Report No. FAA-RD-71-85, II

AD 740514

FAN/COMPRESSOR NOISE RESEARCH

Volume II - Detailed Discussion (II)

M.J. Benzakein R.M. Hochheiser
H.P. Claes S.B. Kazin
W.E. Coward P.R. Knott

Group Engineering Division
Aircraft Engine Group
General Electric Company
Evendale, Ohio

transpo 72
U.S. International Transportation Exposition
Dulles International Airport
Washington, D.C.
May 27-June 4, 1972

DDC
RECEIVED
APR 28 1972
D

March 1972

FINAL REPORT

Reproduced by
NATIONAL TECHNICAL
INFORMATION SERVICE
Springfield, Va. 22151

Availability is unlimited. Document may be released to the National Technical Information Service, Springfield, Virginia 22151, for sale to the public.

Vol. I - 740513

Prepared for

DEPARTMENT OF TRANSPORTATION
FEDERAL AVIATION ADMINISTRATION
Systems Research and Development Service
Washington, D.C. 20591

350

ACCESSION for
NTIS WHITE SECTION
DDC BUFF SECTION
UNANNOUNCED
JUSTIFICATION
DISTRIBUTION/AVAILABILITY CODES
DIST. AVAIL. and/or SPECIAL
A

The contents of this report reflect the views of the General Electric Company, which is responsible for the facts and the accuracy of the data presented herein. The contents do not necessarily reflect the official views or policy of the Department of Transportation. This report does not constitute a standard, specification, or regulation.

TECHNICAL REPORT STANDARD TITLE PAGE

1. Report No.	2. Government Accession No.	3. Recipient's Catalog No.
FAA-RD-71-85, II		

4. Title and Subtitle	5. Report Date
FAN/COMPRESSOR NOISE RESEARCH.VOLUME II - DETAILED DISCUSSION (II)	OCTOBER 1971
	6. Performing Organization Code
7. Author(s)	8. Performing Organization Report No.
M.J.BENZAKEIN, R.M.HOCHHEISER, H.P.CLAES, S.B.KAZIN W.E.COWARD, P.R.KNOTT, W.S.FISK	
9. Performing Organization Name and Address	10. Work Unit No.
GROUP ENGINEERING DIVISION/AIRCRAFT ENGINE GROUP GENERAL ELECTRIC COMPANY/ EVENDALE, OHIO	550-001-01H
	11. Contract or Grant No.
	DOT FA68WA-1960
12. Sponsoring Agency Name and Address	13. Type of Report and Period Covered
FEDERAL AVIATION ADMINISTRATION SYSTEMS RESEARCH AND DEVELOPMENT SERVICE WASHINGTON D.C. 20591	FINAL REPORT JUNE 1968 - OCTOBER 1971
	14. Sponsoring Agency Code

15. Supplementary Notes

Details of illustrations in this document may be better studied on microfiche

16. Abstract

Mechanisms of fan/compressor noise generation, transmission, radiation and propagation were physically defined and mathematically described in terms of functional relationships between acoustic, geometric and aerodynamic parameters. Based on these mechanisms, analytical and semi-empirical predictions of pure tone, broadband and multiple pure tone fan/compressor noise were established in terms of sound power spectra, directivity indices and the resultant sound pressure spectra.

Test data on a variety of fan and compressor vehicles were used to verify the basic prediction techniques and to study the impact of specific design parameters upon fan/compressor noise, including vane-blade spacing, vane and blade numbers, tip speed, blade loading, rotor sweep, inlet guide vanes and vane lean. Effects of refraction on tone directivities were measured and compared with expectations. Propagation of acoustic waves were studied, with specific experiments conducted to investigate ground reflection phase factor and atmospheric absorption at high frequencies.

The prediction systems were summarized in terms of flow charts and tables.

Volumes I and II contain a detailed discussion of the experimentation and analysis. Volumes III and IV are a compilation of the acoustic test data in the form of computer print-out sheets.

17. Key Words		18. Distribution Statement
Acoustics	Multipule pure-tone	Availability is unlimited. Document may be released to the Clearinghouse for Federal Scientific and Technical Information, Springfield, Virginia 22151 for sale to the Public.
Blade-passing noise	Noise	
Broadband noise	Noise prediction	
Compressor noise	Noise reduction	
Fan noise	Discrete-tone noise	

19. Security Classif. (of this report)	20. Security Classif. (of this page)	21. No. of Pages	22. Price
UNCLASSIFIED	UNCLASSIFIED	323	$6/pc $.95/mc

Form DOT F 1700.7 (8-69)

DDC APR 28 1972

ABSTRACT

Mechanisms of fan/compressor noise generation, transmission, radiation and propagation were physically defined and mathematically described in terms of functional relationships between acoustic, geometric and aerodynamic parameters. Based on these mechanisms, analytical and semi-empirical predictions of pure tone, broadband and multiple pure tone fan/compressor noise were established in terms of sound power spectra, directivity indices and the resultant sound pressure spectra.

Test data on a variety of fan and compressor vehicles were used to verify the basic prediction techniques and to study the impact of specific design parameters upon fan/compressor noise, including vane-blade spacing, vane and blade numbers, tip speed, blade loading, rotor sweep, inlet guide vanes and vane lean. Effects of refraction on tone directivities were measured and compared with expectations. Propagation of acoustic waves were studied, with specific experiments conducted to investigate ground reflection phase factor and atmospheric absorption at high frequencies.

The prediction systems were summarized in terms of flow charts and tables.

VOLUME II

TABLE OF CONTENTS

	PAGE
ABSTRACT	II-iii
TABLE OF CONTENTS	II-v
LIST OF ILLUSTRATIONS	II-viii
LIST OF TABLES	II-xxi
VI. EXPERIMENTAL INVESTIGATION OF REFRACTION/PROPAGATION EFFECTS	301
A. Refraction Effects	301
1. Experimental Rig, Test Conducted and Data Analysis	301
2. Results	308
Section VI-A Nomenclature	
B. Experimental Investigation of Propagation Effects	320
1. Reflection Phase Factor	320
2. Atmospheric Absorption	392
VII. SEMI EMPIRICAL FAN NOISE PREDICTION	401
A. Introduction	401
B. Broadband Noise/Multiple Pure Tone Sound Power Levels Generated by IGV Less Fans	403
1. IGV-Less Fans	403
2. IGV Fans	403
3. Frequency Scaling	411
C. Fan Blade Passing Frequency Directivity	417
1. IGV-Less Fans	
2. IGV Fans	417
D. Broadband and Multiple Pure Tone Noise Directivity	423
1. IGV-Less Fan	423
2. IGV Fans	423
3. Frequency Scaling	423
VIII. VERIFICATION OF FAN NOISE PREDICTION METHOD	487
A. Blade Passing Frequency Tones	487

VOLUME II

TABLE OF CONTENTS (Continued)

	PAGE
1. CJ805-23 Fan	487
2. CF700 Fan	487
3. TF39 Fan "Family"	487
4. NASA Two-Stage Fan	510
Section VIII-A References	515
B. Broadband Noise Verification	516
1. LF336 Fans A and B	516
2. Development Vehicle IV	516
C. Verification of Size Parameter	556
Section VIII-C References	561
IX. SEMI EMPIRICAL PREDICTION OF COMPRESSOR NOISE	562
X. VERIFICATION OF COMPRESSOR NOISE PREDICTION METHOD	585
A. Low Speed Single Stage Axial Flow Compressor Pure Tone Levels	585
B. High Speed Multistage Compressor Pure Tone Levels	585
C. Multistage Compressor Directivity Predictions	585
Section X-A References	590
XI. NOISE REDUCTION METHODS	591
A. Results of Analytical Studies	591
1. Rotor-Tip Speed	591
2. Pressure Ratio	594
3. Number of Rotor Blades	594
4. Vane-Blade Number Ratio	594
5. Blade-Vane Spacing	600
6. Vane Lean	600
7. Vane Sweep	603
8. Wake Control	603
9. Inlet Choking	603
Section XI-A References	605

VOLUME II

TABLE OF CONTENTS (Concluded)

		PAGE
	B. Experimental Investigation	606
	1. Rotor Speed	606
	2. Pressure Ratio	606
	3. Vane-Blade Number Ratio	611
	4. Blade-Vane Spacing	611
	5. Swept Rotor	611
	6. Wake Control	615
XII.	SUMMARY AND CONCLUSIONS	635
XIII.	RECOMMENDATIONS	635
XIV.	ACKNOWLEDGEMENT	63[illegible]

VOLUME II

LIST OF ILLUSTRATIONS

Figure		Page
VI-A1	Refraction Test Rig	302
VI-A2	Refraction Test Rig (See Figure VI-A1 for Sketch of Cross Sectional Arrangement)	303
VI-A3	Refraction Rig Nozzle Discharge	304
VI-A4	FAA Refraction Test Ultrasonic Siren Noise Source	305
VI-A5	Refraction Test	306
VI-A6	Predicted Refraction Effects for Conditions of This Test	307
VI-A7	Refraction Test Rig Results 1/3 Octave Band at 20,000 Hz P.R. = 1.2	311
VI-A8	Refraction Test Rig REsults 10 Hz Narrowband at 20,600 Hz P.R. = 1.2	312
VI-A9	ΔdB Relative to Siren Alone Without Flow	314
VI-A10	Calculated Refracted Noise Assuming No Internal Reflection and No Turbulence Scattering	316
VI-A11	Effect of Sound on Far Field Level and Directivity Index	318
VI-B1	Test Set Up to Investigate the Effect of Path Length Differential on Phase Facotr - Configuration A	322
VI-B2	Test Set Up to Investigate the Effects of Incidence Angle on Phase Factor - Configuration B	323
VI-B3 to VI-B41	(Typical Measurement) SPL vs. Frequency - Ground Reflection Tests	325-363
VI-B42	Observed Phase Factor for Dry Concrete and Dry Gravel (Horizontal Distance to Source 50' - Microphone Height 12')	364
VI-B43	Observed Phase Factor for Dry Concrete and Dry Gravel (Horizontal Distance to Source 50' - Microhpone Height 18')	365
VI-B44	Observed Phase Factor for Dry Concrete and Dry Gravel (Horizontal Distance to Source 50' - Microphone Height 24')	366
VI-B45	Observed Phase Factor for Dry Concrete and Dry Gravel (Horizontal Distance to Source 50' - Microphone Height 18')	367

LIST OF ILLUSTRATIONS (Continued)

Figure		Page
VI-B46	Observed Phase Factor for Dry Concrete and Dry Gravel (Horizontal Distance to Source 80' - Microphone Height 24')	368
VI-B47	Effect of Phase Factor of Wetting Concrete Surface (Distance from Source 50' - Microphone Height 12' Configuration A)	371
VI-B48	Effect on Phase Factor of Wetting Concrete Surface (Distance from Source 65' - Microphone Height 18')	372
VI-B49	Effect on Phase Factor of Wetting Concrete Surface (Distance from Source 80' - Microphone Height 24')	373
VI-B50	Effect on Phase Factor of Wetting Concrete Surface (Distance from Source 50' -Microphone Height 12' Configuration B)	374
VI-B51	Effect on Phase Factor of Wetting Concrete Surface (Distance from Source 50' - Microphone Height 18')	375
VI-B52	Effect on Phase Factor of Wetting Concrete Surface (Distance from Source 50' - Microphone Height 24')	376
VI-B53	Effect on Phase Factor of Wetting Gravel Surface (Distance from Source 50' - Microphone Height 12')	377
VI-B54	Effect of Phase Factor of Wetting Gravel Surface (Distance from Source 65' - Microphone Height 18')	378
VI-B55	Effect on Phase Factor of Wetting Gravel Surface (Distance from Source 80' - Microphone Height 24')	379
VI-B56	Effect of Absorbent Pad on Reflected Signal ((Distance from Speaker 50' - Microphone Height 12')	381
VI-B57	Effect of Absorbent Pad on Reflected Signal (Distance from Speaker 65' - Microphone Height 18')	382
VI-B58	Effect of Absorbent Pad on Reflected Signal (Distance from Speaker 80' - Microphone Height 24')	383
VI-B59	Effect of Absorbent Pad on Phase Factor (Horizontal Distance from Speaker 50' - Microphone Height 12')	384
VI-B60	Effect of Absorbent Pad on Phase Factor (Horizontal Distance from Speaker 65' - Microphone Height 18')	385
VI-B61	Effect of Absorbent Pad on Phase Factor (Horizontal Distance from Speaker 80' - Microphone Height 24')	386
VI-B62	Variation of Phase Factor with Incidence Angle (Dry Concrete)	387

VOLUME II

LIST OF ILLUSTRATIONS (Continued)

Figure		Page
VI-B63	Variation of Phase Factor with Incidence Angle (Dry Gravel)	388
VI-B64	Phase Factor as a Function of Angle of Incidence for Gravel	389
VI-B65	Variation of Phase Factor with Path Length Difference (Dry Concrete)	390
VI-B66	Variation of Phase Factor with Path Length Difference (Dry Gravel)	391
VI-B67	Comparison of Spectra Corrected for Ground Absorption and Reflection, Inverse Square Law Decay and Atmospheric Absorption. Polar Angle = 60°	393
VI-B68	Comparison of Spectra Corrected for Ground Absorption and Reflection, Inverse Square Law Decay and Atmospheric Absorption. Polar Angle = 80°	394
VI-B69	Comparison of Spectra Corrected for Ground Absorption and Reflection, Inverse Square Law Decay, and Atmospheric Absorption. Polar Angle = 100°	395
VI-B70	Comparison of Spectra Corrected for Ground Absorption and Reflection, Inverse Square Law Decay, and Atmospheric Absorption. Polar Angle = 120°	396
VI-B71	High Frequency Atmospheric Absorption Test Set-Up	399
VI-B72	Atmospheric Absorption for High Frequency	400
VII-B1	Normalized Power Levels Versus M_R (GE D/V I) for a Number of fD's	405
VII-B2	Normalized Power Levels Versus M_R (GE D/V I) for a Number of fD's	406
VII-B3	Normalized Power Levels Versus M_R (Ge D/V I) for a Number of fD's	407
VII-B4	Broadband Noise/MPT Sound Power Level Trends with Mach Number	408
VII-B5	Broadband Noise/MPT Sound Power Level Trends with Mach Number	409
VII-B6	Broadband Noise/MPT Sound Power Level Trends with Mach Number	410

VOLUME II

LIST OF ILLUSTRATIONS (Continued)

Figure		Page
VII-B7	Normalized Power Levels Versus M_R (GE D/V III) for a Number of fD's	414
VII-B8	Normalized Power Levels Versus M_R (GE D/V III) for a Number of fD's	415
VII-B9	Normalized Power Levels Versus M_R (GE D/V III for a Number of fD's	416
VII-C1	Comparison of D/V I Measured and Calculated Directivity Indices for Rotor Tip Speeds of Mach 0.860 and 1.179	421
VII-C2	Fan Blade Passing Frequency Directivity Index for GE D/V III	422
VII-D1	Broadband Noise Directivity Index (GE D/V I) for fD = 1.118×10^5 in/sec.	431
VII-D2	Broadband Noise Directivity Index (GE D/V I) for fD = 1.42×10^5 in/sec.	432
VII-D3	Broadband Noise Directivity Index (GE D/V I) for fD = 1.775×10^5 in/sec.	433
VII-D4	Broadband Noise Directivity Index (GE D/V I) for fD = 2.237×10^5 in/sec.	434
VII-D5	Broadband Noise Directivity Index (GE D/V I for fD = 2.84×10^5 in/sec .	435
VII-D6	Broadband Noise Directivity Index (GE D/V I) for fD = 3.55×10^5 in/sec.	436
VII-D7	Broadband Noise Directivity Index (GE D/V I) for fD = 1.42×10^4 in/sec.	437
VII-D8	Broadband Noise Directivity Index (GE D/V I) for fD = 1.775×10^4 in/sec.	438
VII-D9	Broadband Noise Directivity Index (GE D/V I) for fD 2.237×10^4 in/sec.	439
VII-D10	Broadband Noise Directivity Index (GE D/V I) for fD = 2.84×10^4 in/sec.	440
VII-D11	Broadband Noise Directivity Index (GE D/V I) for fD = 3.55×10^4 in/sec.	441

VOLUME II

LIST OF ILLUSTRATIONS (Continued)

Figure		Page
VII-D12	Broadband Noise Directivity Index (GE D/V I) for fD = 4.44 x 10^4 in/sec.	442
VII-D13	Broadband Noise Directivity Index (GE D/V I) for fD = 5.68 x 10^4 in/sec.	443
VII-D14	Broadband Noise Directivity Index (GE D/V I) for fD = 7.1 x 10^4 in/sec.	444
VII-D15	Broadband Noise Directivity Index (GE D/V I) for fD = 8.88 x 10^4 in/sec.	445
VII-D16	MPT Noise Directivity Index (GE D/V I) M_T = 1.057	446
VII-D17	MPT Noise Directivity Index (GE D/V I) M_T = 1.057	447
VII-D18	MPT Noise Directivity Index (GE D/V I) M_T = 1.057	448
VII-D19	MPT Noise Directivity Index (GE D/V I) M_T = 1.170	449
VII-D20	MPT Noise Directivity Index (GE D/V I) M_T = 1.170	450
VII-D21	MPT Noise Directivity Index (GE D/V I) M_T = 1.170	451
VII-D22	MPT Noise Directivity Index GE D/V I) M_T = 1 '97	452
VII-D23	MPT Noise Directivity Index (GE D/V I) M_T = 1.197	453
VII-D24	MPT Noise Directivity Index (GE D/V I) M_T = 1.197	454
VII-D25	Broadband Noise Index (GE D/V III) fD = 1.42 x 10^4 in/sec.	464
VII-D26	Broadband Noise Index (GE D/V III) fD = 1.775 x 10^4 in/sec.	465
VII-D27	Broadband Noise Directivity Index (GE D/V III) fD = 2.24 x 10^4 in/sec.	466
VII-D28	Broadband Noise Directivity Index (GE D/V III) fD = 2.84 x 10^4 in/sec.	467
VII-D29	Broadband Noise Directivity Index (GE D/V III) fD = 3.55 x 10^4 in/sec.	468
VII-D30	Broadband Noise Directivity Index (GE D/V III0 fD = 4.44 x 10^4 in/sec.	469

VOLUME II

LIST OF ILLUSTRATIONS (Continued)

Figure		Page
VII-D31	Broadband Noise Directivity Index (GE D/V III) fD = 5.68 x 10^4 in/sec.	470
VII-D32	Broadband Noise Directivity Index (GE D/V III) fD = 7.10 x 10^4 in/sec.	471
VII-D33	Broadband Noise Directivity Index (GE D/V III) fD = 8.88 x 10^4 in/sec.	472
VII-D34	Broadband Noise Directivity Index (GE D/V III) fD = 11.20 x 10^4 in/sec.	473
VII-D35	Broadband Noise Directivity Index (GE D/V III) fD = 1.42 x 10^4 in/sec.	474
VII-D36	Broadband Noise Directivity Index (GE D/VIII) fD = 17.75 x 10^4 in/sec.	475
VII-D37	Broadband Noise Directivity Index (GE D/V III) fD = 22.4 x 10^4 in/sec.	476
VII-D38	Broadband Noise Directivity Index (GE-D/V III) fD = 28.4 x 10^4 in/sec.	477
VII-D39	Broadband Noise Directivity Index (GE-D/V III) fD = 35.5 x 10^4 in/sec.	478
VII-D40	MPT Directivity Index (GE D/V III)	479
VII-D41	MPT Directivity Index (GE D/V III)	480
VII- 42	MPT Directivity Index (GE D/V III)	481
VII-D43	MPT Directivity Index (GE D/V III)	482
VII-D44	MPT Directivity Index (GE D/V III)	483
VII-D45	MPT Directivity Index (GE D/V III)	484
VIII-A1	Cutaway View CJ805-23 Aft Turbofan	490
VIII-A2	Standard CJ805-23 On Test	491
VIII-A3	Fundamental PWL - CJ805-23 Predicted and Measured	492
VIII-A4	CJ-805 Second Harmonic Power Levels	493

VOLUME II

LIST OF ILLUSTRATIONS (Continued)

Figure		Page
VIII-A5	CF700 Engine on Edwards Test Stand	494
VIII-A6	CF700 Fundamental Power Level	495
VIII-A7	Full Scale TF39 Engine	496
VIII-A8	TF39 Fan Configuration	497
VIII-A9	TF39 Development Vehicle	498
VIII-A10	Freon Compressor TF39 Scale Model Hardware	499
VIII-A11	TF39 First Stage Fundamental PWL's	500
VIII-A12	TF39 Second Stage Fundamental PWL's	501
VIII-A13	TF39 Second Stage 2nd Harmonic PWL's	502
VIII-A14	TF39 D/V First Stage Fundamental PWL's	503
VIII-A15	TF39 D/V Second Stage Fundamental PWLS's	504
VIII-A16	TF39 D/V Second Stage 2nd Harmonic PWL's	505
VIII-A17	TF39 O/P Test Rig Fundamental PWL	506
VIII-A18	TF39 Outer Panel Rig 2nd Harmonic PWL	507
VIII-A19	TF39 O/P Freon Model Fundamental PWL	508
VIII-A20	TF39 O/P Freon Model 2nd Harmonic PWL	509
VIII-A21	NASA Two Stage Fan Engine	512
VIII-A22	NASA Two-Stage Fan Configuration	513
VIII-A23	Two Stage Fan 2nd Stage Fundamental Power Levels	514
VIII-B1	LF336 Tests Front View	517
VIII-B2	LF336 Tests Rear View	518
VIII-B3	LF336 Broadband Noise Power Level Spectrum N = 5140 RPM	519
VIII-B4	LF336 Broadband Noise Sound Pressure Level Spectrum N = 5140, θ = 40°	520
VIII-B5	LF336 Broadband Noise Sound Pressure Level Spectrum N = 5140 RPM, θ= 80°	521

VOLUME II

LIST OF ILLUSTRATIONS (Continued)

Figure		Page
VIII-B6	LF336 Broadband Noise Sound Pressure Level Spectrum N = 5140 RPM, θ = 120°	522
VIII-B7	LF336 Broadband Noise Power Level Spectrum N = 5442 RPM	523
VIII-B8	LF336 Broadband Noise Sound Pressure Level Spectrum N = 5442 RPM, θ = 40°	524
VIII-B9	LF336 Broadband Noise Sound Pressure Level Spectrum N = 5442 RPM, θ = 80°	525
VIII-B10	LF336 Broadband Noise Sound Pressure Level Spectrum N = 5442 RPM, θ = 120°	526
VIII-B11	LF336 Broadband Noise Power Level Spectrum N = 5700 RPM	527
VIII-B12	LF336 Broadband Noise Sound Pressure Level Spectrum N = 5700 RPM, θ = 40°	528
VIII-B13	LF336 Broadband Noise Sound Pressure Level Spectrum N = 5700 RPM, θ = 80°	529
VIII-B14	LF336 Broadband Noise Sound Pressure Level Spectrum N = 5700 RPM, θ = 120°	530
VIII-B15	LF336 Broadband Noise Power Level Spectrum N = 6047	531
VIII-B16	LF336 Broadband Noise Sound Pressure Level Spectrum N = 6000 RPM, θ = 40°	532
VIII-B17	LF336 Broadband Noise Sound Pressure Level Spectrum N = 6000 RPM, θ = 80°	533
VIII-B18	LF336 Broadband Noise Sound Pressure Level Spectrum N = 6000 RPM, θ = 120°	534
VIII-B19	GE D/V IV Broadband Noise Power Level Spectrum N = 5510 RPM	535
VIII-B20	GE D/V IV Broadband Noise Sound Pressure Level Spectrum N = 5510 RPM, θ = 40°	536
VIII-B21	GE D/V IV Broadband Noise Sound Pressure Level Spectrum N = 5510 RPM, θ = 80°	537

LIST OF ILLUSTRATIONS (Continued)

Figure		Page
VIII-B22	GE D/V IV Broadband Noise Sound Pressure Level Spectrum N = 5510 RPM, θ = 120°	538
VIII-B23	GE D/V IV Broadband Noise Power Level Spectrum N = 5970 RPM	539
VIII-B24	GE D/V IV Broadband Noise Sound Pressure Level Spectrum N = 5970 RPM, θ = 20°	540
VIII-B25	GE D/V IV Broadband Noise Sound Pressure Level Spectrum N = 5970 RPM, θ = 80°	541
VIII-B26	GE D/V IV Broadband Noise Sound Pressure Level Spectrum N = 5970 RPM, θ = 120°	542
VIII-B27	GE D/V IV Broadband Noise Power Level Spectrum N = 6350 RPM	543
VIII-B28	GE D/V IV Broadband Noise Sound Pressure Level Spectrum N = 6350 RPM, θ = 20°	544
VIII-B29	GE D/V IV Broadband Noise Sound Pressure Level Spectrum N = 6350 RPM, θ = 80°	545
VIII-B30	GE D/V IV Broadband Noise Sound Pressure Level Spectrum N = 6350 RPM, θ = 120°	546
VIII-B31	GE D/V IV Broadband Noise Power Level Spectrum N = 6525 RPM	547
VIII-B32	GE D/V IV Broadband Noise Sound Pressure Level Spectrum N = 6525 RPM, θ = 20°	548
VIII-B33	GE D/V IV Broadband Noise Sound Pressure Level Spectrum N = 6525 RPM, θ = 80°	549
VIII-B34	GE D/V IV Broadband Noise Sound Pressure Level Spectrum N = 6525, θ = 120°	550
VIII-B35	GE D/V IV Broadband Noise Power Level Spectrum N = 6850	551
VIII-B36	GE D/V IV Broadband Noise Sound Pressure Level Spectrum N = 6850 RPM, θ = 20°	552
VIII-B37	GE D/V IV Broadband Noise Sound Pressure Level Spectrum N = 6850 RPM, θ = 80°	553

VOLUME II

LIST OF ILLUSTRATIONS (Continued)

Figure		Page
VIII-B38	GE D/V IV Broadband Noise Sound Pressure Level Spectrum N = 6850 RPM, θ = 120°	554
VIII-C1	Fundamental PWL - CJ805-23 and CF700 Scaled to CJ805-23 Size	558
VIII-C2	Fundamental PWL - TF39 Test Vehicles Scaled to Full Size TF39	559
VIII-C3	Second Harmonic PWL - TF39 Test Vehicles scaled to Full Size TF39	560
IX-A1	Normalized Power Levels Versus M_R for Various 1/3 Octave Band Center Frequencies	564
IX-A2	Normalized Power Levels Versus M_R for Various 1/3 Octave Band Center Frequencies	565
IX-A3	Directivity Index Versus Angular Position for M_R = .35	573
IX-A4	Directivity Index Versus Angular Position for M_R = .35	574
IX-A5	Directivity Index Versus Angular Position for M_R = .48	575
IX-A6	Directivity Index Versus Angular Position for M_R = .48	576
IX-A7	Directivity Index Versus Angular Position for M_R = .61	577
IX-A8	Directivity Index Versus Angular Position for M_R = .61	578
IX-A9	Directivity Index Versus Angular Position for M_R = .95	579
IX-A10	Directivity Index Versus Angular Position for M_R = .95	580
IX-A11	Directivity Index Versus Angular Position for M_R = 1.09	581
IX-A12	Directivity Index Versus Angular Position for M_R = 1.09	582

LIST OF ILLUSTRATIONS (Continued)

Figure		Page
IX-A13	Reference Blade Passing Frequency Versus Tip Relative Mach Number	583
X-A1	Comparison of Measured and Calculated Sound Power Levels for NASA 14.75 Inch Diameter Compressor	586
X-B1	Fundamental PWL - Stage One J79 Compressor	587
X-B2	Fundamental PWL - Stage One GE4 Compressor	588
X-C1	Comparison of Predicted and Measured SPL's for Fundamental Tone of J93 Compressor First Stage	589
XI-A1	Effect of Tip Speed on Rotor Alone Pure Tone Noise for a Typical Fan	592
XI-A2	Effect of Tip Speed on Wake Interaction Pure Tone Noise for a Typical Fan	593
XI-A3	Effect of Pressure Ratio on Rotor Alone Pure Tone Noise for a Typical Fan	595
XI-A4	Effect of Pressure Ratio on Wake Interaction Pure Tone Noise for a Typical Fan	596
XI-A5	Effect of Rotor Blade Numbers on Rotor Alone Pure Tone Noise for a Typical Fan	597
XI-A6	Effect of Rotor Blade Numbers on Wake Interaction Pure Tone Noise for a Typical Fan	598
XI-A7	Effect of Vane/Blade Ratio on Wake Interaction Pure Tone Noise for a Typical Fan	599
XI-A8	Effect of Axial Vane-Blade Spacing on Wake Interaction Pure Tone Noise for a Typical Fan	601
XI-A9	Blade Passing Frequency Noise Reduction with Stator Lean for a Typical Fan	602
XI-A10	Blade Passing Frequency Noise Reduction with Stator Sweep for a Typical Fan	604
XI-B1	Broadband Noise from CJ805-23 Fan	607

VOLUME II

LIST OF ILLUSTRATIONS (Continued)

Figure		Page
XI-B2	TF39 D/V Fan Broadband Fan	608
XI-B3	Fundamental PWL's vs. Fan Tip Speed Two Stage Experimental Fan	609
XI-B4	Isonoise Map - Fundamental PWL (Second Stage) Two Stage Experimental Fan	610
XI-B5	Effect of Variation of IGV-Rotor Spacing on Fundamental PWL - TF39 D/V	612
XI-B6	Variation of Fundamental PWL with OGV Spacing (100% Design Speed)	613
XI-B7	Swept Rotor Tests - Comparison of Configurations	614
XI-B8	Fundamental PWL vs. Percent Speed: Swept Rotor vs. Non-Swept Rotor	616
XI-B9	15 Inch Laboratory Compressor Wake Injection Tests	617
XI-B10	Wake Traverse - .6" Immersion	619
XI B11	Wake Traverse - 1.0" Immersion	620
XI-B12	Wake Traverse = 1.8" Immersion	621
XI-B13	Wake Traverse - 2.4" Immersion	622
XI-B14	50 Hz Bandwidth Spectral Comparison Compressor W/O Rods vs. Compressor with 8 IGV Rods	623
XI-B15	50 Hz Bandwidth Spectral Comparison Compressor with 8 IGV Rods vs. 2.9% Flow Rate Wake Injection Noise	624
XI-B16	50 Hz Bandwidth Spectral Comparison Compressor with 8 IGV Rods vs. 4.0% Flow Rate Wake Injection Noise	625
XI-B17	50 Hz Bandwidth Spectral Comparison Compressor with Rods and No Wake Injection vs. Compressor with Rods and 2.9% Wake Injection Flow	626
XI-B18	50 Hz Bandwidth Spectral Comparison Compressor with Rods and No Wake Injection vs. Compressor with Rods and 4.0% Wake Injection Flow	627

LIST OF ILLUSTRATIONS (Concluded)

Figure		Page
XI-B19	Pure Tone Suppression vs. Injection Angle - Fundamental Tone 2.9% Flow Rate	628
XI-B20	Pure Tone Suppression vs. Injection Angle - Second Harmonic Tone 2.9% Flow Rate	629
XI-B21	Pure Tone Suppression vs. Injection Angle - Third Harmonic Tone 2.9% Flow Rate	630
XI-B22	Measured Reductions in Pure Tone Sound Power Level with Wake Injection	632

VOLUME II

LIST OF TABLES

TABLE NO.		PAGE
VI-A1	10 Hz Narrowband Sound Pressure Level, 20,600 Hz (dB) Refraction Test Rig	309
VI-A2	One-Third Octave Band Sound Pressure Level, 20,600 Hz (dB) Refraction Test Rig	310
VII-B1	IGV Less Fans - Broadband Noise/Multiple Pure Tone Prediction - Polynomial Coefficient	404
VII-B2	IGV Fans - Broadband Noise/Multiple Pure Tone Prediction - Polynomial Coefficients	413
VII-C1	IGV Less Vehicles - Coefficients for Polar Angles 20° - 0 - 80°	418
VII-C2	IGV Less Vehicles - Coefficients for Polar Angles 90° - 0 - 160°	419
VII-C3	IGV Vehicles - Coefficients for Polar Angles 20° - 0 160°	420
VII-D1	IGV Less Fans - Directivity Correlation Coefficients M_R = .76	425
VII-D2	IGV Less Fans - Directivity Correlation Coefficients M_R = .872	425
VII-D3	IGV Less Fans - Directivity Correlation Coefficients M_R = .939	427
VII-D4	IGV Less Fans - Directivity Correlation Coefficients M_R = 1.0	428
VII-D5	IGV Less Fans - Directivity Correlation Coefficients M_R = 1.046	429
VII-D6	IGV Less Fans - Directivity Correlation Coefficients M_R = 1.141	430
VII-D7	IGV Less Fans - Directivity Correlation Coefficients M_R = 1.201	455
VII-D8	IGV Less Fans - Directivity Correlation Coefficients M_R = 1.266	456

VOLUME II

LIST OF TABLES (Continued)

TABLE NO.		PAGE
VII-D9	IGV Less Fans - Directivity Correlation Coefficients $M_R = 1.296$	457
VII-D10	IGV Fans - Directivity Correlation Coefficients $M_R = .637$	458
VII-D11	IGV Fans - Directivity Correlation Coefficients $M_R = .712$	459
VII-D12	IGV Fans - Directivity Correlation Coefficients $M_R = .855$	460
VII-D13	IGV Fans - Directivity Correlation Coefficients $M_R = 1.020$	461
VII-D14	IGV Fans - Directivity Correlation Coefficients $M_R = 1.082$	462
VII-D15	IGV Fans - Directivity Correlation Coefficients $M_R = 1.180$	463
VIII-A1	Fan Design Parameters CJ805-23 and CF700	488
VIII-A2	Fan Design Parameters TF39 Family	489
VIII-A3	NASA Two Stage Fan Design Parameters	511
IX-A1	Coefficient Table for Compressor Noise Power Level Prediction	563
IX-A2	Coefficient Table for Compressor Directivity Indices $M_r = 0.35$	568
IX-A3	Coefficient Table for Compressor Directivity Indices $M_r = 0.48$	569
IX-A4	Coefficient Table for Compressor Directivity Indices $M_r = 0.61$	570
IX-A5	Coefficient Table for Compressor Directivity Indices $M_r = 0.95$	571
IX-A6	Coefficient Table for Compressor Directivity Indices $M_r = 1.09$	572

VI. EXPERIMENTAL INVESTIGATION OF REFRACTION/PROPAGATION EFFECTS

(A) Refraction Effects. An experiment was conducted as part of this program in order to explore the validity of the effects predicted in Section III-C, namely:

- Is sound refracted outward from the jet axis as a result of the velocity and elevated temperature of the airstream containing the sound?

- Can this trend be reversed by using a hot shroud of air around the sound source so that, rather than an increase, a reduction in the maximum sideline noise is attainable?

(1) Experimental Rig, Tests Conducted, and Data Analysis. The experimental rig is shown by the sketch in Figure VI-A1 and the photograph in Figure VI-A2; the nozzle discharge is shown by the photograph in Figure VI-A3. It consisted of a pipe, terminated with a conical nozzle enclosed by a larger concentric pipe also with a conical nozzle, arranged so that the two nozzle exhausts were concentric and co-planar. The inside diameters of the two nozzles are shown on the sketch, the outer one being slightly more than 8" and the inner one being less than 6", so that the annular width between the two was about 1-1/4". This annular thickness is large relative to the wave length of the siren tone, so acoustic ray analysis is applicable.

Air was supplied to the outer pipe; a burner was included upstream so that the shroud air could be heated. A high frequency (20,600 Hz) siren was used to introduce a high intensity tone into the inner pipe. The siren was located as shown in Figures VI-A1 and VI-A2. The siren was contained in a box chamber as shown in Figure VI-A4. A microphone was included inside the box so that the tone frequency and sound pressure level in the box could be set by appropriate regulation of the air supply to the siren motor and to the siren disc plenum. The sound pressure level of the one-third octave band containing the tone was controlled within $\pm$ 1 dB for all tests. The rig was assembled outdoors over a concrete and gravel field (see background of Figure VI-A2) with nine microphones on a circular arc of 20 ft. radius from the center of the nozzle discharge plane. These microphones were in fixed positions shown by the diagram in Figure VI-A5 . Eight microphones were placed at 10° increments between 20° and 90° from the jet axis, the ninth being placed at 25°. The jet efflux precluded reliable measurements any nearer to the jet axis, although this would have been desirable to detect any channeling of sound which might have occurred within the shroud jet. During each run, noise measurements were made at each far field microphone and in the siren box; since the sound level of the one-third octave band containing the siren tone was controlled in the box within $\pm$ 1 dB, any larger change in the far field microphone level was caused by the refraction/reflection effects of the shroud air flow.

After measuring the siren noise level in the far field without air flow, the shroud air Mach number was fixed by setting the nozzle pressure ratio at 1.20, and measurements were made at all positions for shroud air temperatures of 520°R, 960°R, 1460°R and 1960°R. The theoretical angle, θ_R, of complete internal reflection under these test conditions is shown in Figure VI-A6, calculated from

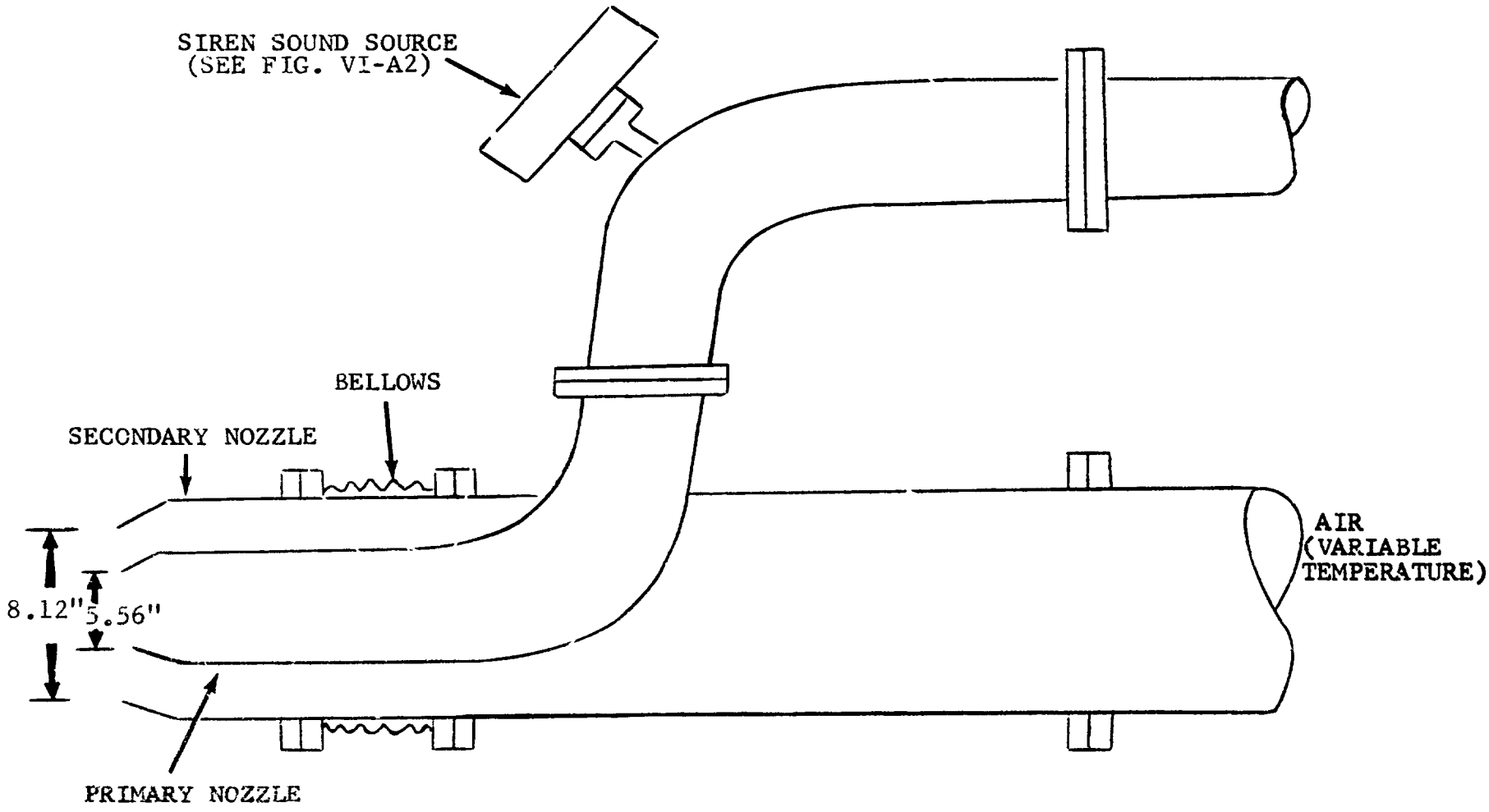

FIGURE VI-A1 REFRACTION TEST RIG

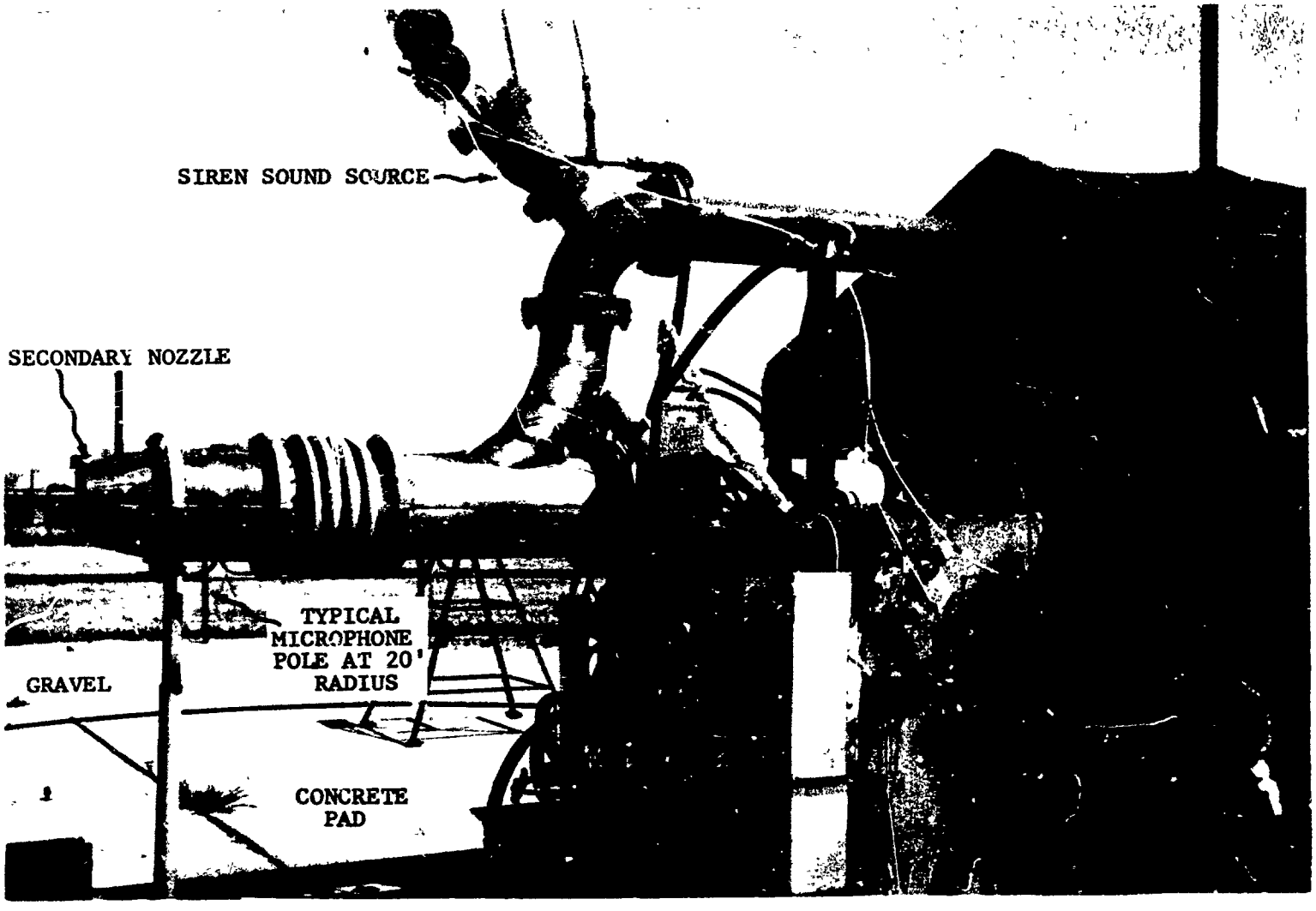

FIGURE VI-A2 REFRACTION TEST RIG (SEE FIG.VI-A1 FOR SKETCH OF CROSS SECTIONAL ARRANGEMENT)

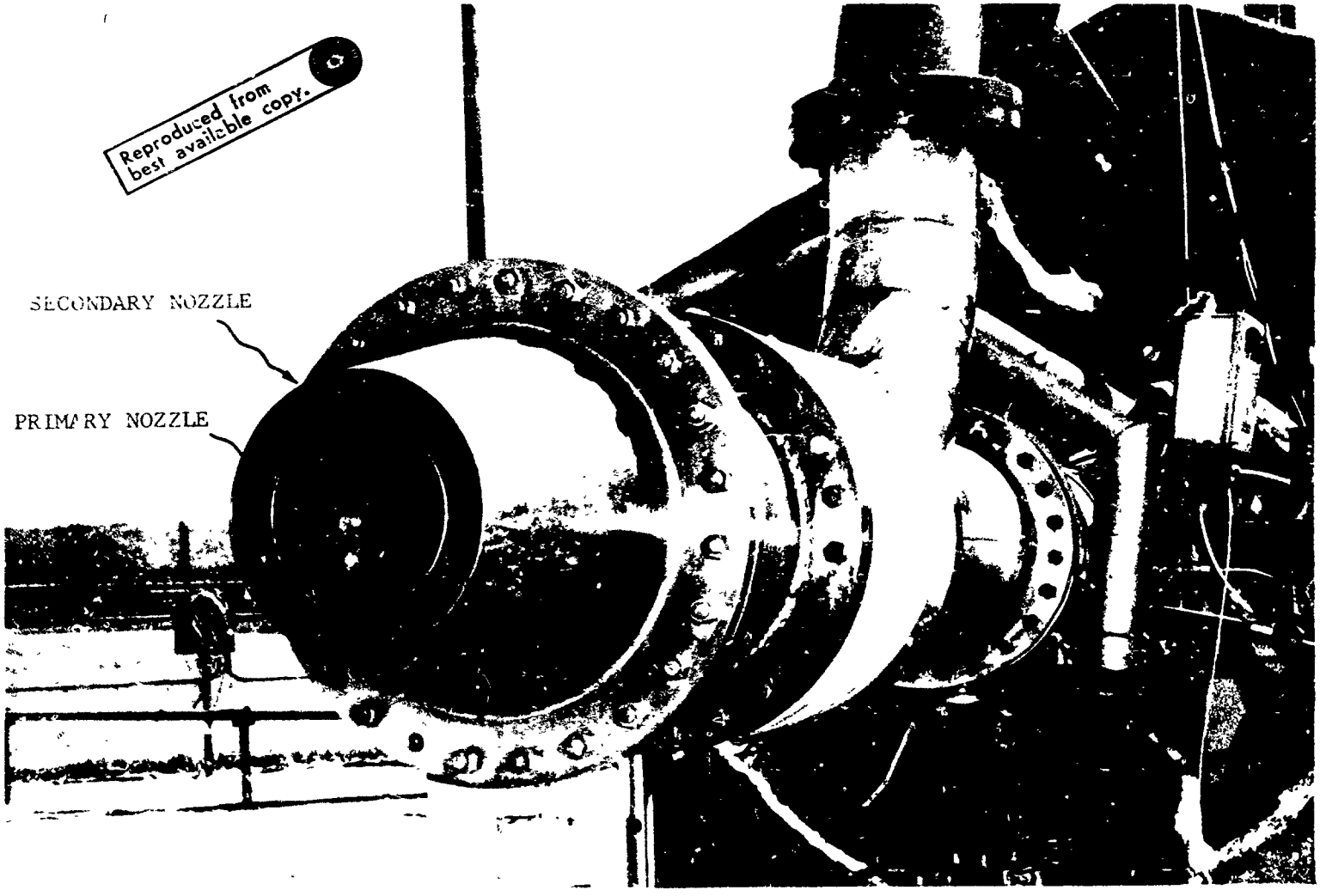

Reproduced from best available copy.

FIGURE VI-A3 REFRACTION RIG NOZZLE DISCHARGE

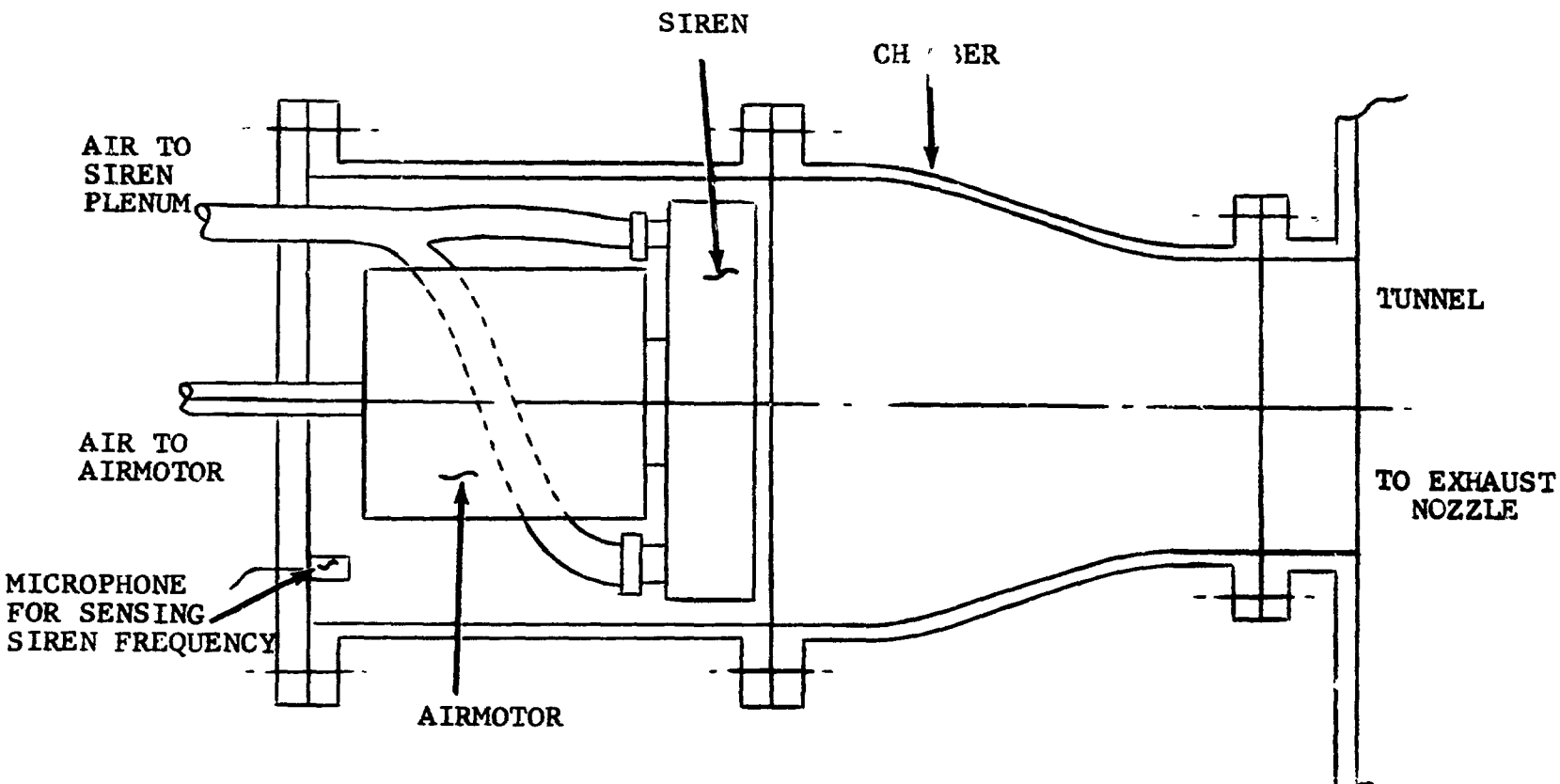

FIGURE VI-A4 FAA REFRACTION TEST ULTRASONIC SIREN NOISE SOURCE

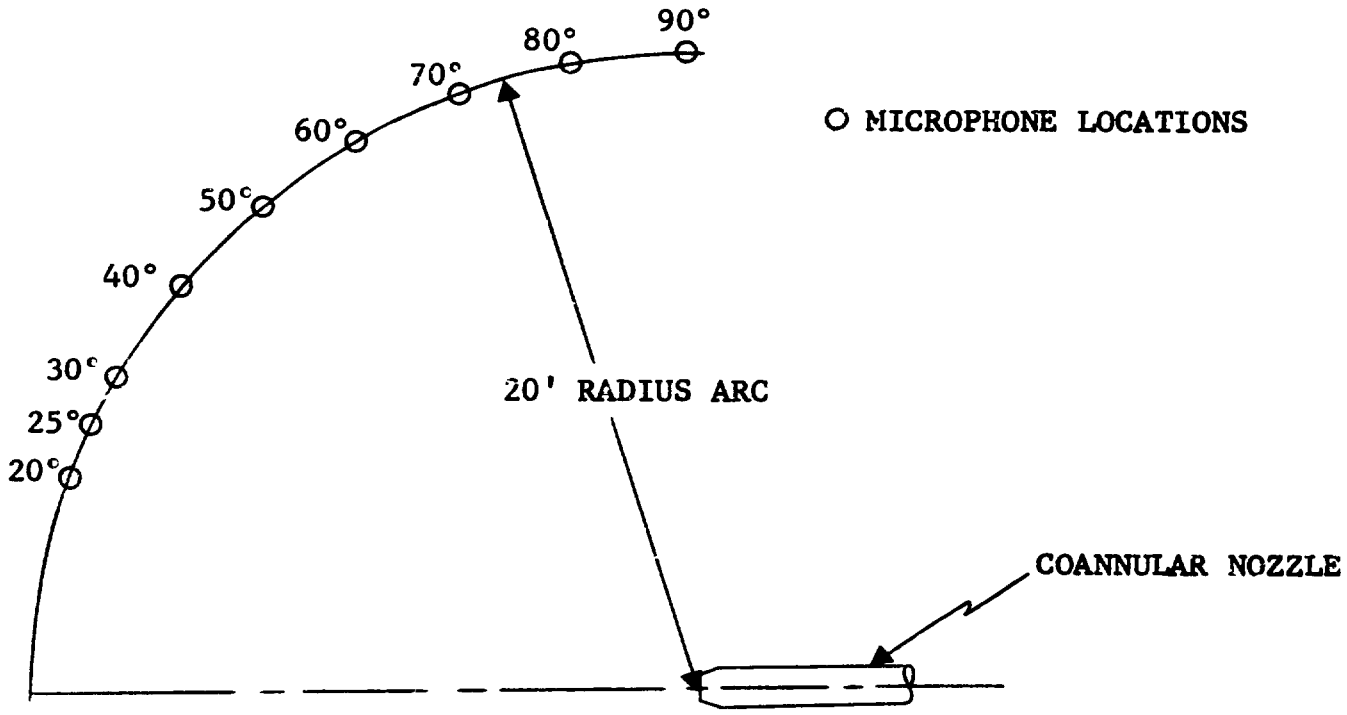

FIGURE VI-A5 REFRACTION TEST

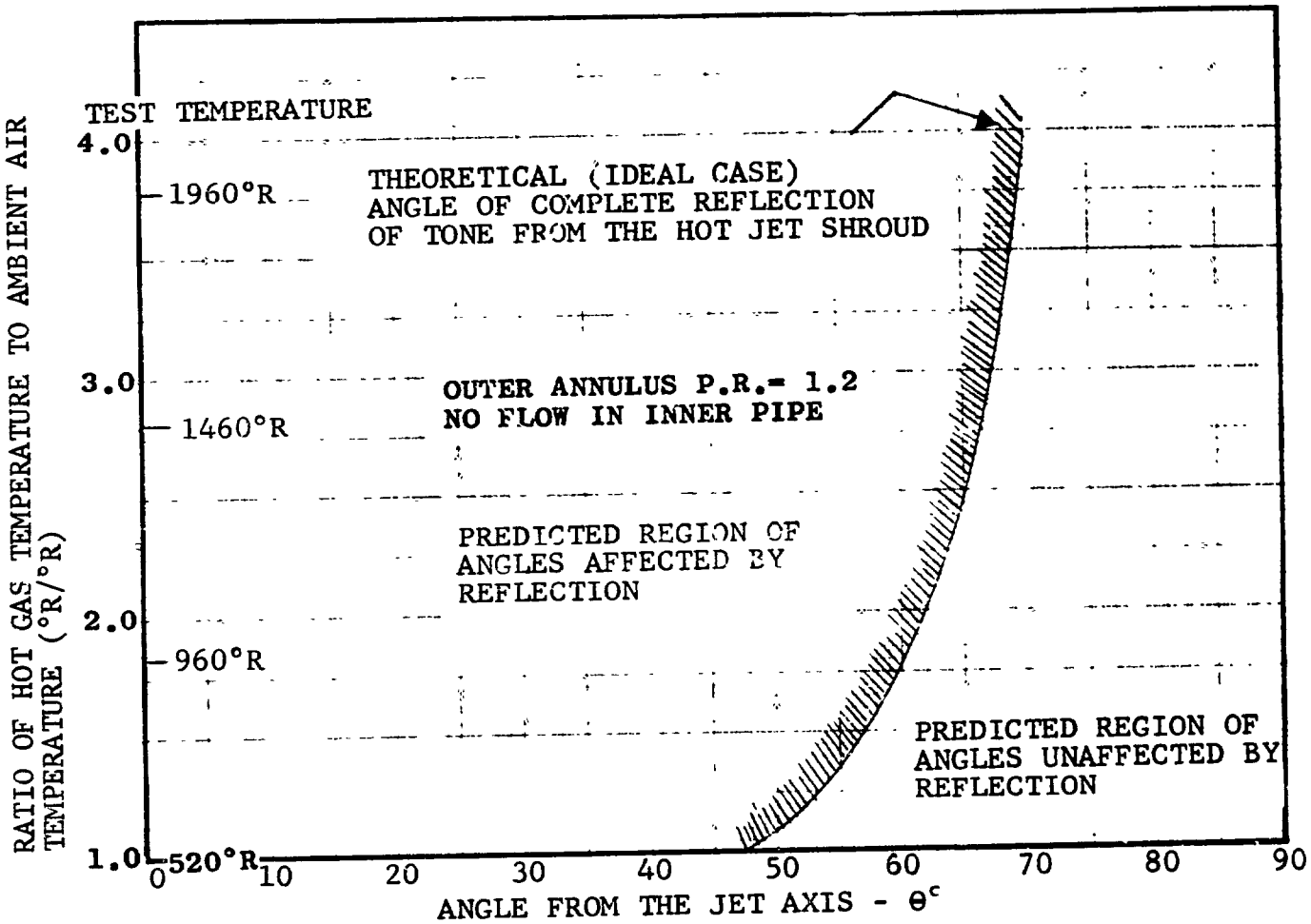

FIGURE VI-A6 PREDICTED REFRACTION EFFECTS FOR CONDITIONS OF THIS TEST

$$\theta_c = \sin^{-1}\left[\frac{C_o}{C_2 + V_2}\right]$$

C_2, V_2 = Shroud sonic velocity and convection velocity, respectively

C_o = Ambient sonic velocity

The figure shows that at ambient temperature of the shroud, only the angles of 50° or less from the jet axis are expected to be affected. At 960°R the critical angle moves to 60°. Finally, at 1960°R, it moves to 70°. Noise originally at angles less than the critical angle is expected to be captured in the shroud.

Data reduction included both narrowband (10 Hz bandwidth) and one-third octave band analyses for the frequency band containing the 20,600 Hz signal. Both kinds of data are required because the noise spike generated by the siren was not only affected by refraction (reflection) but also by modulation introduced by the turbulence in the jet mixing zone. This modulation caused scattering of the sound energy into adjacent frequencies within the one-third octave band limits (18,000 to 22,400)Hz. The siren noise spike was sufficiently near the midpoint frequency so that, as revealed by the narrowband data, the scattered energy remained within the one-third octave band limits. The siren noise spike as measured in the siren box contained sideband noise at 20,600 ± 1550 Hz because of modulation associated with the siren disc rotational frequency. Except for the sideband noise spikes, which were generally 10 dB below the primary siren spike, the signal-to-noise ratio of the siren spike was more than 15 dB, generally being 20 dB.

(2) Results. The narrowband results are given in Table VI-A1 and the one-third octave band, in Table VI-A2. Graphical presentation of these same data is given in Figures VI-A7 and VI-A8. In the tables and in the graphs, the measured far-field sound pressure levels are shown.

(a) For the siren alone - This gives the levels at each microphone without any flow effects. These are the datum levels used in Figures VI-A7 and VI-A8.

(b) For the shroud air flow alone - This shows how much of the noise was introduced by the jet.

(c) For the siren with the shroud air flow - This shows the combined siren and jet noise.

Data for each far field angle measured from the jet axis, are given for each of the four shroud air temperatures. In the two figures, the arrows indicate the changes in far field levels induced by the shroud air flow, and the bars indicate the jet noise contribution. The jet noise shows an increase with shroud air temperature because, with constant Mach number (fixed by nozzle pressure ratio the velocity increases with temperature.

Microphone Location	Siren Alone	Shroud Air Temperature (P.R. = 1.20							
		550°R		960°R		1460°R		1960°R	
		Jet Alone	Jet + Siren	Jet Alone	Jet + Siren	Jet Alone	Jet + Siren	Jet Alone	Jet + Siren
20+	77	42.5	55	47.5	50.5	53.5	53	57	53.5*
25	70	39	44	52	52*	53	52*	57.5	56*
30	66	39.5	48	44.5	45*	53	53.5*	54	56.5*
40	77	51	66	52	56.5	55.5	55.5*	60	58.5*
50	74	45	67.5	49	61.5	56	57.5*	61	59*
60	70	43.5	70	48	67	54	61	58	58*
70	72	43	72	48	66	53.5	63.5	56.5	59
80	63	(47)	58	45	58.5	50	58.5	52.5	56
90	62	40	57	45	56	52	55	55	53.5
Siren Box	135	-	134	-	135	-	135	-	132

*Tone completely absent; the value given is the broadband noise level.

+Angle from jet axis (degrees)

TABLE VI-A1

10 Hz Narrowband Sound Pressure Level, 20,600 Hz (dB)

Refraction Test Rig

Microphone Location	Siren Alone	Shroud Air Temperature (P.R. = 1.20)							
		550°R		960°R		1460°R		1960°R	
		Jet Alone	Jet + Siren	Jet Alone	Jet + Siren	Jet Alone	Jet + Siren	Jet Alone	Jet + Siren
20+	89	72	79	79	79	82	83.5	87.5	85.5
25	81	70	71	81	82	84	84	86	86.5
30	80	66	72	73.5	74	84	84	84.5	88
40	89	76.5	88.5	82	84	87	87.5	91.5	90
50	85	76	91	81	85	87.5	89	93	91
60	83	76.5	90	79.5	88	86	87.5	90	90
70	80	78	87	79	87	84	86	87.5	88
80	75	(77)	81	76	81.5	82	83.5	85	85
90	70.5	73.5	77	76	79	81	82	84	84
Siren Box	148	-	147	-	148.5	-	149	-	148

+ Angle from jet axis, degrees

TABLE VI-A2

One-Third Octave Band Sound Pressure Level, 20,000 Hz (dB)

Refraction Test Rig

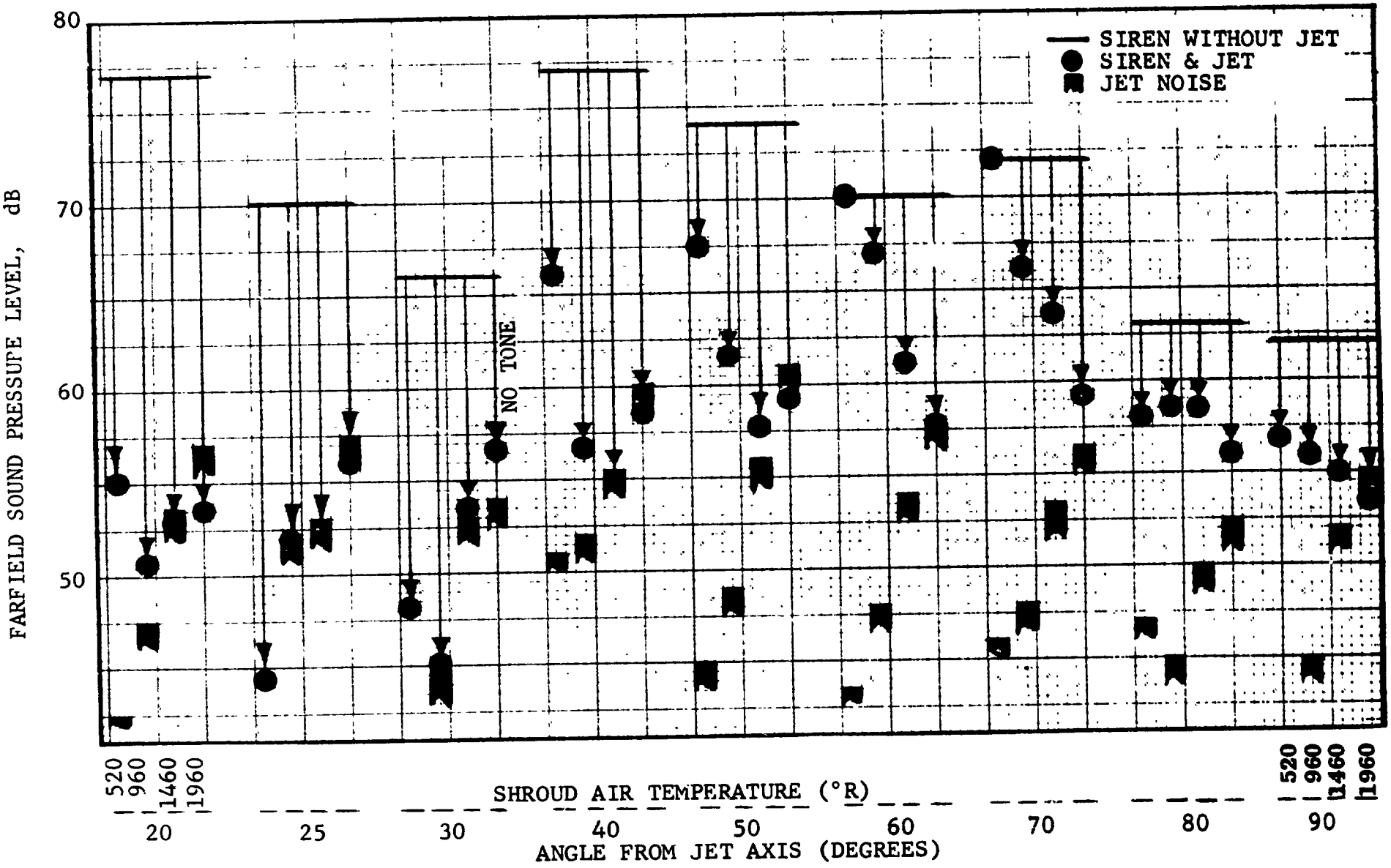

FIGURE VI- A7 REFRACTION TEST RIG RESULTS 10 Hz NARROWBAND @ 20,600 Hz

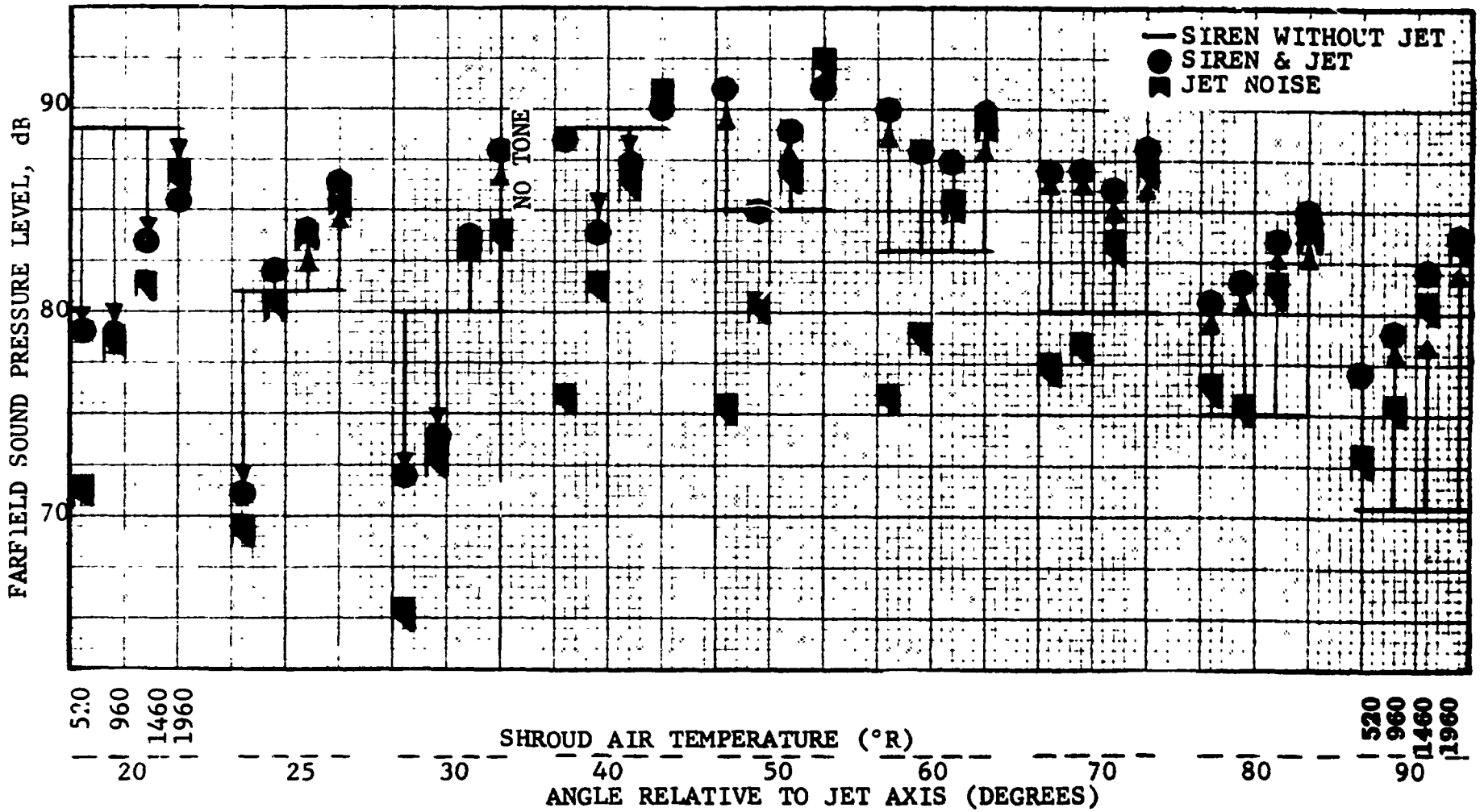

FIGURE VI- A8 REFRACTION TEST RIG RESULTS, 1/3 OCTAVE BAND (20 KHz)

(3) Discussion of Results. The narrowband analysis was originally intended to provide the data to show the refraction/reflection effect, using a filter bandwidth of 10 Hz to permit identifying the tone level without interference by the jet noise floor. Thus, relative to a one-third octave filter, the 10 Hz filter provides an improvement of 26 dB in the signal-to-noise ratio. The data in Figure VI-A7 shows that in most cases the jet noise floor was more than 20 dB below the siren tone level datum (no flow case).

The data in Figure VI-A7 do, in fact, show an impressive reduction in the siren tone level when the air shroud is used. This reduction occurs at all angles and for all shroud air temperatures, excepting only two out of 36 data points. Even the 80° and 90° locations showed a reduction in the tone level; here, the narrowband data indicate that the reduction is a result of modulation of the tone by the jet mixing turbulence such that the tone energy is scattered into a range of frequencies. Therefore, the one-third octave band data analysis must be used to separately evaluate whether the siren tone was captured within the shroud (consistent with the prediction of Figure VI-A6) or was merely scattered into a wider frequency band.

When the data is analyzed by the one-third octave filter, the jet noise floor begins to intrude in some cases. Also, the datum level for the siren-alone has strong directionality around the measurement arc. For these reasons, the data has been normalized relative to the datum and corrected for jet noise, with the results as shown in Figure VI-A9. The data show that:

(a) The siren noise level is reduced for all angles of 40° or less relative to the jet axis.

(b) At 50° the siren noise level is increased for the 520°R shroud temperature, but decreased for the higher shroud temperatures. Note that Figure VI-A6 shows the 50° angle to be marginally outside the region of internal reflection when the shroud temperature is 520°R, but is it is well within it for the higher shroud temperatures. Thus, the changeover point between the 520°R and 960°R shroud temperatures for the 50° angle is confirmed.

(c) At 60° the siren noise level is increased for the 520° and 960°R shroud temperatures, there is not much change for the 1460°R case, but it is decreased for the 1960°R case. Here Figure VI-A6 shows the 60° to be well outside the captive region for 520°R, to be marginal for the 960°R case, slightly within the capture region for the 1460°R case, and somewhat further within it for the 1960°R case.

(d) At 70°, the siren noise level is increased for all shroud temperatures excepting the 1960°R case, for which a reduction still occurs. Again this is consistent with the crossover from affected to unaffected regions predicted by Figure VI-A6.

(e) Finally, at 80° and 90° an increase in the noise level occurs except for the highest shroud temperature (1960°R). In that case the jet noise level is the same with or without the siren, so the tone has not contributed significantly to the jet noise. The narrowband results in Figure VI-A7 show that some trace of tone was remaining at 80° but none at 90° for the 1960°R case.

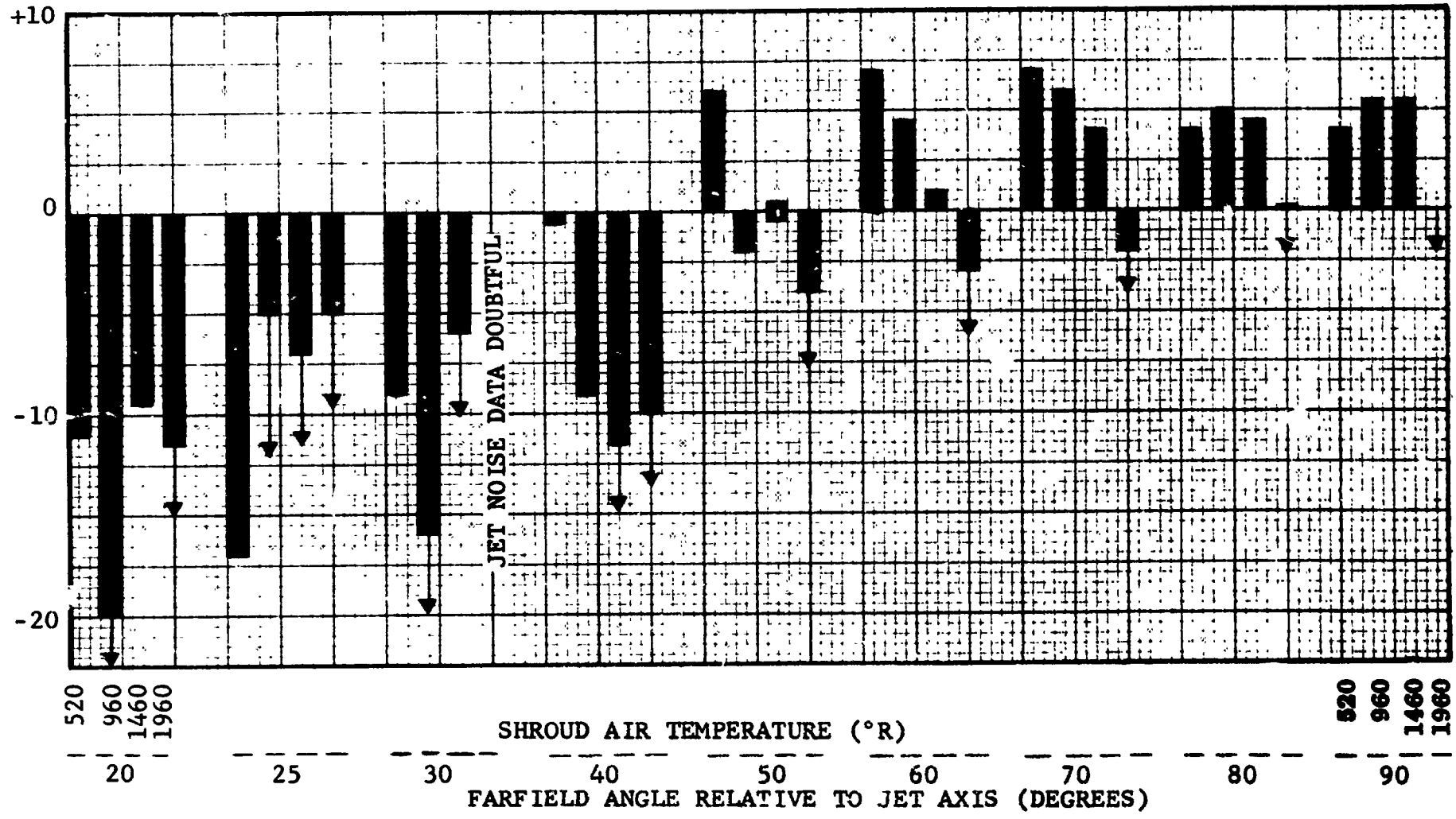

FIGURE VI-A9 ΔdB RELATIVE TO SIREN ALONE WITHOUT FLOW (1/3 OCTAVE BAND) CORRECTED FOR JET NOISE

These comparisons indicate that the shroud does capture the noise by internal reflection, consistent with the predicted trends.

The increases in noise shown by Figure VI-A9, however, show that the directivity of the siren-alone noise (without flow) has, in fact, been changed by the shroud air. Even though the narrowband data of Figure VI-A7 show that the tone level did not in any case exceed the siren alone tone level, the one-third octave band data of Figure VI-A8 show that siren-plus-jet noise was well above the siren alone noise for angles 50° and greater, even when the jet noise is so low that it makes no contribution. Therefore, the data in Figure VI-A9 raises the question whether the shroud, rather than reducing the sideline noise, actually causes it to increase. This would be possible if there had been no internal reflections such that the nozzle of the inner pipe became a sound source, completely inserting the siren noise into the shroud air, resulting in subsequent refraction toward the side.

To evaluate whether this could have happened, the refraction effect was calculated assuming that there was no internal reflection within the shroud and no spatial scattering by the jet-mixing turbulence, with the results as shown in Figure VI-A10. The calculated directivity index was obtained from:

$$DI_{\theta r} = DI_{\theta i} + 20 \log (1 + M \sin \theta_i) + 5 \log \frac{T_1}{T_o}$$

$$\theta_r = \sin^{-1}\left[\frac{\sin\theta_i}{\sqrt{\frac{T_1}{T_o}}\,(1 + M \sin\theta_i)}\right] \qquad M = \text{airflow Mach number}$$

It is pertinent to note that the shadow angle, shown in Figure VI-A10 by the downward pointing arrow, is the same as the critical angle for internal reflection (Figure VI-A6). As a result, the previously discussed trends of Figure VI-A9 which were given to support the concept of internal reflections, now can be seen to be consistent with the possibility that the higher temperature shroud merely moved the shadow angle more and more toward the sideline. That is, rather than the noise being captured by the shroud and redirected toward the axis, this suggests the possibility that the noise was merely refracted without internal reflections, and the observed decrease in noise, say at 60°, as the shroud temperature was increased, could have occurred simply because that microphone was in the shadow zone for the higher temperature. A contrary indication from the data is the fact that the calculated refraction level of Figure VI-A10 would require at 70° and 80° the siren noise level should increase with increasing shroud temperature. The data in Figure VI-A9 show this did not happen; the trend is strongly in the opposite direction, indicating that although there was some sidewise refraction with the unheated air shroud, internal reflection reversed the effect as the shroud temperature was increased.

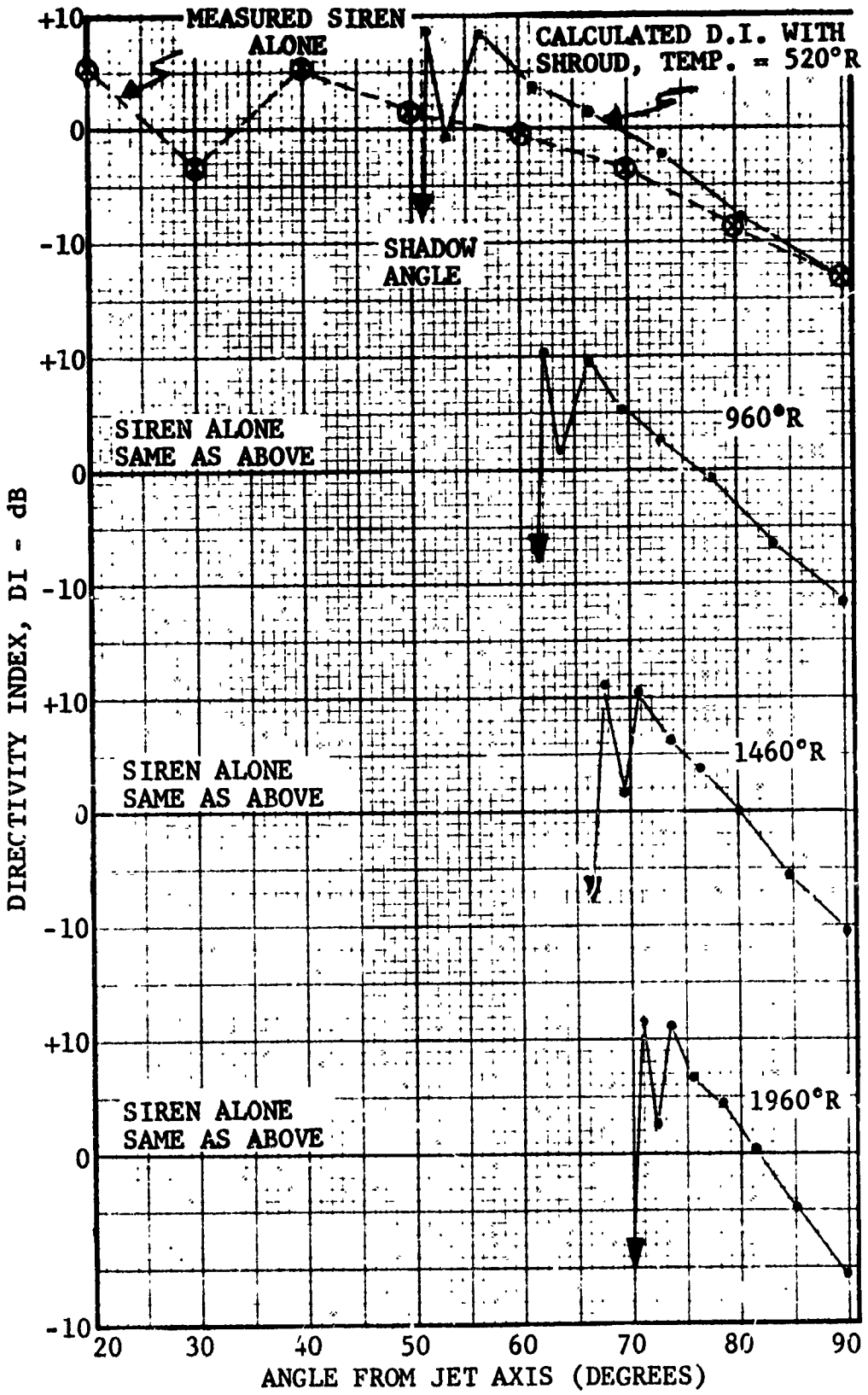

FIGURE VI-A10 CALCULATED REFRACTED NOISE ASSUMING NO INTERNAL REFLECTION AND NO TURBULENCE SCATTERING

This is more clearly shown by the data as presented in Figure VI-A11, a plot of directivity index versus polar angle for the siren without shroud airflow and for the siren noise with airflow corrected for jet noise. The space averaged sound pressure level is 83.6 dB for the no-flow case, but 86.7 dB for the 520°R shroud temperature case. The reason for the higher value with flow is not understood, since the sound level at the source (siren box) was the same within 1 dB. This change in average level is one of the factors that makes the data in Figure VI-A 9 subject to misinterpretation. The space averaged sound pressure levels for each case are tabulated below, showing that after the initial increase caused by flow, the space averaged level then decreased as the shroud temperature was raised.

Space-Averaged Sound Pressure Level (dB)

	Siren Alone	Siren, corrected for Jet Noise at Shroud Temperature of:			
		520°R	960°R	1460°R	1960°R
Space Avg. SPL	83.6	86.7	83.6	80.1	*

*Could not be determined because jet noise too high.

Thus, while the value is higher at 520°R, it is the same at 960°R, and lower at 1460°R than the siren-alone value. The space averaged value of 86.7 dB was used as the reference for all cases with shroud flow, thereby permitting graphic illustration in Figure VI-A11 of the noise reduction achievable by elevating the shroud air temperature, all other factors being held constant. Such a reduction could result only from capture of the noise within the shroud.

A final point of interest in Figure VI-A11 is that the initial directivity "without flow" still has a strong influence on shape of the directivity "with flow" for the 80° and 90° locations. This shows that the modal patterns of the inner nozzle were not completely randomized by the air flow turbulence in the shroud. This is believed to be the result of having no air flow and the associated turbulence in the pipe through which the siren noise was channelled, as would be the case in an engine exhaust.

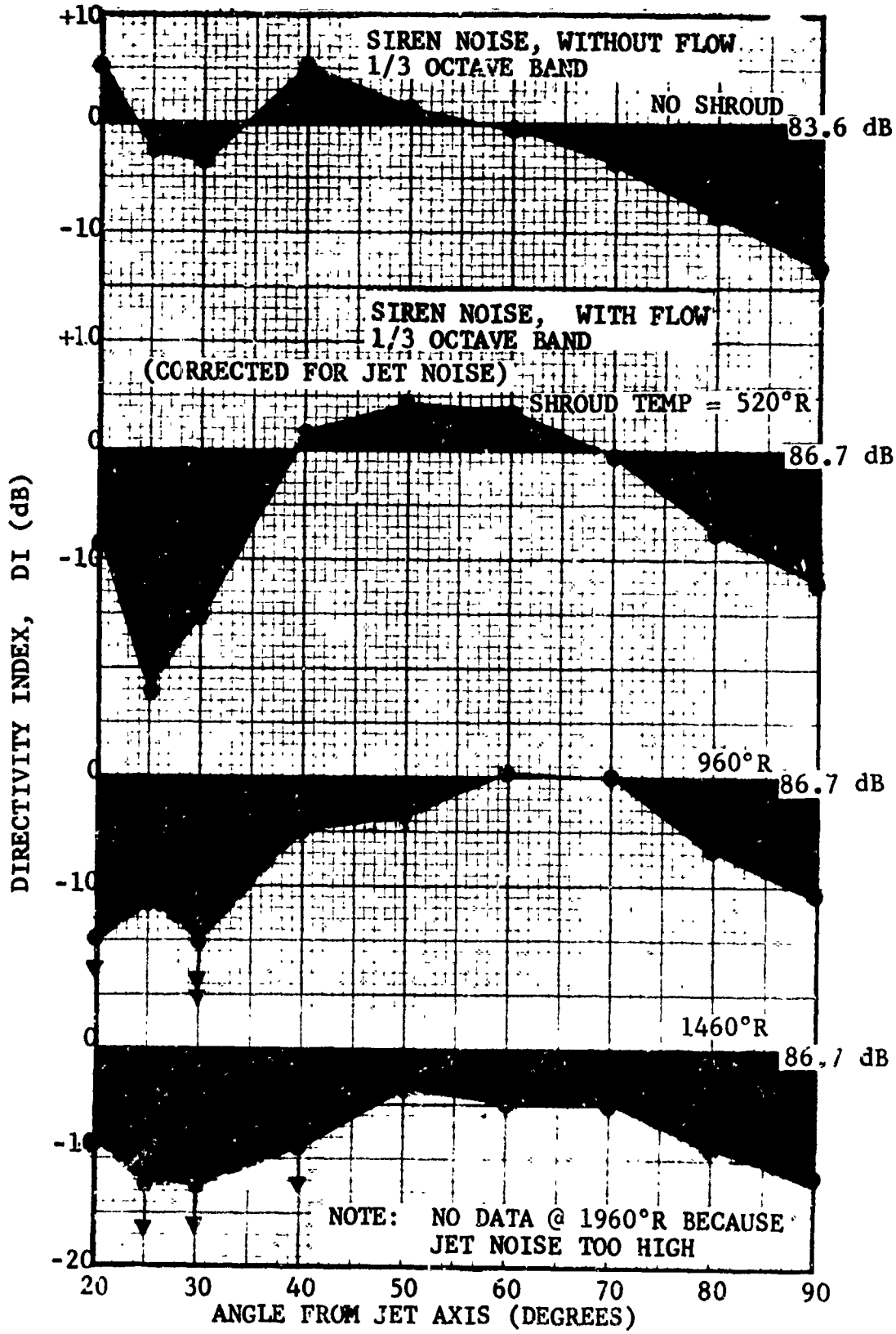

FIGURE VI-A11 EFFECT OF SHROUD ON FARFIELD LEVEL AND DIRECTIVITY INDEX

NOMENCLATURE - SECTION VI-A

$DI_{\theta r}$	Directivity Index of the sound after refraction.
$DI_{\theta i}$	Directivity Index of the sound before refraction.
M	Mach number of the following airstream containing the sound.
θ_i	Angle of incidence of the sound measured from the normal to the plane of the interface between two media.
θ_r	Angle of refraction of the sound measured from the normal to the plane of the interface between two media.
T_1	Absolute temperature of moving air containing the sound.
T_o	Absolute temperature of ambient air.

(B) Experimental Investigation of Propagation Effects. The mechanisms associated with the propagation of sound in the atmosphere were discussed and mathematical models describing these mechanisms were described in Section III-D of this report. The phenomena were treated in four parts:

- Inverse Square Law Divergence
- Atmospheric Absorption of Acoustic Energy
- Additional Absorption by the Ground Boundary Layer
- Reflection of Sound Waves by the Ground

As indicated in Section III-D, the interpretation of atmospheric absorption and reflection are complicated by inhomogeneities in the atmosphere (for example atmospheric turbulence, thermal gradients, etc) and by the deviation of any real surface from an ideal reflector due to surface roughness, absorption by the surface, and by a phase shift in reflected sound at the surface. Thus, the models used to represent the propagation phenomena must include factors which are derived from experimentation. The two semi-empirical factors from Section III-D that most require experimental determination are:

- Reflection phase factor, ϕ
- Atmospheric Absorption Coefficients for high frequency data

A series of tests were conducted at the General Electric test facility near Peebles, Ohio to investigate the phenomena associated with acoustic propagation. The first part of the tests was aimed at an investigation of the reflection phase factor, and the second portion of the series consisted of an investigation of atmospheric absorption at high frequencies. No systematic investigation of the reflection coefficient was included in this test series; however, observed values were used in the tests to verify the models.

(1) Reflection phase Factor. The phase factor, ϕ, was defined in Section III-D to be

$$\phi = \frac{\Delta r}{\Delta r'},$$

where

Δr = ideal path length difference (reflected signal path minus direct signal path)

$\Delta r'$ = effective path length difference, a function of Δr, non-ideal surface, and atmospheric inhomogeneities (turbulence, gradients, etc.)

The phase factor may also be expressed as:

$$\phi = \frac{2}{2n + 1} \times \frac{\Delta r}{c} \times f_{null\ actual} \qquad n = 0, 1, 2, \ldots.$$

where

c = acoustic velocity

$f_{null\ actual}$ = frequency at which maximum cancellation of direct and reflected signal occur.

The phase factor is a function of surface, distance (Δr), angle of incidence, frequency and meteorological conditions (wind, etc.).

(a) Phase Factor - Test Objectives and Set-up. This series of tests attempted to determine the variation of phase factor with type of surface, angle of incidence, and geometric path length difference (Δr).

Two types of surfaces were considered: concrete and gravel. In addition, the surfaces were wetted in order to determine the sensitivity of the surface to weather conditions.

Two test configurations were designed for the testing of phase factor. The first, Configuration A (Figure VI-B1), was designed to test the variation of phase factor at nearly constant angle of incidence, while the path length difference varied. The second, Configuration B (Figure VI-B2), was designed to test the variation of phase factor with angle of incidence. The microphone located ten feet from the speaker was used to monitor the speaker output so that any null noted (local minimum) at other microphones can be assigned to reflection and not to speaker output.

The sound for these tests was produced by driving a speaker with a sine wave generator that produced a one minute linear frequency sweep from 450 to 10,000 Hz. Generator output was set at the highest power level attainable. The pure tone sweep was recorded by the microphones at various locations.

In order to obtain an indication of the location of the reflection point, a 4 foot x 4 foot x 4 inch Scottfoam pad was placed at 21, 25 and 29 feet from the speaker with the microphones located in Configuration A.

With the exception of tests performed for the concrete surface with the mikes in Configuration A (Figures VI-B1) the tests were performed with negligible wind speeds. For the noted tests wind gusts of one to five miles per hour were observed. While the wind may have introduced some scatter in the data, the consistency between data for repeat runs indicates the effect was negligible.

For each combination of configuration and surface, a minimum of 4 repeats (frequency sweeps) were performed. This was done so that such random effects as atmospheric turbulence may be eliminated through the averaging process.

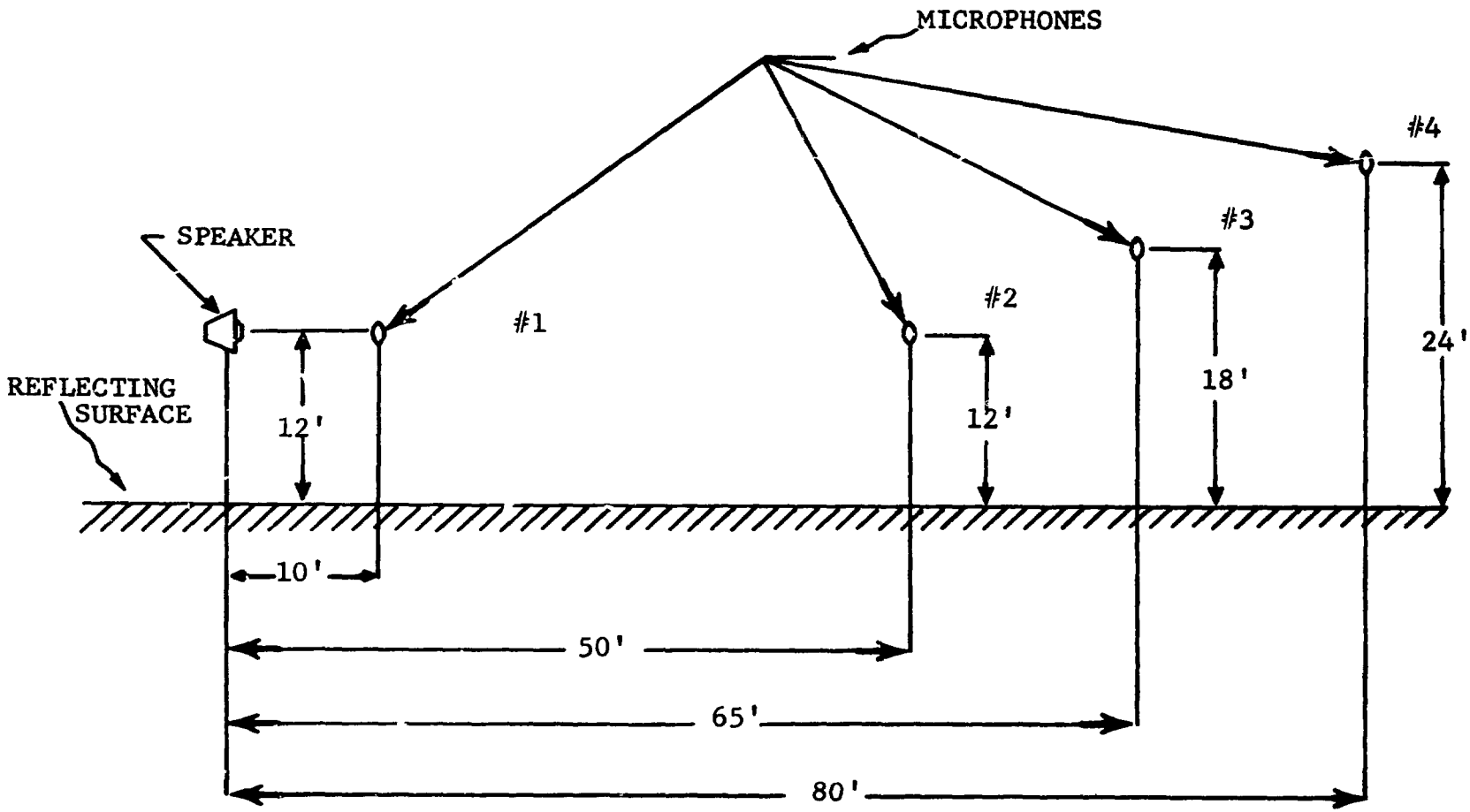

FIGURE VI-B1 TEST SETUP TO INVESTIGATE THE EFFECT OF PATH LENGTH DIFFERENTIAL ON PHASE FACTOR - CONFIGURATION A

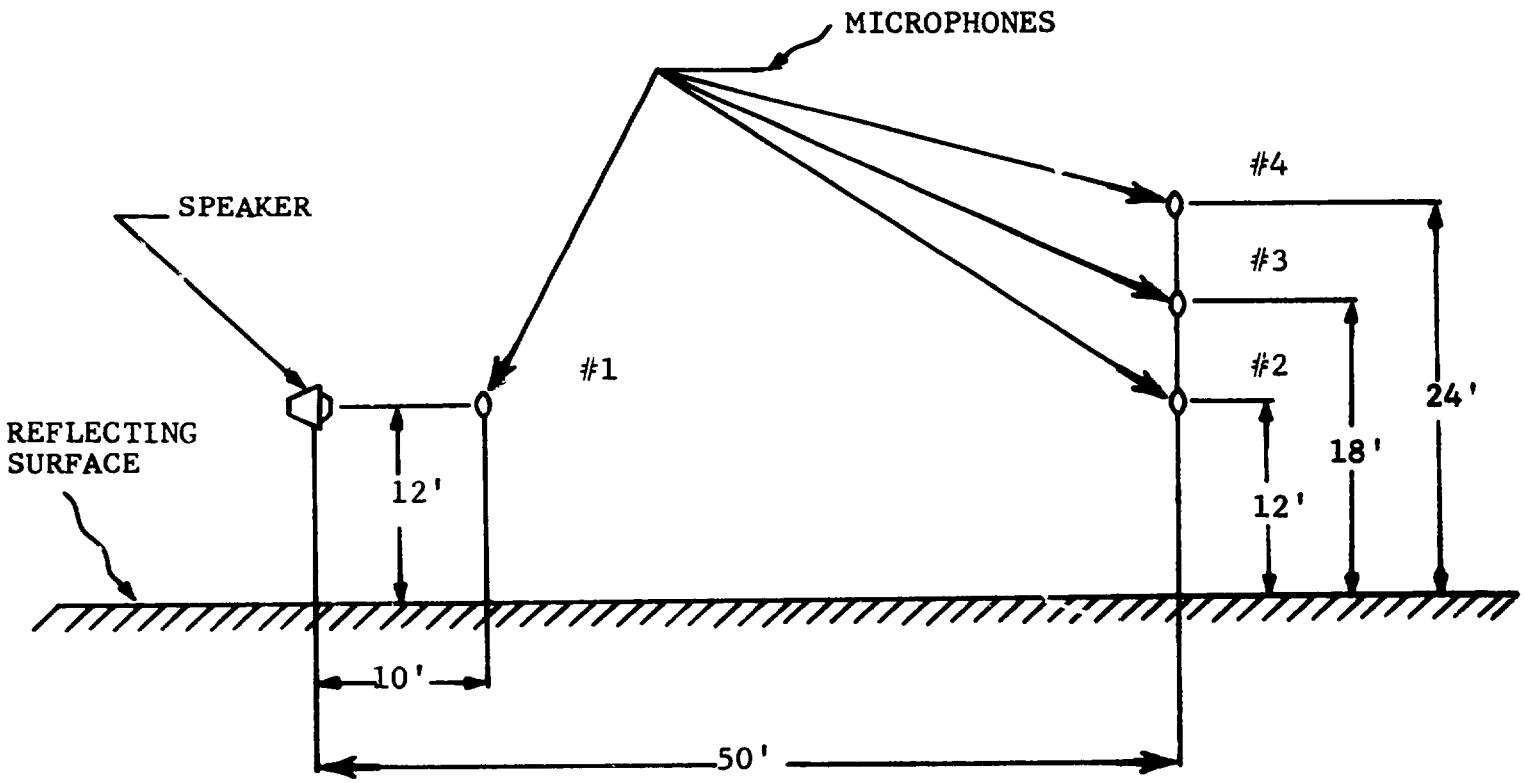

FIGURE VI-32 TEST SETUP TO INVESTIGATE THE EFFECT OF INCIDENCE ANGLE ON PHASE FACTOR - CONFIGURATION B

(b) Phase Factor - Results and Analysis. Typical values of Sound Pressure Level (SPL) recorded, versus frequency, are presented in Figures VI-B3 through VI-B41.

(1) Type of Surface. Using the relationship between phase factor (ϕ) and test measurements:

$$\phi = \frac{2}{2n+1} \times \frac{\Delta r}{c} \times f_{null\ action} \qquad n = 0, 1, 2, \ldots.$$

yields, for the recorded sound pressure levels, ϕ as a function of frequency (and surface). Results of the above calculation for each microphone over concrete and over gravel are presented in Figures VI-B42 through VI-B46.

Prior to discussion of the test results the expected variations in phase factor due to measurement errors must be determined. Taking the differential of the equation relating phase factor to test measurements yields

$$\left[\frac{d\phi}{\phi}\right]_{rss} = \pm\sqrt{\left[\frac{d(\Delta r)}{r}\right]^2 + \left(\frac{d\ f_{null}}{f_{null}}\right)^2 + \left(\frac{dc}{c}\right)^2}$$

where

rss - denotes root sum square of the variances

Δr - geometric path length differential (reflected minus direct signal)

f_{null} - frequency at which a null is observed

c - acoustic velocity

Now c is const.$^{x}\sqrt{T}$

where T = absolute temperature.

So

$$\frac{dc}{c} = \frac{1}{2} x\left(\frac{dT}{T}\right)$$

Now, considering the geometry of the problem, it can be shown that:

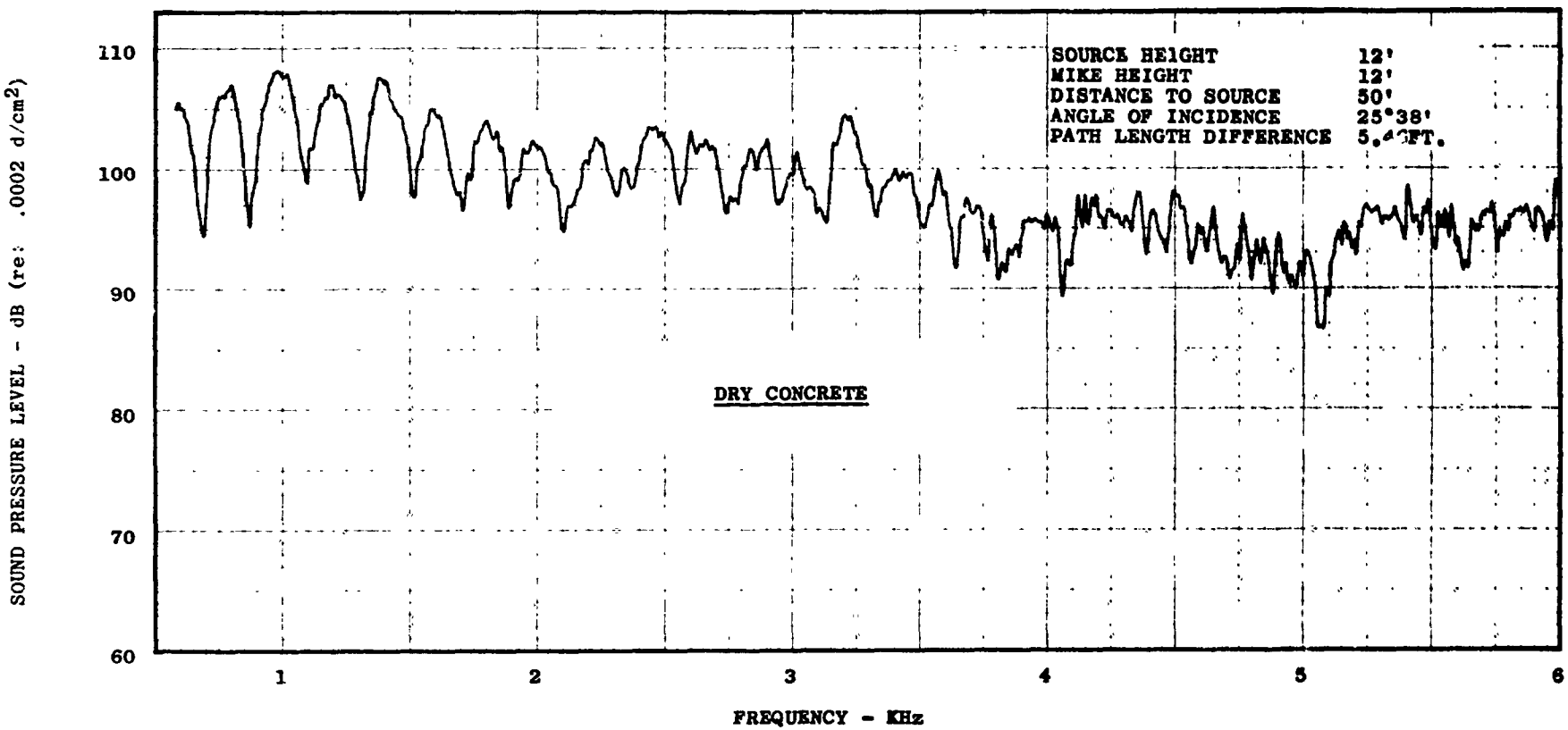

FIGURE VI -B3 SPL vs. FREQUENCY - GROUND REFLECTION TESTS CONFIGURATION A , MIKE #2

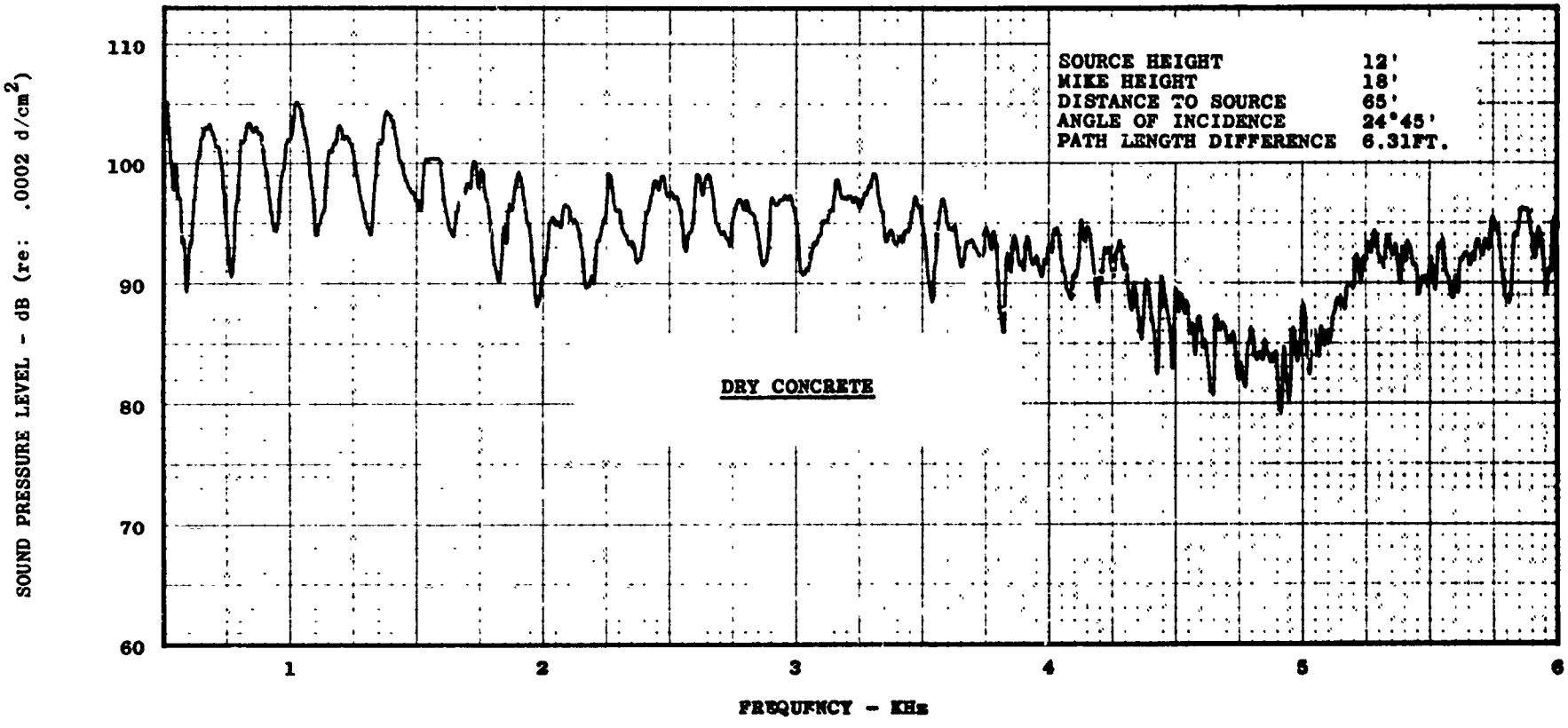

FIGURE VI-B4 SPL vs. FREQUENCY - GROUND REFLECTION TESTS CONFIGURATION A, MIKE #3

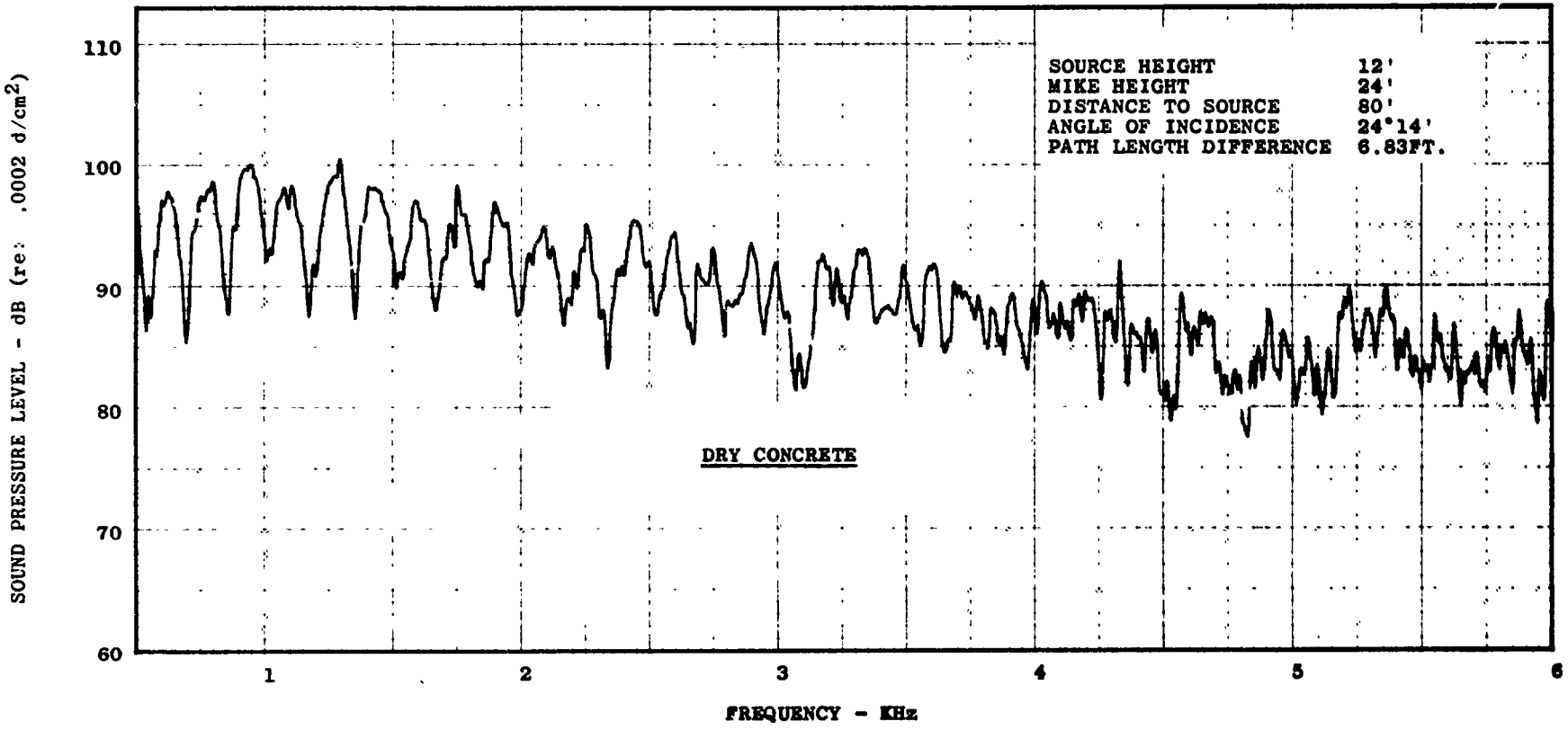

FIGURE VI-B5 SPL vs. FREQUENCY - GROUND REFLECTION TESTS CONFIGURATION A, MIKE #4

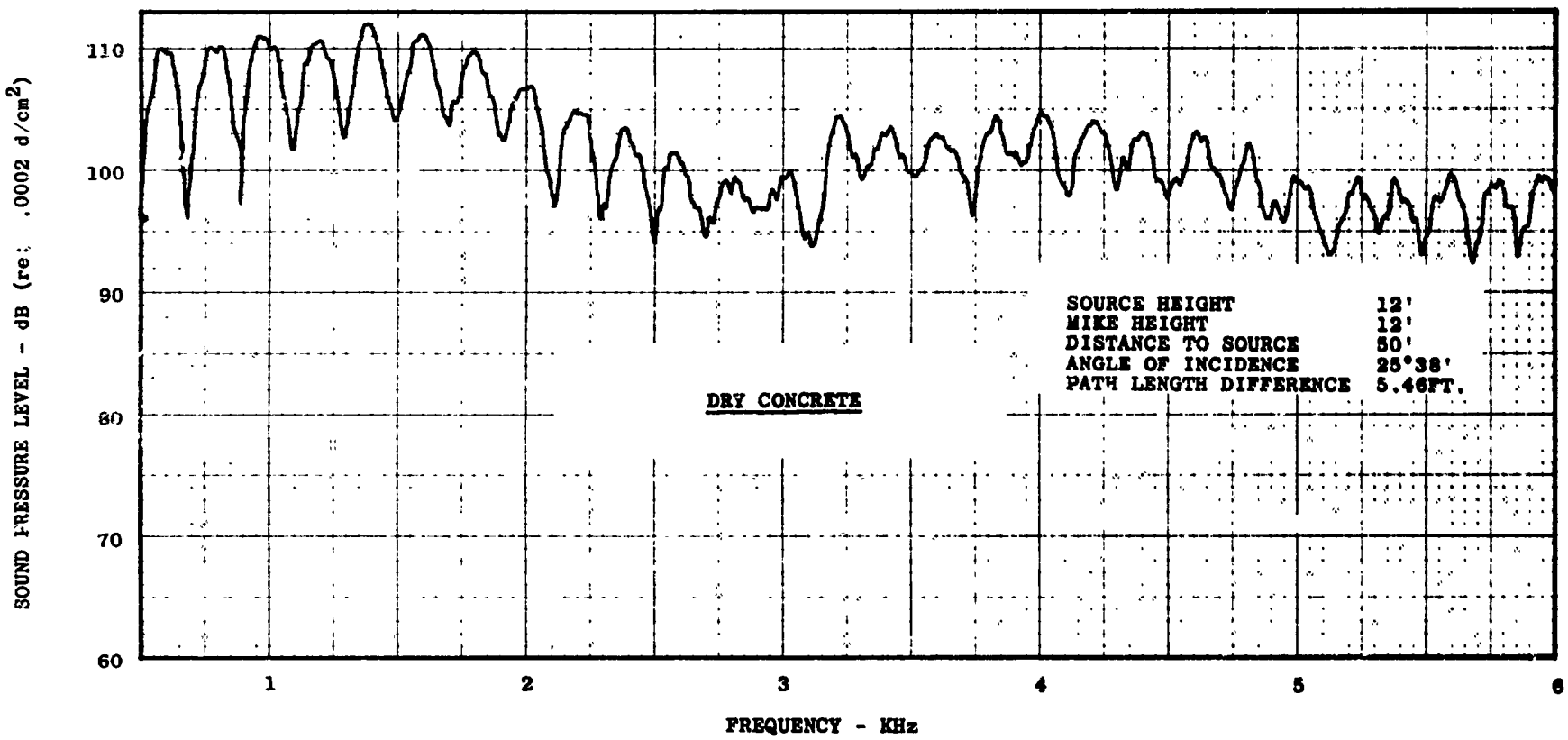

FIGURE VI-B6 SPL vs. FREQUENCY - GROUND REFLECTION TESTS CONFIGURATION B, MIKE #2

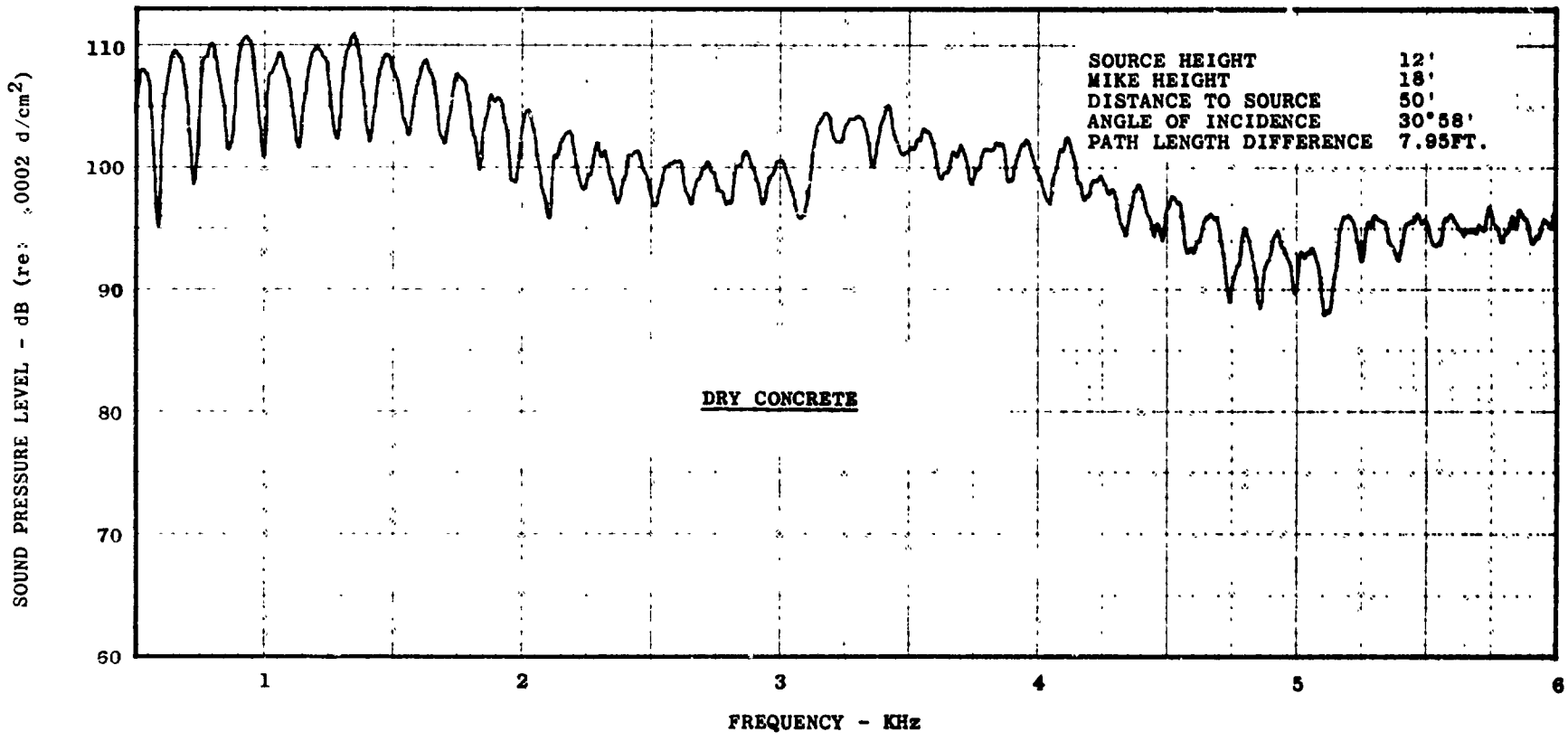

FIGURE VI-B7 SPL vs. FREQUENCY - GROUND REFLECTION TESTS CONFIGURATION B, MIKE #3

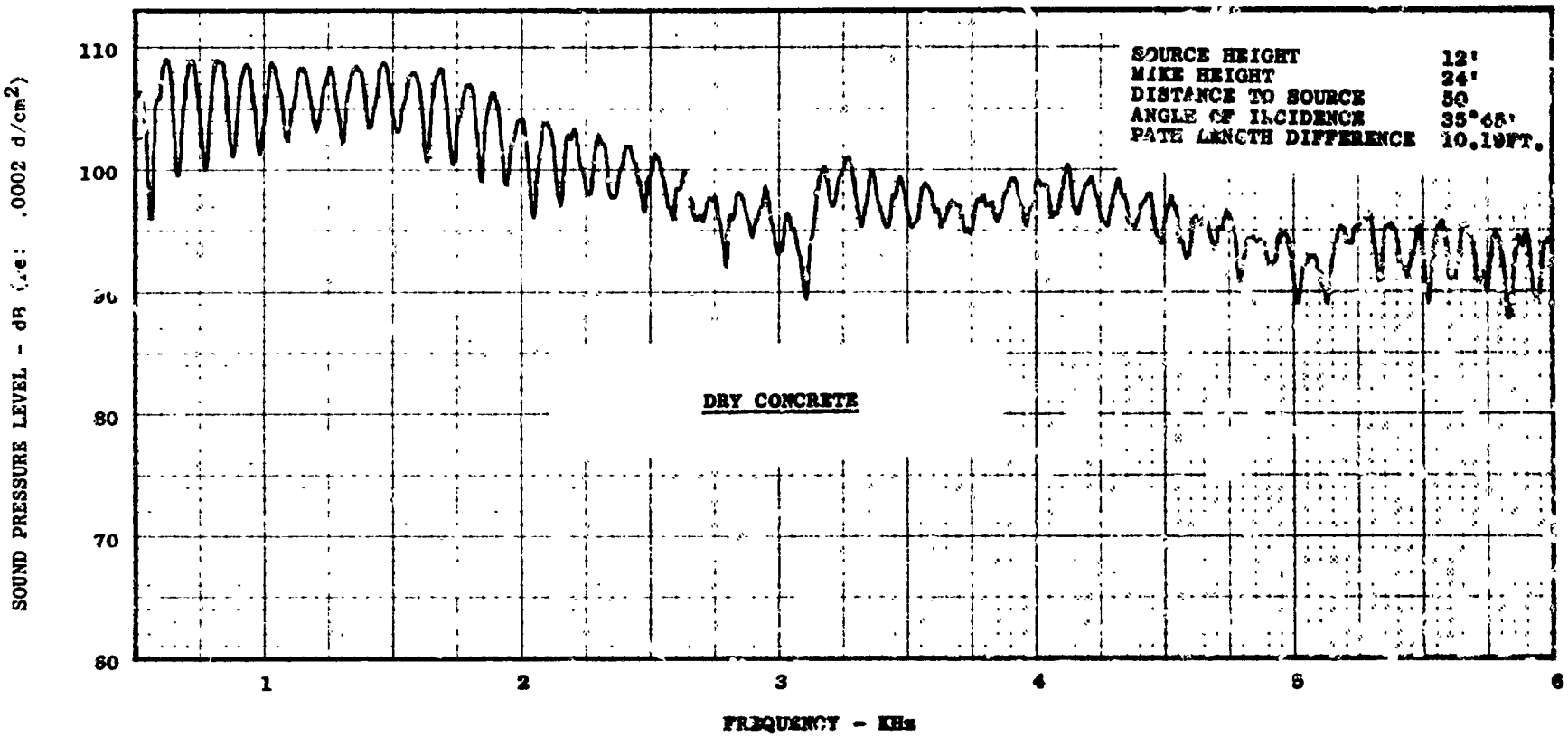

FIGURE VI-B8 SPL vs. FREQUENCY - GROUND REFLECTION TESTS CONFIGURATION 8, MIKE #4

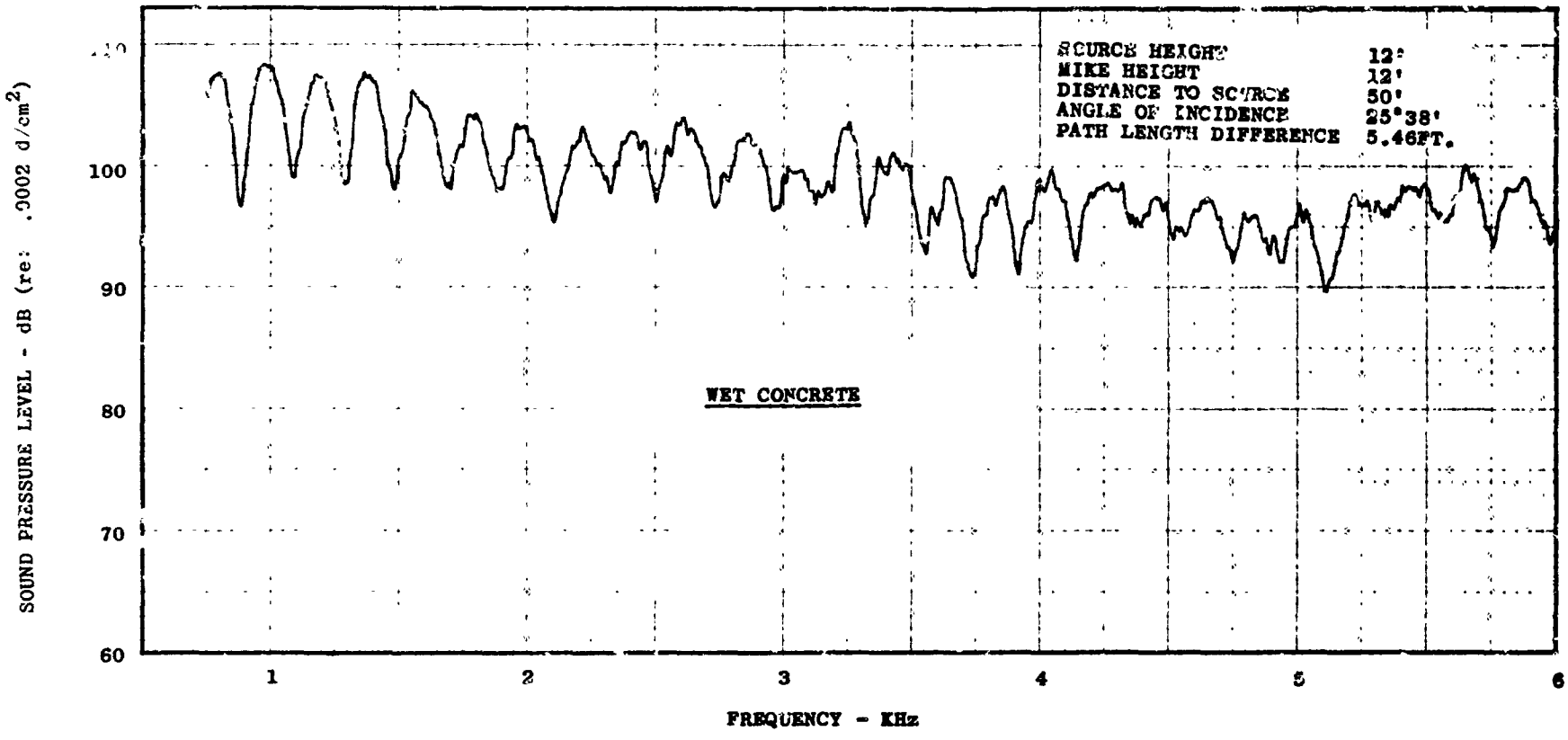

FIGURE VI-B9 SPL vs. FREQUENCY - GROUND REFLECTION TESTS CONFIGURATION A, MIKE #2

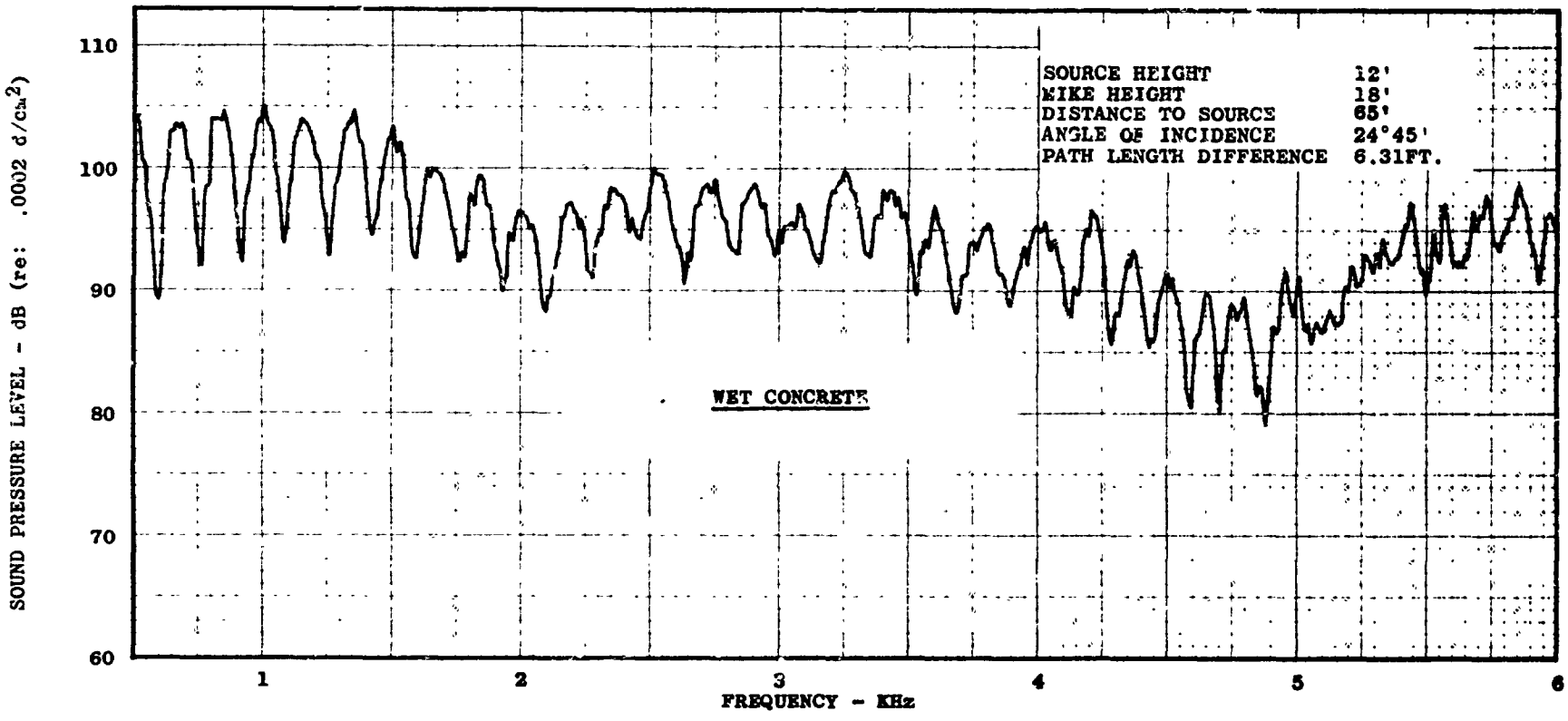

FIGURE VI-B10 SPL vs. FREQUENCY - GROUND REFLECTION TESTS CONFIGURATION A, MIKE #3

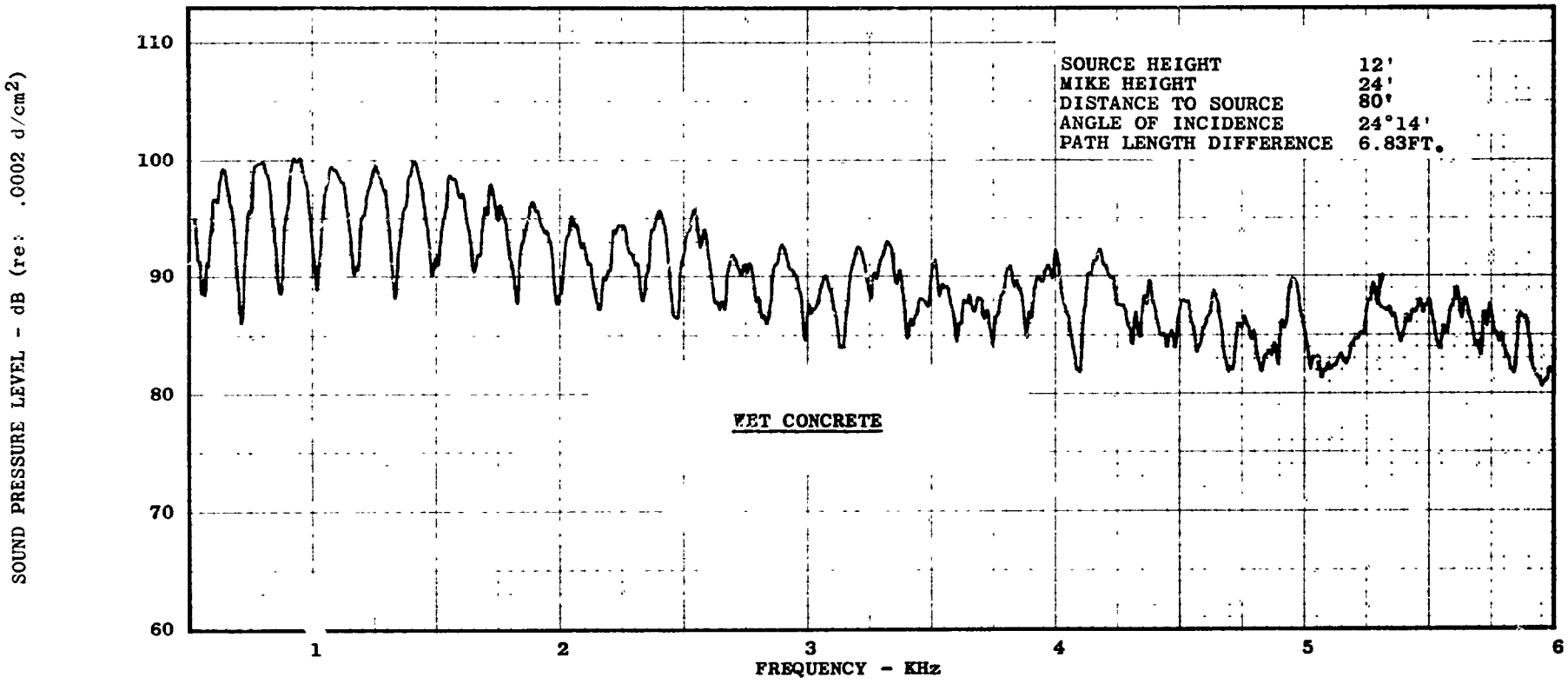

FIGURE VI-B11 SPL vs. FREQUENCY - GROUND REFLECTION TESTS CONFIGURATION A, MIKE #4

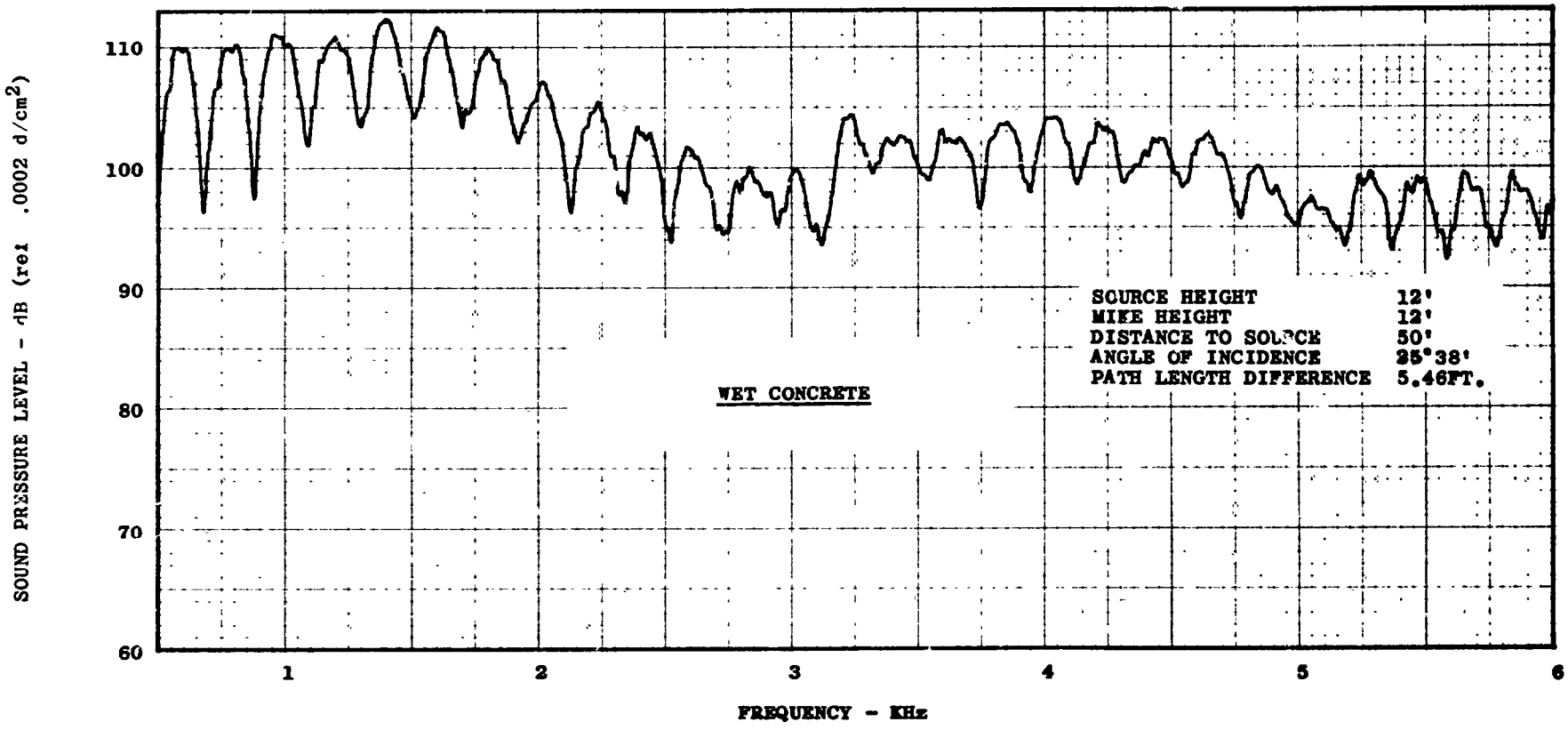

FIGURE VI-B12 SPI vs. FREQUENCY - GROUND REFLECTION TESTS CONFIGURATION B, MIKE #2

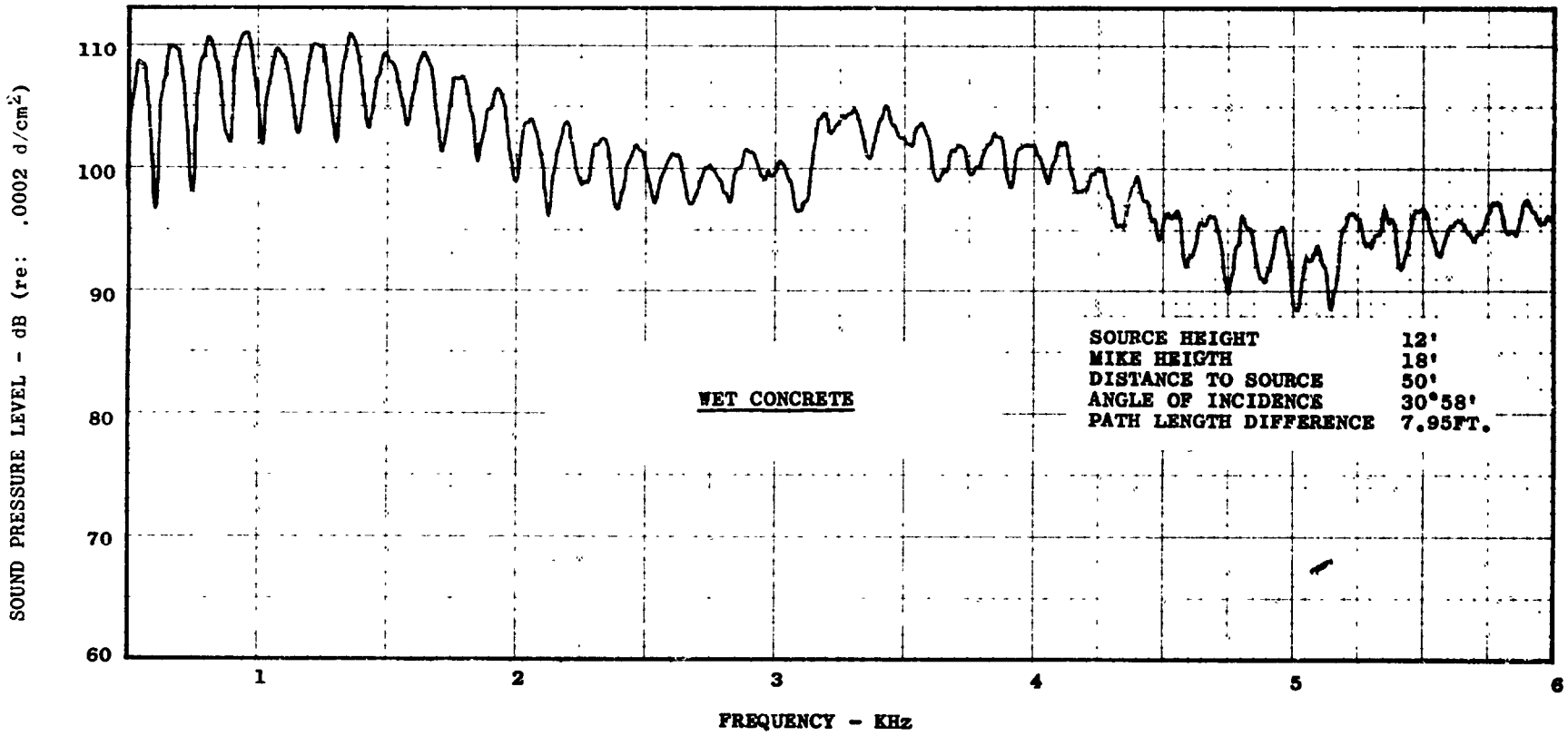

FIGURE VI-B13 SPL vs. FREQUENCY - GROUND REFLECTION TESTS CONFIGURATION B, MIKE #3

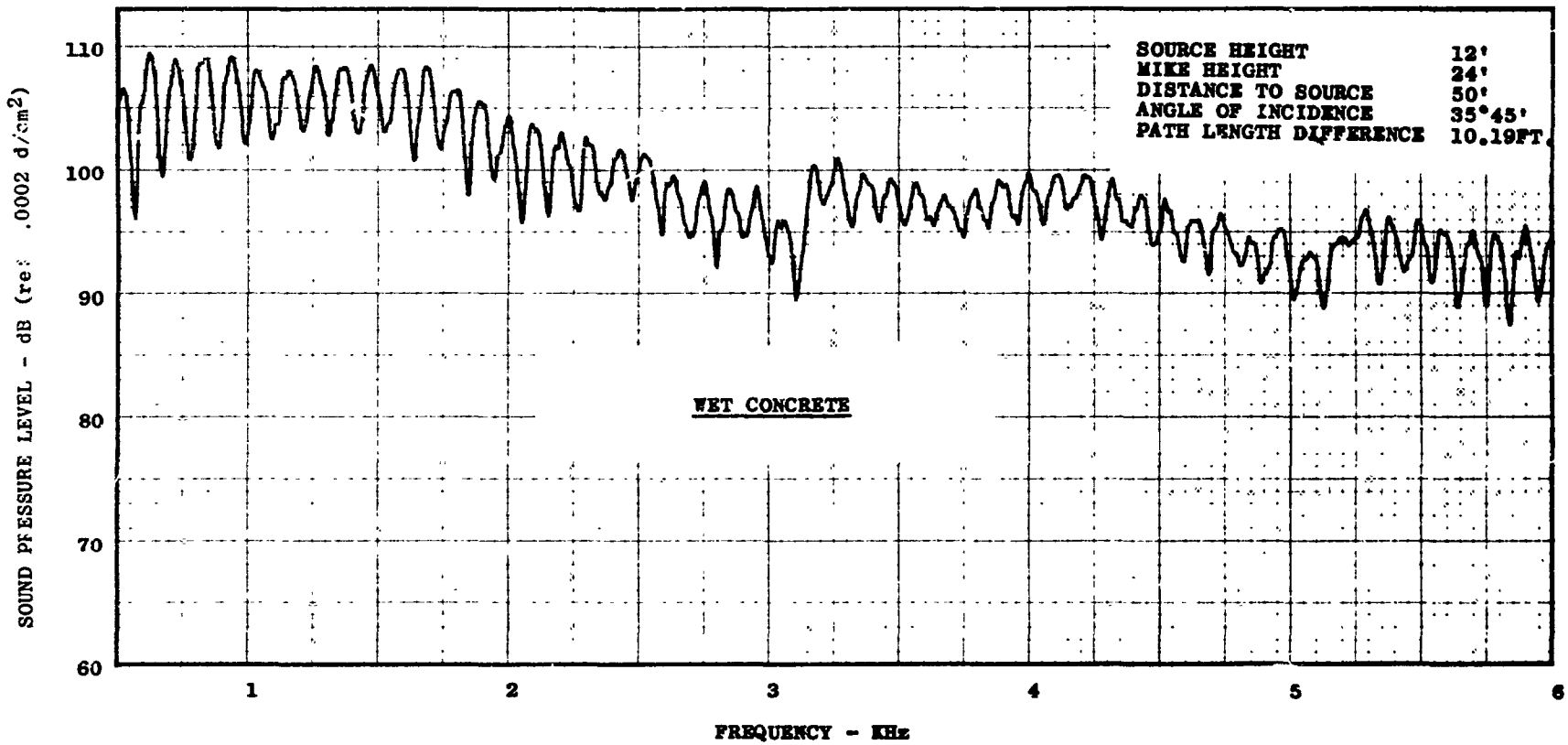

FIGURE VI-B14 SPL vs. FREQUENCY - GROUND REFLECTION TESTS CONFIGURATION B, MIKE #4

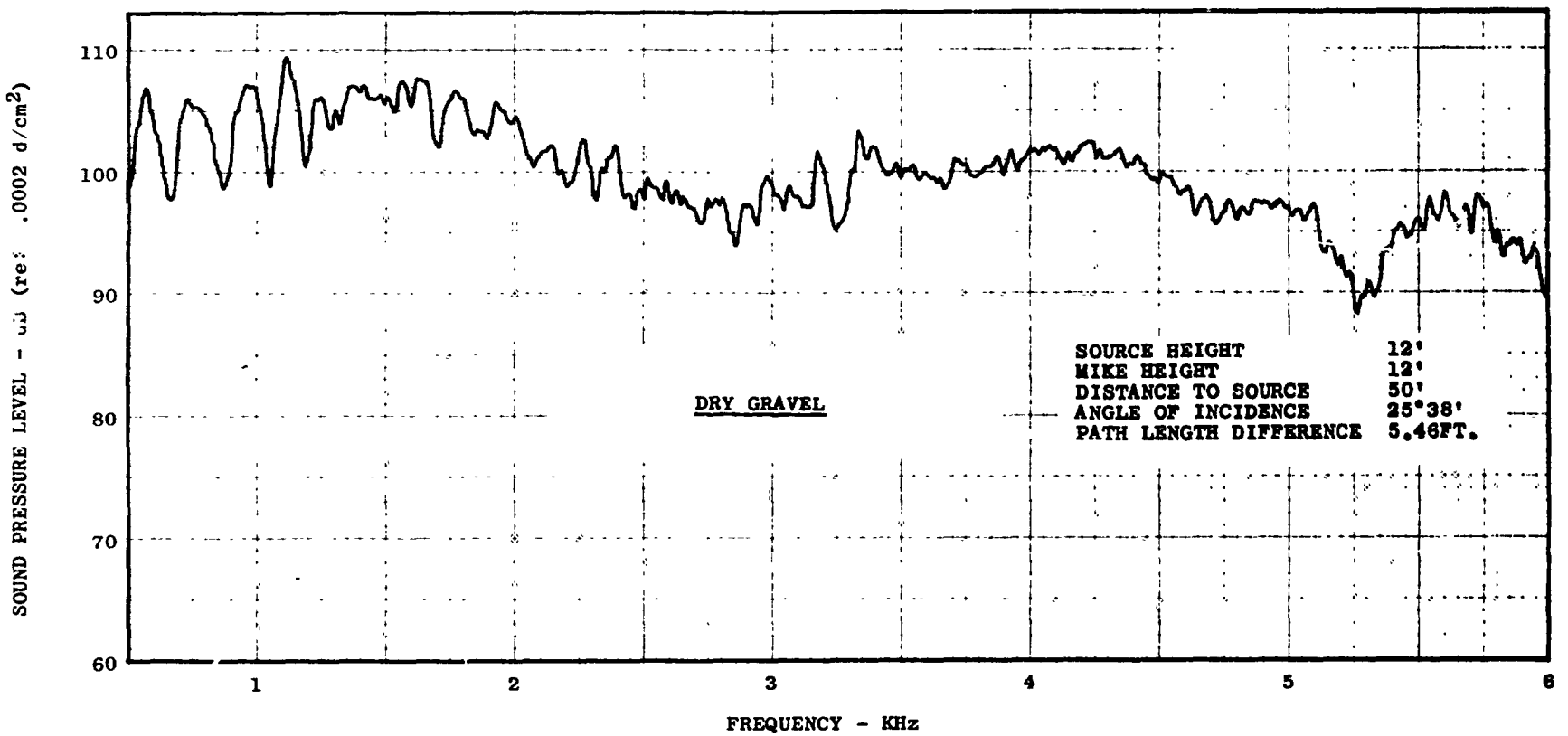

FIGURE VI-B15 SPL vs. FREQUENCY- GROUND REFLECTION TESTS CONFIGURATION A, MIKE #2

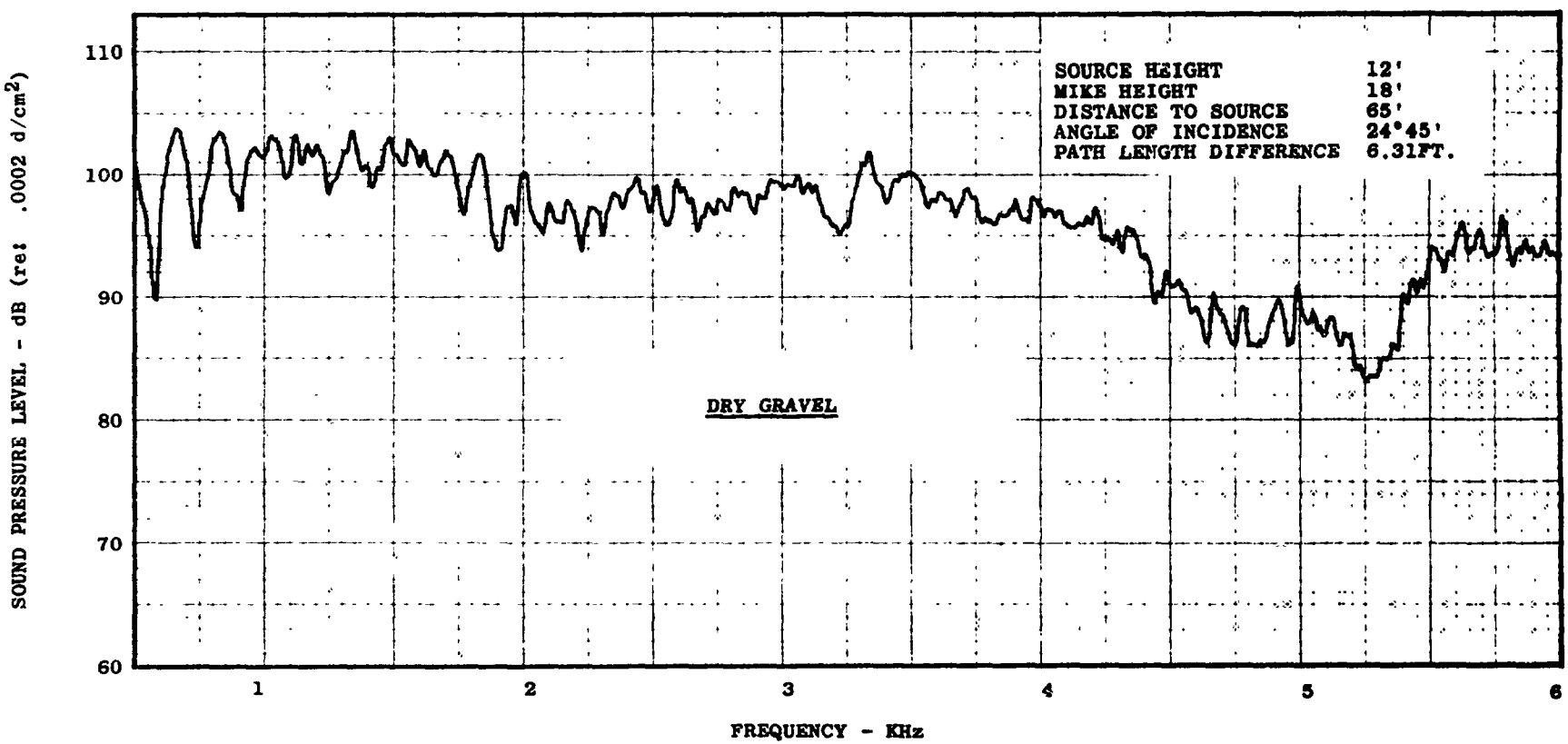

FIGURE VI-B16 SPL vs. FREQUENCY - GROUND REFLECTION TESTS CONFIGURATION A, MIKE #3

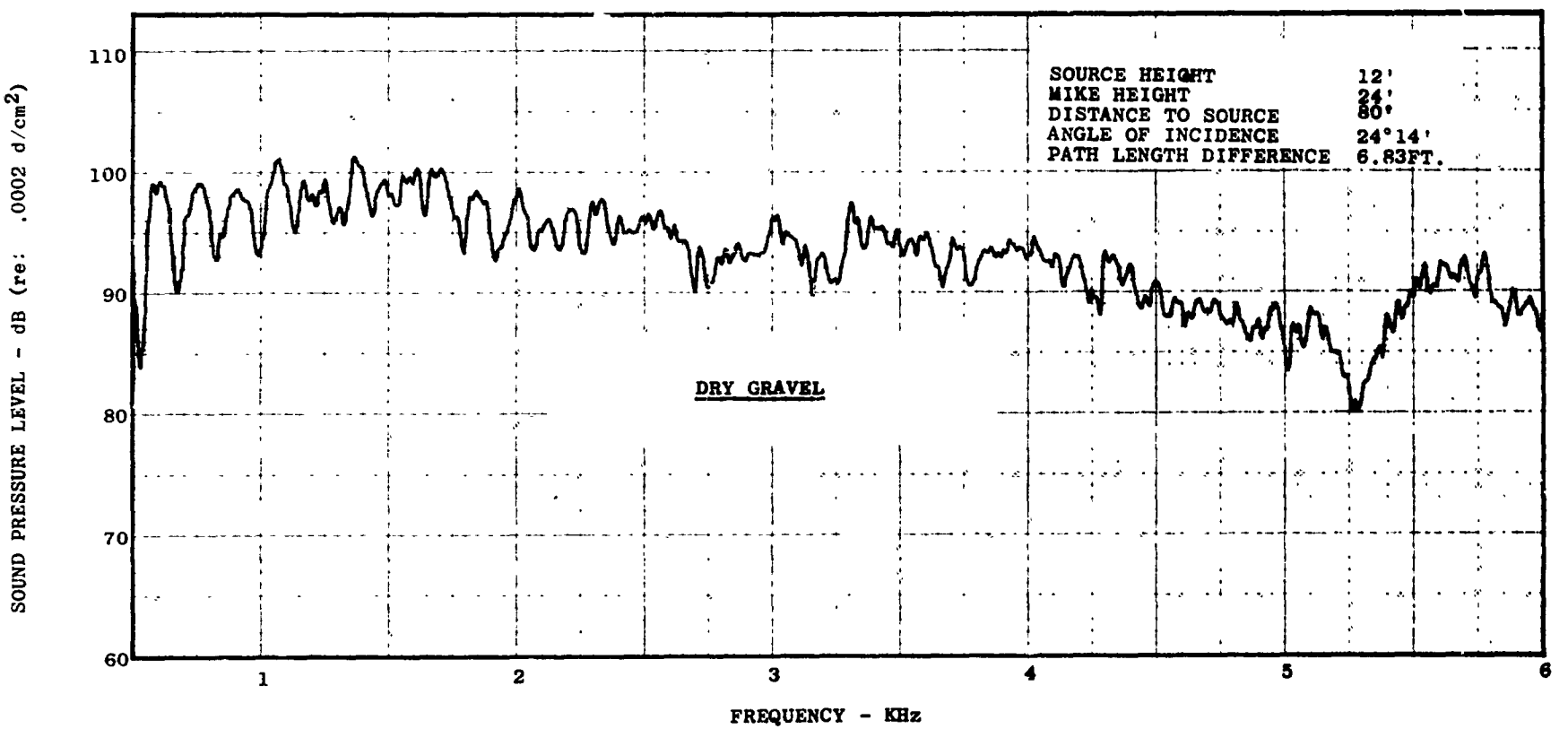

FIGURE VI-B17 SPL vs. FREQUENCY - GROUND REFLECTION TESTS CONFIGURATION A, MIKE #4

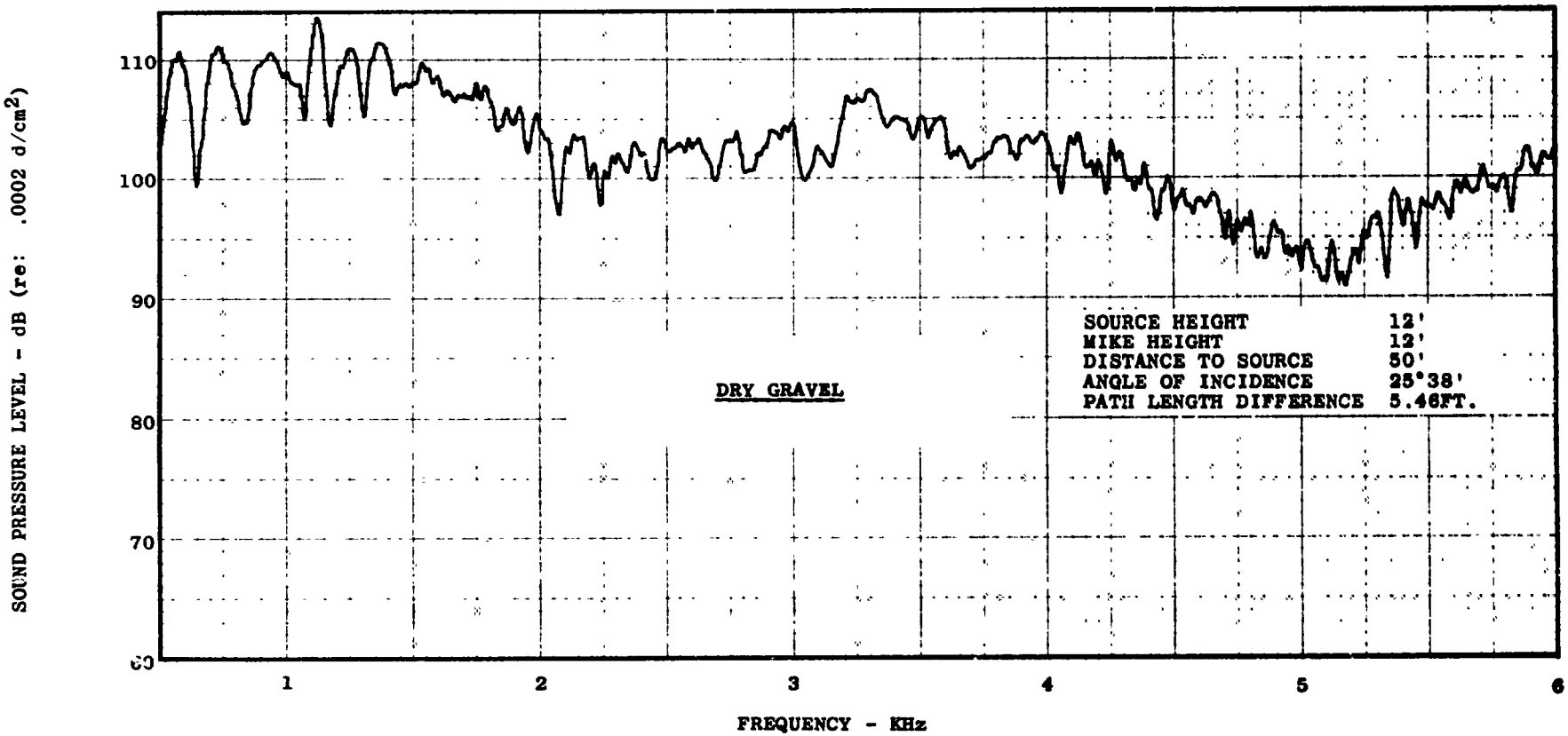

FIGURE VI-B18 SPL vs. FREQUENCY - GROUND REFLECTION TESTS CONFIGURATION B, MIKE #2

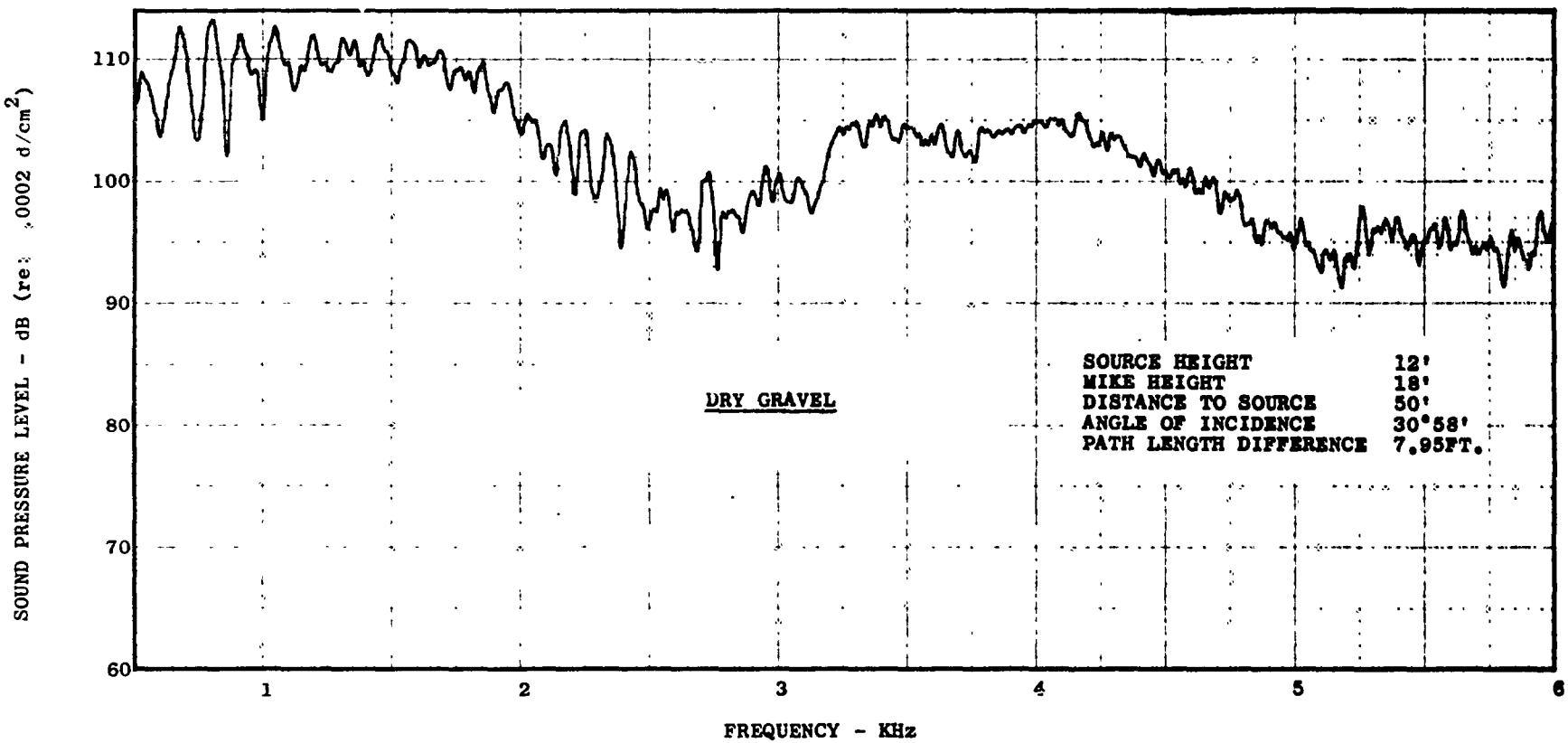

FIGURE VI-B19 SPL vs. FREQUENCY - GROUND REFLECTION TESTS CONFIGURATION B, MIKE #3

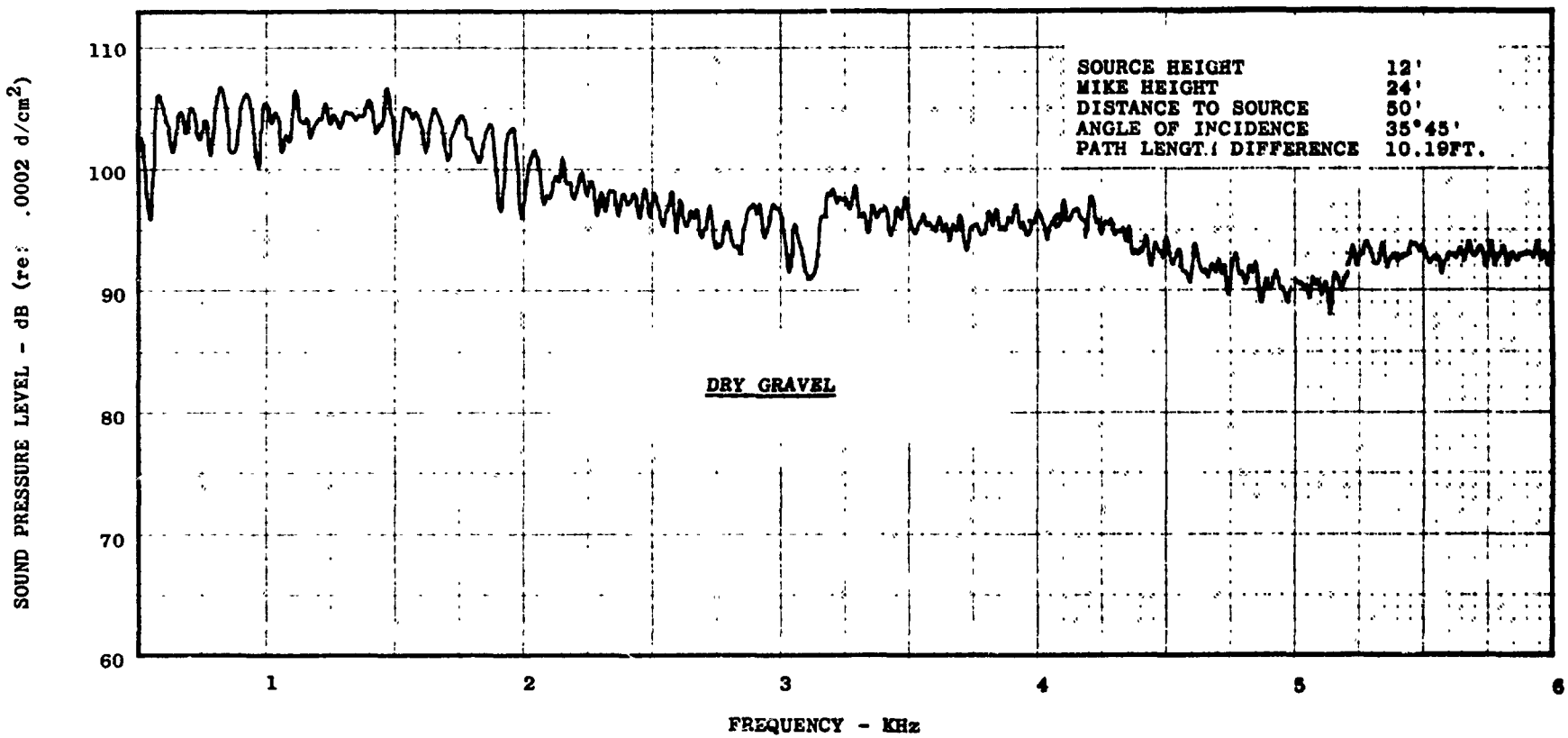

FIGURE VI-B20 SPL vs. FREQUENCY - GROUND REFLECTION TESTS CONFIGURATION B, MIKE #4

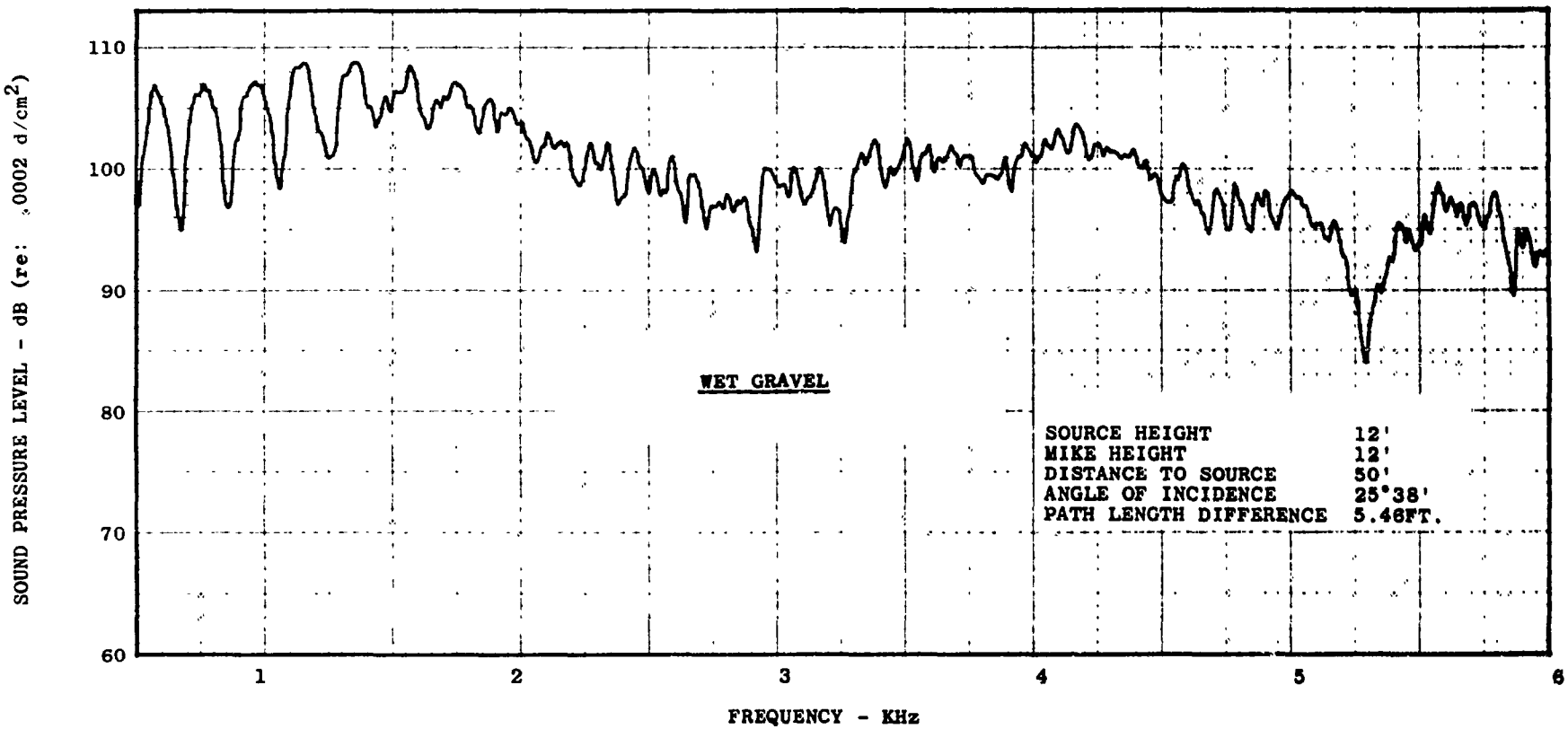

FIGURE VI-B21 SPL vs. FREQUENCY - GROUND REFLECTION TESTS CONFIGURATION A, MIKE #2

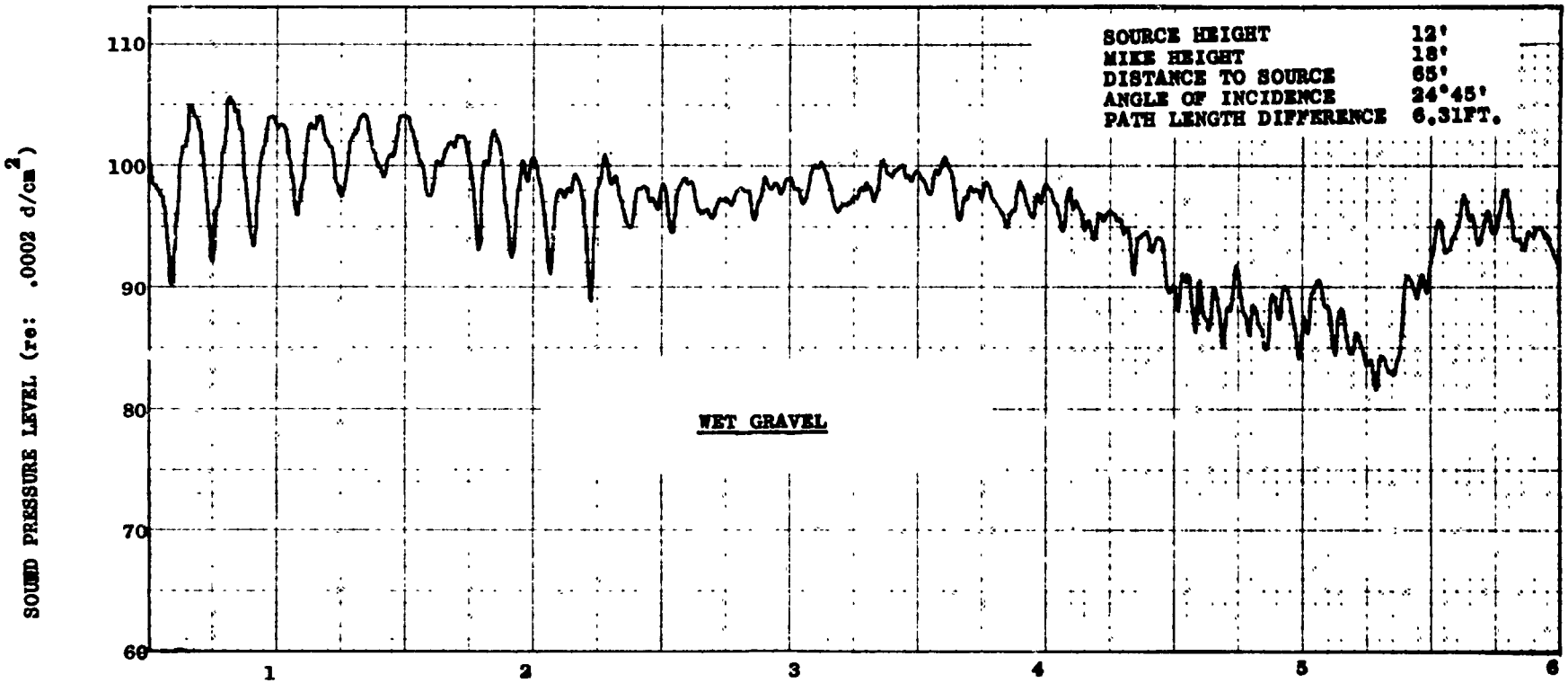

FIGURE VI-B22 SPL vs. FREQUENCY - GROUND REFLECTION TESTS CONFIGURATION A, MIKE #3

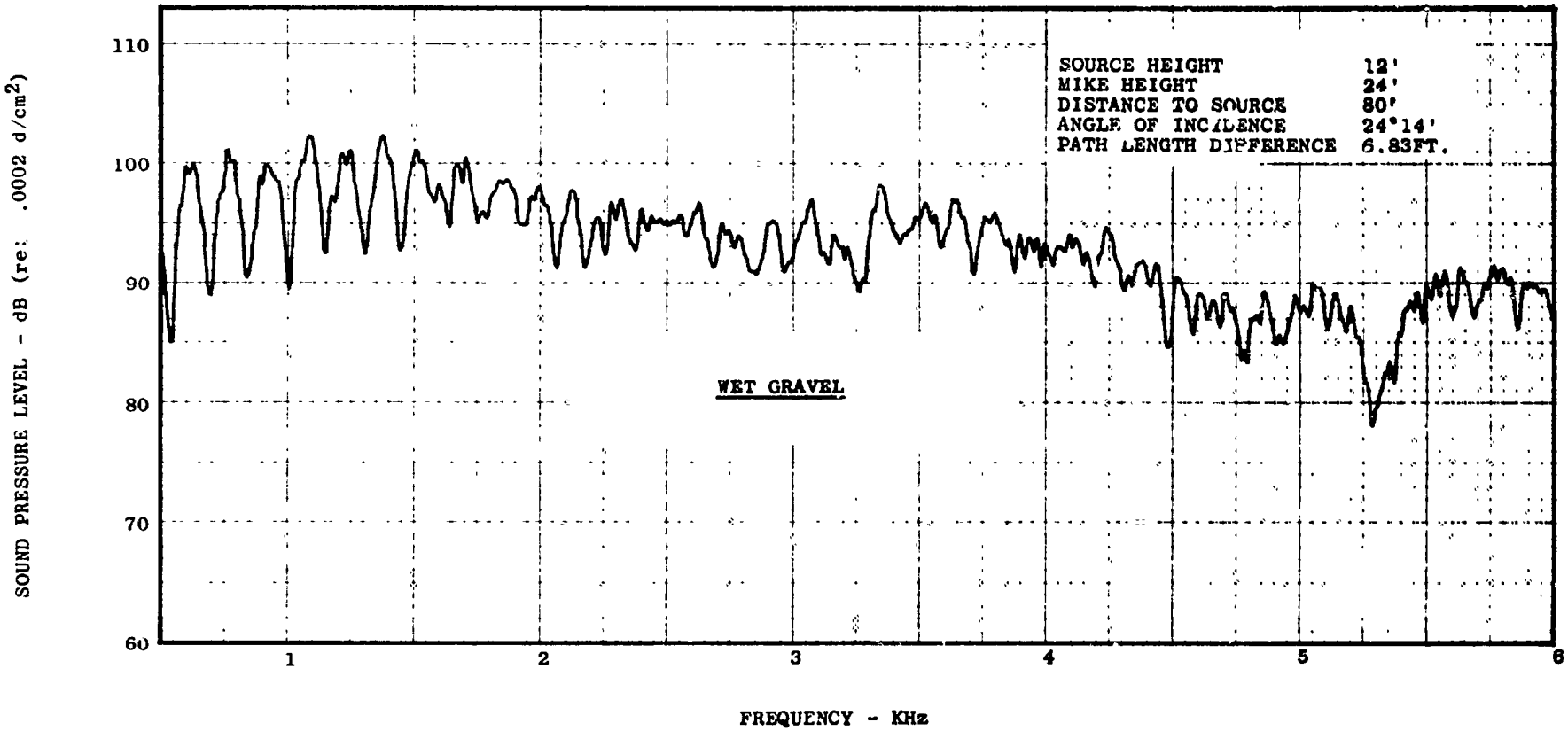

FIGURE VI-B23 SPL vs. FREQUENCY - GROUND REFLECTION TESTS CONFIGURATION A, MIKE #4

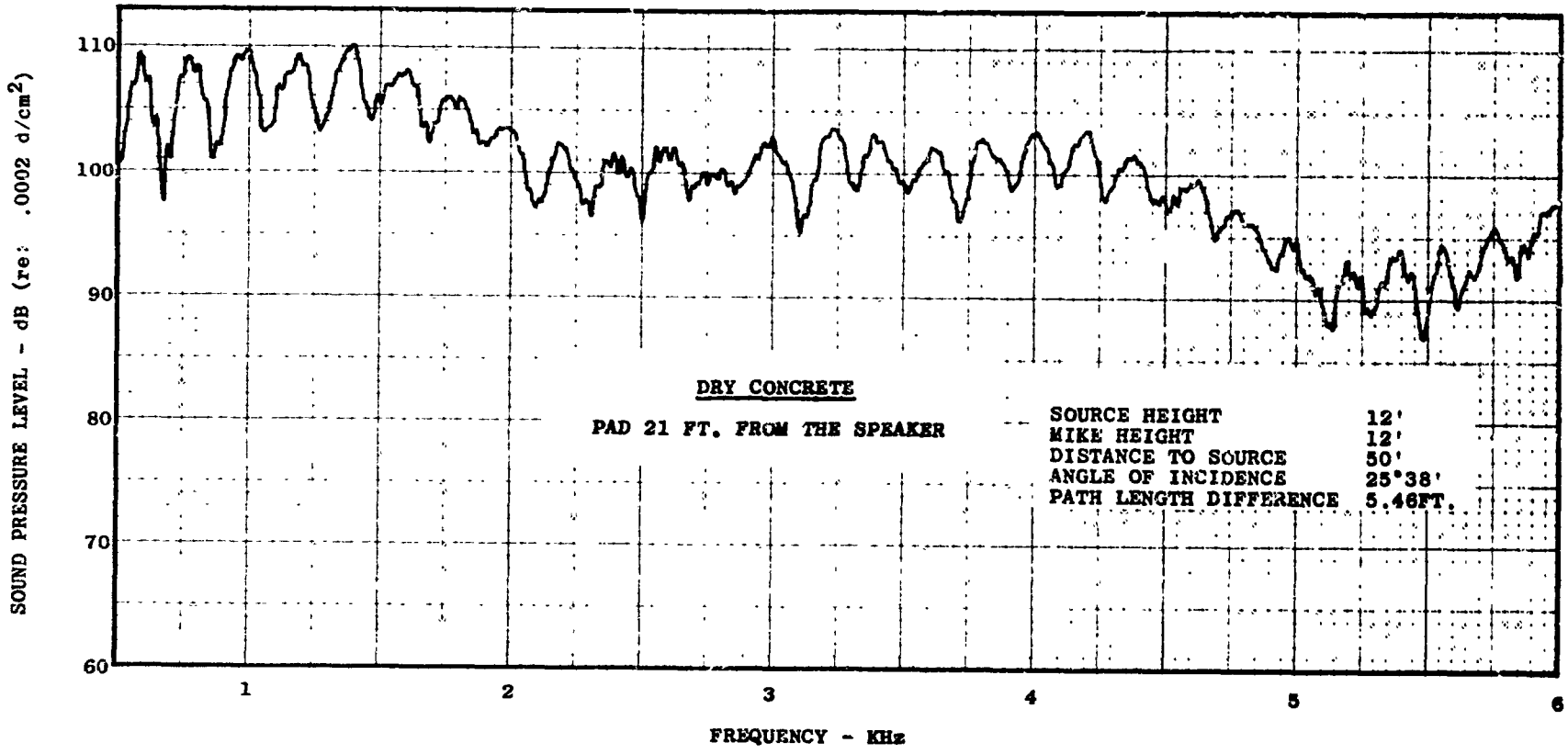

FIGURE VI-B24 SPL vs. FREQUENCY - GROUND REFLECTION TESTS CONFIGURATION A, MIKE #2

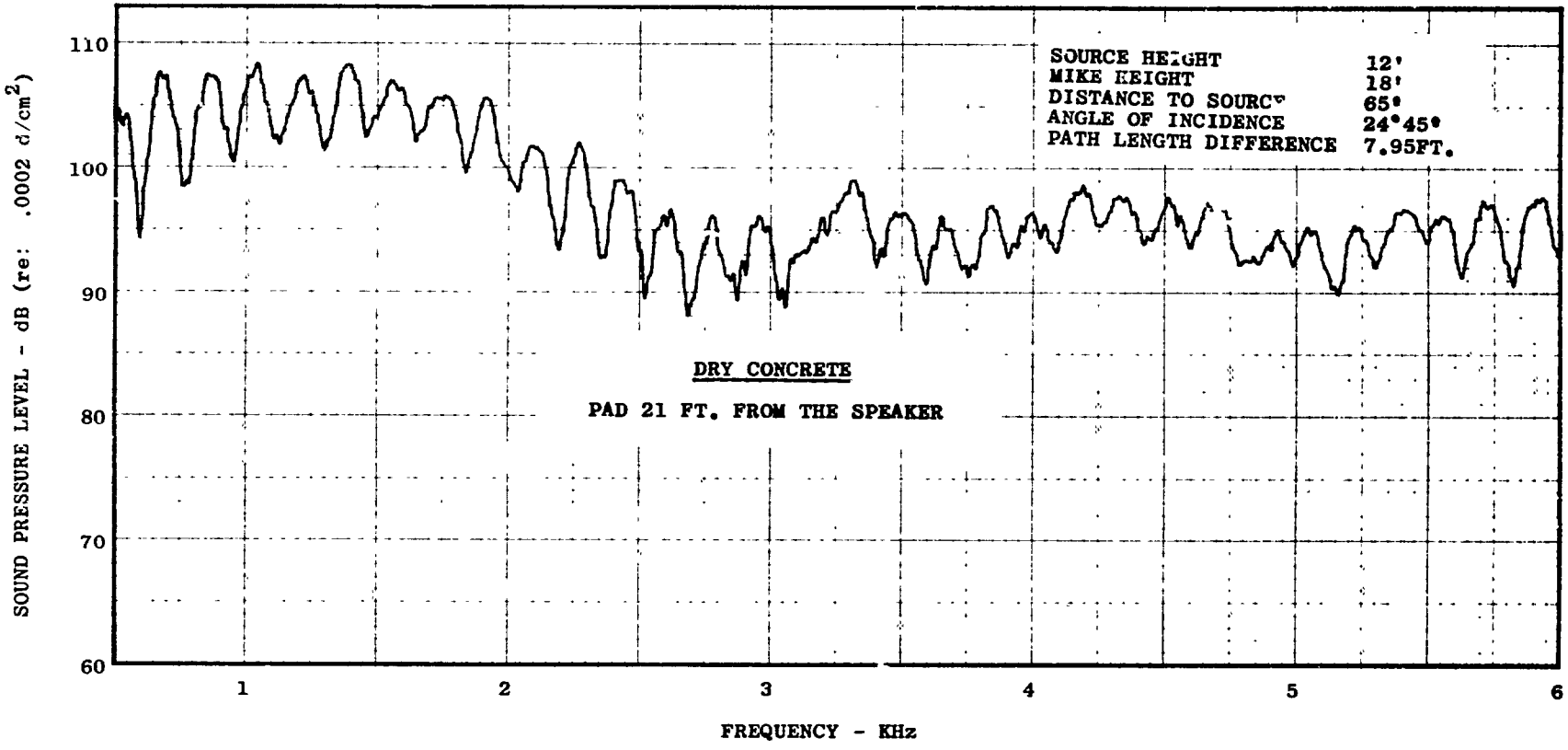

FIGURE VI-B25 SPL vs. FREQUENCY - GROUND REFLECTION TESTS CONFIGURATION A, MIKE #3

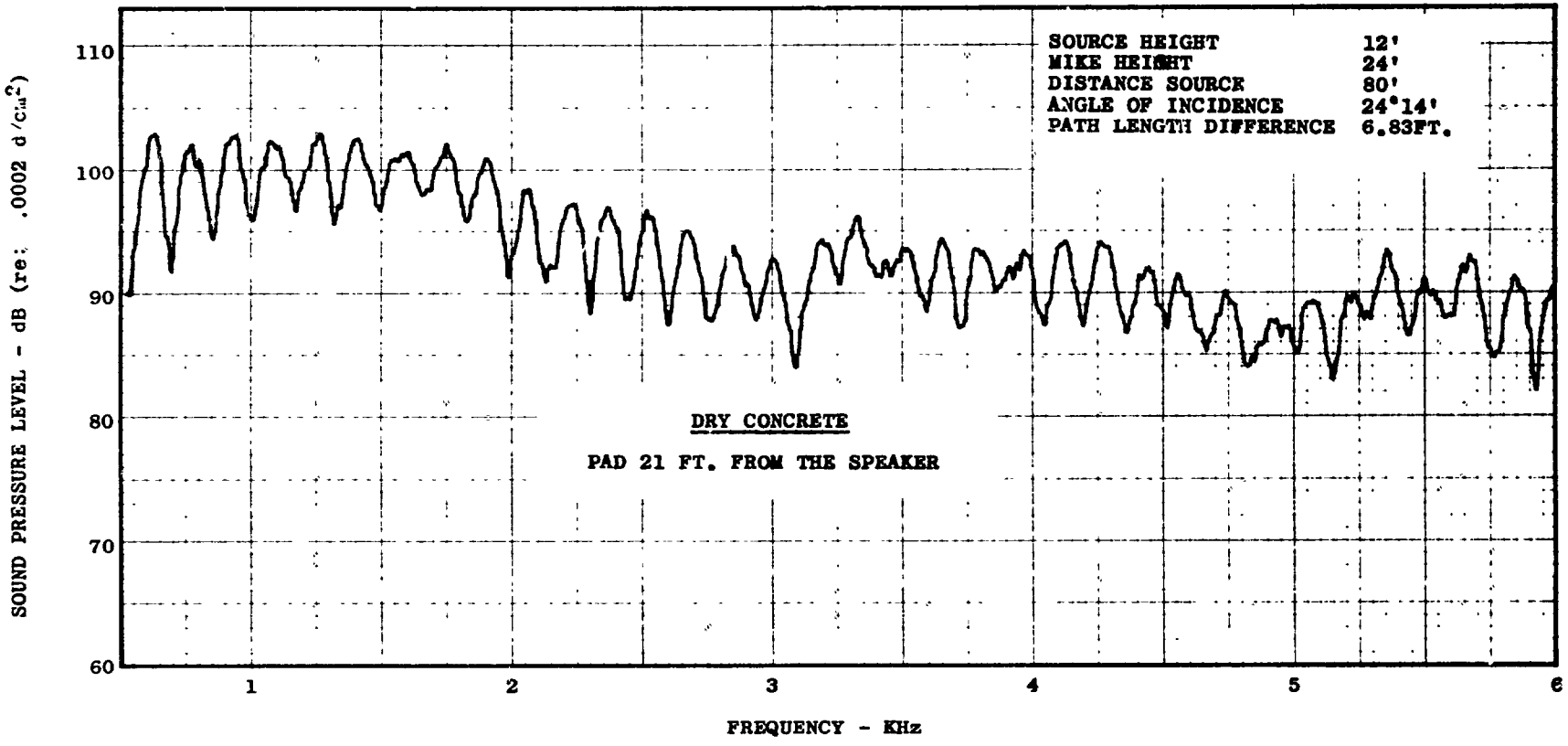

FIGURE VI-B26 SPL vs. FREQUENCY - GROUND REFLECTION TESTS CONFIGURATION A, MIKE #4

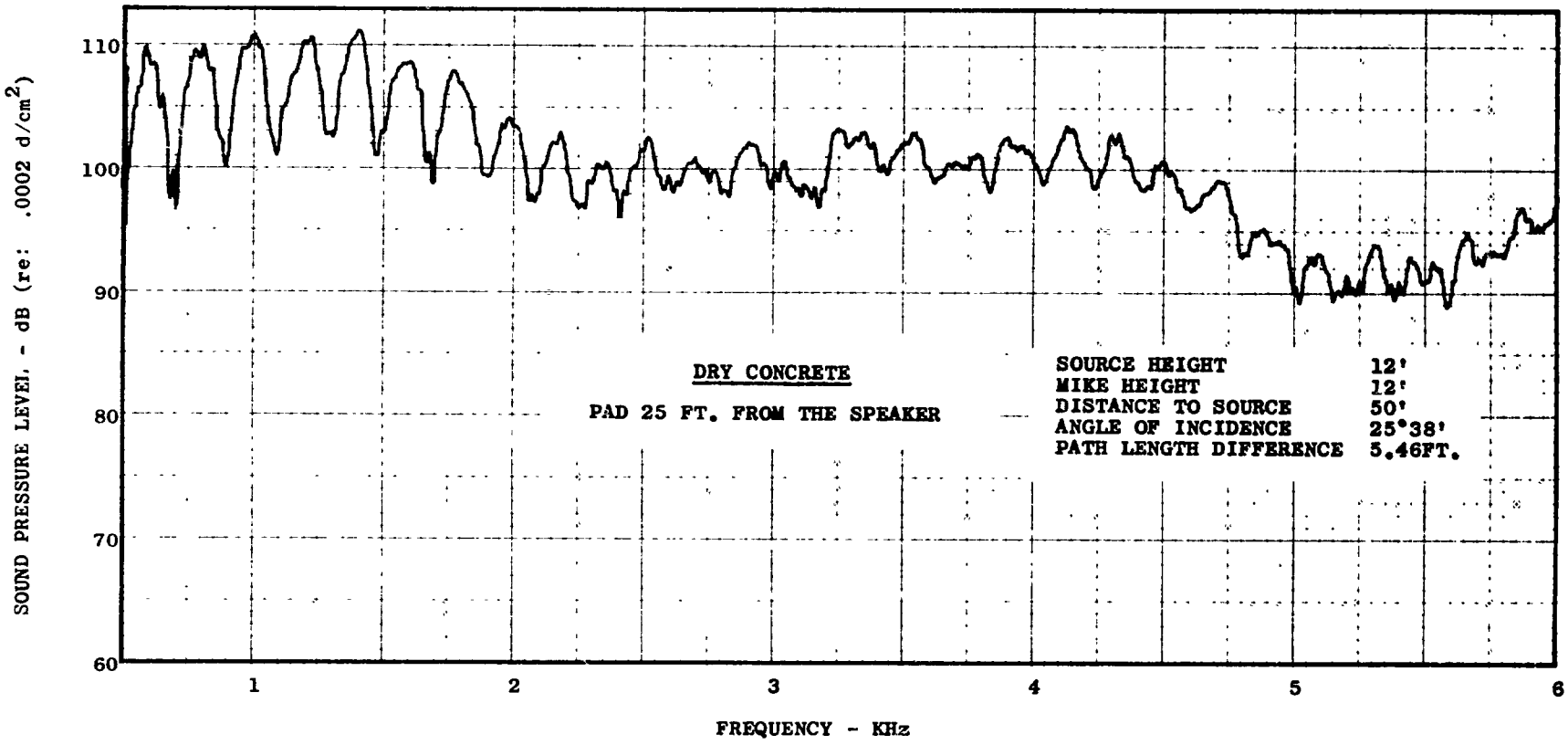

FIGURE VI-B27 SPL vs. FREQUENCY - GROUND REFLECTION TESTS CONFIGURATION A, MIKE #2

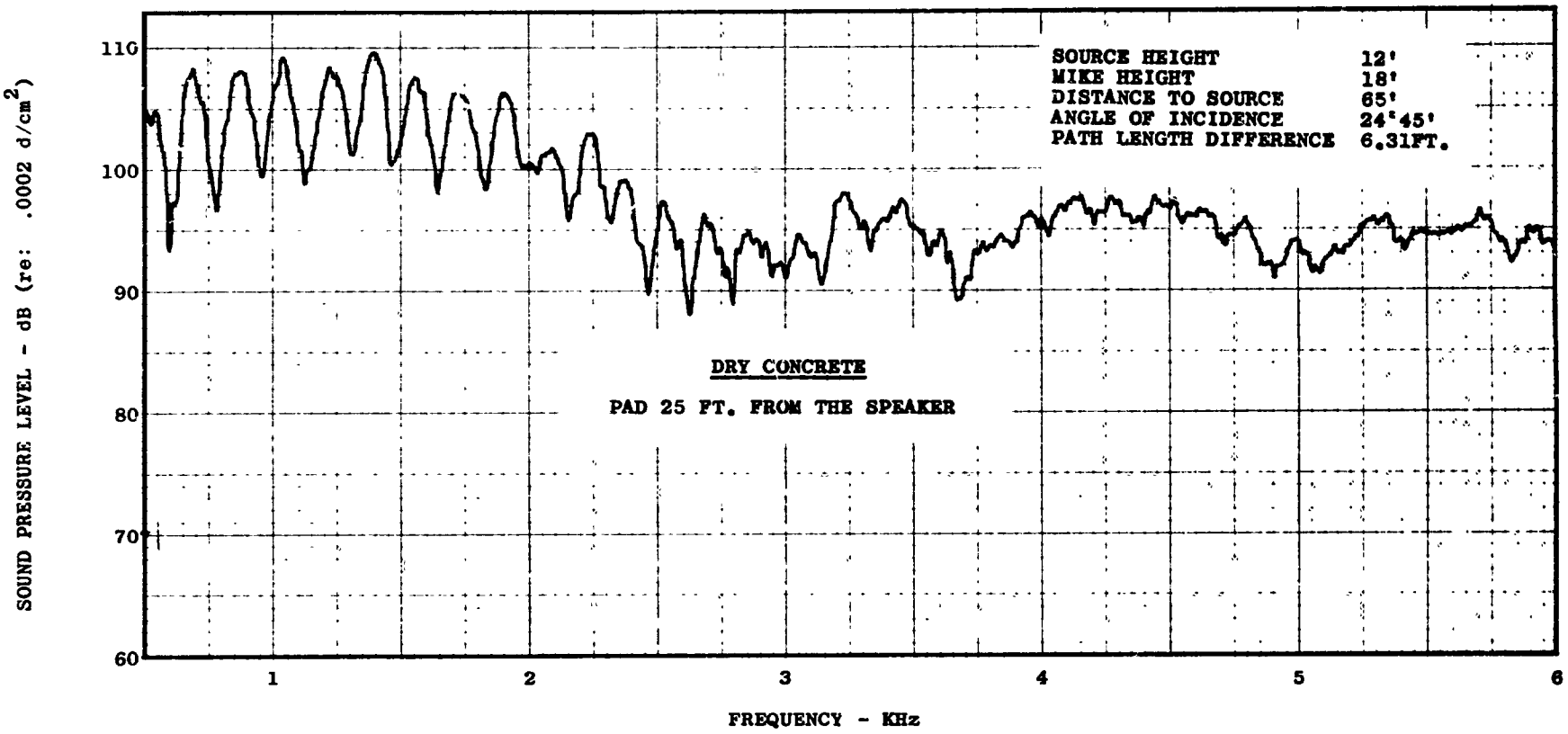

FIGURE VI-B28 SPL vs. FREQUENCY - GROUND REFLECTION TESTS CONFIGURATION A, MIKE #3

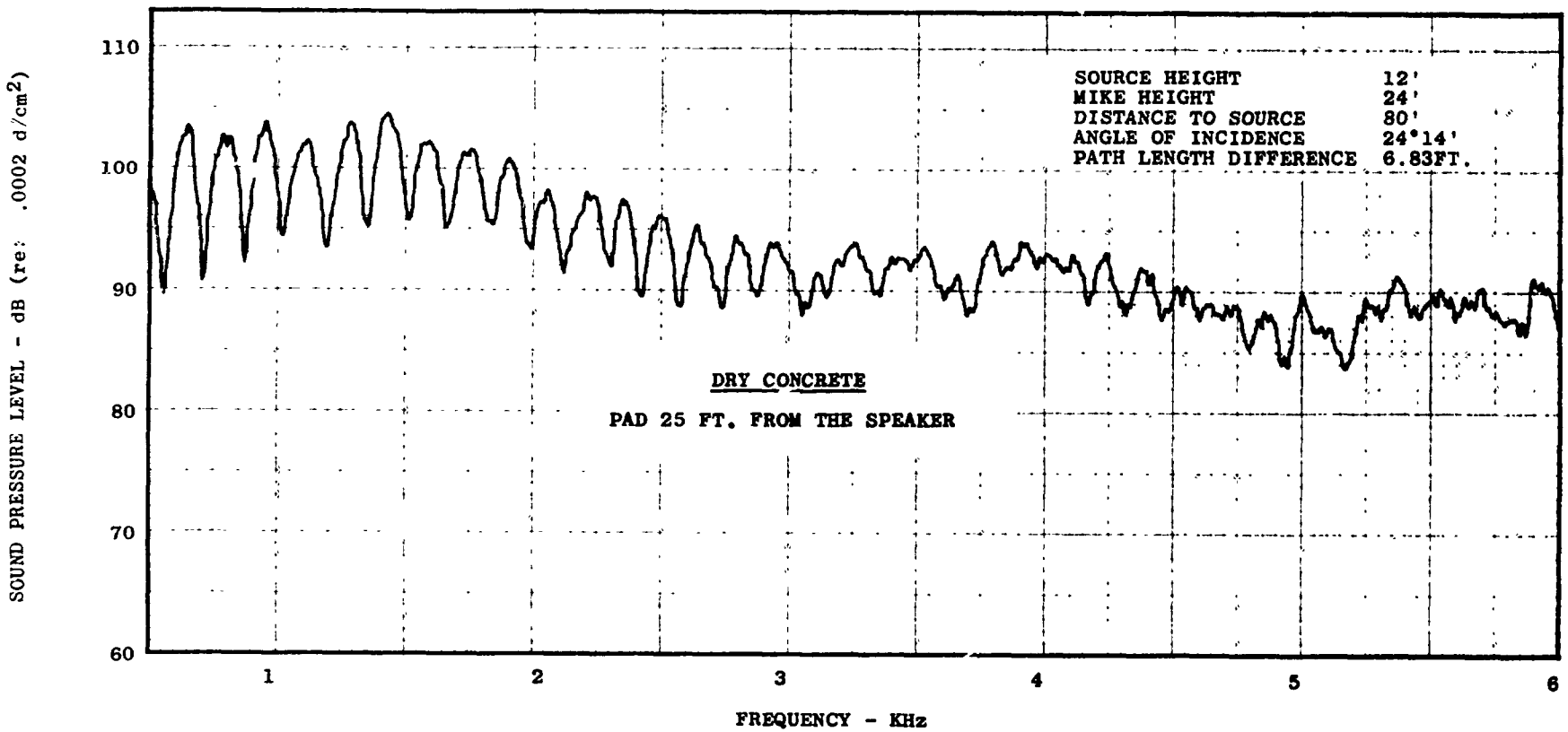

FIGURE VI-B29 SPL vs. FREQUENCY - GROUND REFLECTION TESTS CONFIGURATION A, MIKE #4

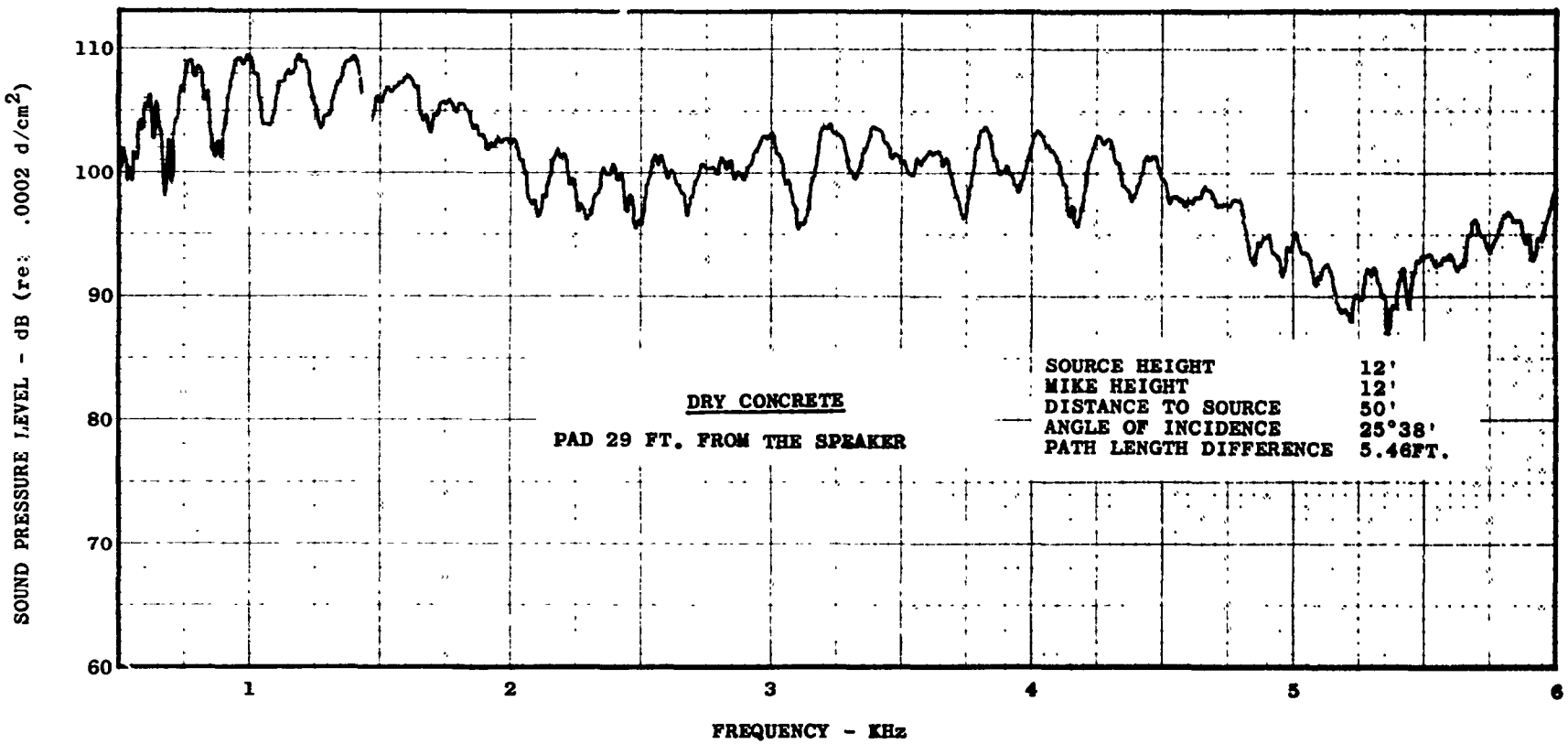

FIGURE VI-B30 SPL vs. FREQUENCY - GROUND REFLECTION TESTS CONFIGURATION A, MIKE #2

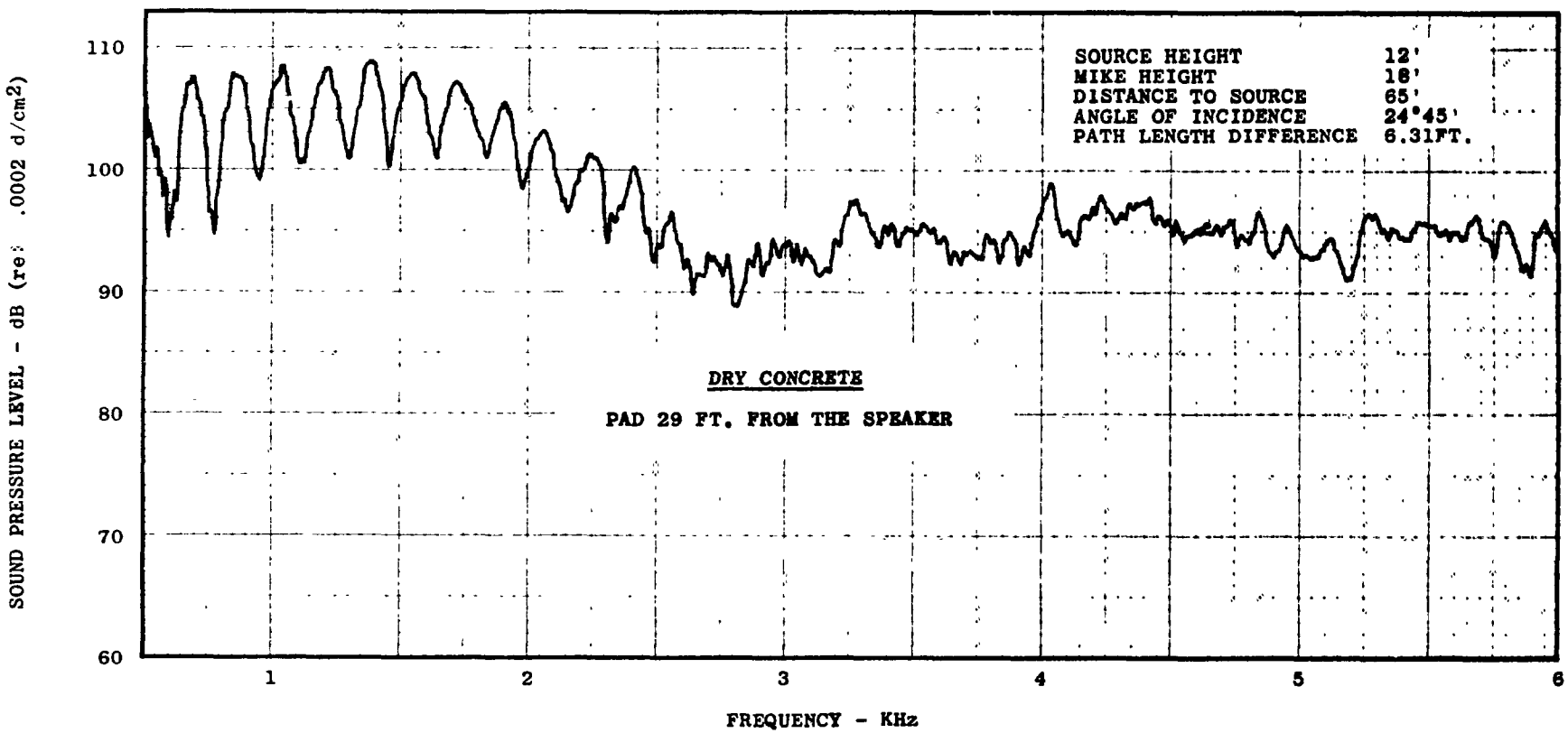

FIGURE VI-B31 SPL vs. FREQUENCY - GROUDN REFLECTION TESTS CONFIGURATION A, MIKE #3

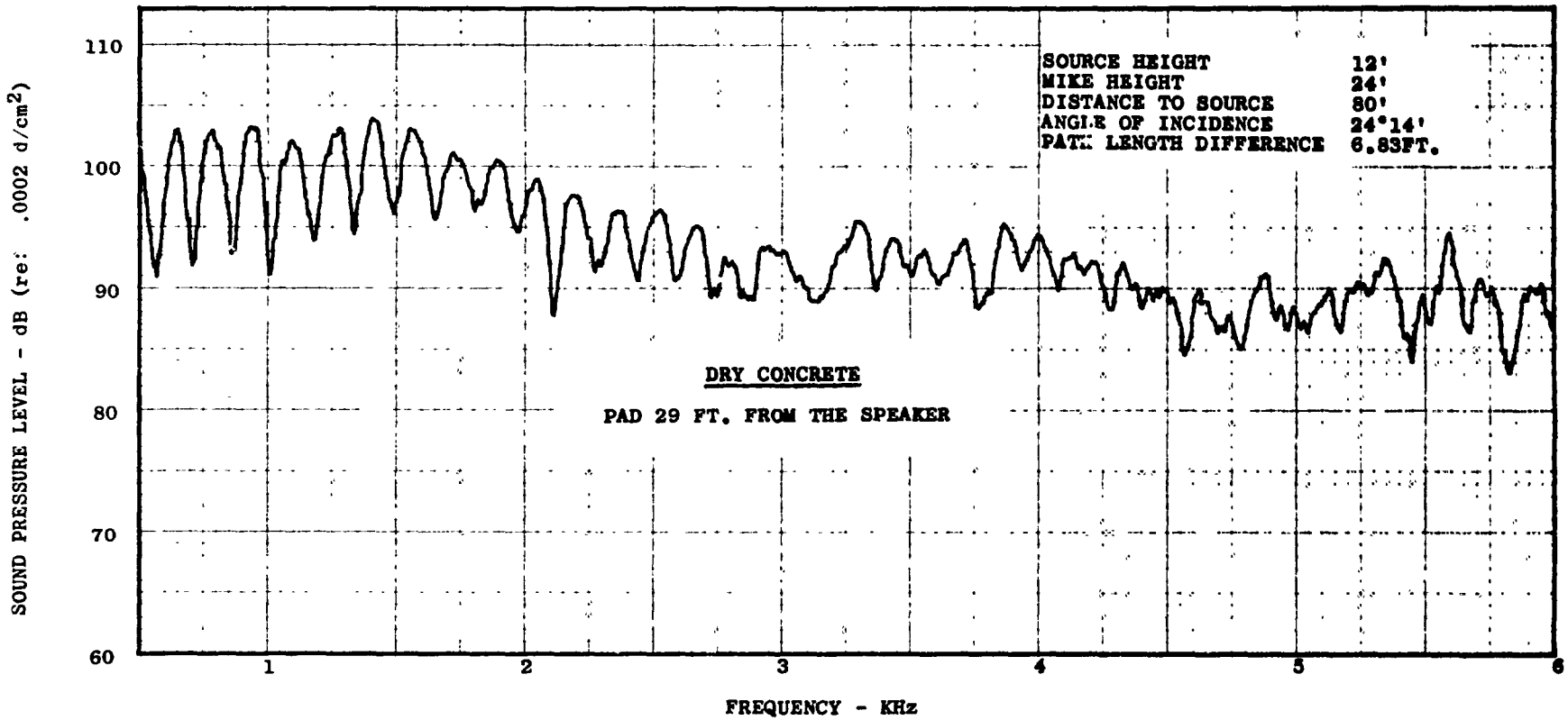

FIGURE VI-B32 SPL vs. FREQUENCY - GROUND REFLECTION TESTS CONFIGURATION A; MIKE #4

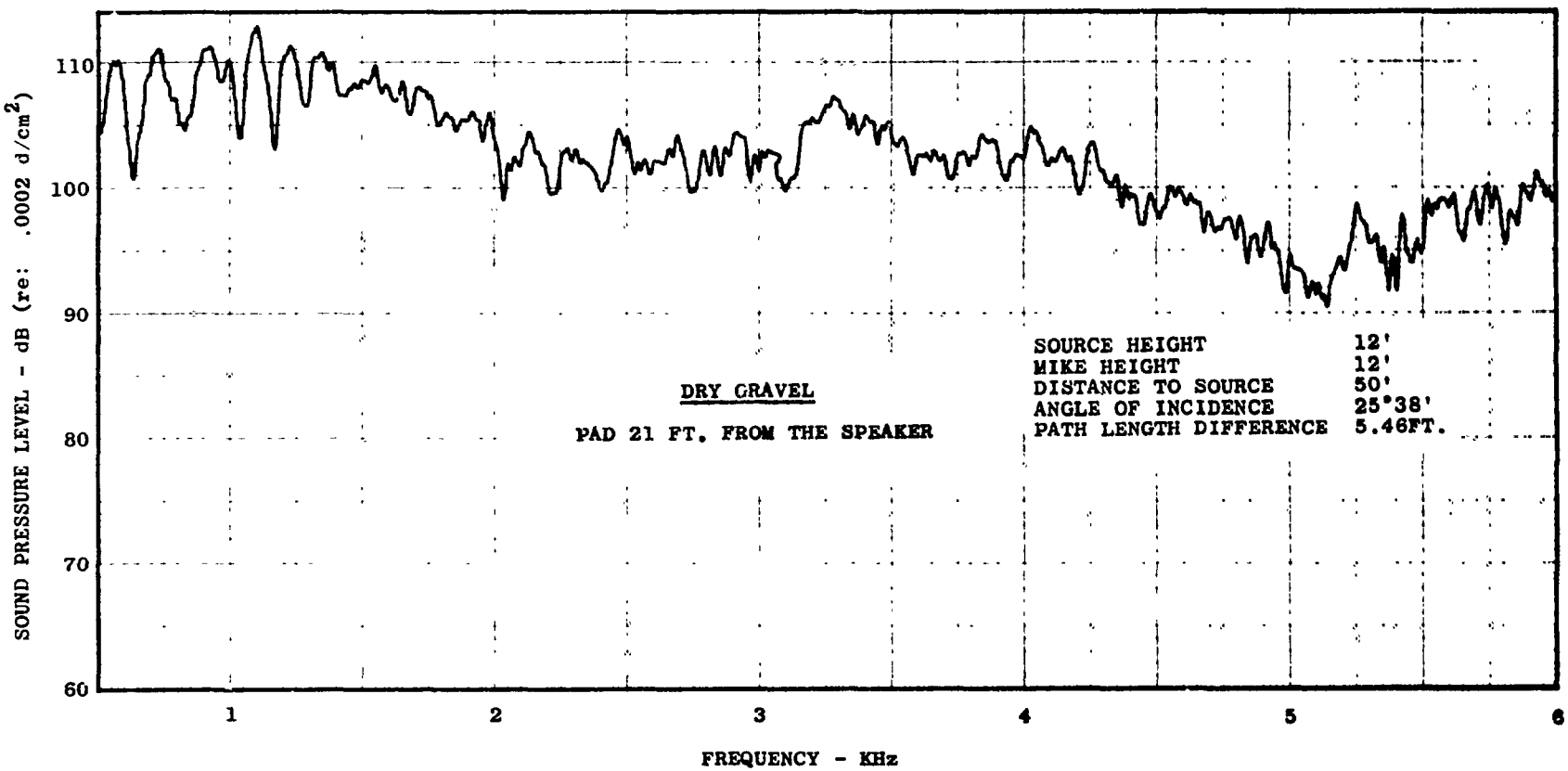

FIGURE VI-B33 SPL vs. FREQUENCY - GROUND REFLECTION TESTS CONFIGURATION A, MIKE #2

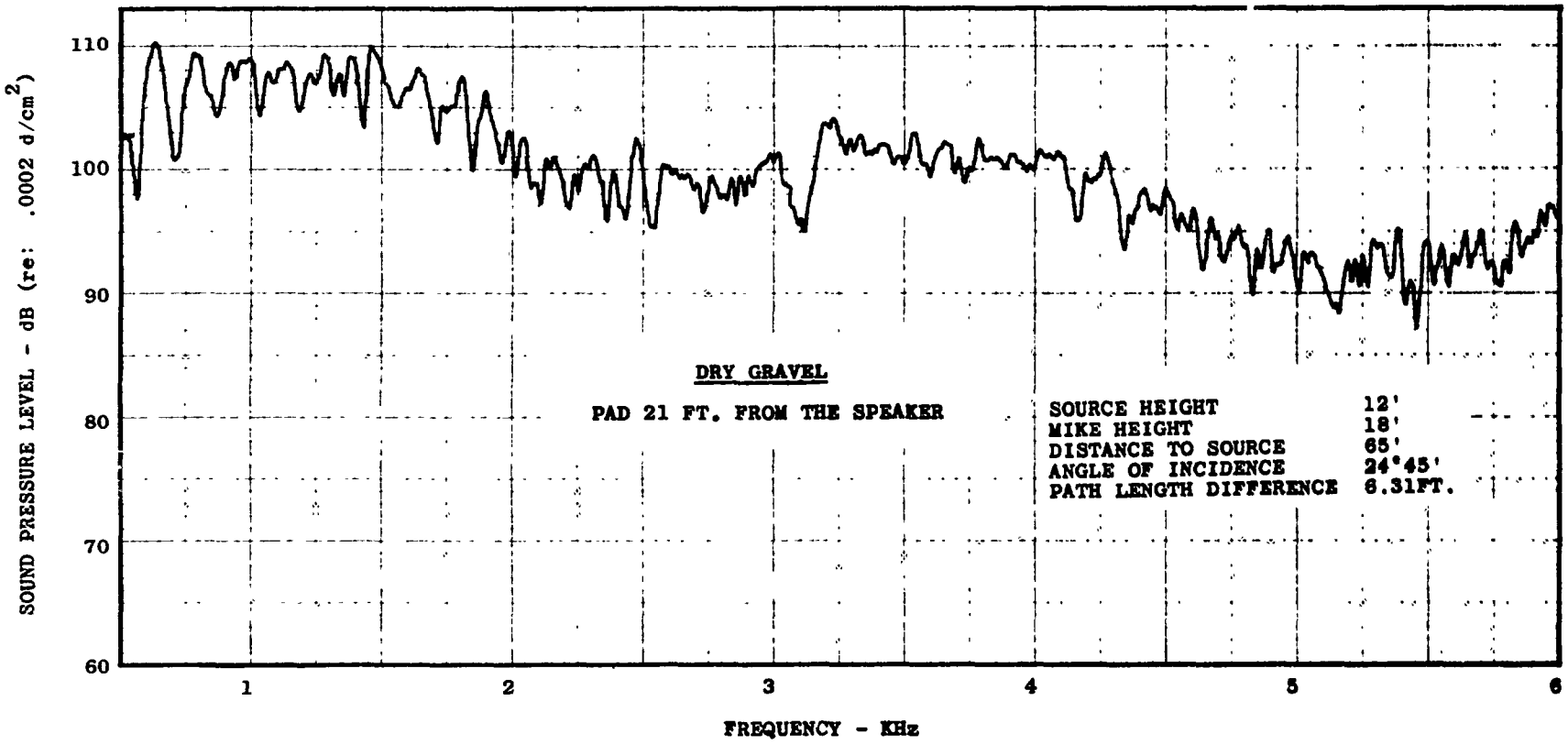

FIGURE VI-B34 SPL vs. FREQUENCY - GROUND REFLECTION TESTS CONFIGURATION A, MIKE #3

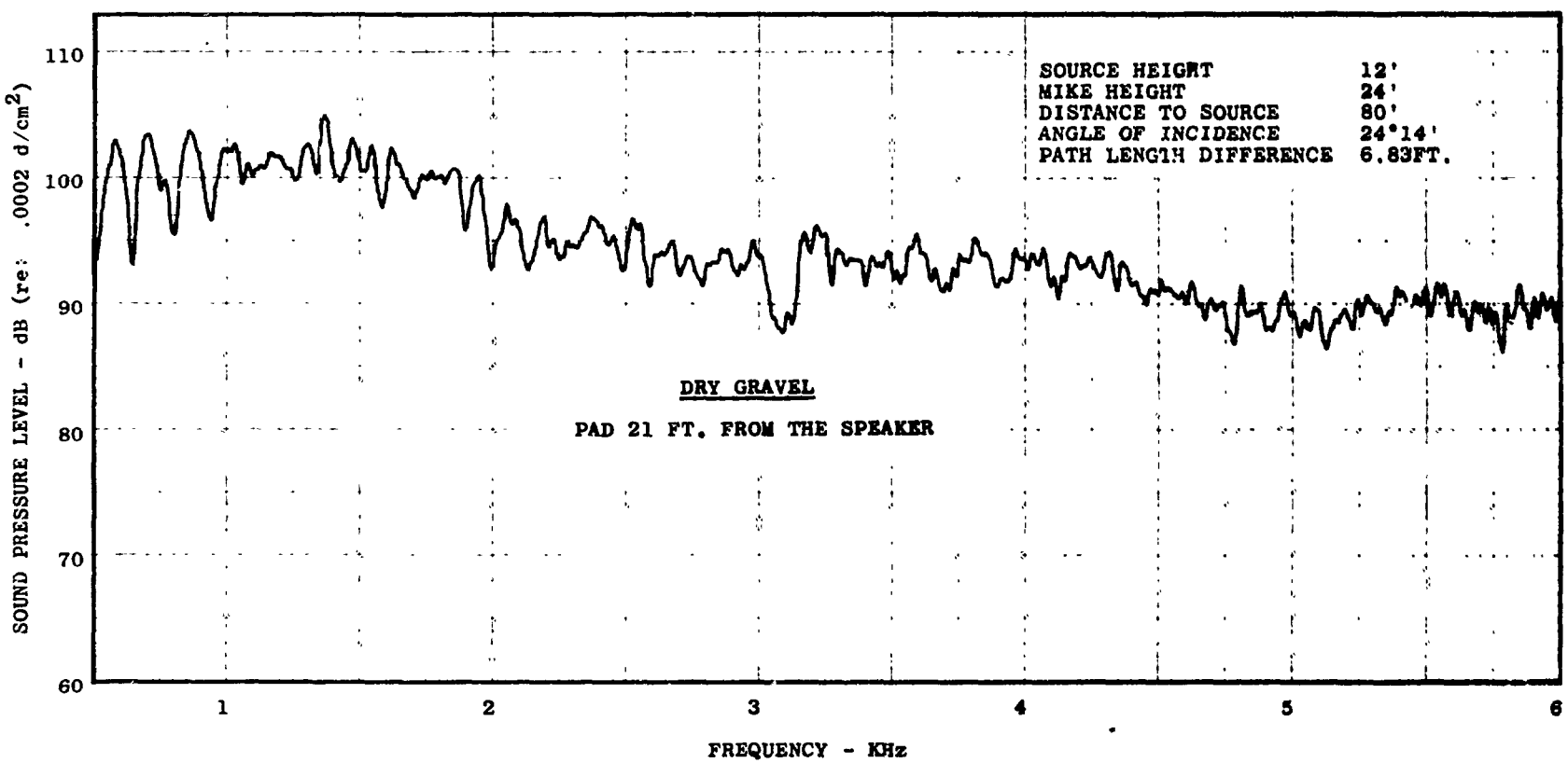

FIGURE VI-B35 SPL vs. FREQUENCY - GROUND REFLECTION TESTS CONFIGURATION A, MIKE #4

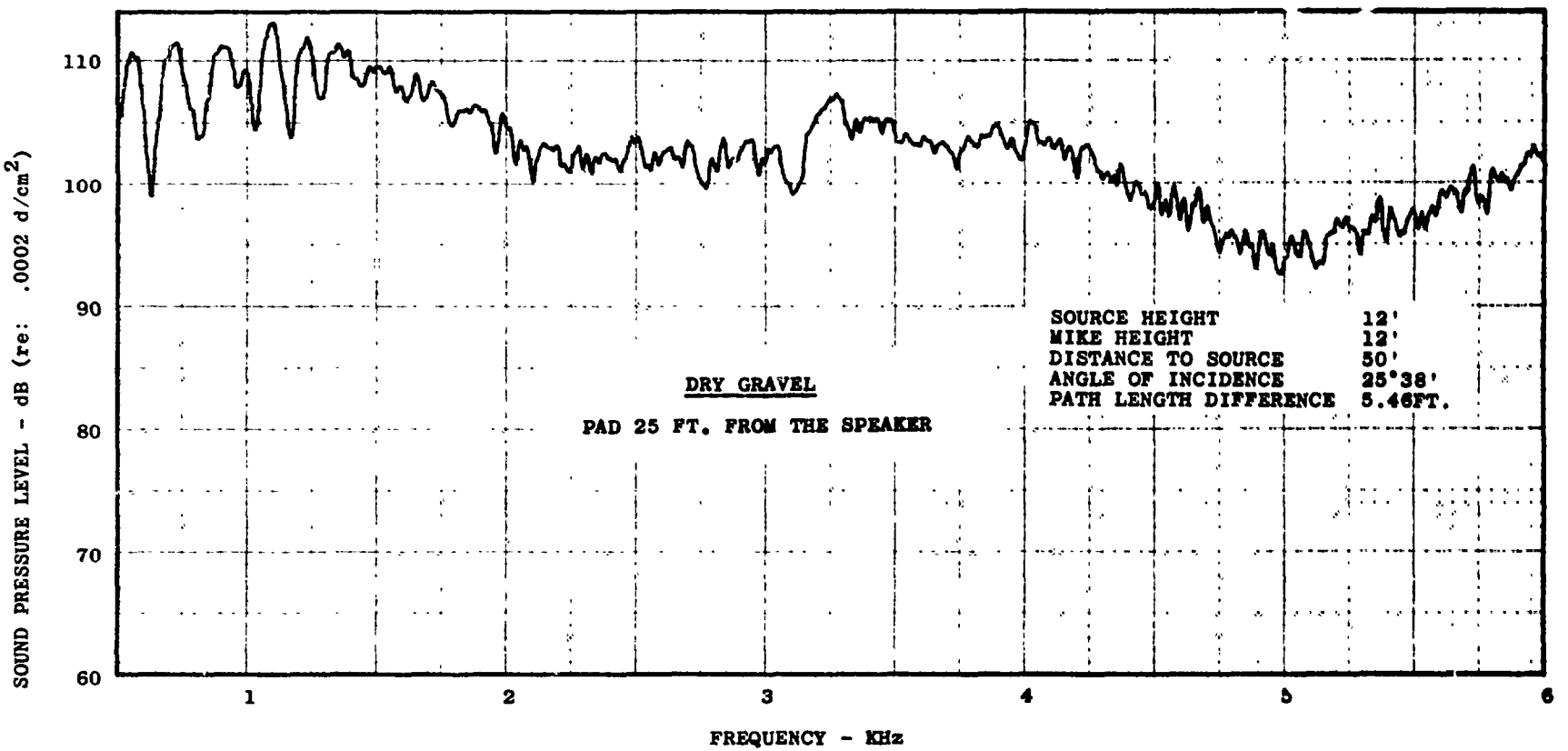

FIGURE VI-B36 SPL vs. FRIQUENCY - GROUND REFLECTION TESTS CONFIGURATION A, MIKE #2

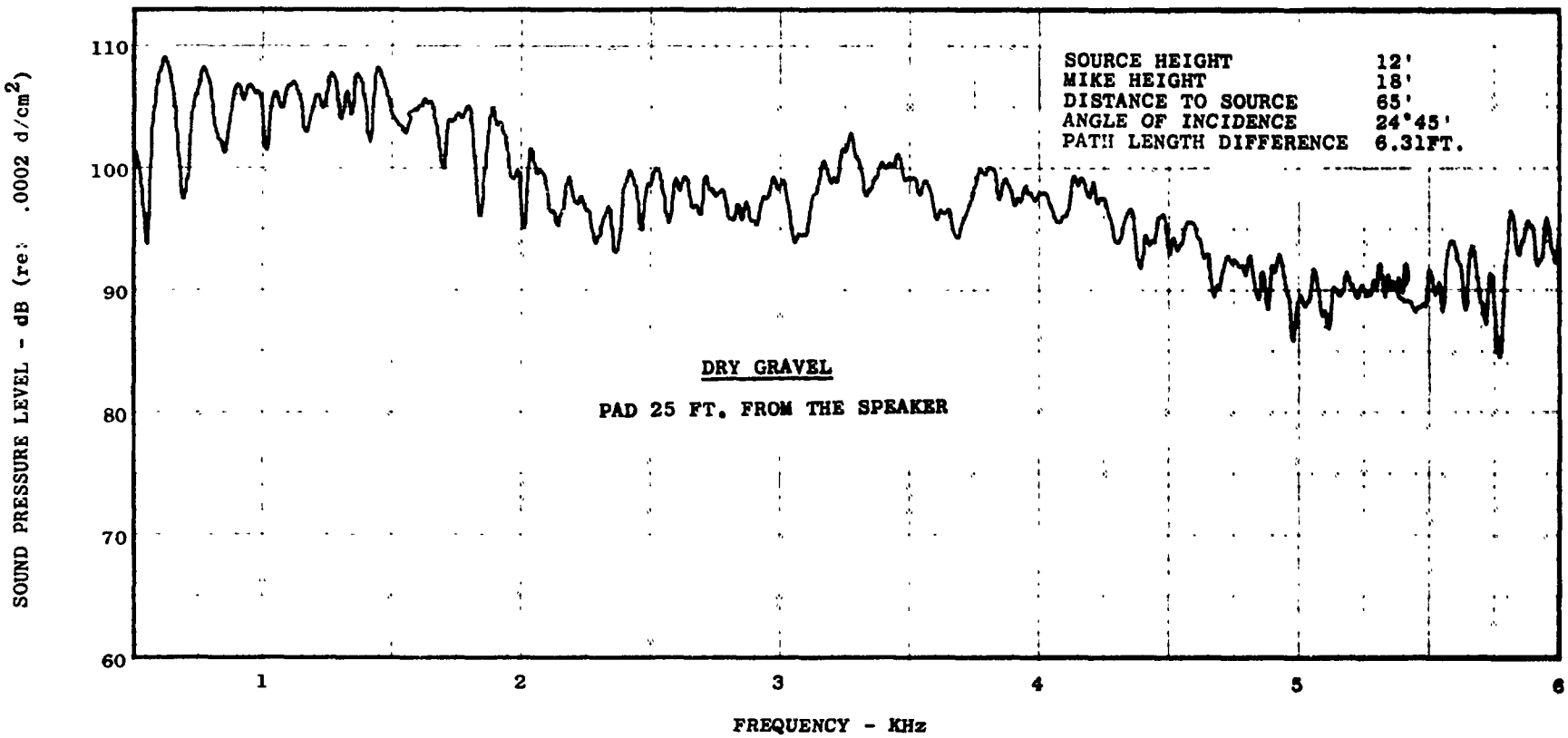

FIGURE VI-B37 SPL s. FREQUENCY - GROUND REFLECTION TESTS CONFIGURATION A, MIKE #3

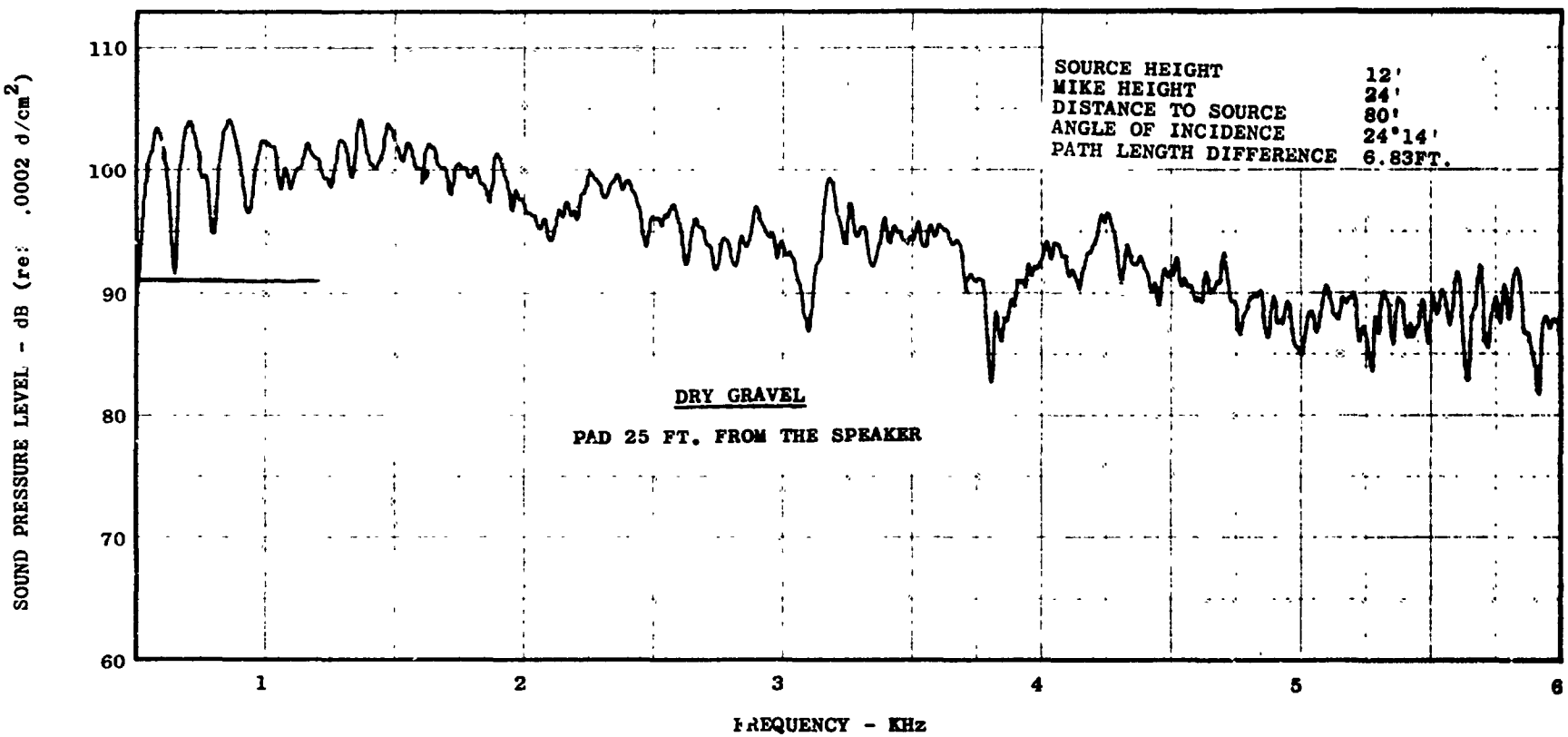

FIGURE VI-B38 SPL vs. FREQUENCY - GROUND REFLECTION TESTS CONFIGURATION A, MIKE #4

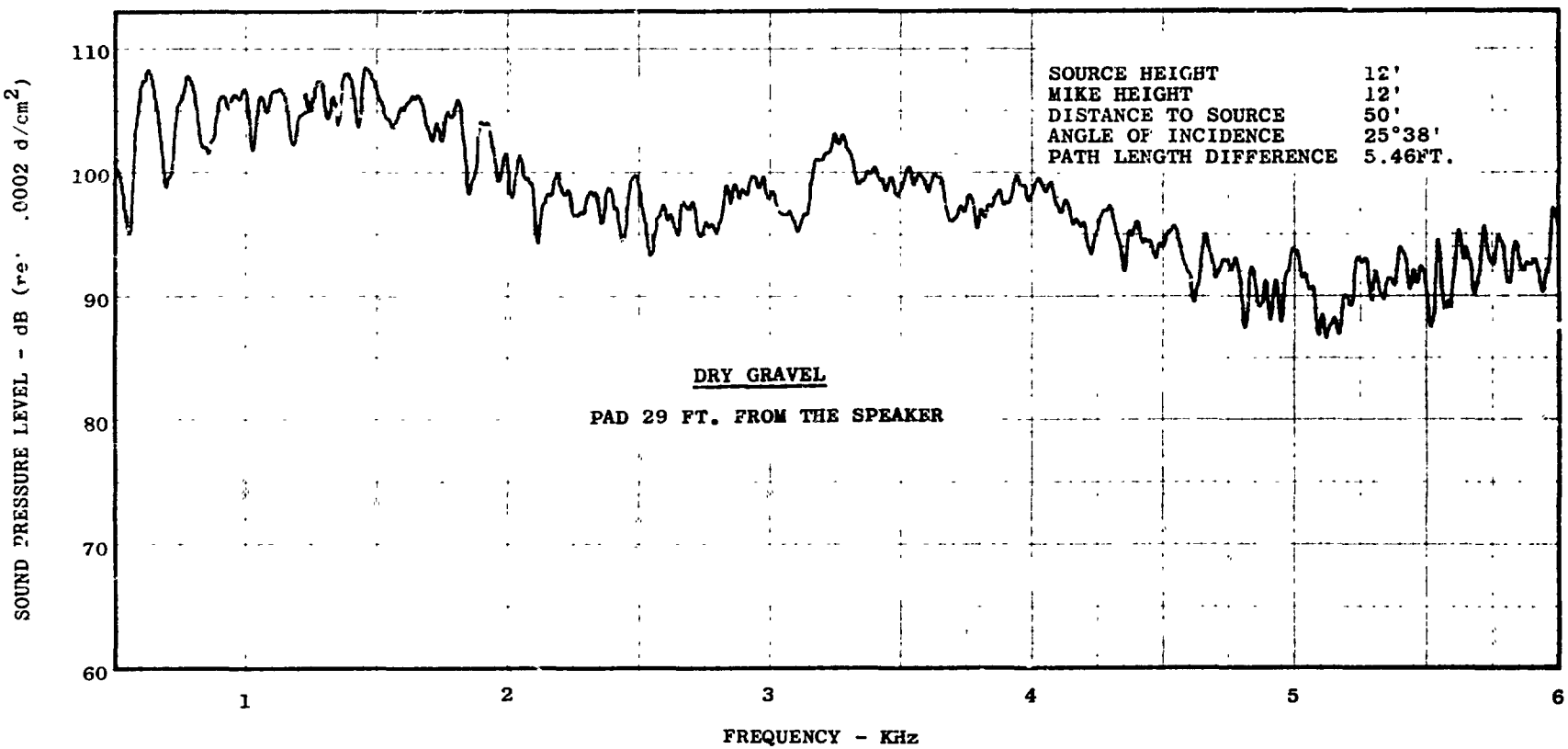

FIGURE VI-39 SPL vs. FREQUENCY - GROUND REFLECTION TESTS CONFIGURATION A, MIKE #2

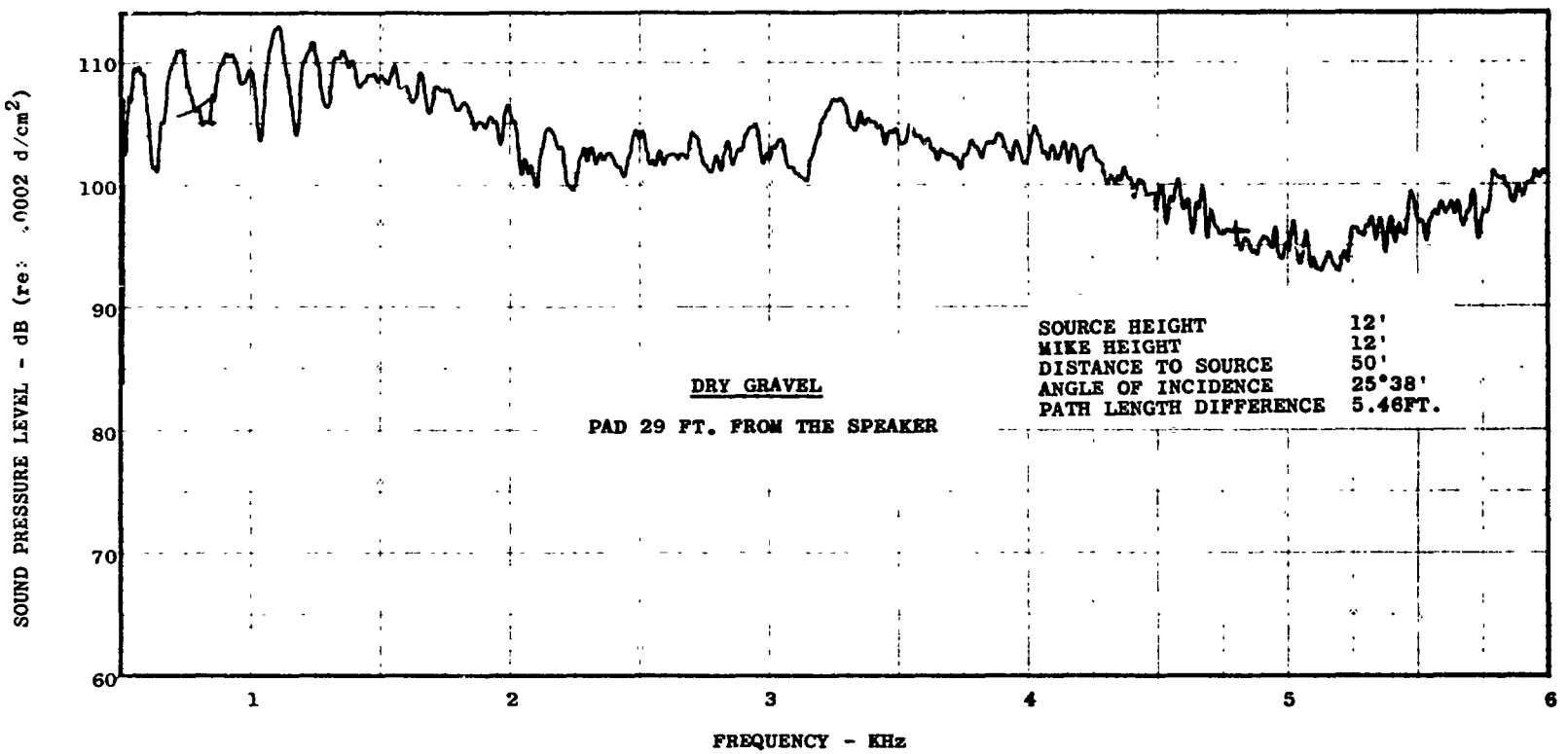

FIGURE VI-B40 SPL vs. FREQUENCY - GROUND REFLECTION TESTS CONFIGURATION A, MIKE #2

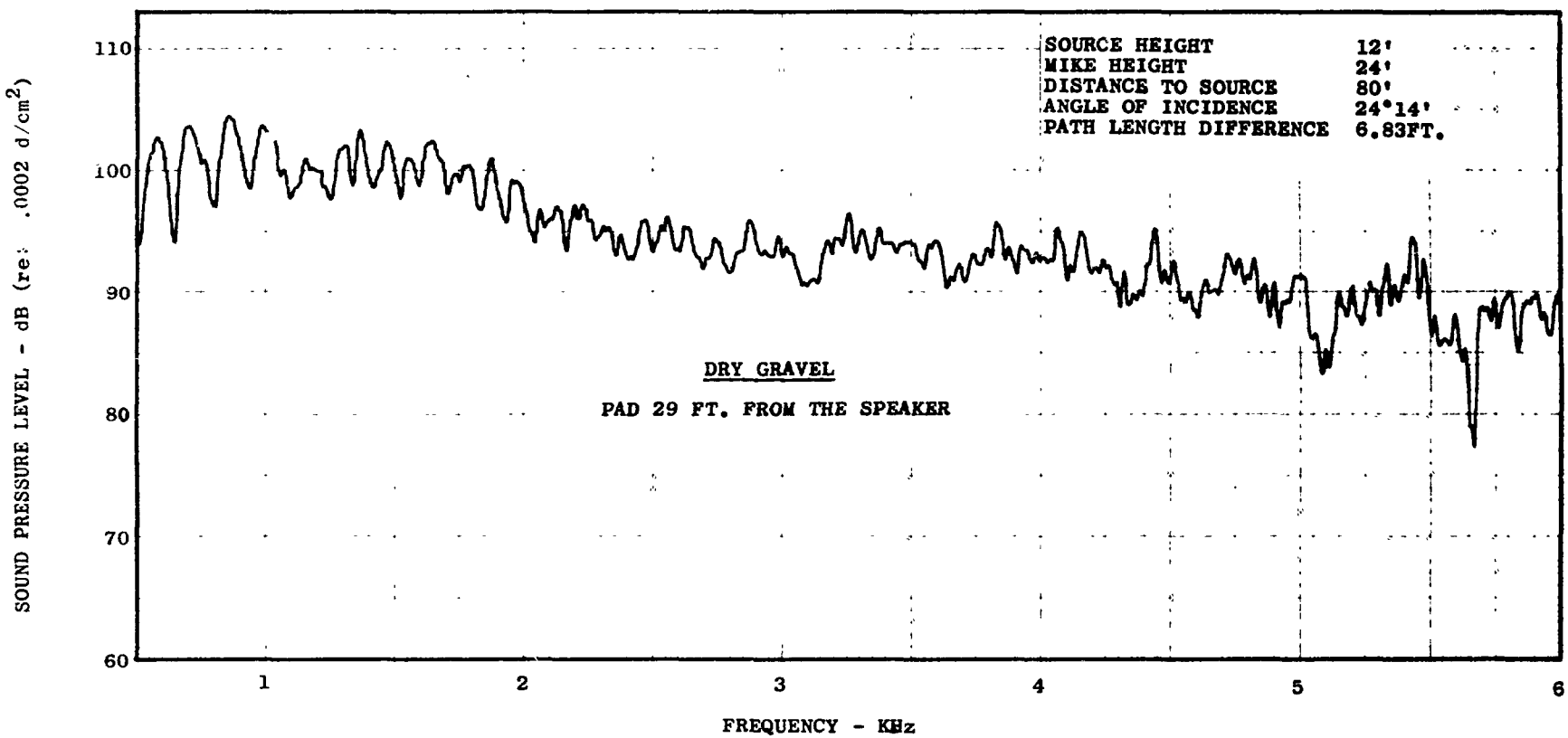

FIGURE VI-B41 SPL vs. FREQUENCY - GROUND REFLECTION TESTS CONFIGURATION A, MIKE #4

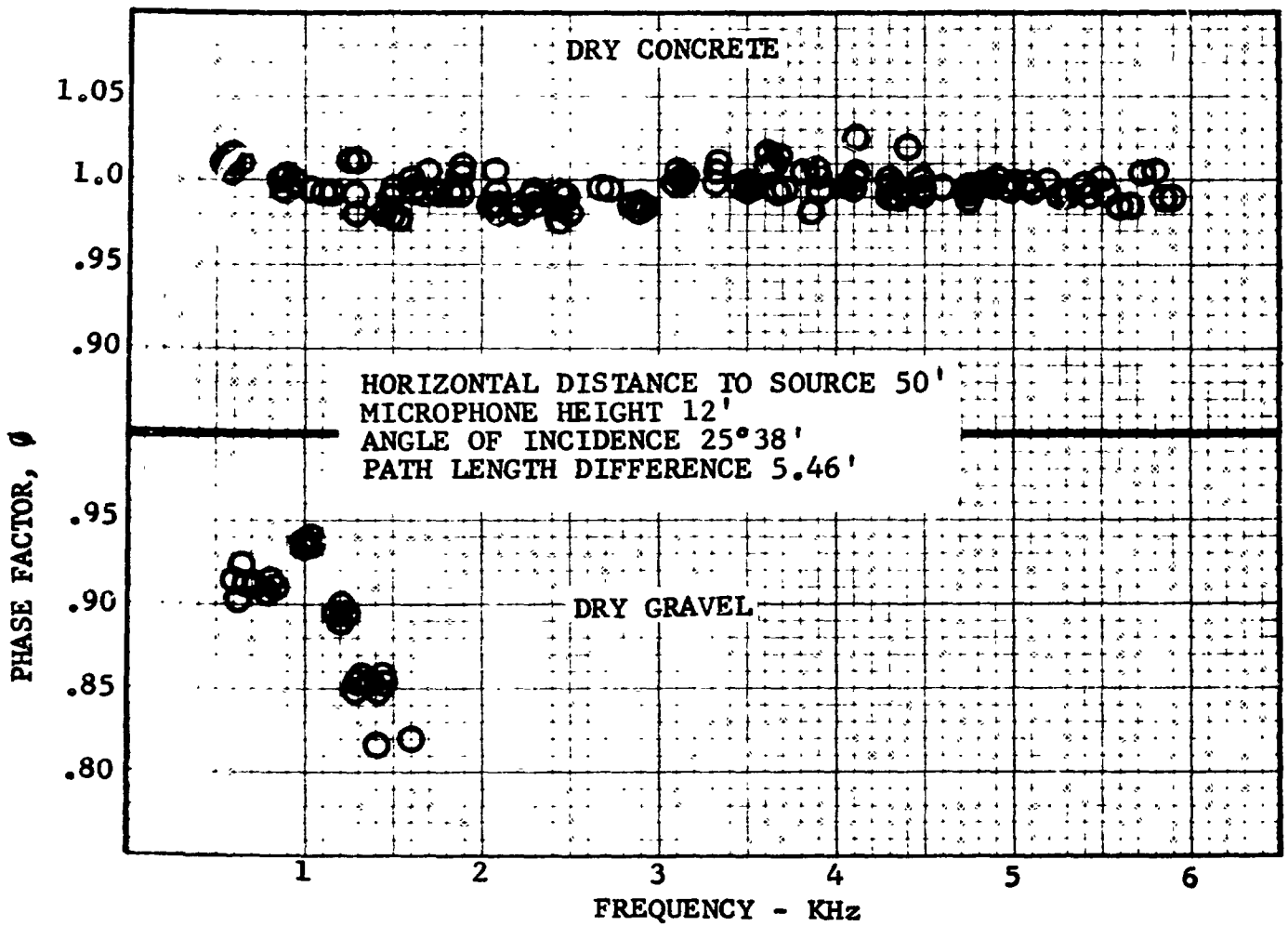

FIGURE VI-B42 OBSERVED PHASE FACTOR FOR DRY CONCRETE AND DRY GRAVEL

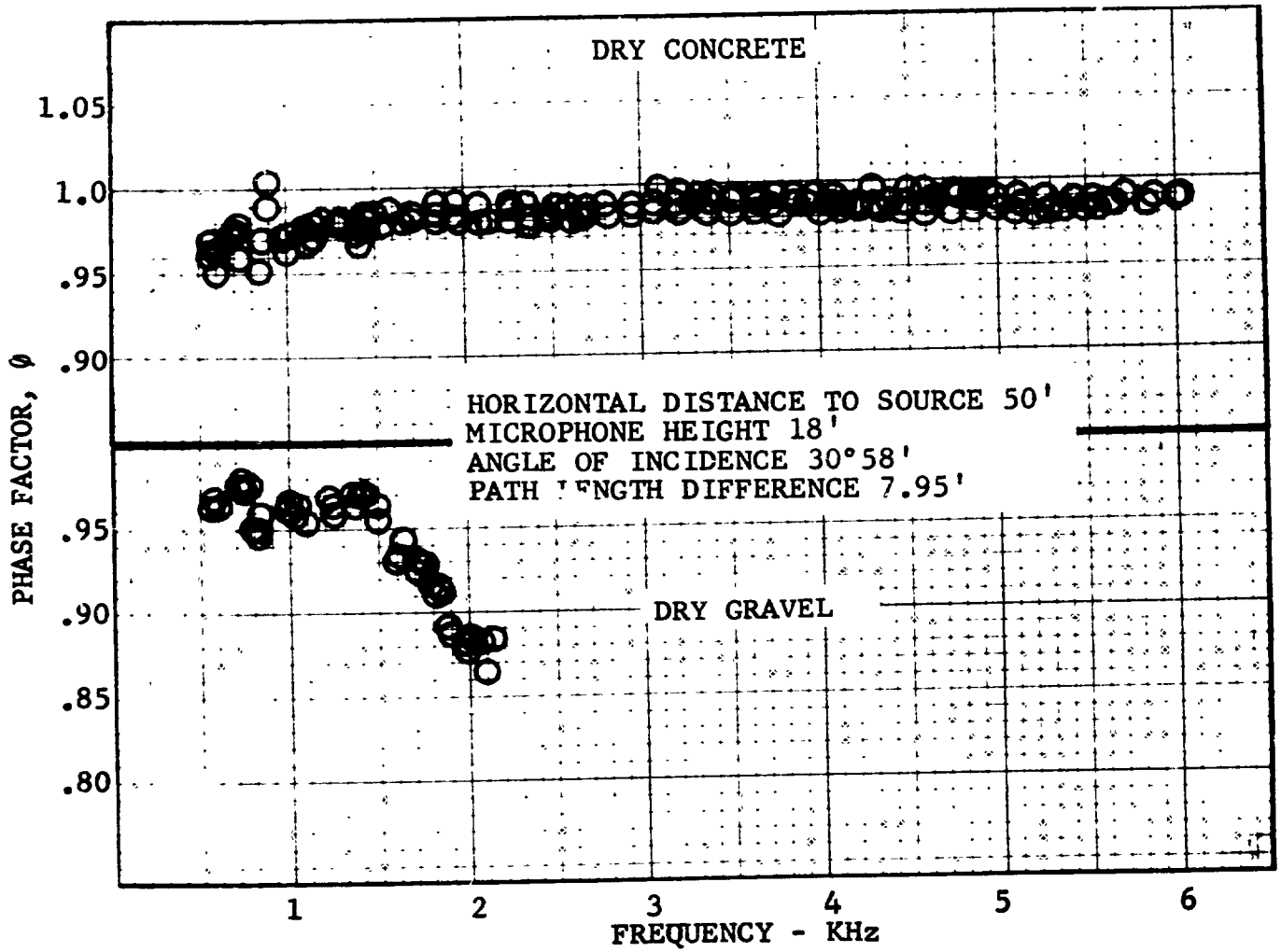

FIGURE VI-B43 OBSERVED PHASE FACTOR FOR DRY CONCRETE AND DRY GRAVEL

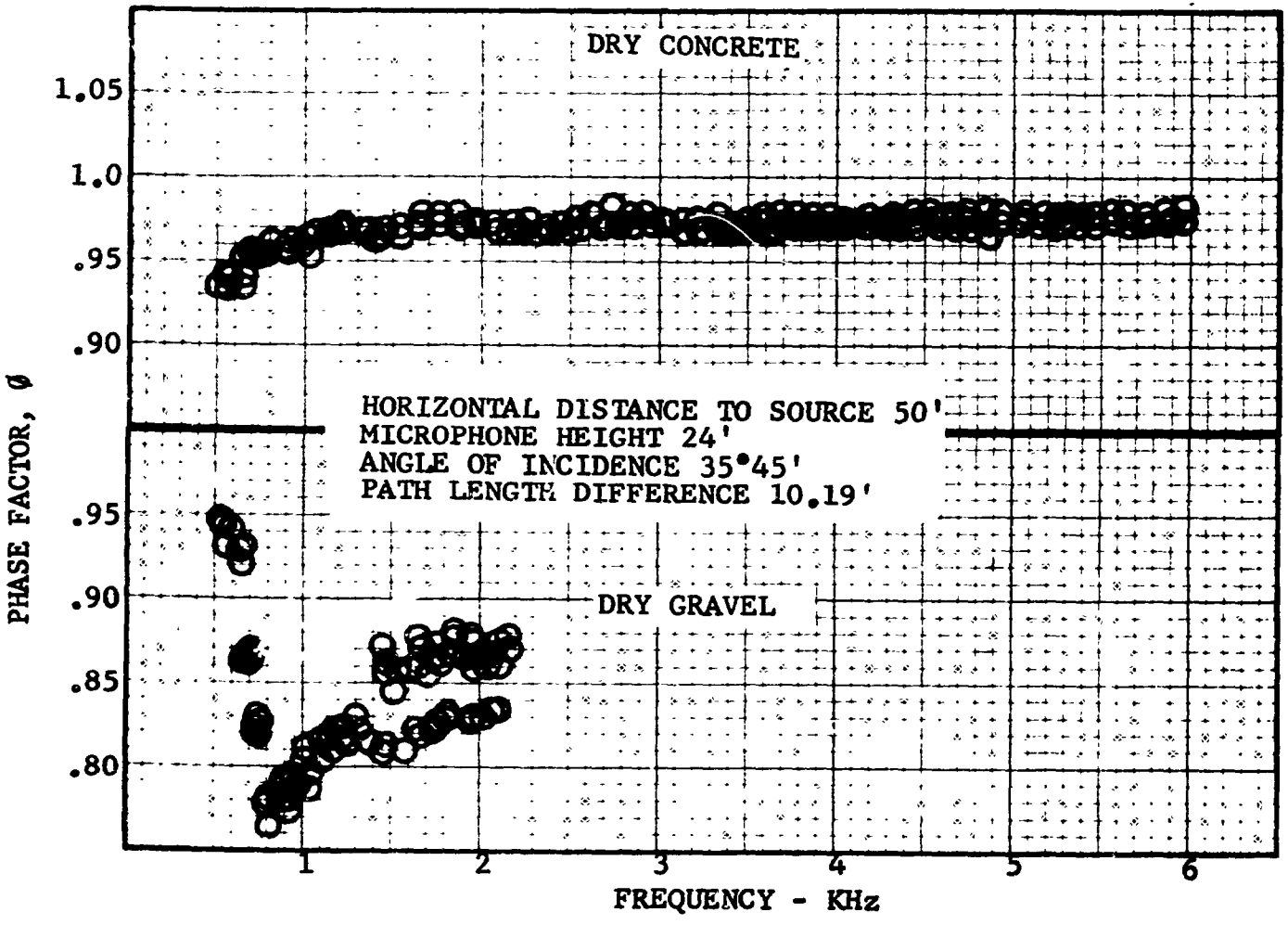

FIGURE VI-B44 OBSERVED PHASE FACTOR FOR DRY CONCRETE AND DRY GRAVEL

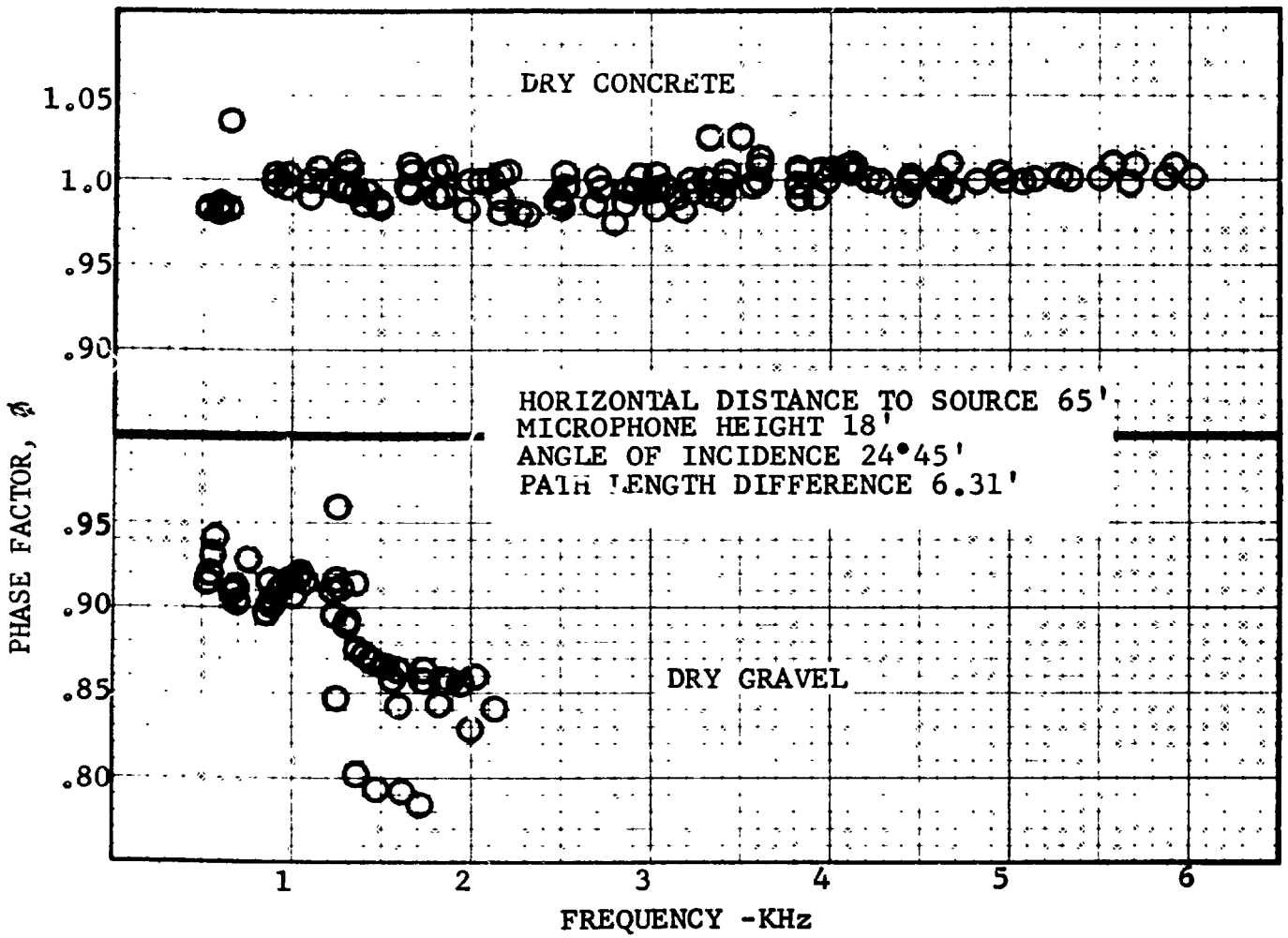

FIGURE VI-B45 OBSERVED PHASE FACTOR FOR DRY CONCRETE AND DRY GRAVEL

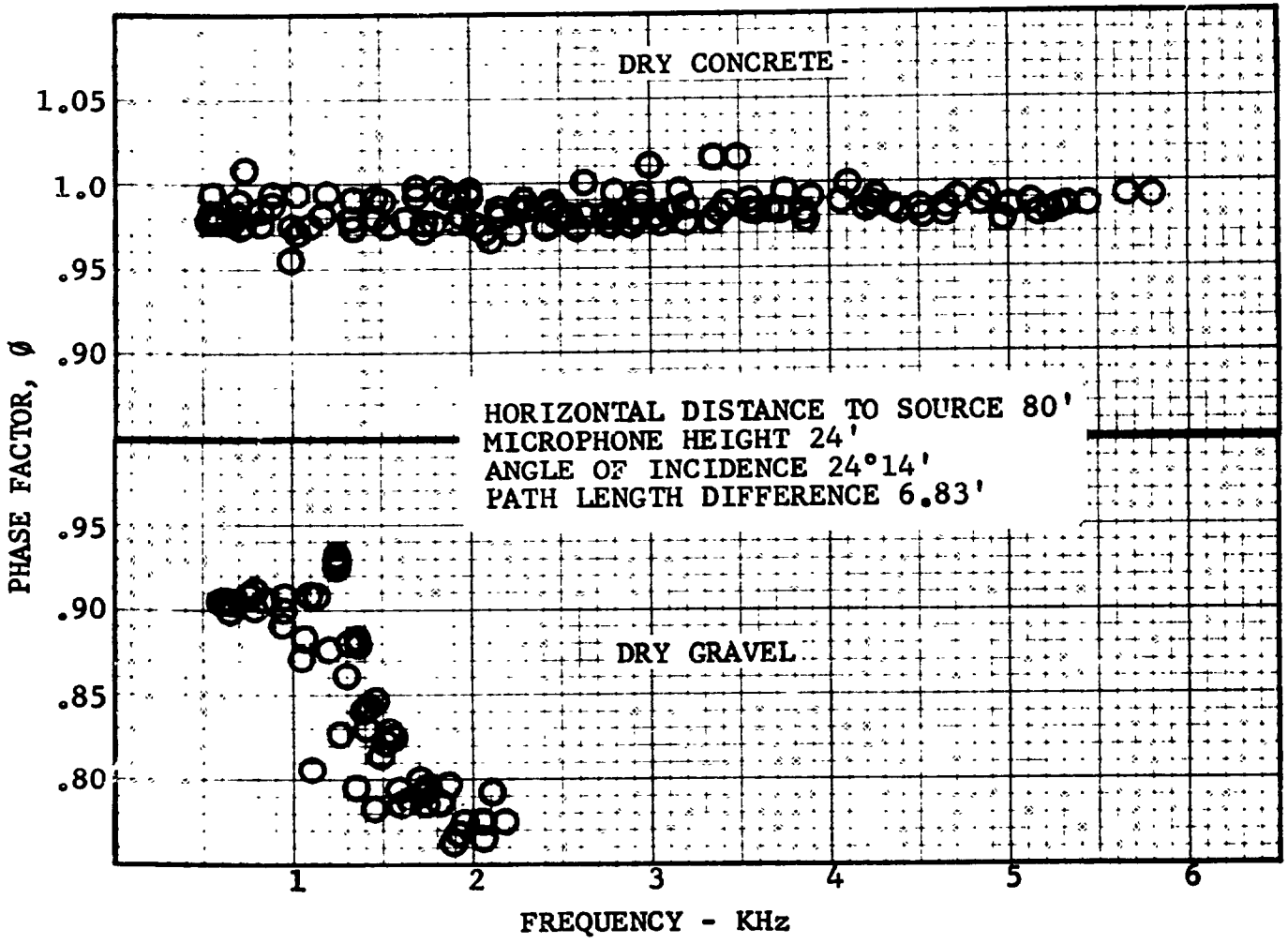

FIGURE VI-B46 OBSERVED PHASE FACTOR FOR DRY CONCRETE AND DRY GRAVEL

$$d(\Delta r)^2 = \left[\frac{L}{r_r} - \frac{L}{r_d}\right]^2 (dL)^2 + \left[\frac{h_s + h_r}{r_r} - \frac{h_s - h_r}{r_d}\right]^2 (dh_s)^2$$

$$+ \left[\frac{h_s + h_r}{h_r} + \frac{h_s - h_r}{r_d}\right]^2 (dh_r)^2$$

where

r = horizontal separation between source and receiver

h_s = height of sound source

h_r = height of receiver

$r = \sqrt{(h_s + h_r)^2 + L^2}$

$r_d = \sqrt{(h_s - h_r)^2 + L^2}$

Thus we have 5 types of possible measurement errors to contend with (dh_s, dh_r, dL, dT, and df_{null}).

The values dh_s and dh_r indicate (in addition to measurement error) the uncertainty with which we know the exact location of sound source and receiver, respectively. The value dL reflects a physical measurement error. For example if the microphone stand is 2° out of perpendicular for the 18 foot microphone this alone introduces an error of 6 inches in L.

The error dT is strictly a measurement error.

The value of df_{null} is not only a function of the measurement system but also the resolution of the frequency scale for reading f_{null}. This is, to a large part a random error and should be cancelled through the averaging procedure. For any given sweep, df_{null}/f_{null} should be significant only for the lower frequencies, i.e., in comparing repeats one would expect more scatter (due to measurement error and reading f_{null}) in the values of ϕ at low frequencies.

Using the following values

dL = 1 foot

dh_s = 2 inches

dh_r = 1 inch

dT = 1°

df_{null} = 0

Yields for these tests

$$\frac{d\phi}{\phi} \pm .02$$

Thus, one would assume that, if an ideal reflecting surface ($\phi = 1$) were used in these tests, the observed values of ϕ would be

$$\phi_{ideal} = 1 \pm .02$$

Referring again to Figures VI-B42 through VI-B46, it may be seen that concrete essentially behaves as an ideal reflecting surface. There is, however a "breakdown" in the cancellation/reinforcement pattern at frequencies greater than $\approx$6 KHz (see for example Figure VI-B3).

This breakdown at the high frequencies is assumed to be a result of the variation of the effective path length difference ($\Delta r'$) with time (the wave lengths are of the same order of magnitude as the variation in $\Delta r'$). Because ϕ varies with time, $f_{null\ actual}$ also varies in time. Thus, a pure tone (above breakdown frequency) measured near a reflecting surface will have a time varying amplitude. The variation in amplitude recorded for a pure tone results in no discernable nulls or peaks when a frequency sweep is being recorded. The contribution to measurements as a result of reflection then approaches $10 \log_{10} (1 + Q^2/Z^2)$ (see Section III-D) at high frequencies where the effects of cancellation and reinforcement average to zero over the time sample.

The phenomenon of breakdown occurred at lower frequencies for gravel (2 - 2.5 KHz) than it did for concrete ($\approx$6 KHz). In addition, the phase factor varied between .95 and .75 over the frequency range of .5 to 2KHz.

This is due to a result of two effects (1) the surface acting as a resonator, and (2) at higher frequencies the wave length approaches the magnitude of the surface roughness, resulting in a diffuse reflecting surface, causing extreme scattering of the reflected signal. For surfaces such as gravel, no consistent prediction of phase factor seems apparent, so that the phase factor must be determined experimentally for use in any analysis of the propagation problem.

Values of the phase factor (average of the repeats) versus $(2n + 1)/2$ (for all microphones Configurations A and B for concrete and Configuration A for gravel) for wet and dry surfaces are presented in Figures VI-B47 through VI-B55.

It should be emphasized again that the expected accuracy is $\pm$ 2%. The expanded scales used in these and subsequent figures, are used only to observe trends, while actual values are accurate to $\pm$ .02 x ϕ.

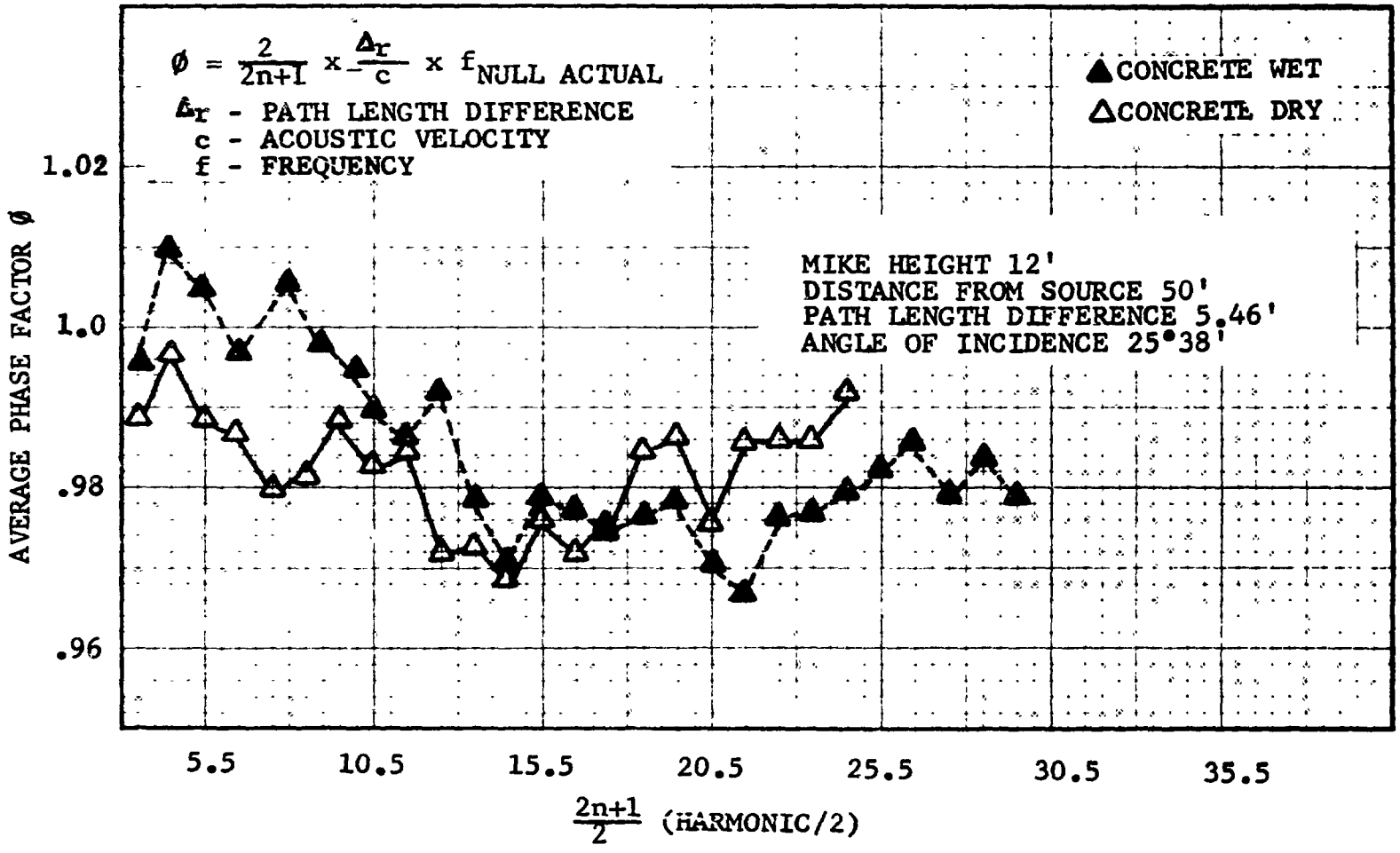

FIGURE VI-B47 EFFECT ON PHASE FACTOR OF WETTING CONCRETE SURFACE

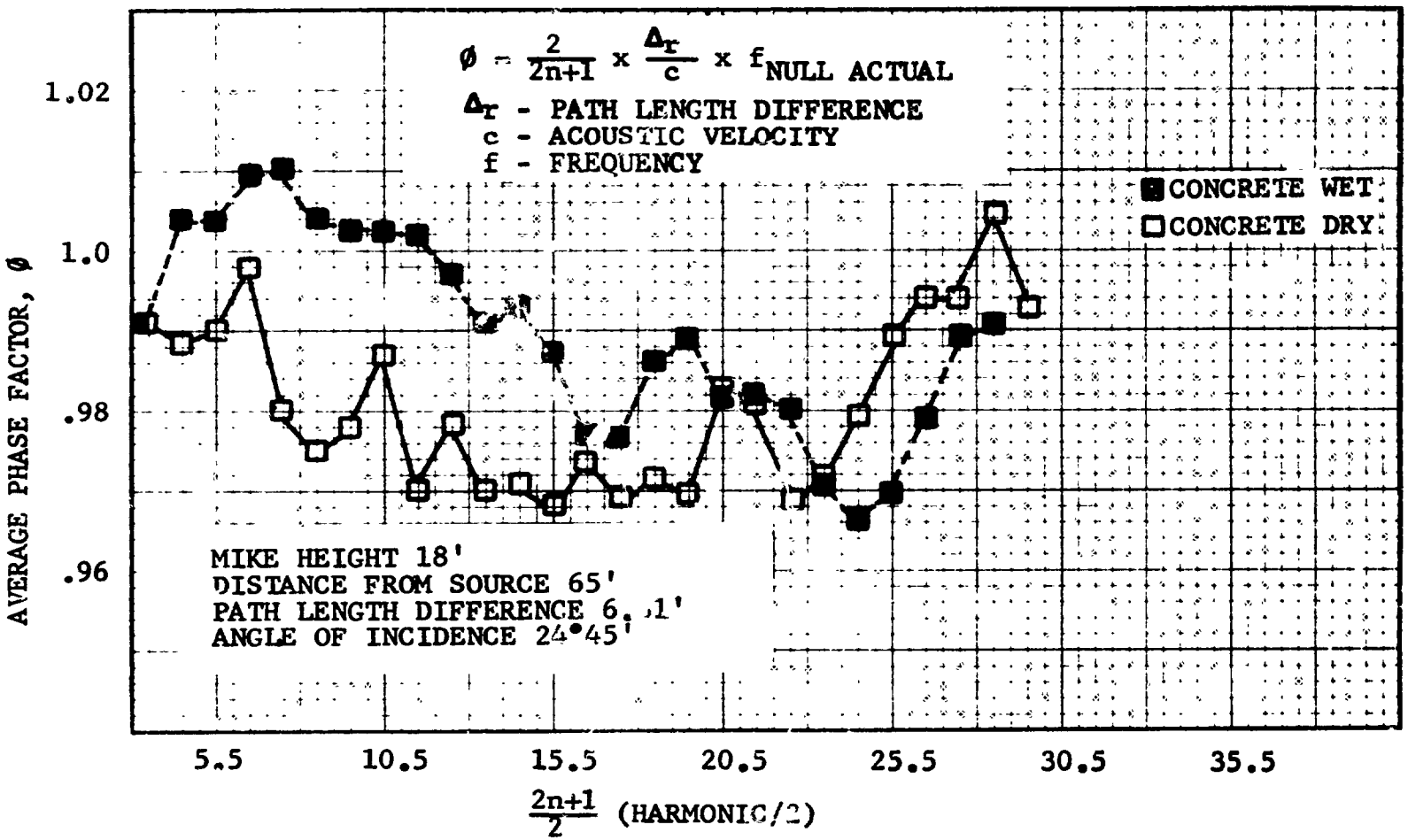

FIGURE VI-B48 EFFECT ON PHASE FACTOR OF WETTING CONCRETE SURFACE

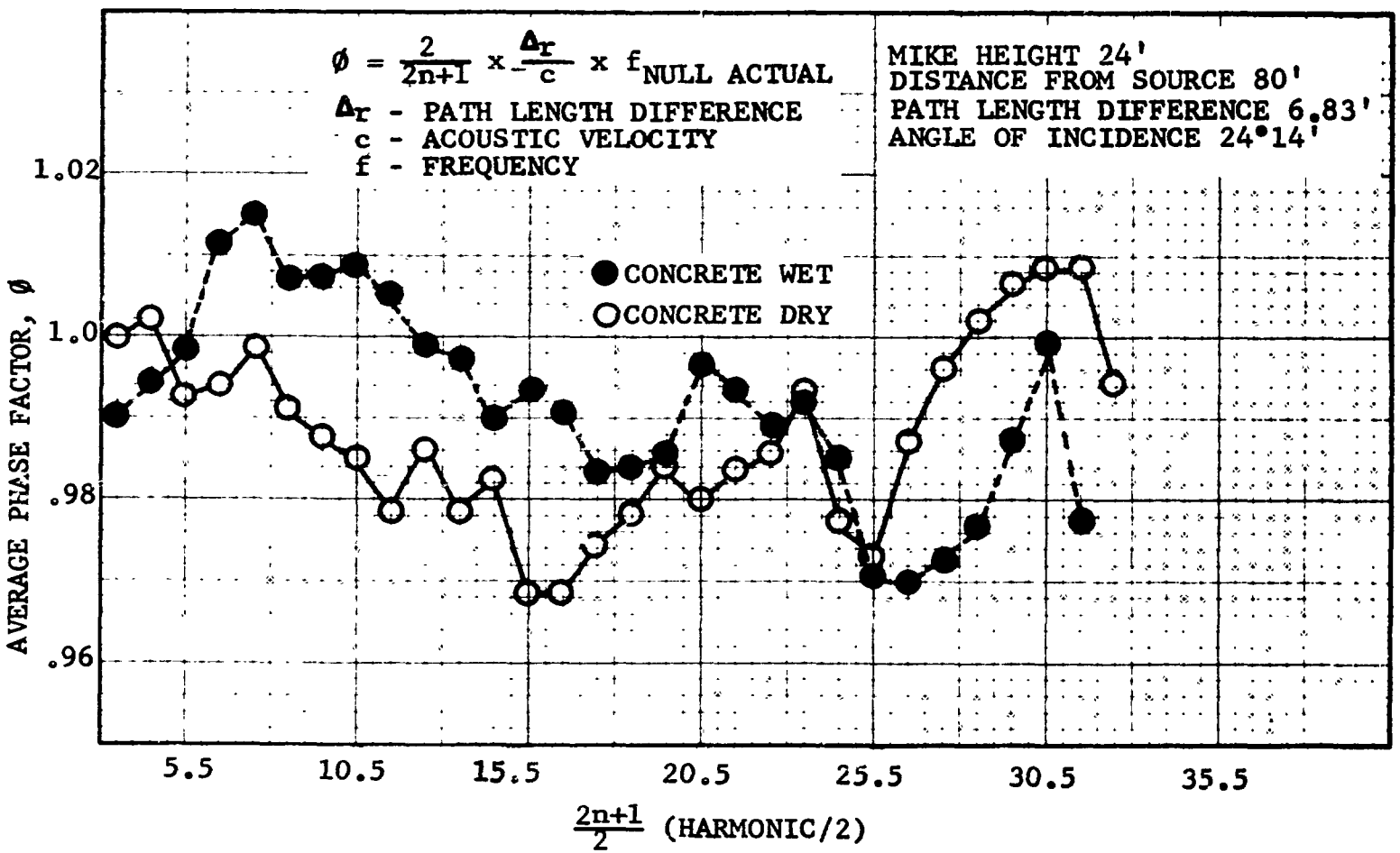

FIGURE VI-B49 EFFECT ON PHASE FACTOR OF WETTING CONCRETE SURFACE

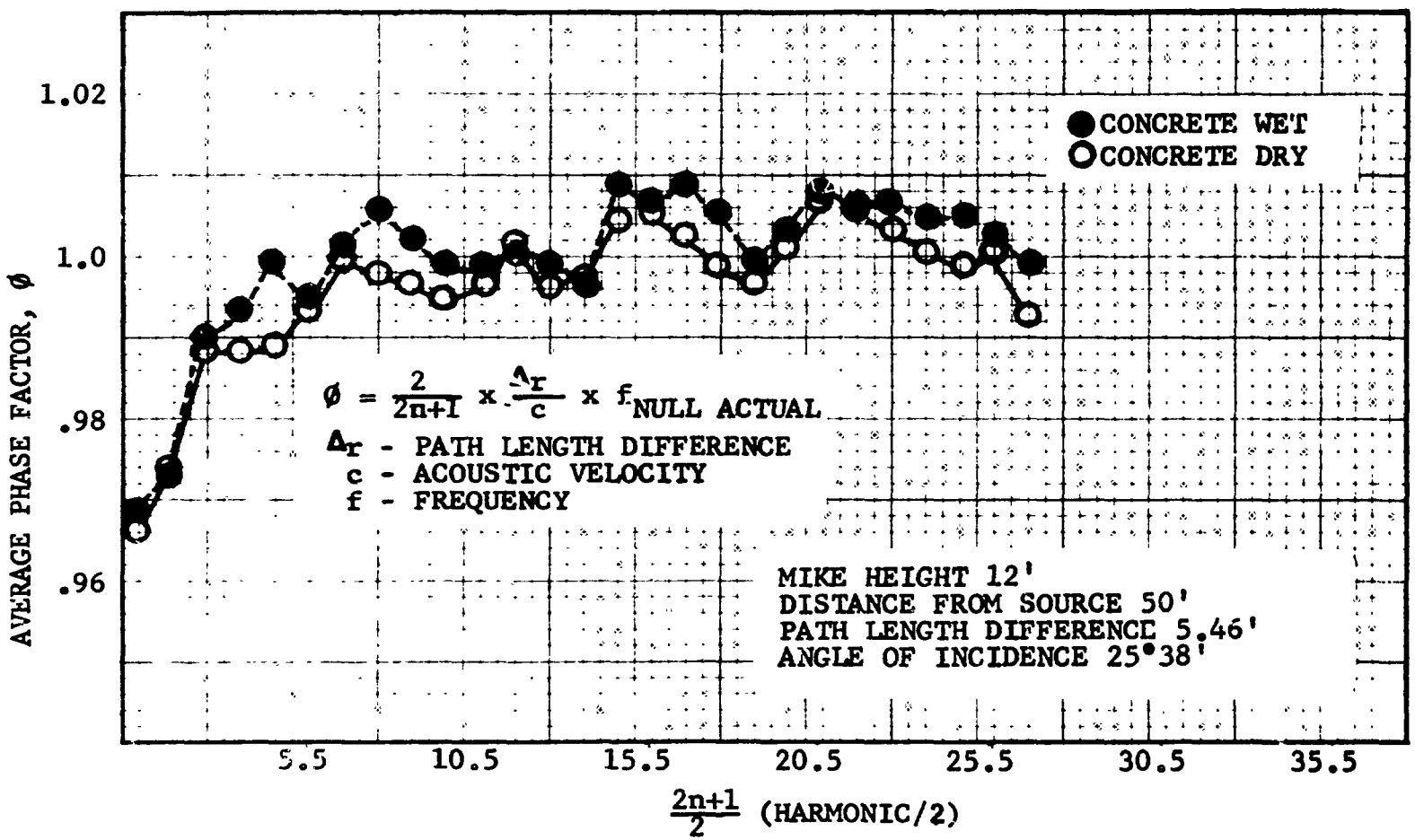

FIGURE VI-B50 EFFECT ON PHASE FACTOR OF WETTING CONCRETE SURFACE

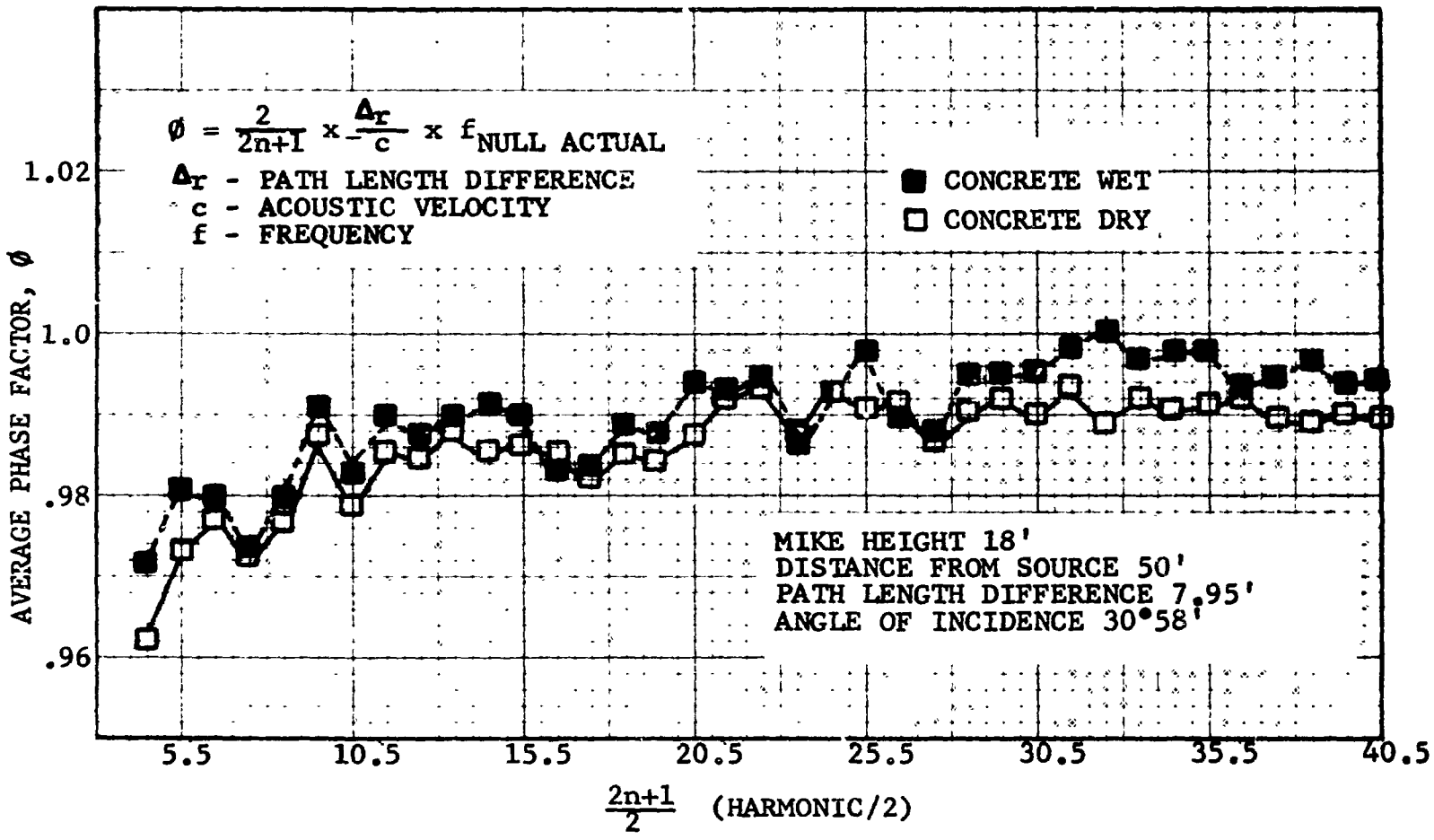

FIGURE VI-B51 EFFECT ON PHASE FACTOR OF WETTING CONCRETE SURFACE

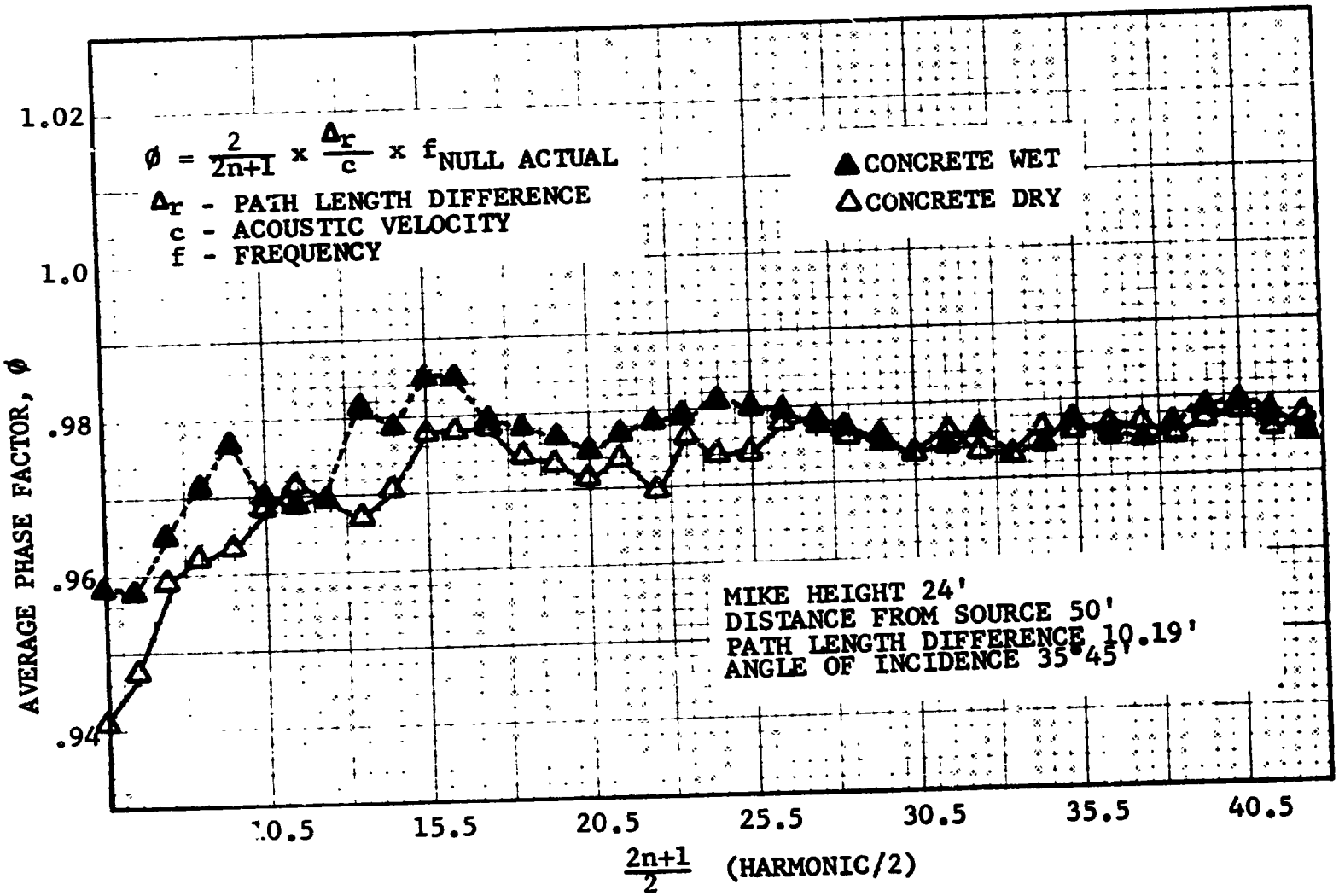

FIGURE VI-B52 EFFECT ON PHASE FACTOR OF WETTING CONCRETE SURFACE

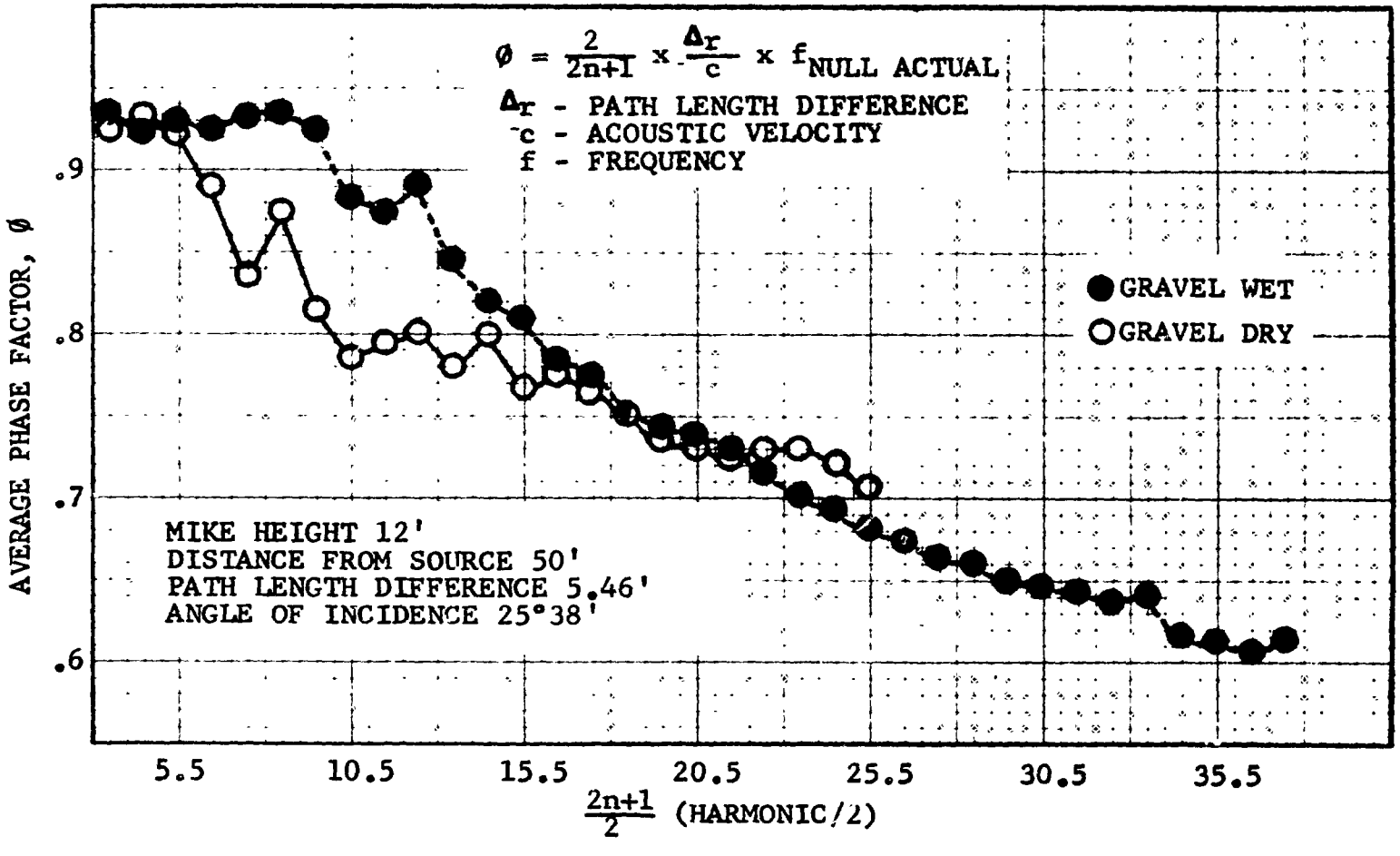

FIGURE VI-B53 EFFECT ON PHASE FACTOR OF WETTING GRAVEL SURFACE

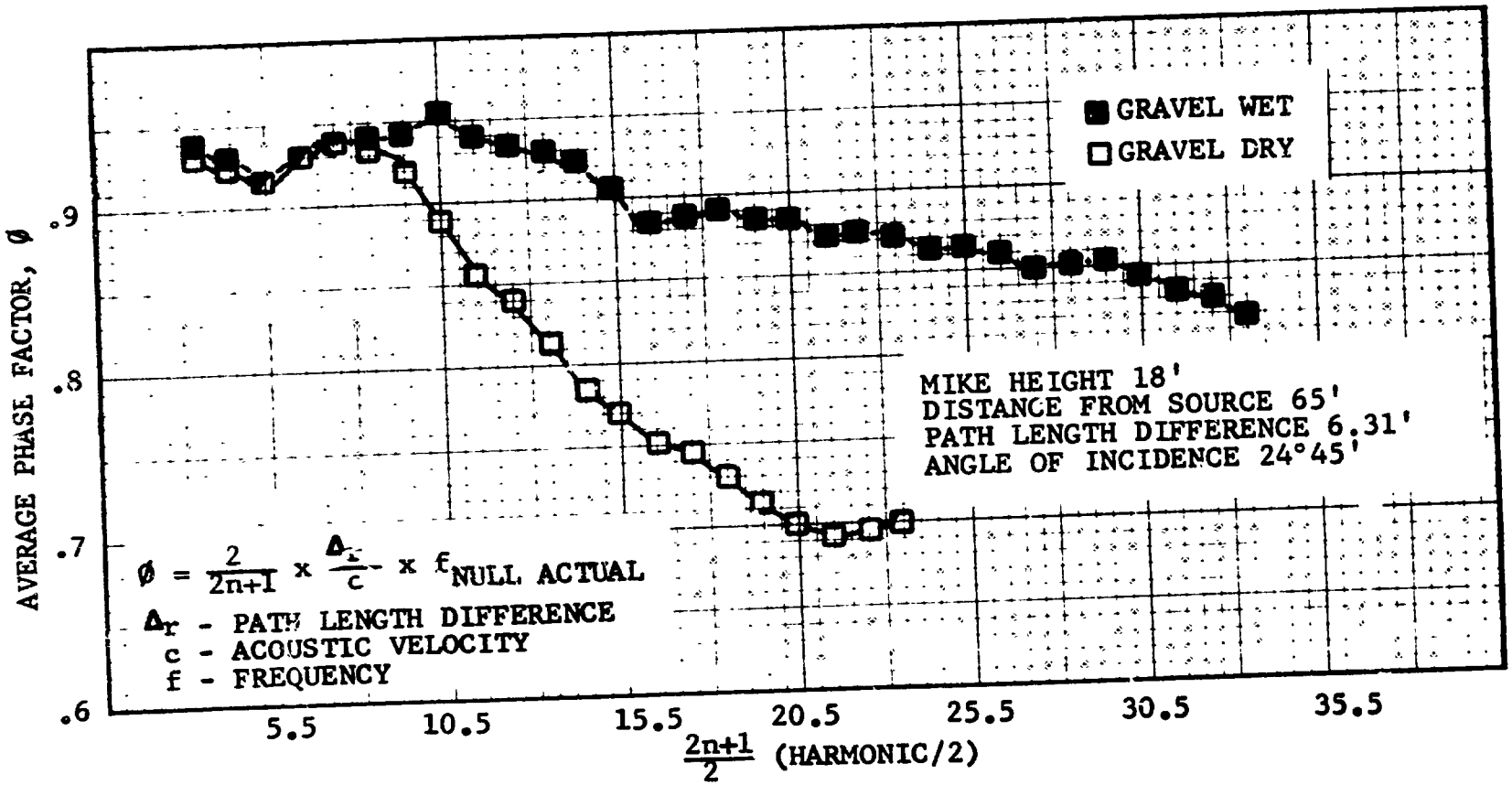

FIGURE VI-B54 EFFECT ON PHASE FACTOR OF WETTING GRAVEL SURFACE

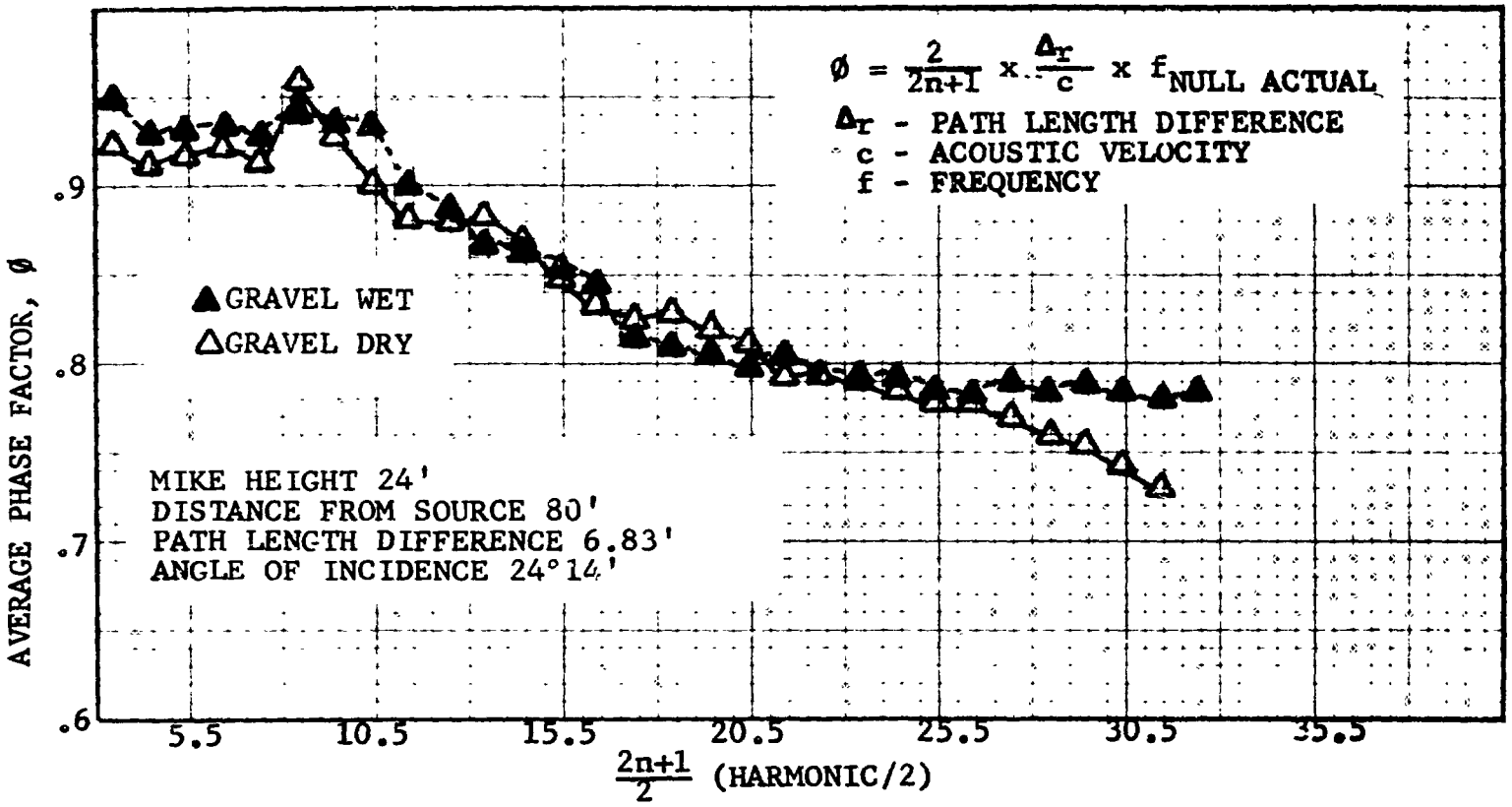

FIGURE VI-B55 EFFECT ON PHASE FACTOR OF WETTING GRAVEL SURFACE

The effect of water on the surface is to raise the value of the phase factor for both gravel and concrete. This is probably caused by water filling the "gaps" in the surface and thus presenting a more uniform reflector. In addition, breakdown occurs at higher frequencies for wet gravel. This also indicates that breakdown is not only a function of time variation of atmospheric properties alone but a function of surface roughness.

The initial objective of placing Scottfoam on the surface was to locate the reflection point and its effective dimensions, but the results of this portion of the tests indicate a greater effect on phase factor than on the strength of the reflected signal.

Over gravel, no effect of placing the pad on the surface could be seen (Figures VI-B17 and VI-B41).

This result is caused by the fact that the gravel field is reflecting over a broad area, and not at a point or small region. Little effect in the level of the reflected signal was produced by placing the pad on the concrete. The peak to null spread versus frequency (shown in Figures VI-B56 through VI-B58) for concrete without the pad and with the pad at various locations shows almost no evidence of the pad affecting the recorded levels; however, the pad did affect the value of the phase factor. Values of average phase factor versus pad position are presented in Figures VI-B59 through VI-B61. As noted above, the pad tends to lower the phase factor when placed at the area of maximum reflection.

(2) Angle of Incidence Variation. For the configuration designed to test the variation of ϕ with angle of incidence, the angle was varied between 25.5° and 35.75°. The observed phase factors versus $(2n + 1)/2$ for the three microphones are presented in Figure VI-B62 for concrete and Figure VI-B63 for gravel.

For concrete the phase factor was apparently higher for lower angles of incidence. However, the data was within the range expected for an ideal reflecting surface, and the range of angle variation is small.

For gravel, phase factor tends to go down as incidence angle decreases. Many measurements of engine noise are performed with a gravel surface. Using observed phase factors from engine tests and from these tests, phase factor (50 Hz < frequency < 1500 Hz) versus angle of incidence for gravel is presented in Figure VI-B64.

(3) Path Length Difference Variation. Phase factors versus $2n + 1)/2$, for the configuration to test variation with Δr (Configuration A), are presented for the three microphones in Figures VI-B65 (concrete) and VI-B66 (gravel). Referring to the recorded SPL's for concrete (Figures VI-B3 through VI-B8), the phenomenon of breakdown occurred at lower frequencies for larger Δr's This is a result of atmospheric variations affecting the signal over a greater distance.

For the gravel surface the larger Δr appeared to produce a larger phase factor. Further tests involving Δr variation, however, are necessary in order to arrive at any definite conclusion about this effect.

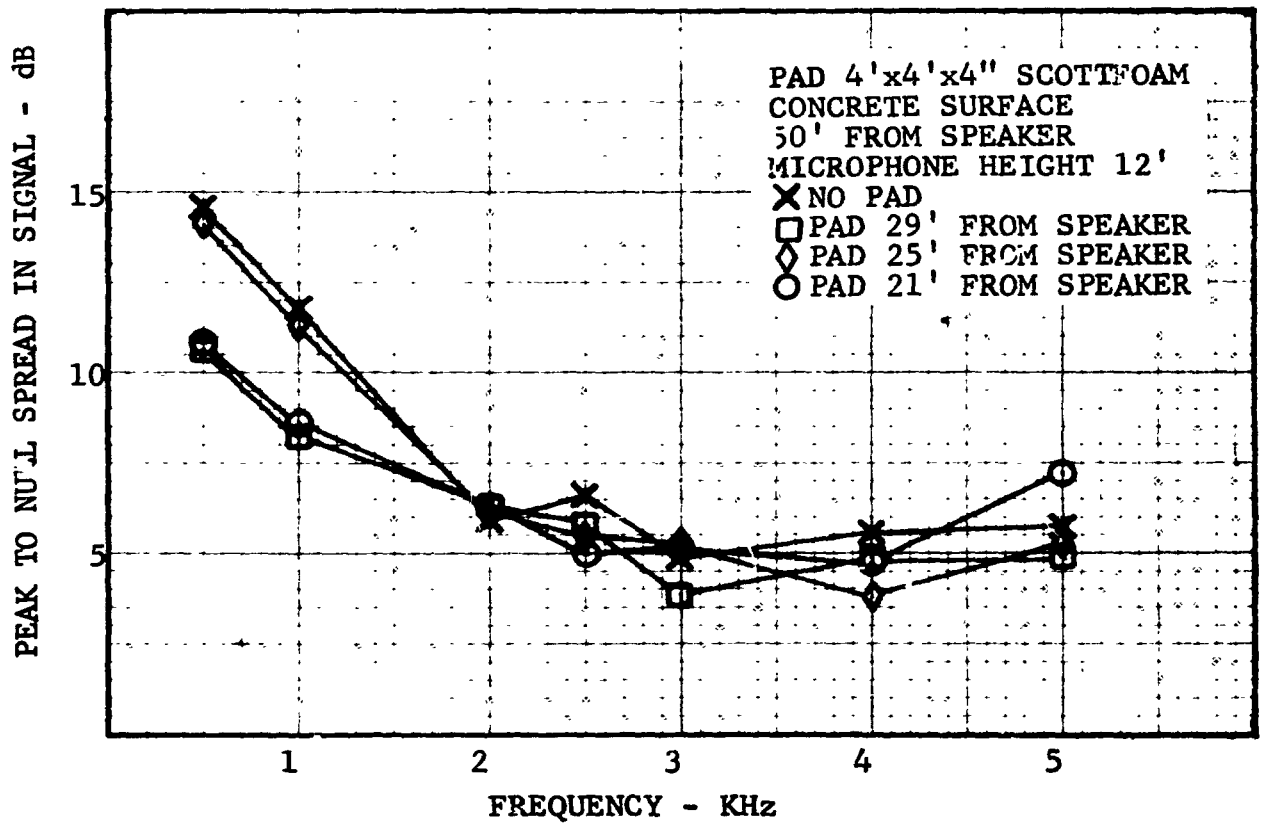

FIGURE VI-B56 EFFECT OF ABSORBENT PAD ON REFLECTED SIGNAL

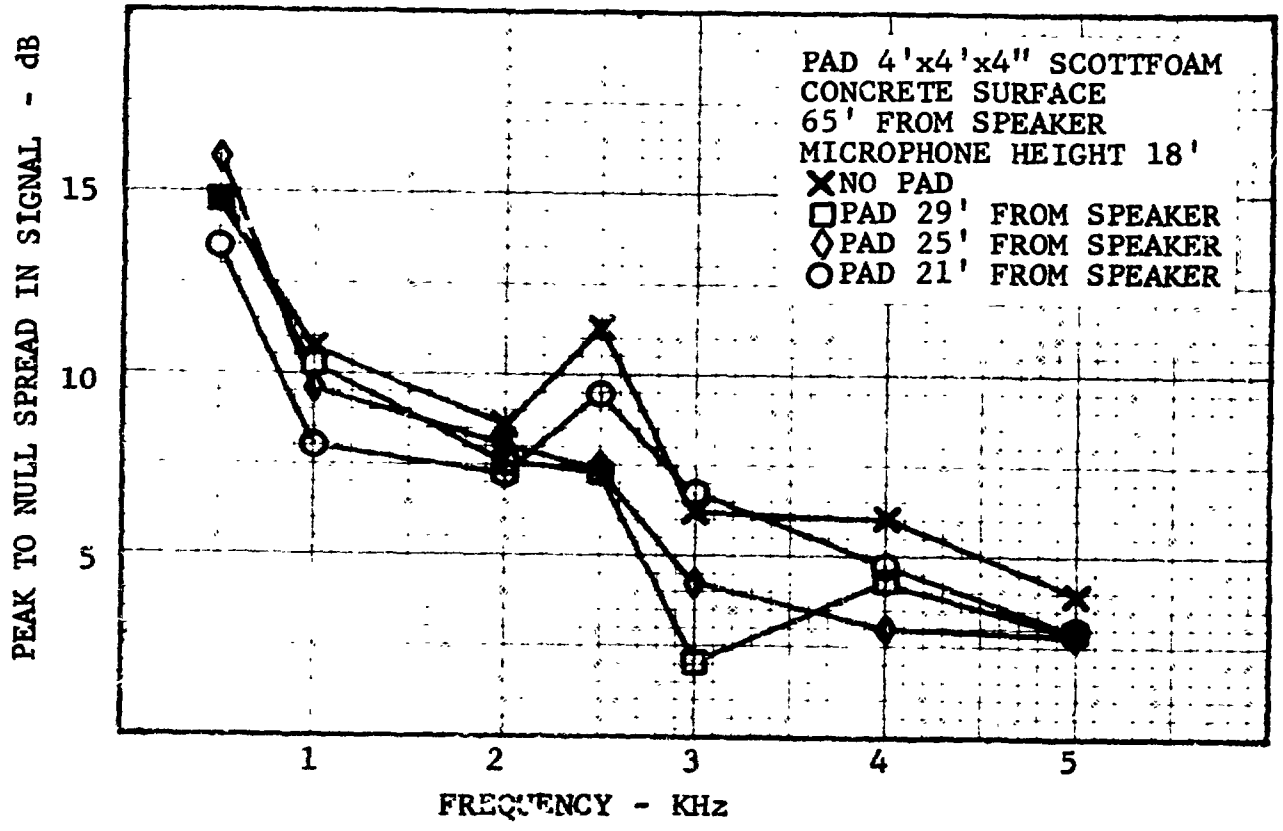

FIGURE VI-B57 EFFECT OF ABSORBENT PAD ON REFLECTED SIGNAL

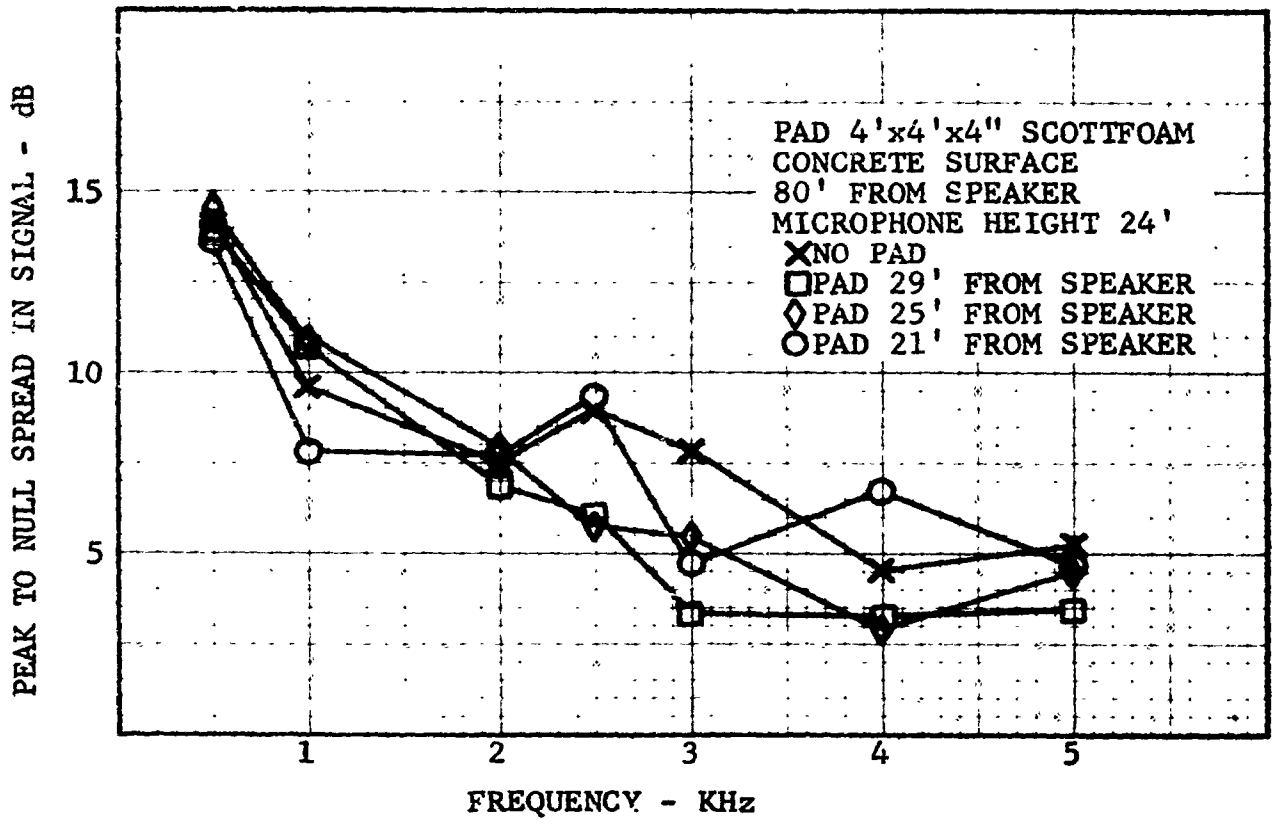

FIGURE VI-B58 EFFECT OF ABSORBENT PAD ON REFLECTED SIGNAL

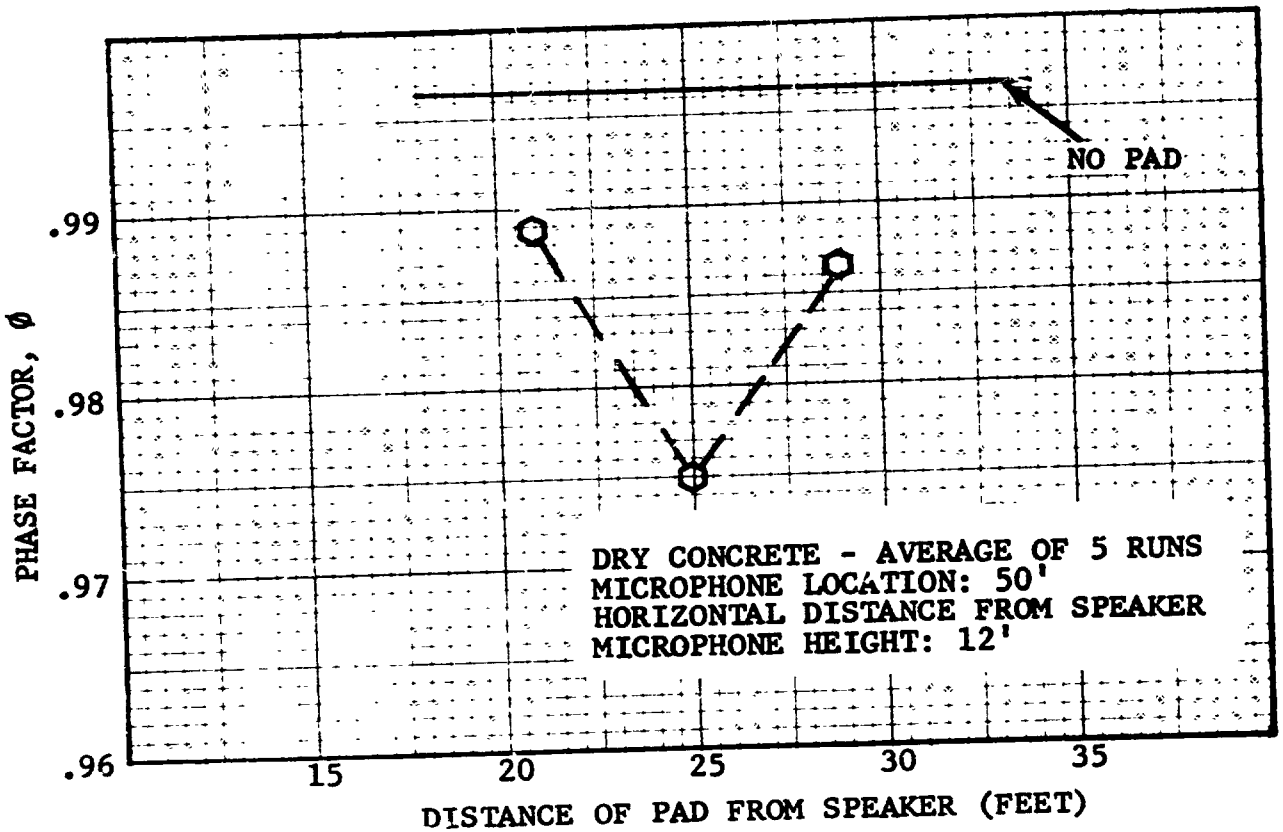

FIGURE VI-B59 EFFECT OF ABSORBENT PAD ON PHASE FACTOR

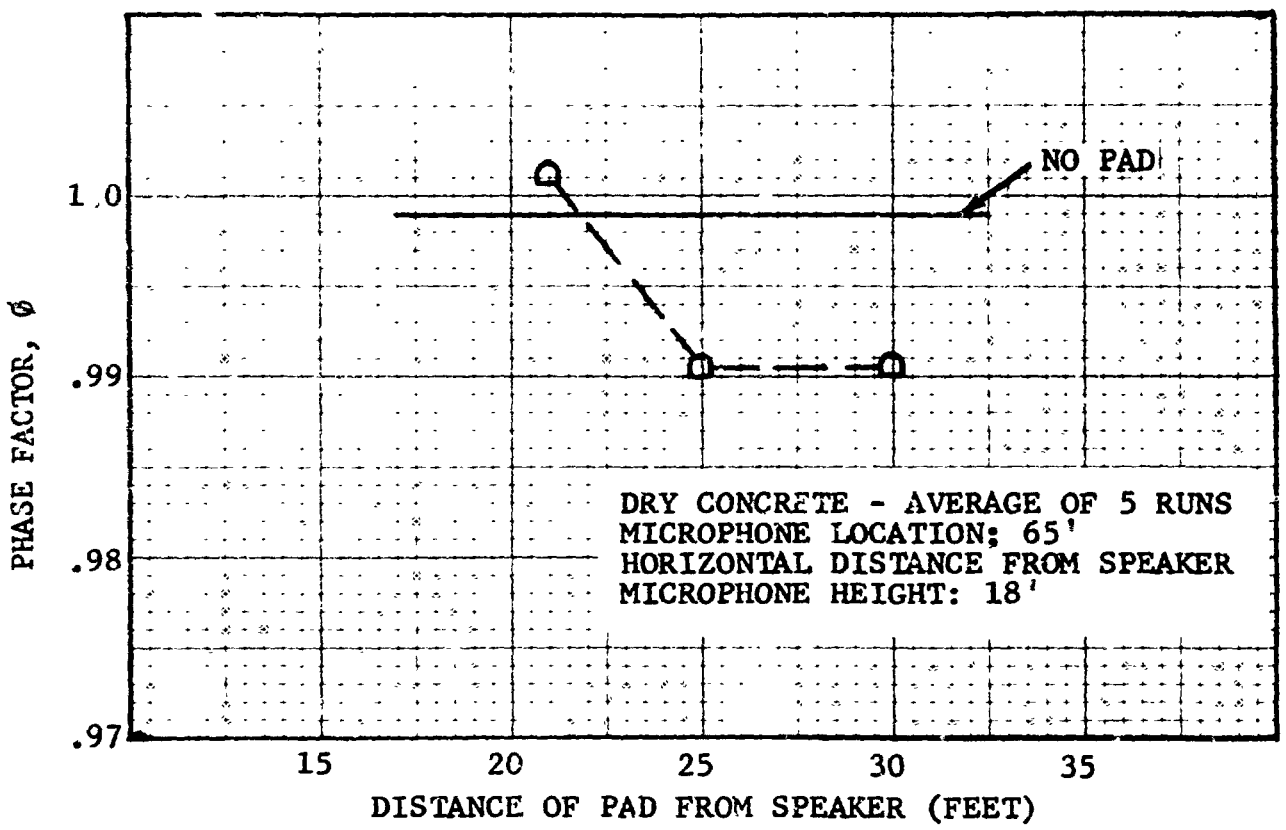

FIGURE VI-B60 EFFECT OF ABSORBENT PAD ON PHASE FACTOR

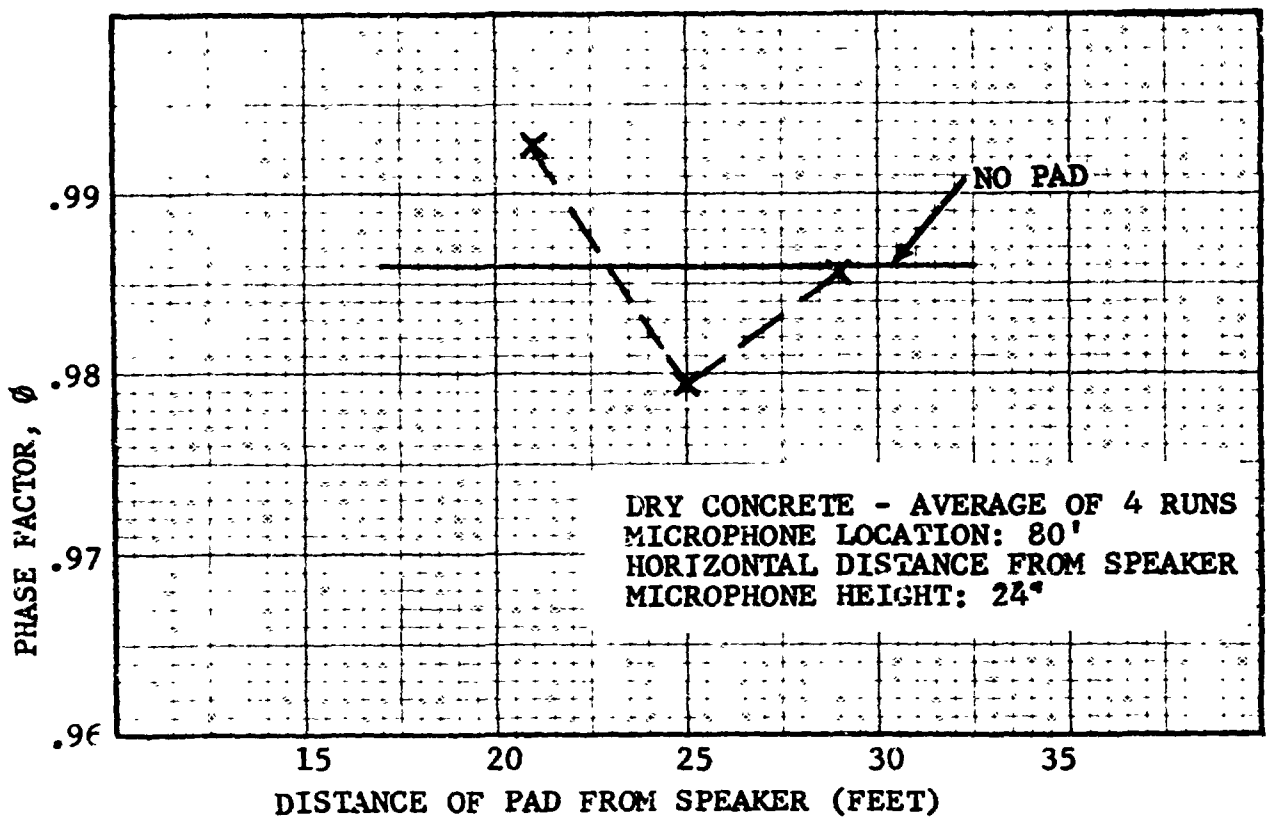

FIGURE VI-B61 EFFECT OF ABSORBENT PAD ON PHASE FACTOR

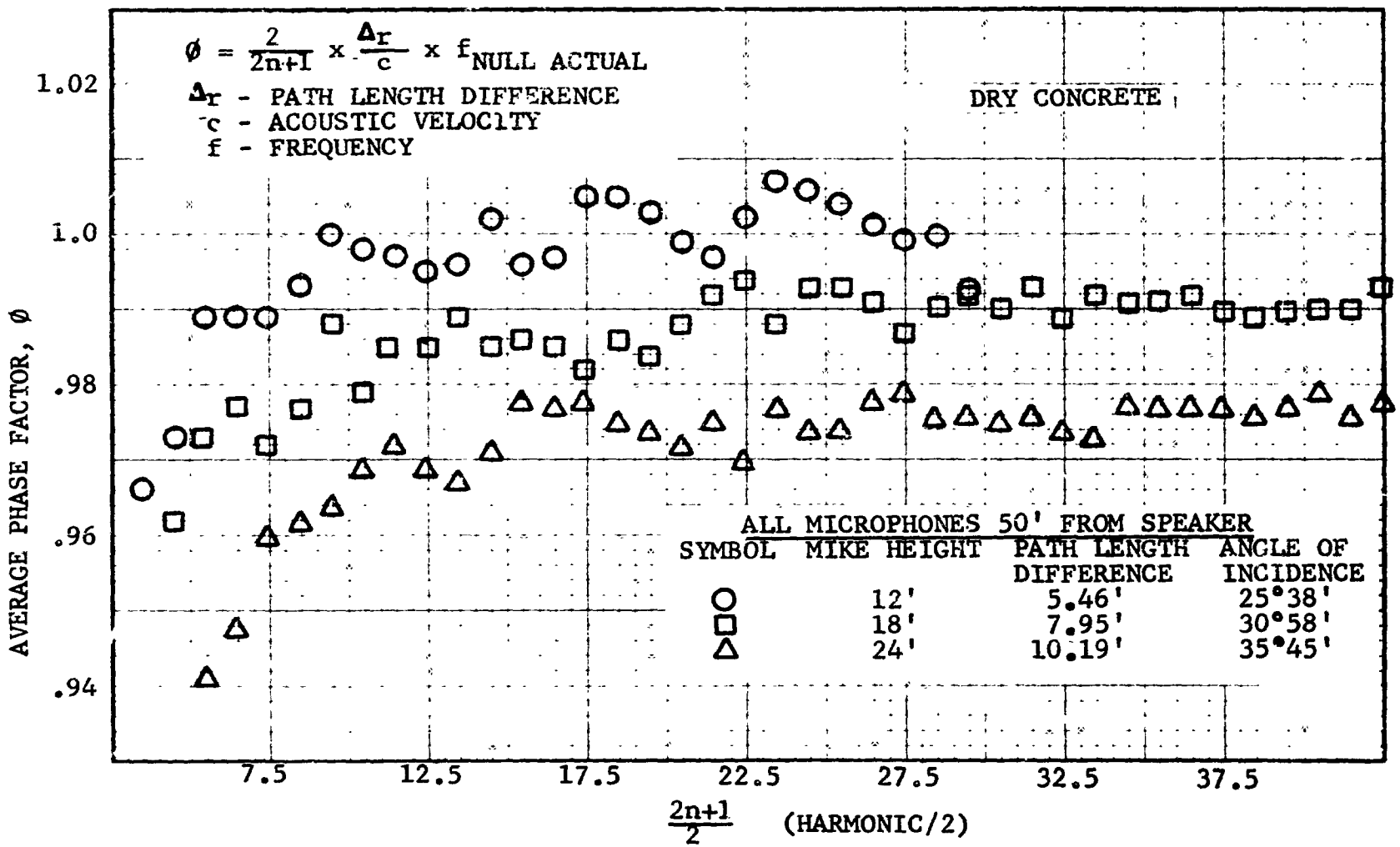

FIGURE VI-B62 VARATION OF PHASE FACTOR WITH INCIDENCE ANGLE

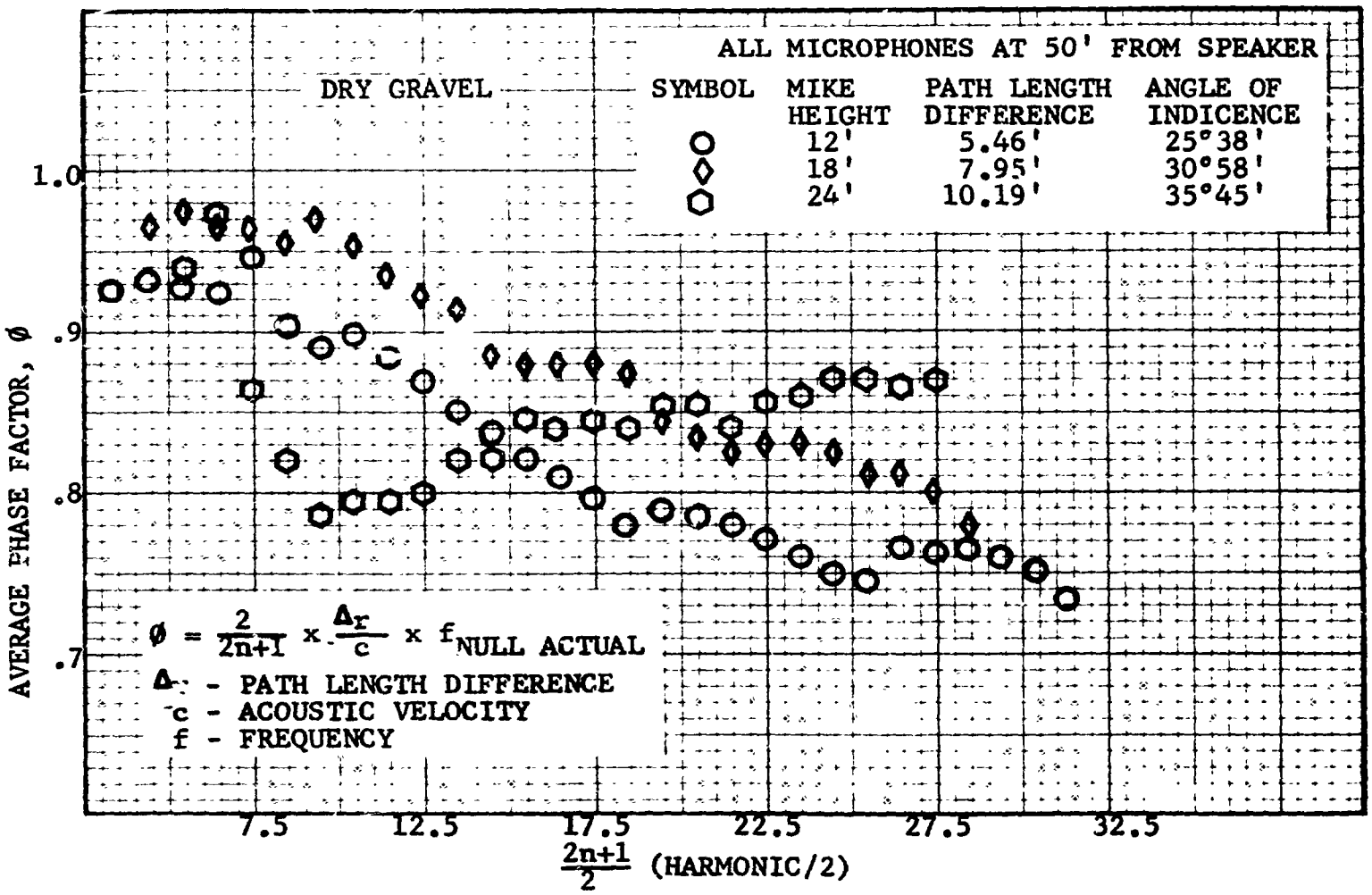

FIGURE VI-B63 VARIATION OF PHASE FACTOR WITH INCIDENCE ANGLE

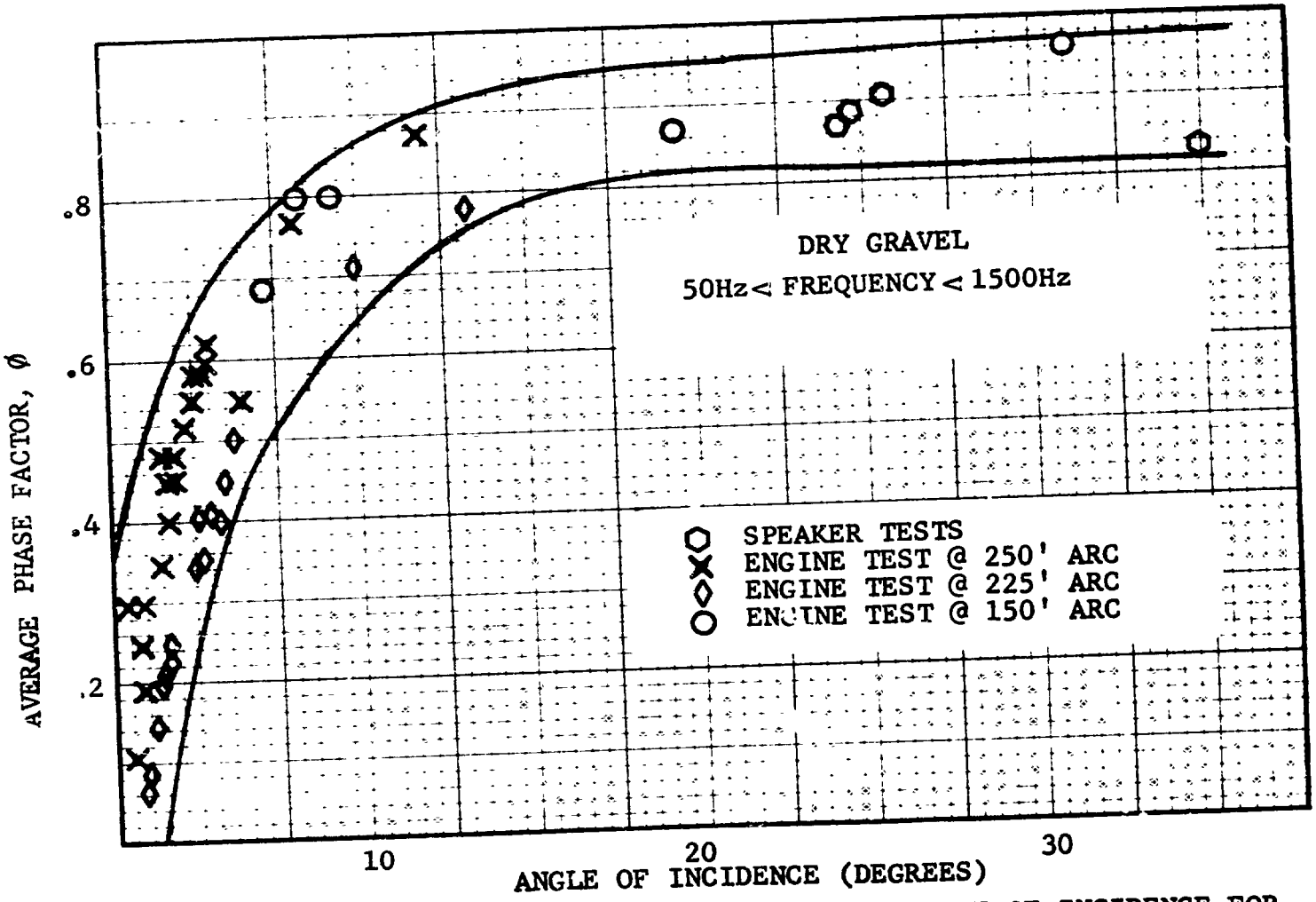

FIGURE VI-B64 PHASE FACTOR AS A FUNCTION OF ANGLE OF INCIDENCE FOR GRAVEL

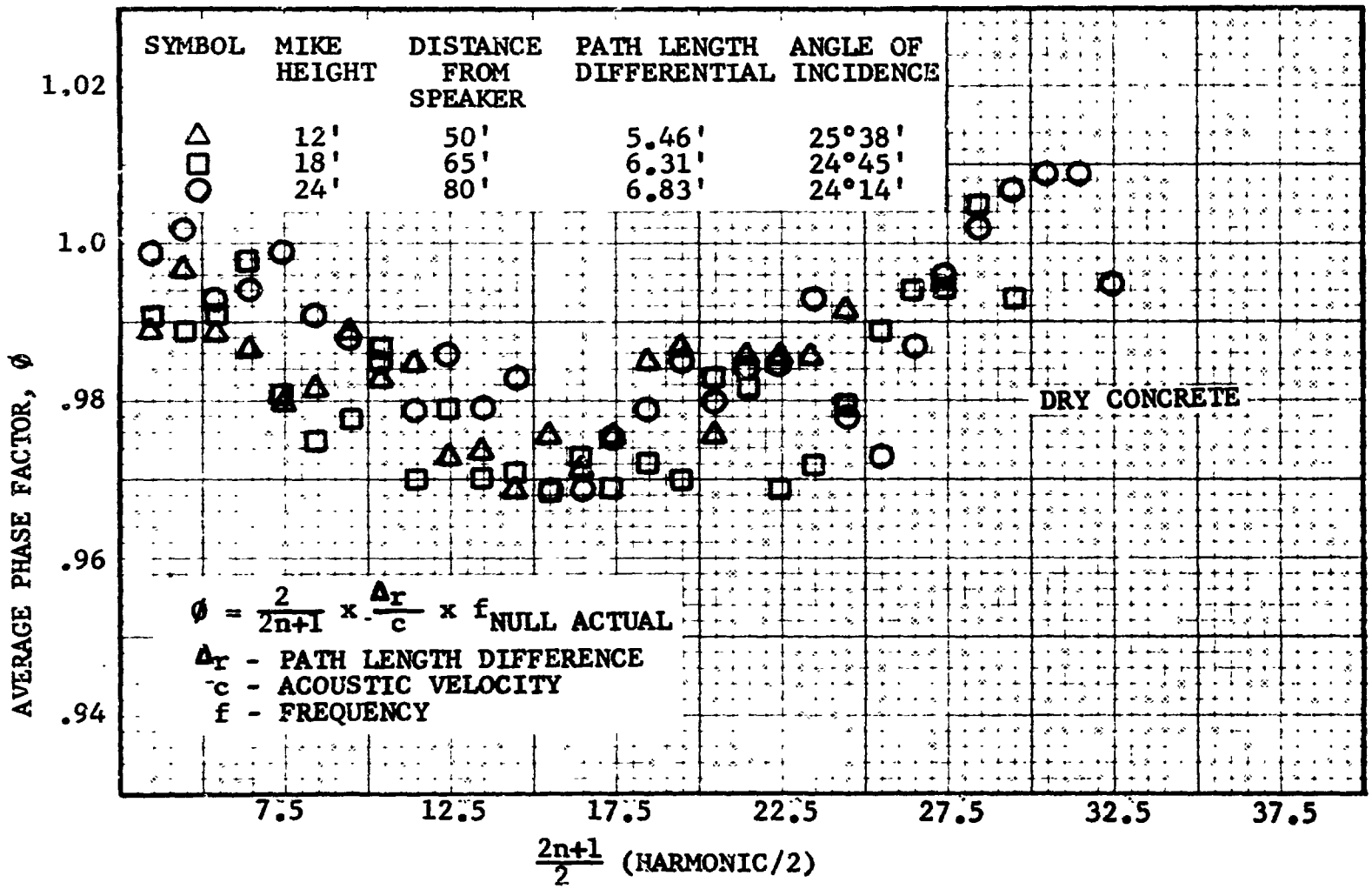

FIGURE VI-B65 VARIATION OF PHASE FACTOR WITH PATH LENGTH DIFFERENCE

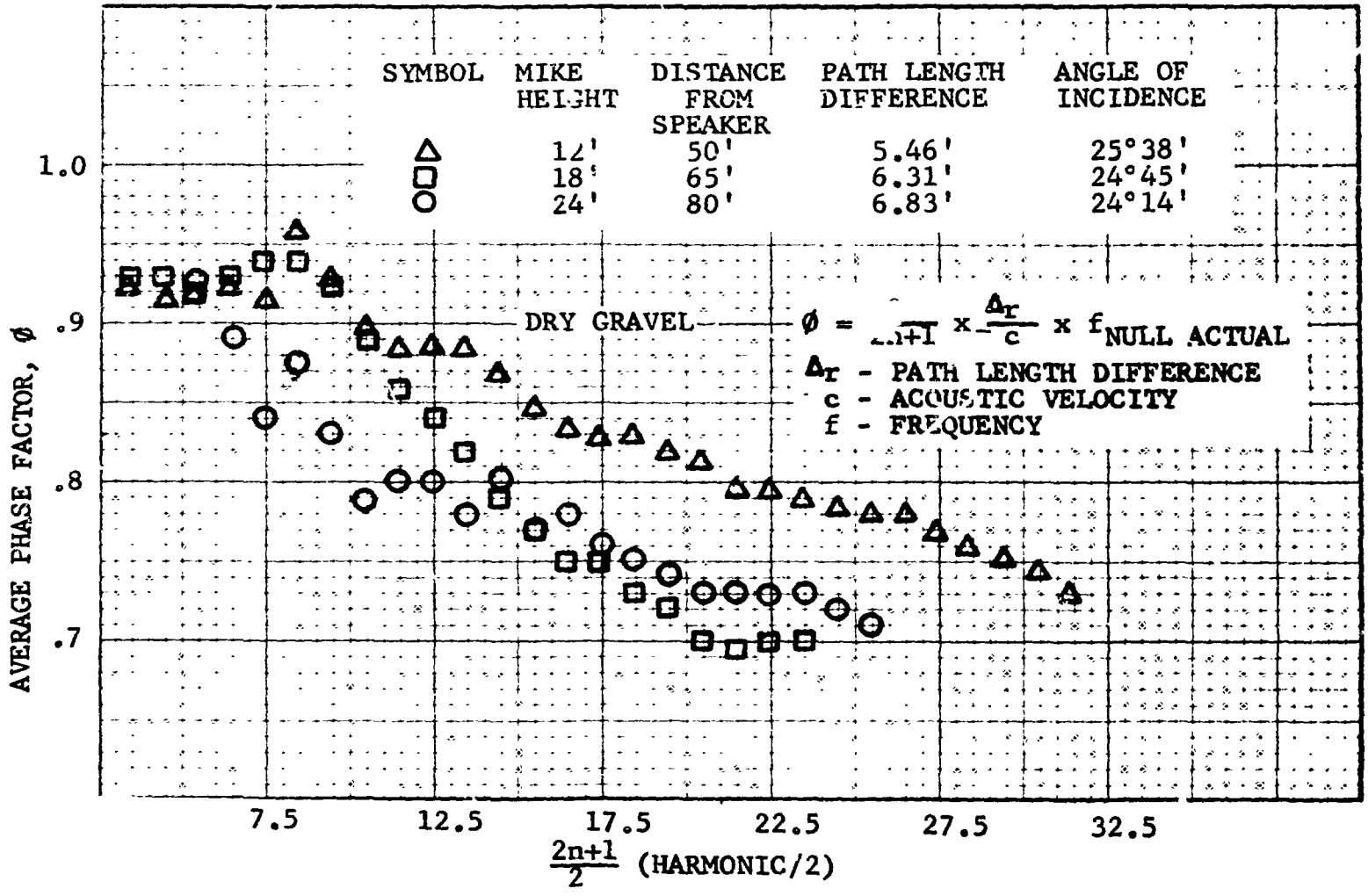

FIGURE VI-b56 VARIATION OF PHASE FACTOR WITH PATH LENGTH DIFFERENCE

(4) Substantiation of Reflection Analyses. In order to verifty the models and empirical results, engine data (1/3 octave bands) taken at 150' and 250' arc radius were corrected to 150' arc in "free field" (no reflection). The corrections applied were

- Inverse square low divergence
- Atmospheric absorption per Reference 1.
- Extra ground attenuation per Reference 2.
- Reflection effects computed using (see Section III-D) $Q = .6$; $\phi = .8$.

Figures VI-B67 through VI-B70 are typical results of this effort. The remaining differences in the spectra are probably due to use of constant ϕ and Q, where in reality they vary with frequency. The comparison, however, is quite good and indicates that, while further efforts in the investigation of phase factor are necessary, the results to date may be used with confidence in accounting for the major effects of ground surface reflection in noise data.

(2) Atmospheric Absorption. Acoustic testing of scale models presents an advantage from the lower time and cost involved in developing test vehicles and instrumentation, and also allows acoustic data to be taken early enough in the design process to influence the final vehicle design. Projecting scale model data to full scale value, however, does require projection of high frequency values of sound into the audible range. For instance, a half-scale model will require data at 20 KHz to provide an estimate of the 10 KHz level for full scale. This in turn requires a knowledge of atmospheric absorption of high frequency sound, so that source levels may be determined.

Values of atmospheric absorption for 1/3 octave bands for the acoustic range 50 Hz to 10 KHz (geometric mean frequency) are given in Reference 1, but no values are available for higher frequencies. The following curve fits have been developed for the values presented in Reference 1.

Given input of T_{amb} = temperature °F

and H_{amb} = absolute humidity in gm/meter^3.

Calculate for each band

$$H_{max} = 0.0289618 \times F^{(0.510939)}$$

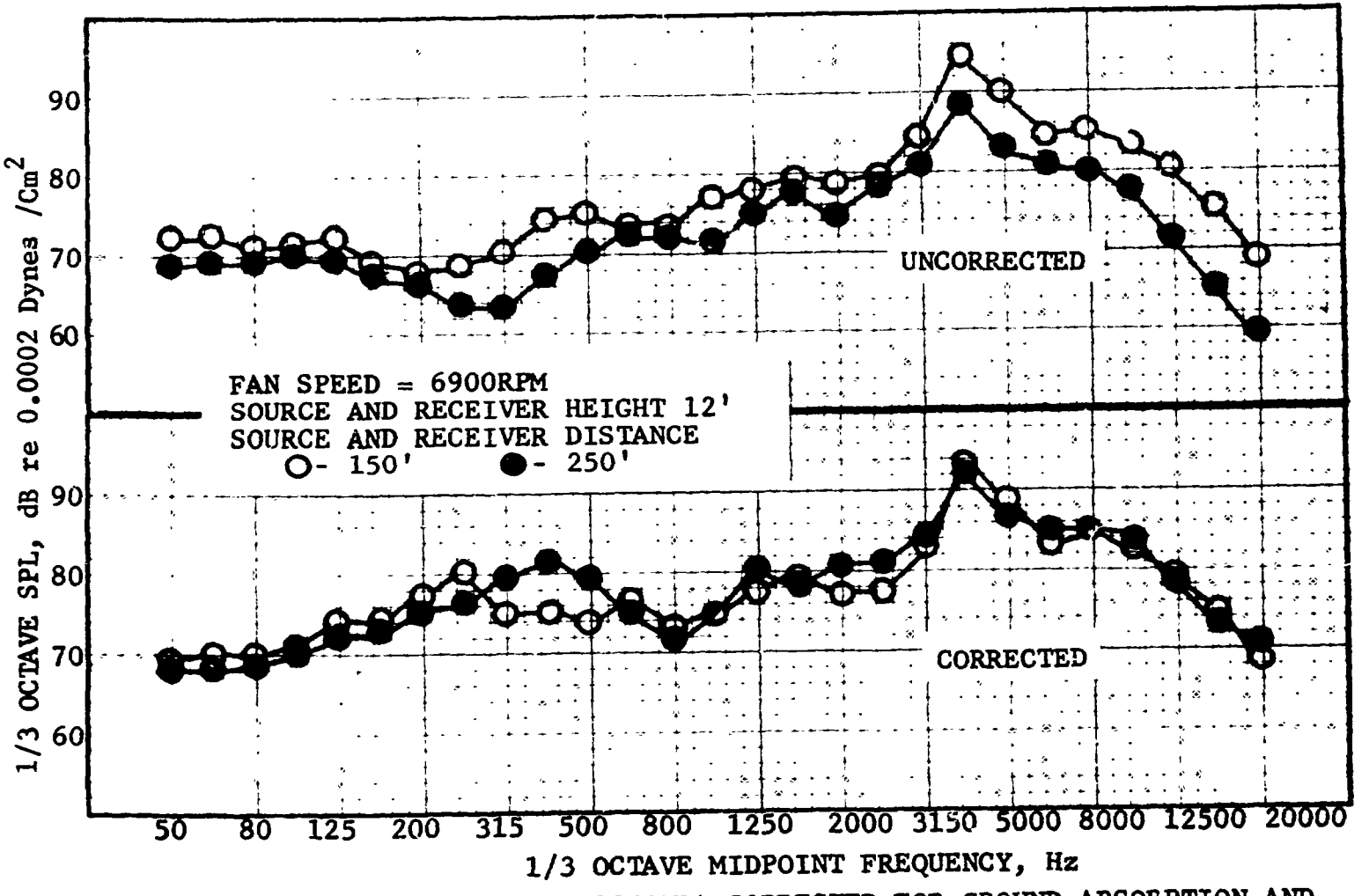

FIGURE VI-B67 COMPARISON OF SPECTRA CORRECTED FOR GROUND ABSORPTION AND REFLECTION, INVERSE SQUARE LAW DECAY, AND ATMOSPHERIC ABSORPTION. POLAR ANGLE = 60°

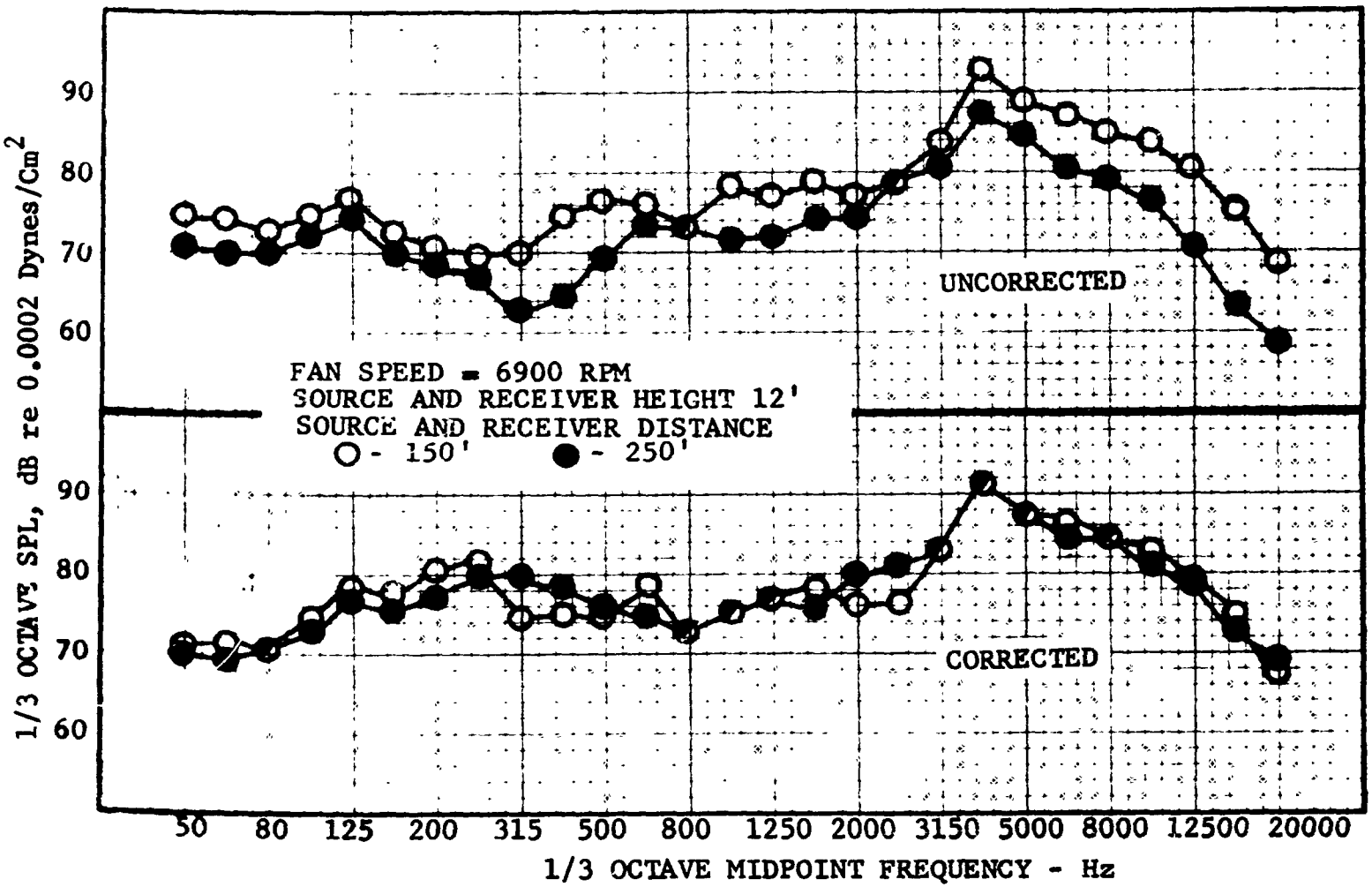

FIGURE VI-568 COMPARISON OF SPECTRA CORRECTED FOR GROUND ABSORPTION AND REFLECTION, INVERSE SQUARE LAW DECAY, AND ATMOSPHERIC ABSORPTION. POLAR ANGLE =80°

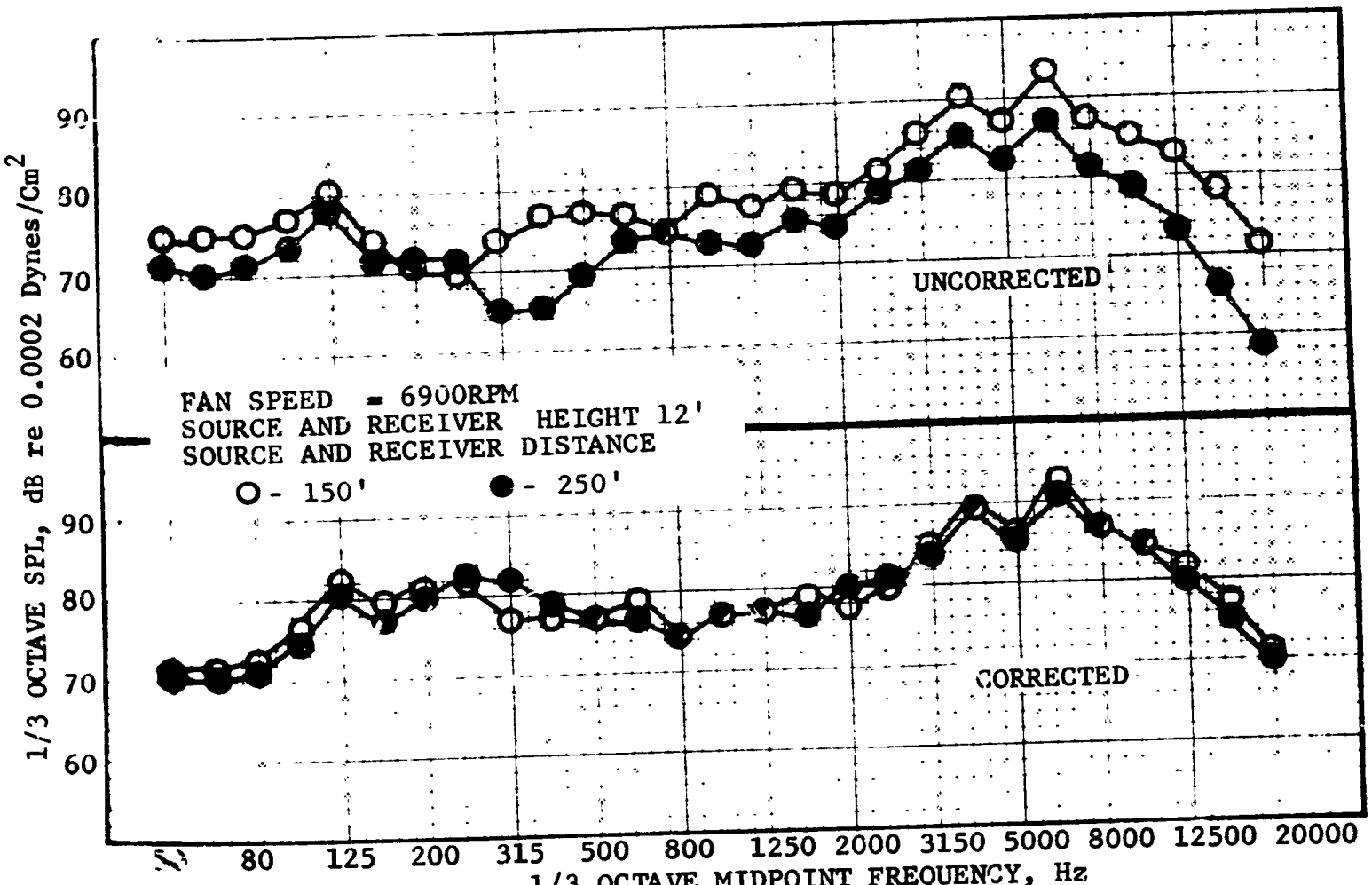

FIGURE V2-869 COMPARISON OF SPECTRA CORRECTED FOR GROUND ABSORPTION AND REFLECTION, INVERSE SQUARE LAW DECAY, AND ATMOSPHERIC ABSORPTION. POLAR ANGLE = 100°

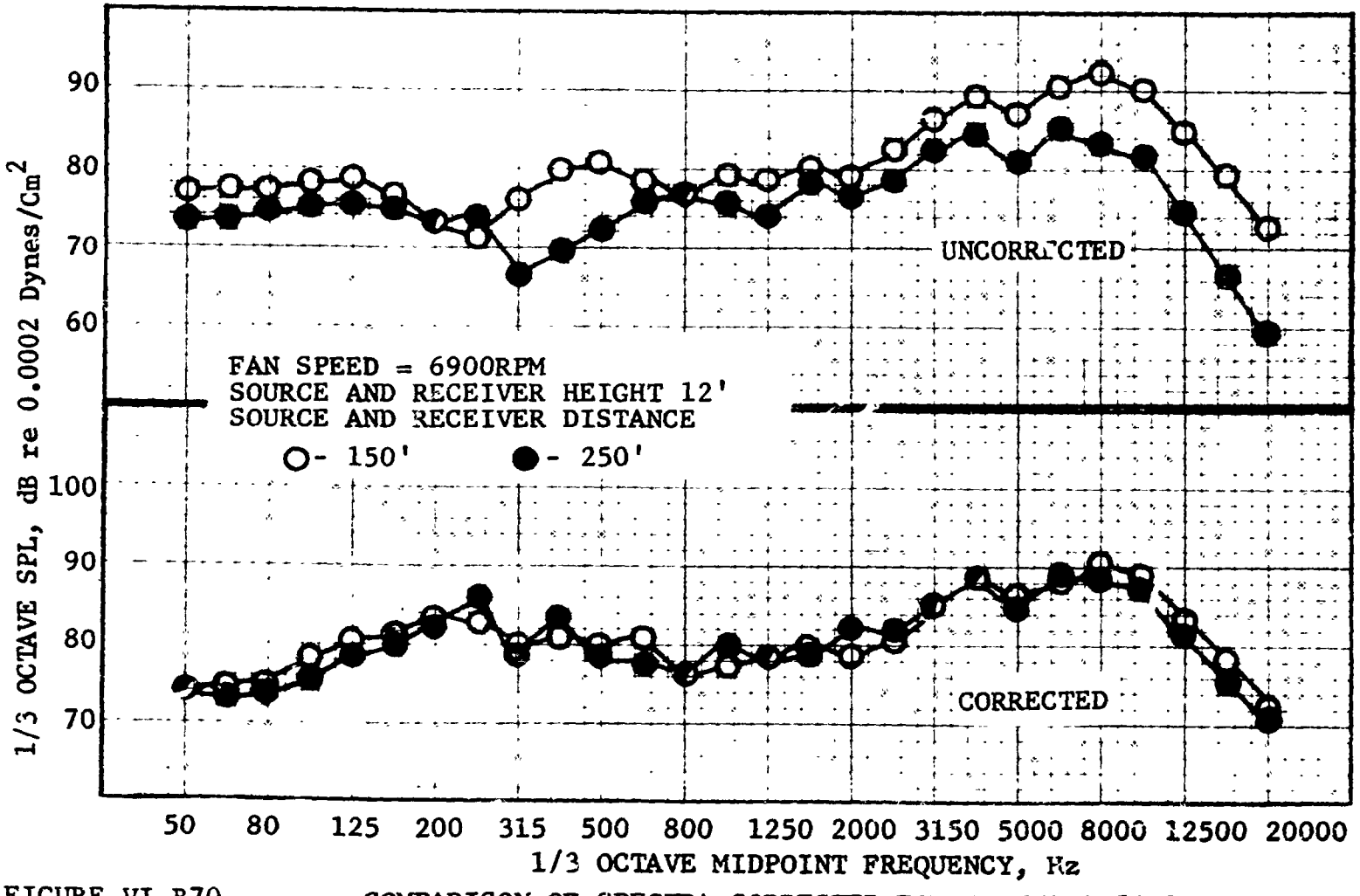

FIGURE VI-B70 COMPARISON OF SPECTRA CORRECTED FOR GROUND ABSORPTION AND REFLECTION, INVERSE SQUARE LAW DECAY, AND ATMOSPHERIC ABSORPTION. POLAR ANGLE = 120°

where:

$$F = f_c \text{ for } f_c \leq 4000$$

$$F = 0.89 \times f_c \text{ for } f_c > 4000$$

where f_c - Geometric Mean Frequency

$$\alpha_{max} = F \times 0.00357451 \times e^{(0.0117537 \times T_{amb})}$$

If $H_{amb}/H_{max} \leq 1.0$

$$\frac{\alpha_{act}}{\alpha_{max}} = (.74335316 \times 10)\, X^5 - (.17186058 \times 10^2)\, X^4$$

$$+ (.11814166 \times 10^2)\, X^3 - (.23793759 \times 10)\, X^2$$

$$+ (.13220157 \times 10)\, X + (.52305810 \times 10^{-3})$$

where $X = H_{amb}/H_{max}$.

If $H_{amb}/H_{max} > 1.0$ but < 6.5

$$\frac{\alpha_{act}}{\alpha_{max}} = (1.6955546 \times 10^{-2})\, X^4 - (.35055924 \times 10^{-1})\, X^3$$

$$+ (.28070973)\, X^2 - (.10581673 \times 10^1)\, X$$

$$+ (.18209020 \times 10^1)$$

where $H = H_{amb}/H_{max}$.

If $H_{amb}/H_{max} \geq 6.5$

$$\frac{\alpha_{act}}{\alpha_{max}} = 0.2$$

Solve for $\alpha_{act} = \alpha_{max} \times \frac{\alpha_{act}}{\alpha_{max}}$.

α_{act} represents the dB per 1000 ft. of distance of atmospheric absorption in each frequency band.

For the purposes of scaling data, these curve fits have been used for values of f_c >10 KHz. In order to verify this extrapolation, a series of tests were performed to determine high frequency atmospheric absorption coefficients.

The pertinent atmospheric conditions range from 69°F to 71°F and from 77% to 83% relative humidity. There was no measurable wind during the test.

The source for the test was an airhorn with a fundamental of 140 Hz with harmonics out to the higher frequencies. The data were recorded at distances of 25 ft., 50 ft., 100 ft., and 200 ft. from the source (Figure VI-B71). All noise below 5 KHz was filtered out.

Because the sound pressure decreases inversely with the distance from the source, there is a 6 dB decrease in sound pressure level for each doubling of distance. There will also be different EGA (Excess Ground Attenuation - see Reference 2), and ground reflection spectra recorded at each mike position. Any other difference in the data recorded at the four microphones will be attributed to atmospheric absorption.

The test was conducted over a two-hour period, during which 8 one-minute samplings of data were recorded. Despite the time differential and small changes in ambient weather, the data recorded in the repeats were remarkably consistent. At any selected frequency, the scatter about the average recorded SPL was less than ± 1 dB.

Figure VI-B72 shows the average sound pressure levels recorded at each microphone and adjusted by "square law" and EGA. The slope of the line connecting the data points represents the atmospheric absorption rate. Due to the frequency response of the recording system, data recorded above 30 KHz was not believed to be valid. Although there is a significant amount of scatter, the extrapolated curve fits of the SAE Specification (Reference 1) do approach the average absorption rates recorded in the test.

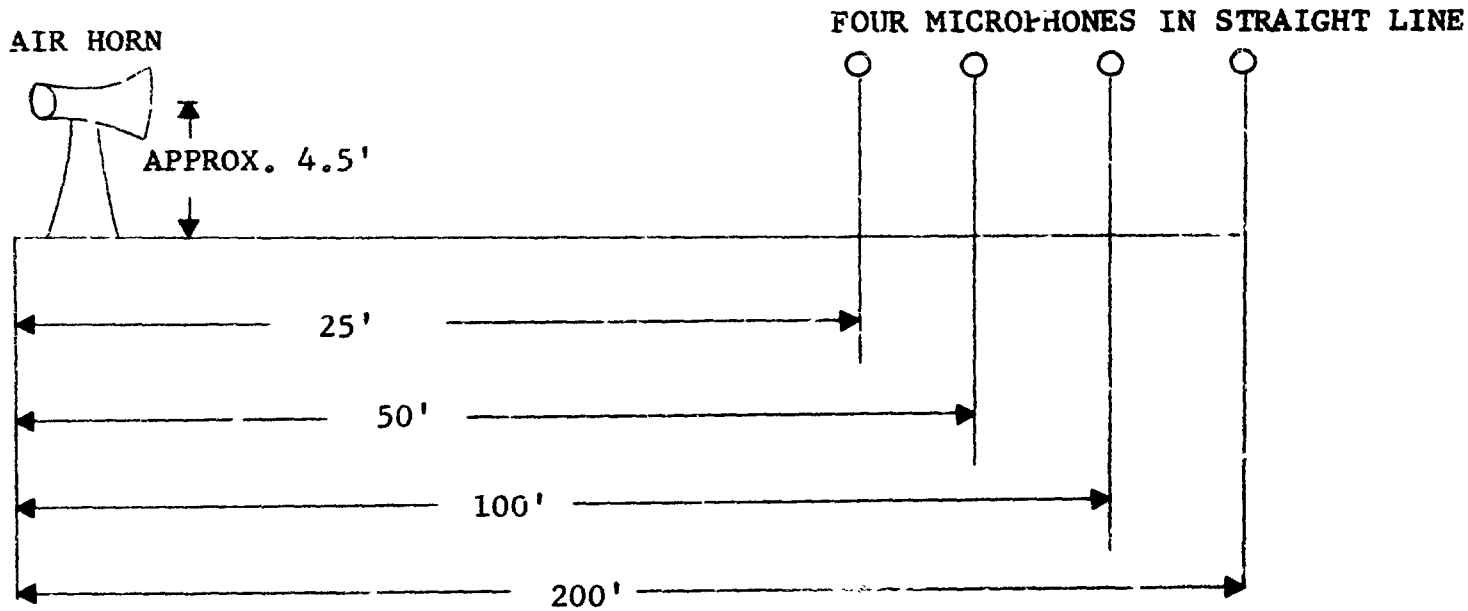

FIGURE VI-B71 HIGH FREQUENCY ATMOSPHERIC ABSORPTION TEST SETUP

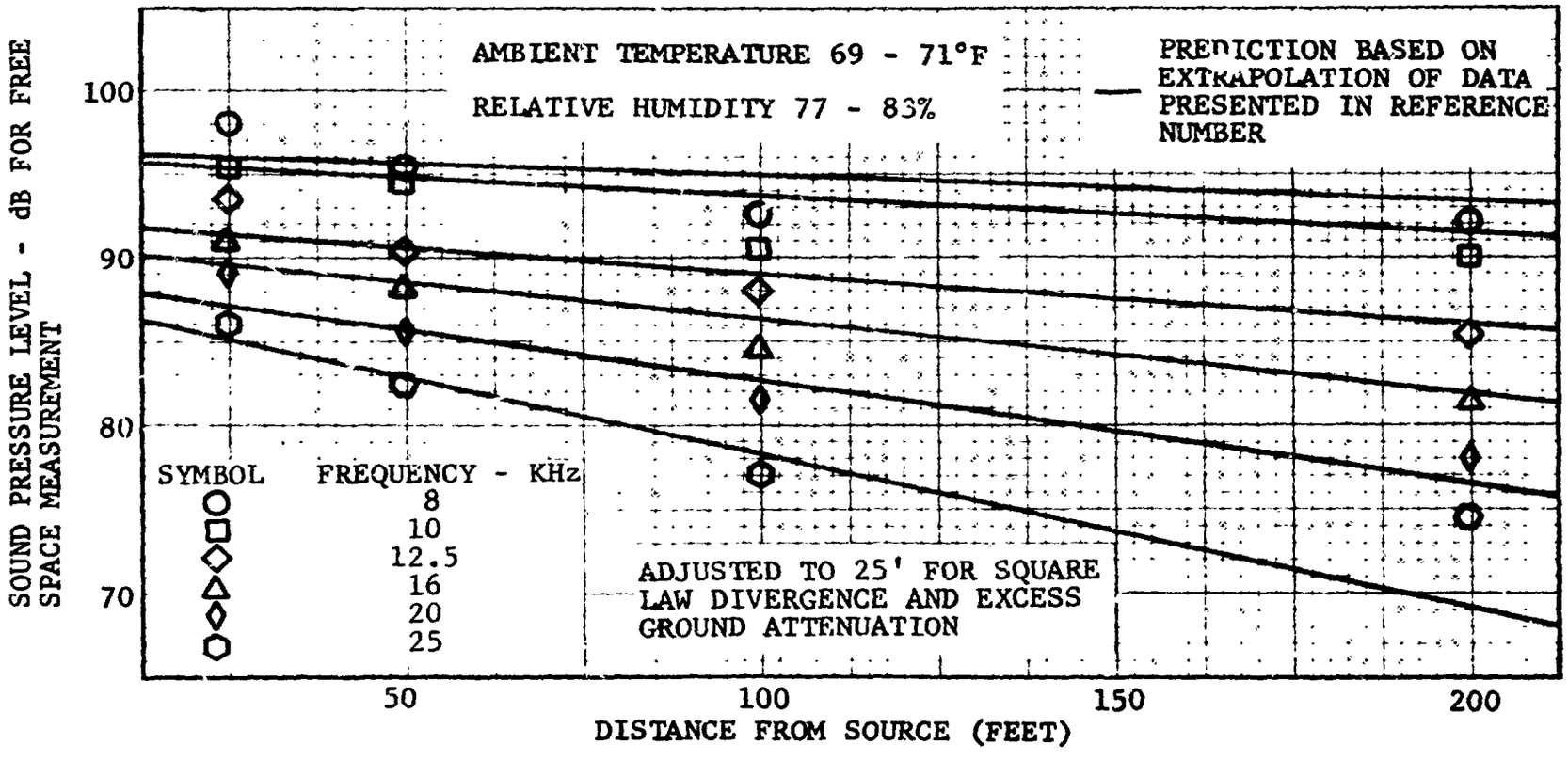

FIGURE VI-B72 ATMOSPHERIC ABSORPTION FOR HIGH FREQUENCIES

VII. SEMI EMPIRICAL FAN NOISE PREDICTION

(A) Introduction. The overall objective of this program has been the establishment of a network of techniques which would enable comprehensive and accurate prediction of fan/compressor noise. A primary requirement on each of these techniques, established at the inception of the program, was that each aspect of the prediction had to be based upon a mechanism which represented a functional relationship between acoustic parameters and aerodynamic and/or geometric parameters. For this purpose, sections II and III have described in detail the pertinant mechanisms of fan/compressor noise generation, transmission, radiation and propagation.

With respect to fan/compressor pure tone generation the mechanisms derived in Section III can be incorporated directly into the over-all predictor model. Pure tone transmission and radiation, on the other hand are complex noise phenomena. As demonstrated in Section III, certain aspects of transmission and radiation can be accurately predicted when the prediction is applied towards experiments performed under highly selective and/or controlled conditions. In this regard, the phased speaker modal pattern analysis, the low tip speed research compressor modal pattern analysis, the plane wave refraction experiments, and the transmission loss tests through a laboratory cascade indicate that the mechanisms presented in this report are in fact significant and valid. When these concepts are used to evaluate large size, high speed and high flow turbomachinery, however, other data are necessary to factor into the mechanisms. In this category are the effects of turbulence on blade row transmission and modal pattern generation and the effect of incipient modal radiation or external nacelle aerodynamic flow fields upon inlet or exhaust refraction. The prediction of these effects is feasible, but in many instances the aerodynamic data necessary to establish the prediction parameters is not available. It is either extremely difficult to measure or has not been measured on vehicles from which existing acoustic data has been used in this program. Certainly, derivation of such data was clearly beyond the scope of this program.

Broadband fan noise predictions entail similar problems. The mechanisms have clearly shown the importance of turbulence intensity and blade relative Mach number to broadband noise levels. It has also been shown that controlled two and three dimensional cascade experiments provide verification of these effects on a relative basis. Turbulence intensity data on fan stages, is not, however, information that is accurately calculated in the design phase of engine development. Accordingly, the use of these analytical mechanisms is limited to the availability of parameters which are necessary for input into the equations. Clearly the most accurate of predictions is of little use if the input parameters are not known.

Consequently, it was decided to perform specific aspects of the prediction in a semi-empirical manner. In each semi-empirical derivation, the formulations were based upon that parameter which, according to the mechanisms developed in Sections II and III, was most influential on the type of noise under consideration.

The results of this effort are described in subsequent pages of this section. It entails a useable system of predictions which requires use of normally available design parameters and, as shown in Section VIII is reliably accurate.

(B) Broadband Noise/Multiple Pure Tone Sound Power Levels Generated by IGV Less Fans. The correlation of experimental data was done on a one third octave basis and the results were non-dimensionalized with weight flow. Experimental data indicates that the one third octave band levels below 400 Hz are dominated by fan jet noise and were therefore left out of the correlation. It was shown in Section II that the key parameter affecting broadband noise generation is the blade relative Mach number. It was also shown that even though overall sound power level trends provide a qualitative valuable piece of information, they do not quantitatively represent the right trends in every one third octave band.

(1) IGV-Less Fans. The power levels of a number of vehicles (Development Vehicle I and II, CJ805-23 Fan) were, therefore, correlated on a one third octave power level spectrum basis as a function of blade tip relative Mach number M_R. The following relationships were obtained (one for every one third octave band).

$$[PWL - 10 \log \dot{W}/\dot{W}_o]_f = A_{f_0} + A_{f_1} M_R + A_{f_2} M_R^2 + A_{f_3} M_R^3 + A_{f_4} M_R^4 = \sum_{n=0}^{4} A_{f_n} M_R^n \qquad \text{(VII-B1)}$$

The A_{f_n} were derived using the General Electric computer program POLFIT***. Table VII-B1 lists the calculated coefficients. Figures VII-B1 to VII-B3 compare the normalized experimental power levels with the derived curves. These curves are replotted on a dimensionalized basis five one third octave at a time in Figure VII-B4 to VII-B6. It is interesting to note that the average power dependence on relative Mach number is 5.7 in the region $M_R = 1$. At sonic Mach numbers one can notice a flattening of the curves due to inlet choking. At supersonic Mach numbers the sound power levels rise sharply at the frequencies below the blade passing frequency due to the presence of multiple pure tones. The special handling of blade sub-harmonic tones(MPT's) will be discussed in the latter part of this Section.

(2) IGV Fans. The experimental results of Section V indicate that a basic difference exists between the broadband/multiple pure tone characteristics of IGV and IGV-less fans. It was, therefore, decided to use an empirical prediction applicable exclusively to IGV fans. The data obtained on several vehicles (D/V III, TF39 D/V) were used in that correlation. Here again a third octave power level spectrum prediction was obtained and the same relationship as defined by Equation VII-B1 resulted.

$$[PWL - 10 \text{ Log } \dot{W}/\dot{W}_o]_f = \sum_{n=0}^{4} A_{f_n} M_R^n \qquad \text{(VII-B2)}$$

$$[PWL - 10 \log_{10} (\dot{W}/\dot{W}_o)]_f = \sum_{n=0}^{4} A_n (M_R)^n$$

f	A_o	A_1	A_2	A_3	A_4
400	86.0019	14.3208	6.6665	0	0
500	85.9315	17.3125	5.9072	0	0
630	- 154.543	887.377	-1111.27	597.794	- 108.901
800	- 65.8737	524.330	- 543.590	194.362	0
1000	-2293.78	9775.47	-14754.1	9776.13	-2394.67
1250	-4275.99	17862.8	-26967.0	17877.4	-4385.01
1600	-3076.80	13038.5	-19787.4	13198.3	-3258.63
2000	-3561.08	15012.9	-22755.6	15152.4	-3734.95
2500	-1686.07	7270.56	-10919.1	7215.87	-1767.31
3150	-2732.12	11443.6	-17064.9	11186.2	-2719.12
4000	-1396.10	6034.49	- 8962.63	5867.10	-1426.25
5000	806.943	-2991.15	4720.36	-3225.10	808.644
6300	860.663	-3222.96	5128.08	-3556.19	909.602
8000	- 153.176	763.546	703.176	213.614	0
10000	81.9917	68.5888	- 28.6312	0	0

TABLE VII-B1

Broadband Noise/Multiple Pure Tone Prediction - Polynomial Coefficient

IGV Less Fans

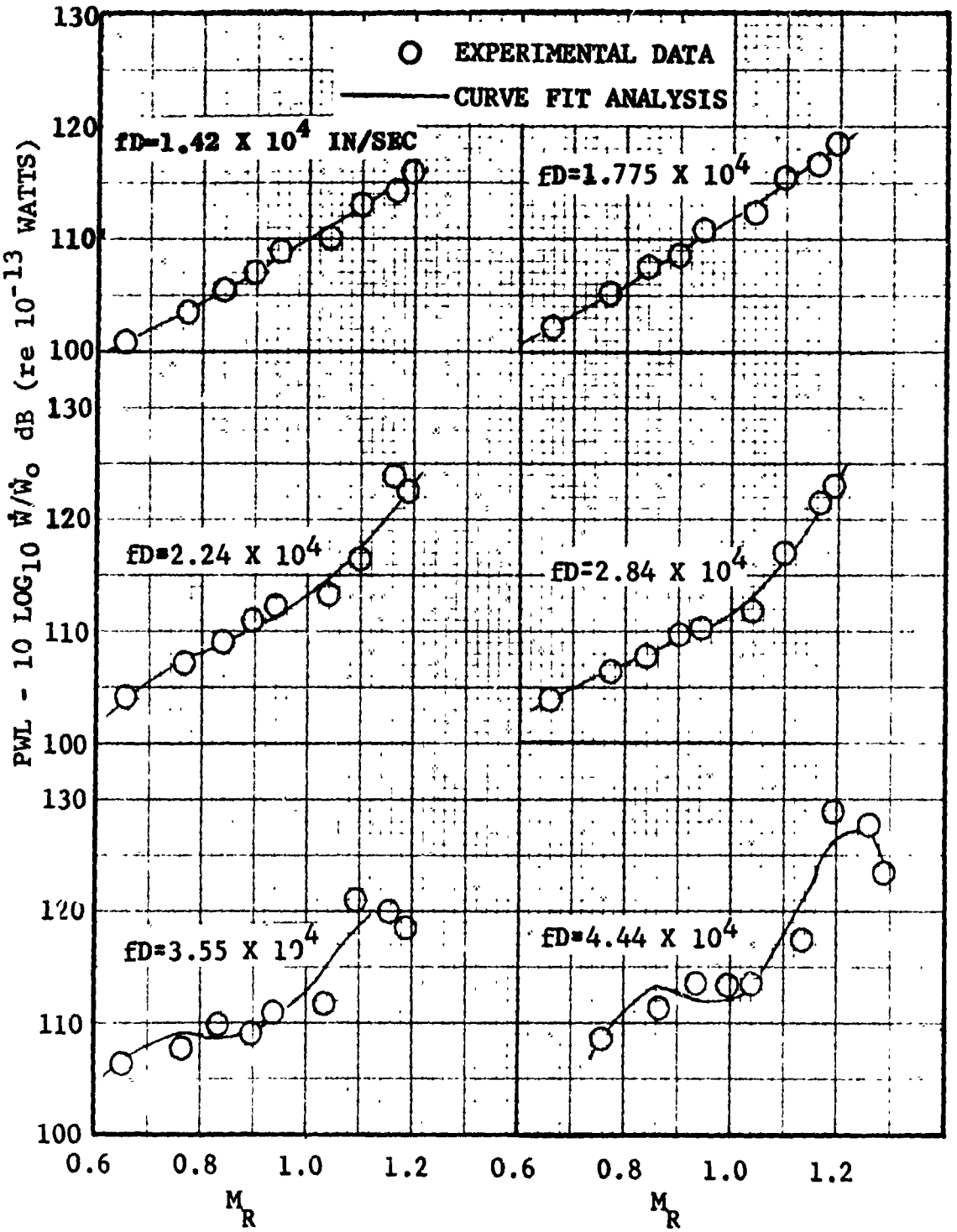

FIGURE VII-B1 NORMALIZED POWER LEVELS VERSUS M_R

(GE D/V-I) FOR A NUMBER OF fD's

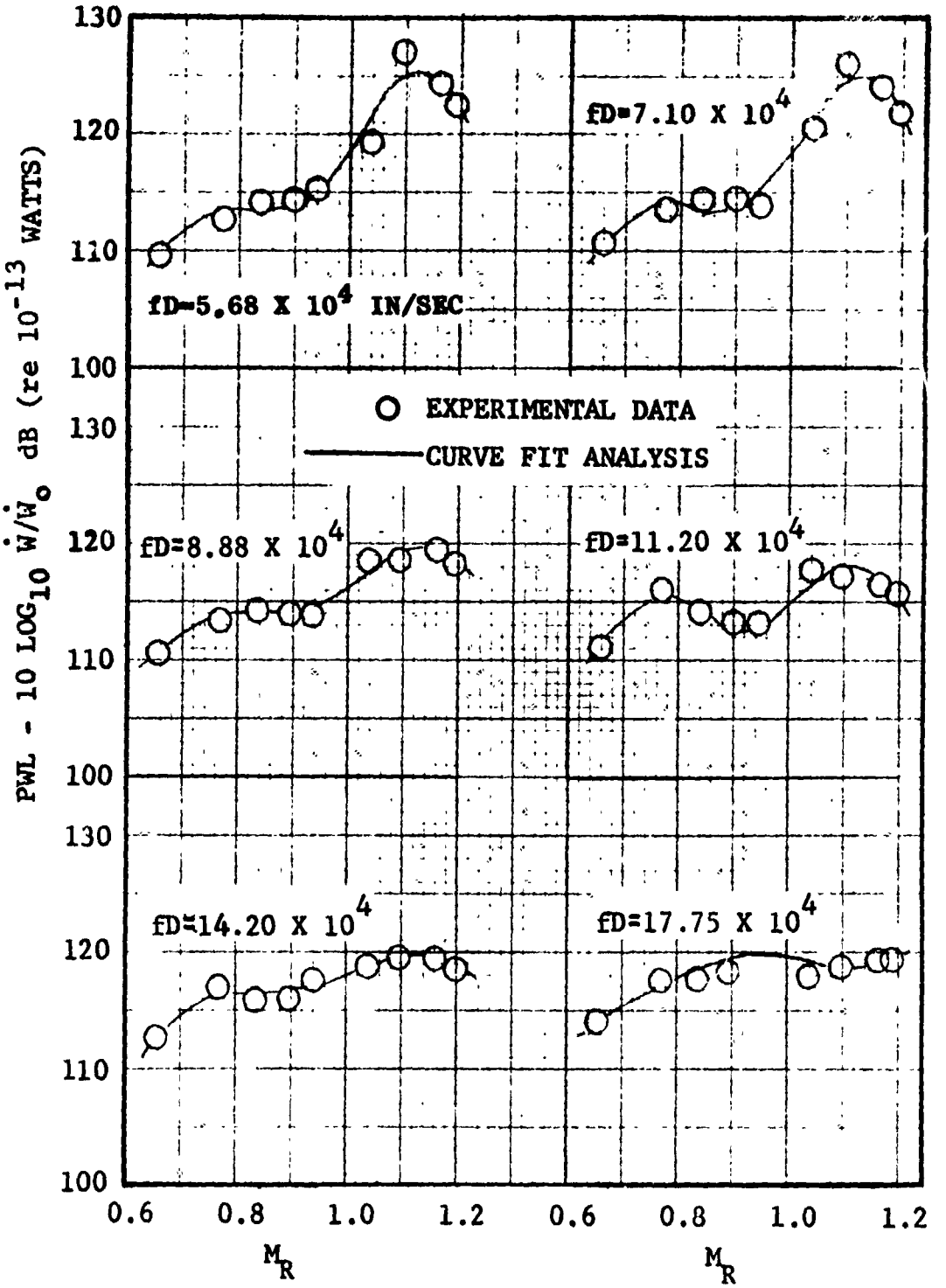

FIGURE VII-B2 NORMALIZED POWER LEVELS VERSUS M_R

(GE D/V-X) FOR A NUMBER OF fD's

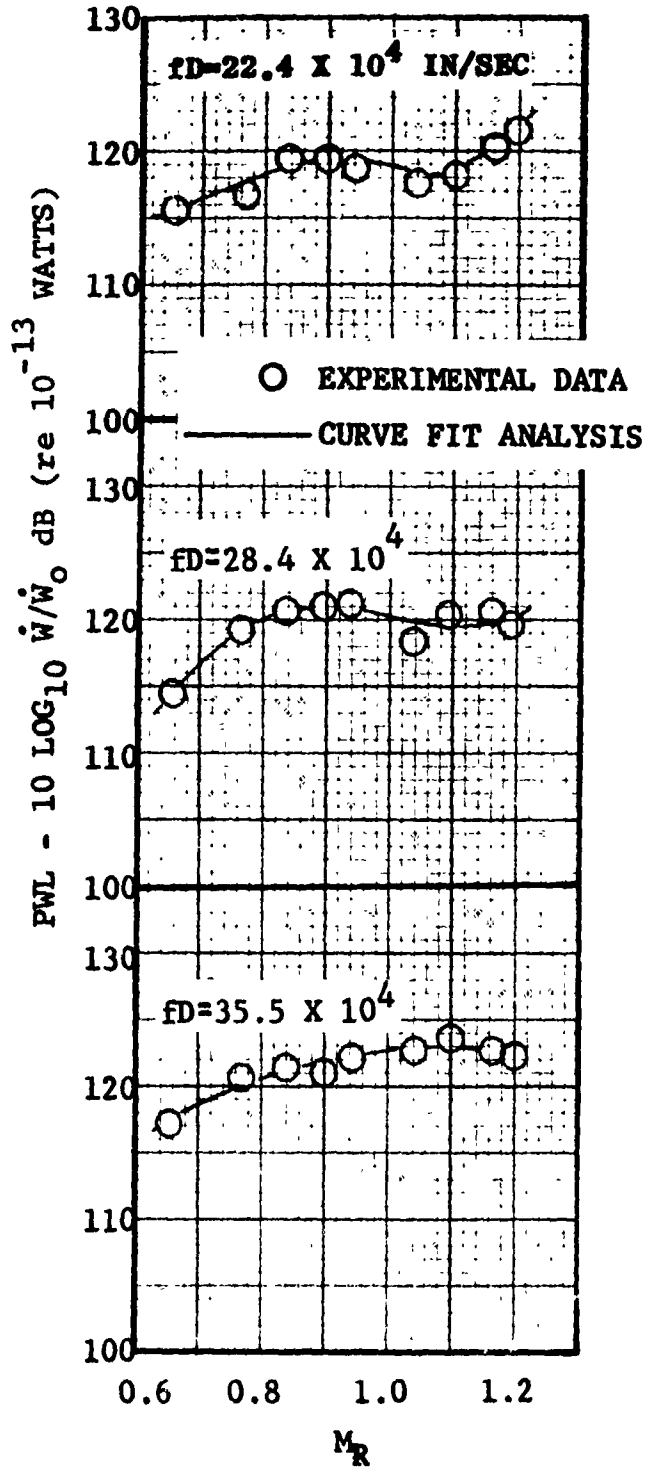

FIGURE VII-B3 NORMALIZED POWER LEVELS VERSUS M_R (GE D/V-1) FOR A NUMBER OF fD's

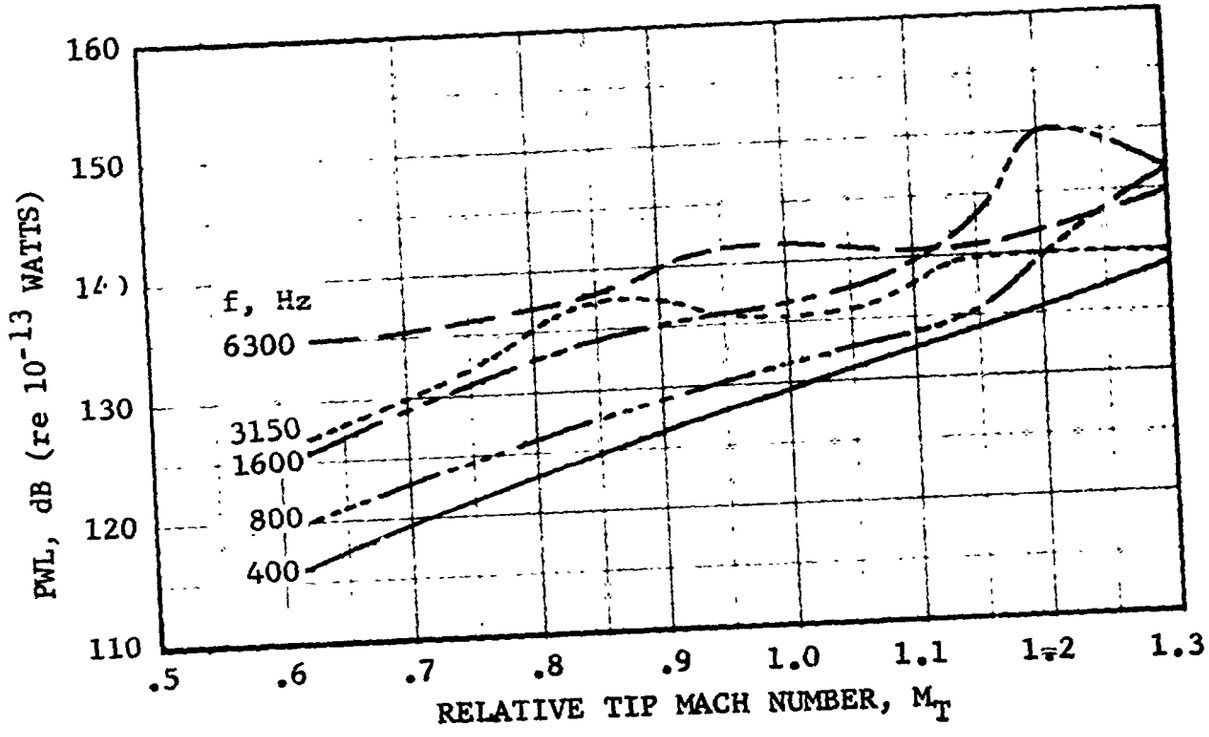

FIGURE VII-B4. BROADBAND NOISE/ MPT SOUND POWER LEVEL TRENDS WITH MACH NUMBER

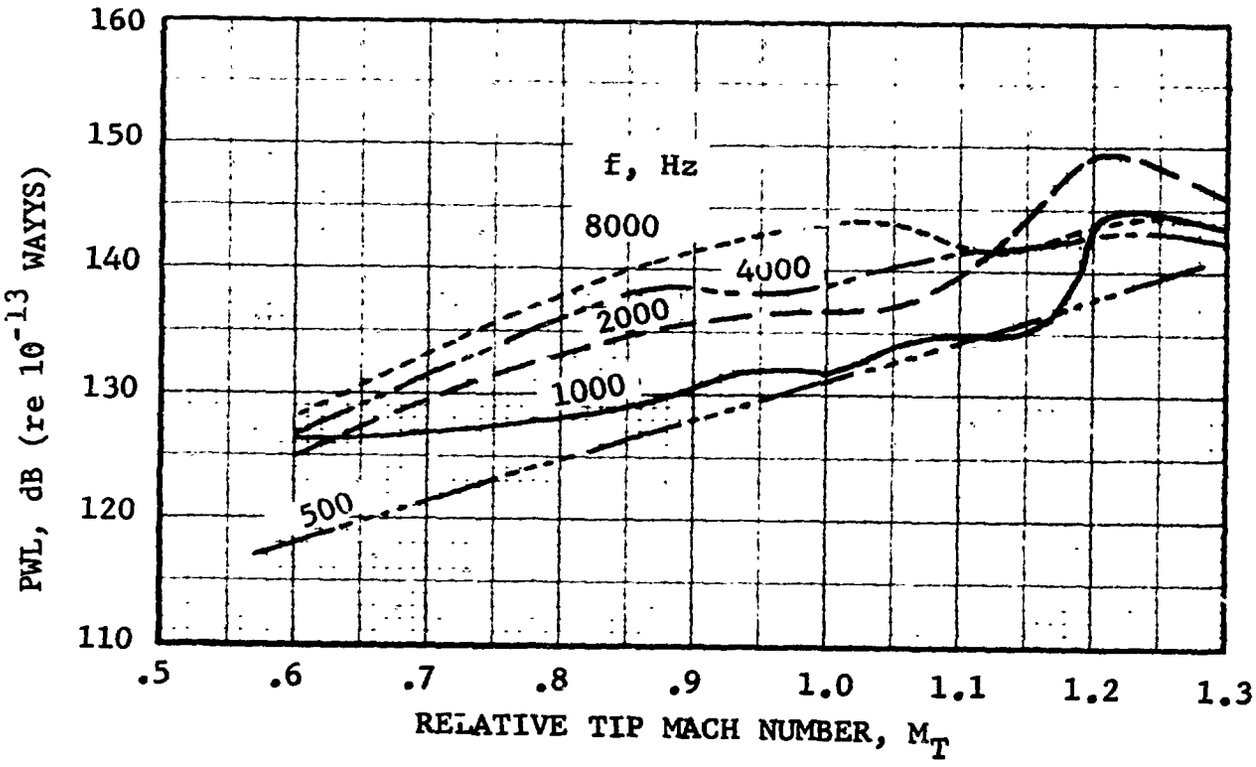

FIGURE VII-B5. BROADBAND NOISE/ MPT SOUND POWER LEVEL TRENDS WITH MACH NUMBER

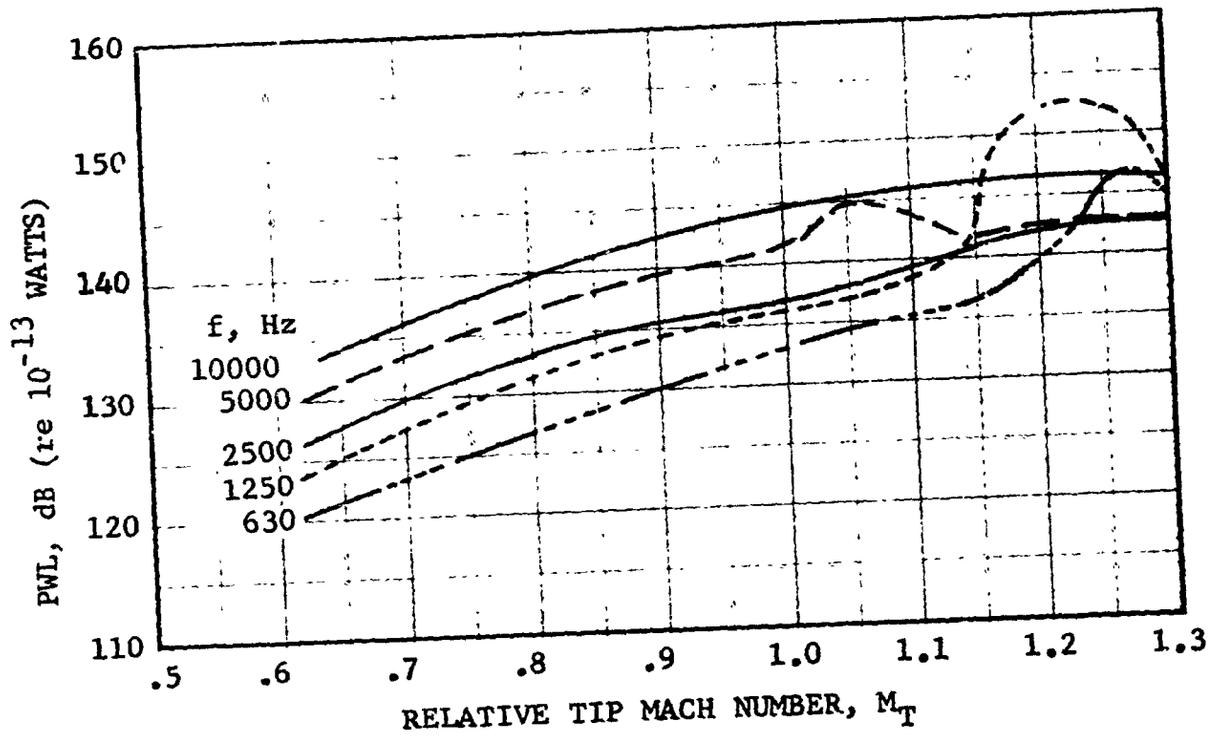

FIGURE VII-B6. BROADBAND NOISE/MPT SOUND POWER LEVEL TRENDS WITH MACH NUMBER

The correlation coefficients for IGV fans were again derived with the POLFIT*** Program and are shown on Table VII-B2. Figures VII-B7 to VII-B9 show a comparison of the normalized experimental power levels with the derived curves. A comparison between Figures VII-B1 to B3 and VII-B7 to B9 indicate that as previously shown in Section V the IGV fan has a higher broadband noise but a lower multiple pure tone (low frequency) contribution due to inlet guide vane blocking.

(3) Frequency Scaling. When the empirical prediction is applied to a vehicle of a different size than the one that has provided the data for the initial correlation, the resulting sound power level frequency spectrum has to be frequency scaled.

Careful examination of experimental data has shown that when the physical tip Mach number M_T is less than one, broadband power levels maybe scaled by keeping the parameter fD constant (D = fan outer diameter). This comes from the fact that in standard practice there is a very close relationship between fan O.D. and rotor blade chord which is the key parameter defining broadband noise characteristics. The frequency scaling procedure for broadband noise is as follows: If one is interested in PWL at a frequency f on a fan of diameter D and a weight flow (W), one goes through the following steps: One finds first which third octave bands f_1 and f_2 are such than $(fD)_1 < fD < (fD)_2$ one calculates PWL_1^* and PWL_2^* corresponding to $fD)_1$ and $(fD)_2$ using either Table VII-B1 or B2 depending on whether the fan under investigation does not or does have an IGV. One then finds

$$PWL^*_f = 10 \log_{10} \frac{(fD)_2 - fD}{(fD)_2 - (fD)_1} 10^{\frac{PWL^*_1}{10}} + \frac{fD - (fD_1)}{(fD)_2 - (fD)_1} 10^{\frac{PWL^*_2}{10}} \qquad \text{(VII-B3)}$$

Having found the normalized PWL_f one calculates PWL by just adding $10 \log_{10} (\dot{W}/\dot{W}_o)$.

The prediction of multiple pure tone frequency scaling is very similar to the above procedure except that the scaling parameter is fD/f_{BPF} (f_{BPF} = blade passing frequency). This technique applied only to the frequency bands below f_{BPF} with $M_T > 1$. The scaling parameter was derived from the fact that MPT's are essentially sub-harmonics and are, therefore, directly dependent on the blade passing frequency. Now if one is interested in $(PWL)_{MPT}$ on a fan of diameter D at a given Mach number M_R one first finds what one third octave bands would give $(fD/f_{BPF})_1 < fD/f_{BPF} < (fD/f_{BPF})_2$. One calculates PWL^*_1 and PWL^*_2 using either Table VII-B1 or VII-B2. The interpolation formula becomes

$$PWL^*_{MPT} = 10 \log \frac{\left(\frac{fD}{f_{BPF}}\right)_2 - \frac{fD}{f_{BPF}}}{\left(\frac{fD}{f_{BPF}}\right)_2 - \left(\frac{fD}{f_{BPF}}\right)_1} 10^{\frac{PWL^*_1}{10}} + \frac{\frac{fD}{f_{BPF}} - \left(\frac{fD}{f_{BPF}}\right)_1}{\left(\frac{fD}{f_{BPF}}\right)_2 - \left(\frac{fD}{f_{BPF}}\right)_1} 10^{\frac{PWL^*_2}{10}}$$

One adds 10 log $\dot{W}/\dot{W}_o$ and obtains the desired power level.

$$[PWL - 10 \log_{10} \dot{W}/\dot{W}_o] = \sum_{n=0}^{4} A_n (M_r)^n$$

f	A_o	A_1	A_2	A_3	A_4
400	67.3349	91.1491	- 70.1414	23.9973	0
500	88.2161	26.1668	0	0	0
630	- 3.4689	350.187	- 377.341	142.560	0
800	131.684	- 70.795	52.1573	0	0
1000	9.2752	348.681	- 392.262	148.661	0
1250	-630.786	3480.62	-6039.63	4596.00	-1288.77
1600	- 42.2946	529.630	- 591.815	220.258	0
2000	-392.080	2148.36	-3362.95	2302.69	- 581.214
2500	95.4247	- 104.694	479.959	- 557.677	202.245
3150	- 95.0009	684.170	- 712.917	242.641	0
4000	- 31.7717	484.119	- 502.018	170.355	0
5000	87.4706	61.1089	- 28.0562	0	0
6300	- 25.8840	493.040	- 541.961	195.252	0
8000	- 70.701	600.918	- 614.873	206.471	0
10000	187.986	- 281.592	361.662	- 142.452	0

TABLE VII-B2

Broadband Noise/Multiple Pure Tone Prediction - Polynomial Coefficients

IGV Fans

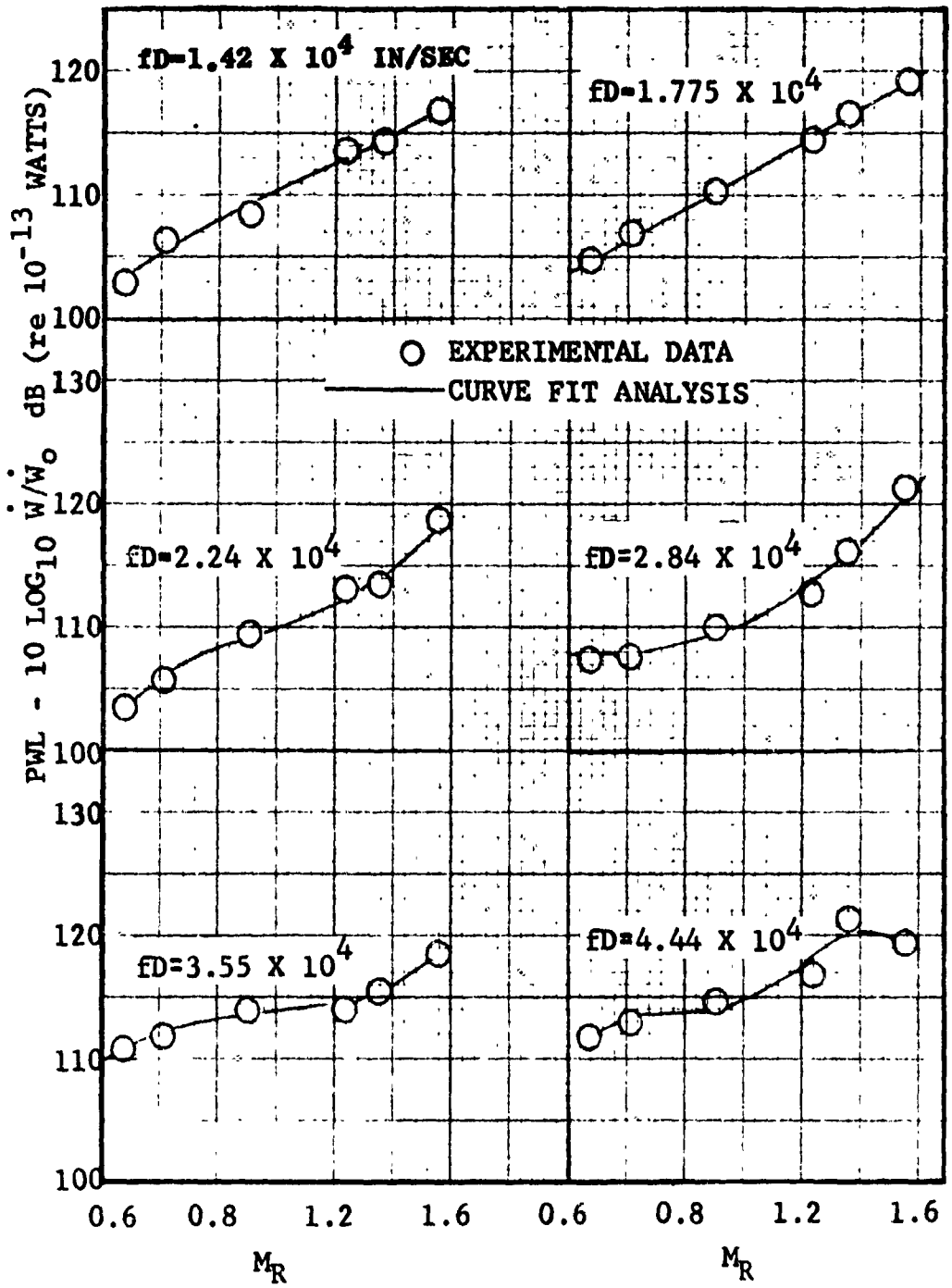

FIGURE VII-B7 NORMALIZED POWER LEVELS VERSUS M_R

(GE D/V-III) FOR A NUMBER OF fD's

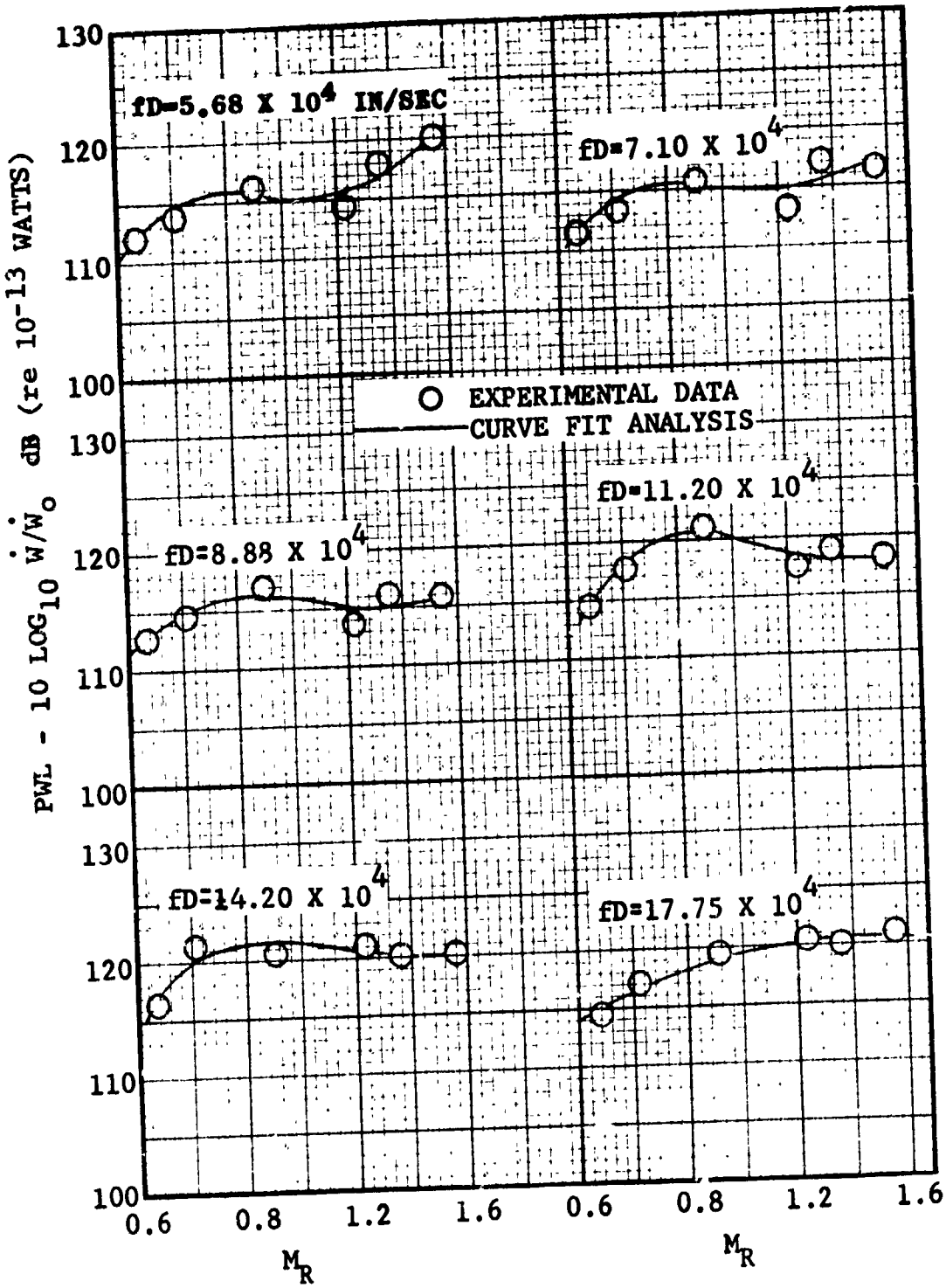

FIGURE VII-B8 NORMALIZED POWER LEVELS VERSUS M_R

(GE D/V III) FOR A NUMBER OF fD's

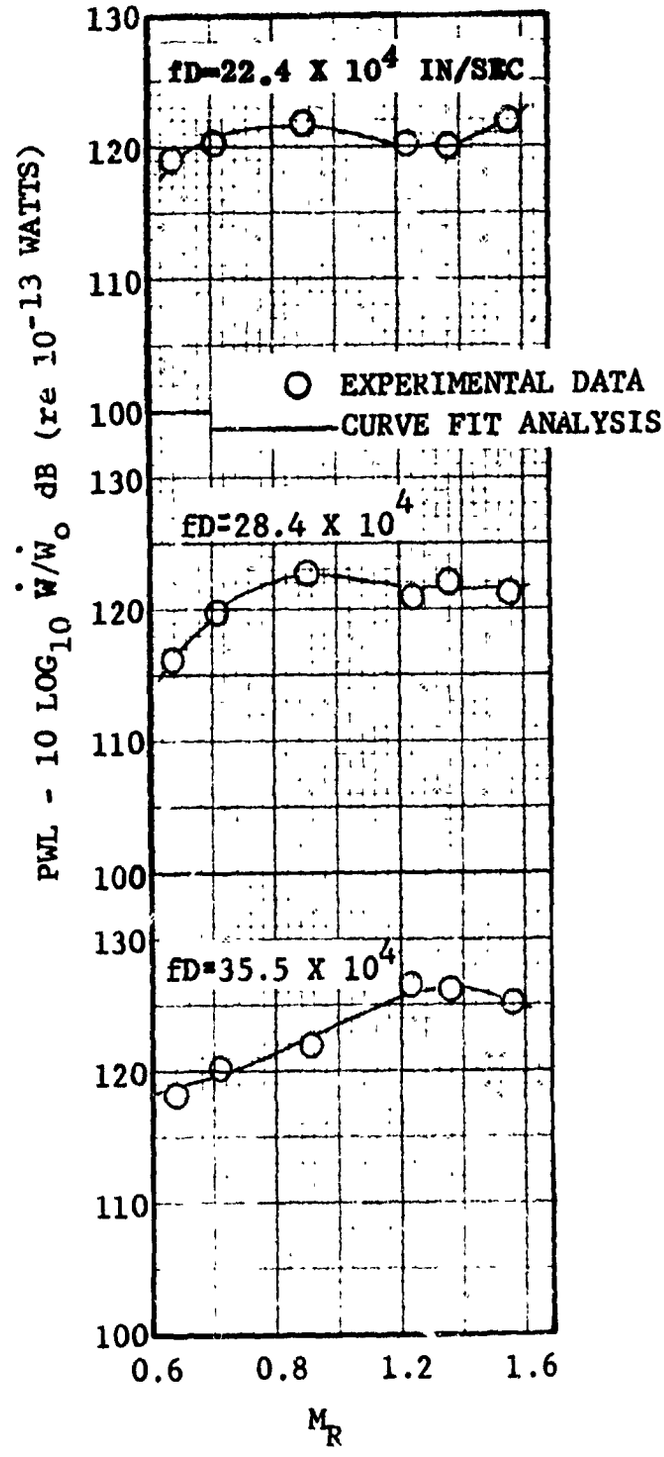

FIGURE VII-B9 NORMALIZED POWER LEVELS VERSUS M_R

(GE D/V-III) FOR A NUMBER OF fD's

(C) Fan Blade Passing Frequency Directivity. To predict at a point along an arc or a sideline the correct radiated sound pressure level one has to have a detailed knowledge of the radiation pattern, i.e., the sound directivity index distribution vs. polar angle. Section II discussed in some detail the different mechanisms affecting blade passing frequency tone radiation. It was shown that tip speed, spinning lobe number and refraction parameters have an effect on tone directivities. Examination of experimental data indicates that fan tip speed and refraction effects overshadow the spinning lobe (vane/blade ratio) effects. This is shown very clearly in Section IV. Refraction effects are directly related to inlet/exhaust velocities and temperatures, which are related to fan pressure ratio which has a fairly constant relationship to fan tip speed in a modern fan design. Because of these considerations it was decided to correlate the fan directivity index with fan tip physical Mach number M_T.

(1) IGV-Less Fans. Experimental results obtained on a number of fan vehicles (D/V I and II, CJ805-23) were correlated. Directivity indices as a function of angular position (angles of interest 20 to 160° in increments of 10°) were obtained for nine different tip Mach numbers M_T using a General Electric regression analysis program MULFT$***. The following relationship was obtained

$$DI = A_o + A_1 \sin\theta + A_2 \sin^2\theta + A_3 \sin^3\theta + A_4 \sin^6\theta + A_5 \cos\theta \qquad \text{(VIII-C1)}$$

Where directivity index $DI = SPL_{angle} - SPL_{average}$. The coefficients for $A_o, \ldots A_5$ are listed in Table VII-C1 and VII-C2 for respectively the front and the rear quadrant directivities. Comparisons between experimental results and data computed from the correlation formulas are shown on Figure VII-C1.

(2) IGV Fans. Experimental results on directivities obtained on vehicles D/V III and TF39 D/V were correlated. The following relationship was obtained

$$DI = A_o + A_1 \sin 1.5\theta + A_2 \cos 2\theta + A_3 \sin 2\theta + A_4 \cos^2 2\theta + A_5 \sin 1.5\theta$$

$$+ A_5 \sin 1.5\,\theta \sin^2\theta$$

The coefficients A_o, $A_1, \ldots A_5$ are presented on Table VII-C3. Comparisons between experimental results and data computed from the correlation formula are shown on Figure VII-C2.

IGV LESS VEHICLE

M_T	A_o	A_1	A_2	A_3	A_4	A_5
0.422	-102.836	114.424	- 99.423	26.436	47.505	81.488
0.507	- 77.279	-1082.050	2578.48	-1875.15	424.546	233.796
0.591	- 58.321	36.397	132.484	- 207.609	93.234	40.527
0.675	-165.339	477.971	- 918.473	638.333	- 46.505	92.408
0.759	- 9.182	1391.70	3092.40	-2160.20	442.348	222.312
0.798	-218.682	- 199.551	814.532	672.045	247.542	225.543
0.832	-156.996	- 292.958	935.266	- 724.538	216.503	180.007
0.860	-151.550	245.296	751.293	- 546.802	170.034	172.391
0.894	- 164.782	- 192.079	731.479	- 589.806	194.345	170.292
0.916	- 163.053	- 48.975	413.838	- 369.097	149.218	145.953
0.957	- 75.285	65.943	98.629	- 165.526	71.441	43.385
1.041	- 50.825	534.433	-982.373	608.906	- 106.140	- 54.092
1.068	9.097	343.901	-668.204	425.197	- 102.935	- 79.697
1.096	- 28.358	550.682	-1049.73	660.607	- 124.161	- 80.042
1.124	- 3.974	373.125	- 686.65	408.752	- 82.08	- 77.836
1.151	45.209	481.123	-1004.31	649.478	- 154.455	- 140.791
1.179	34.999	656.952	-1426.16	978.165	- 226.125	- 156.881

TABLE VII-C1

Coefficients for Polar Angles $20° \leq \theta \leq 80°$

$$D.I. = A_o + A_1 \sin\theta + A_2 \sin^2\theta + A_3 \sin^3\theta + A_4 \sin^6\theta + A_5 \cos\theta$$

IGV LESS VEHICLE

M_T	A_o	A_1	A_2	A_3	A_4	A_5
0.422	-83.556	322.493	-687.879	529.730	- 87.999	- 27.341
0.507	-25.924	- 43.337	23.645	62.287	- 21.426	- 32.270
0.591	11.718	-192.879	349.063	-181.93	12.267	- 15.514
0.675	-29.246	398.087	-995.243	811.252	-185.889	31.709
0.759	- 7.909	- 12.697	- 25.816	72.350	- 27.683	- 8.163
0.798	-71.994	334.162	-670.823	470.609	- 62.024	- 12.821
0.832	-67.878	325.297	-678.377	484.551	- 63.515	- 11.985
0.860	-50.352	141.072	-268.098	188.338	- 11.149	- 20.681
0.894	-45.556	171.756	-340.753	243.88	- 29.253	- 10.821
0.916	-41.217	66.200	-122.419	95.290	1.870	- 24.910
0.957	-30.646	210.379	-514.43	411.05	- 75.387	1.382
1.041	-37.589	45.326	-185.081	215.203	- 38.859	- 32.181
1.068	-50.951	277.828	-678.828	558.926	-106.959	- 8.124
1.096	-35.232	238.639	-649.968	576.305	-130.10	- 1.716
1.124	-27.977	63.488	-233.634	259.857	- 61.814	- 18.507
1.151	-49.147	219.149	-544.984	475.042	- 99.667	- 11.362
1.179	-35.822	248.570	-643.764	556.826	-124.003	4.092

TABLE VII-C2

Coefficients for Polar Angles $90° \leq \theta \leq 160°$

$$D.I. = A_o + A_1 \sin\theta + A_2 \sin^2\theta + A_3 \sin^3\theta + A_4 \sin^6\theta + A_5 \cos\theta$$

IGV VEHICLE

M_t	f^*_{BPF} (H_z)	A_o	A_1	A_2	A_3	A_4	A_5
.706	3150	26.211	-38.658	-21.085	32.422	-22.457	-23.380
.777	3150	8.865	- 7.315	- 5.160	8.008	- 9.547	-10.016
.91	4000	2.841	- .232	- 2.557	3.585	- 1.744	- 7.707
1.059	5000	-16.053	28.367	8.188	-21.046	7.070	9.626
1.115	5000	3.038	.336	- 2.361	1.362	- 3.761	- 6.226
1.2	5000	- 2.091	7.144	.777	- 4.082	1.882	- 5.117

*f_{BPF} is the center frequency of the 1/3 octave band which contains the blade passing frequency

TABLE VII-C3

Coefficients for Polar Angles $20° \leq \theta \leq 160°$

$$D.I. = A_o + A_1 \sin 1.5\theta + A_2 \cos 2\theta + A_3 \sin 2\theta + A_4 \cos^2 2\theta$$

$$+ A_5 \sin\theta\ 1.5\theta \sin 2\theta$$

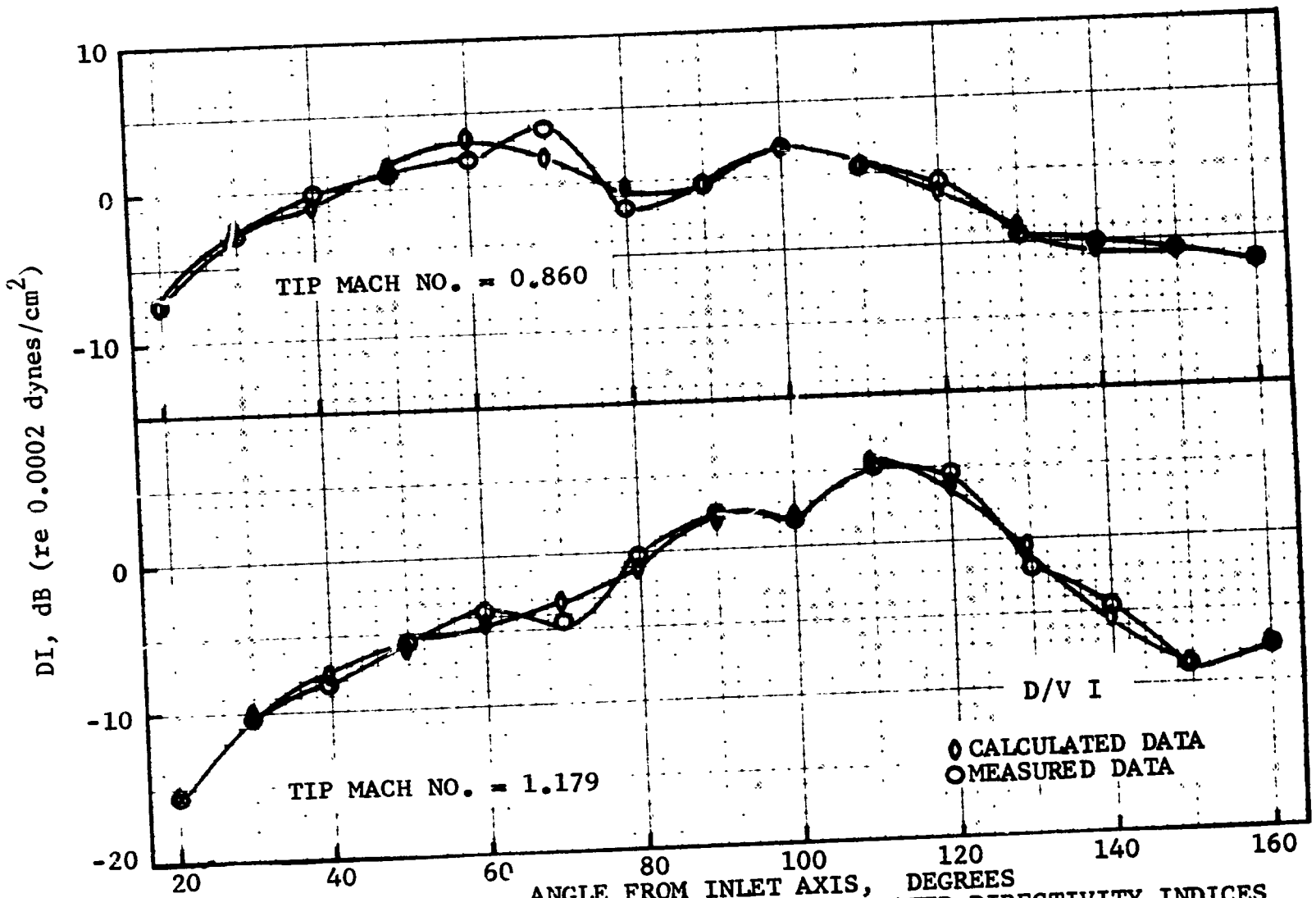

FIGURE VII-C1 COMPARISON OF D/V I MEASURED AND CALCULATED DIRECTIVITY INDICES FOR ROTOR TIP SPEEDS OF MACH 0.860 AND 1.179

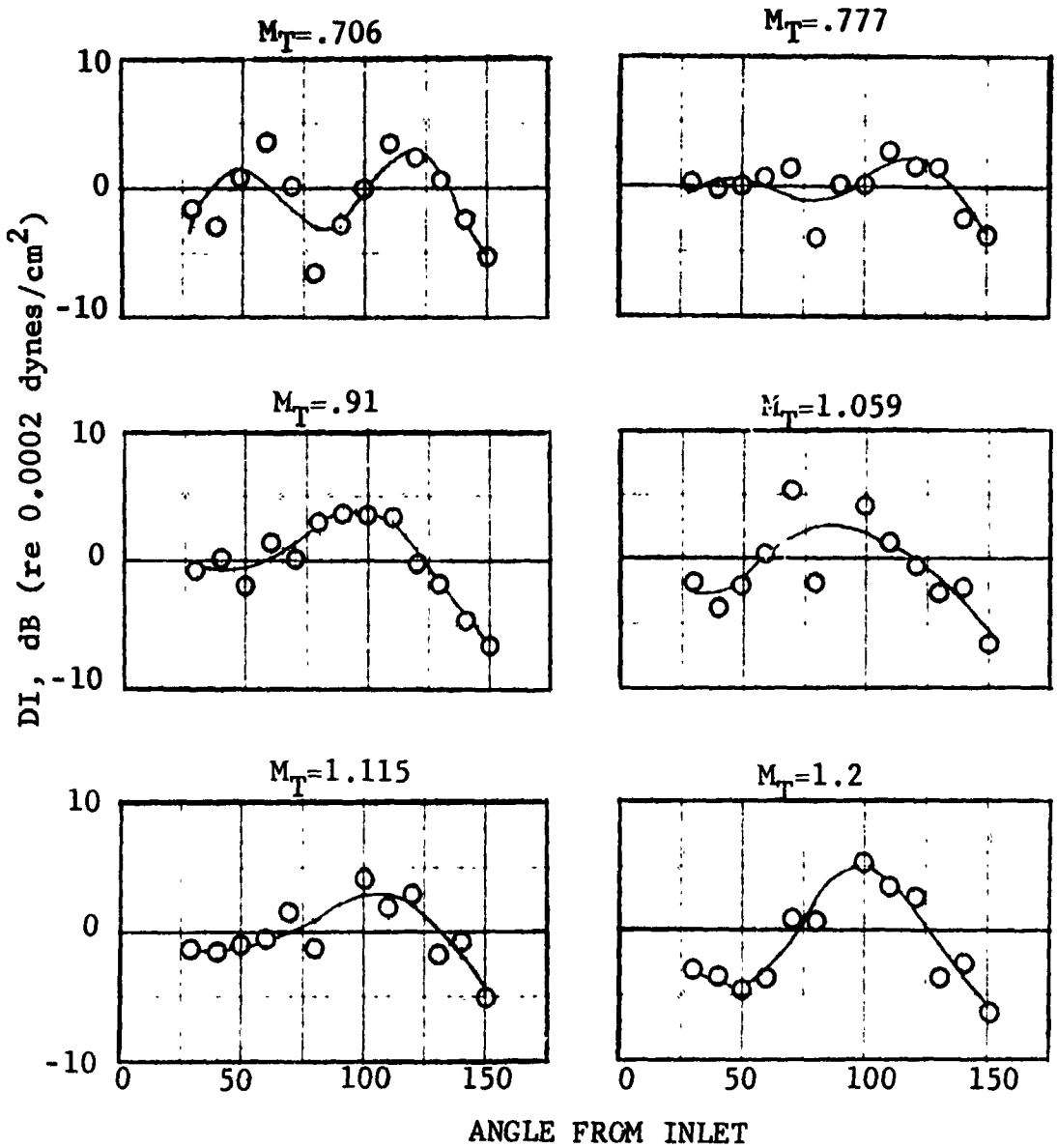

FIGURE VII-C2 FAN BLADE PASSING FREQUENCY DIRECTIVITY INDEX FOR GE D/V-III

(D) Broadband and Multiple Pure Tone Noise Directivity . Broadband noise and multiple pure tone radiation mechanisms are essentially similar to blade passing frequency tone radiation mechanisms and are functions of the same parameters. Therefore, following the same considerations it was originally decided to correlate broadband noise and multiple pure tone directivities in function of fan tip Mach number M_T. There is however in IGV fans and IGV-less fans respectively, a close relationship between M_T and the tip relative Mach number M_R. Due to the fact that all sound power level predictions for broadband noise and MPT's were already derived in terms of M_R, it was decided to use M_R as a correlating parameter to facilitate the use of the prediction procedure.

(1) IGV-Less Fans. Experimental data obtained on D/V I and II and the CJ805-23 fan were used for correlations done for each of nine relative Mach numbers. The range of angles covered was 20 to 160° in 10° increments. Fifteen third octave band frequencies (from 400 Hz to 10000 Hz) were considered. The following directivity index formula was obtained

$$D.I. = A_0 + A_1 \sin 1.5\,\theta + A_2 \cos 2\theta + A_3 \sin 2 \quad + A_4 \cos^2 2\theta$$
$$+ A_5 \sin 1.5\theta \sin 2\theta \qquad \text{(VII-D1)}$$

The coefficients A_j, j = 0, 1, ----- 5 are a function of M_R and frequency. They were obtained by regression analysis. The results are presented in Tables VII-D1 to VII-D6. The comparison between experimental results and data derived from equation VII-D1 are shown on Figures VII-D1 to VII-D24.

(2) IGV Fans. Similar correlations were derived for IGV fans using the experimental data obtained on D/V III and the TF39 D/V. Correlating formulas were obtained for six tip relative Mach numbers, for fifteen one third octave frequency bands ranging from 400 to 10000 Hz as a function of polar angles varying from 20 to 160° in 10° increments. Same equation D.I. = f (θ).

As shown previously, the coefficients A_j, j = 0, 1,----, 5 were derived by regression analysis. The coefficients are here again functions of M_R and third octave frequencies. The results are listed in Tables VII-D7 to VII-D15. Comparisons between experimental results and data computed from the correlation's relationships are shown on Figures VII-D25 to VII-D39.

(3) Frequency Scaling. Broadband noise and multiple pure tone frequencies have to be scaled to fit the vehicle under consideration. The directivity indices will be scaled using the same scaling frequency parameter used in the sound power level prediction, namely "fD" for broadband noise and "fD/f_{BPF} "for MPT's. Again using the same nomenclature with the subscripts "1" and "2" representing the adjacent bands one obtains:

For Broadband Noise

$$D.I. = 10 \log_{10} \frac{(fD)_2 - (fD)}{(fD)_2 - (fD)_1} 10^{\frac{DI_1}{10}} + \frac{(fD) - (fD)_1}{(fD)_2 - (fD)_1} 10^{\frac{DI_2}{10}} \qquad \text{(VII-D2)}$$

For Multiple Pure Tones

$$D.I. = 10 \log_{10} \frac{(fD/F_{BPF})_2 - (fD/f_{BPF})}{(fD/f_{BPF})_2 - (fD/f_{BPF})_1} 10^{\frac{DI_1}{10}}$$

$$+ \frac{(fD/f_{BPF}) - fD/f_{BPF})_1}{(fD/f_{BPF})_2 - (fD/f_{BPF})_1} 10^{\frac{DI_2}{10}} \qquad \text{(VII-D3)}$$

Comparisons between experimental results and data computed from the correlation's relationships are shown on Figures VII-D40 to VII-D45.

$$D.I. = A_o + A_1 \sin 1.5\theta + A_2 \cos 2\theta + A_3 \sin 2\theta + A_4 \cos^2 2\theta + A_5 \sin 1.5\theta \sin 2\theta$$

f	A_o	A_1	A_2	A_3	A_4	A_5
400	- 4.20788	13.6514	4.77902	-10.3642	4.63938	7.44632
500	- 4.66136	7.70959	2.23694	- 6.74423	1.91658	3.95528
630	3.62761	- 2.40796	- 2.37659	2.0617	- 4.44452	- 4.27851
800	8.77786	- 9.81079	- 5.68278	8.29568	- 8.33415	- 8.52029
1000	15.6428	-22.5526	-12.3904	19.5415	-13.1878	-13.4805
1250	20.6013	-29.696	-15.3382	26.1269	-16.2398	-18.2162
1600	17.6397	-24.5695	-12.7671	21.4834	-13.9844	-16.0016
2000	21.0922	-30.4234	-15.3625	26.5853	-16.107	-18.9901
2500	20.4726	-29.9483	-15.3603	26.1322	-15.8636	-18.3664
3150	22.4349	-30.9152	-15.6202	27.6452	-17.218	-20.891
4000	23.7936	-31.8587	-15.9236	29.0571	-18.5572	-23.2488
5000	24.0169	-32.9657	-16.9303	29.42	-18.3156	-23.333
6300	23.0943	-34.5125	-17.6344	29.9345	-17.8326	-20.7523
8000	20.727	-27.4378	-15.3374	24.5304	-19.5603	-18.5908
10000	22.545	-31.0919	-16.6452	28.0617	-18.6151	-21.0071

TABLE VII-D1

Directivity Correlation Coefficients

$M_R = .76$

IGV Less Fans

$$D.I. = A_o + A_1 \sin 1.5\theta + A_2 \cos \quad + A_3 \sin 2\theta$$

$$+ A_4 \cos^2 2\theta + A_5 \sin 1.5\theta \sin 2\theta$$

f	A_o	A_1	A_2	A_3	A_4	A_5
400	- 2.02454	4.59299	1.06747	- 4.06662	- .571258	2.2396
500	- .0263473	.0346881	- 1.22965	- 1.52511	- 1.32449	.39963
630	4.97094	- 5.47146	- 3.71518	4.63716	- 4.80629	- 4.9369
800	10.9286	-14.6174	- 7.21522	12.6878	- 8.2843	-10.1969
1000	16.9511	-23.9908	-12.2799	20.9778	-13.4438	-14.7943
1250	19.2056	-28.4791	-15.4213	24.8556	-15.3652	-16.9943
1600	19.8542	-29.2705	-15.5842	25.8817	-15.3253	-17.91
2000	19.8265	-30.2837	-16.4326	26.6177	-15.0444	18.2718
2500	21.0895	-31.8012	-17.0762	28.3366	-16.3786	-19.5646
3150	18.263	-27.8539	-16.5758	25.9226	-15.7416	-17.317
4000	20.044	-29.7637	-17.1103	27.0278	-16.0	-19.5112
5000	21.7294	-31.9453	-17.7653	28.3781	-16.3261	-21.825
6300	22.4441	-33.3209	-18.4500	29.3216	-17.2908	-22.0727
8000	16.8959	-22.5625	-14.5168	21.1202	-17.0452	-16.1402
10000	27.6474	-37.4746	-18.5834	33.8154	-21.3287	-26.344

TABLE VII-D2

Directivity Correlation Coefficients

$M_R = .872$

IGV Less Fans

$$D.I. = A_o + A_1 \sin 1.5\theta + A_2 \cos 2\theta + A_3 \sin 2\theta + A_4 \cos^2 2\theta + A_5 \sin 1.5\theta \sin 2\theta$$

f	A_o	A_1	A_2	A_3	A_4	A_5
400	- 3.59116	7.11721	1.67373	- 6.75803	- 1.30712	5.36451
500	- 2.59696	3.90171	.421011	- 4.93813	- .357312	3.32725
630	6.28865	- 7.37793	- 4.6982	5.6888	- 6.06076	- 6.1228
800	13.7308	-18.1741	- 8.60166	15.5234	-10.266	-12.8969
1000	18.053	-24.7486	-12.4865	21.8227	-14.1284	-16.3454
1250	20.6317	-29.4921	-15.4574	25.7617	-16.0982	-18.8559
1600	21.3096	-31.0242	-16.1102	27.3046	-16.0654	-19.6894
2000	19.3817	-28.0934	-15.5077	24.8206	-15.265	-18.2968
2500	22.2096	-33.1287	-17.5228	29.1877	-16.6365	-20.9147
3150	20.2293	-29.2157	-16.3797	26.8074	-16.3144	-19.4715
4000	20.8372	-30.068	-16.569	27.421	-16.0229	-20.7363
5000	21.9237	-31.4352	-16.9844	28.5251	-16.1681	-22.5144
6300	20.7115	-30.8259	-17.7763	26.8737	-15.725	-21.778
8000	16.7158	-23.2358	-14.9707	21.5263	-16.3616	-15.9759
10000	23.9157	-29.1762	-14.7565	26.1	-19.8588	-24.0328

TABLE VII-D3

Directivity Correlation Coefficients

$M_R = .939$

IGV Less Fans

$$D.I. = A_o + A_1 \sin 1.5\theta + A_2 \cos 2\theta + A_3 \sin 2\theta$$

$$+ A_4 \cos^2 2\theta + A_5 \sin 1.5\theta \sin 2\theta$$

f	A_o	A_1	A_2	A_3	A_4	A_5
400	- 2.75201	4.28498	.182494	- 4.66253	- 1.71304	4.92215
500	1.04546	- 2.45452	- 2.46922	.127913	- 2.06936	- .296157
630	6.62462	- 8.73723	- 5.71048	6.61372	- 6.09545	- 6.43996
800	10.925	-15.4367	- 7.7783	11.9846	- 8.19129	-10.0897
1000	12.7385	-20.7788	-10.8099	16.41	- 9.41934	-10.3092
1250	4.84951	-32.4248	-17.3239	28.6215	17.6074	-20.7193
1600	19.7448	-28.9348	-15.3181	25.1707	-15.0114	-18.2429
2000	21.4598	-33.9245	-18.4602	29.3661	-16.0036	-19.4089
2500	22.1457	-34.4989	-18.3869	30.0383	-16.3035	-20.5454
3150	22.5588	-33.5741	-18.1213	30.2609	-17.4023	-21.1375
4000	22.7234	-34.1178	-18.4915	30.6608	-17.0698	-21.6597
5000	22.6462	-34.6619	-18.8882	30.9406	-16.5882	-21.998
6300	23.2827	-36.6057	-20.5757	30.7893	-17.3993	-24.1162
8000	18.6556	-26.222	-15.9084	23.5945	-16.7682	-17.9313
10000	22.4003	-30.1801	-16.3793	25.4346	-18.6123	-21.9162

TABLE VII-D4

Directivity Correlation Coefficients

$M_R = 1.0$

IGV Less Fans

$$D.I. = A_o + A_1 \sin 1.5\theta + A_2 \cos 2\theta + A_3 \sin 2\theta + A_4 \cos^2 2\theta + A_5 \sin 1.5\theta \sin 2\theta$$

f	A_o	A_1	A_2	A_3	A_4	A_5
400	- 4.24077	9.72514	2.32412	- 9.77427	- 3.24979	7.37988
500	- 2.85547	3.41317	- .163555	- 5.32308	.00046	3.14353
630	5.77718	- 6.82988	- 5.1058	4.56778	- 6.09956	- 6.30357
800	9.01658	-12.5733	- 7.30492	9.45716	- 7.4492	- 8.85498
1000	10.6588	-14.6139	- 8.0368	12.3985	- 8.61093	- 9.96737
1250	1.23463	-16.1947	- 9.89852	13.9314	10.1904	-10.2781
1600	16.7785	-23.6497	-13.1481	21.1885	-13.4567	-15.8003
2000	14.9167	-22.4633	-13.1722	19.5309	-11.8533	-14.1734
2500	17.2195	-26.3872	-15.1844	23.1869	-13.4671	-16.4582
3150	18.404	-26.5437	-14.9643	24.4801	-14.7184	-18.122
4000	16.2821	-24.2797	-14.3266	22.2956	-12.8467	-16.308
5000	14.2726	-22.3391	-13.6818	20.3662	-11.2446	-14.8821
6300	15.8519	-25.4543	-16.0257	21.9928	-12.5019	-17.7686
8000	17.9056	-23.0371	-14.1159	21.4972	-16.264	-18.5805
10000	17.4904	-21.4959	-12.9975	19.2803	-15.9199	-18.4019

TABLE VII-D5

Directivity Correlation Coefficients

$M_R = 1.046$

IGV Less Fans

$$D.I. = A_o + A_1 \sin 1.5\theta + A_2 \cos 2\theta + A_3 \sin 2\theta$$

$$+ A_4 \cos^2 2\theta + {}_5 \sin 1.5\theta \sin 2\theta$$

f	A_o	A_1	A_2	A_3	A_4	A_5
400	- 2.88414	- 1.24977	- 1.36796	- 1.13598	3.15487	1.95452
500	4.47598	- 7.4793	- 3.89521	3.12806	- 6.32898	- 2.02739
630	7.55105	-10.7457	- 6.199	6.36166	- 8.56214	- 6.2225
800	10.2075	-14.6896	- 7.23588	9.81511	- 8.86773	- 9.38458
1000	9.8063	-17.8086	-10.0765	13.2662	- 8.58302	- 6.78217
1250	11.5635	-18.2594	-10.7718	15.5277	-11.1668	- 9.6176
1600	6.96344	-16.5356	-11.5808	13.7024	- 7.82446	- 5.09148
2000	7.3155	-19.3	-14.2598	15.8546	- 6.46598	- 5.64919
2500	5.74722	-18.0172	-13.7468	14.9591	- 7.56692	- 3.30214
3150	7.17885	-19.5947	-13.9565	17.9578	[illegible].6892	- 5.83013
4000	20.6252	-32.2636	-16.9227	29.5378	-15.0349	-20.0491
5000	20.197	-32.257	-17.4213	28.8454	-14.4328	-18.9178
6300	20.5889	-33.7013	-18.3991	29.3958	-15.2252	-18.7252
8000	20.3054	-31.4655	-17.8133	27.929	-15.8876	-19.319
10000	27.0133	-38.5504	-19.9365	33.098	-20.8752	-26.4796

TABLE VII-D6

Directivity Correlation Coefficients

$M_R = 1.141$

IGV Less Fans

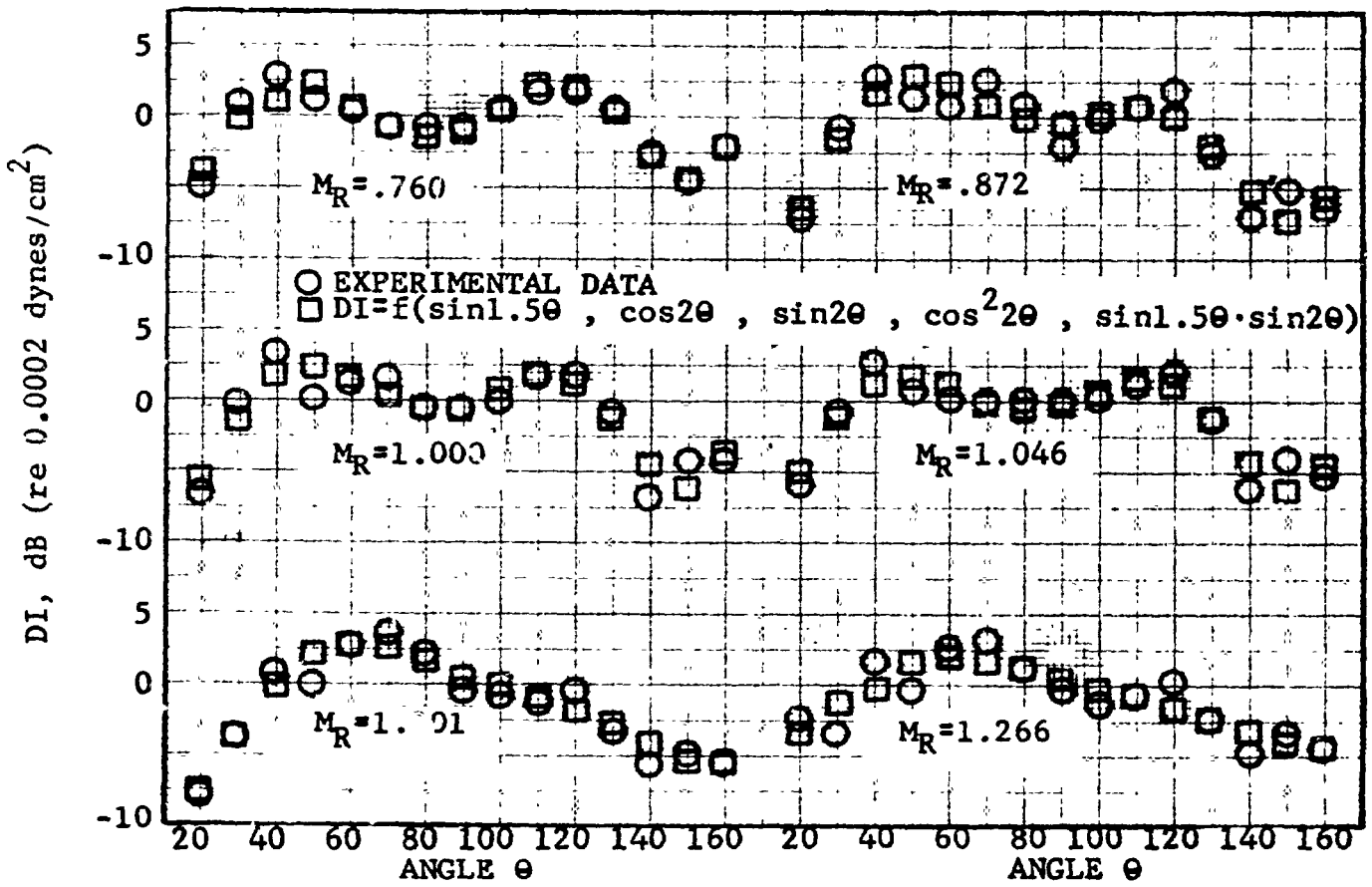

FIGURE VII-D1 BROADBAND NOISE DIRECTIVITY INDEX (GE D/V-I) FOR $fD=1.118 \times 10^5$ IN/SEC

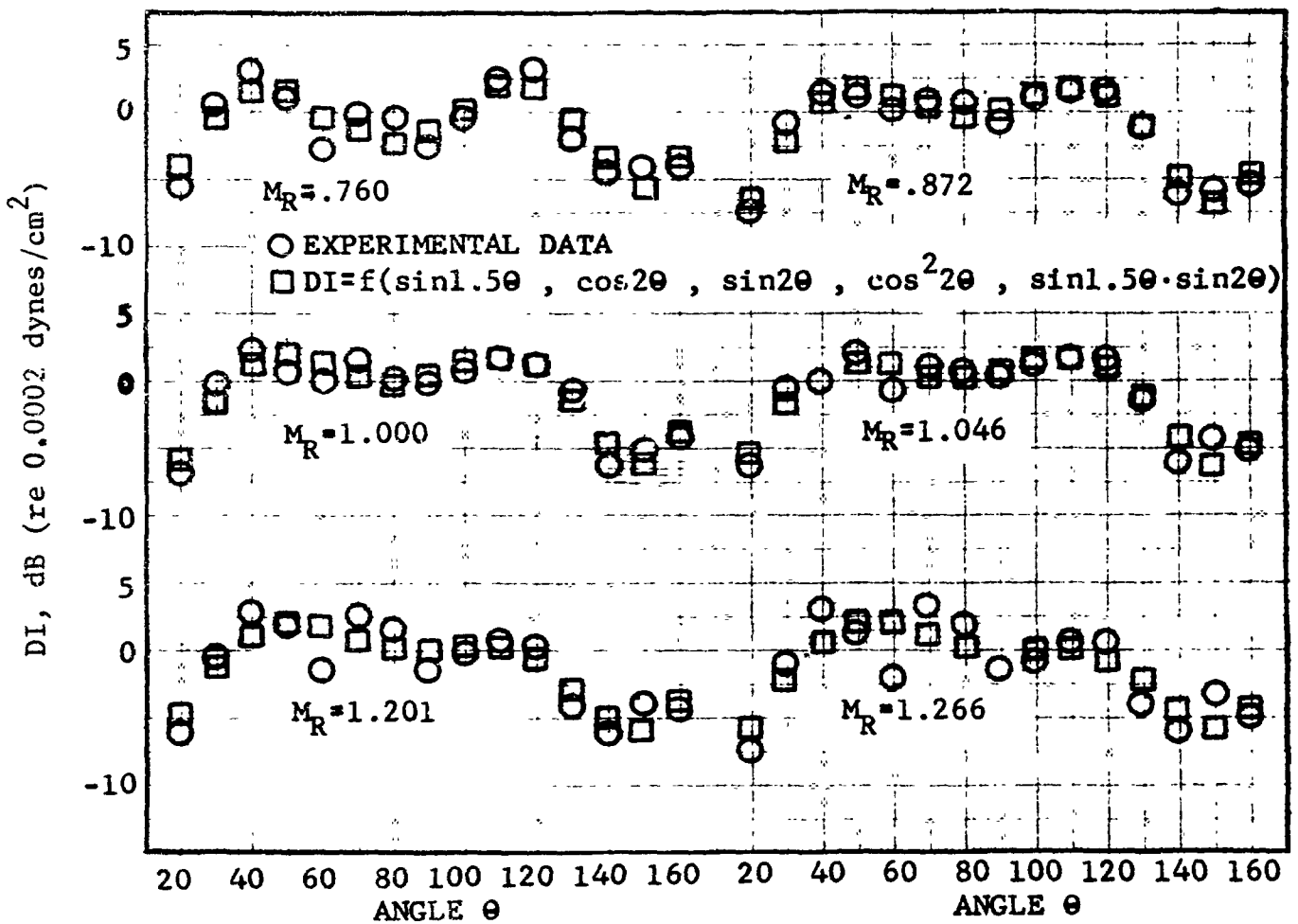

FIGURE VII-D2 BROADBAND NOISE DIRECTIVITY INDEX (GE D/V-I) FOR $fD=1.42 \times 10^5$ IN/SEC

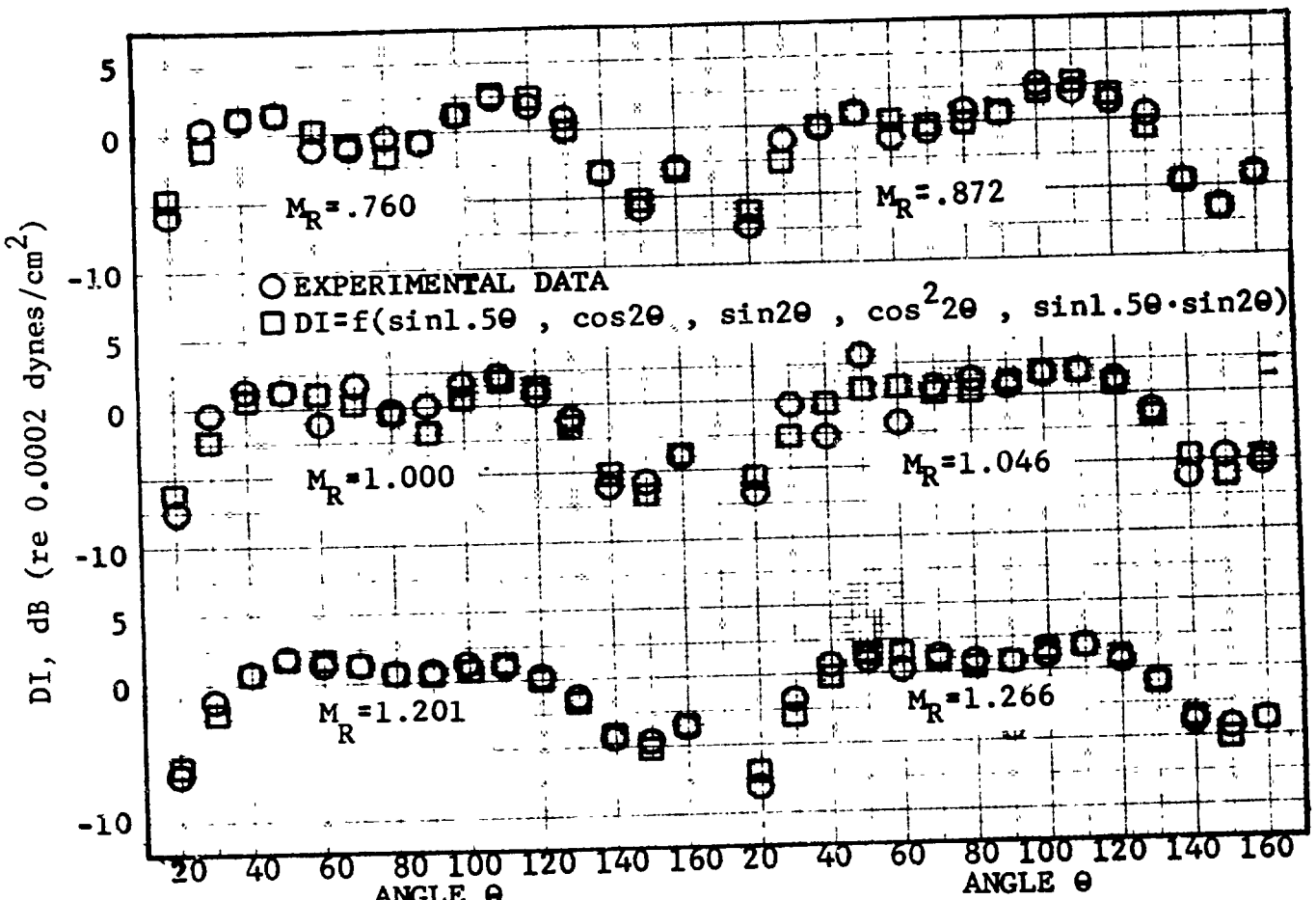

FIGURE VII-D3 BROADBAND NOISE DIRECTIVITY INDEX (GE D/V-I) FOR $fD=1.775 \times 10^5$ IN/SEC

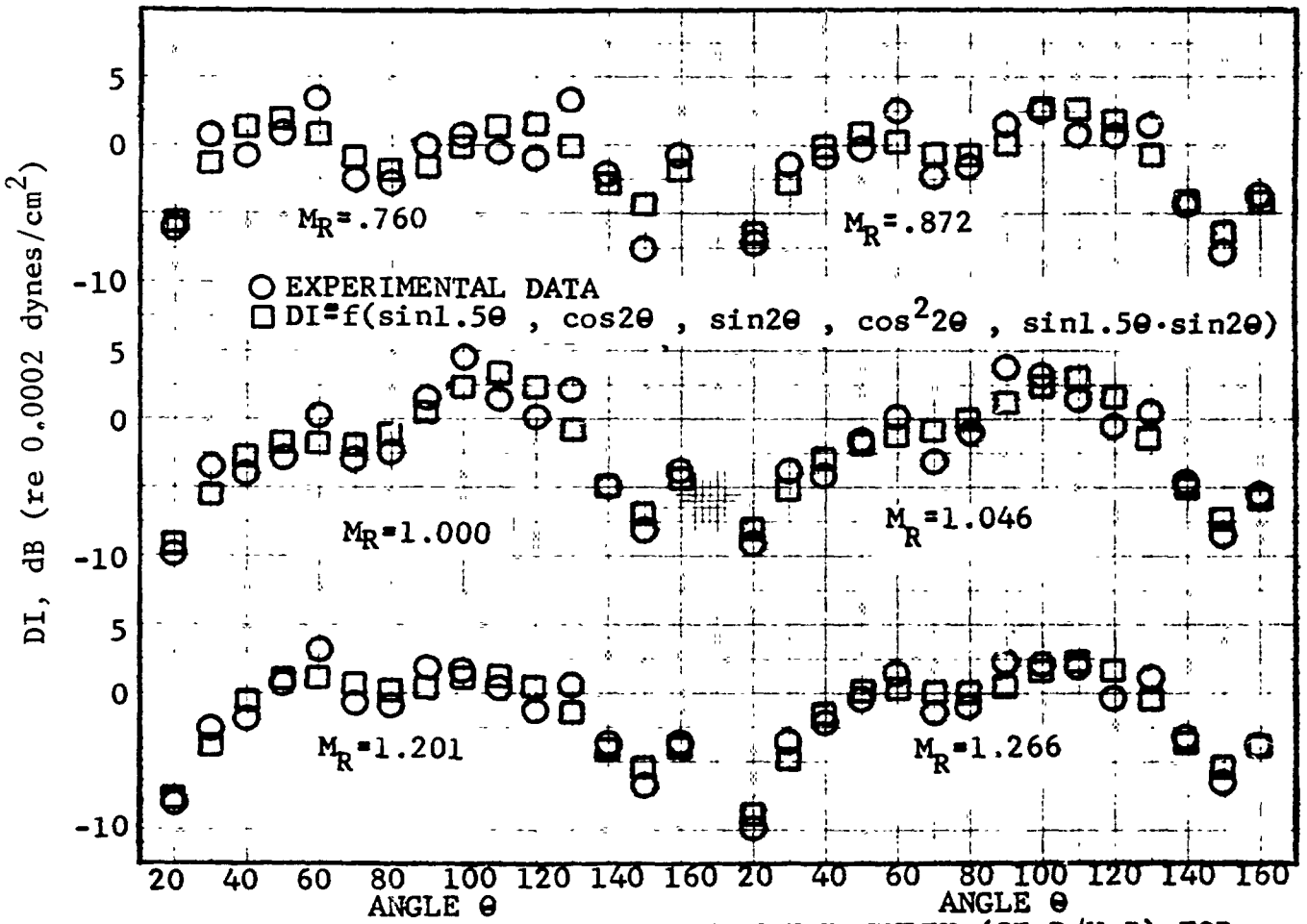

FIGURE VII-D4 BROADBAND NOISE DIRECTIVITY INDEX (GE D/V-I) FOR $fD=2.237 \times 10^5$ IN/SEC

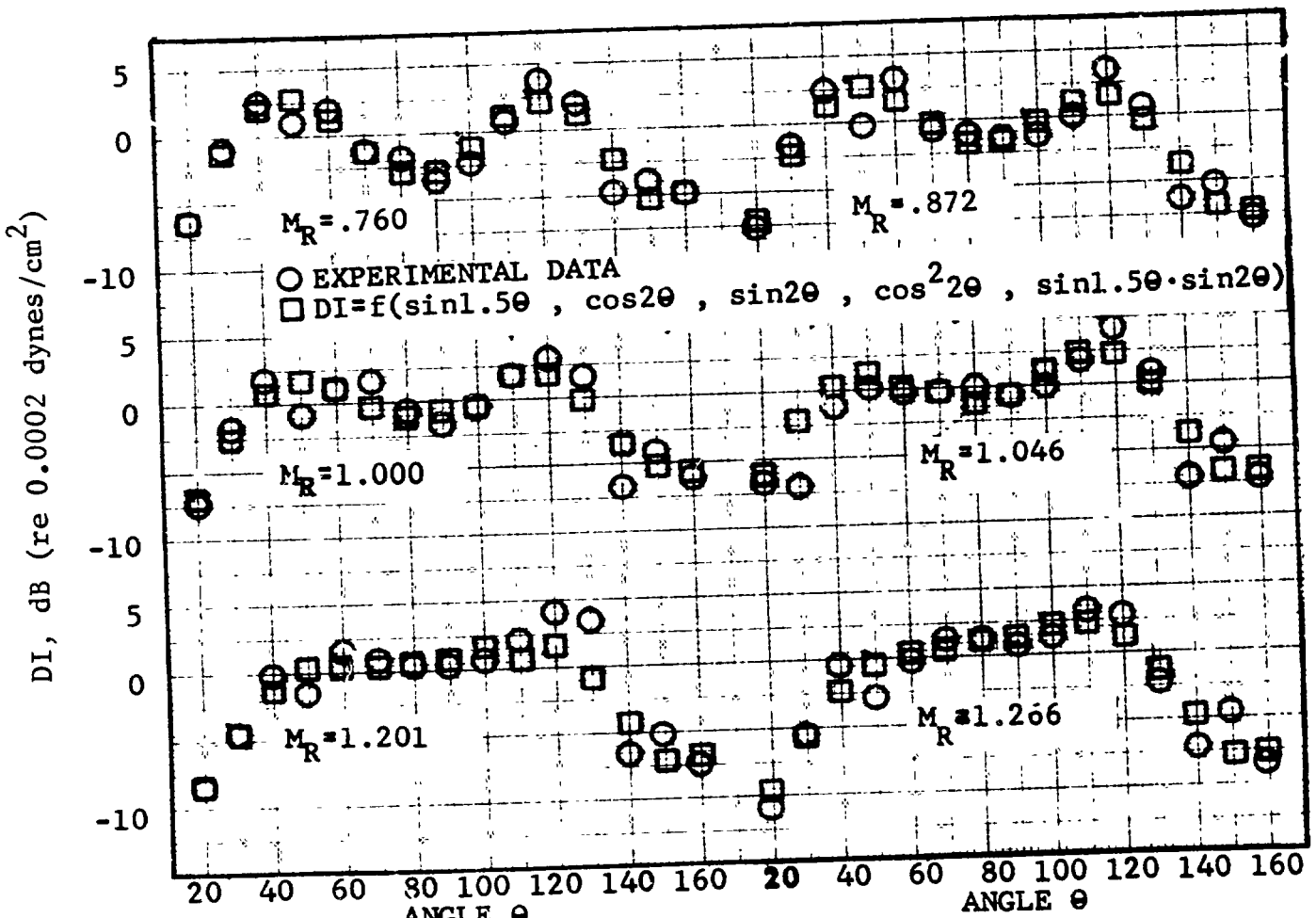

FIGURE VII-D5 BROADBAND NOISE DIRECTIVITY INDEX (GE D/V-I) FOR $fD=2.84 \times 10^5$ IN/SEC

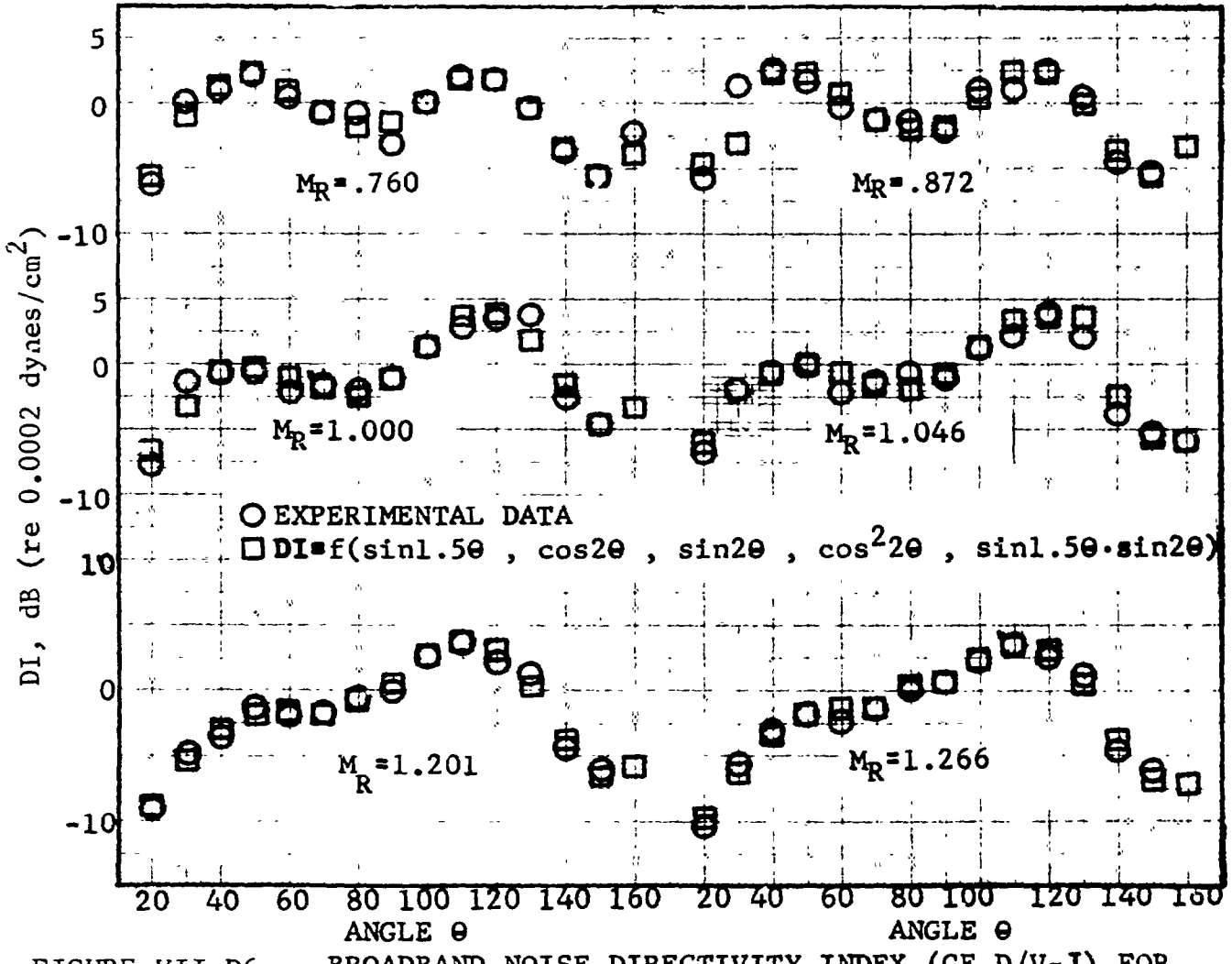

FIGURE VII-D6 BROADBAND NOISE DIRECTIVITY INDEX (GE D/V-I) FOR $fD=3.55 \times 10^5$ IN/SEC

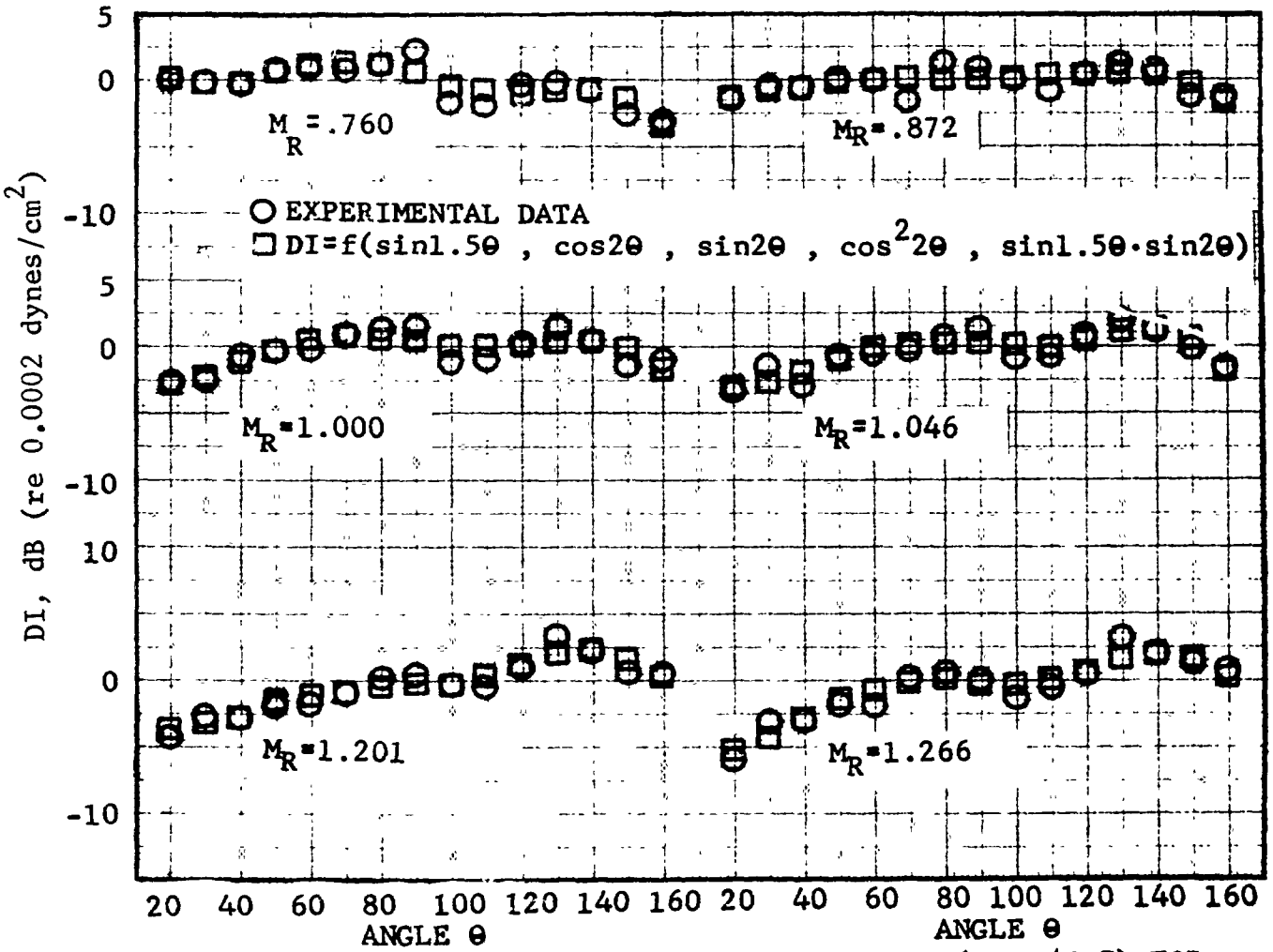

FIGURE VII-D7 BROADBAND NOISE DIRECTIVITY INDEX (GE D/V-I) FOR $fD = 1.42 \times 10^4$ IN/SEC

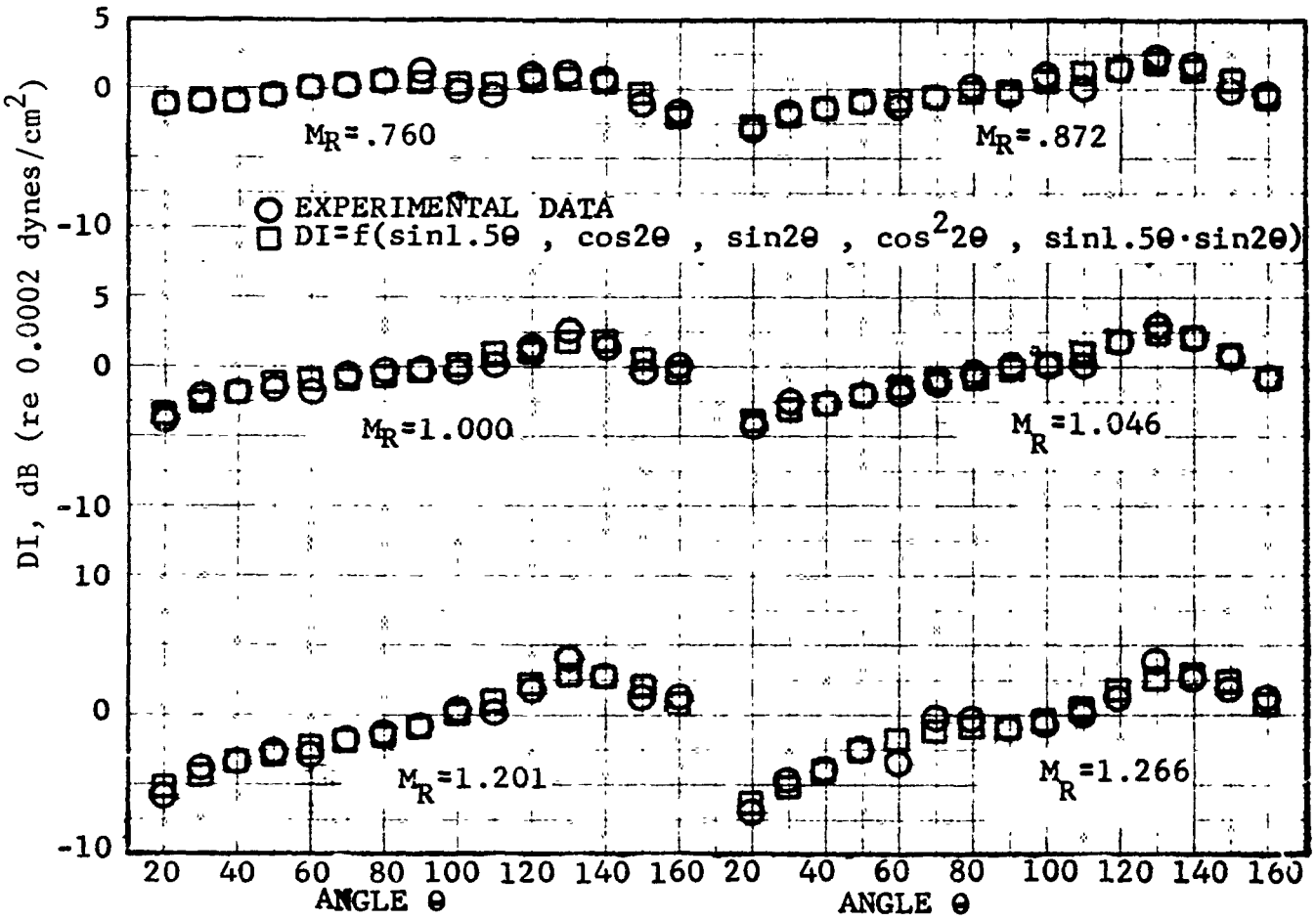

FIGURE VII-D8 BROADBAND NOISE DIRECTIVITY INDEX (GE D/V-I) FOR $fD=1.775 \times 10^4$ IN/SEC

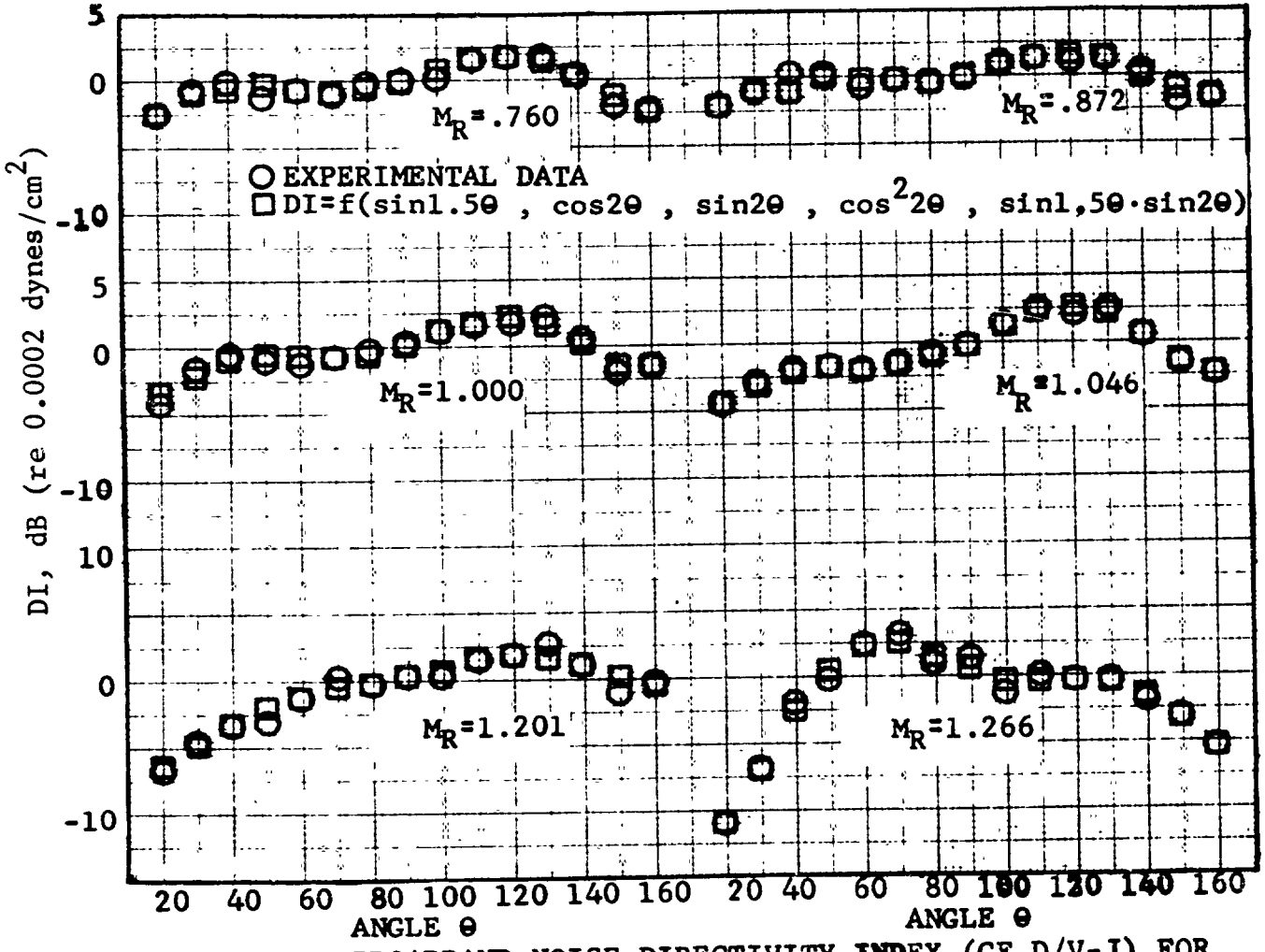

FIGURE VII-D9 BROADBAND NOISE DIRECTIVITY INDEX (GE D/V-I) FOR $fD=2.237 \times 10^4$ IN/SEC

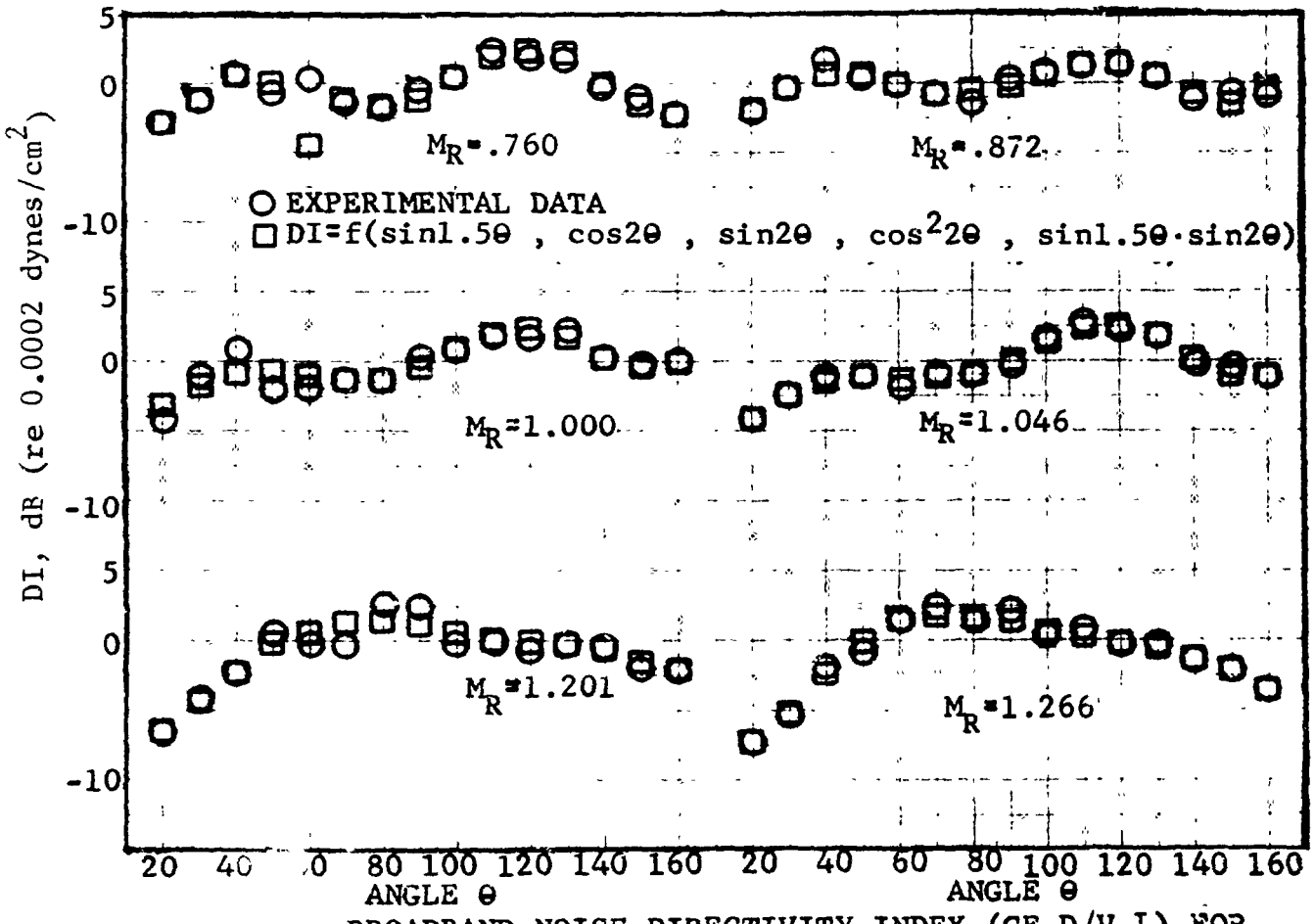

FIGURE VII-D10 BROADBAND NOISE DIRECTIVITY INDEX (GE D/V-I) FOR $fD=2.84 \times 10^4$ IN/SEC

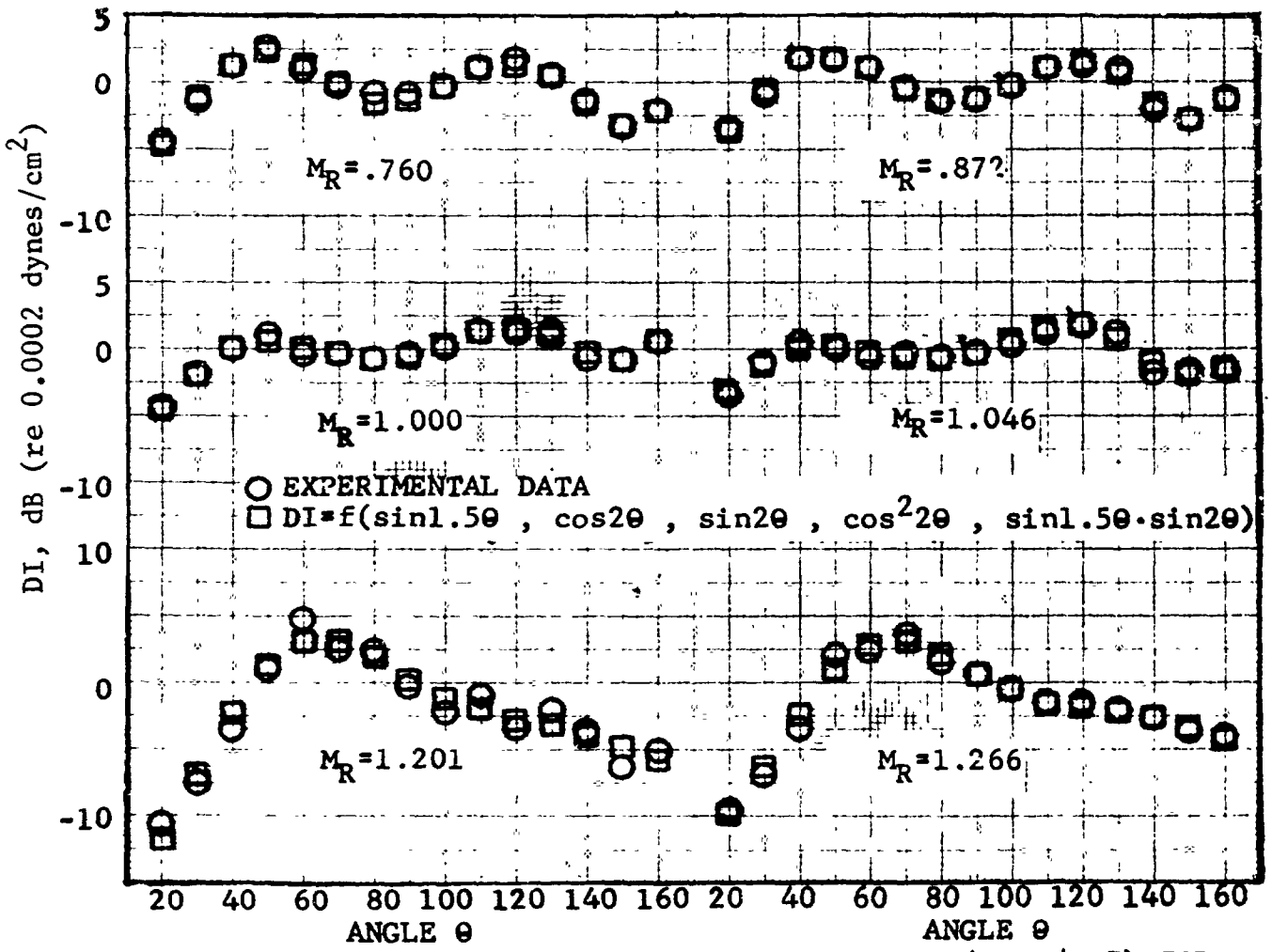

FIGURE VII-D11 BROADBAND NOISE DIRECTIVITY INDEX (GE D/V-I) FOR $fD=3.55 \times 10^4$ IN/SEC

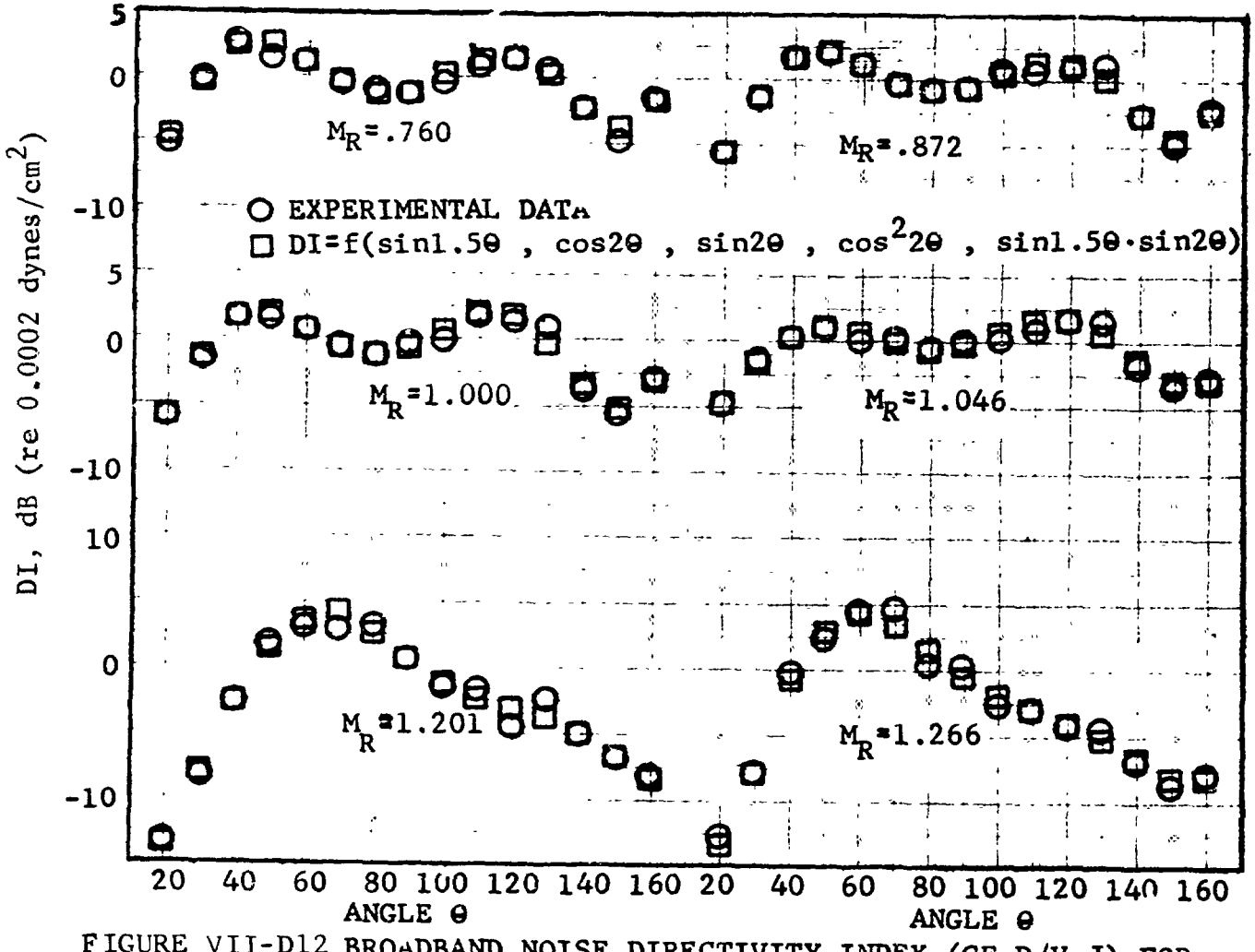

FIGURE VII-D12 BROADBAND NOISE DIRECTIVITY INDEX (GE D/V-I) FOR fD=4.44 X 10^4 IN/SEC

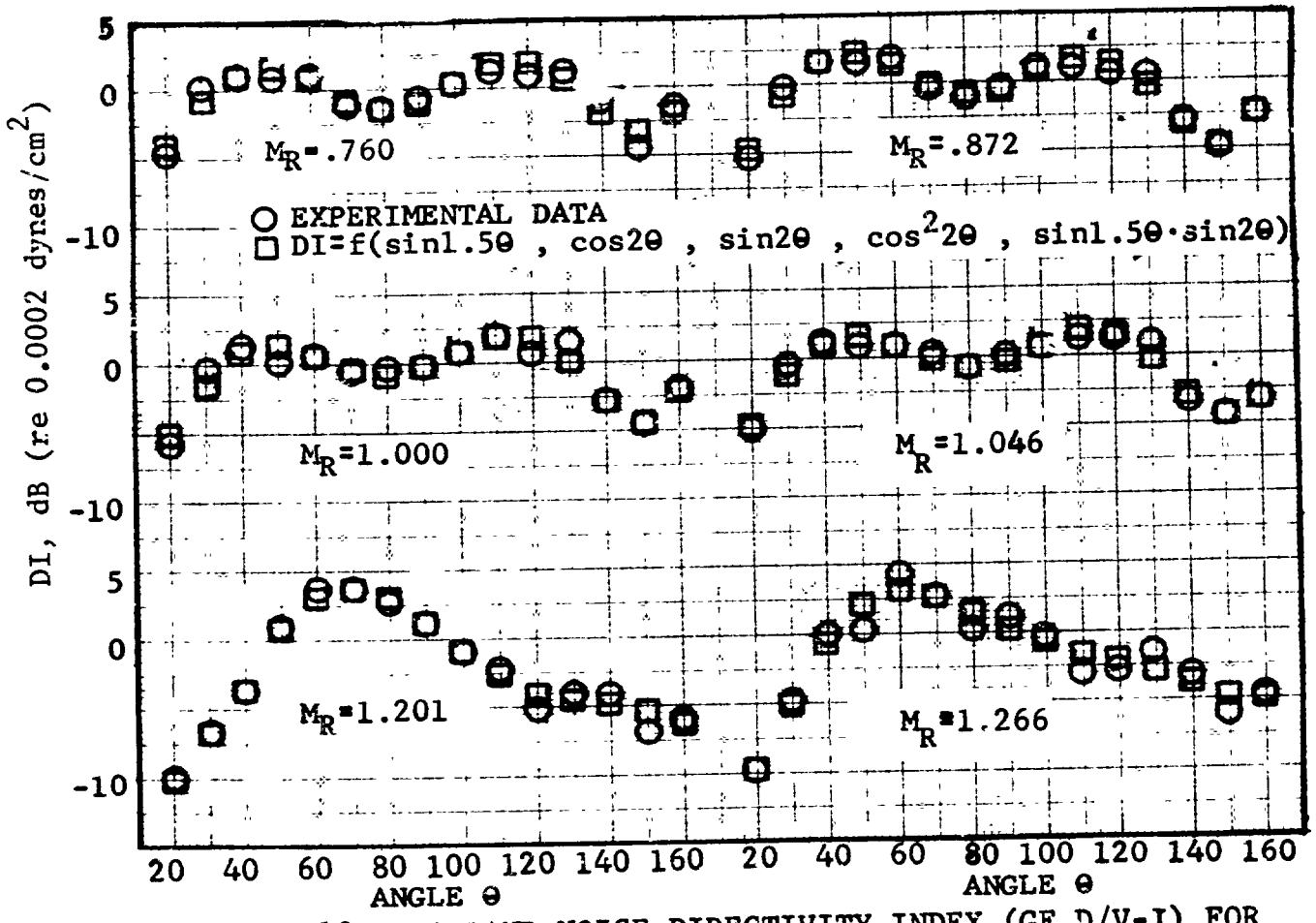

FIGURE VII-D13 BROADBAND NOISE DIRECTIVITY INDEX (GE D/V-I) FOR $fD=5.68 \times 10^4$ IN/SEC

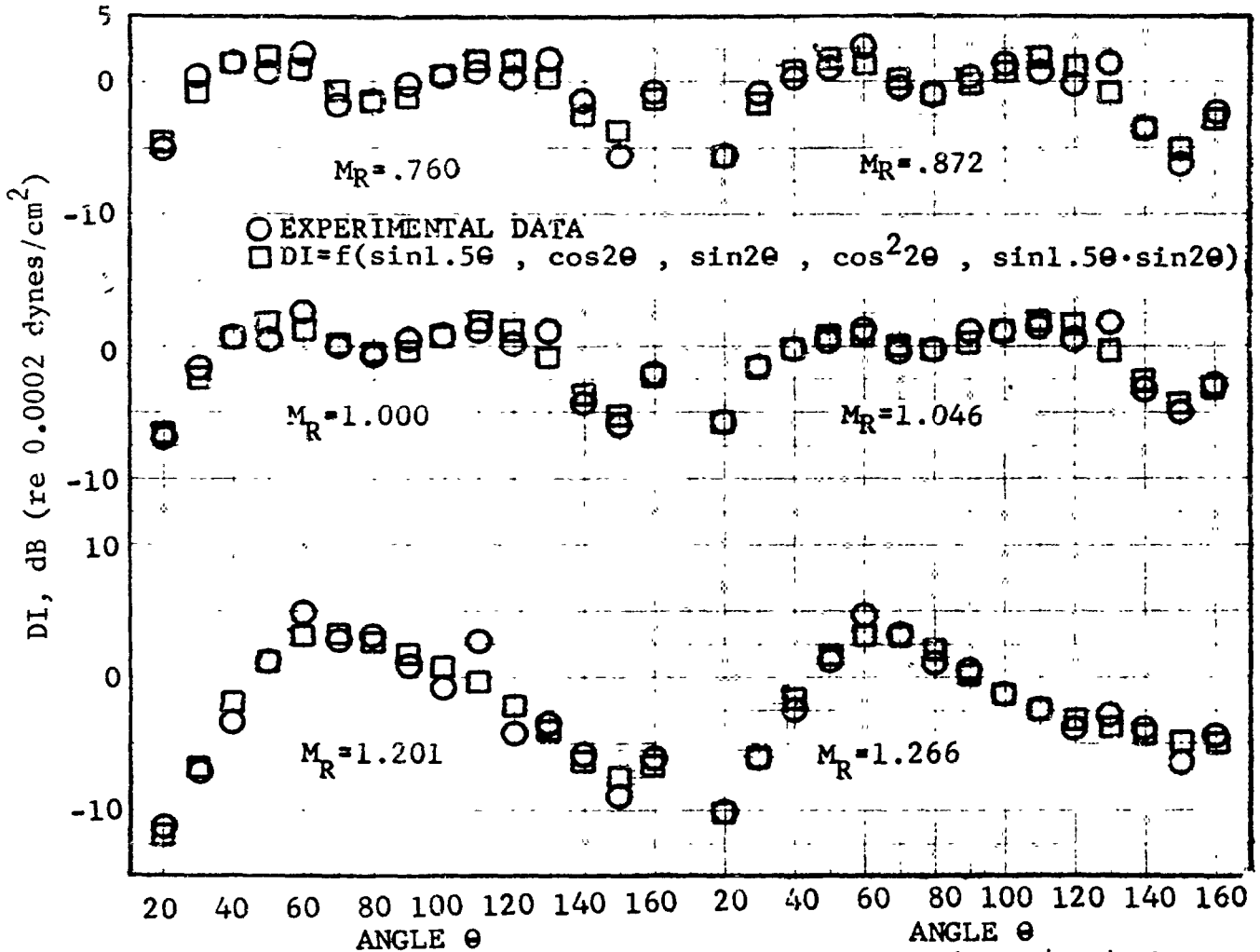

FIGURE VII-D14 BROADBAND NOISE DIRECTIVITY INDEX (GE D/V-I) FOR fD=7.1 X 10^4 IN/SEC

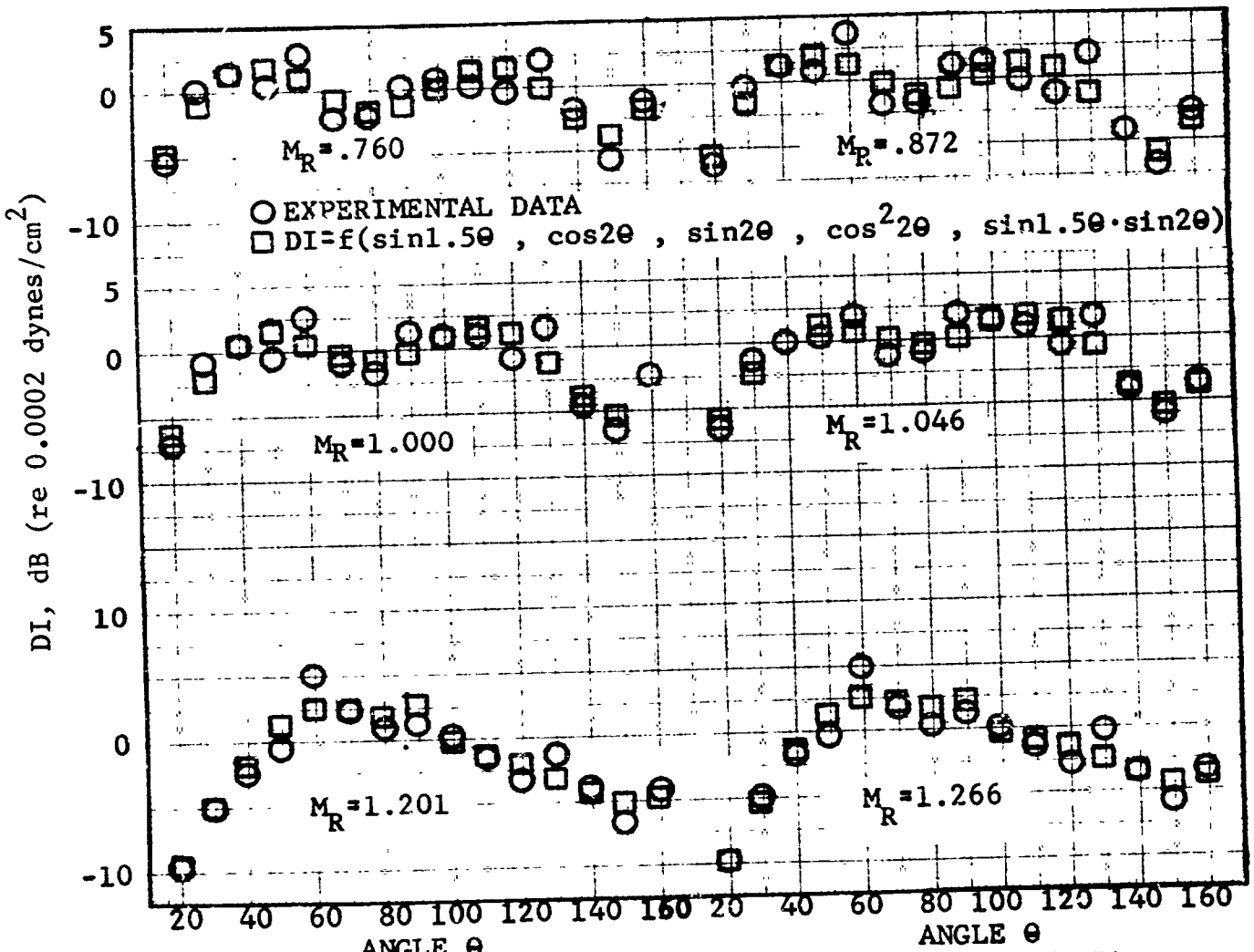

FIGURE VII-D15 BROADBAND NOISE DIRECTIVITY INDEX (GE D/V-I) FOR $fD=8.88 \times 10^4$ IN/SEC

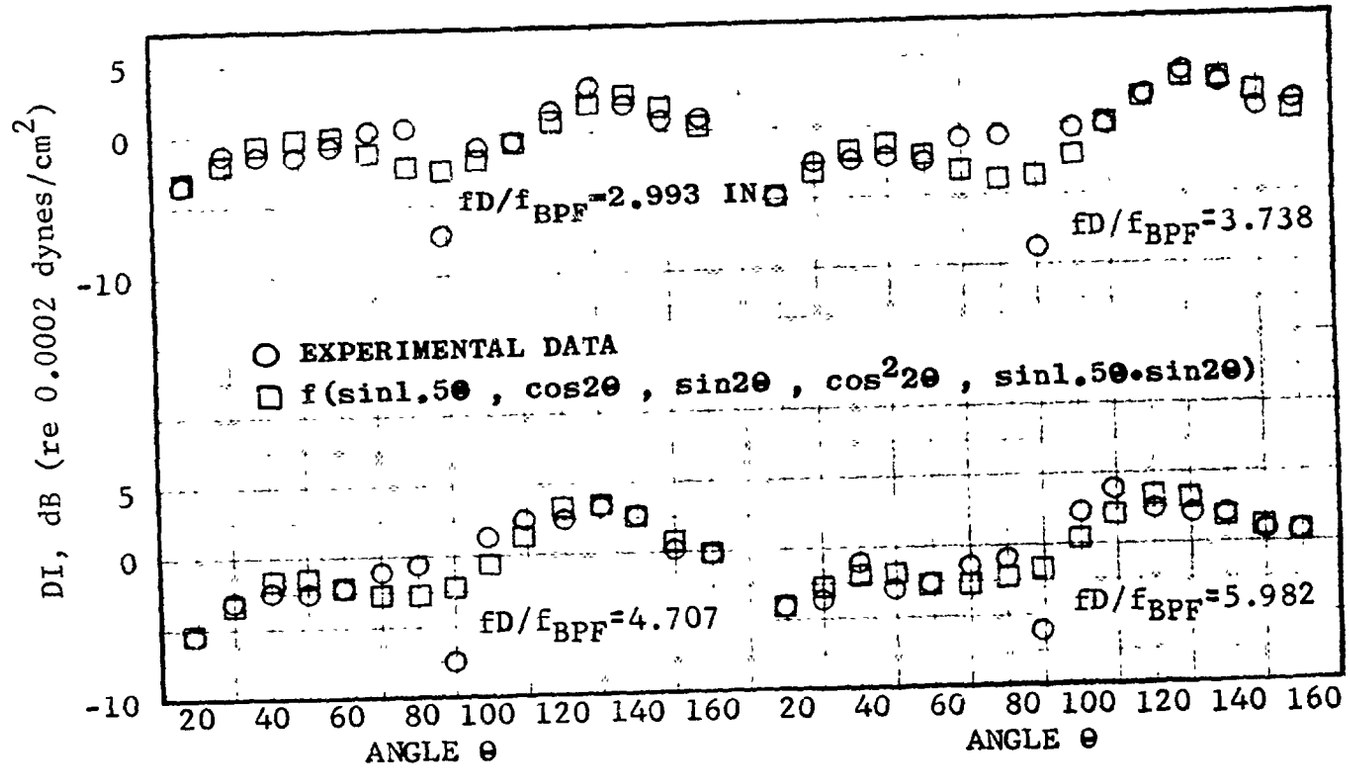

FIGURE VII-D16 MPT NOISE DIRECTIVITY INDEX (GE D/V-I)
M_T=1.057

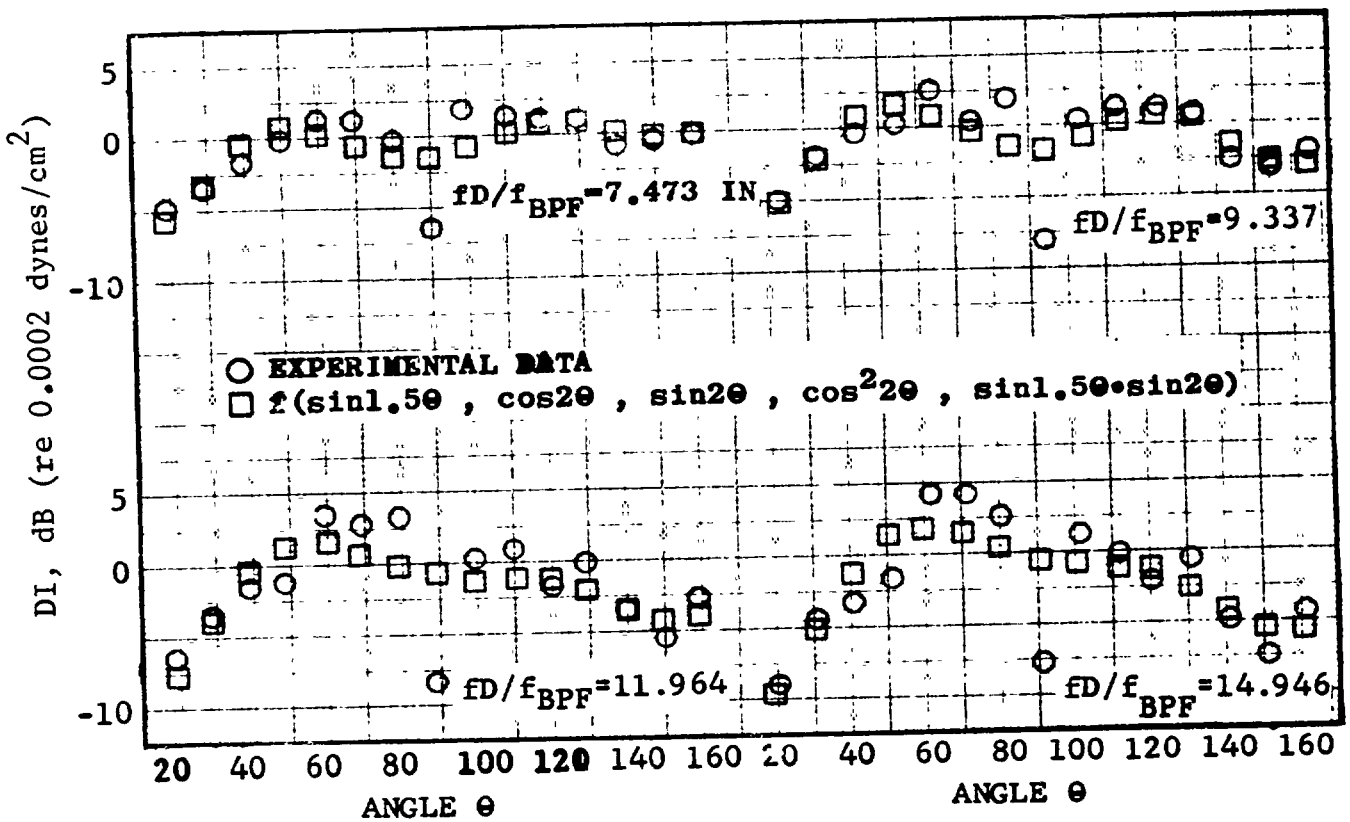

FIGURE VII-D17 MPT NOISE DIRECTIVITY INDEX (GE D/V-I)
M_T=1.057

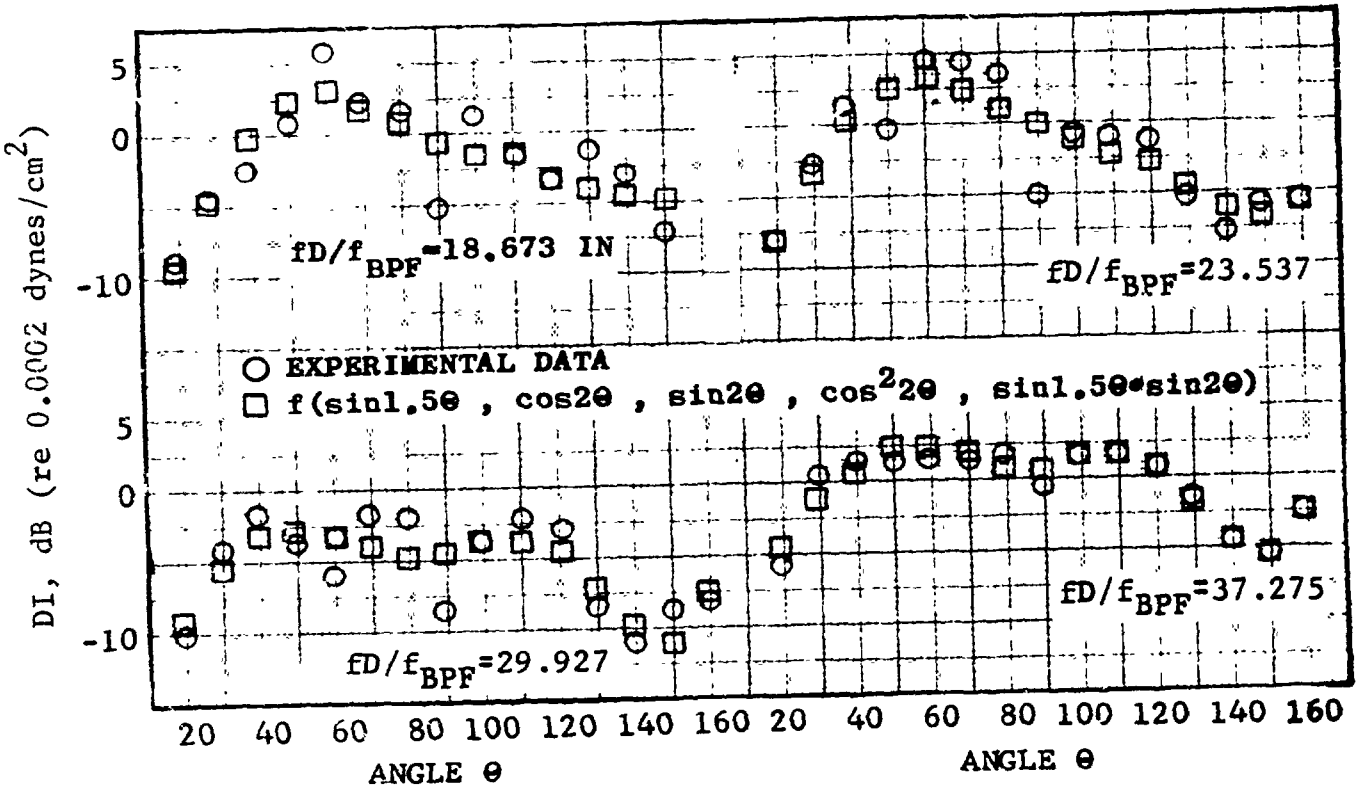

FIGURE VII-D18 MPT NOISE DIRECTIVITY INDEX (GE D/V-I)
M_T=1.057

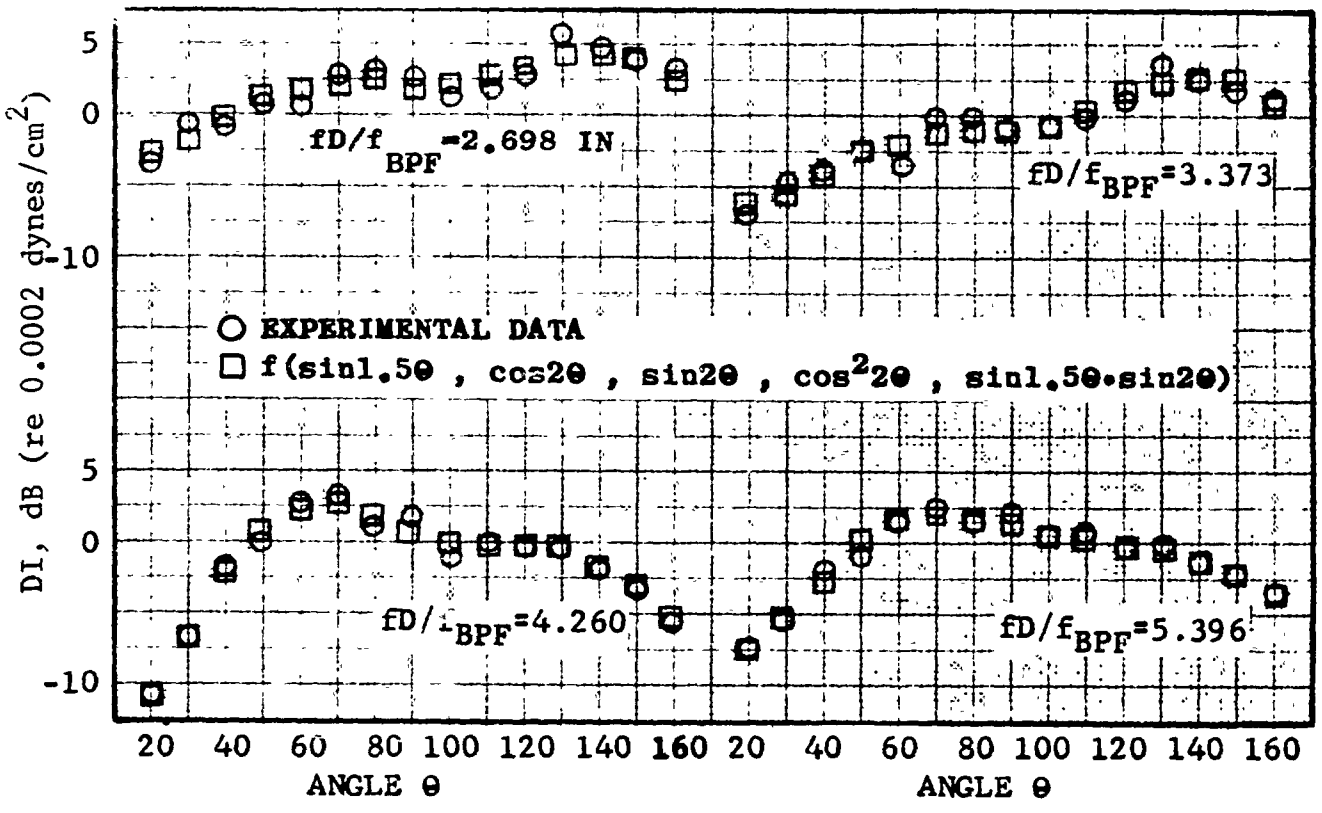

FIGURE VII-D19 MPT NOISE DIRECTIVITY INDEX (GE D/V-I)
M_T=1.170

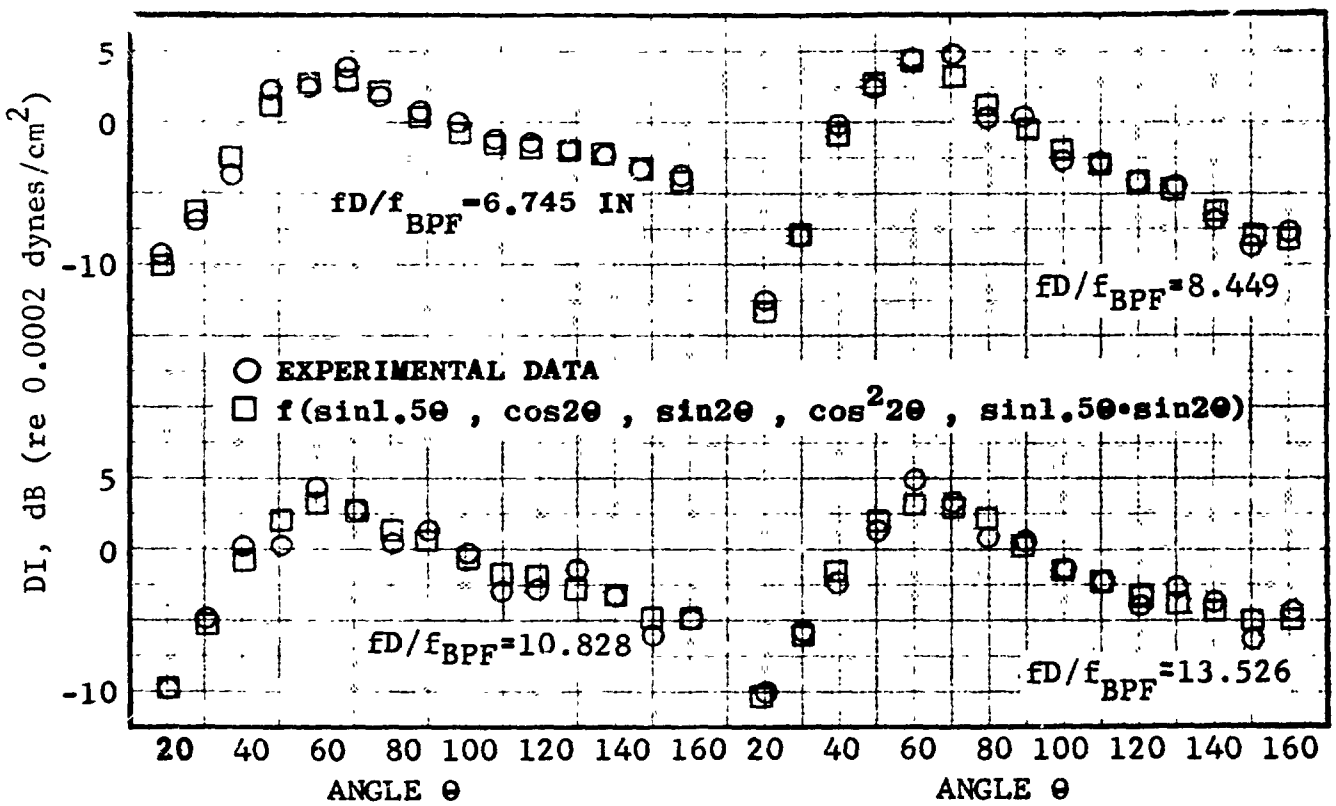

FIGURE VII-D20 MPT NOISE DIRECTIVITY INDEX (GE D/V-I)
M_T=1.170

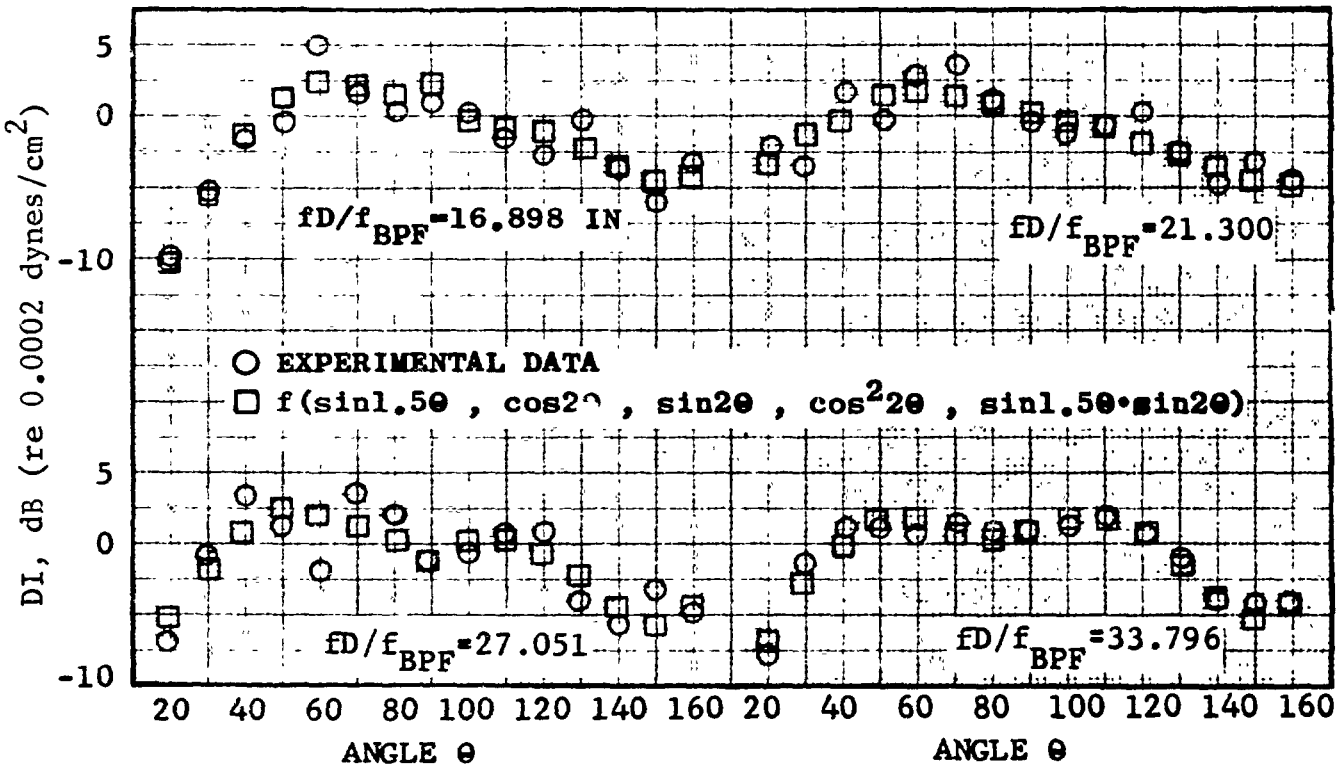

FIGURE VII-D21 MPT NOISE DIRECTIVITY INDEX (GE D/V-I)
M_T=1.170

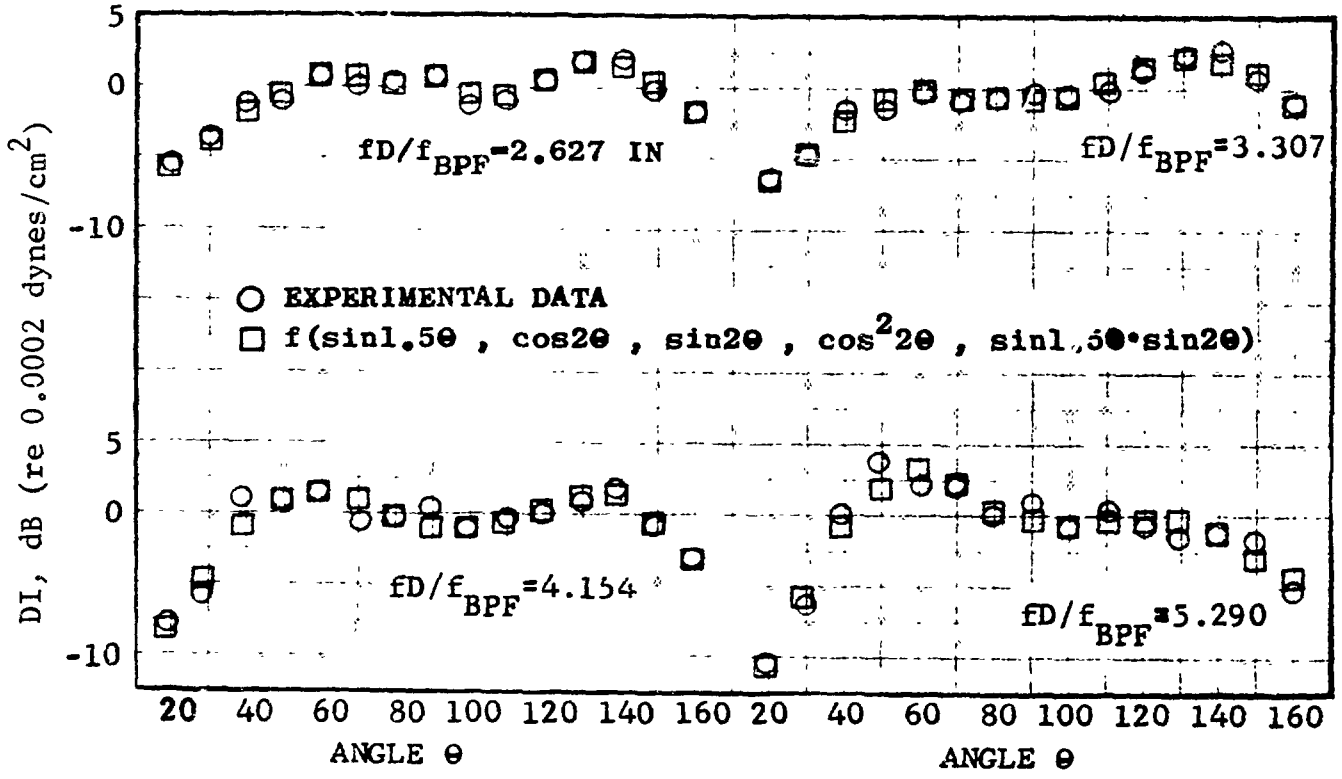

FIGURE VII-D22 MPT NOISE DIRECTIVITY INDEX (GE D/V-I)
M_T=1.197

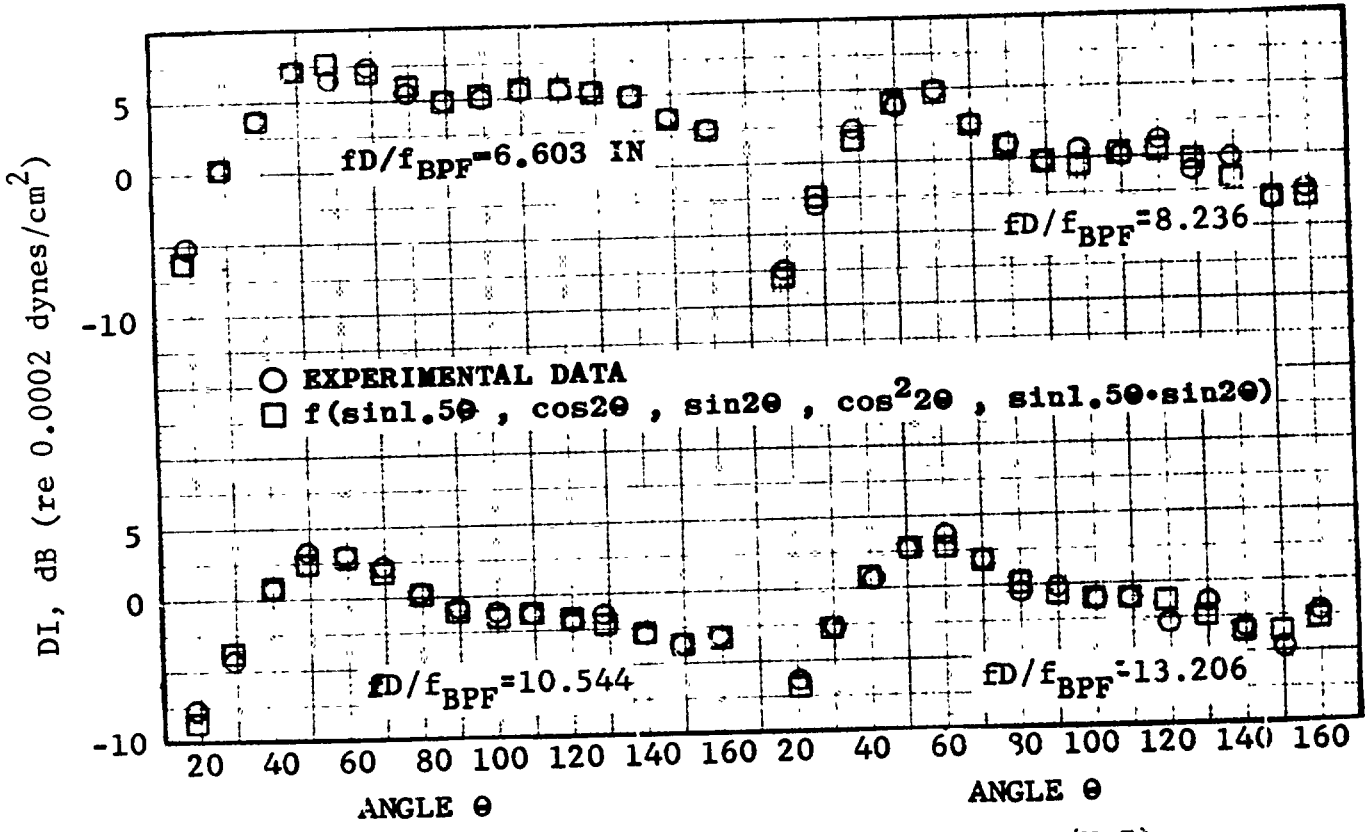

FIGURE VII-D23 MPT NOISE DIRECTIVITY INDEX (GE D/V-I)
M_T=1.197

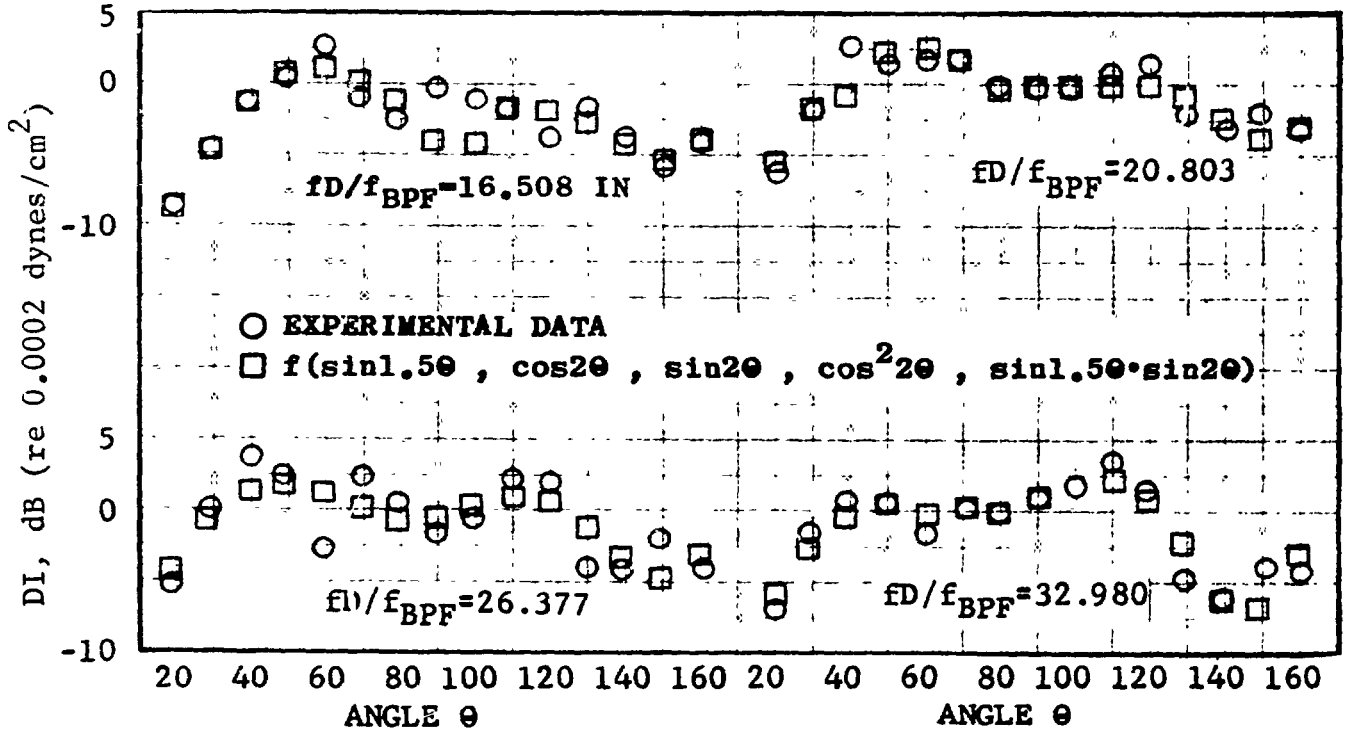

FIGURE VII-D24 MPT NOISE DIRECTIVITY INDEX (GE D/V-I)
M_T=1.197

$$D.I. = A_o + A_1 \sin 1.5\theta + A_2 \cos 2\theta + A_3 \sin 2\theta$$

$$+ A_4 \cos^2 2\theta + A_5 \sin 1.5\theta \sin 2\theta$$

f	A_o	A_1	A_2	A_3	A_4	A_5
400	- 2.40276	2.20092	- .577555	- 4.74369	- .821832	4.10939
500	.930953	- 4.43444	- 3.55397	- .156473	- 2.34824	.399302
630	2.59917	- 7.99954	- 6.5893	3.56536	- 3.22735	- 1.57442
800	- 1.77976	- 3.72026	- 5.65463	1.37433	- .07594	2.72261
1000	- 1.35856	-10.7001	-12.1213	7.50228	- 2.75428	3.83613
1250	- 6.073	- 8.16369	-12.5543	5.75193	2.46127	5.61144
1600	- 7.13347	- 3.08357	- 8.56047	1.81351	2.09064	8.09075
2000	7.55704	-23.1435	-18.1984	19.4123	- 7.65627	- 6.11388
2500	2.71925	-14.5119	-12.6451	11.5317	- 4.17531	- 1.05552
3150	4.75387	-13.9523	-11.4623	12.429	- 5.7974	- 3.41653
4000	15.7835	-26.2205	-14.7115	24.1043	-11.9327	-14.8839
5000	15.6855	-26.2262	-15.4609	23.2617	-12.0969	-14.3324
6300	15.0866	-26.3009	-16.2035	22.5032	-12.2427	-13.8524
8000	14.5262	-22.7053	-15.5292	20.1211	-13.457	-15.1276
10000	18.0649	-26.5416	-16.497	22.3949	-15.1929	-19.4138

TABLE VII-D7

Directivity Correlation Coefficients

$M_R = 1.201$

IGV Less Fans

$$D.I. = A_o + A_1 \sin 1.5\theta + A_2 \cos 2\theta + A_3 \sin 2\theta$$

$$+ A_4 \cos^2 2\theta + A_5 \sin 1.5\theta \sin 2\theta$$

f	A_o	A_1	A_2	A_3	A_4	A_5
400	- 3.04357	1.99589	- 1.41493	- 5.24981	- 1.67821	6.45927
500	- 2.30701	- 2.12288	- 3.25809	- 2.7989	- .152388	4.21297
630	- 2.1725	- 5.75528	- 9.62145	2.61634	- 2.73762	4.59917
800	- 2.27026	- 3.20682	- 6.41665	1.012	- .484741	3.18849
1000	- 2.25596	- 7.95076	- 9.97899	4.80772	- 1.19049	4.70835
1250	- 3.39182	-20.8223	-17.719	17.7979	8.06404	- 1.92084
1600	2.41297	-13.2879	-12.0709	10.6163	- 4.92038	.168453
2000	.193454	-13.2833	-12.6085	10.1775	- 2.98776	2.42645
2500	5.9018	-18.8164	-14.3309	14.7958	- 6.35046	- 3.38154
3150	.476763	- 3.43495	- 4.59511	4.33776	- 2.15029	- .554869
4000	12.4684	-21.9565	-13.4324	19.945	-10.3729	-11.4011
5000	15.5332	-26.1522	-15.9073	22.5611	-12.3681	-14.198
6300	17.9889	-30.34	-18.3971	25.1653	-14.3252	-16.9431
8000	11.8916	-20.5744	-15.3605	17.9283	-11.3468	-13.1628
10000	14.9269	-22.2595	-15.5041	18.6176	-13.9105	-16.5607

TABLE VII-D8

Directivity Correlation Coefficients

$M_R = 1.266$

IGV Less Fans

$$D.I. = A_o + A_1 \sin 1.5\theta + A_2 \cos 2\theta + A_3 \sin 2\theta$$

$$+ A_4 \cos^2 2\theta + A_5 \sin 1.5\theta \sin 2\theta$$

f	A_o	A_1	A_2	A_3	A_4	A_5
400	- 4.3082	3.85515	- 1.37059	- 5.5285	- .396448	6.38641
500	- .950525	2.15015	- 4.1563	- 1.36668	- 2.46364	3.24755
630	- .599979	- 3.46275	- 6.10395	.721951	- 3.90684	3.69019
800	2.15915	-11.5668	-11.6883	8.00608	- 6.13066	1.5028
1000	2.80135	-10.4559	- 9.53963	6.91688	- 4.97502	.273533
1250	- .484699	-21.6864	-14.7338	18.1024	10.912	- 6.65073
1600	9.05361	-21.0027	-14.1348	17.2553	- 9.10672	- 5.18276
2000	9.9253	-21.5157	-13.4395	18.3211	- 8.63536	- 6.74735
2500	11.2824	-22.549	-14.1809	18.7356	- 9.7619	- 8.38627
3150	11.9455	-20.55	-12.6873	18.0037	-10.6202	- 9.71424
4000	16.4814	-24.8593	-13.3676	22.6914	-12.8546	-15.5668
5000	22.5015	-35.6056	-19.0102	31.447	-15.4367	-22.6433
6300	27.7145	-46.1653	-24.6119	40.0198	-17.9076	-29.5891
8000	14.3323	-21.4314	-14.3803	19.091	-12.8518	-15.8871
10000	15.9585	-23.4999	-15.4027	20.0428	-13.6475	-18.3499

TABLE VII-D9

Directivity Correlation Coefficients

$M_R = 1.296$

IGV Less Fans

$$D.I. = A_o + A_1 \sin 1.5\theta + A_2 \cos 2\theta + A_3 \sin 2\theta$$

$$+ A_4 \cos^2 2\theta + A_5 \sin 1.5\theta \sin 2\theta$$

f	A_o	A_1	A_2	A_3	A_4	A_5
400	- 2.1200	7.4402	3.1168	- 5.5490	- .1005	1.6379
500	- 6.5442	14.1351	5.9877	-12.6894	2.6017	4.6543
630	.0039	- 1.2254	- 2.8841	- 1.3392	- 2.1464	.4046
800	8.5851	- 6.7480	- 2.3274	7.1856	- 7.9406	- 7.9373
1000	- 3.4393	14.7231	6.9861	-10.1304	- .9848	1.1175
1250	- 3.4855	12.4406	4.2714	- 8.1452	- 1.3014	1.4787
1600	.3863	9.2264	4.1404	- 5.1036	- 2.8973	- 3.5909
2000	- 4.1652	18.2667	7.9971	-12.1353	- .8529	- .2429
2500	- 2.3415	14.5545	5.0783	- 9.5090	- 4.1072	- .3920
3150	2.5909	6.0967	2.1009	- 2.2846	- 5.1661	- 5.4994
4000	6.9773	- 1.7811	- .5857	4.4571	- 6.0377	-10.3737
5000	- 5.2233	19.1819	6.8633	-13.0843	- 1.3290	.3023
6300	4.9165	.6416	- .3810	1.7812	- 6.1852	- 7.3043
8000	- 9.3895	27.5911	11.1439	-19.2993	.1669	4.4597
10000	- 3.9744	13.5100	4.0473	- 8.3058	- 2.3538	1.5623

TABLE VII-D10

Directivity Correlation Coefficients

$M_R = .637$

IGV Fans

$$D.I. = A_o + A_1 \sin 1.5\theta + A_2 \cos 2\theta + A_3 \sin 2\theta$$

$$+ A_4 \cos^2 2\theta + A_5 \sin 1.5\theta \sin 2\theta$$

f	A_o	A_1	A_2	A_3	A_4	A_5
400	11.8669	-19.7694	- 7.9371	14.0726	- 6.5011	- 9.0206
500	- 5.5007	10.9647	4.1175	-10.8092	1.7179	4.2302
630	-15.1083	25.3753	10.1438	-24.4479	6.3741	12.6797
800	6.4939	- 4.5241	- 1.6770	4.8094	- 6.5705	- 5.6629
1000	- 2.9748	12.7747	5.1691	- 8.9413	- 1.5489	1.0344
1250	3.8631	- .6591	- 2.0287	2.0595	- 5.9503	- 4.2744
1600	4.2444	.5055	- 1.1735	1.5206	- 5.6390	- 6.2302
2000	3.9797	2.8237	.2541	.1330	- 5.7397	- 6.7863
2500	13.1117	-14.2271	- 8.3043	13.6207	-12.2608	-13.0660
3150	12.8027	-13.7418	- 7.6227	13.3436	-10.9219	-13.5560
4000	11.2281	-11.1816	- 6.0822	11.4215	- 9.0761	-13.1585
5000	4.1095	.7232	- 2.2560	1.4311	- 6.2193	- 7.5430
6300	10.6015	- 9.9540	- 5.8856	10.3392	- 9.8594	-11.9746
8000	4.2[illegible]9	3.5812	.6555	.1081	- 7.0103	- 6.9591
10000	- 1.8312	7.2097	1.1001	- 3.9540	- 2.5466	- .1299

TABLE VII-D11

Directivity Correlation Coefficients

$M_R = .712$

IGV Fans

$$D.I. = A_o + A_1 \sin 1.5\theta + A_2 \cos 2\theta + A_3 \sin 2\theta$$

$$+ A_4 \cos^2 2\theta + A_5 \sin 1.5\theta \sin 2\theta$$

f	A_o	A_1	A_2	A_3	A_4	A_5
400	- 4.4581	11.9733	5.3523	- 9.7883	.7922	3.3416
500	- 7.1817	15.4337	6.5356	-14.2140	2.4170	5.3750
630	-11.6780	21.2593	7.2808	-20.3597	2.8725	9.1757
800	8.9551	-8.9050	-3.4889	8.0270	-7.3522	-8.2680
1000	- 5.2016	17.1159	7.9229	-12.2669	.4304	2.4827
1250	- 4.0170	12.8766	4.9969	- 9.0670	.3424	1.2202
1600	2.1259	3.7126	- .0222	- 1.3926	-4.4207	-4.9034
2000	8.2829	-7.2382	-4.4970	8.1304	-7.0522	-10.2363
2500	13.3204	-16.3666	-9.8043	15.1336	-11.8604	-13.2508
3150	28.4735	-42.7356	-19.9853	36.6143	-17.7187	-27.9833
4000	15.7991	-20.7637	-11.1649	18.7915	-11.4076	-17.4640
5000	2.8585	1.5900	- 2.1736	.6994	- 4.9599	- 6.8157
6300	7.4484	- 8.7666	- 7.1131	8.4555	- 7.2735	- 9.7316
8000	-14.8968	34.4871	12.3455	-25.3893	3.2344	8.3921
10000	-10.0870	24.8217	7.9918	-18.2312	.5069	5.3435

TABLE VII- D12

Directivity Correlation Coefficients

$M_R = .855$

IGV Fans

$$D.I. = A_o + A_1 \sin 1.5\theta + A_2 \cos 2\theta + A_3 \sin 2\theta$$

$$+ A_4 \cos^2 2\theta + A_5 \sin 1.5\theta \sin 2\theta$$

f	A_o	A_1	A_2	A_3	A_4	A_5
400	-23.5073	44.2195	19.3434	-37.1008	10.7105	18.6955
500	- 8.0936	13.1108	4.9472	-15.0088	3.2822	8.3723
630	-10.0453	19.6905	8.2710	-17.3635	4.3056	7.9340
800	2.3308	- 3.1449	- 2.9233	.6311	- 2.9699	- 2.1595
1000	-11.1716	20.4684	6.9583	-18.4687	3.8140	8.6351
1250	2.0157	- 5.2480	- 6.2018	3.1721	- 3.7090	- 1.5718
1600	- 3.0121	7.7044	1.0976	- 6.9049	- .7055	.9554
2000	4.4025	- 5.1226	- 4.5669	3.9906	- 4.6098	- 5.4459
2500	2.5998	- 5.0730	- 4.7504	5.0417	- 2.0784	- 3.5024
3150	5.0130	- 7.6651	- 5.3237	8.0407	- 3.7612	- 6.0040
4000	2.4338	- 1.4246	- [illegible].8975	2.9921	- 2.4395	- 5.7307
5000	3.1853	- 1.1450	- 1.6765	3.4350	- 2.3856	- 6.2589
6300	3.3702	- .1741	- .1860	3.3237	- 2.1367	- 6.4509
8000	- 8.5135	20.0696	7.1655	-13.3759	2.9983	2.4932
10000	-16.3671	28.6084	8.6185	-21.4567	7.2175	10.2479

TABLE VII- D13

Directivity Correlation Coefficients

$M_R = 1.020$

IGV Fans

$$D.I. = A_o + A_1 \sin 1.5\theta + A_2 \cos 2\theta + A_3 \sin 2\theta$$

$$+ A_4 \cos^2 2\theta + A_5 \sin 1.5\theta \sin 2\theta$$

f	A_o	A_1	A_2	A_3	A_4	A_5
400	-11.6556	19.0963	6.9392	-18.2886	4.3537	11.0377
500	- 9.8739	13.7516	4.3969	-16.0783	3.5042	8.8407
630	- 3.1517	7.8436	2.8414	- 7.6384	.2179	2.4849
800	-14.2917	22.4715	5.8643	-19.6547	4.7502	13.0470
1000	-11.2707	16.5793	3.8832	-16.6357	3.9331	9.9773
1250	-21.0711	22.7372	1.6285	-19.9428	7.0546	20.5839
1600	-14.6335	19.0917	1.6787	-17.3539	4.3697	12.6556
2000	- 6.4625	5.2563	- 4.2138	- 5.1758	- .5144	6.4142
2500	2.7373	-10.7718	-10.1594	9.0100	- 4.2855	- 1.4481
3150	5.4034	-12.9826	- 9.7054	11.6959	- 5.7421	- 3.6718
4000	9.0831	-13.0048	- 8.3483	12.3463	- 7.2166	- 9.7936
5000	6.0794	- 6.8220	- 4.9166	7.7681	- 5.0316	- 7.5488
6300	3.3753	- 1.1048	- 1.6191	3.5806	- 3.0471	- 5.6242
8000	.0795	4.7222	.1830	- 1.3569	- 1.9389	- 3.9408
10000	2.0977	- .7706	- 4.2794	1.5792	- 4.6284	- 5.0727

TABLE VII-D14

Directivity Correlation Coefficients

$M_R = 1.082$

IGV Fans

$$D.I. = A_o + A_1 \sin 1.5\theta + A_2 \cos 2\theta + A_3 \sin 2\theta$$

$$+ A_4 \cos^2 2\theta + A_5 \sin 1.5\theta \sin 2\theta$$

f	A_o	A_1	A_2	A_3	A_4	A_5
400	- 7.6352	11.7524	3.5983	-12.0753	2.5574	7.8072
500	- 5.7206	6.4609	1.0783	- 9.9233	1.4201	5.5798
630	1.5798	.1628	.1812	- 1.1155	2.0868	- 1.2164
800	- 1.0497	- 3.7295	- 7.2350	2.3720	- 2.5533	1.9880
1000	- 5.7916	4.4464	- 1.7084	- 7.1090	1.8355	6.2209
1250	- 6.4967	5.0006	- 2.6224	- 5.9474	.6269	8.2072
1600	4.6580	-12.3141	-10.1699	8.7077	- 6.0678	- 2.0824
2000	5.8394	-10.3527	- 6.9998	7.6891	- 5.0034	- 4.8389
2500	13.1096	-25.0886	-13.5114	20.2097	- 7.6947	-10.7320
3150	13.5687	-24.3314	-12.0586	20.4246	- 7.8902	-11.1220
4000	11.0920	-16.3847	- 8.1115	14.8223	- 6.1380	-12.0871
5000	7.2793	- 9.8253	- 5.5594	9.3311	- 3.9675	- 9.4425
6300	2.8490	- 2.3165	- 2.5588	3.1374	- 1.5323	- 6.4975
8000	- 6.2151	13.1141	3.1221	- 9.1727	1.9245	1.3778
10000	- 7.4245	11.1922	.4102	- 8.8992	2.0230	2.2743

TABLE VII-D13

Directivity Correlation Coefficients

$M_R = 1.180$

IGV Fans

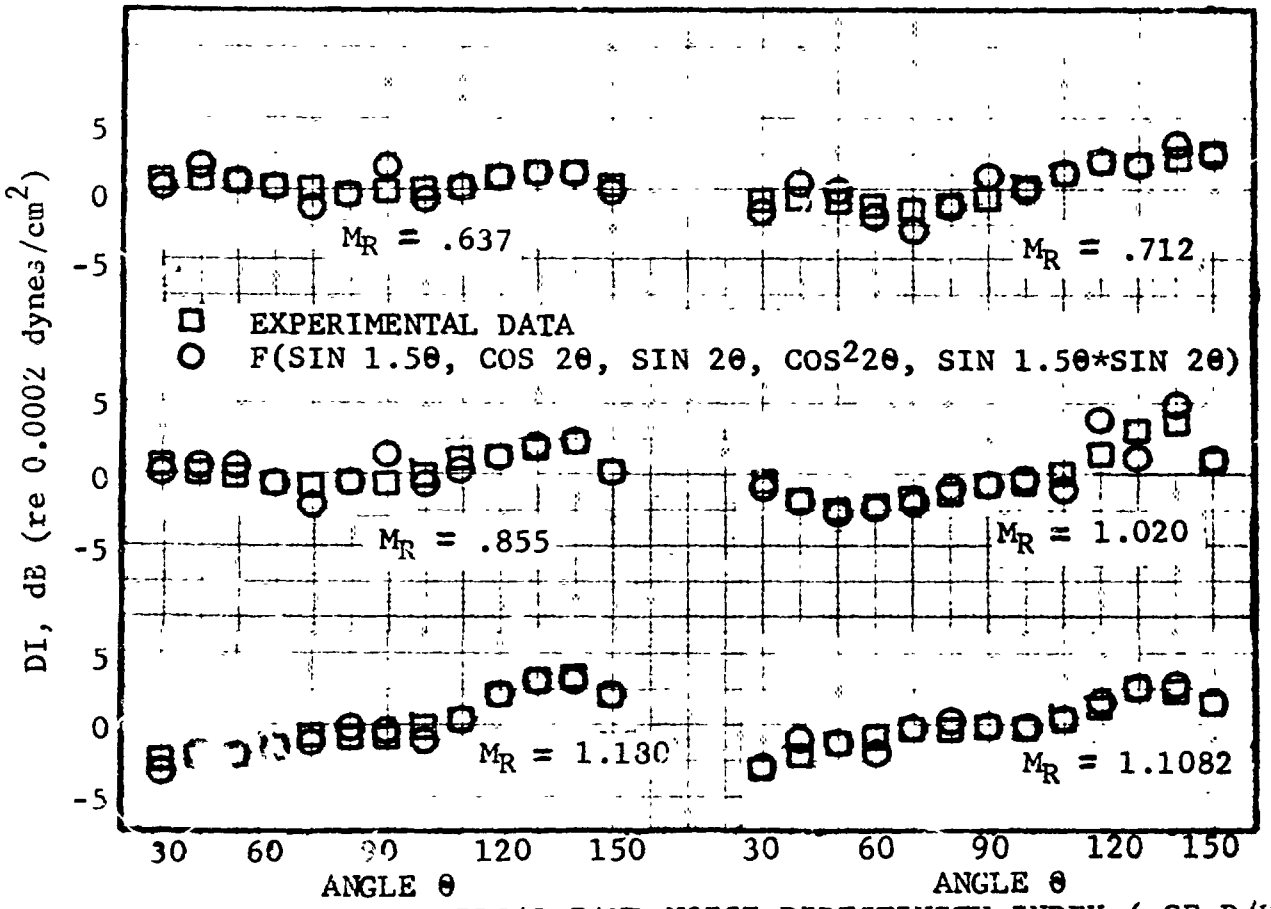

FIGURE VII-D25 BROAD BAND NOISE DIRECTIVITY INDEX (GE D/V - III)
f_D = 1.42 X 10^4 IN./SEC.

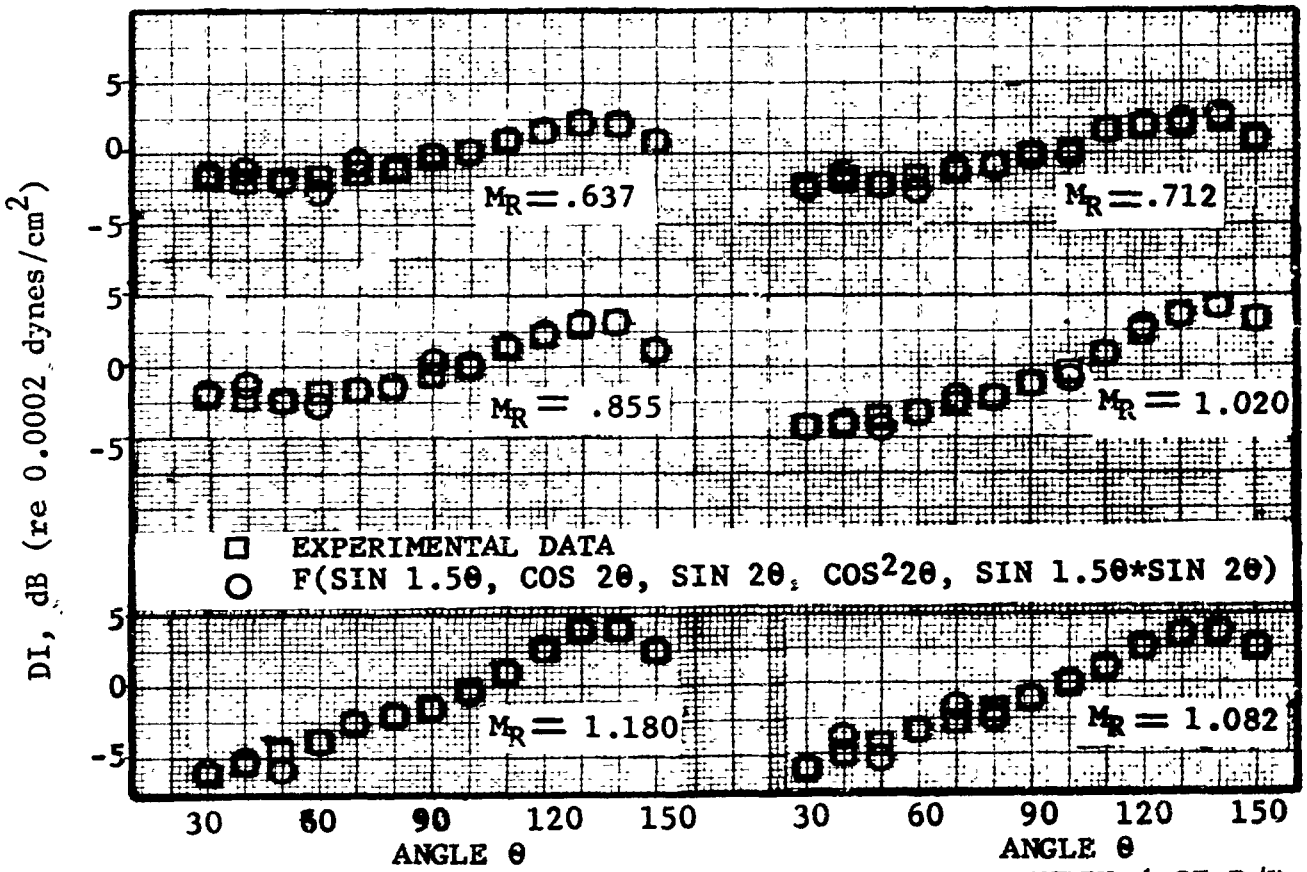

FIGURE VII-D26 BROAD BAND NOISE DIRECTIVITY INDEX (GE D/V - III)
$fD = 1.775 \times 10^4$ IN./SEC.

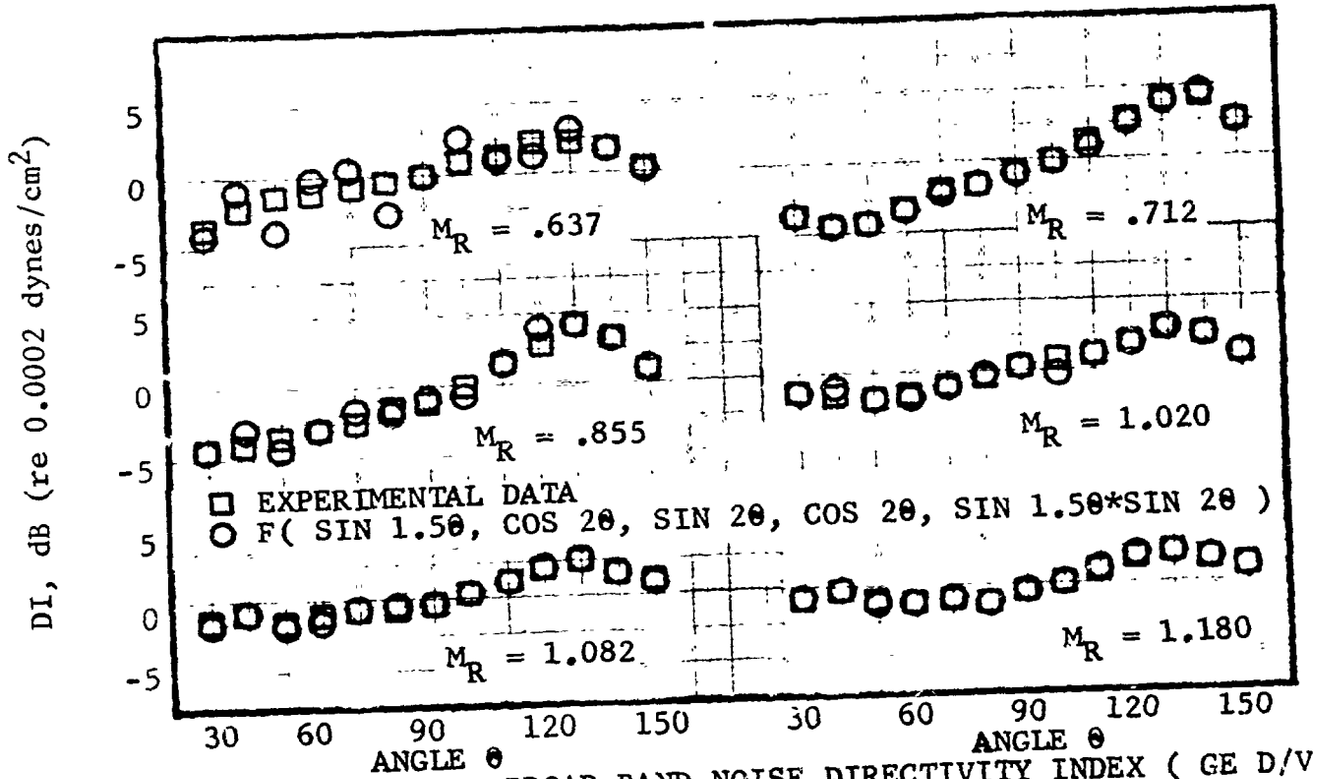

FIGURE VII-D27 BROAD BAND NOISE DIRECTIVITY INDEX (GE D/V - III) AT fD = 2.24 X 10^4, IN./SEC.

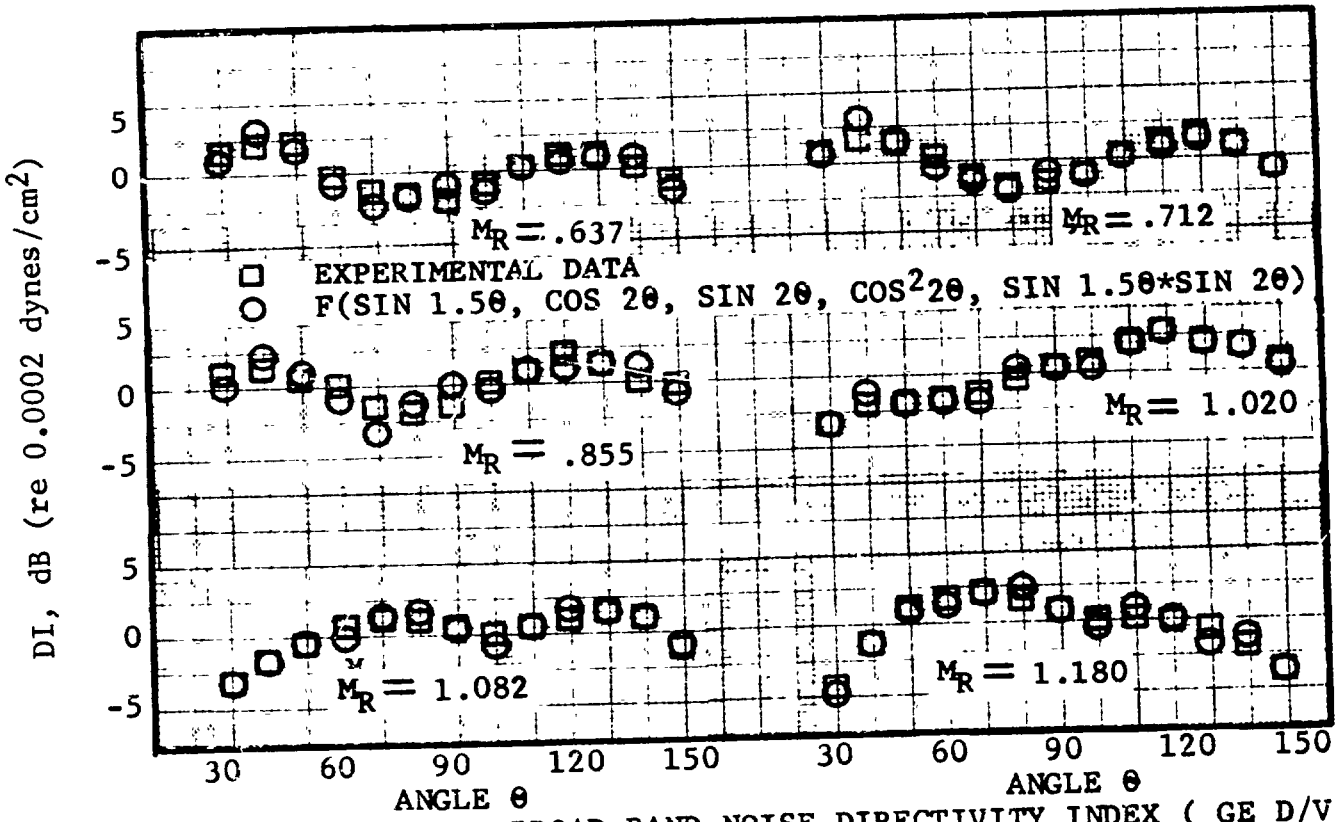

FIGURE VII-D28 BROAD BAND NOISE DIRECTIVITY INDEX (GE D/V - III)
$fD = 2.84 \times 10^4$, IN./SEC.

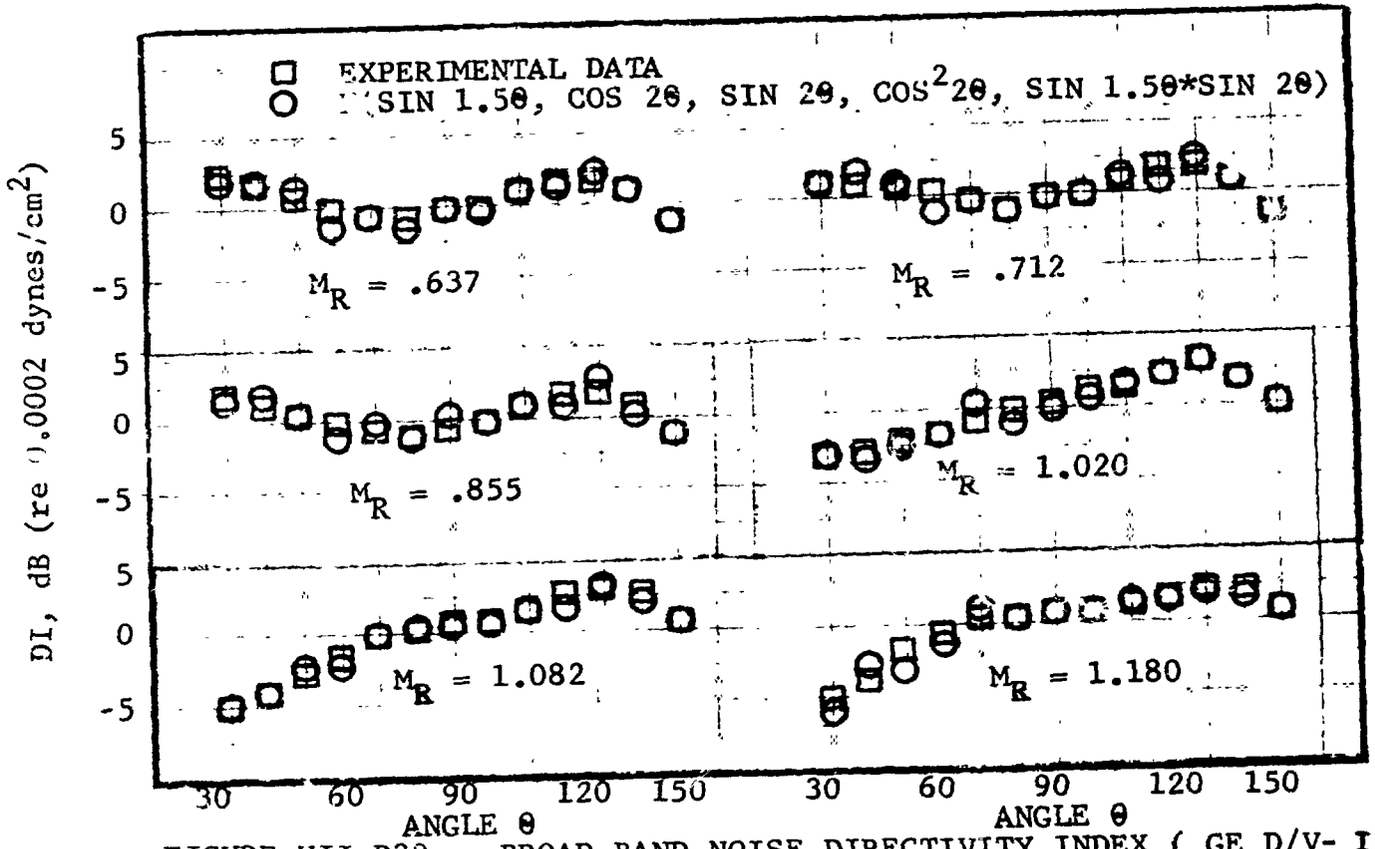

FIGURE VII-D29 BROAD BAND NOISE DIRECTIVITY INDEX (GE D/V- III) AT fD = 3.55×10^4, IN./SEC.

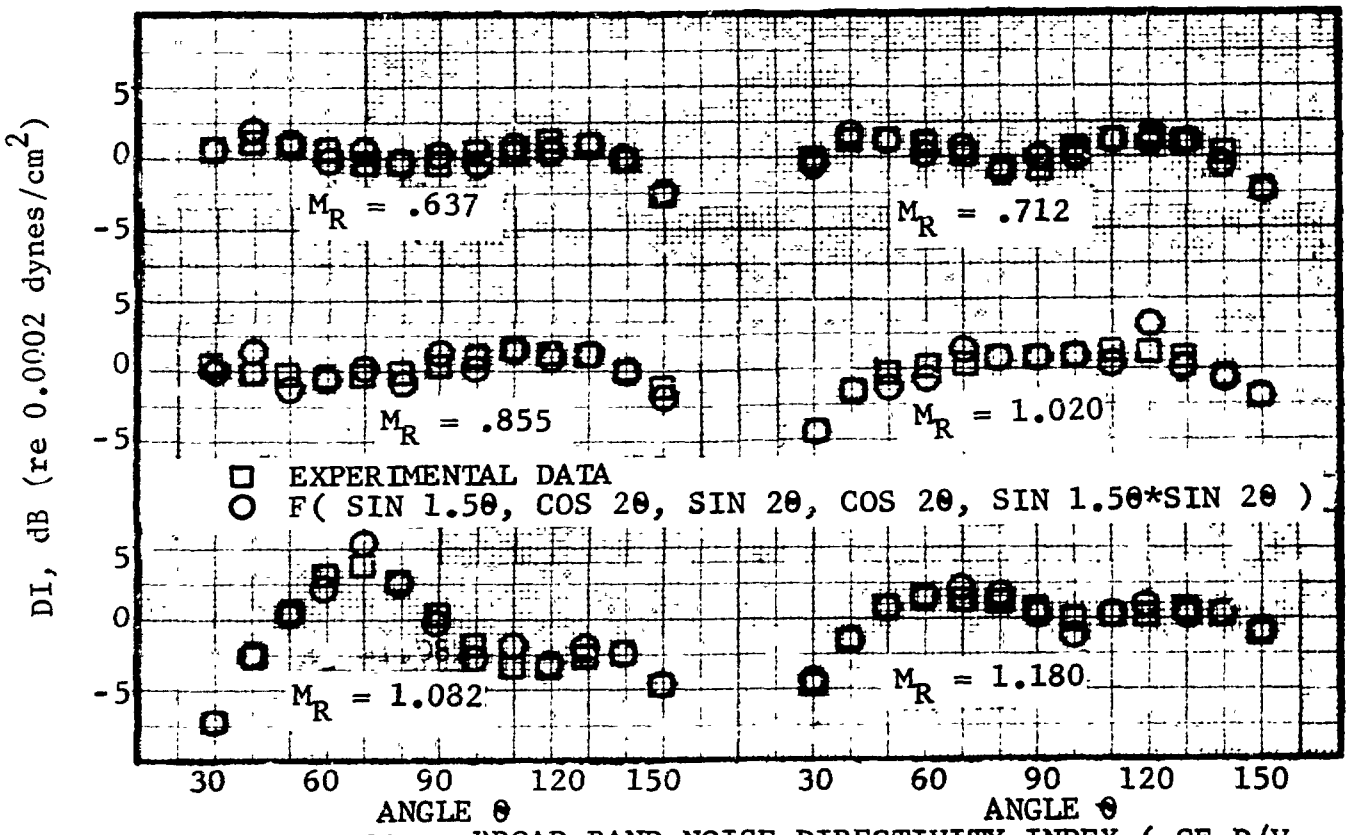

FIGURE VII-D30 BROAD BAND NOISE DIRECTIVITY INDEX (GE D/V - III) AT fD = 4.44 X 10^4 IN./SEC.

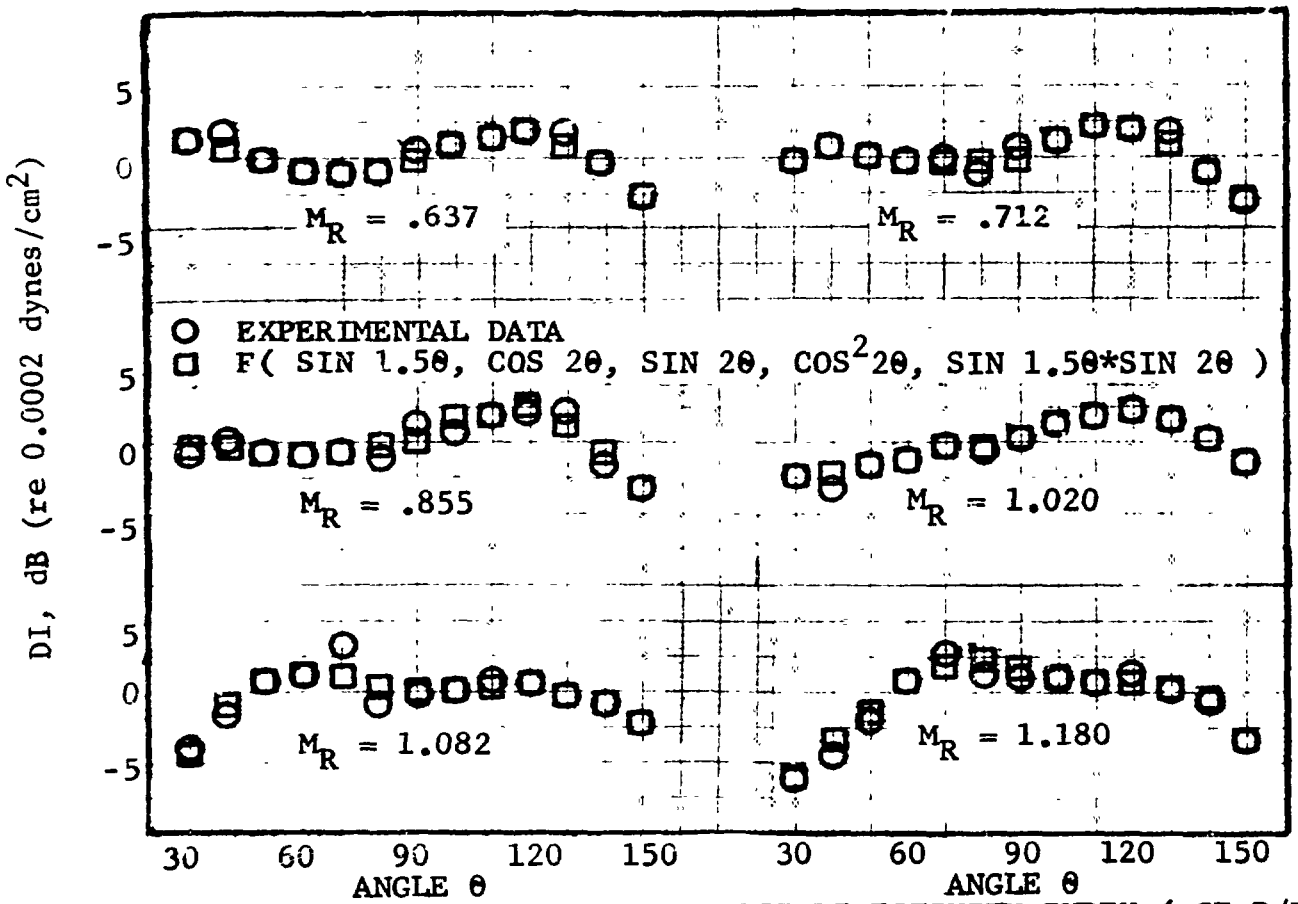

FIGURE VII-D31 BROAD BAND NOISE DIRECTIVITY INDEX (GE D/V - III) AT fD = 5.68 X 10^4 IN./SEC.

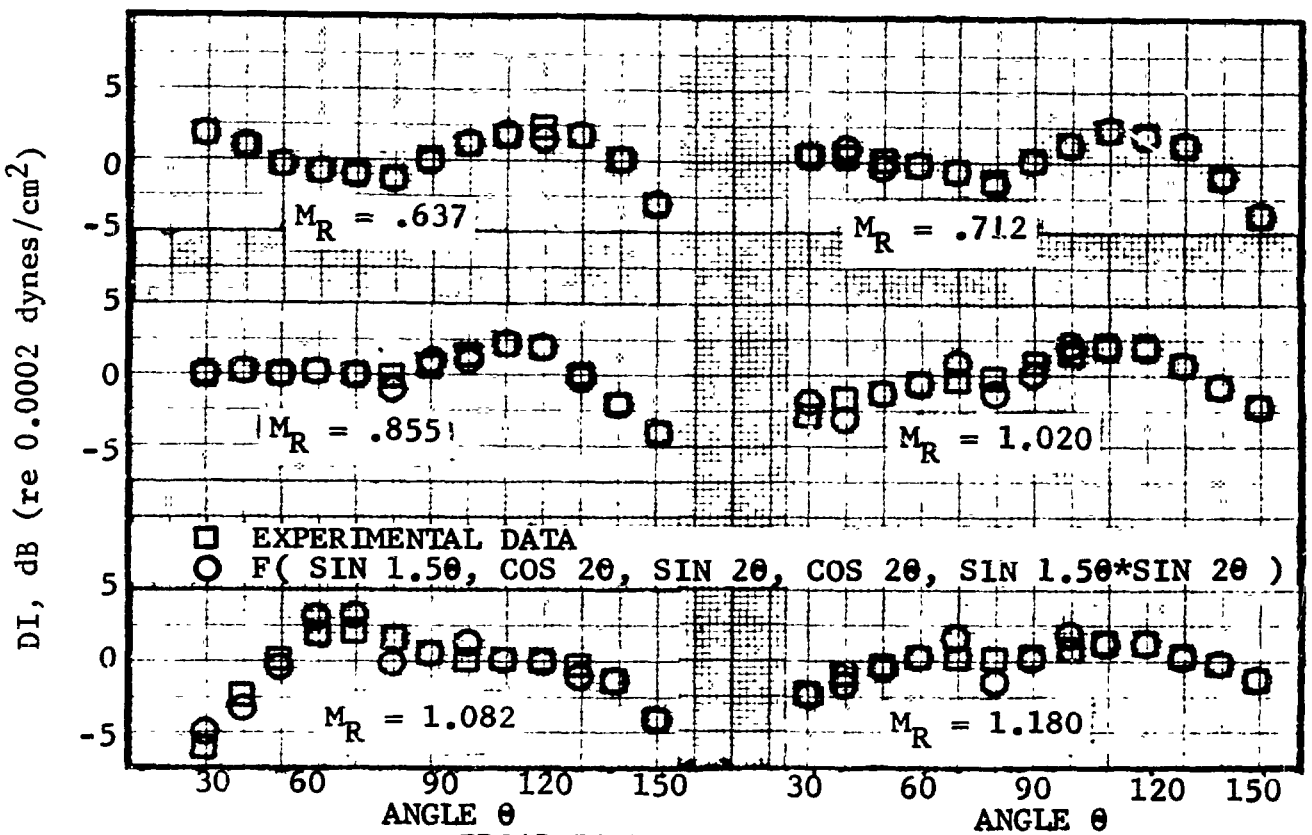

FIGURE VII-D32 BROAD BAND NOISE DIRECTIVITY INDEX (GE D/V - III) AT fD = 7.10 X 10^4, IN./SEC.

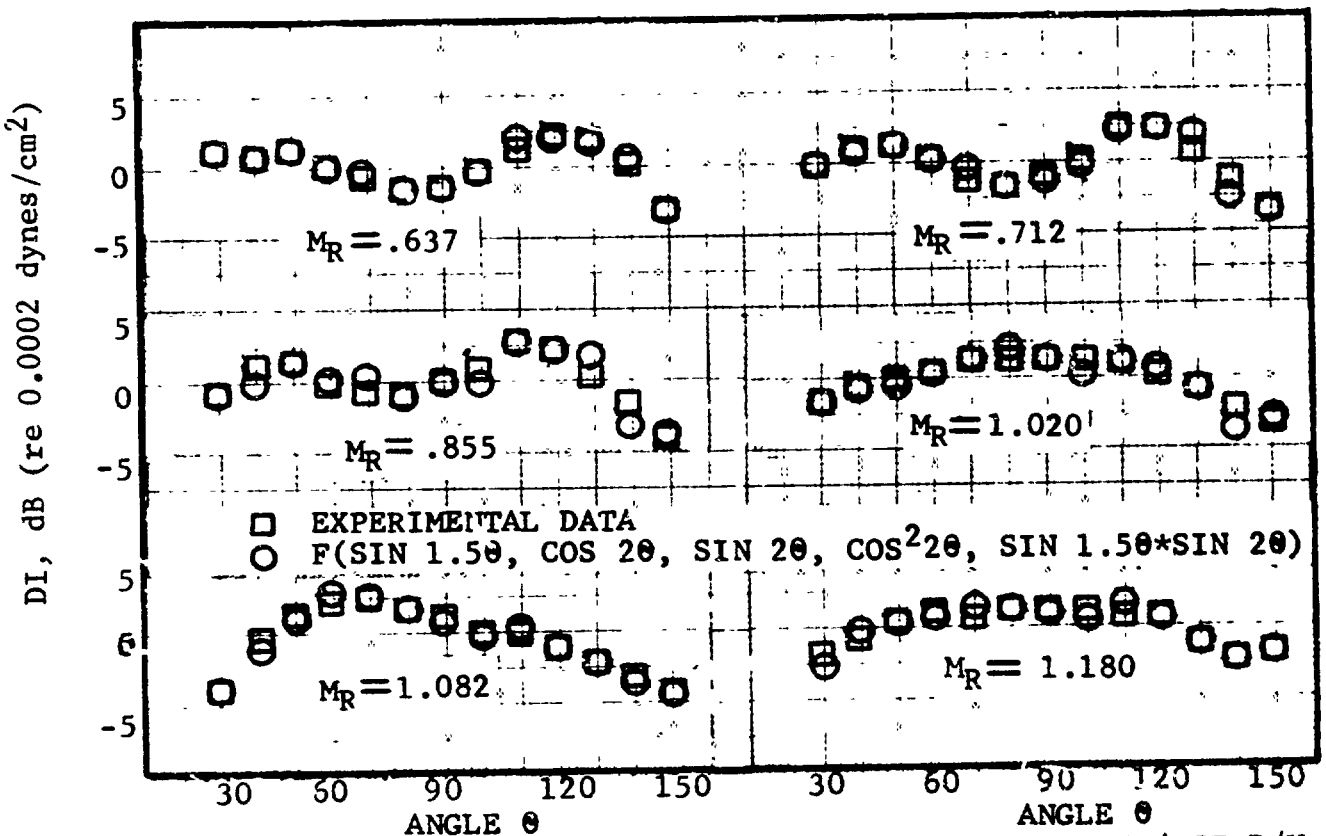

FIGURE VII-D33 BROAD BAND NOISE DIRECTIVITY INDEX (GE D/V - III)
fD = 8.88 X 10^4 IN./SEC.

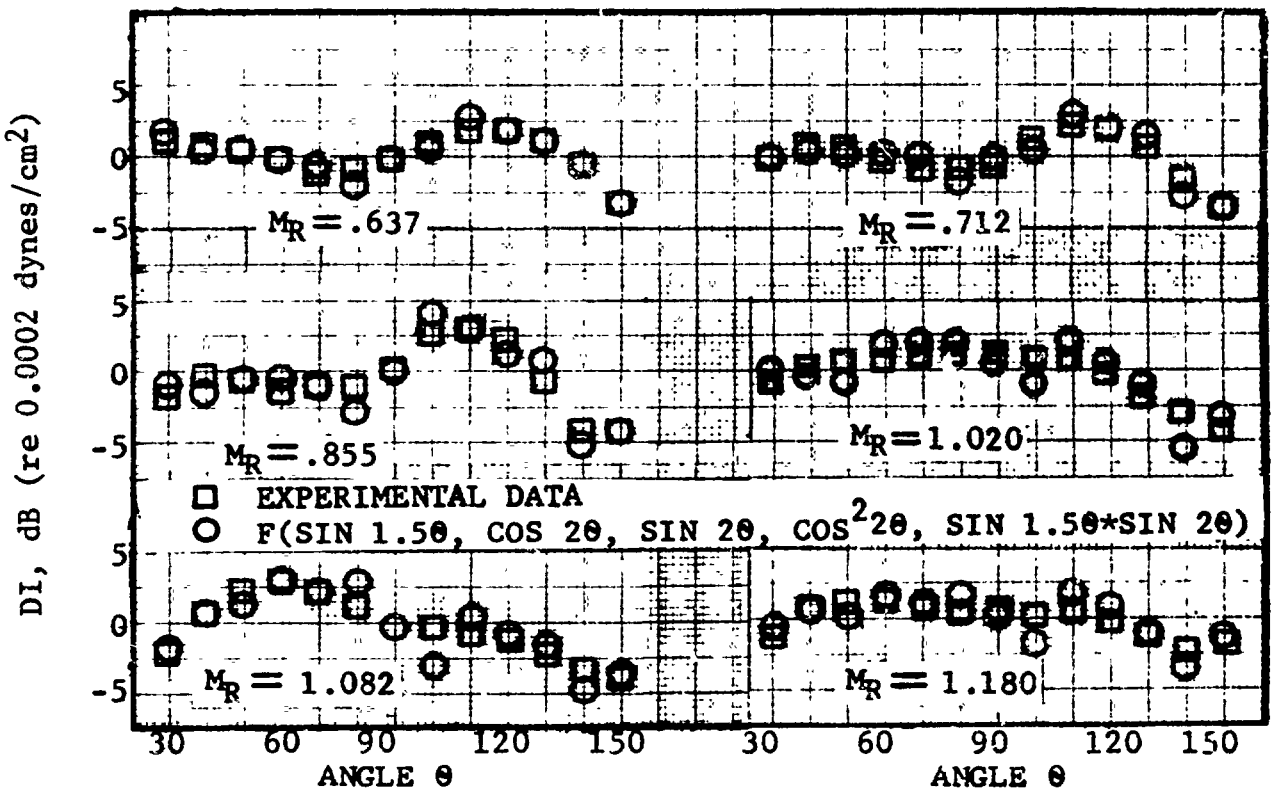

FIGURE VII-D34 BROAD BAND NOISE DIRECTIVITY INDEX (GE D/V - III)
$fD = 11.20 \times 10^4$, IN./SEC.

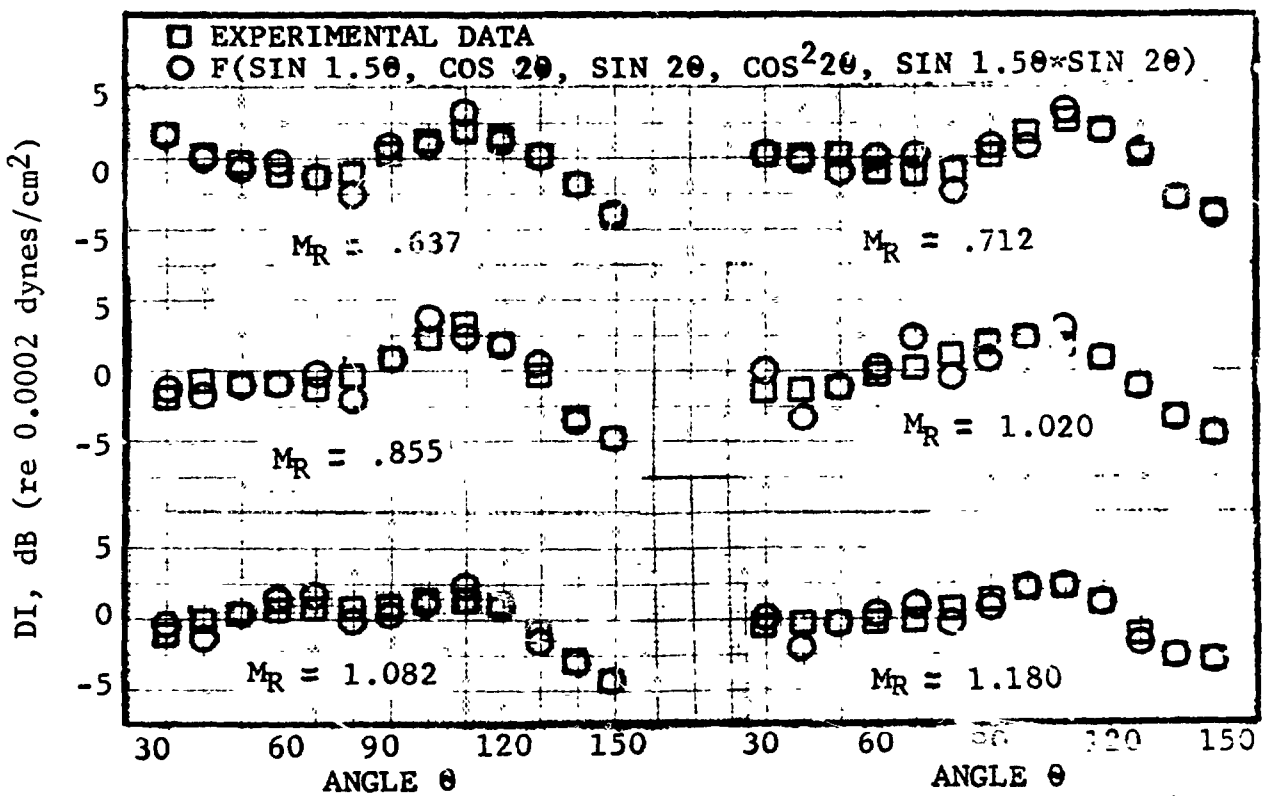

FIGURE VII-D35 BROAD BAND NOISE DIRECTIVITY INDEX (GE [illegible])
AT fD=14.2 X 10^4, IN./SEC.

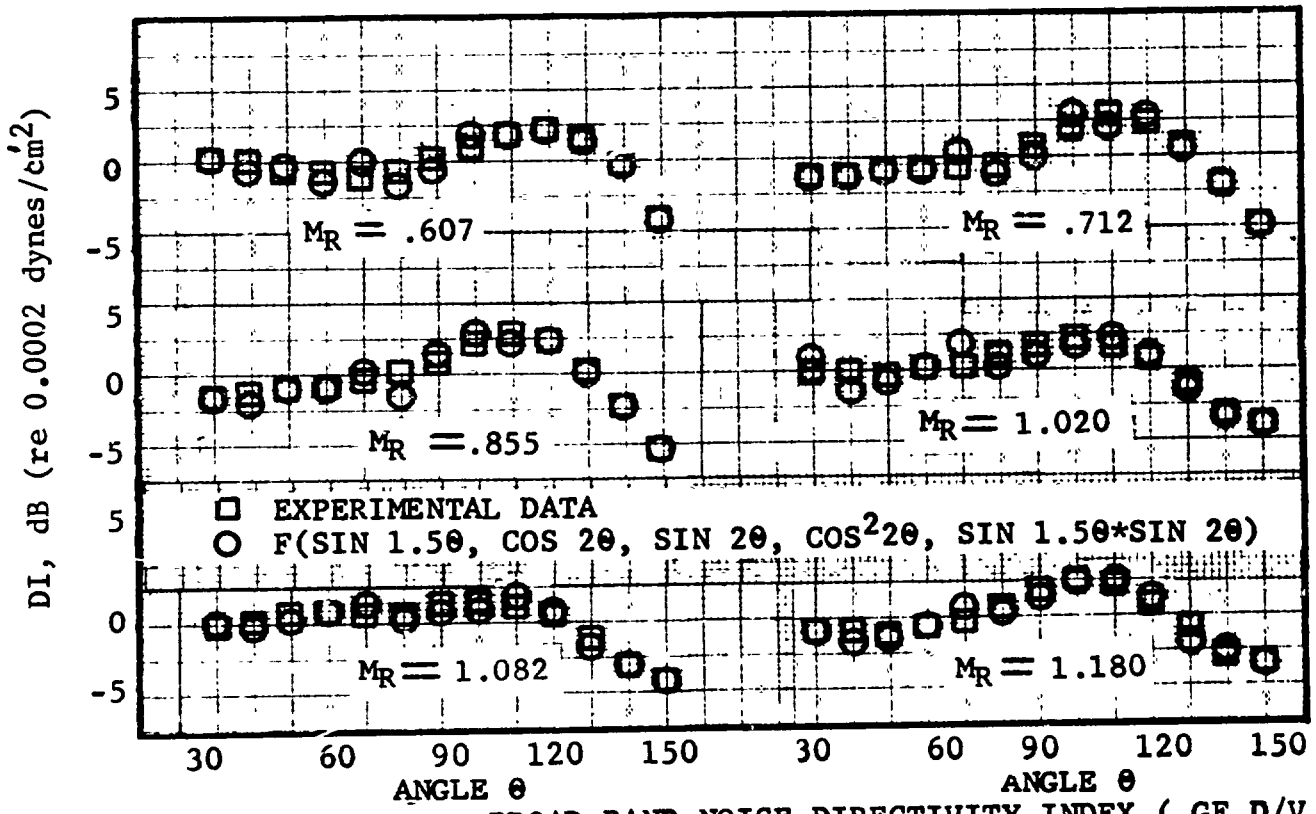

FIGURE VII-D36 BROAD BAND NOISE DIRECTIVITY INDEX (GE D/V - III) AT $fD = 17.75 \times 10^4$, IN./SEC.

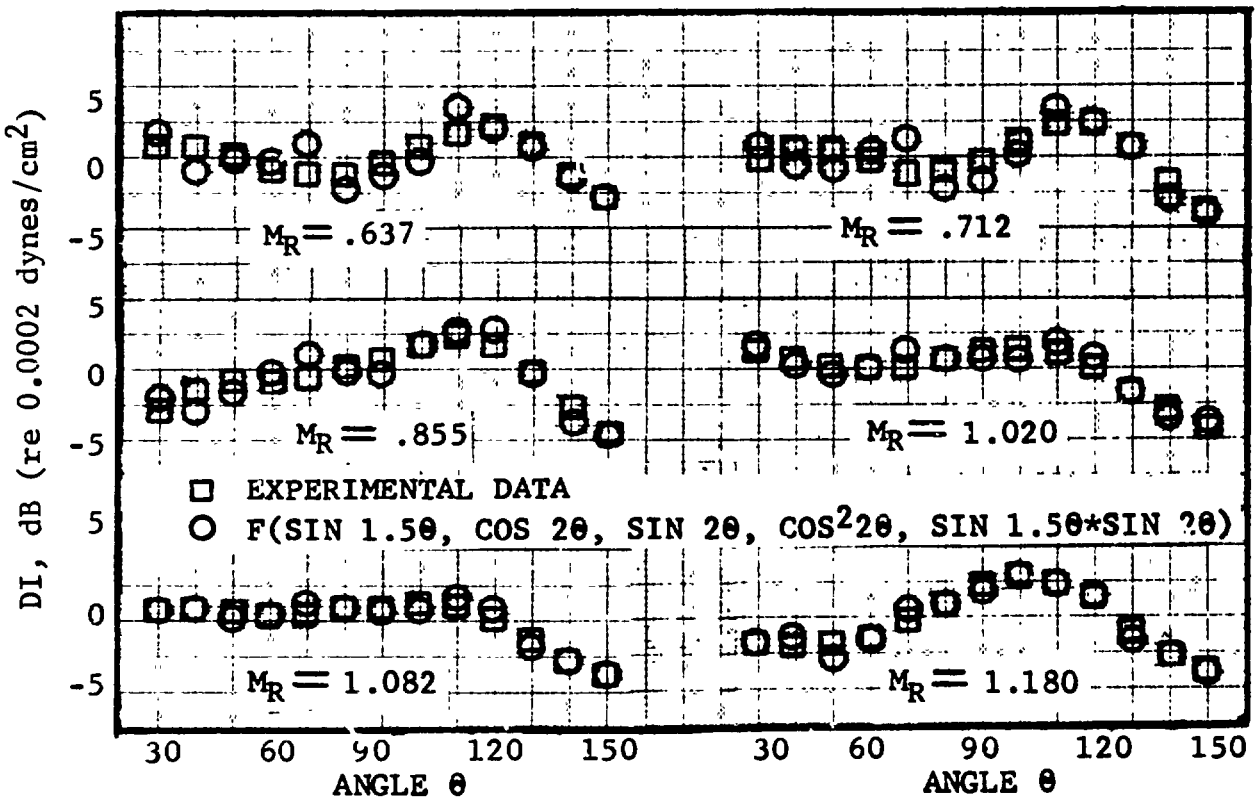

FIGURE VII-D37 BROAD BAND NOISE DIRECTIVITY INDEX (GE D/V - III)
$fD = 22.4 \times 10^4$, IN./SEC.

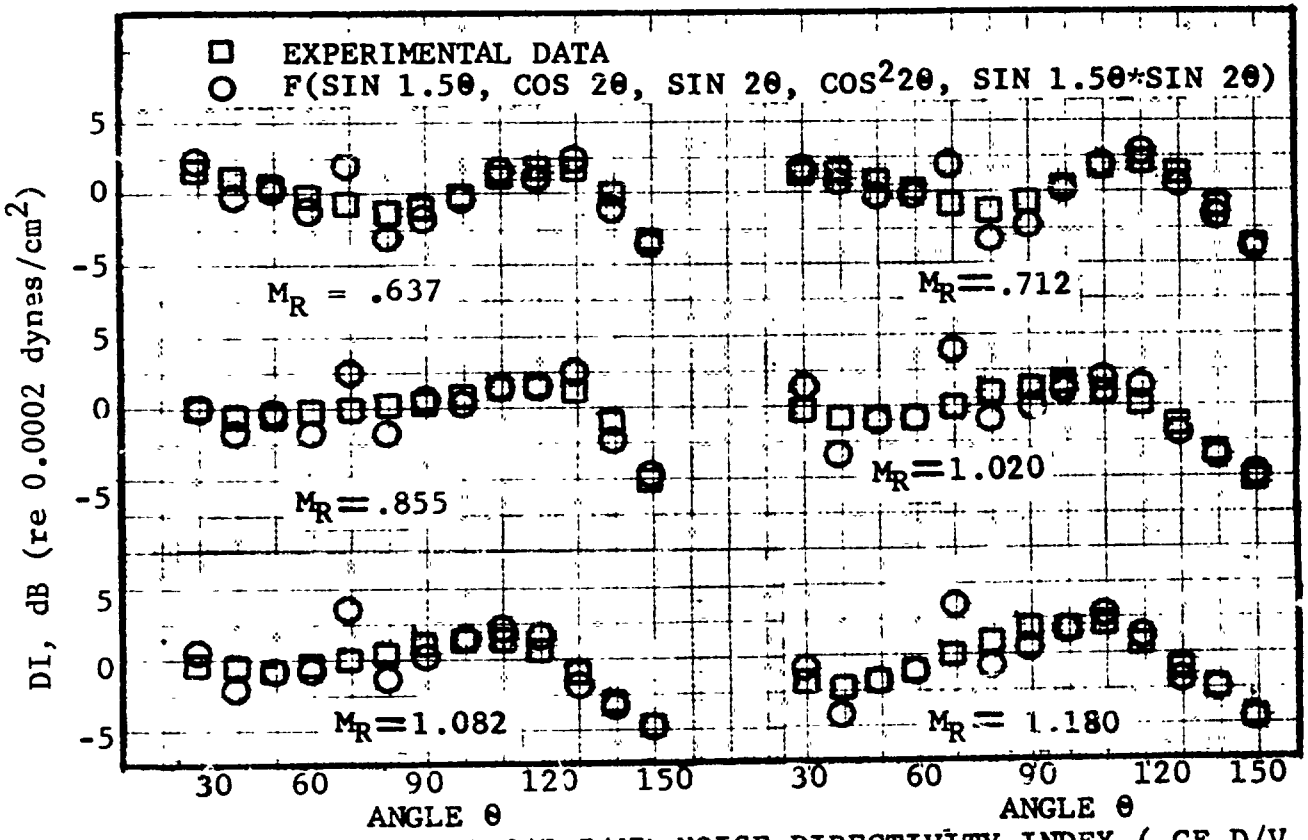

FIGURE VII-D38 BROAD BAND NOISE DIRECTIVITY INDEX (GE D/V - III) AT fD = 28.4 X 10^4 IN./SEC.

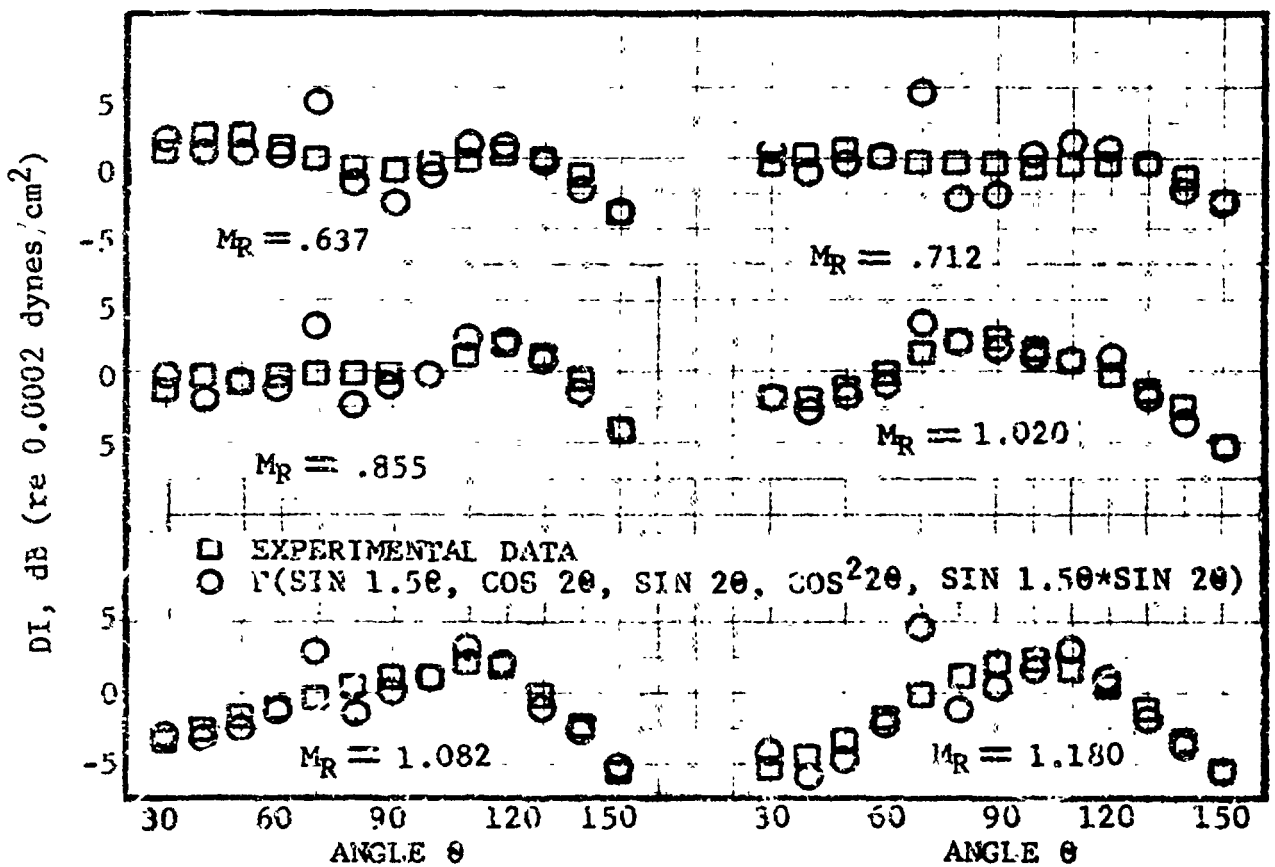

FIGURE VII-D39 BROAD BAND NOISE DIRECTIVITY INDEX (GE D/V - III) AT $fD = 35.5 \times 10^4$, IN./SEC.

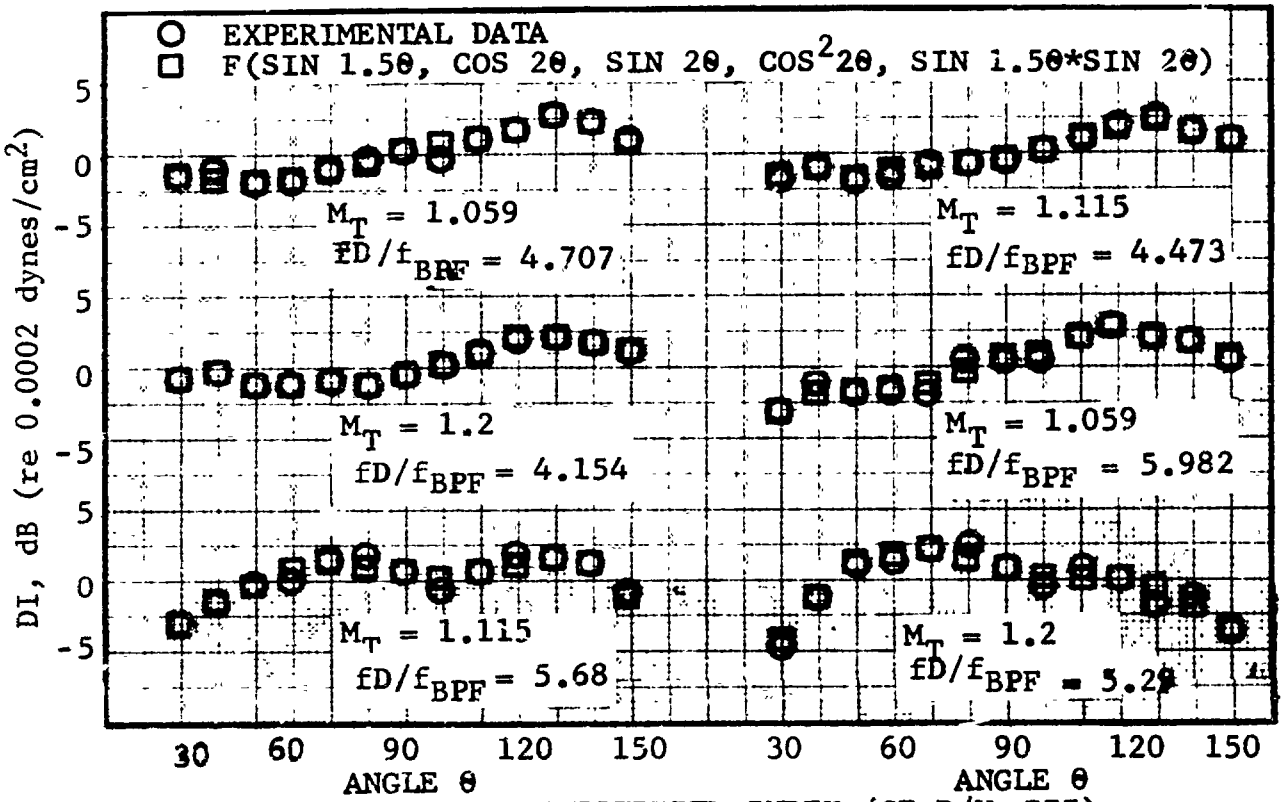

FIGURE VII-D40 MPT DIRECTIVITY INDEX (GE D/V- III)

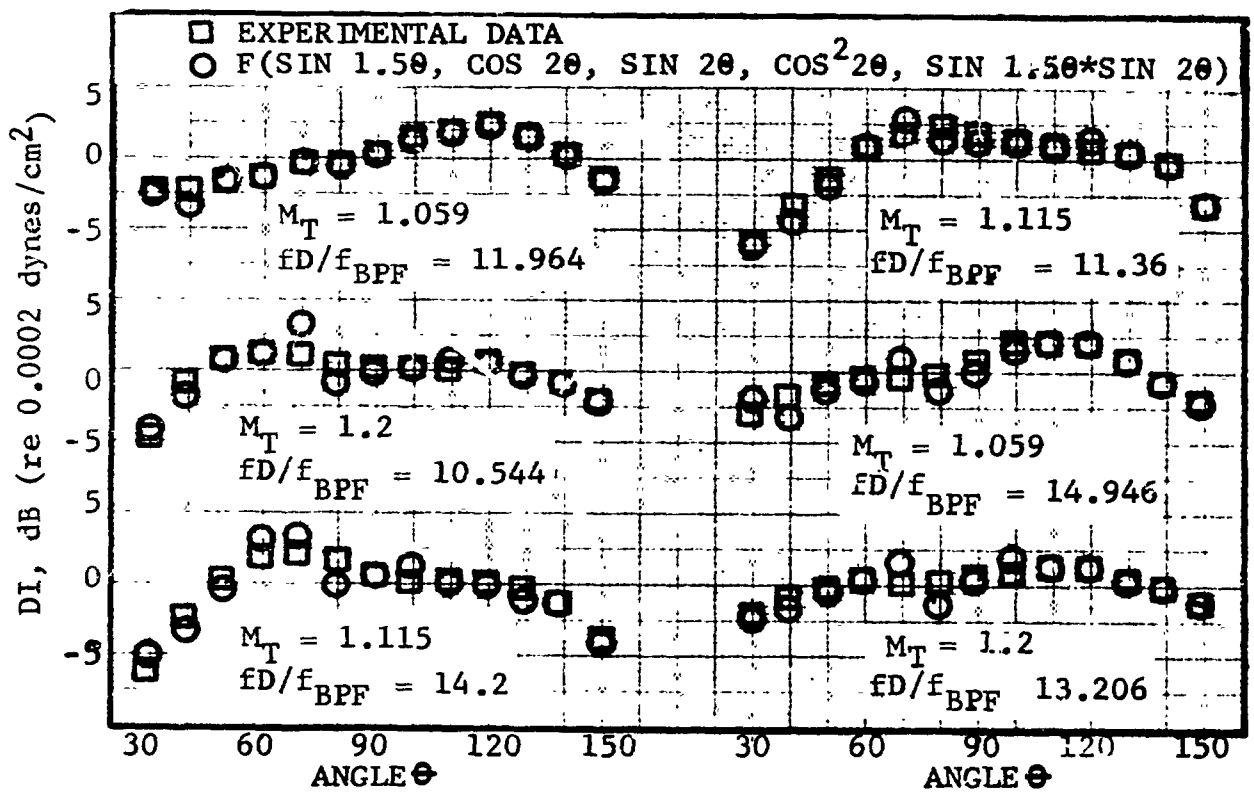

FIGURE VII-D41 MPT DIRECTIVITY INDEX (GE D/V- III)

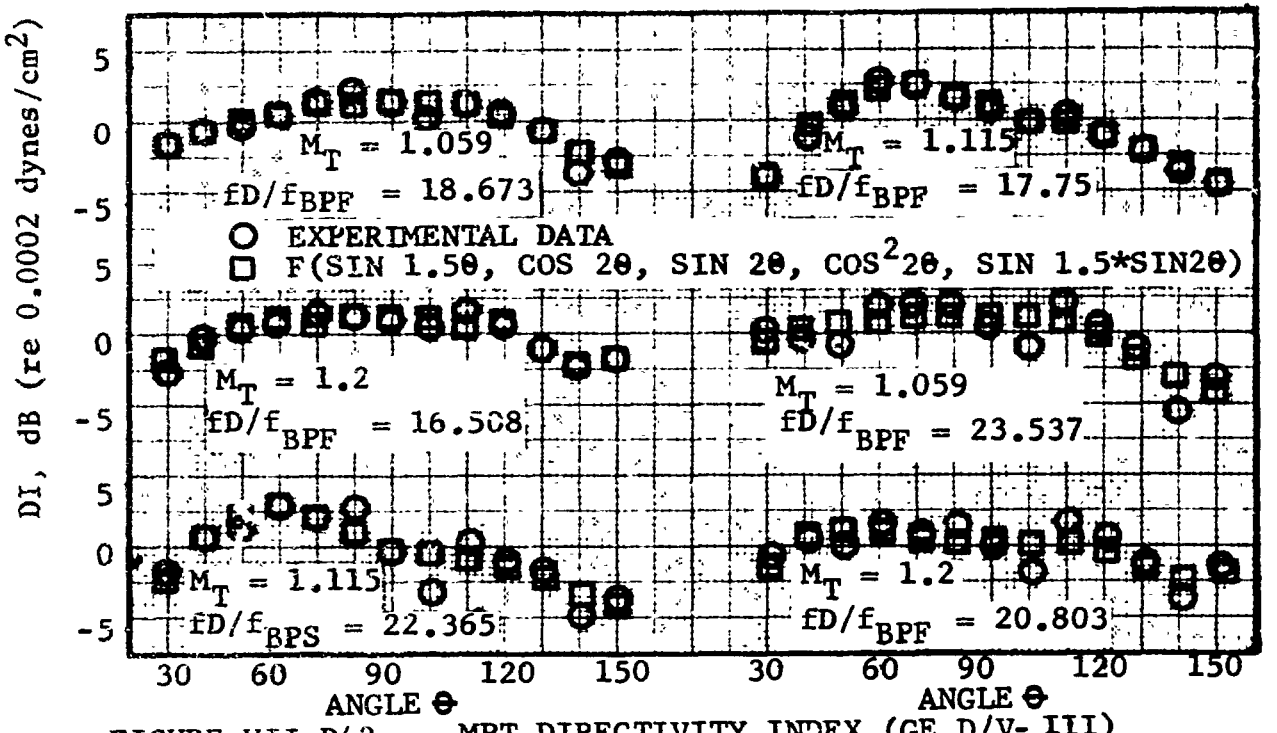

FIGURE VII-D42 MPT DIRECTIVITY INDEX (GE D/V- III)

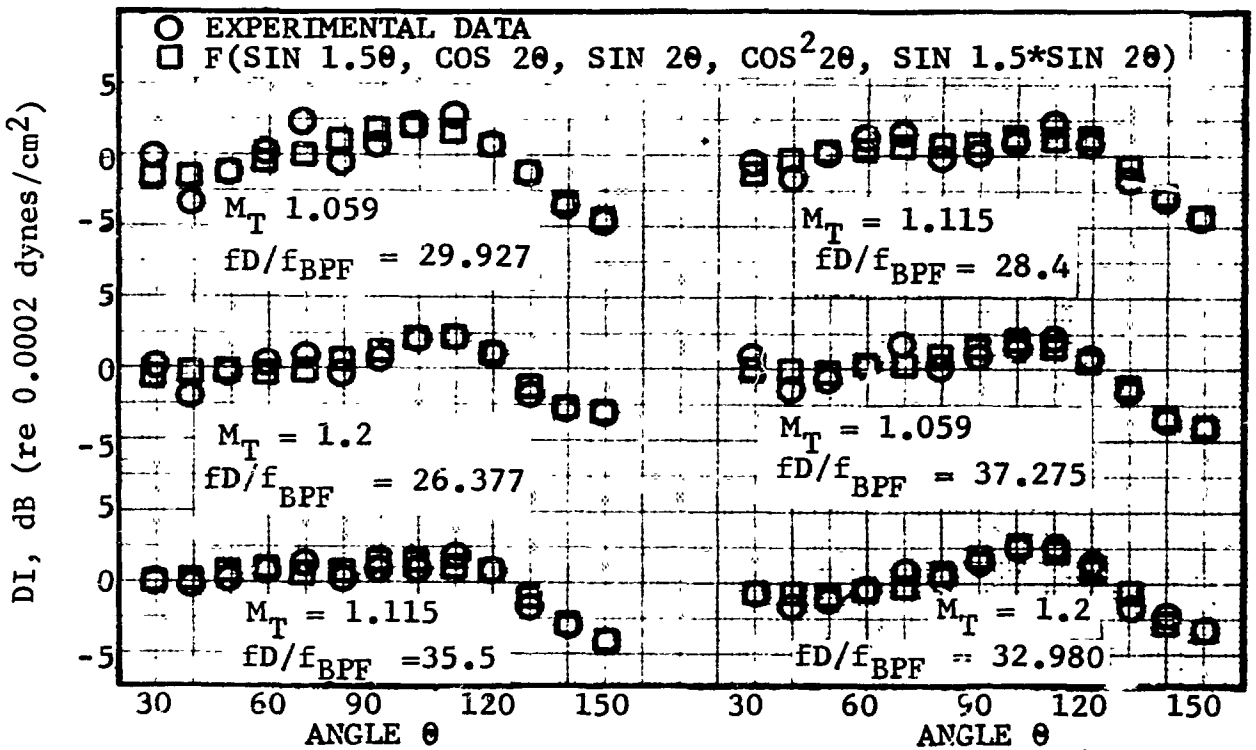

FIGURE VII-D43 MPT DIRECTIVITY INDEX (GE D/V- III)

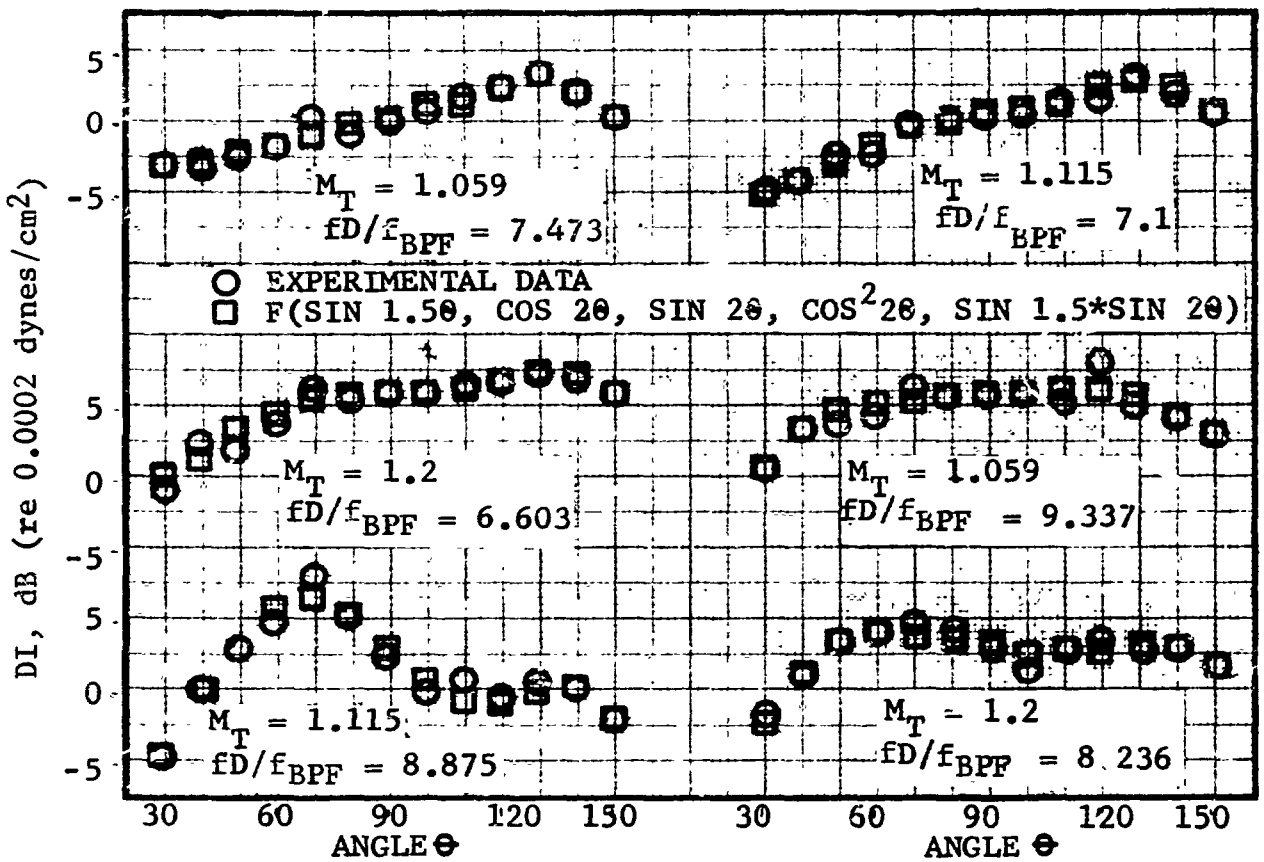

FIGURE VII-D44 MPT DIRECTIVITY INDEX (GE D/V-III)

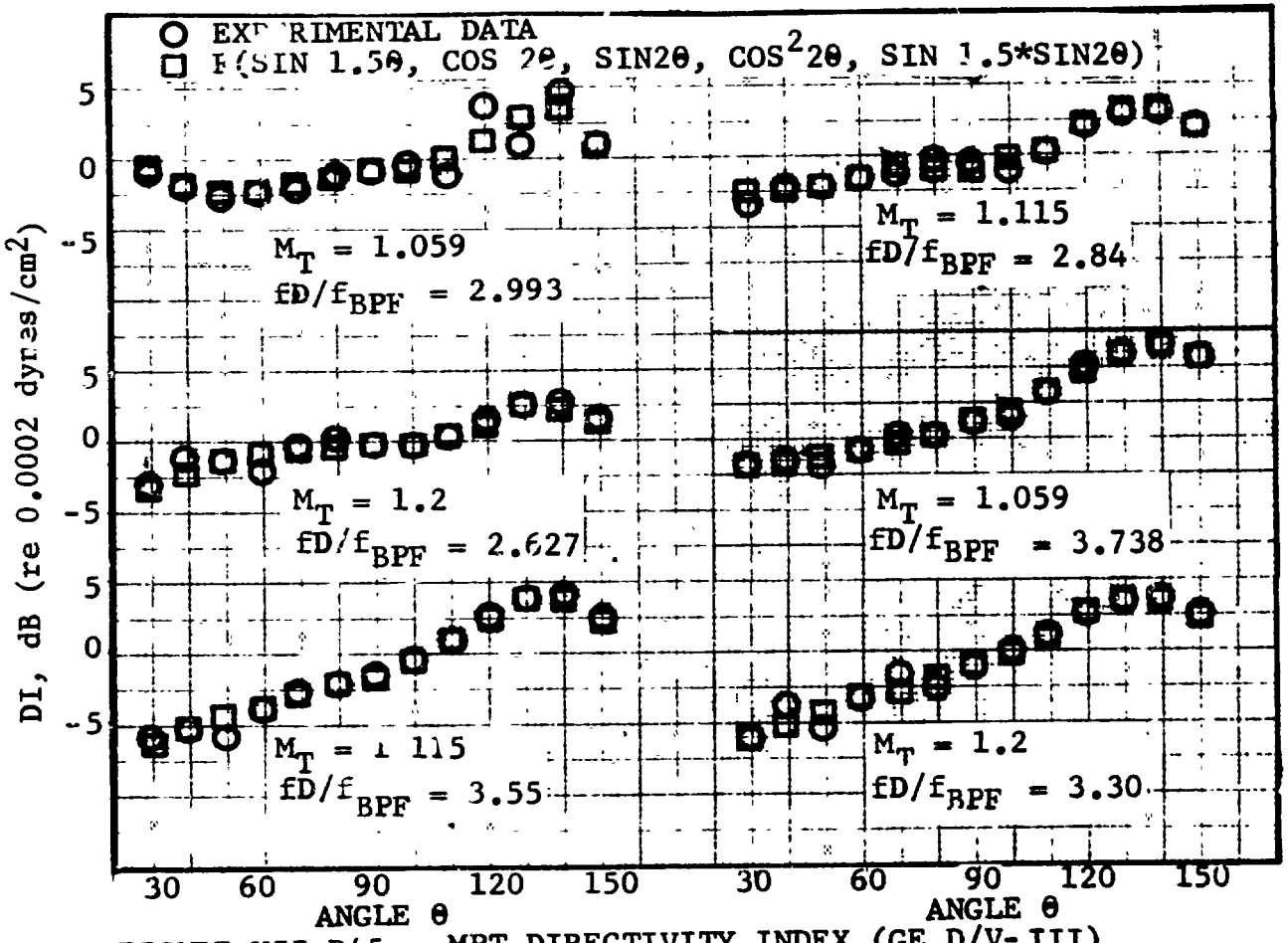

FIGURE VII-D45 MPT DIRECTIVITY INDEX (GE D/V-III)

(E) Summary. The following represents a block diagram of the developed semi-empirical fan noise prediction technique.

INPUTS

- Fan hub/tip diameter
- Fan weight flow
- Fan RPM
- Fan velocity diagram at three radial stations
- Fan detailed blading geometry (inlet/outlet angles, solidities, etc.) at three radial stations
- Interblade spacing at three radial stations

(Program will calculate all necessary other parameters to be input in the following)

1. Calculate BPF tone sound power level using model developed in section VII-A.

2. Calculate D.I. for BPF tone using Tables VII-C1 and VII-C2 for IGV less fans; Table VII-C3 for IGV fans; (Interpolate to obtain D.I. at required M_T)

3. Calculate BPF tone SPL at a given point on an arc or a sideline using the results of 1 + 2 and the results of Section VI (Air and Ground Attenuation)

4. Calculate broadband/noise MPT sound power level. Spectrum (in 1/3 octave bands) using Tables VII-B1 for IGV less fans Table VII-B2 for IGV fans Frequency scale using VII-B3 relationship for broadband noise VII-B4 relationship for MPT's

5. Calculate D.I. for 15 1/3 octave bands using Table VII-D1 to VII-D6 for IGV less fans; Tables VII-D7 to VII-D15 for IGV fans; (Interpolate to obtain D.I. at required M_R frequency scale using relationship (VII-D2) for broadband noise and (VII-D3) for MPT's

6. Calculate 1/3 octave bands SPL's at a given point on an arc or a sideline using the results of 4 and 5 and the results of Section VI (Air and Ground Attenuation)

7. Combine the results of 3 and 6 to give total fan spectrum and PNdB

OUTPUT

Fan SPL spectrum plus PNdB at angles ranging between 20 to 160° (in 10° increments) along any given arc or sideline

The semi-empirical prediction technique developed in this Section has been checked successfully against experimental data obtained on a variety of vehicles. The details of these comparisons are discussed in the following section.

VIII. VERIFICATION OF FAN NOISE PREDICTION METHOD

(A) Blade Passing Frequency Tones. In order to substantiate the accuracy of the pure tone noise prediction procedure, described in Section II-A, it was applied to a number of fan vehicles for which extensive acoustic test data already existed. The fans chosen represented a wide variety of sizes and design features, to emphasize the general applicability of the prediction technique. Comparisons between measured and predicted pure tone sound power levels, for each fan studied, are presented herein. Pertinent design details of each fan are included.

(1) CJ805-23. The CJ805-23 (Figure VIII-A1) is a low bypass ratio aft fan engine; the single-stage fan is a first-generation design. The acoustic data was taken from a standard production engine configuration which was tested at the Edwards Flight Test Center (Figure VIII-A2). Basic physical and aerodynamic design parameters for the CJ805-23 fan are listed in Table VIII-A1. Figure VIII-A3 is a comparison of measured and predicted blade-passing frequency fundamental PWL's for this fan, plotted as function of fan tip Mach number; Figure VIII-A4 is a similar comparison of the second harmonic PWL's. A good correlation between measured and predicted values was achieved for both pure tones.

(2) CF700 Fan. The CF700 (Figure VIII-A5) is a 62% scale model of the CJ805-23. Design parameters for the CF700 fan are also presented in Table VIII-A1. Figure VIII-A6 is a comparison between measured and predicted values, for the fundamental PWL's; a good prediction of the data was again achieved.

(3) TF39 Fan "Family". There are four vehicles in the TF39 "family". The full-scale TF39 fan (Figure VIII-A7) is a high bypass ratio front fan of second generation design. It has a "one and one half stage" configuration, which is effectively divided into an inner panel and an outer panel flowpath (Figure VIII-A8). The TF39 Development Vehicle (D/V) (Figure VIII-A9) is a 68% Scale Model of the full-scale TF39; it has, of course, the same configuration. The TF39 Outer Panel (O/P) test rig is a 45% scale model of only the outer panel portion of the full scale fan. (This vehicle thus includes only the second stage rotor). The TF39 Outer Panel Freon Model is described in Reference 1 and is shown in Figure VIII-A10. It is a 14% scale model of the O/P rig, run with Freon C318 as the test flow media.

The basic design parameters for all four vehicles are listed in Table VIII-A2. Inclusion of this series of vehicles was thought to be a good test of the accuracy of the prediction technique over a large range of fan sizes. Figures VIII-A11 to 20 compare measured and predicted pure tone power levels (plotted as a function of fan tip Mach number) for the following:

Figure VIII-A11 - TF39 Full Scale - Stg. 1 rotor fundamental
Figure VIII-A12 - TF39 Full Scale - Stg. 2 rotor fundamental
Figure VIII-A13 - TF39 Full Scale - Stg. 2 rotor 2nd harmonic
Figure VIII-A14 - TF39 D/V - Stg. 1 rotor fundamental
Figure VIII-A15 - TF39 D/V - Stg. 2 rotor fundamental
Figure VIII-A16 - TF39 D/V - Stg. 2 rotor 2nd harmonic
Figure VIII-A17 - TF39 Outer Panel - fundamental
Figure VIII-A18 - TF39 Outer Panel - 2nd harmonic
Figure VIII-A19 - TF39 Outer Panel - Freon Model - fundamental
Figure VIII-A20 - TF39 Outer Panel - Freon Model - 2nd harmonic

PARAMETER	CJ805-23	CF700
Fan Diameter (in.)	49.0	30.0
Blade and Vane Numbers		
Rotor	54	54
OGV	55	57
OGV Spacing	.33 Rotor Chord	.33 Rotor Chord
Design Weight Flow (lbs/sec)	240	90.6
Design Pressure Ratio	1.58	1.58
Design Tip Speed (ft/sec)	1185	1185
Design Bypass Ratio	1.49	1.49

TABLE VIII-A1

Fan Design Parameters-CJ805-23 and CF700

PARAMETER	TF39	TF39 D/V	TF39 O/P RIG	TF39 O/P FREON
Fan Diameter (in.)				
Outer Panel	93.3	64.0	42.5	6.0
Inner Panel	66.6	45.8	----	----
Blade and Vane No.				
Outer Panel				
IGV	36	36	36	36
Rotor	40	40	40	40
OGV	50	72	72	72
Inner Panel				
Rotor 1	25	25	----	----
Stator 1	36	36	----	----
Rotor 2	40	40	----	----
Stator 2	25	36	----	----
Outer Panel IGV Spacing	.25 Chord	.25 Chord	.25 Chord	.25 Chord
Outer Panel OGV Spacing	.25 Chord	.55 Chord	.55 Chord	.55 Chord
Design Weight Flow (lbs/sec)	1549	725	180	8.65 (Freon C3)
Overall Fan Pressure Ratio	1.45	1.46	1.55	1.50
Design Tip Speed(ft/sec.)				
Outer Panel	1426	1425	1500	547
Overall Design Bypass Ratio	7.88	7.88	----	----

TABLE VIII-A2

Fan Design Parameters-TF39 Family

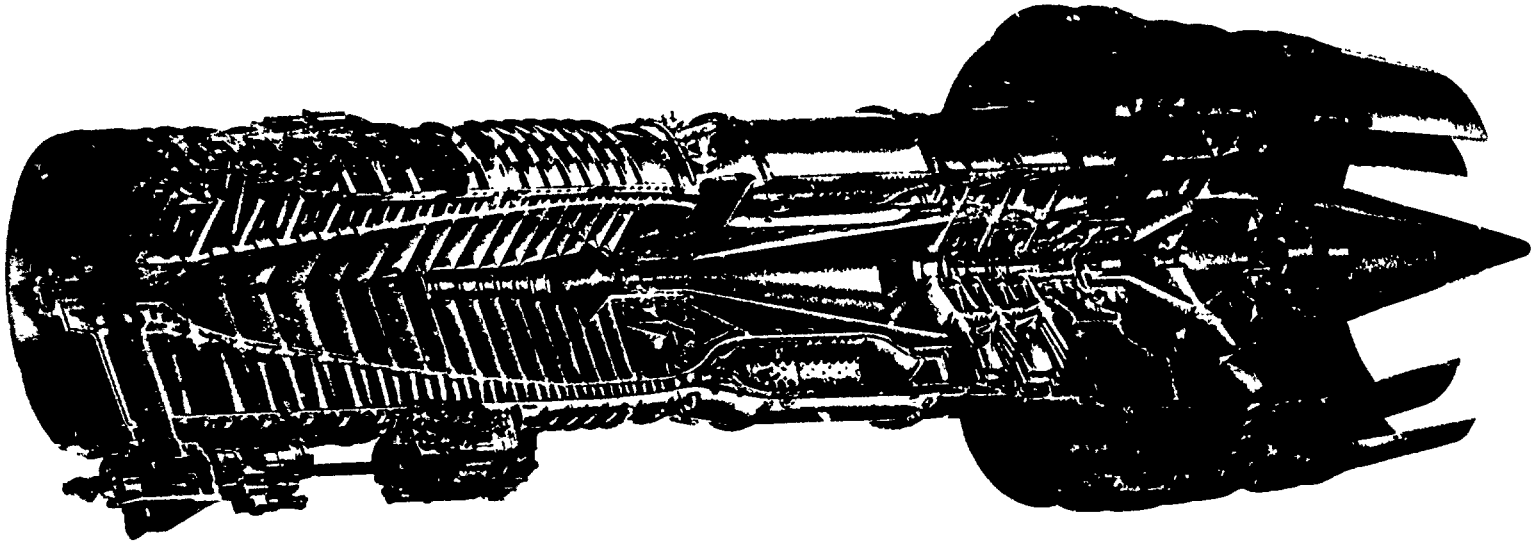

FIGURE VIII-A1 CUTAWAY VIEW CJ805-23 AFT TURBOFAN

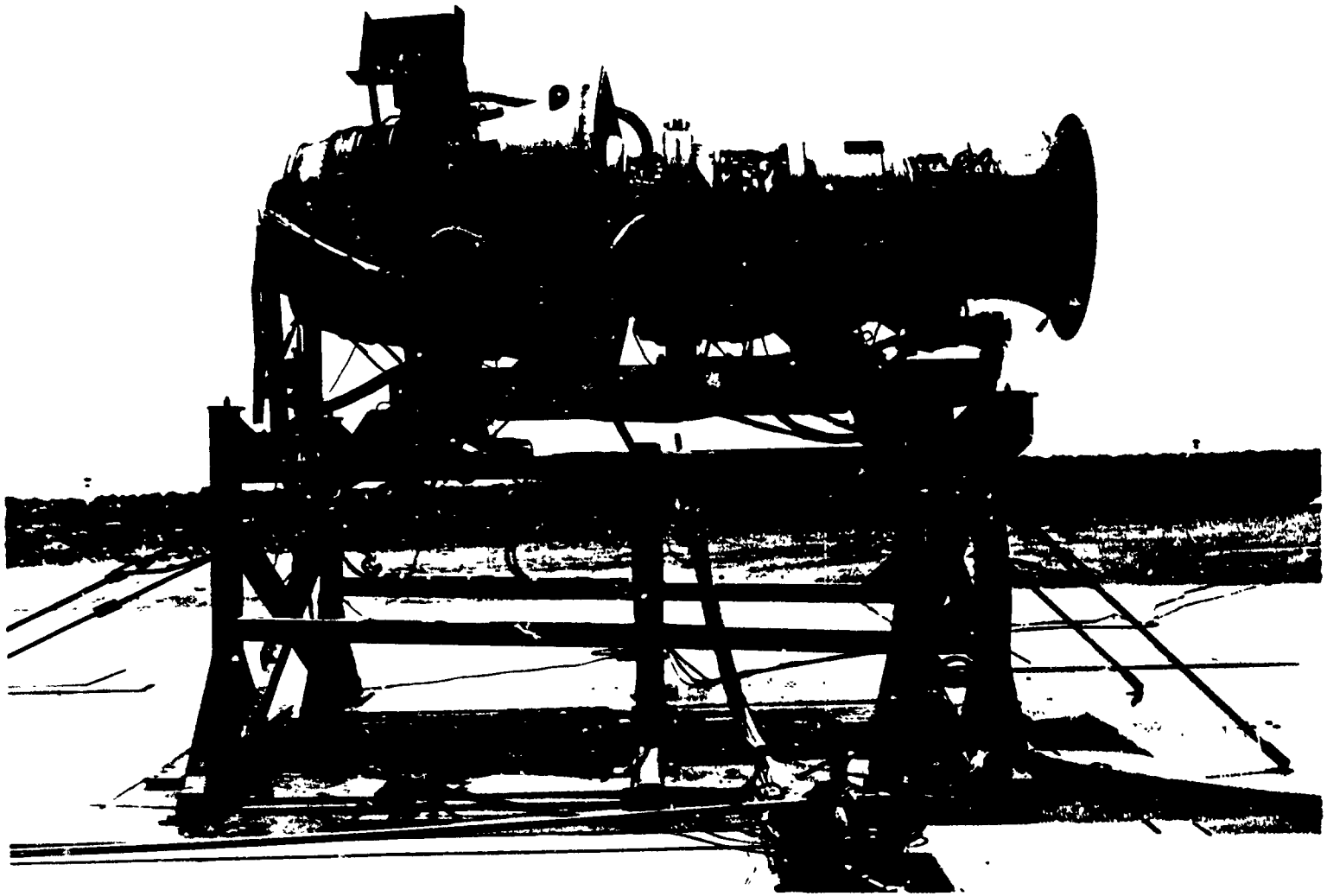

FIGURE VIII-A2 STANDARD CJ805-23 ON TEST

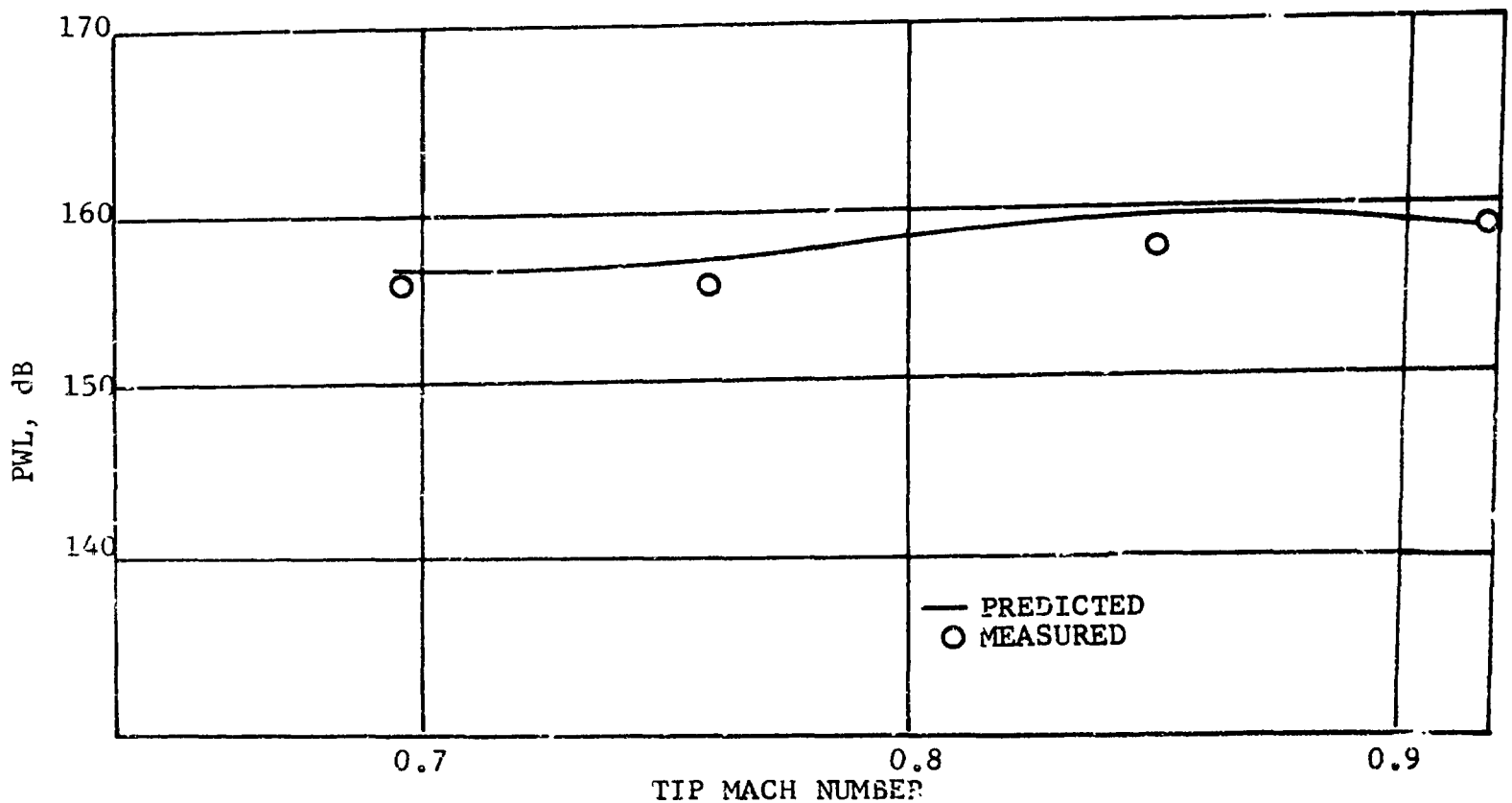

FIGURE VIII-A3 FUNDAMENTAL PWL - CJ805-23 PREDICTED AND MEASURED

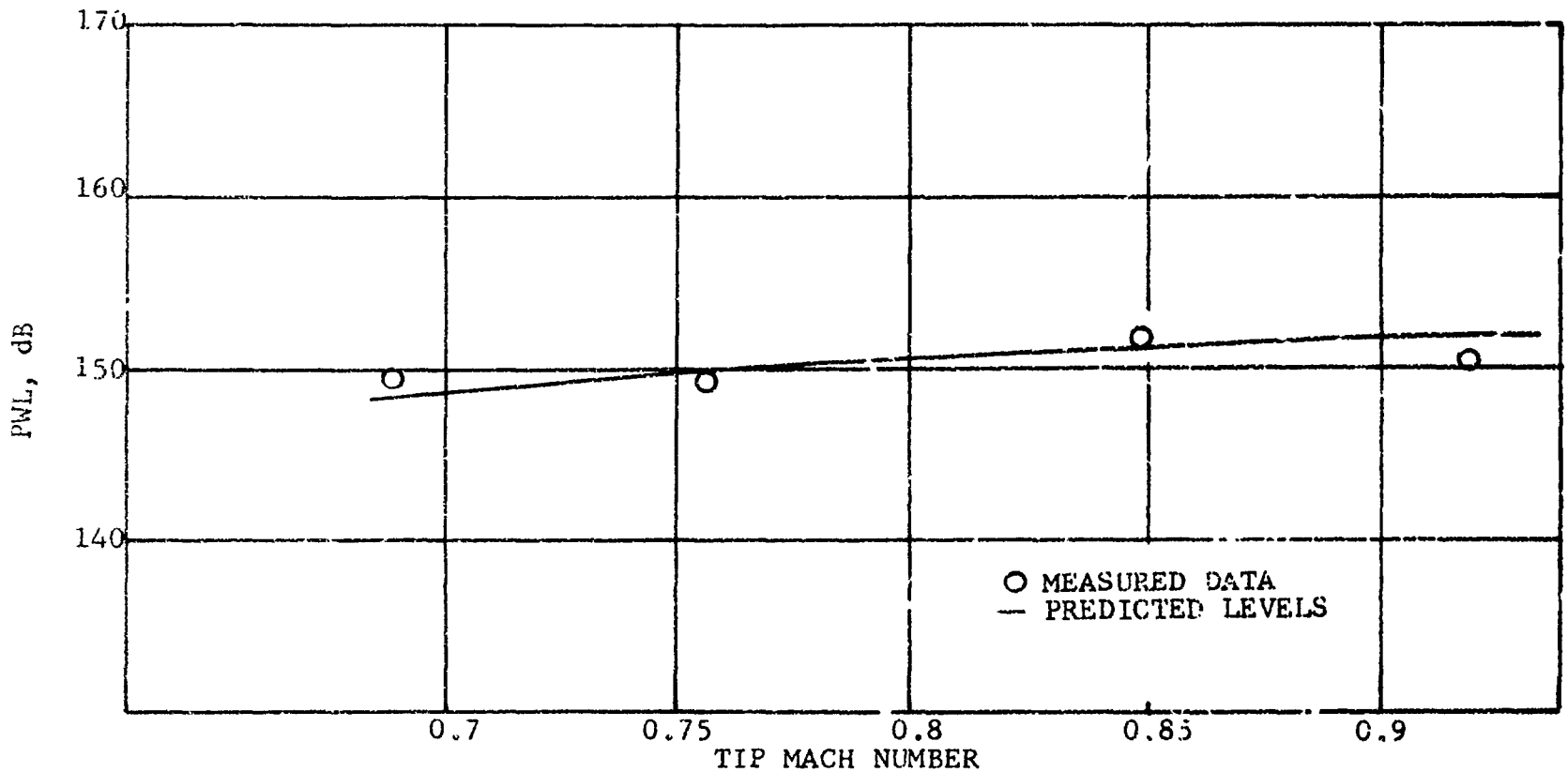

FIGURE VIII-A4 CJ805-23 SECOND HARMONIC POWER LEVELS

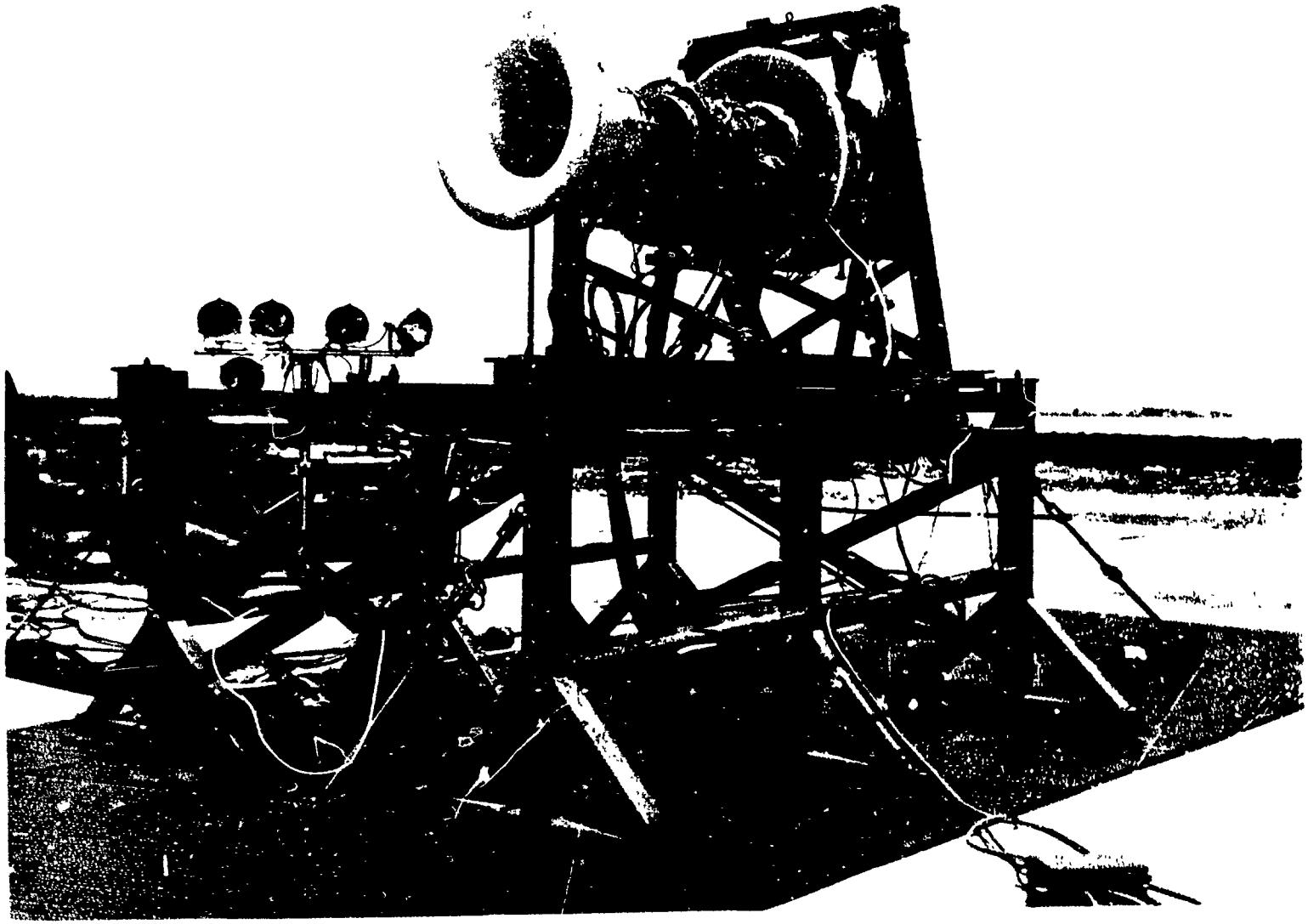

FIGURE VIII-A5 CF700 ENGINE ON EDWARDS TEST STAND

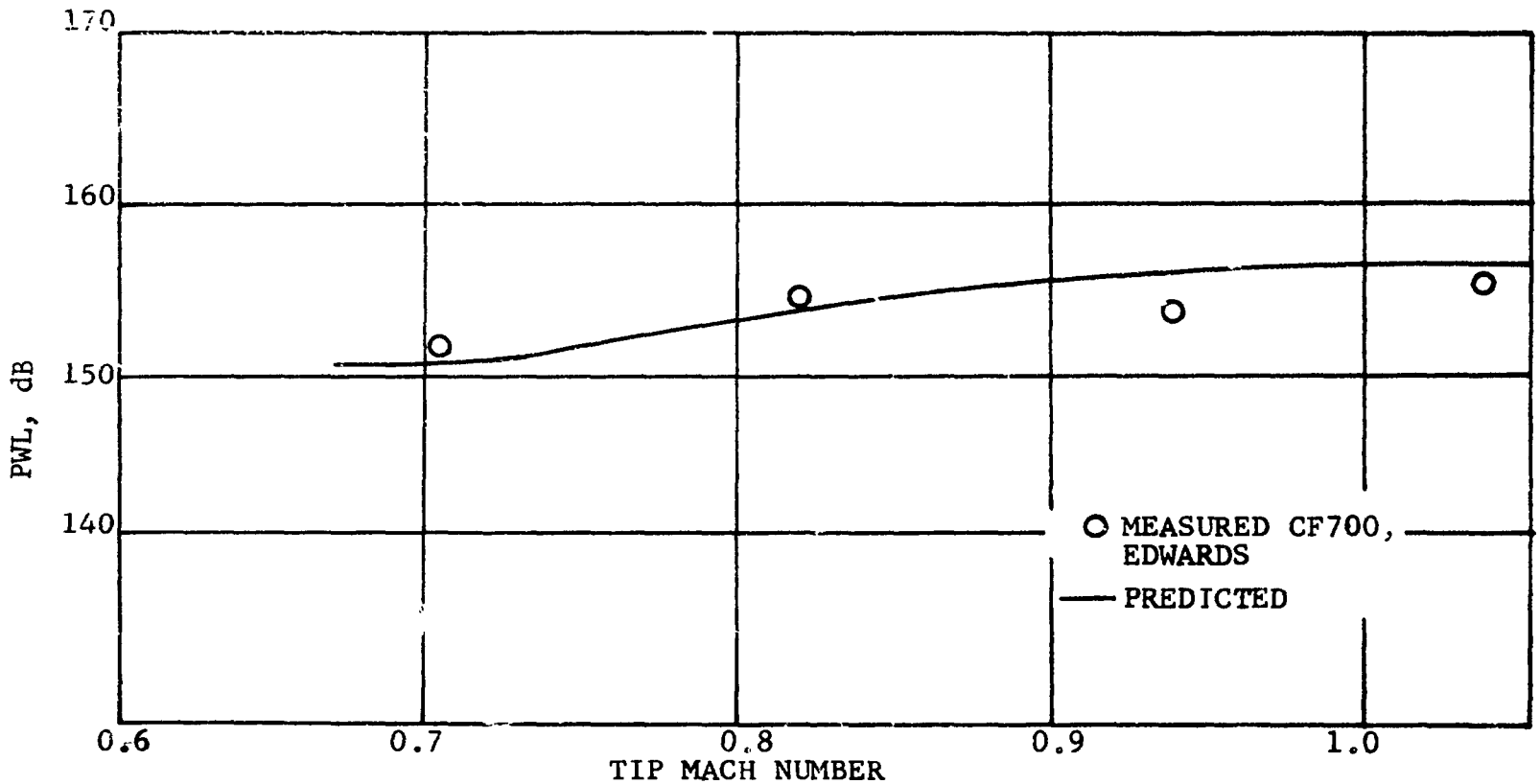

FIGURE VIII-A6 CF700 FUNDAMENTAL POWER LEVEL

FIGURE VIII-A7 FULL SCALE TF39 ENGINE

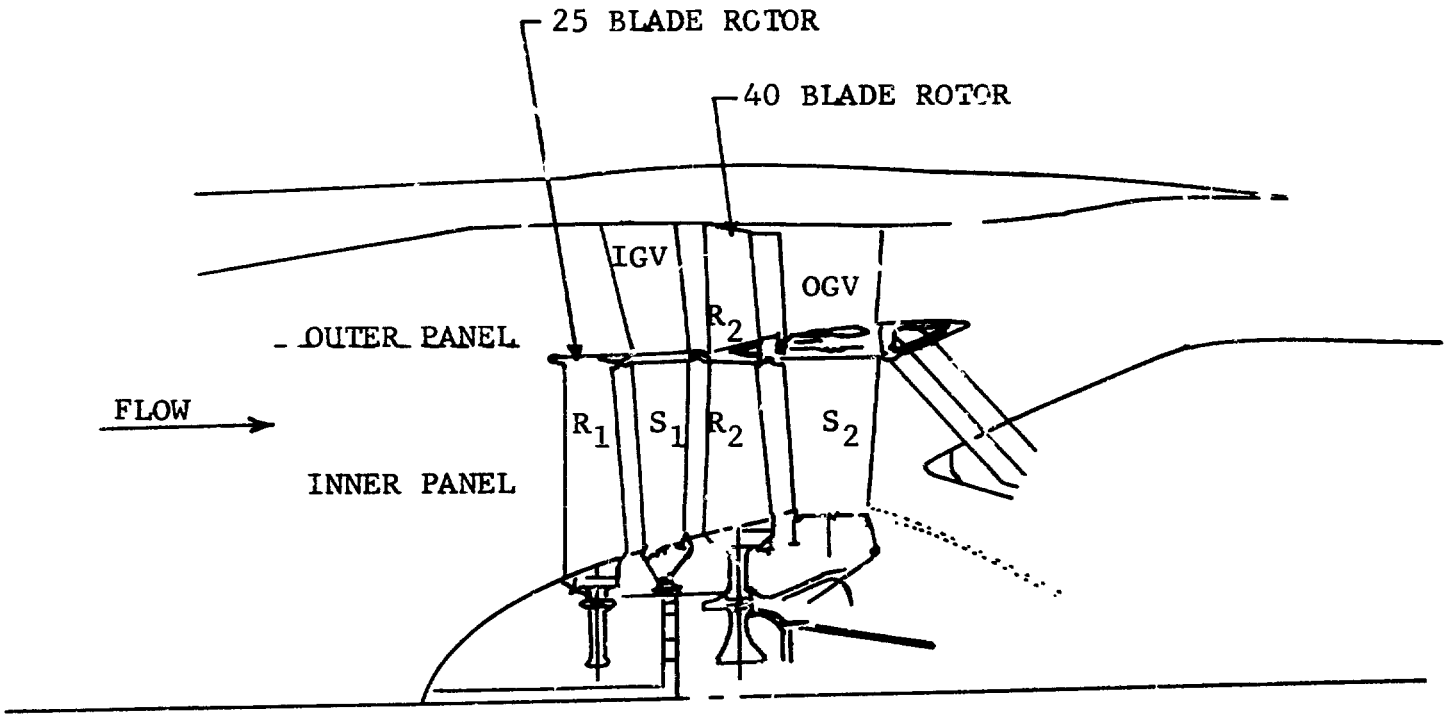

FIGURE VIII-A8 TF39 FAN CONFIGURATION

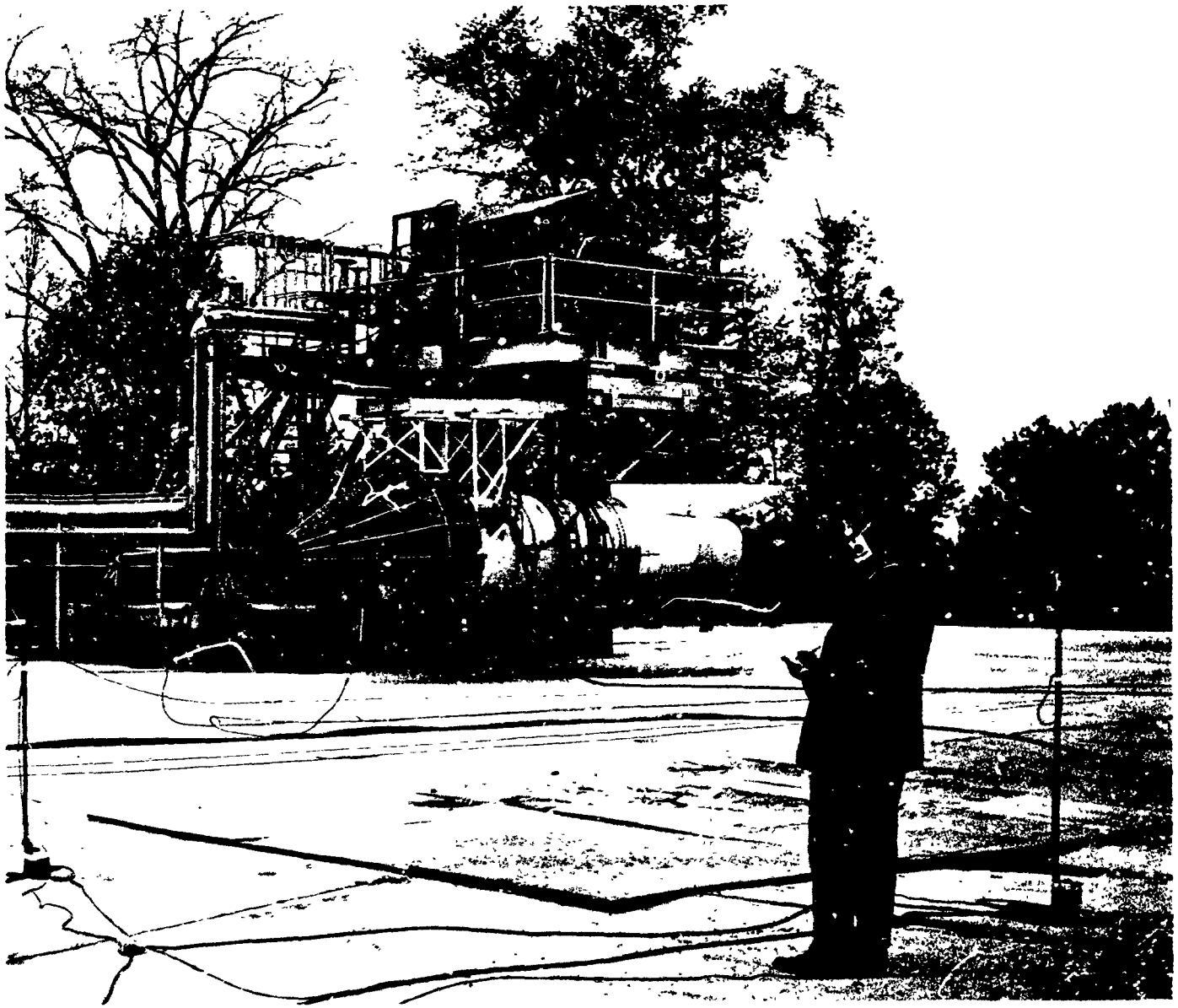

FIGURE VIII-A9 TF39 DEVELOPMENT VEHICLE

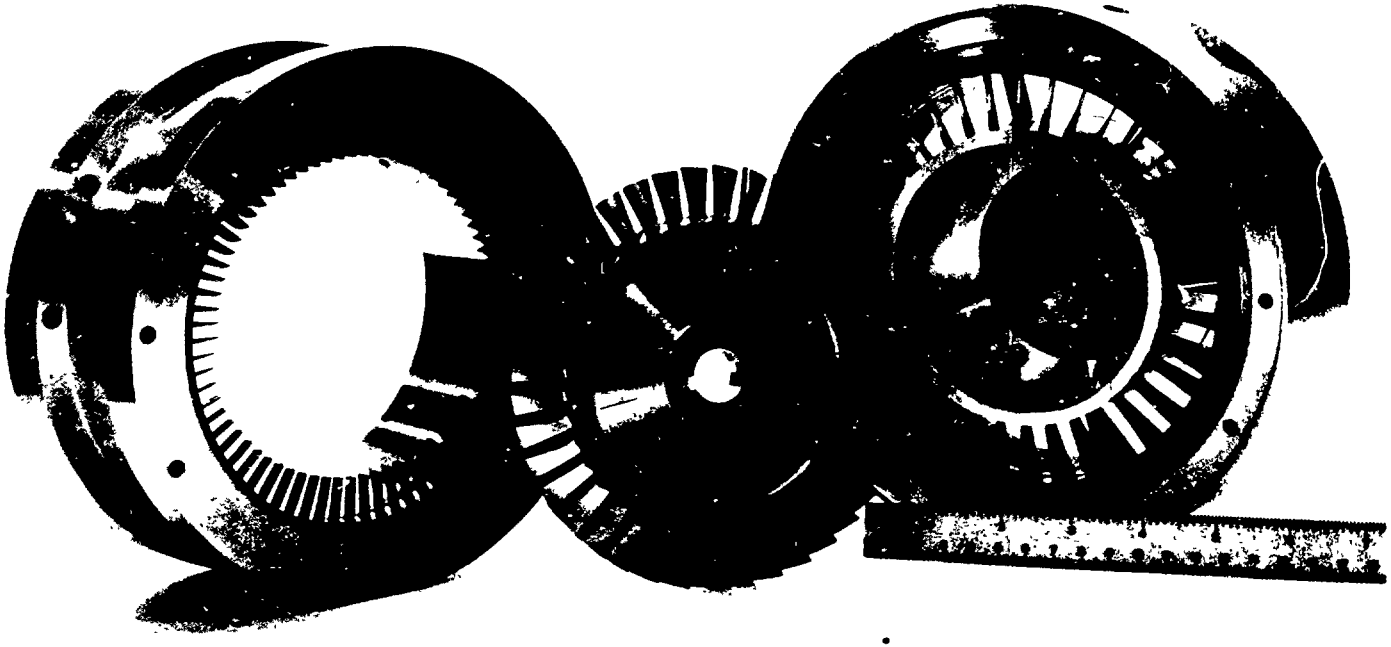

FIGURE VIII-A10 FREON COMPRESSOR TF39 SCALE MODEL HARDWARE

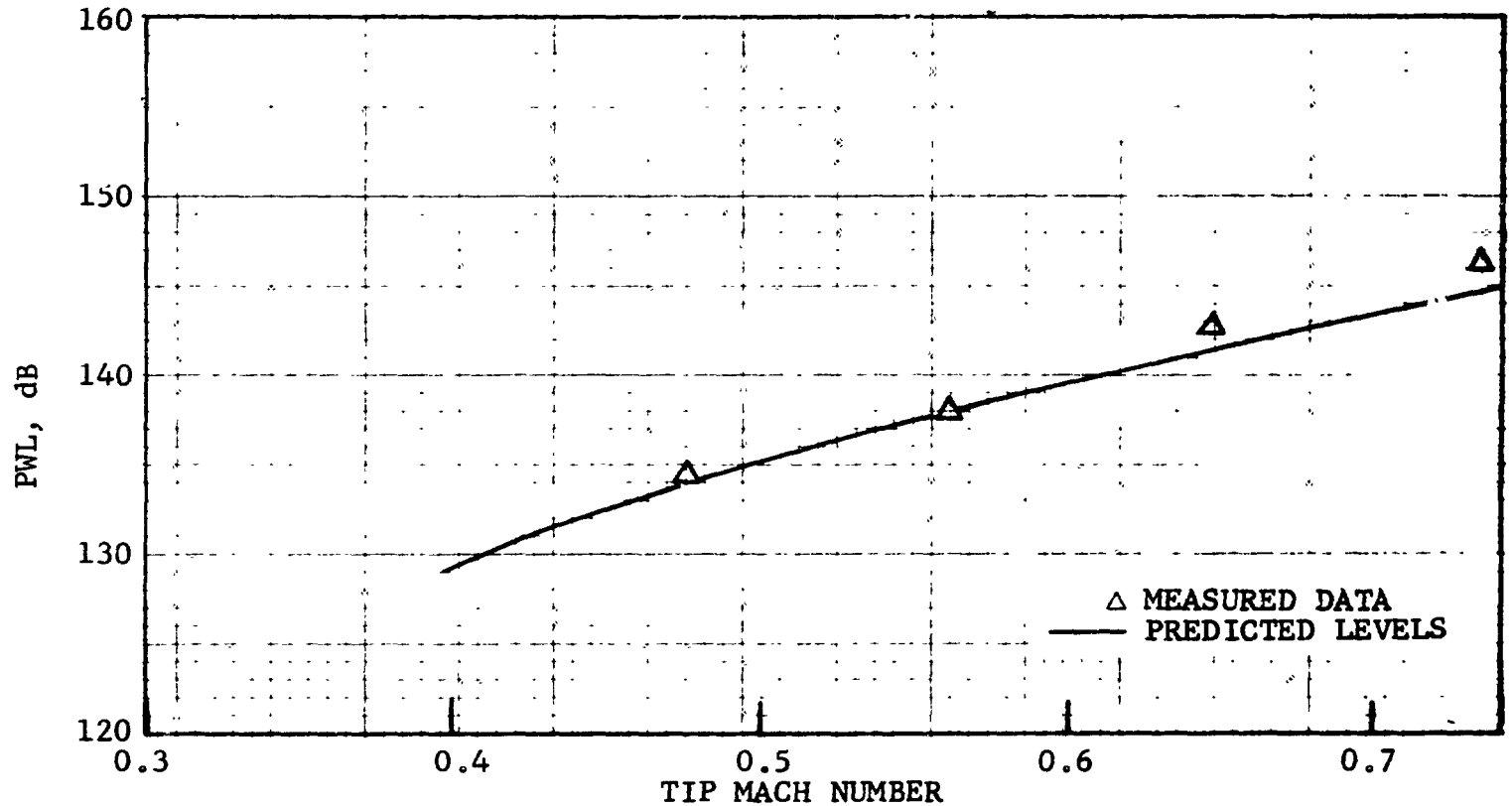

FIGURE VIII-A11 TF39 FIRST STAGE FUNDAMENTAL PWL

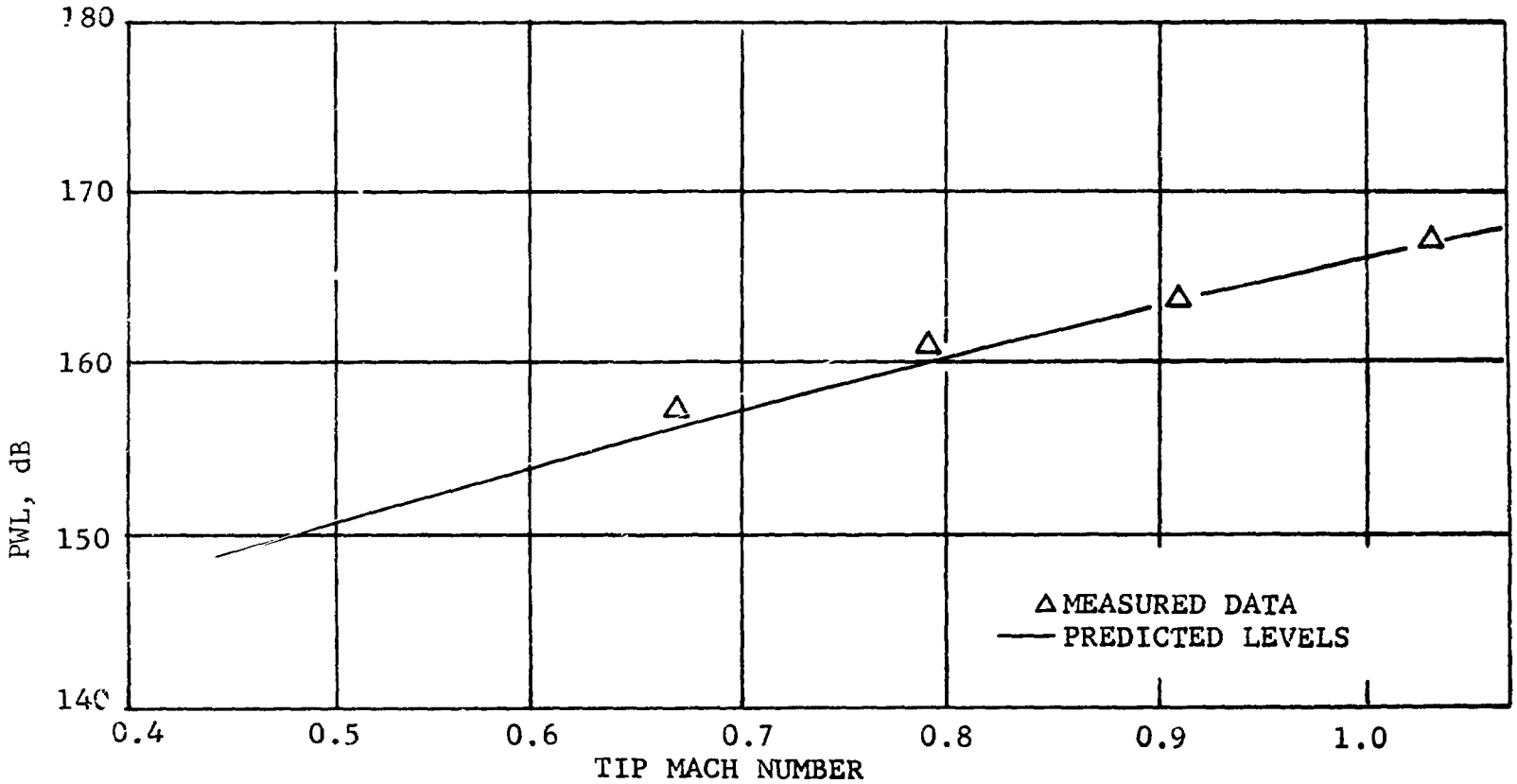

FIGURE VIII-A12 TF39 SECOND STAGE FUNDAMENTAL PWL

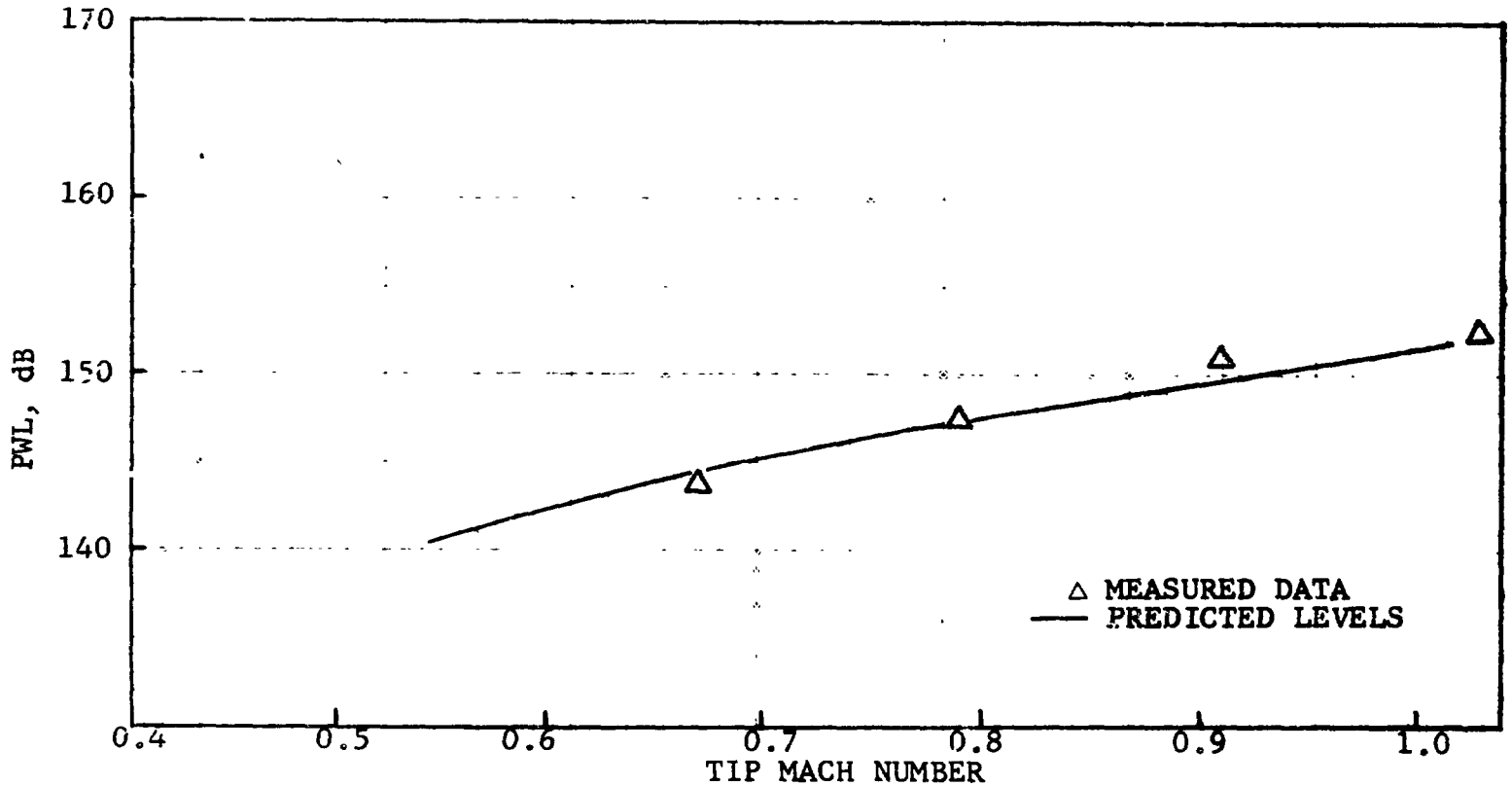

FIGURE VIII-A13 TF39 SECOND STAGE 2ND HARMONIC PWL

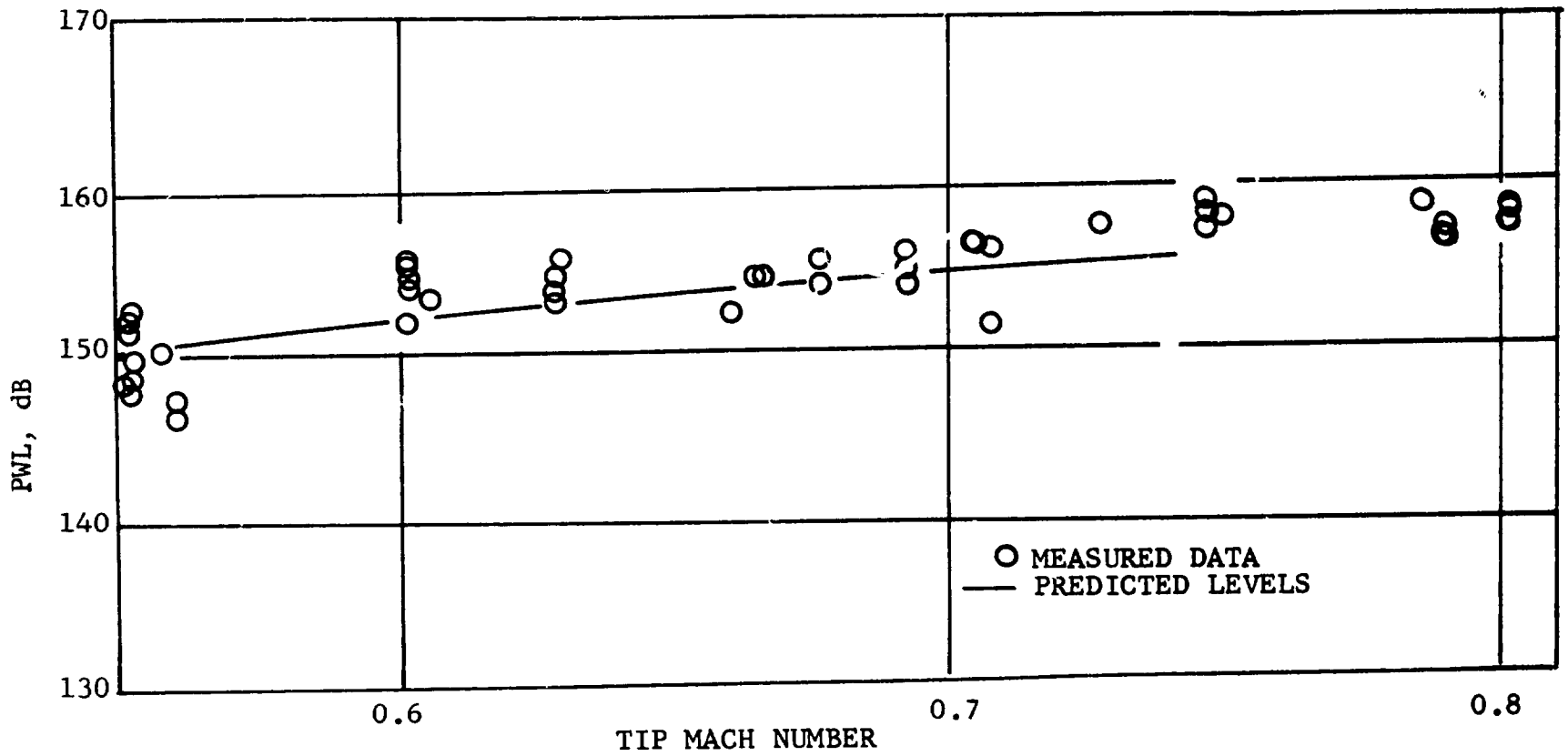

FIGURE VIII-A14 TF39 D/V FIRST STAGE FUNDAMENTAL PWL

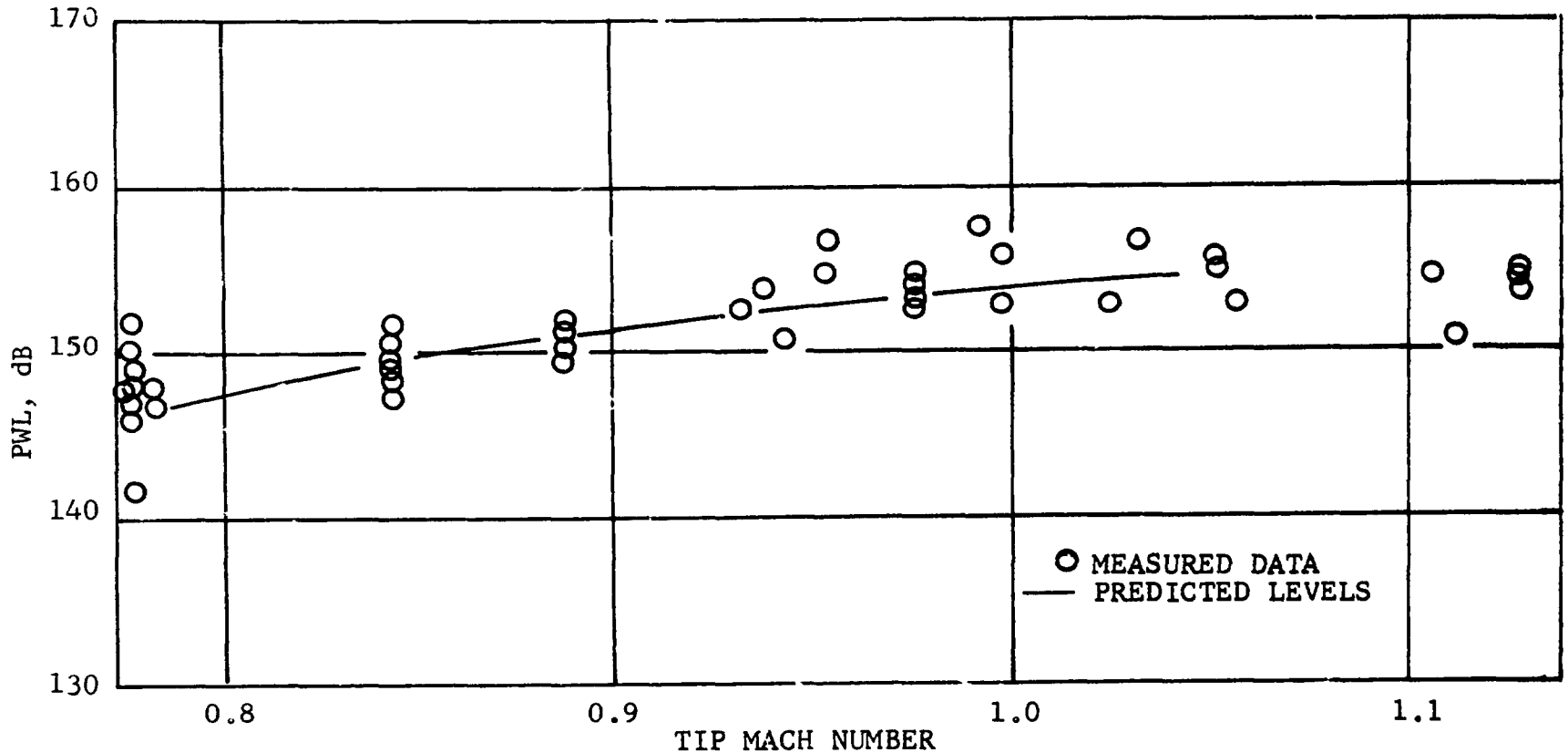

FIGURE VIII-A15 TF39 D/V SECOND STAGE FUNDAMENTAL PWL

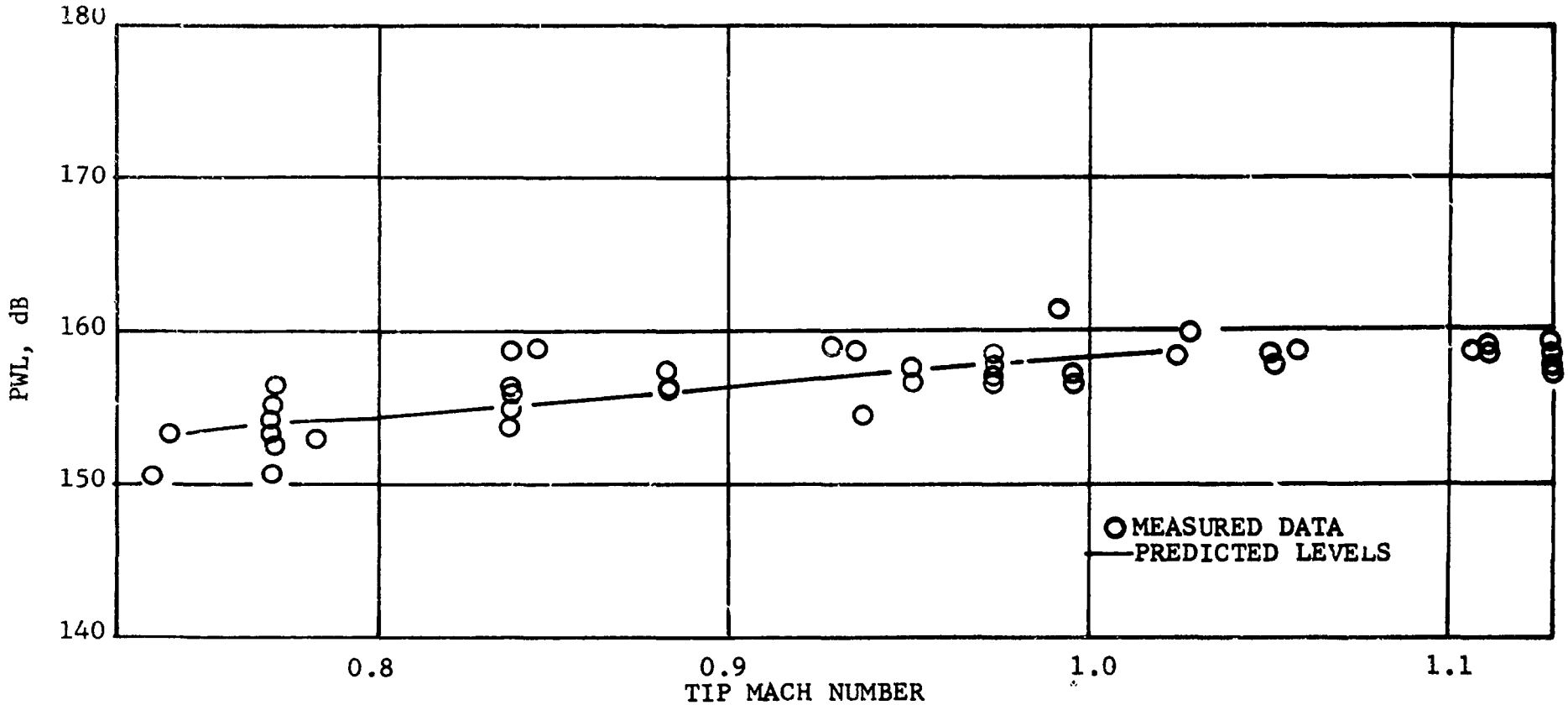

FIGURE VIII-A16 TF39 D/V SECOND STAGE 2ND HARMONIC PWL

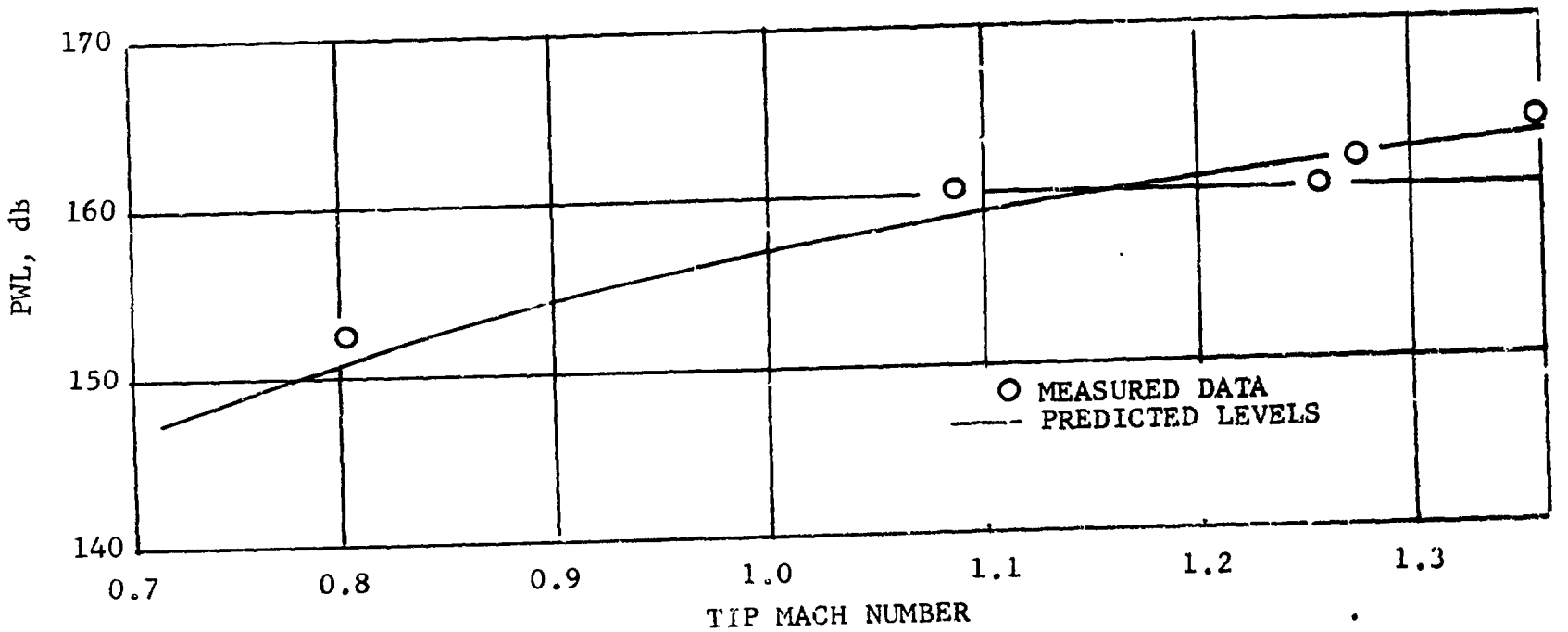

FIGURE VIII-A17 TF39 O/P TEST RIG FUNDAMENTAL PWL

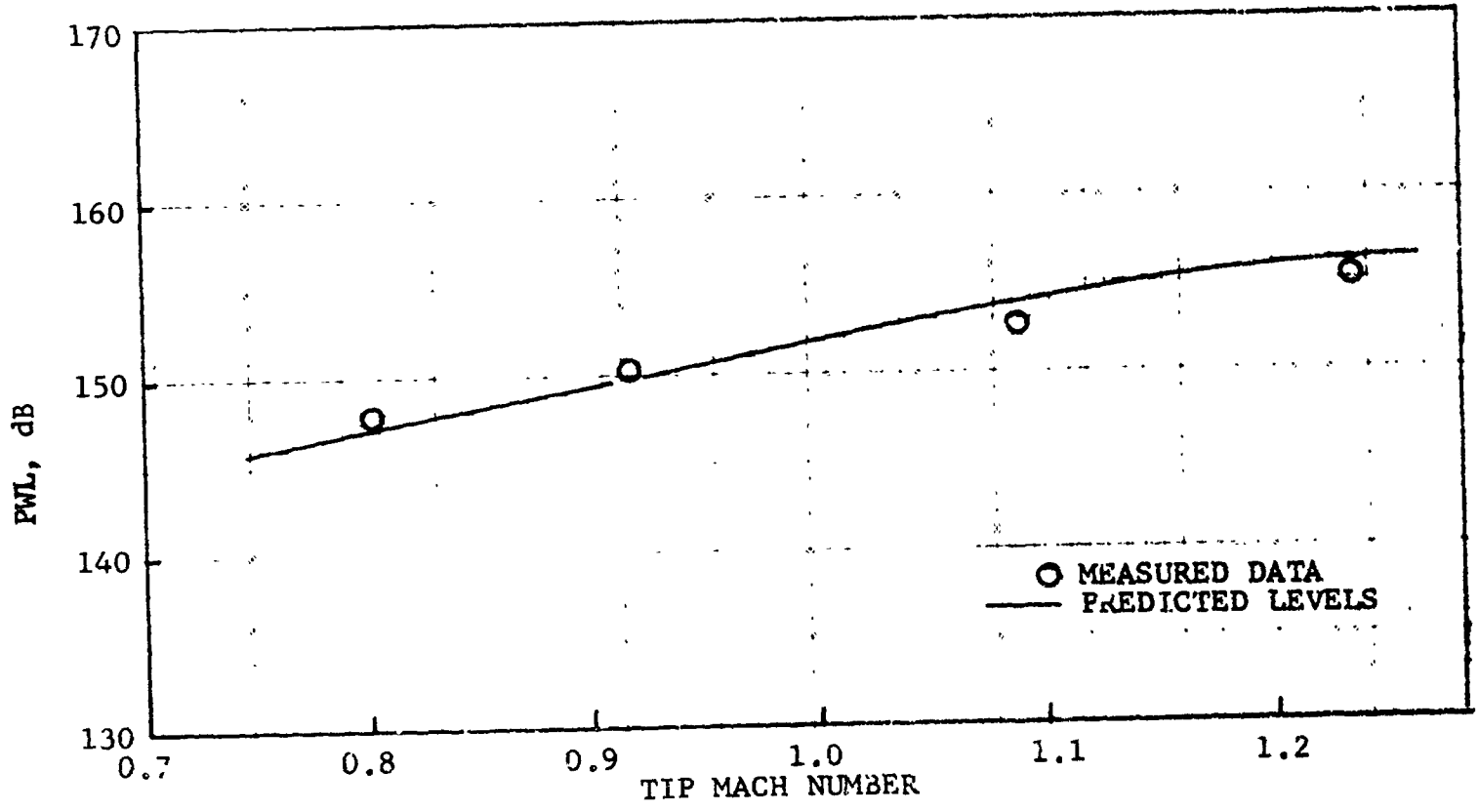

FIGURE VIII-A18 TF39 OUTER PANEL RIG 2nd HARMONIC PWL

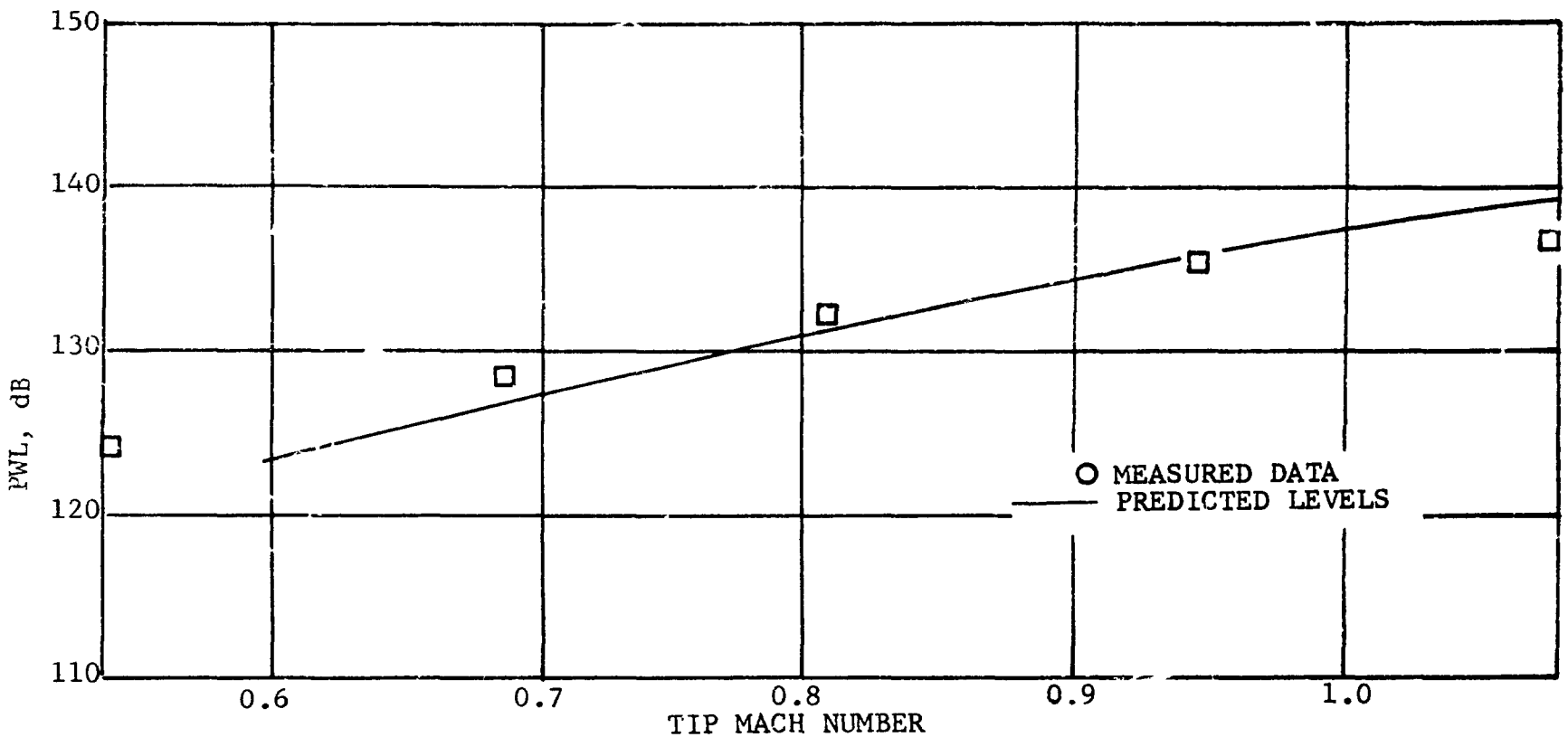

FIGURE VIII-A19 TF39 O/P FREON MODEL FUNDAMENTAL PWL

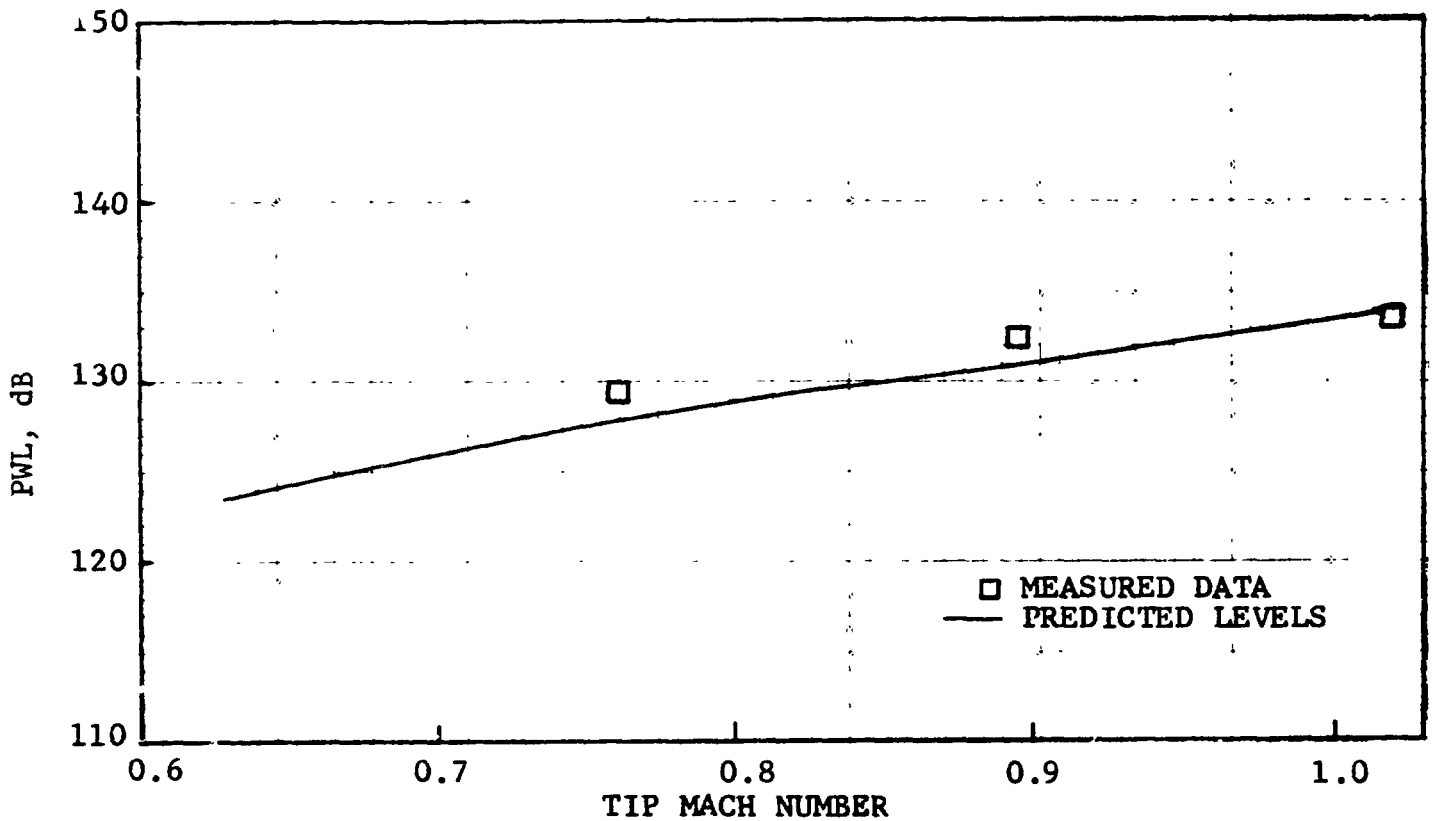

FIGURE VIII-A20 TF39 O/P FREON MODEL 2nd HARMONIC PWL

It is apparent from examination of these comparisons that good correlation was achieved for all vehicles, regardless of size or test flow media employed.

(4) NASA Two-Stage Fan. A full scale TF39 fan was modified (Reference 2) to form a low-tip-speed fan test vehicle (Figure VIII-A21). The outer panel portion of the TF39 fan was removed, and the inner panel blade-vane spacings were increased (Figure VIII-A22). Three separate fan exhaust nozzles were employed on the vehicle. The nozzles were sized to provide pressure ratios of 1.50, 1.45, and 1.35, for a fan design airflow of 750 lb/sec; fan design parameters are listed in Table VIII-A3. Figure VIII-A23 is a comparison of predicted and measured sound power levels for the second stage rotor fundamental tone; three sets of data are presented, one for each fan nozzle area variation. The prediction was accurate for all operating lines.

Fan Diameter (in.)	66.88	
Blade and Vane Numbers		
Rotor 1	25	
Stator 1	36	
Rotor 2	40	
OGV	25	
Blade - Vane Spacings		
Rotor 1 - Stator 1	1.06 Chords	
Stator 2 - Rotor 2	1.24 Chords	
Rotor 2 - OGV	1.22 Chords	
Design Weight Flow (lbs/sec)	750	
Pressure Ratio		
Small Nozzle	1.50	(All with 750 lbs/sec weight flow)
Nominal (Design) Nozzle	1.45	
Large Nozzle	1.35	
Design Tip Speed (ft/sec)	1015	

TABLE VIII-A3

NASA Two-Stage Fan Design Parameters

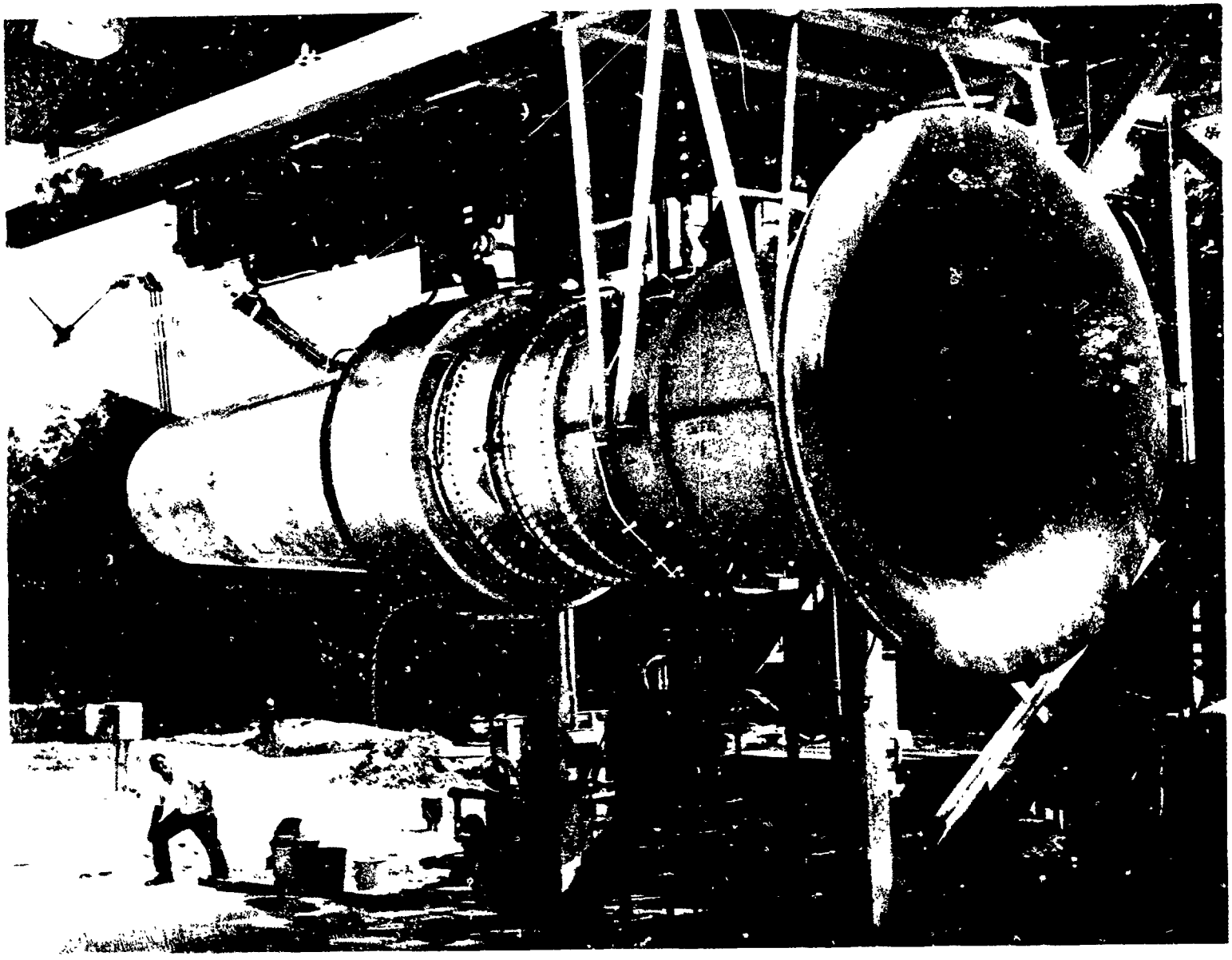

FIGURE VIII-A21 NASA TWO STAGE FAN ENGINE

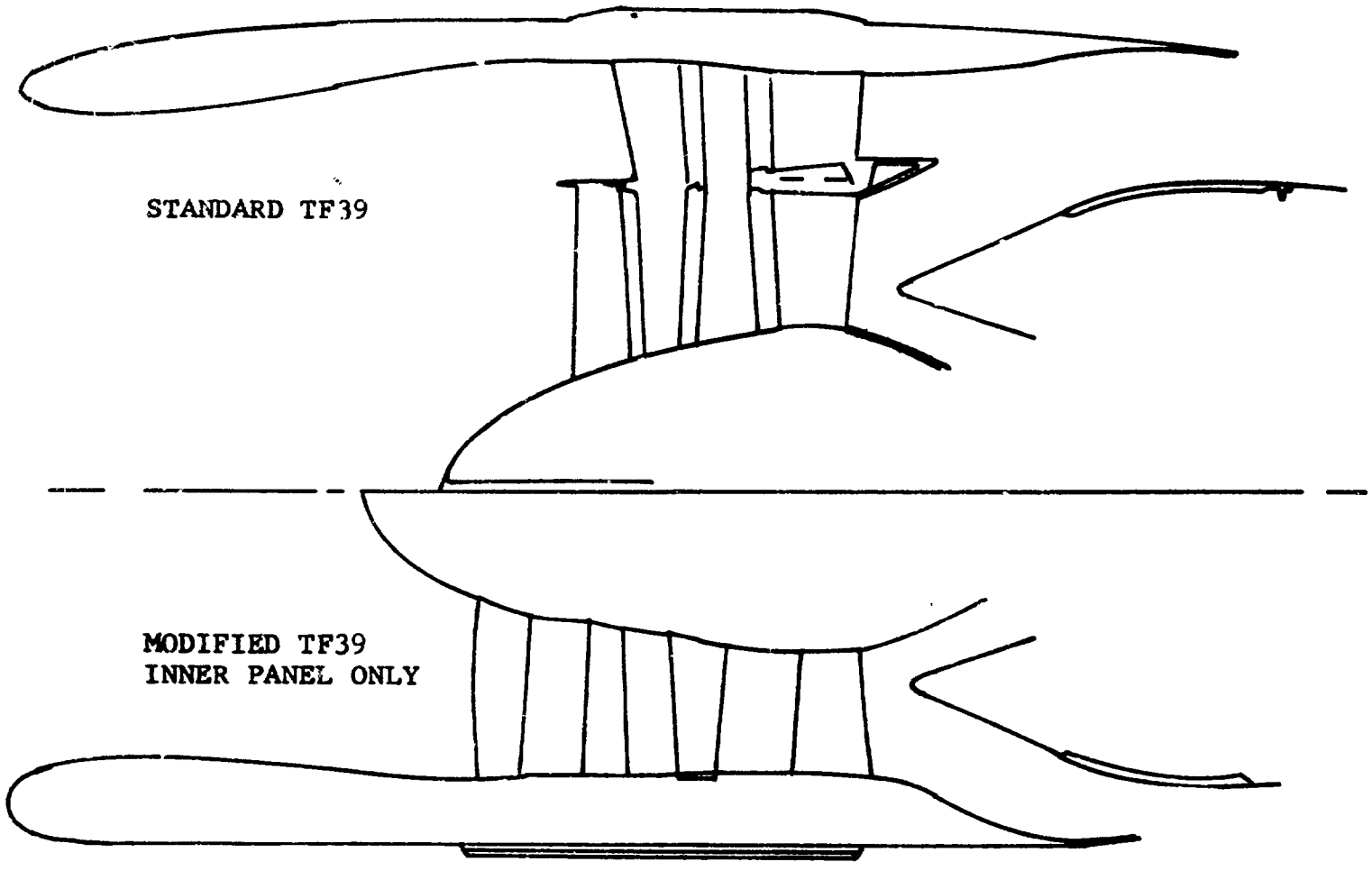

FIGURE VIII-A22 NASA TWO-STAGE FAN CONFIGURATION

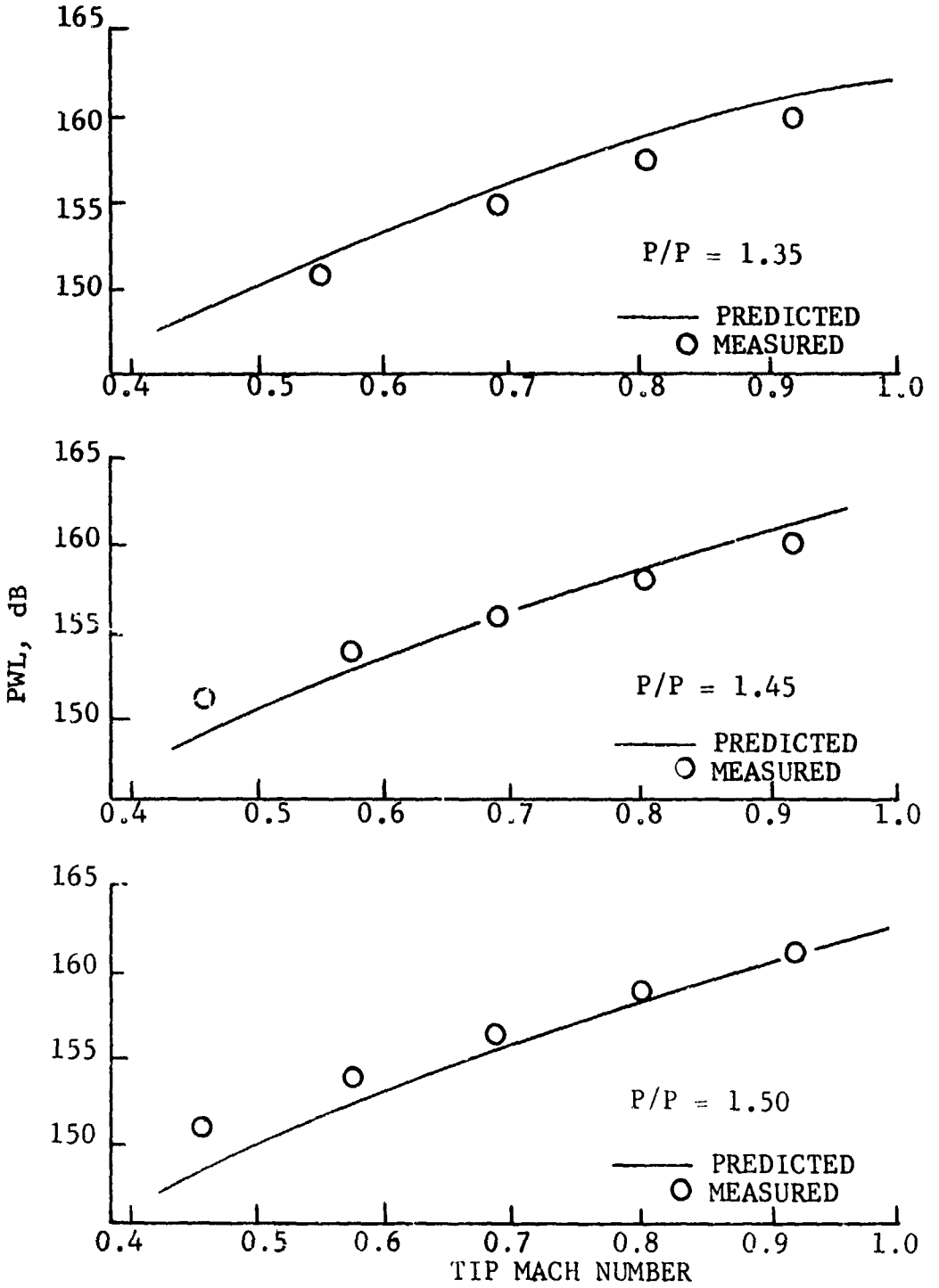

FIGURE VIII-A23 TWO STAGE FAN 2nd STAGE FUNDAMENTAL POWER LEVELS

MEASURED vs. PREDICTED

REFERENCE SECTION VIII-A

1. Wells, R. J. and McGrew, J. M. "Model Freon Compressor Acoustical Studies", FAA Report FAADS-68-5, February 1968.

2. Motsinger, R., et. al. "Low Tip Speed Fan Noise Demonstration Program", NASA Report NASA CR72456, 1968.

(B) Broadband Noise Verification. In order to verify the method for predicting broadband noise presented in Section VII, the suggested prediction technique was applied to several turbofan engines and compared with experimental data. Three fans were considered: NASA's LF336, Fans A and B; GE development vehicle IV and GE's CJ805. For each of the fans considered sound power-level and sound-pressure level spectral predictions were compared with 1/3 octave band noise measurements. The sound-pressure level spectral comparisons were made for angular positions relative to the engine inlet duct of 20°, 80° and 120°.

(1) LF336 Fans A and B. NASA's LF336 Fans (tested under NASA Contract NAS2-5462) are 1.3 pressure ratio, thirty-six inch diameter lift fan propulsion systems. (See Figures VIII-B1 and VIII-B2). They are designed to power high speed vertical takeoff and landing aircraft utilizing two General Electric J85 turbojets and a tip turbine to drive the fan. Fan A was designed by NASA to demonstrate installation and propulsion system technology. Fan B is a modified Fan A. Fan B's axial spacing (rotor-outlet guide vane distance was increased from 15% of the rotor chord, to a two rotor tip chord spacing.

All of the predictions and data comparisons were made on a 250 foot arc distance. The fan speeds considered were: N = 5140, 5442, 5700, and 6047 RPM. corresponding to power settings of 85, 90. 95 and 100%.

The results of the LF336 broadband noise predictions are illustrated in Figures VIII-B3 through VIII-B18. For each of the fans speeds considered there are four figures. The first of each group of four figures is the sound-power level spectrum comparison and the three remaining figures are the sound-pressure level spectrum comparisons at different angular positions.

For all of the cases considered, reasonable agreement between predicted and measured values was obtained for frequencies up to the blade passing frequency (the location of blade passing frequency is designated by a solid vertical line at the center frequency of the 1/3 octave band at which it occurs) and marked as BPF. At the higher frequencies the predictions usually fall in between the Fan A and Fan B data points. The difference in the noise levels between Fan A and Fan B data seems to be due to the unusually close spacing on Fan A.

(2) Development Vehicle IV. The development vehicle IV is a low tip speed 36" Diameter fan with twenty-six (26) rotor blades and a 2.3 vane-blade ratio. The fan pressure ratio at design is 1.5. Its design tip speed is 1100 ft/sec.

All of the prediction-data comparisons were done for 100 foot arc distances. The fan speeds considered were: N = 5510, 5970, 6350, 6525 rpm; corresponding to power settings of 72, 77.9, 82.0, 86.3 and 90.7%.

The results of the Development Vehicle IV broadband noise predictions are illustrated in Figure VIII-B19 through VIII-B38. For each of the fan speeds considered there are four figures illustrating the prediction-data comparison. The first figure of each group of four figures is the sound power level spectrum comparison, and the remaining three figures are the sound pressure level spectrum comparisons.

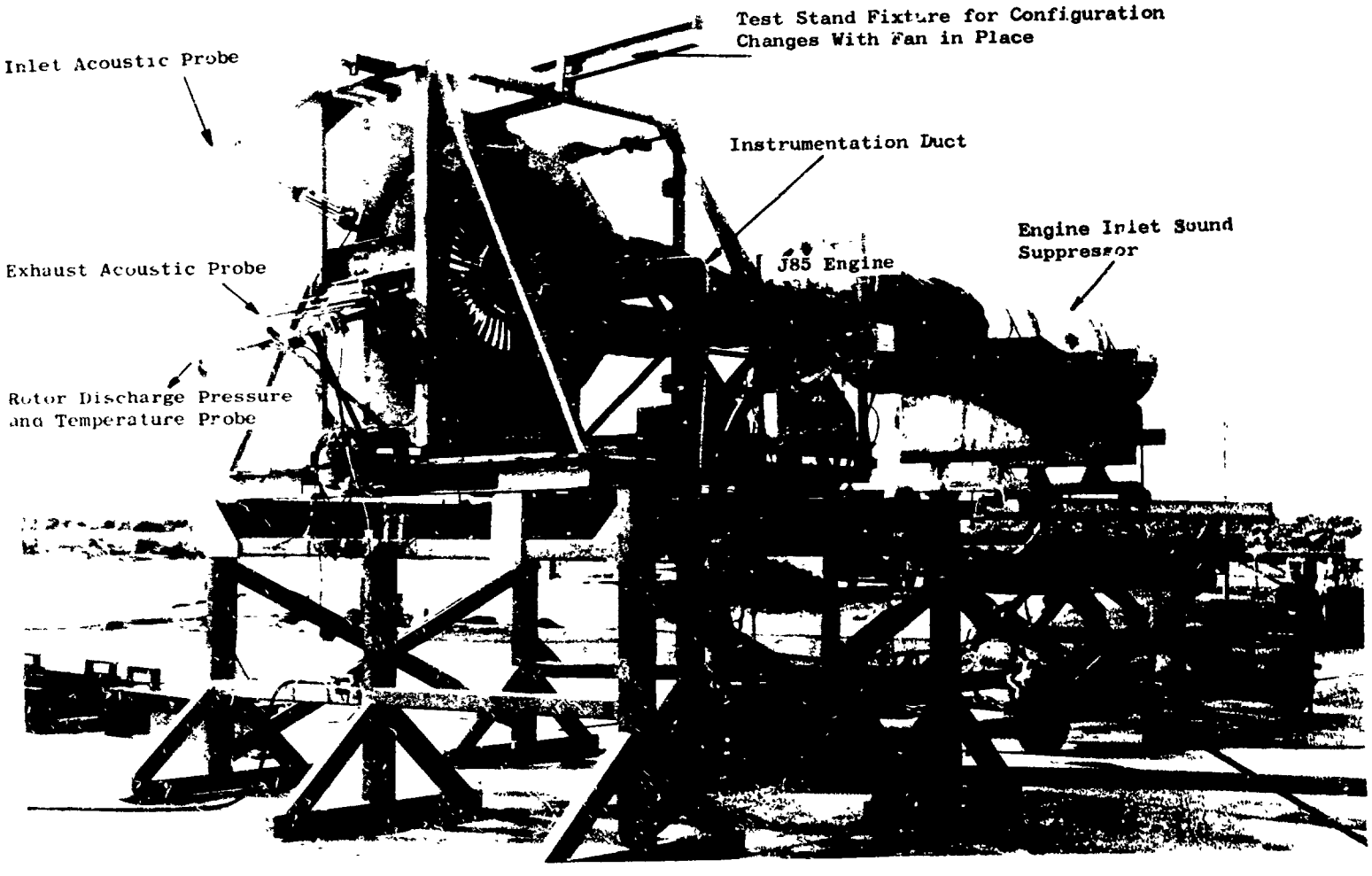

FIGURE VIII-B1 LF336 TESTS FRONT VIEW

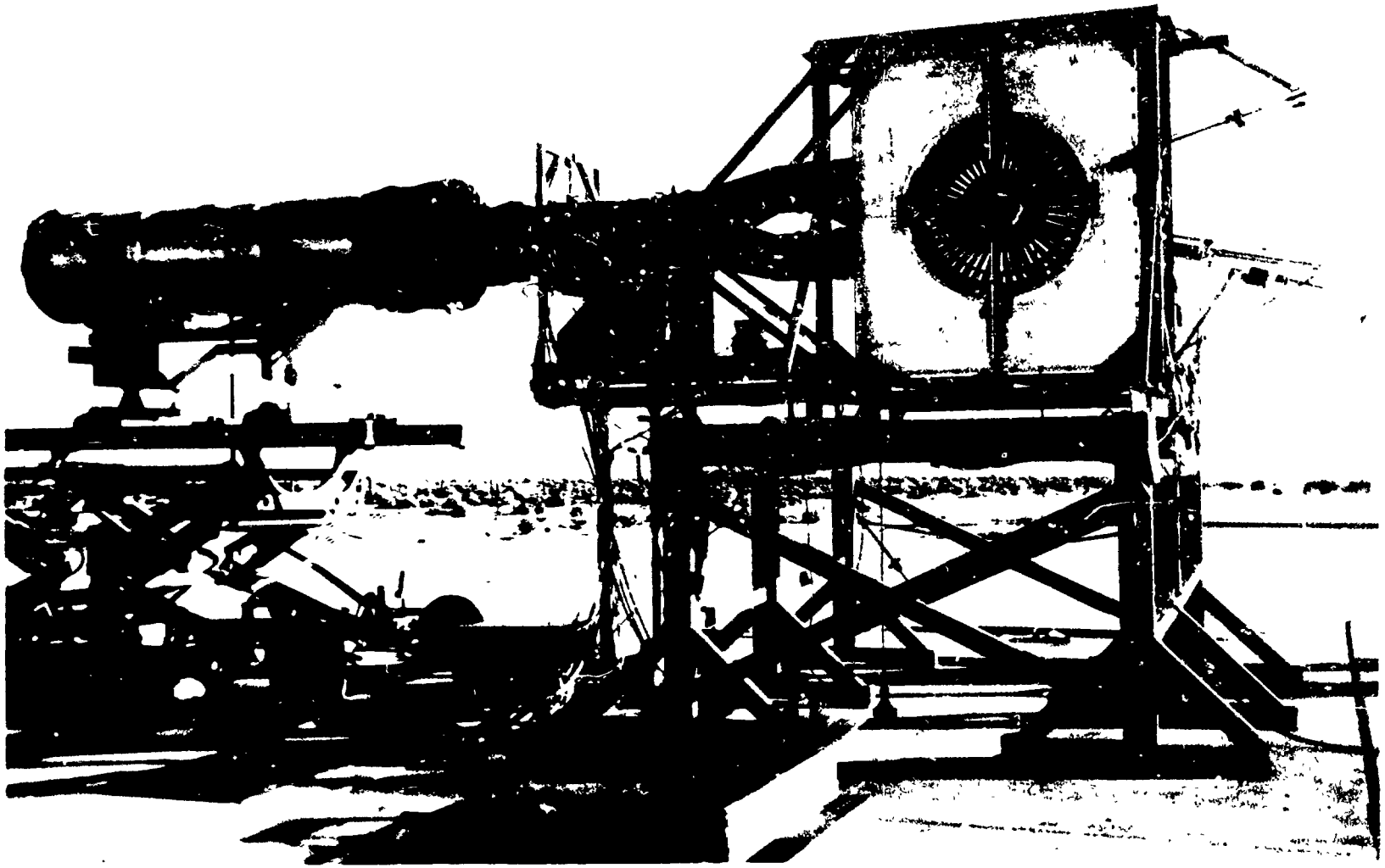

FIGURE VIII-B2 LF336 TESTS REAR VIEW

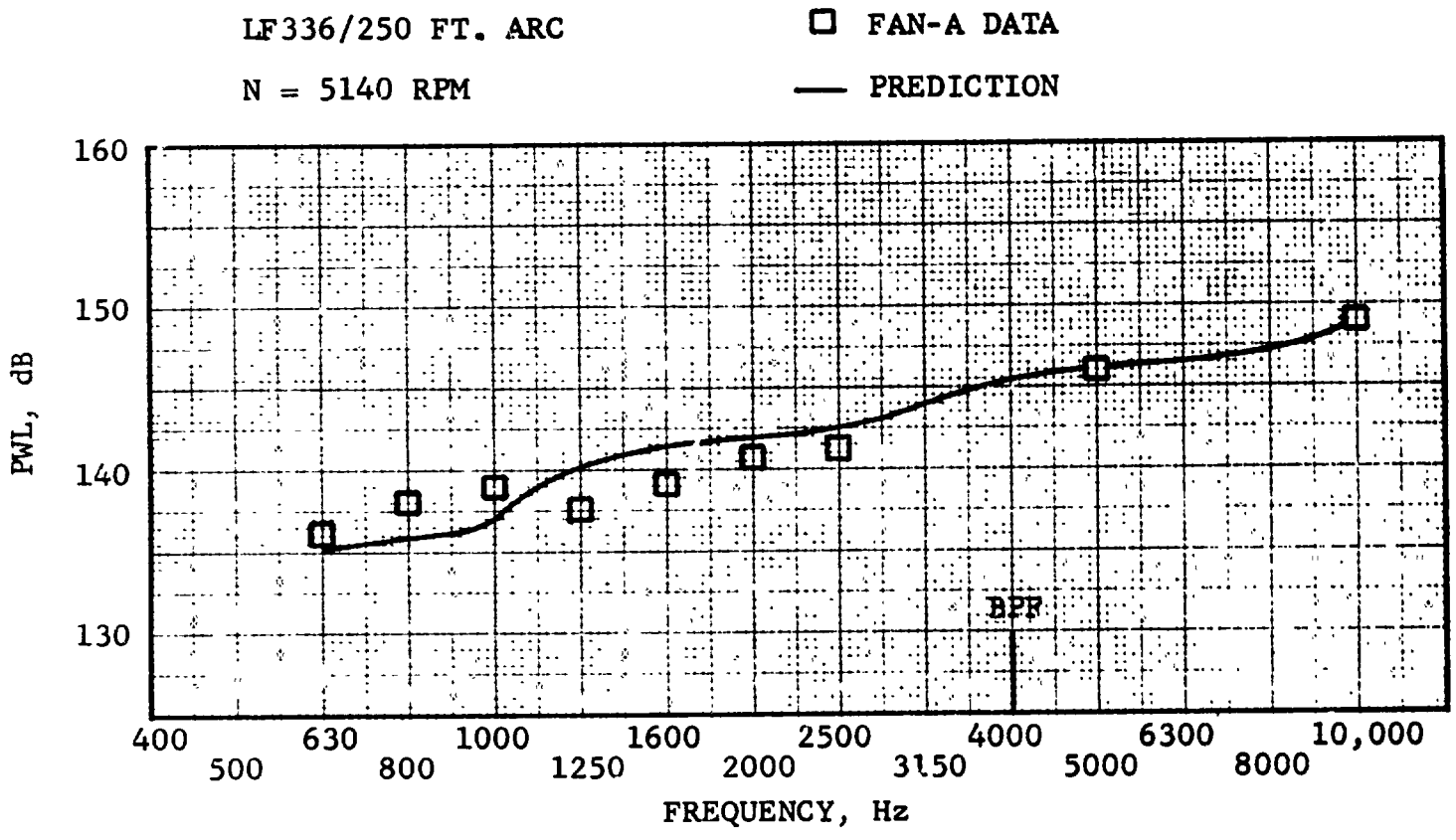

FIGURE VIII-B3 LF336 BROAD BAND NOISE POWER-LEVEL SPECTRUM N = 5140 RPM

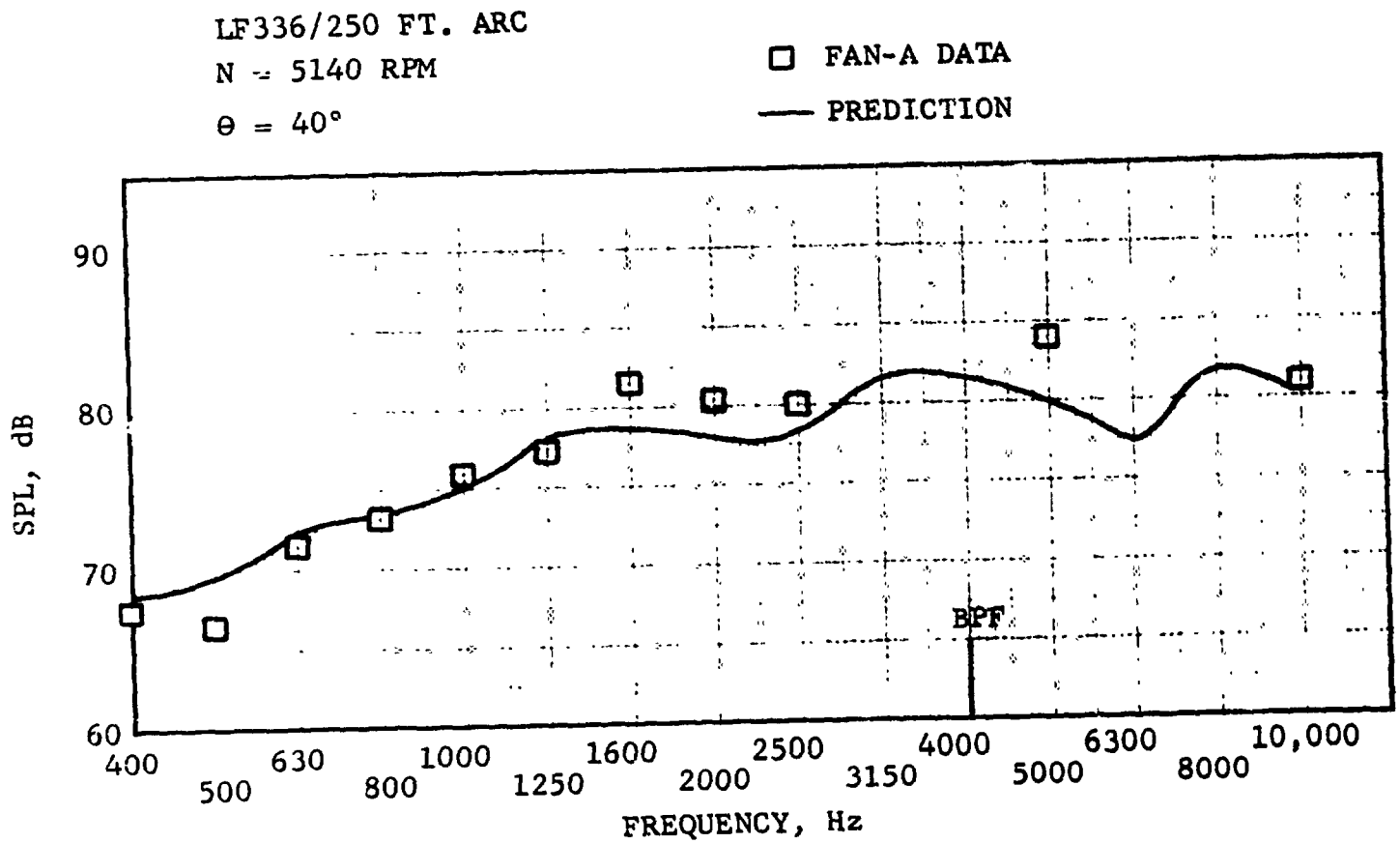

FIGURE VIII-B4 LF336 BROAD BAND NOISE SOUND-PRESSURE LEVEL SPECTRUM N = 5140 RPM, θ = 40°

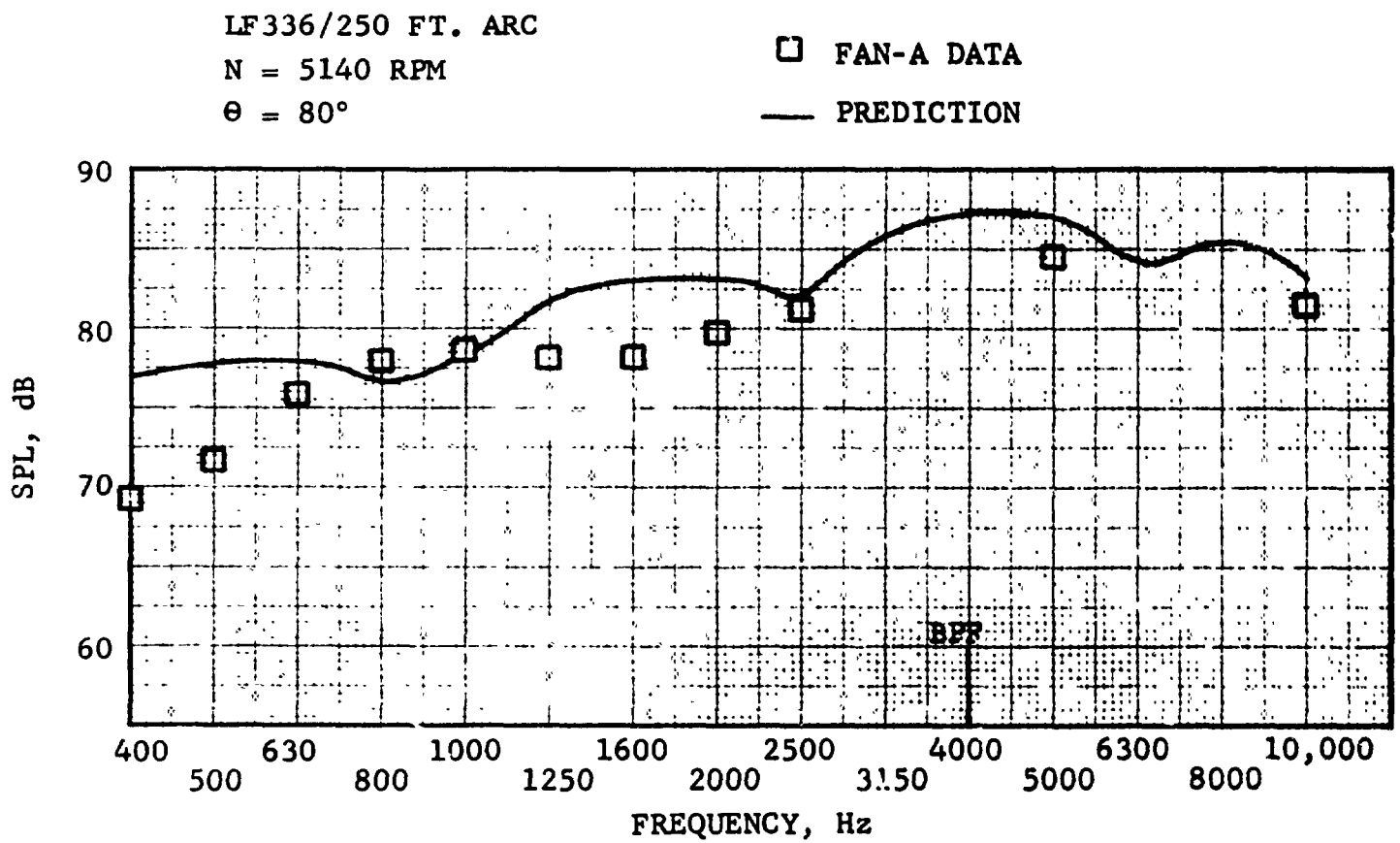

FIGURE VIII-B5 LF336 BROAD BAND NOISE SOUND-PRESSURE LEVEL SPECTRUM N = 5140 RPM, θ = 80°

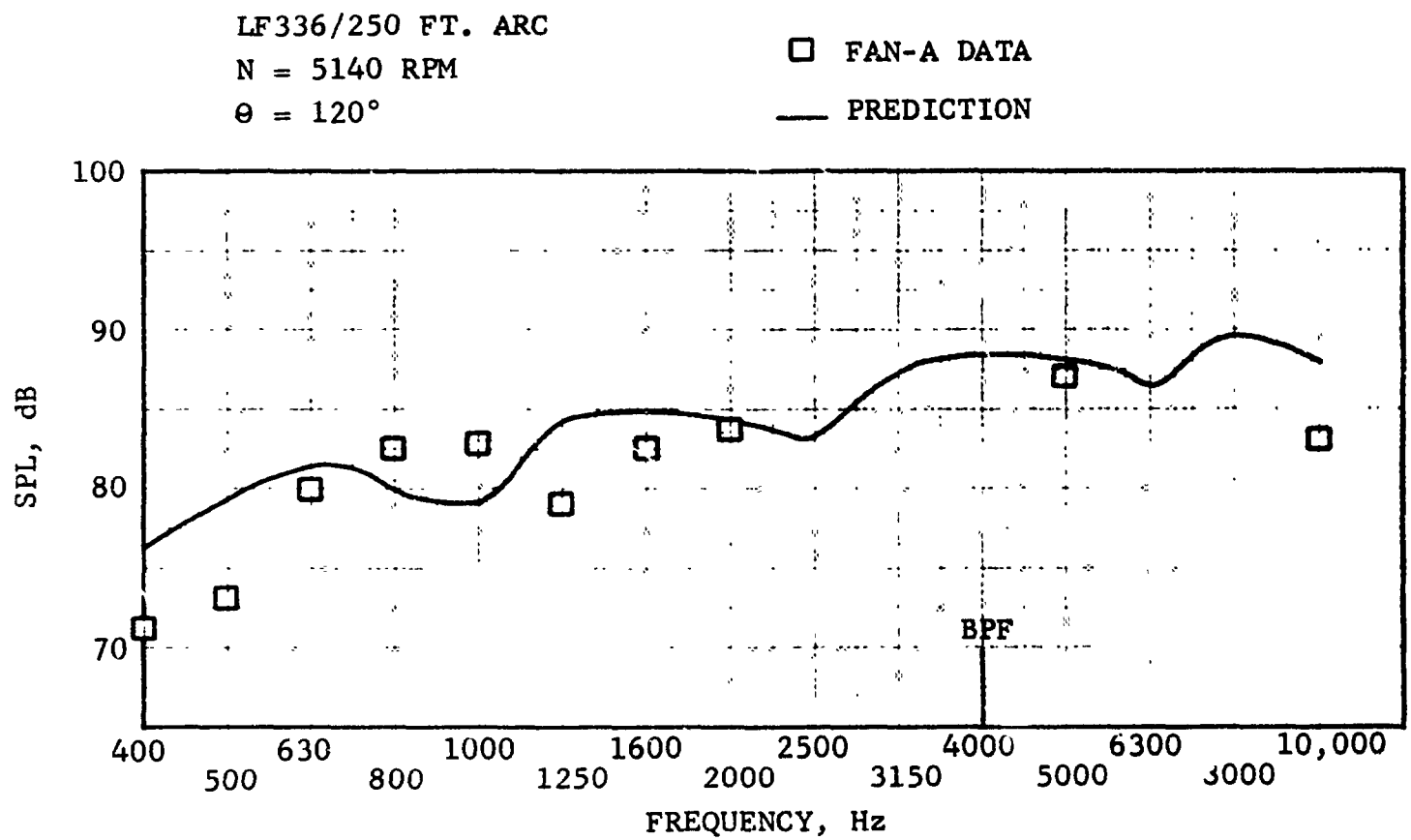

FIGURE VIII-B6 LF336 BROAD BAND NOISE SOUND-PRESSURE LEVEL SPECTRUM N = 5140 RPM, θ = 120°

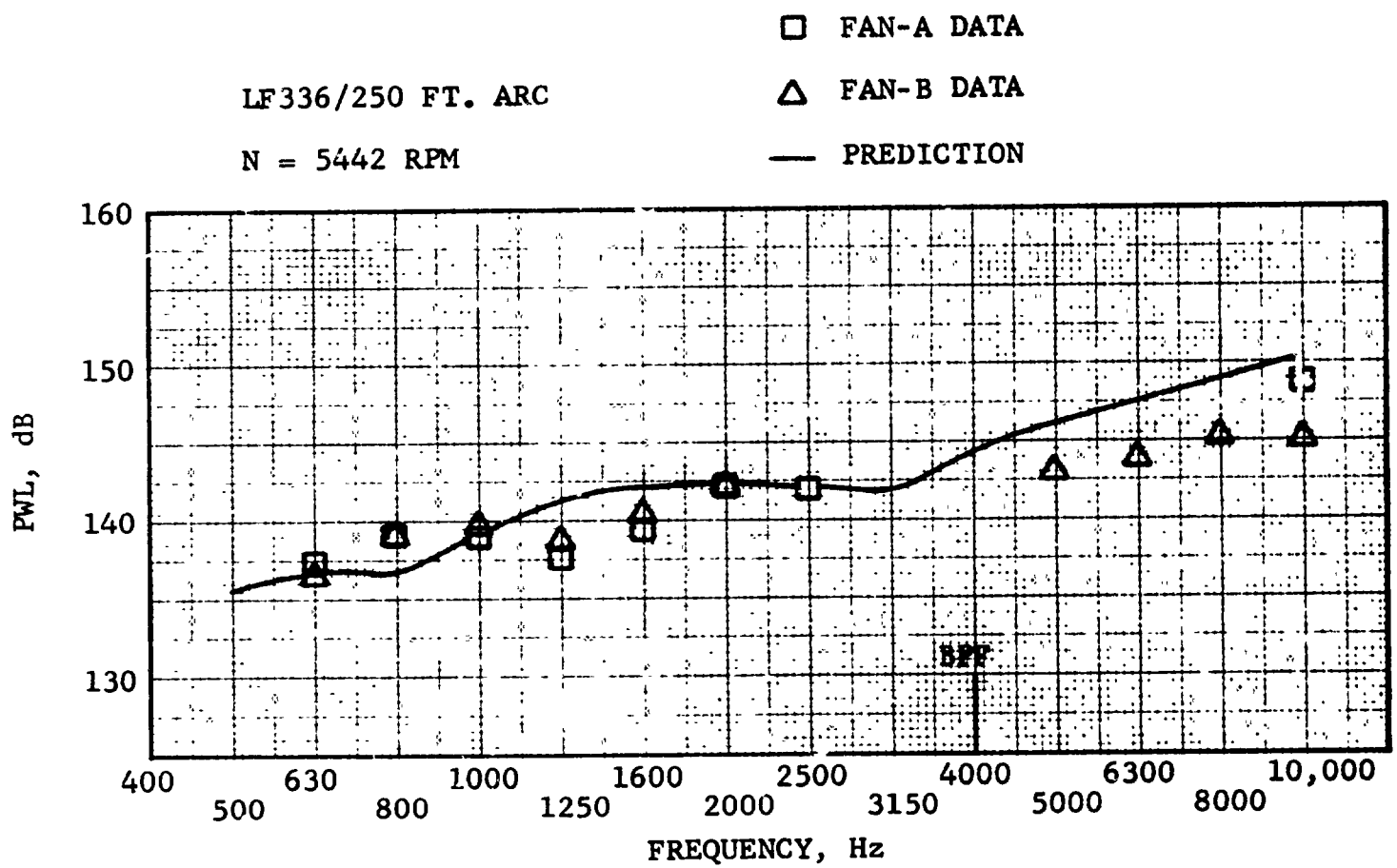

FIGURE VIII-B7 LF336 BROAD BAND NOISE POWER-LEVEL SPECTRUM N = 5442 RPM

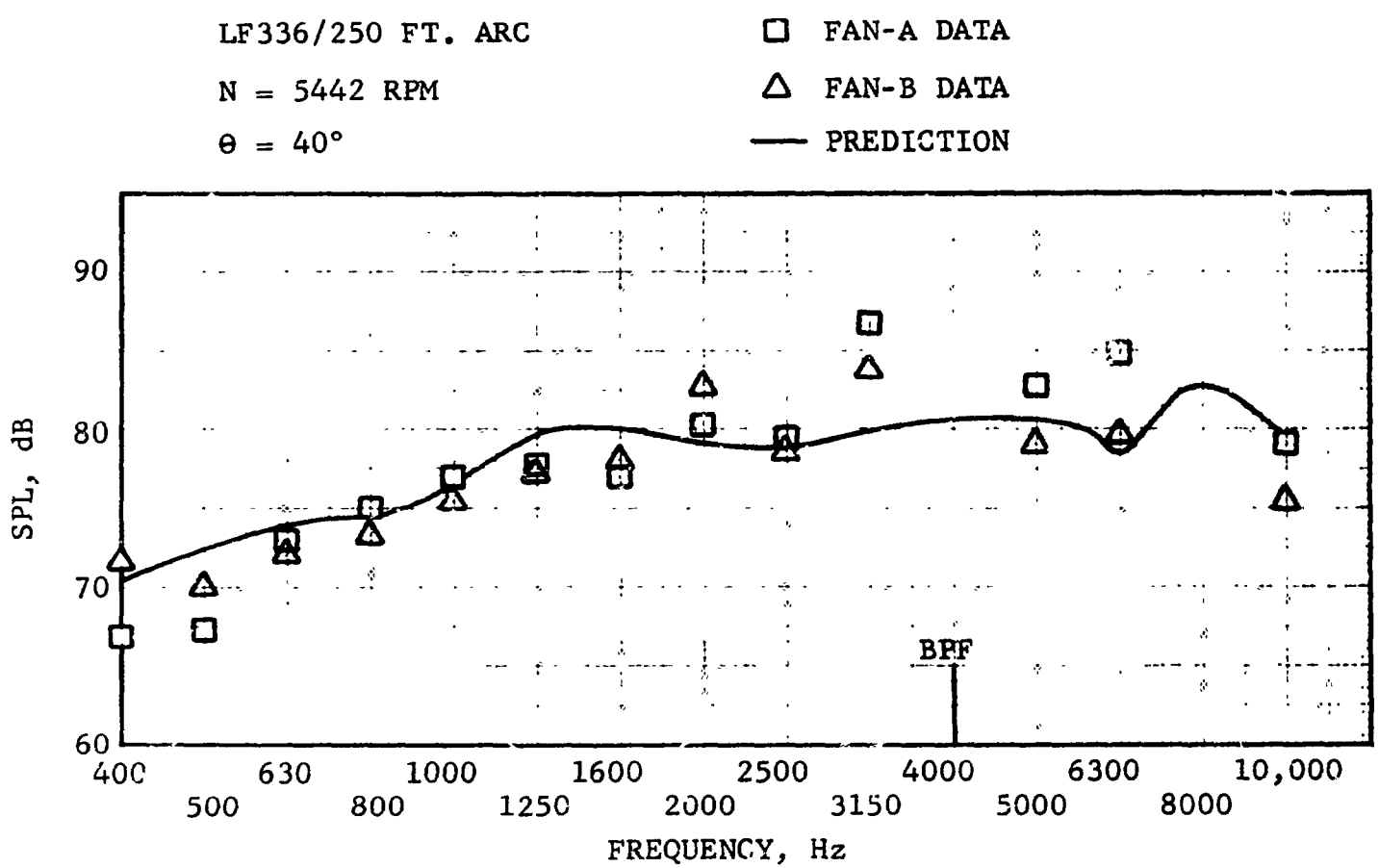

FIGURE VIII-B8 LF336 BROAD BAND NOISE SOUND-PRESSURE LEVEL SPECTRUM N = 5442 RPM, θ = 40°

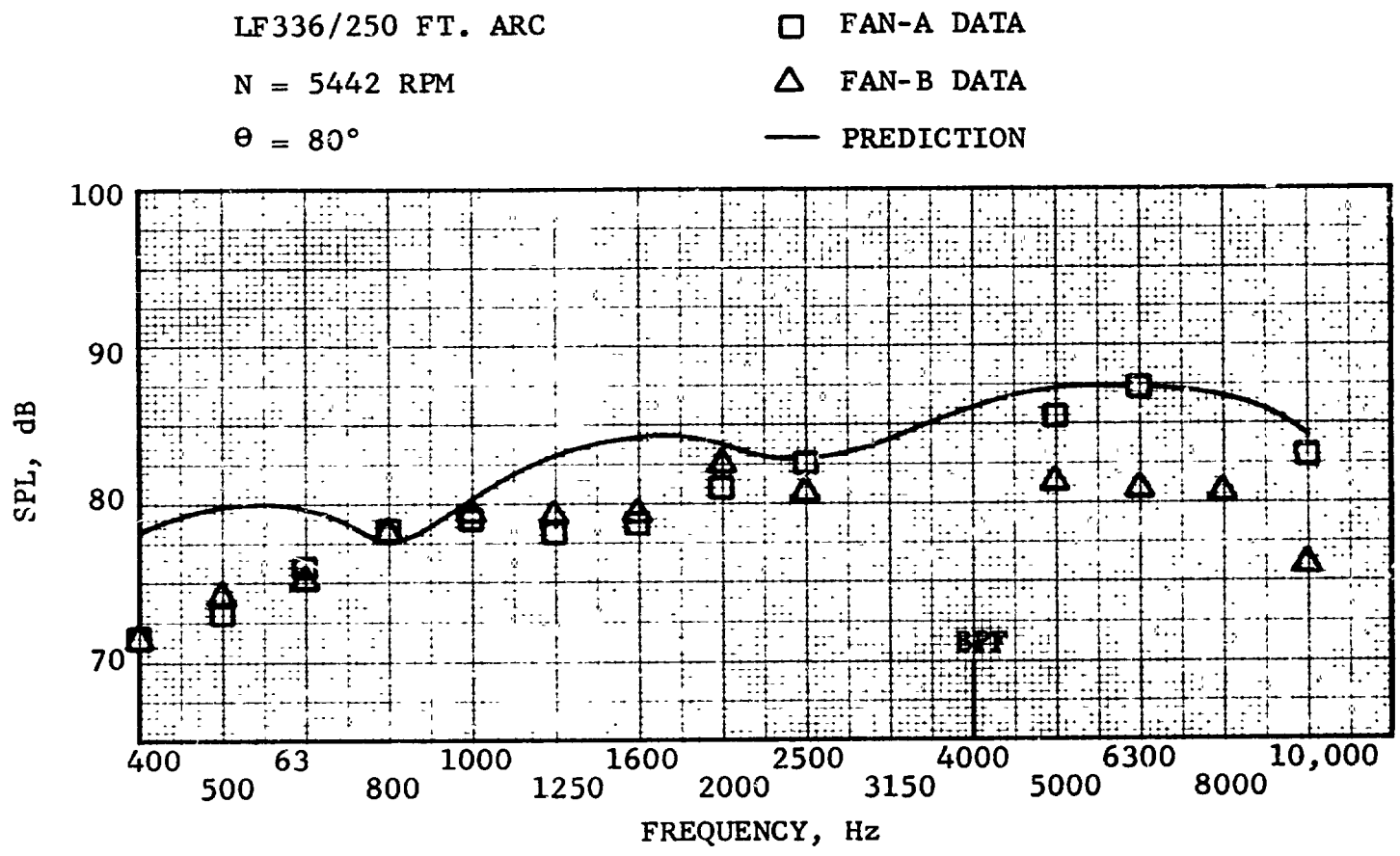

FIGURE VIII-B9 LF336 BROAD BAND NOISE SOUND-PRESSURE LEVEL SPECTRUM N = 5442 RPM, θ = 80°

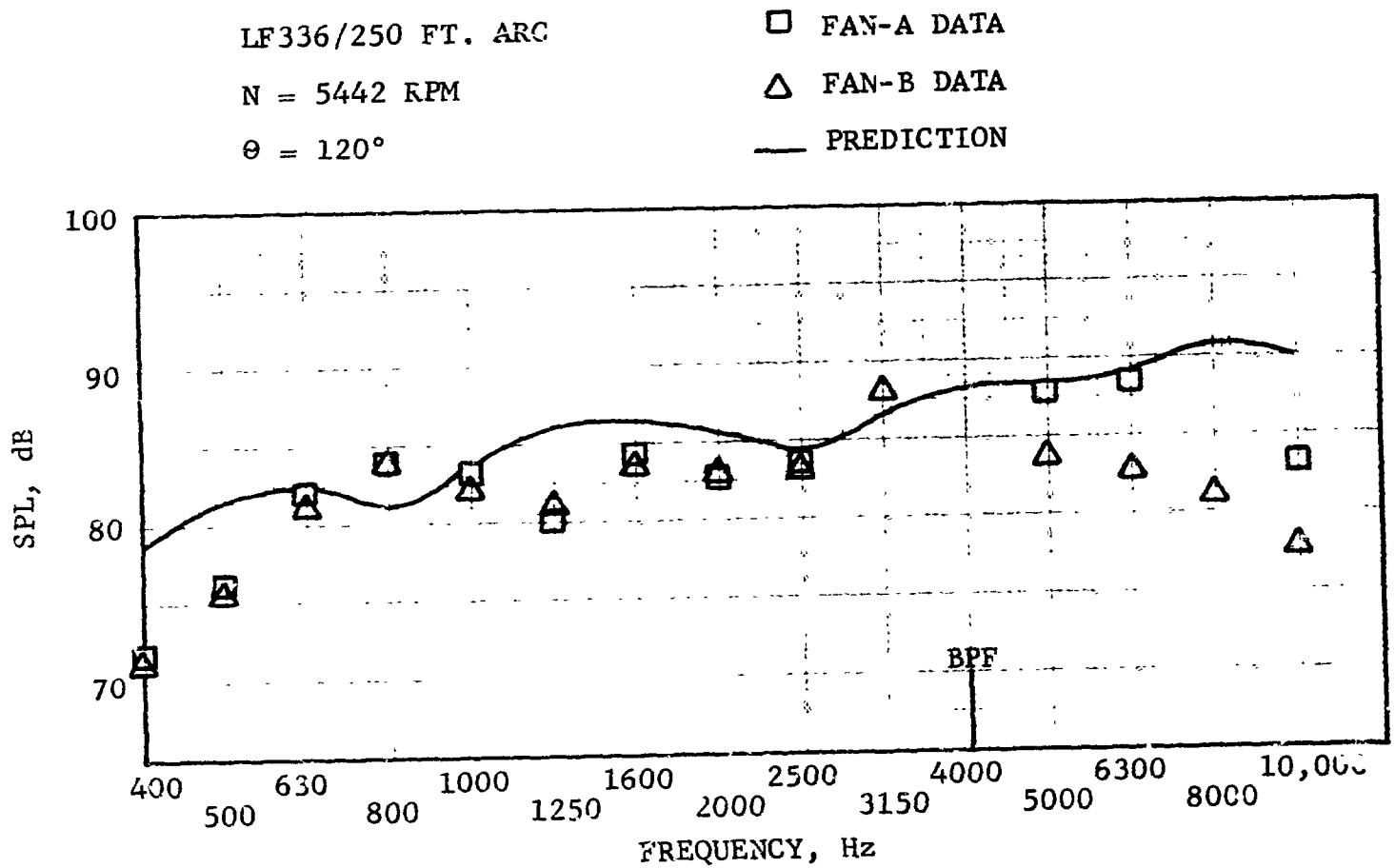

FIGURE VIII-B10 LF336 BROAD BAND NOISE SOUND PRESSURE LEVEL SPECTRUM N = 5442 RPM, θ = 120°

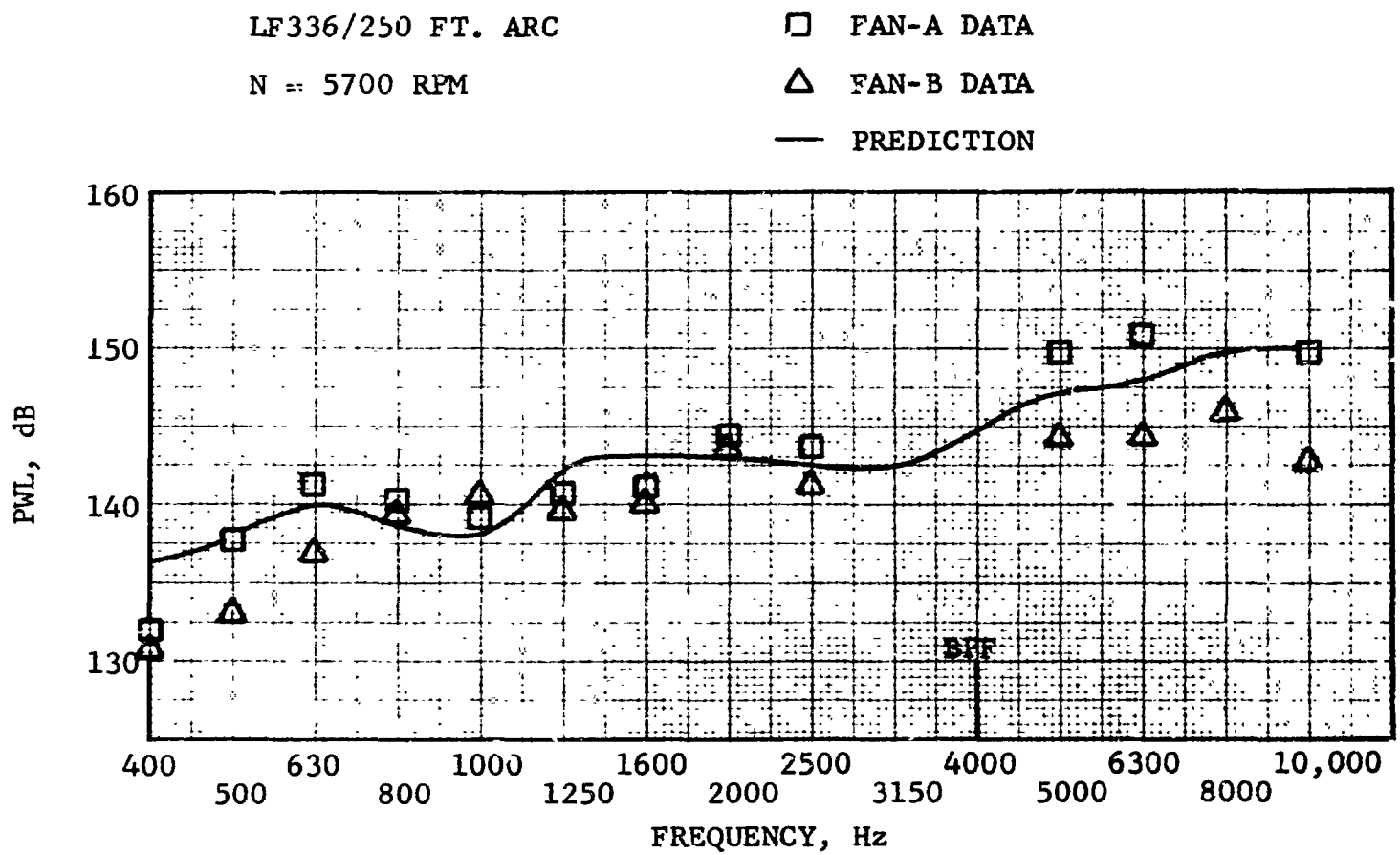

FIGURE VIII-B11 LF336 BROAD BAND NOISE POWER-LEVEL SPECTRUM N = 5700 RPM

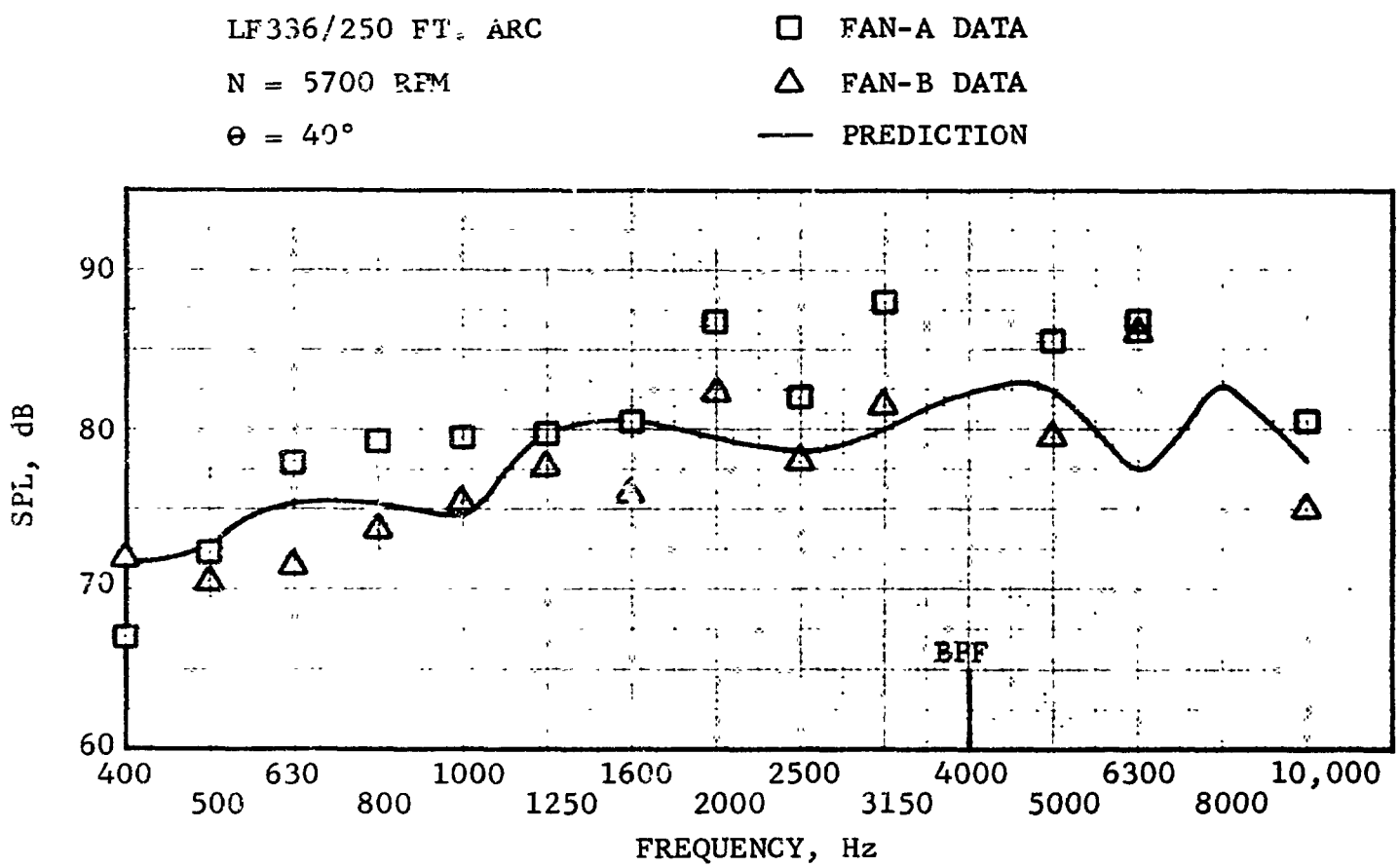

FIGURE VIII-B12 LF336 BROAD BAND NOISE SOUND-PRESSURE LEVEL SPECTRUM N = 5700 RPM, θ = 40°

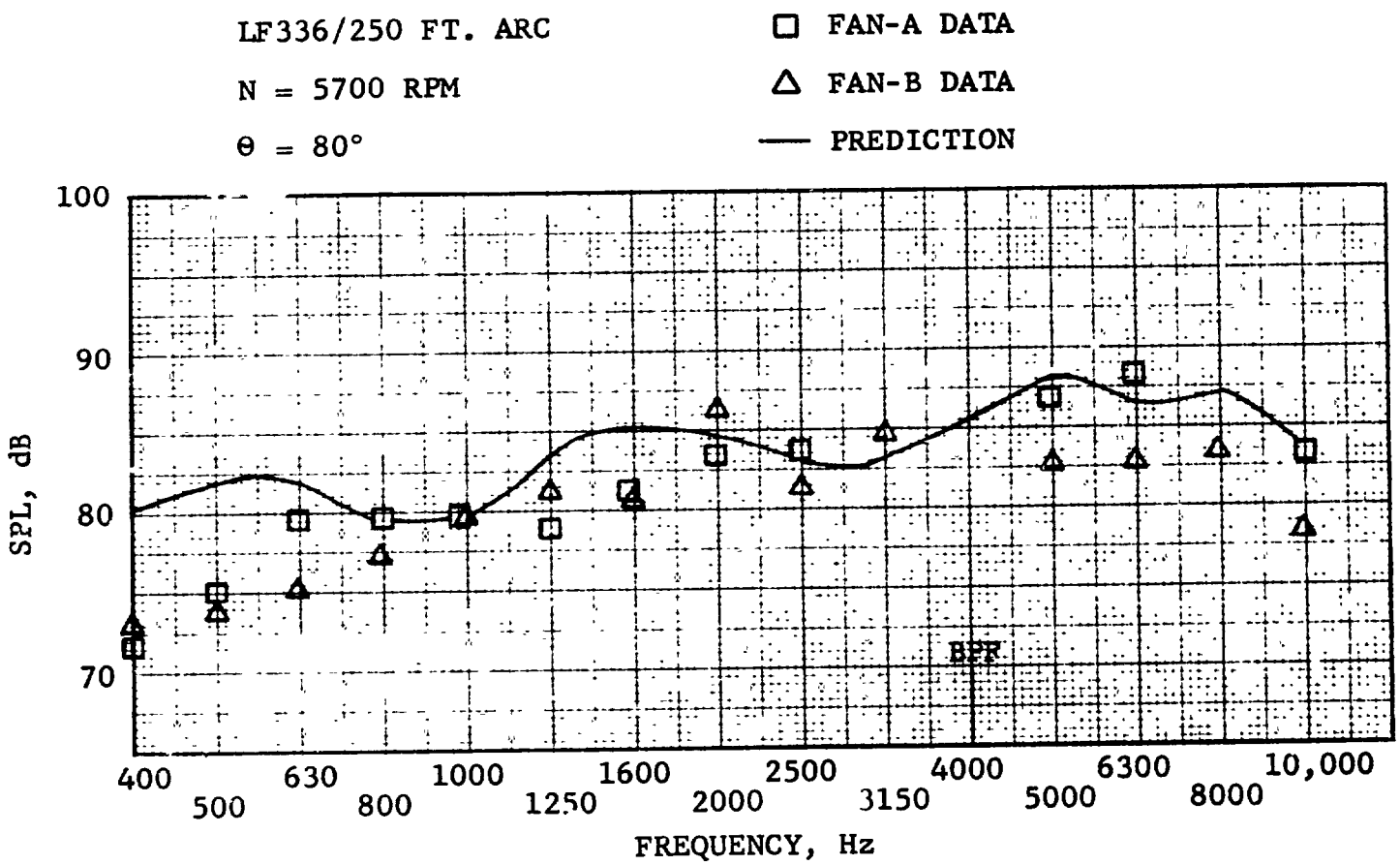

FIGURE VIII-B13 LF336 BROAD BAND NOISE SOUND-PRESSURE LEVEL SPECTRUM N = 5700 RPM, θ = 80°

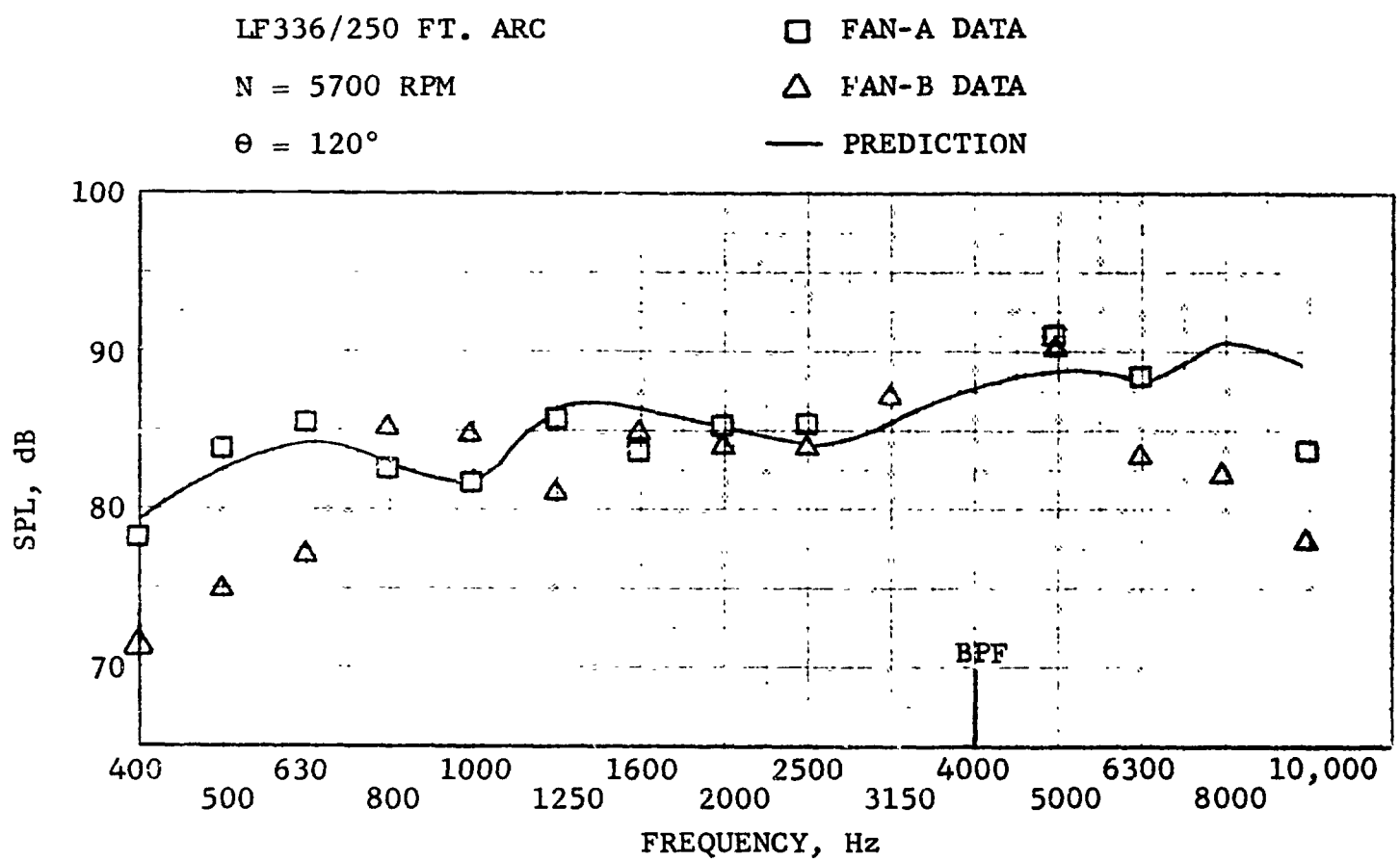

FIGURE VIII-B14 LF336 BROAD BAND NOISE SOUND-PRESSURE LEVEL SPECTRUM N = 5700 RPM, θ = 120°

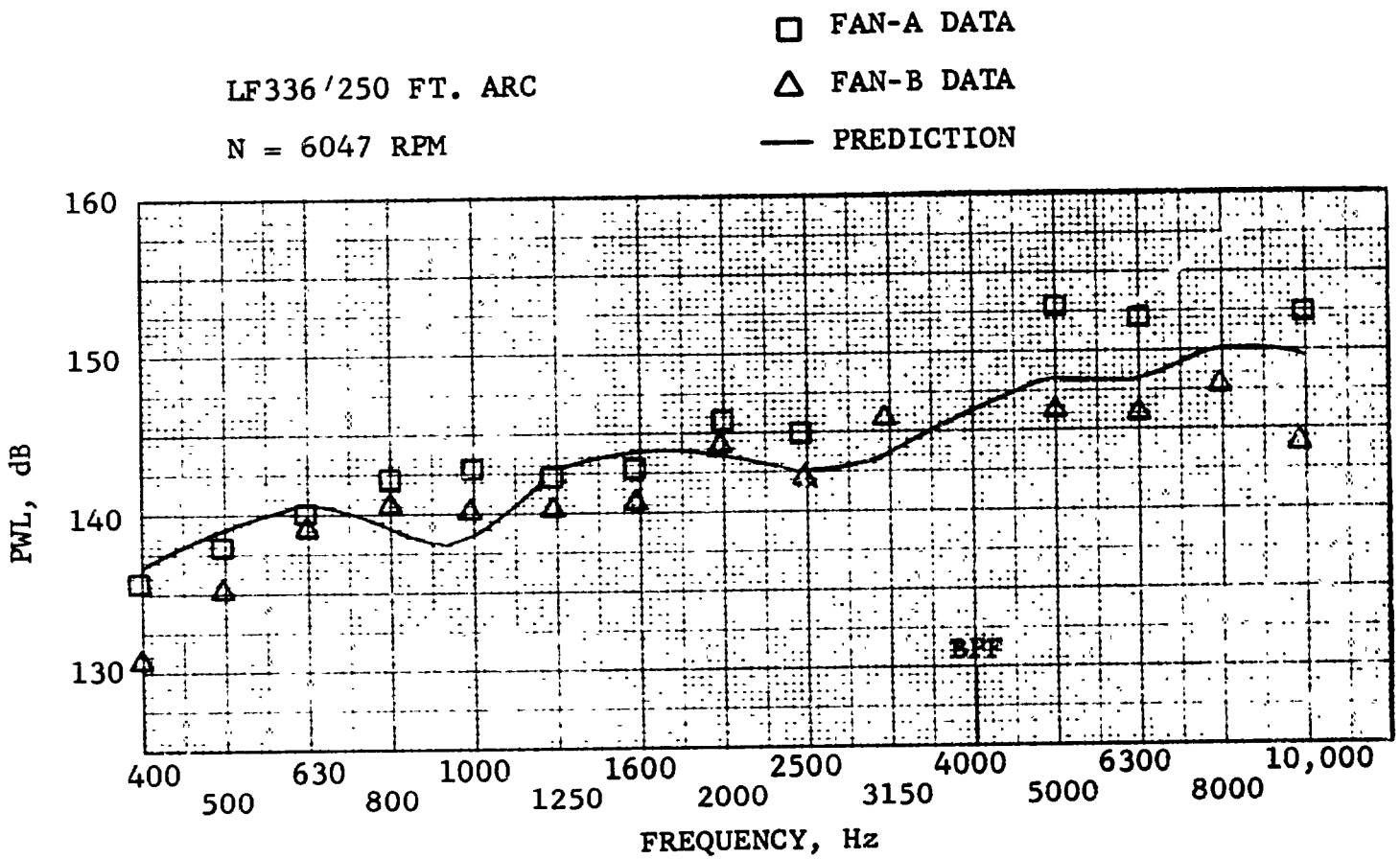

FIGURE VIII-B15 LF336 BROAD BAND NOISE POWER-LEVEL SPECTRUM N = 6047

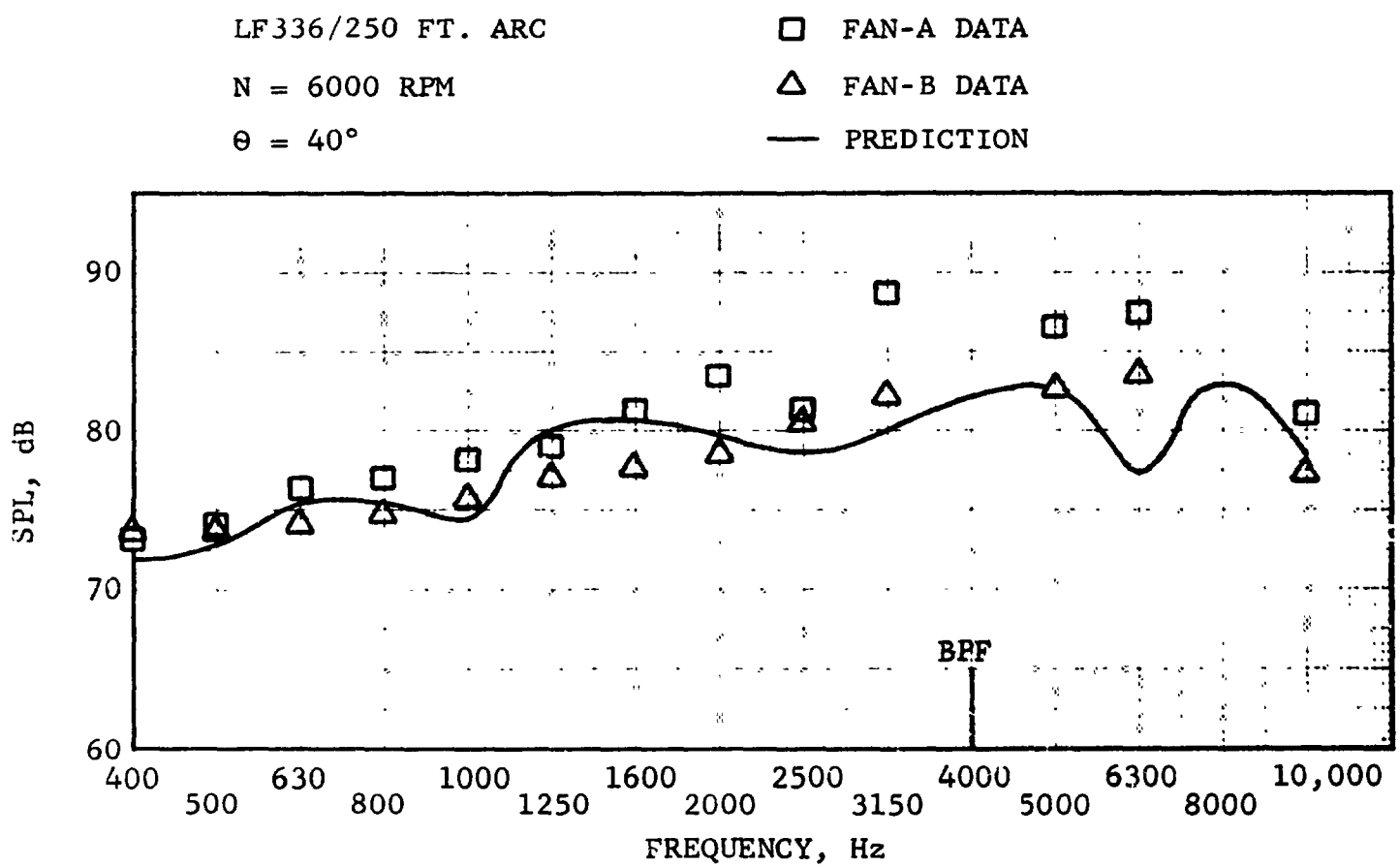

FIGURE VIII-B16 LF336 BROAD BAND NOISE SOUND-PRESSURE LEVEL SPECTRUM N = 6000 RPM, Θ = 40°

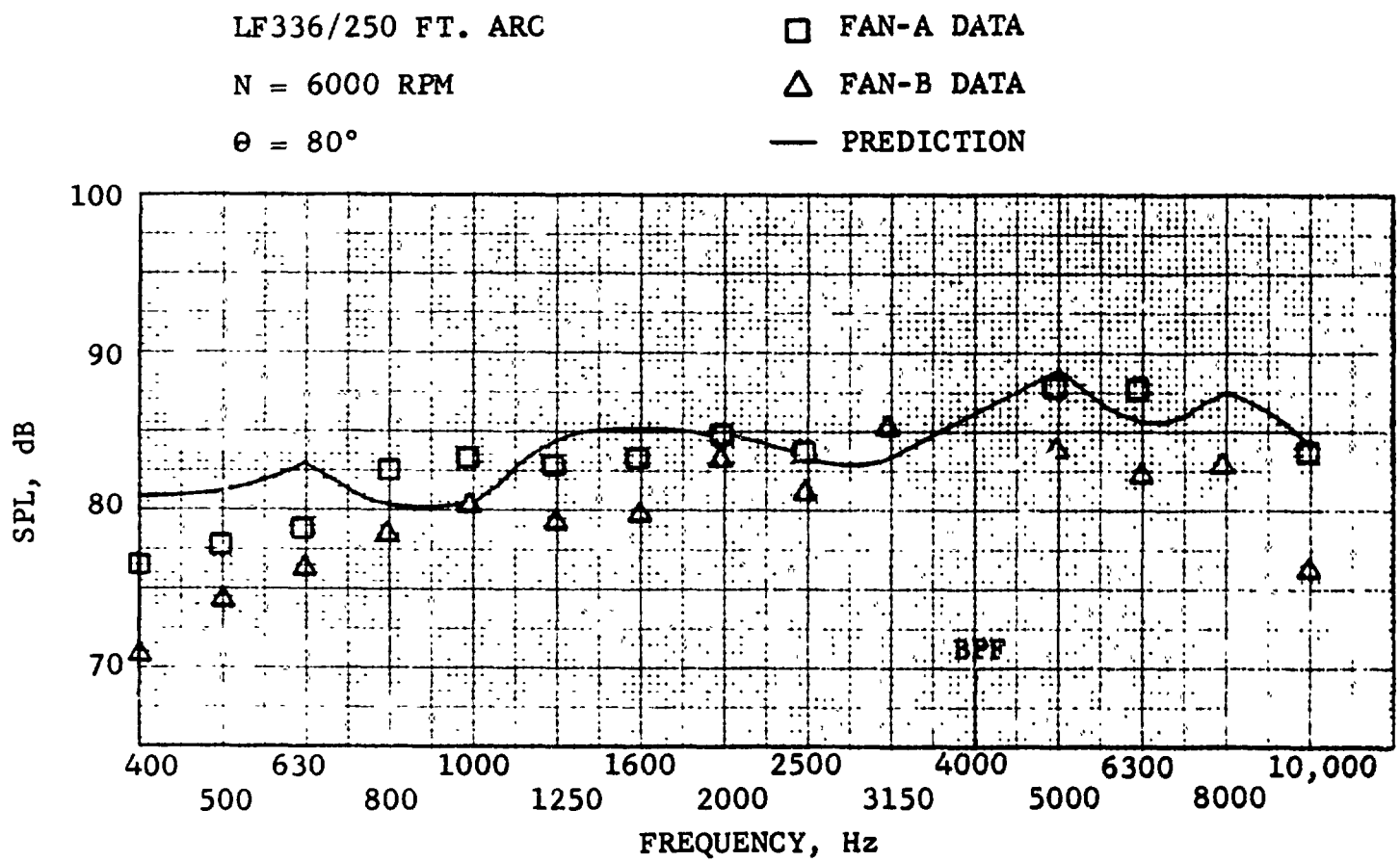

FIGURE VIII-B17 LF336 BROAD BAND NOISE SOUND-PRESSURE LEVEL SPECTRUM N = 6000 RPM, θ = 80°

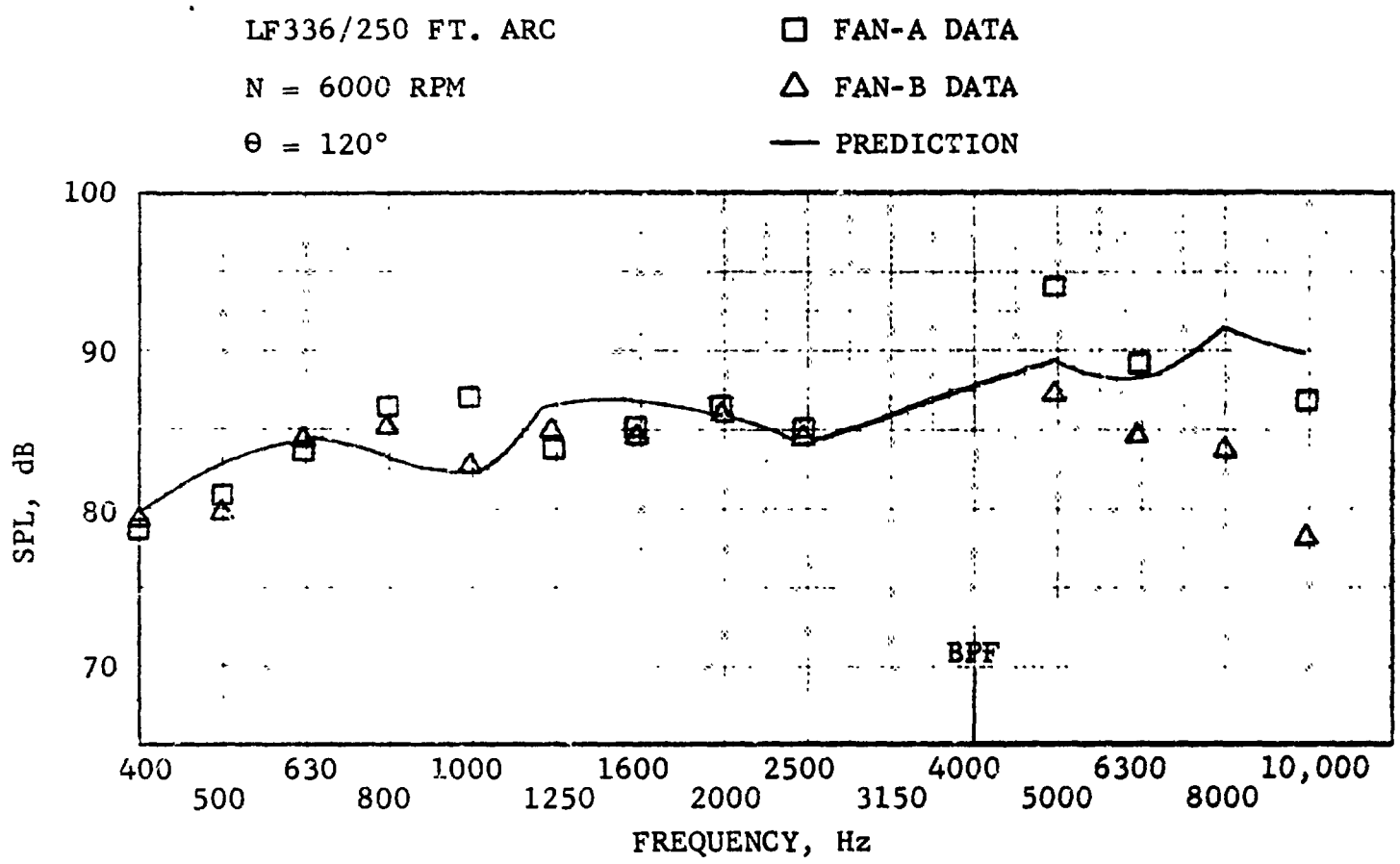

FIGURE VIII-B18 LF336 BROAD BAND NOISE SOUND-PRESSURE LEVEL SPECTRUM N = 6000 RPM, θ = 120°

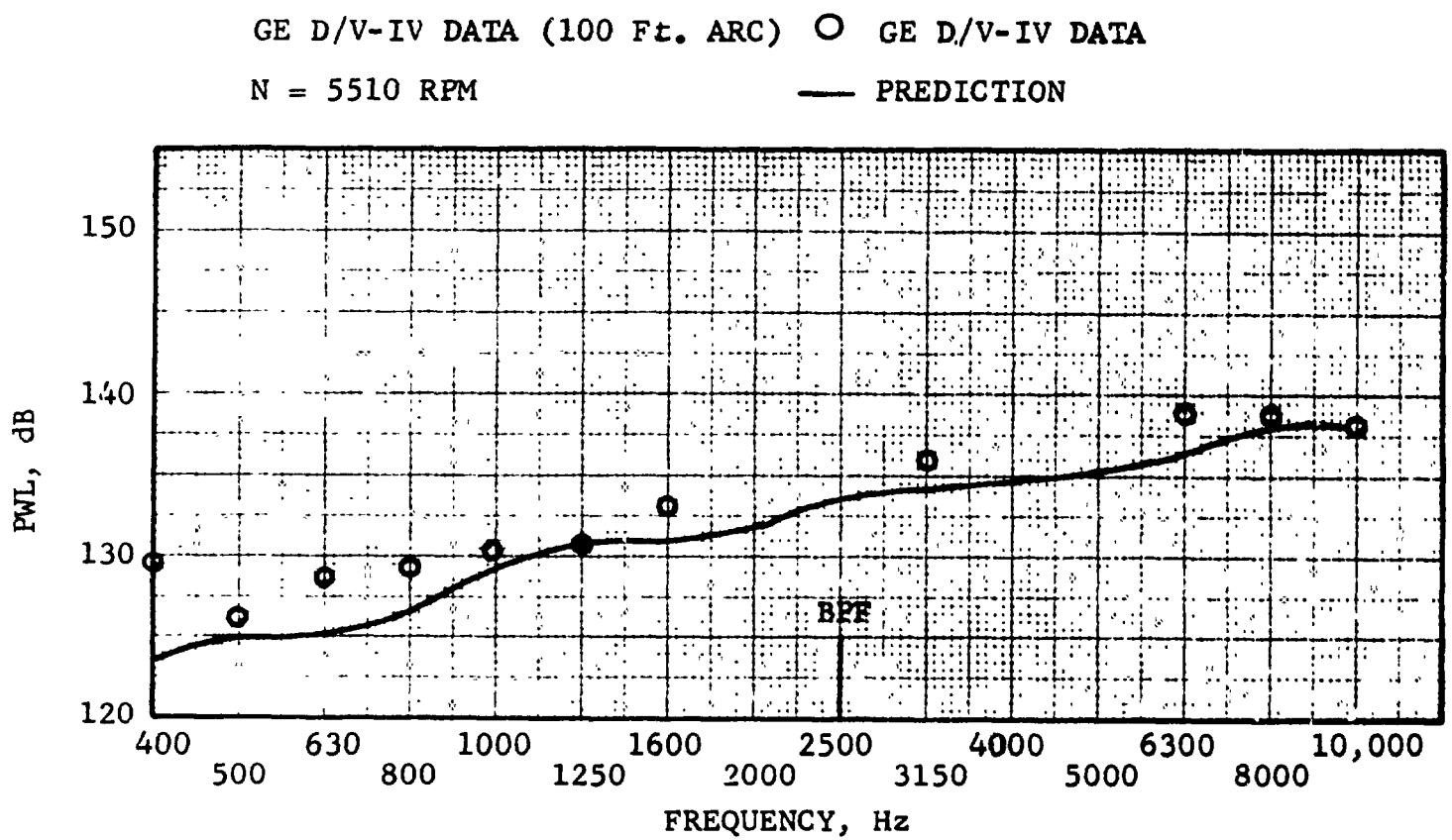

FIGURE VIII-B19 GE D/V-IV BROAD BAND NOISE POWER LEVEL SPECTRUM N = 5510 RPM

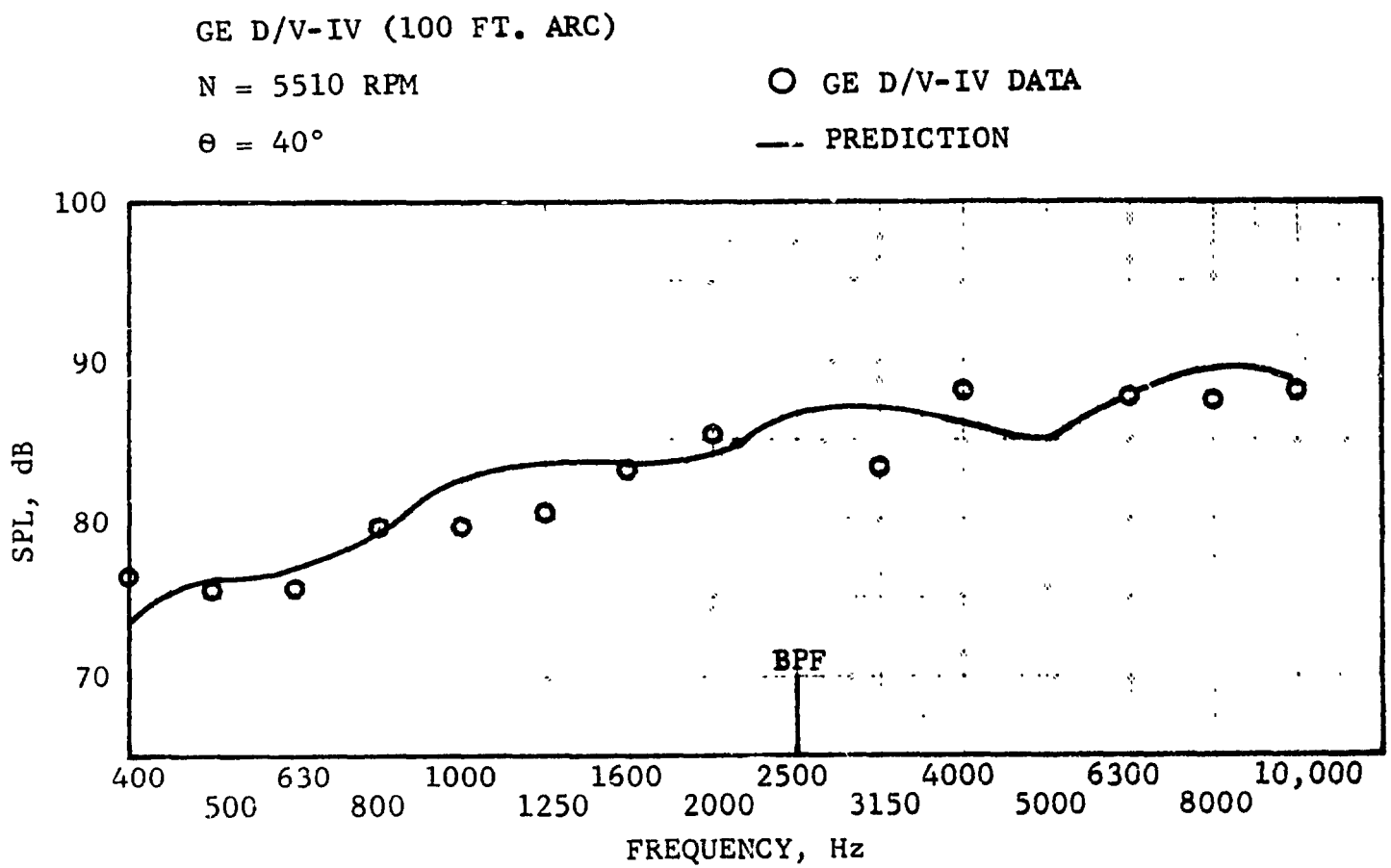

FIGURE VIII-B20 GE D/V-IV BROAD BAND NOISE SOUND-PRESSURE LEVEL SPECTRUM N = 5510 RPM, θ = 40°

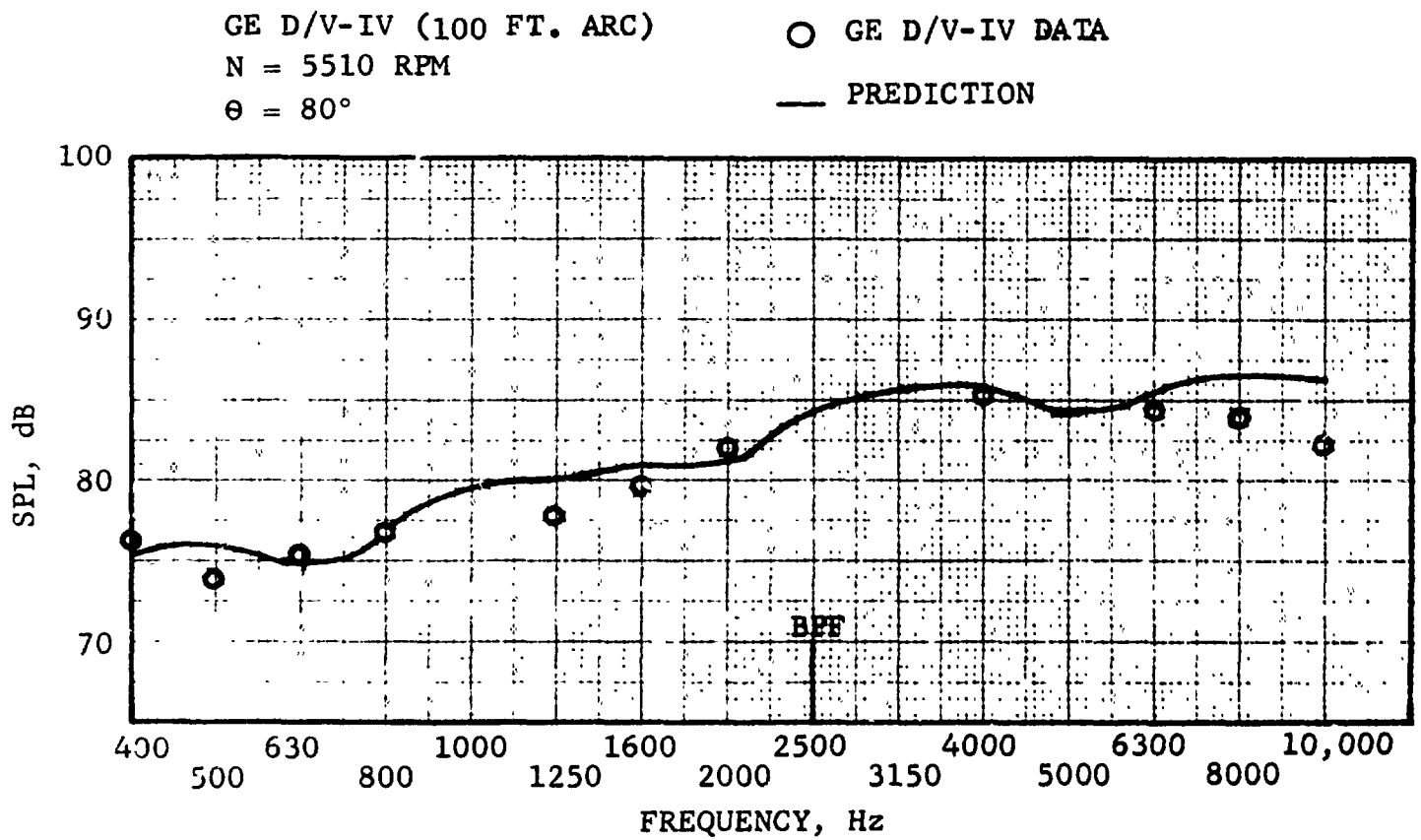

FIGURE VIII-B21 GE D/V-IV BROAD BAND NOISE SOUND-PRESSURE LEVEL SPECTRUM N = 5510 RPM θ = 80°

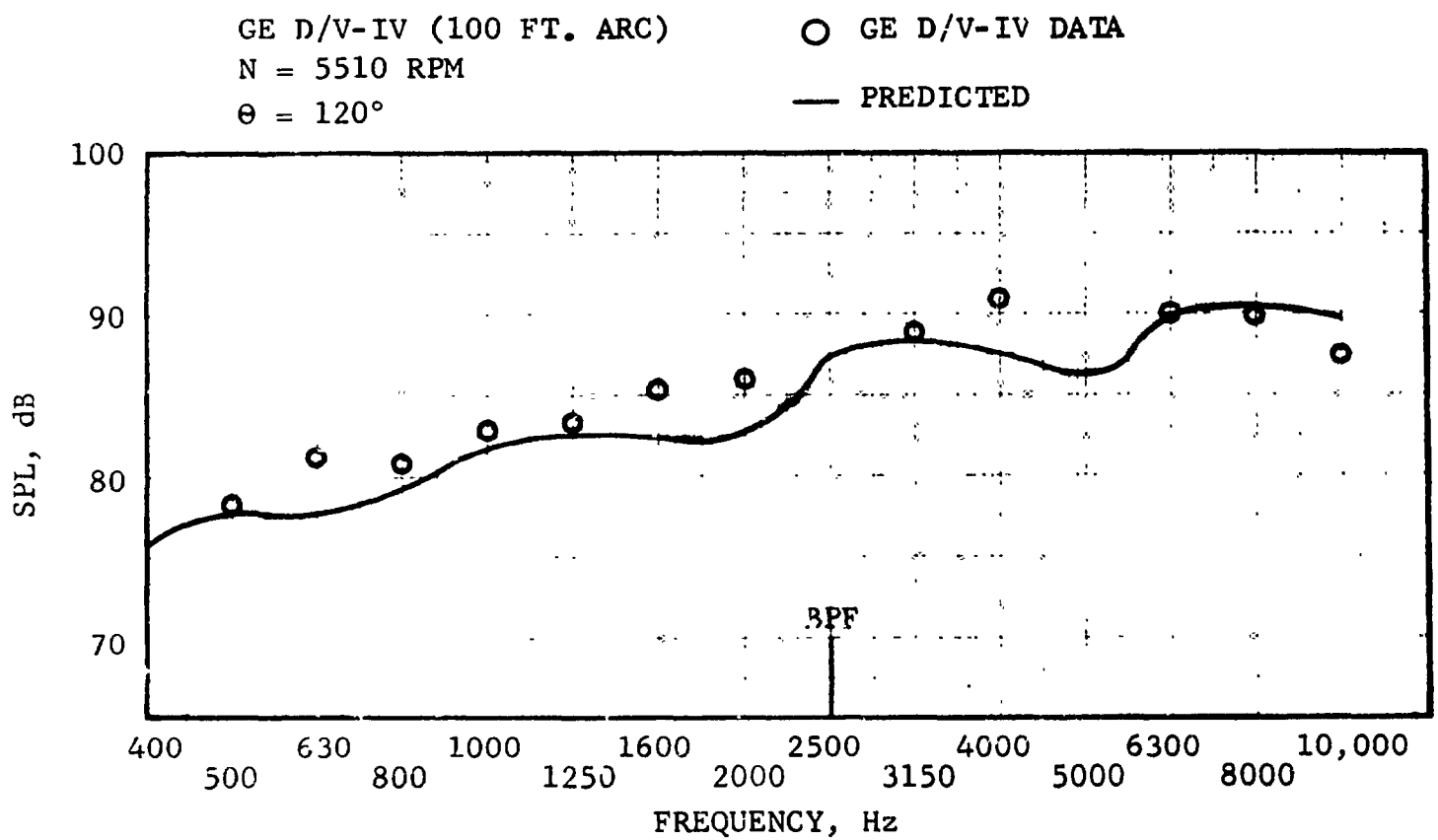

FIGURE VIII-B22 GE D/V-IV BROAD BAND NOISE SOUND-PRESSURE LEVEL SPECTRUM N = 5510 RPM, θ = 120°

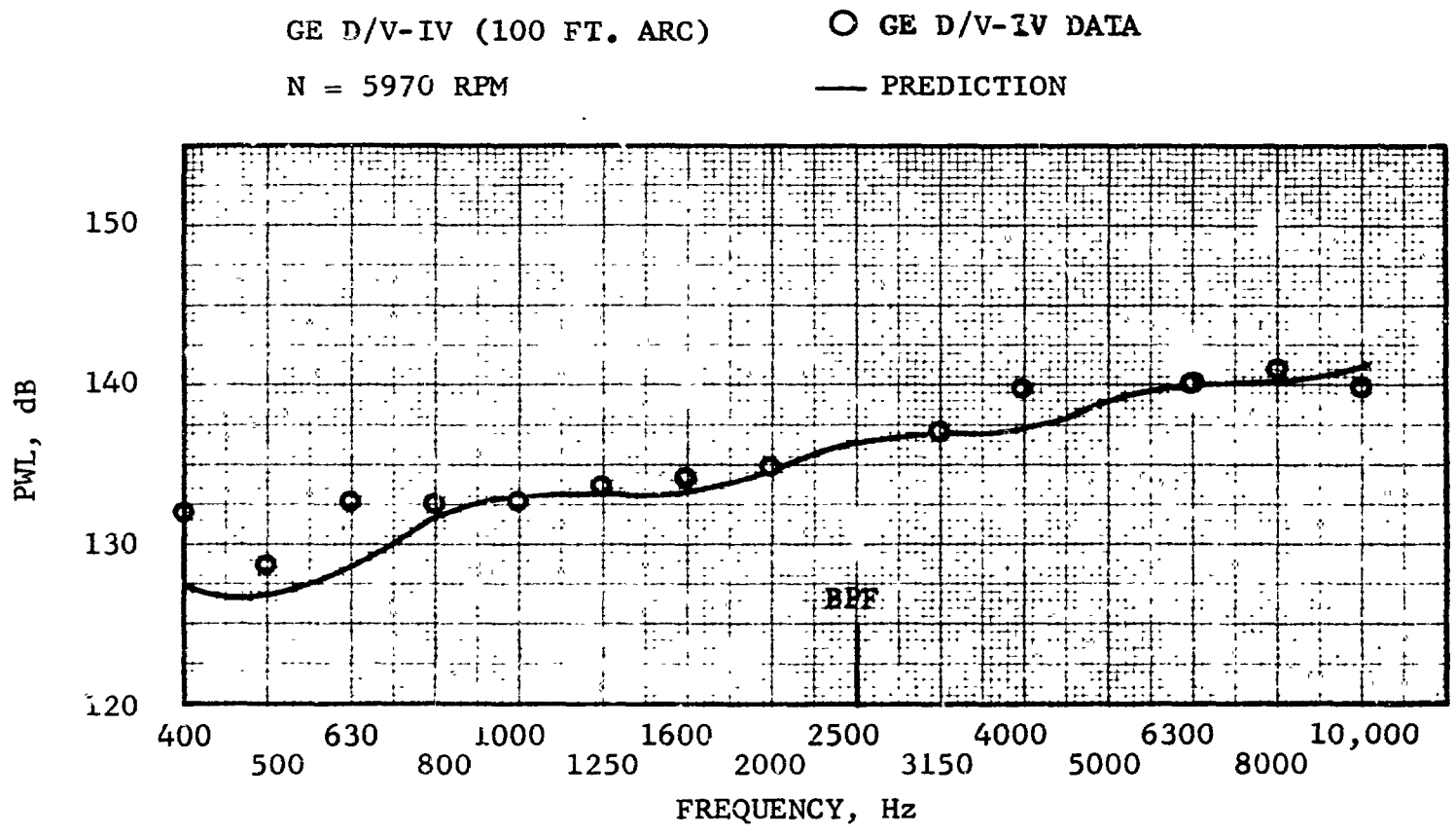

FIGURE VIII-B23 GE D/V-IV BROAD BAND NOISE POWER-LEVEL SPECTRUM N = 5970 RPM

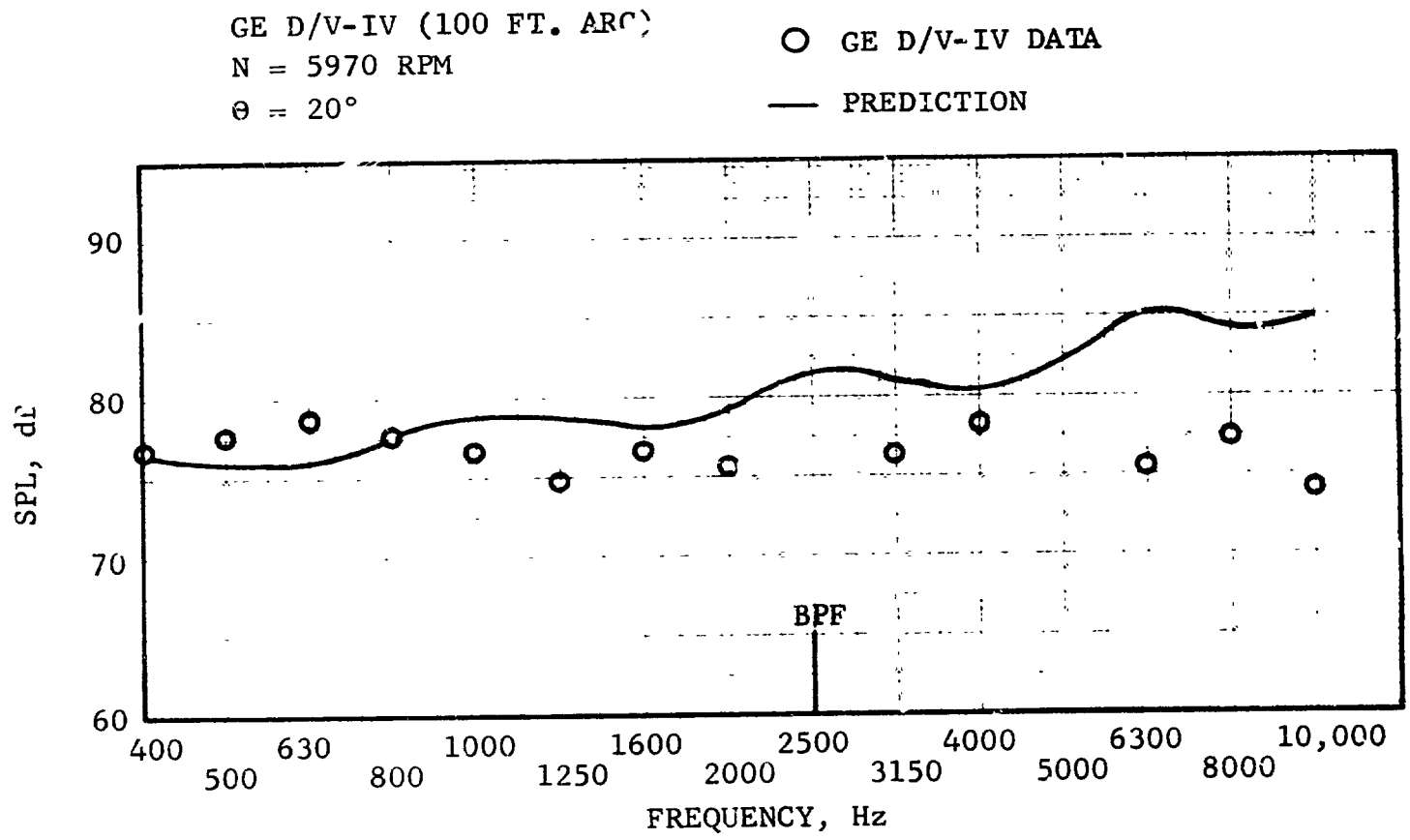

FIGURE VIII-B24 GE D/V-IV BROAD BAND NOISE SOUND-PRESSURE LEVEL SPECTRUM N = 5970 RPM, θ = 20°

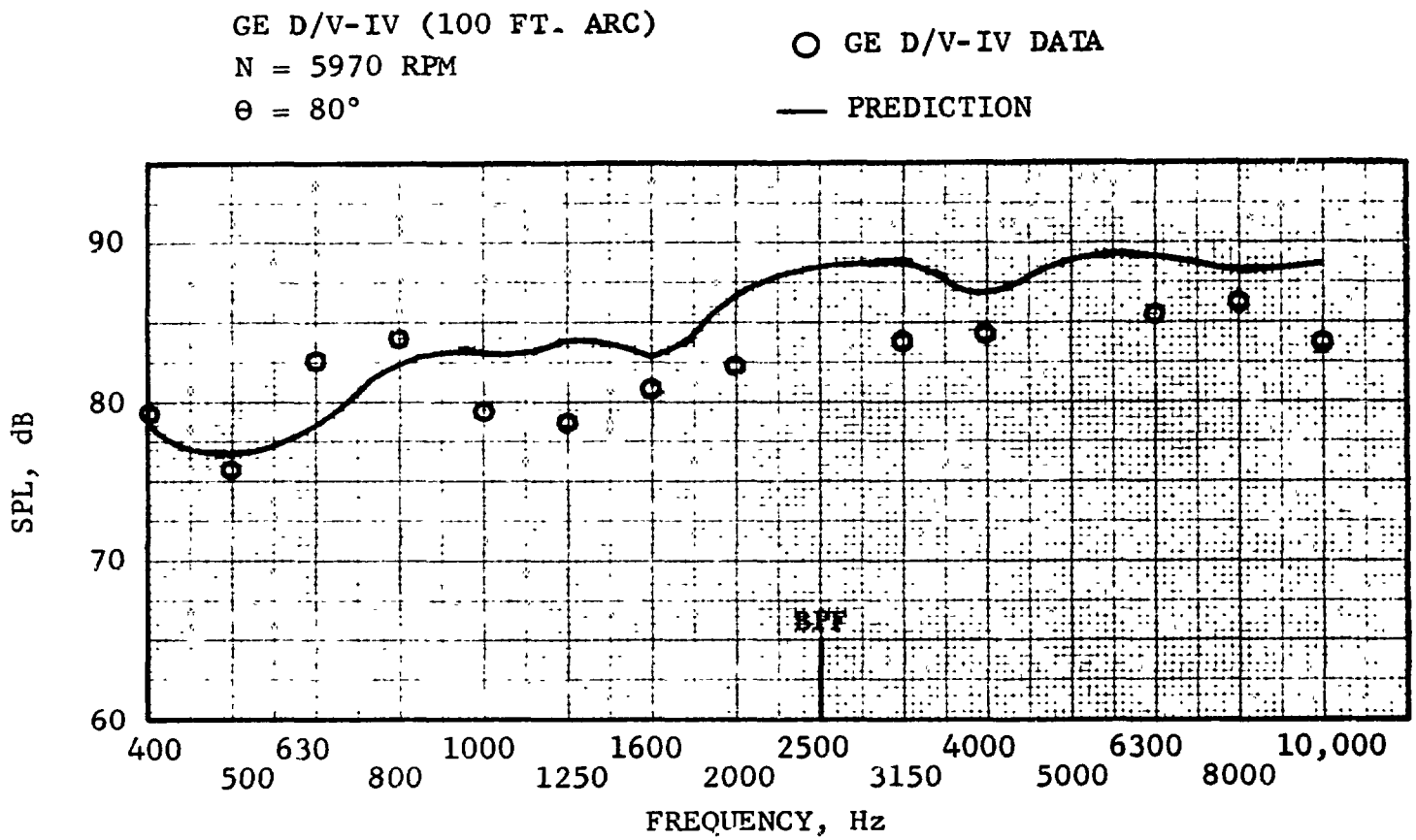

FIGURE VIII-B25 GE D/V-IV BROAD BAND NOISE SOUND-PRESSURE LEVEL SPECTRUM N = 5970 RPM, θ = 80°

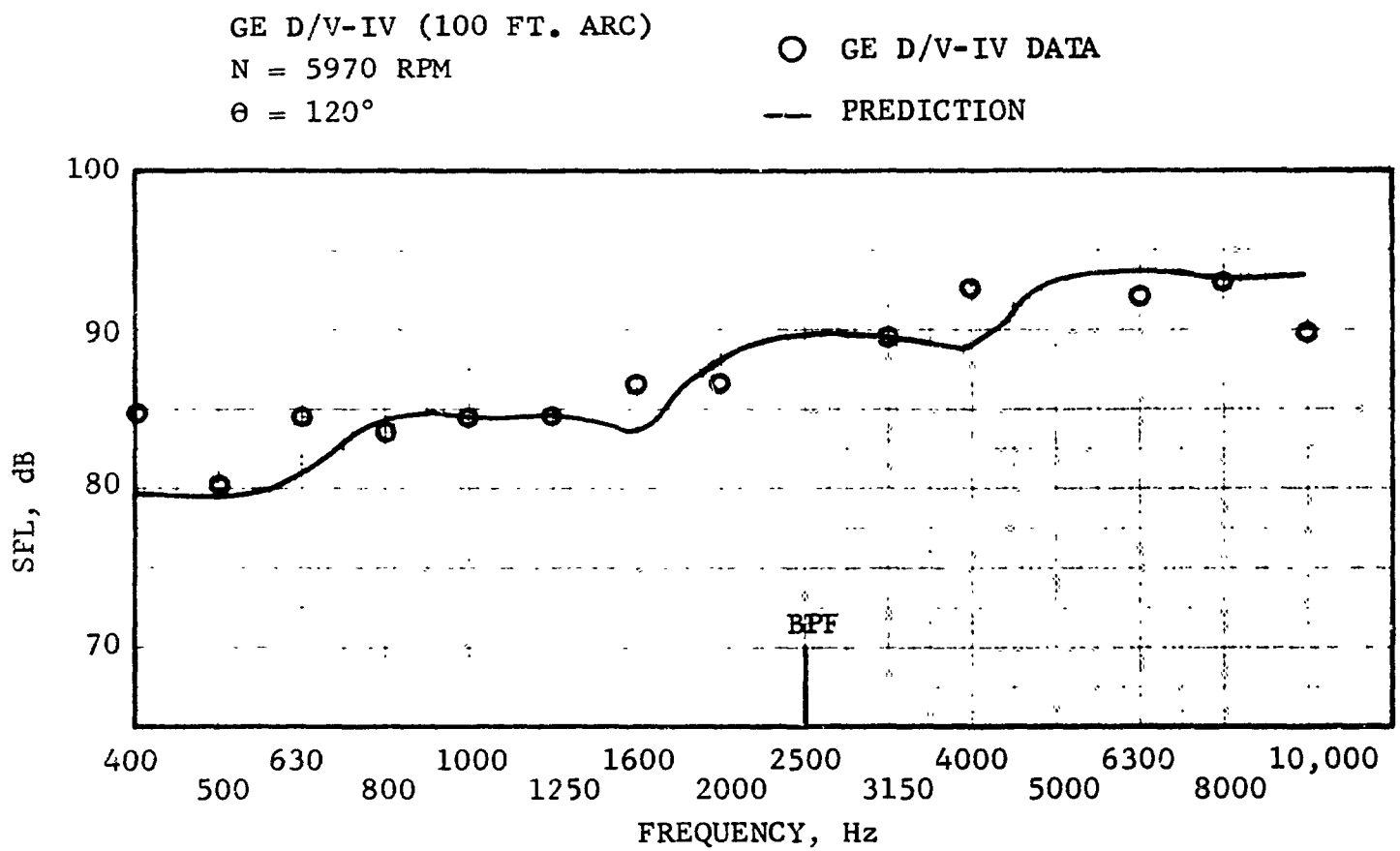

FIGURE VIII-B26 GE D/V-IV BROAD BAND NOISE SOUND-PRESSURE LEVEL SPECTRUM N = 5970 RPM, θ = 120°

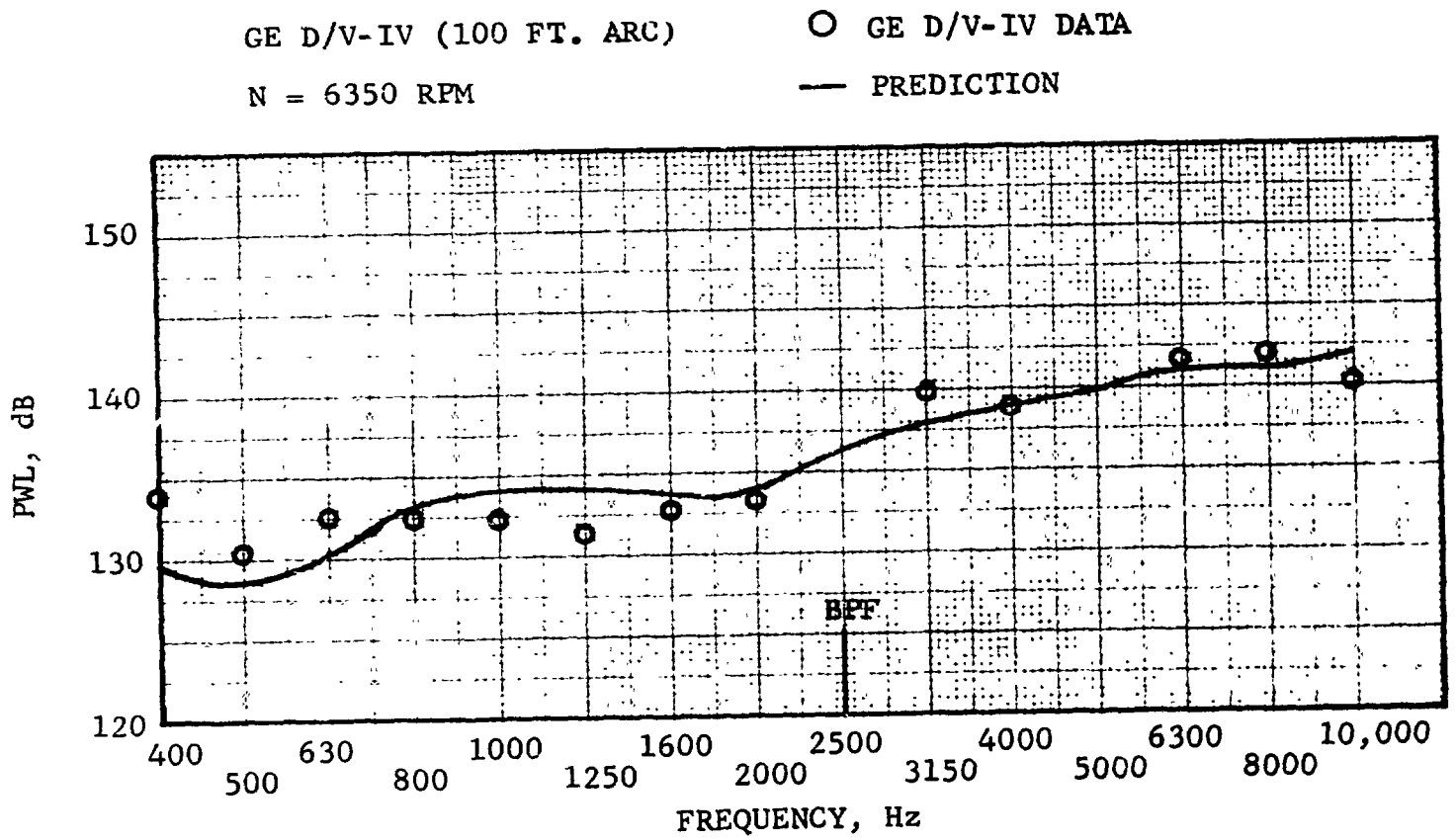

FIGURE VIII-B27 GE D/V-IV BROAD BAND NOISE POWER-LEVEL SPECTRUM N = 6350 RPM

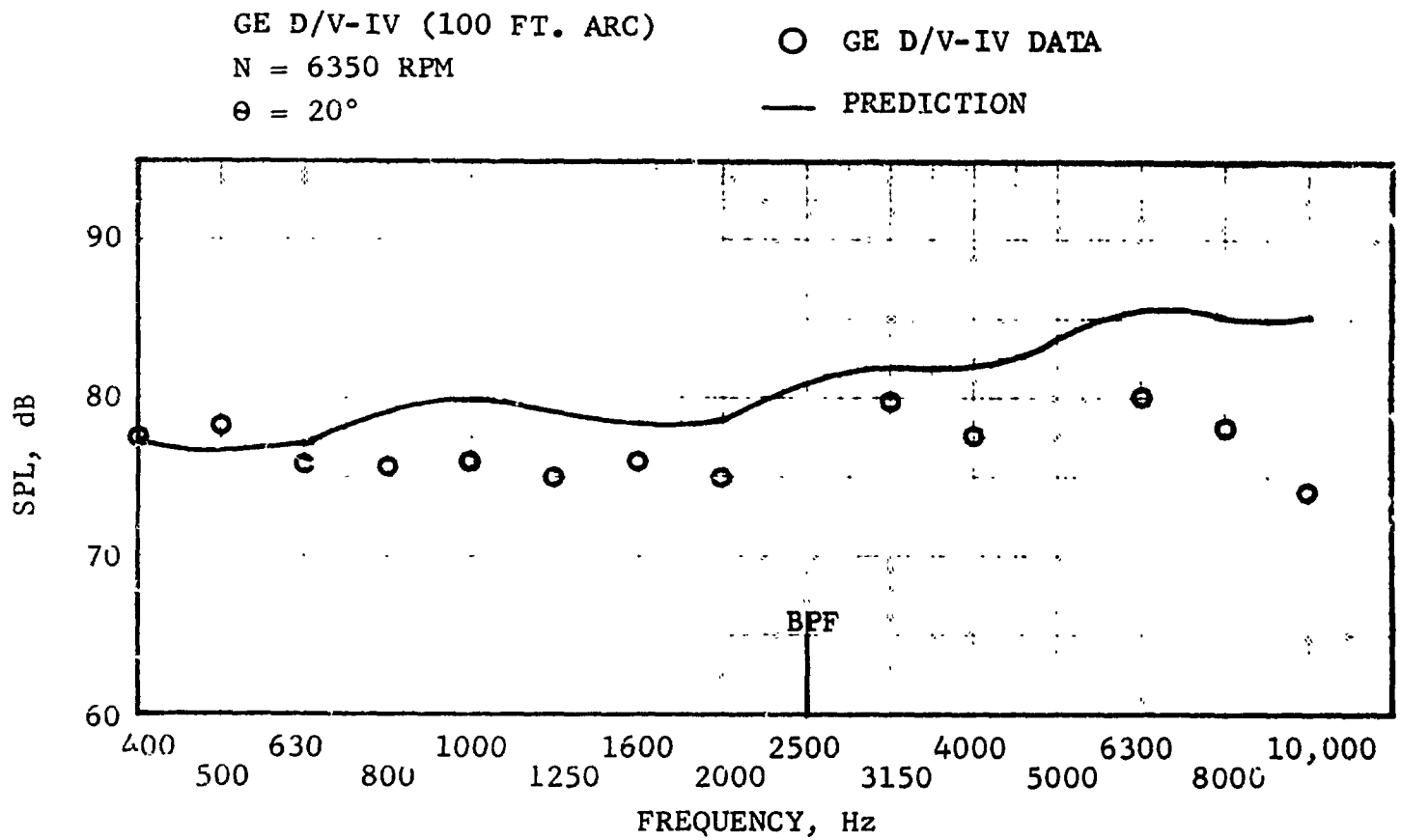

FIGURE VIII-B28 GE D/V-IV BROAD BAND NOISE SOUND-PRESSURE LEVEL SPECTRUM N = 6350 RPM, Θ = 20°

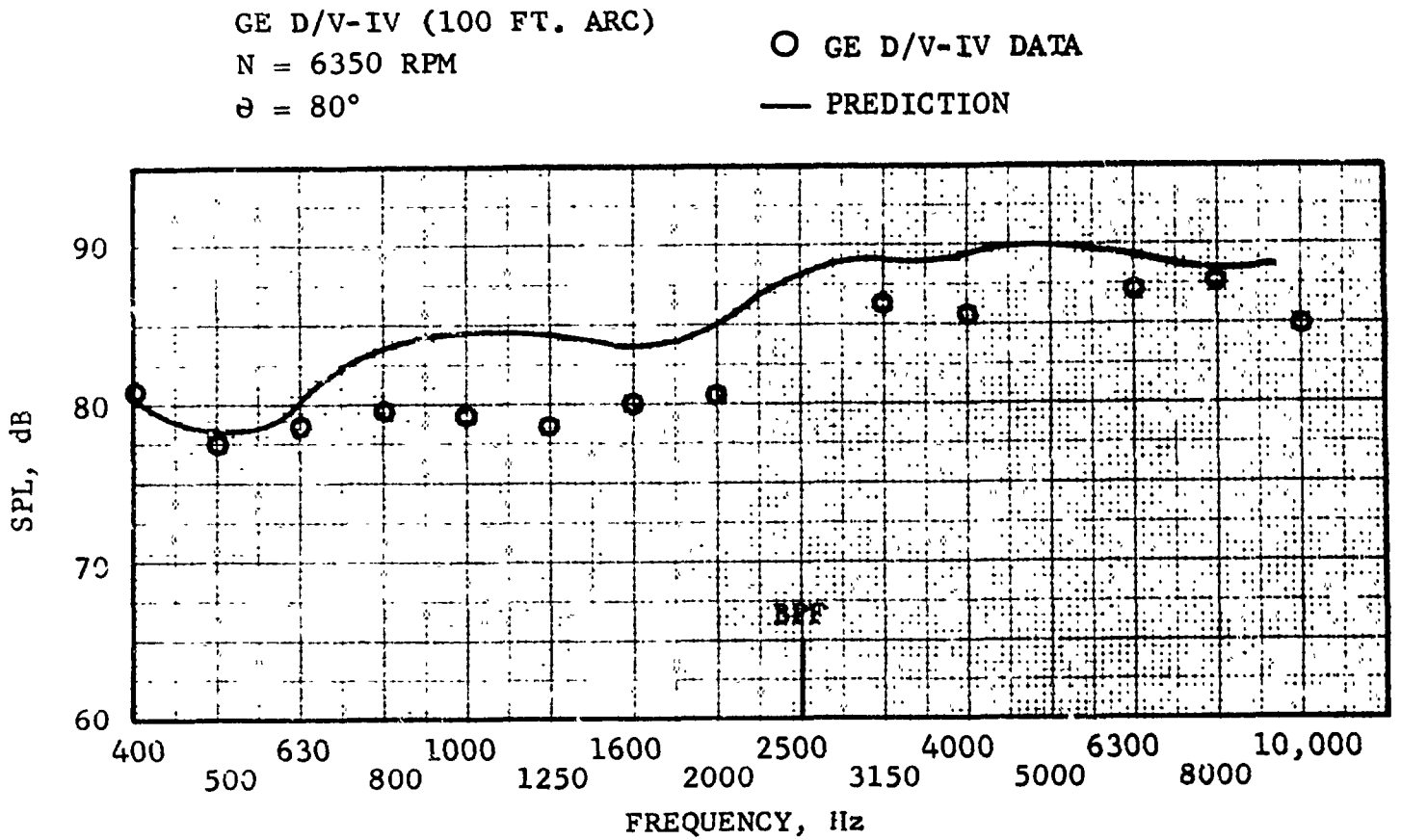

FIGURE VIII-B29 GE D/V-IV BROAD BAND NOISE SOUND-PRESSURE LEVEL SPECTRUM N = 6350 RPM, θ = 80°

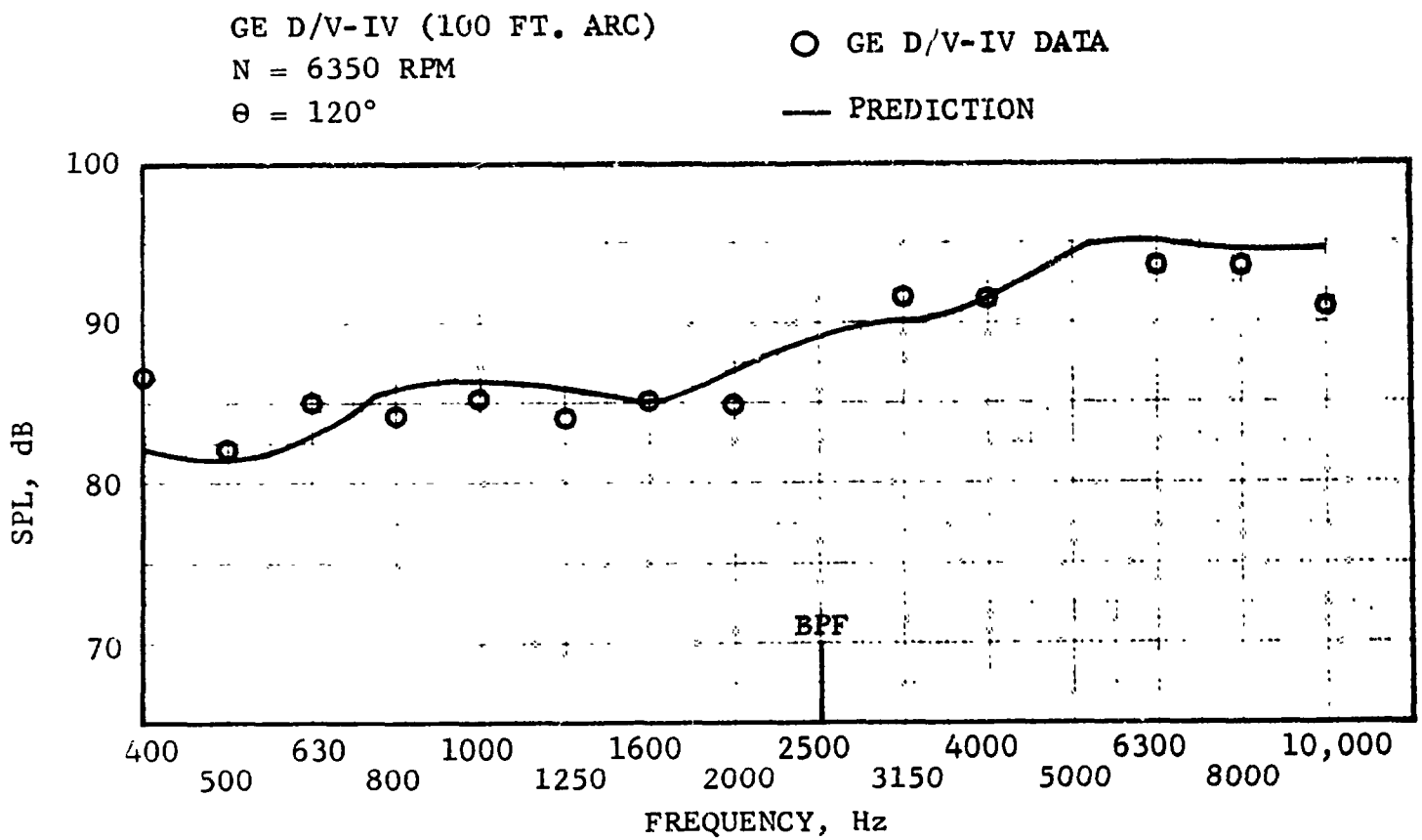

FIGURE VIII-B30 GE D/V-IV BROAD BAND NOISE SOUND-PRESSURE LEVEL SPECTRUM N = 6350 RPM, θ = 120°

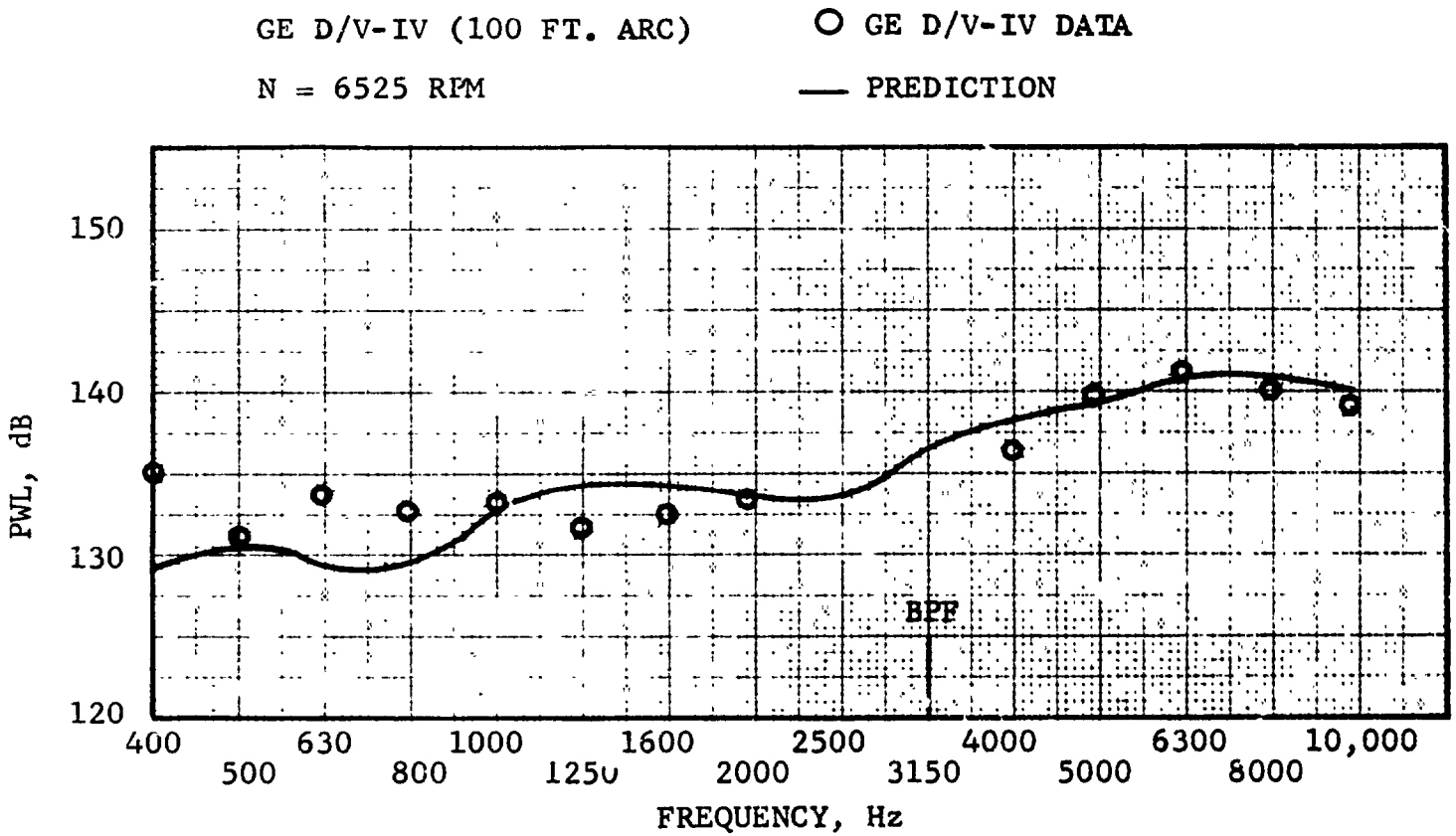

FIGURE VIII-B31 GE D/V-IV BROAD BAND NOISE POWER-LEVEL SPECTRUM N = 6525 RPM

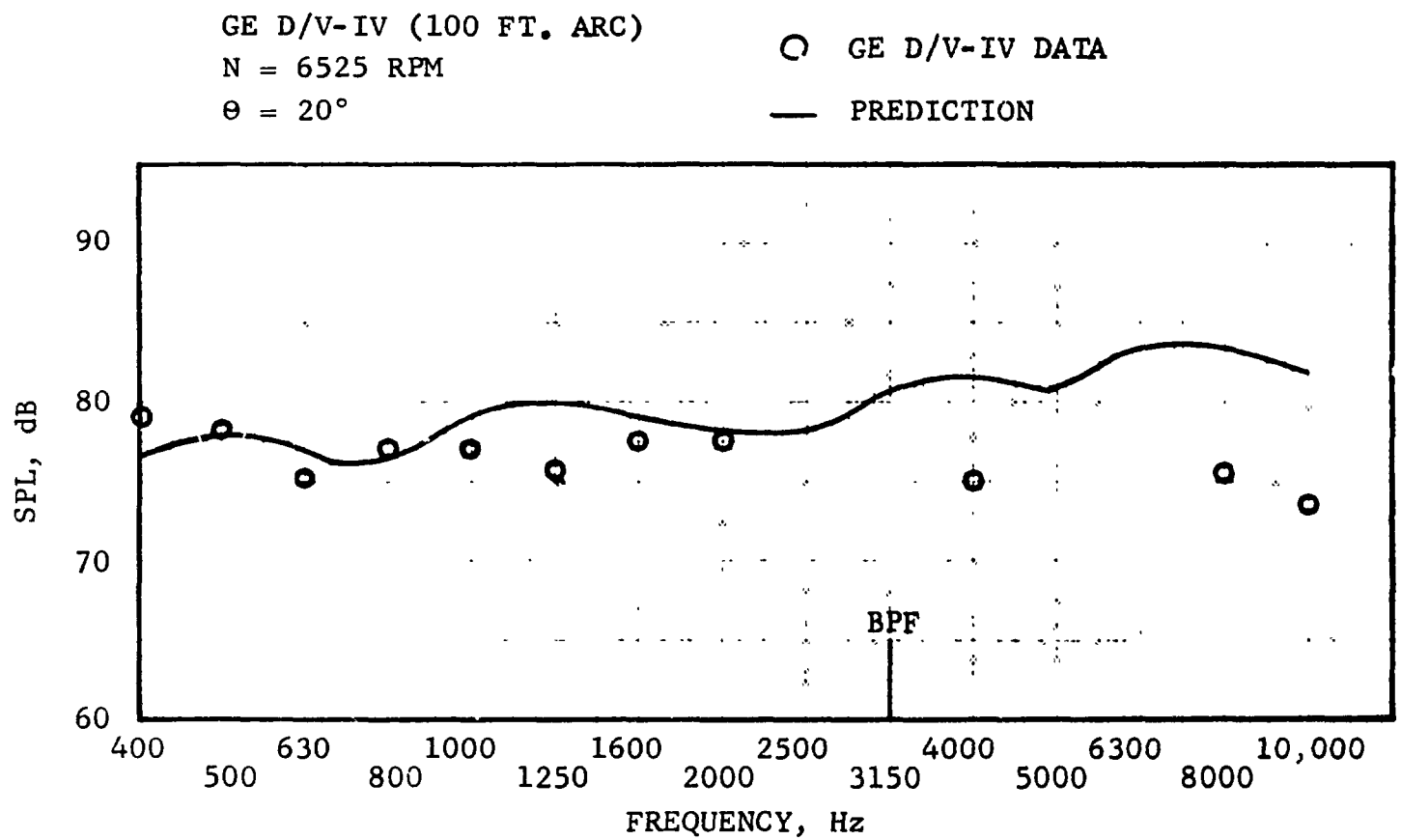

FIGURE VIII-B32 GE D/V-IV BROAD BAND NOISE SOUND-PRESSURE LEVEL SPECTRUM N = 6525 RPM, θ = 20°

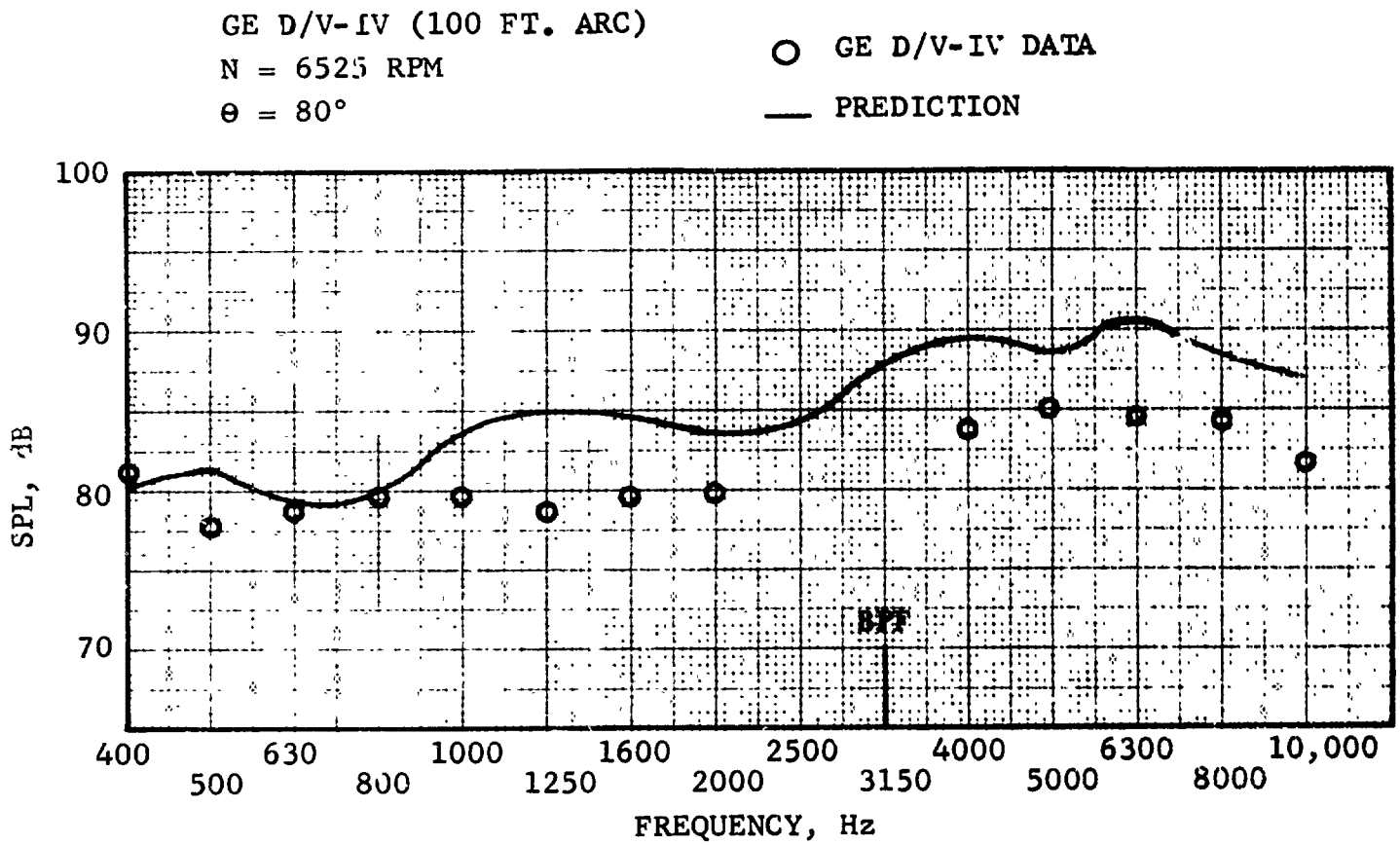

FIGURE VIII-B33 GE D/V-IV BROAD BAND NOISE SOUND-PRESSURE LEVEL SPECTRUM N = 6525 RPM, θ = 80°

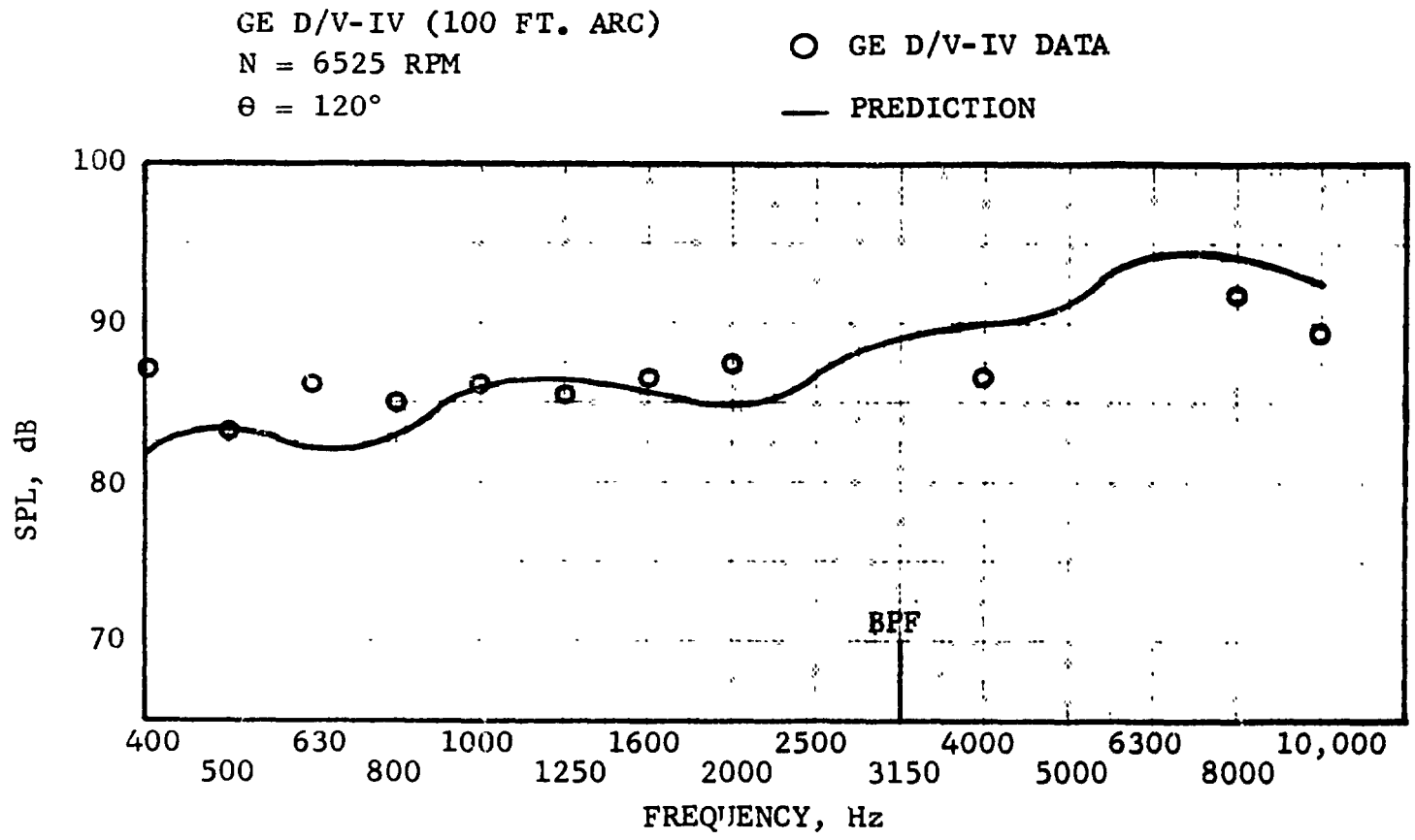

FIGURE VIII-B34 GE D/V-IV BROAD BAND NOISE SOUND-PRESSURE LEVEL SPECTRUM N = 6525 RPM, θ = 120°

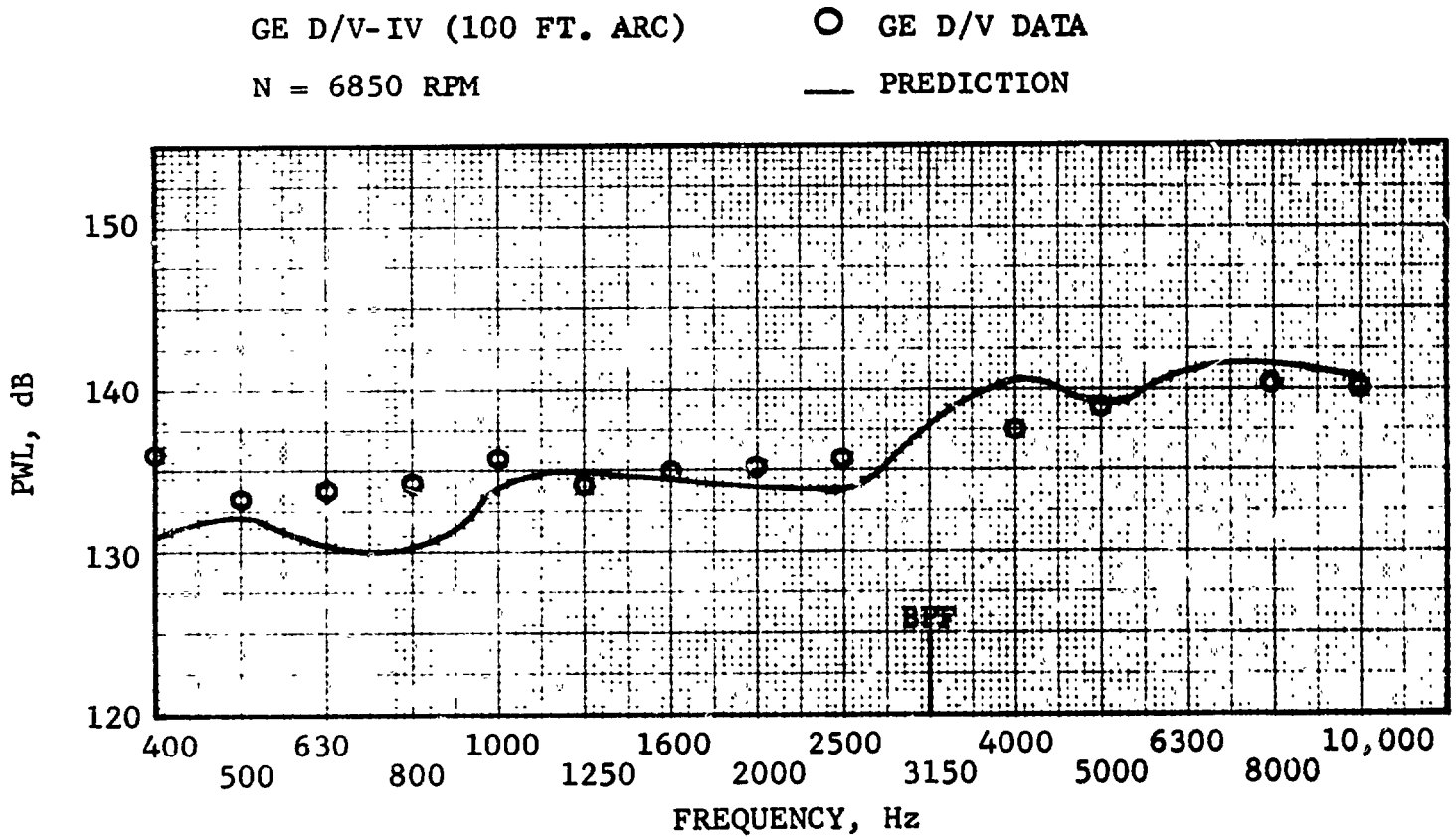

FIGURE VIII-B35 GE D/V-IV BROAD BAND NOISE POWER-LEVEL SPECTRUM N = 6850 RPM

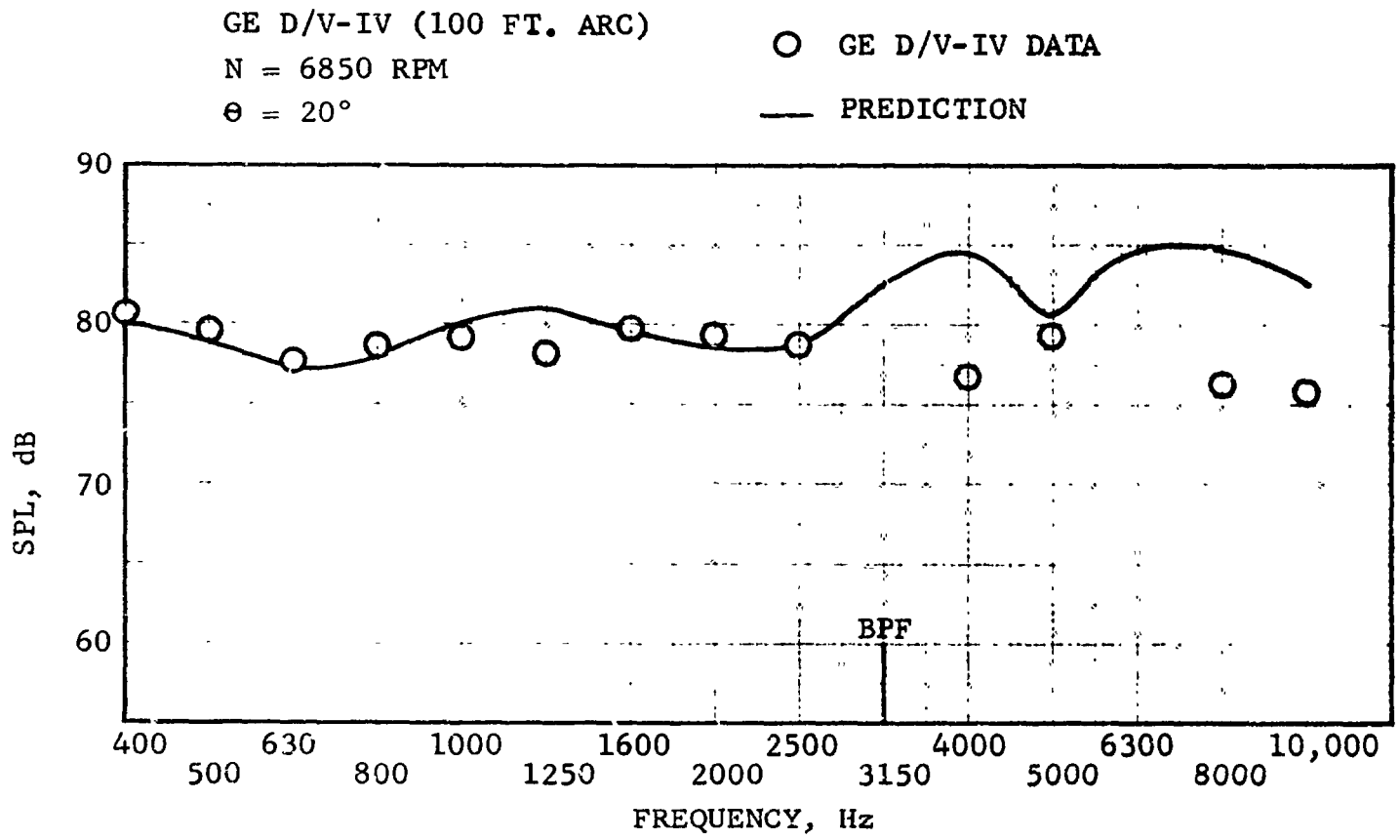

FIGURE VIII-B36 GE D/V-IV BROAD BAND NOISE SOUND-PRESSURE LEVEL SPECTRUM N = 6850 RPM, Θ = 20°

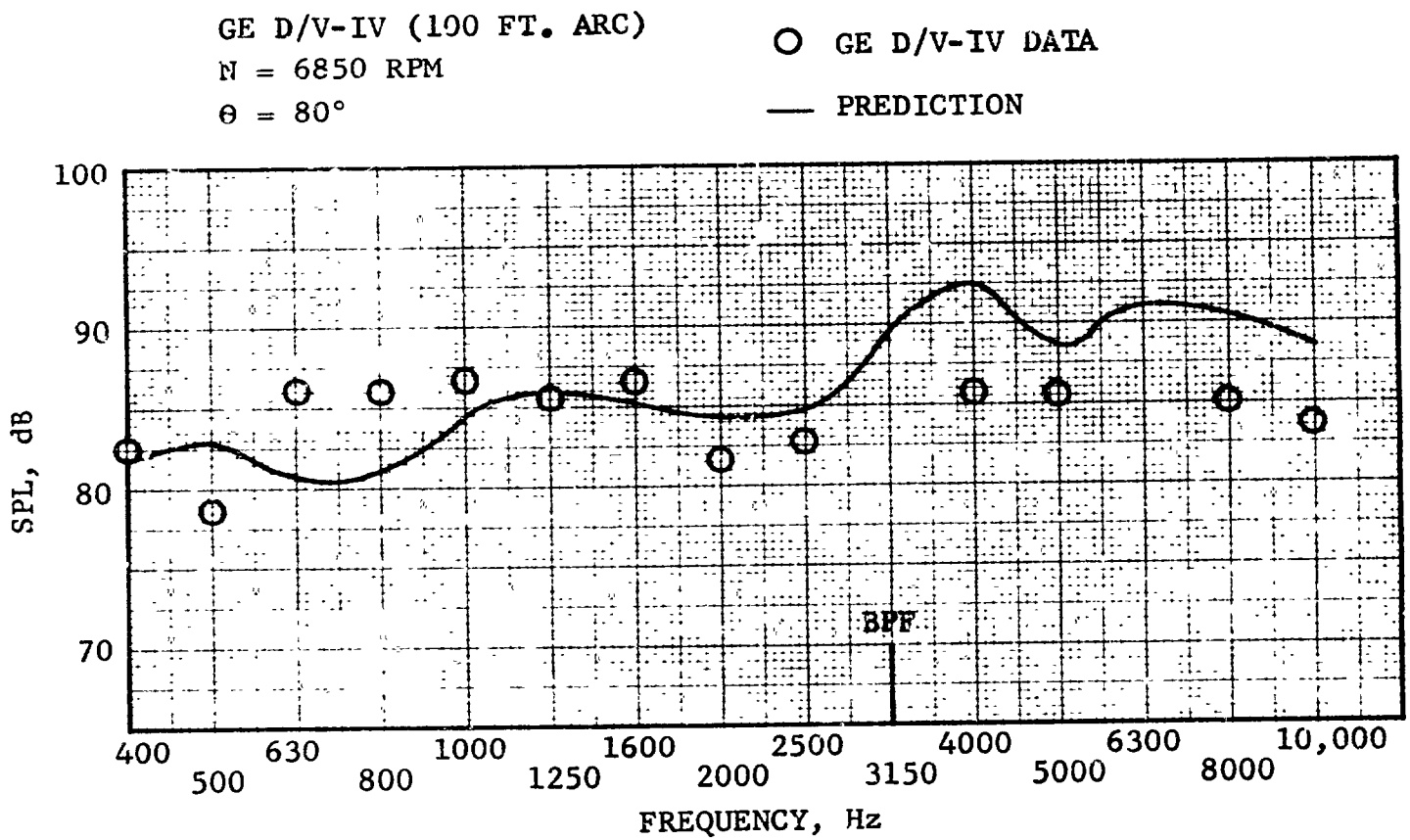

FIGURE VIII-B37 GE D/V-IV BROAD BAND NOISE SOUND-PRESSURE LEVEL SPECTRUM N = 6850 RPM, θ = 80°

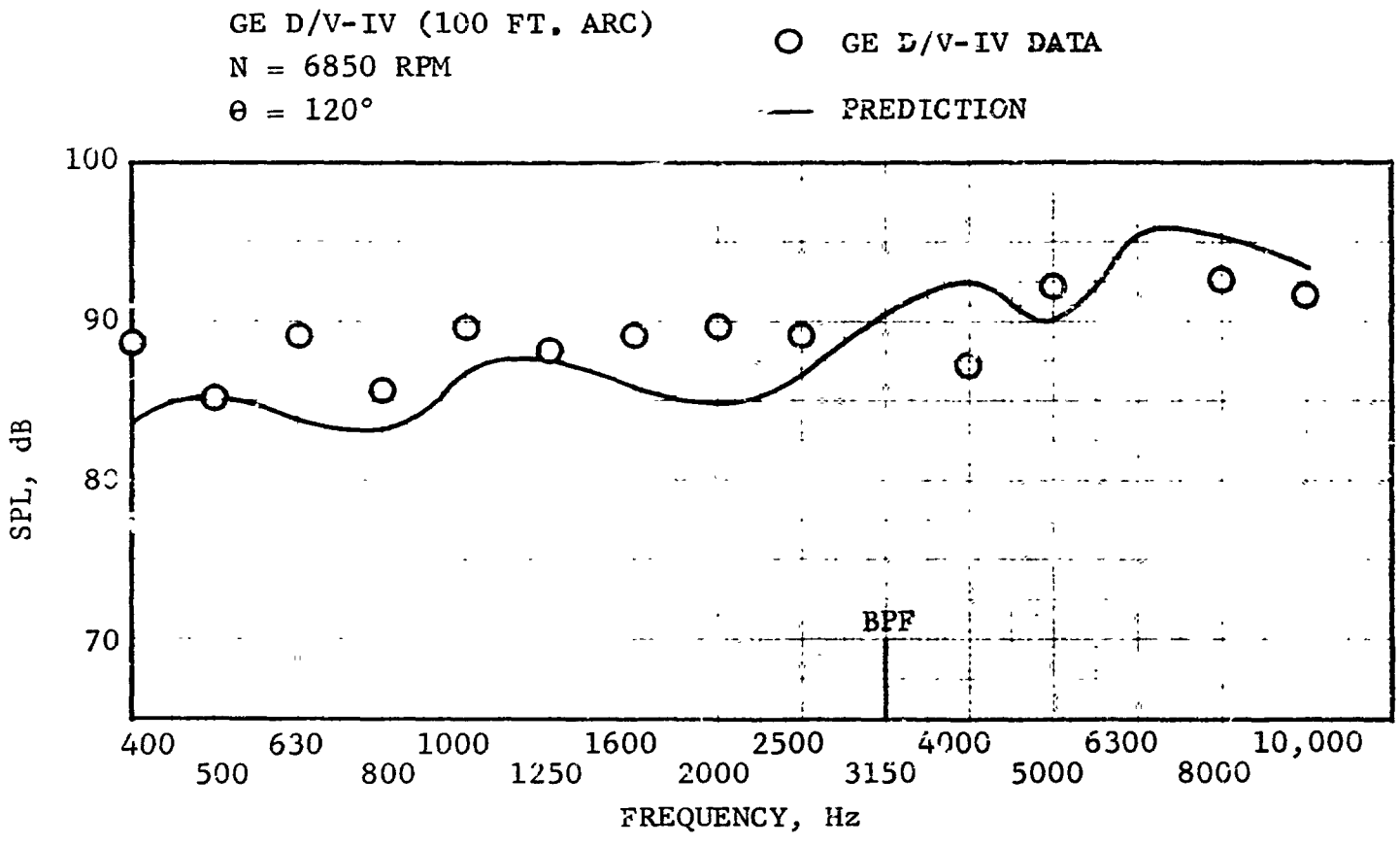

FIGURE VIII-B38 GE D/V-IV BROAD BAND NOISE SOUND-PRESSURE LEVEL SPECTRUM N = 6850 RPM, θ = 120°

For all the fan speeds considered, the power-level spectrums show a good comparison between the predicted broadband noise levels and the measured data.

(C) Verification of Size Parameter. A common practice in the design of fans and compressors is the building of scale models for use in test programs. These much less expensive scale models can be used to verify the performance of the final design. It is important, from an acoustic standpoint, to be able to project noise measurements recorded for the model in order to accurately predict the noise characteristics of the full-scale machine. With this end in mind, investigations have been carried out to determine the necessary acoustic scaling relationships.

The mechanisms derived in Section II indicate that in addition to physical similarity, scale models should be aerodynamically designed in such a manner that their Mach diagrams are identical to those of the full scale vehicle, at "scaled" rotor speeds. If the model and prototype are tested in the same gases (at essentially the same temperature), it can be seen that the identical Mach diagrams prescribe identical velocity diagrams. Thus, the only remaining difference between the two vehicles (at scaled speeds) is in their relative annular flow areas, which are directly proportional to their relative weight flow rates. The difference in pure tone sound power levels generated by the model and full scale vehicle would thus be expected to be functionally dependent on this weight flow ratio. For equal airflow densities, this becomes:

$$\Delta \text{ PWL} = 10 \log_{10} \frac{\dot{W} \text{ Prototype}}{\dot{W} \text{ Model}}$$

It is sometimes advantageous to test the model in a gas other than air. It is readily apparent that identical Mach diagrams then do not necessarily indicate identical velocity diagrams. The difference in acoustic power level thus becomes a function of the physical properties of the test gases as well as of the relative flow areas, and the simple weight flow relationship no longer holds. Studies of the Model Freon Compressor (Reference 1) have provided the derivation of the following scaling relationship for a model run in a different test gas (at scaled speeds):

$$\Delta \text{ PWL} = 20 \text{ Log}_{10} \frac{r_p}{r_m} + 5 \text{ Log}_{10} \frac{R_p}{R_m} + 15 \text{ Log}_{10} \frac{\gamma_p}{\gamma_m}$$

r = radius of rotor blade
R = gas constant
γ = ratio of specific heats

Subscripts:

m = model
p = prototype

These factors are employed in the pure tone noise prediction procedure, to project scale model predictions to those for the prototype. Figure VIII-C1 through 3 provide examples of their use.

Figure VIII-C1 is a plot of fundamental blade-passing PWL versus speed, for the CJ805-23 fan and the "scaled", CF700 fan. Both vehicles are described in Section VIII-A. Figure VIII-C1 presents both measured and predicted fundamental PWL's. The CF700 acoustic data and predictions were scaled to the CJ805-23 size by taking PWL's at equal blade tip Mach numbers then adding the " Δ PWL" calculated from the aforementioned relationships. (The scaled predictions are, of course, identical.) As can be seen, close agreement was achieved between scaled model data and the full size data; both sets of data, in turn, are very close to the predicted values.

A similar analysis was carried out for the TF39 "family" of fans (Reference Section VIII-A). The measured fundamental PWL's (second stage) for all vehicles were scaled to the full size TF39, and these data are presented in Figure VIII-C2 along with the predictions. The scaled data is seen to once again agree closely with the full size levels, as do the scaled predictions.

The TF39 scaling study was repeated, this time for the power levels recorded for the second harmonic of the blade-passing frequency. The results are presented in Figure VIII-C3. It is apparent that the scaling relationships apply equally well to the harmonic power levels as to the fundamental.

The scaling relationships examined in this study provide an accurate means of predicting pure tone noise levels for the full scale vehicle, from scale model data. The predictions are valid, regardless of the size of the model or the test flow medium employed.

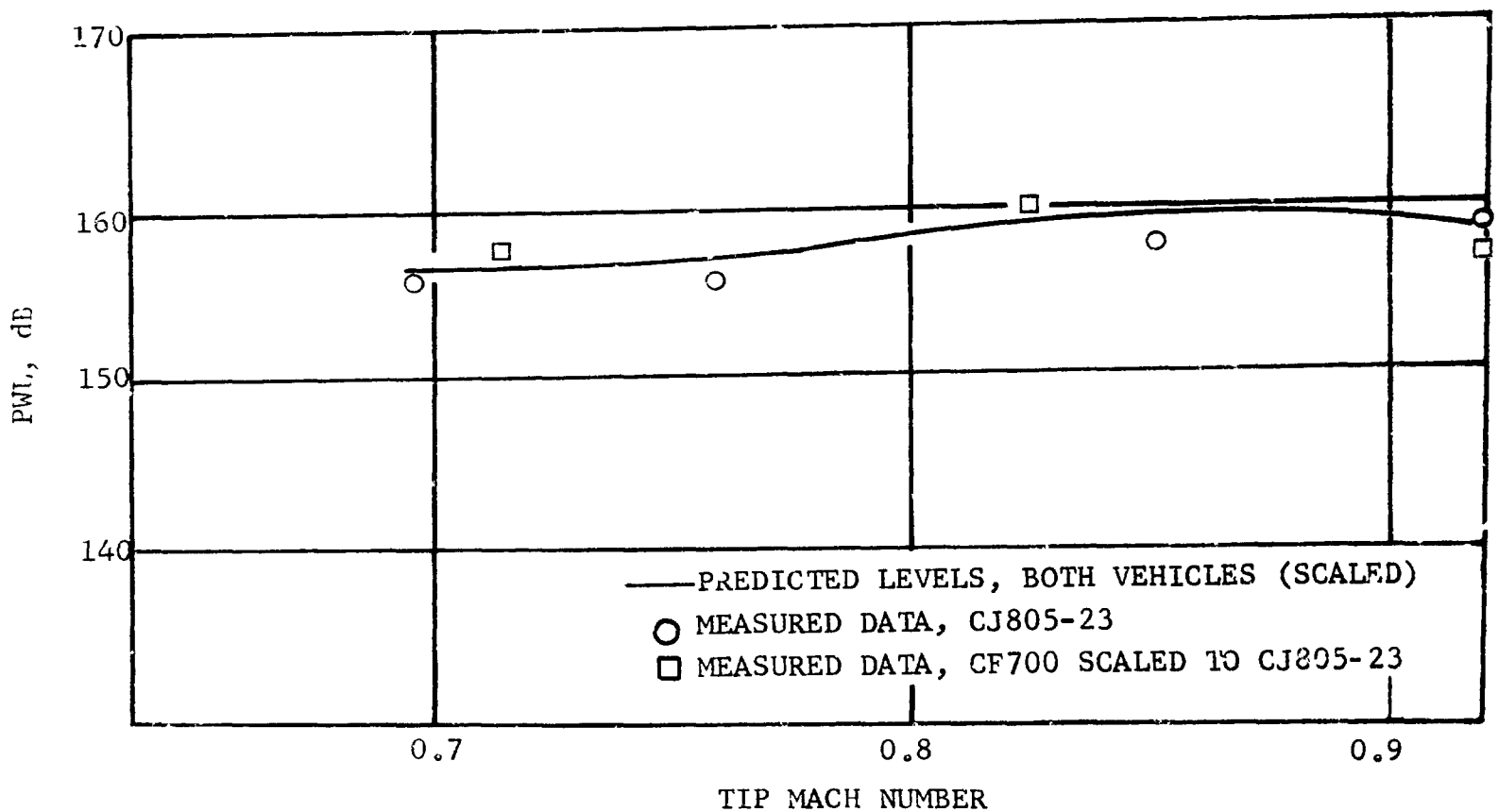

FIGURE VIII-C1 FUNDAMENTAL PWL - CJ805-23 AND CF700 SCALED TO CJ805-23 SIZE

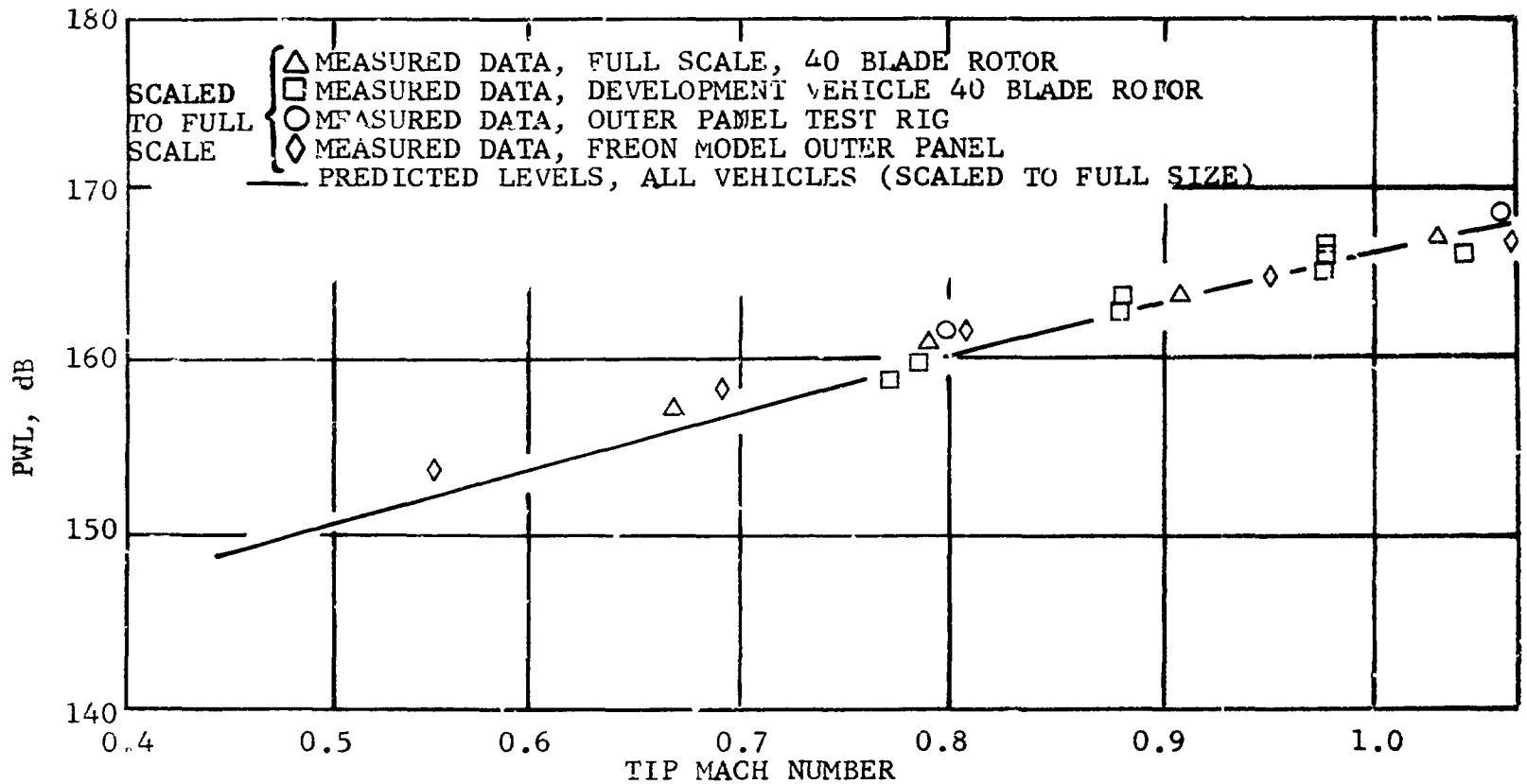

FIGURE VIII-C2 FUNDAMENTAL PWL - TF39 TEST VEHICLES - SCALED TO FULL SIZE TF39

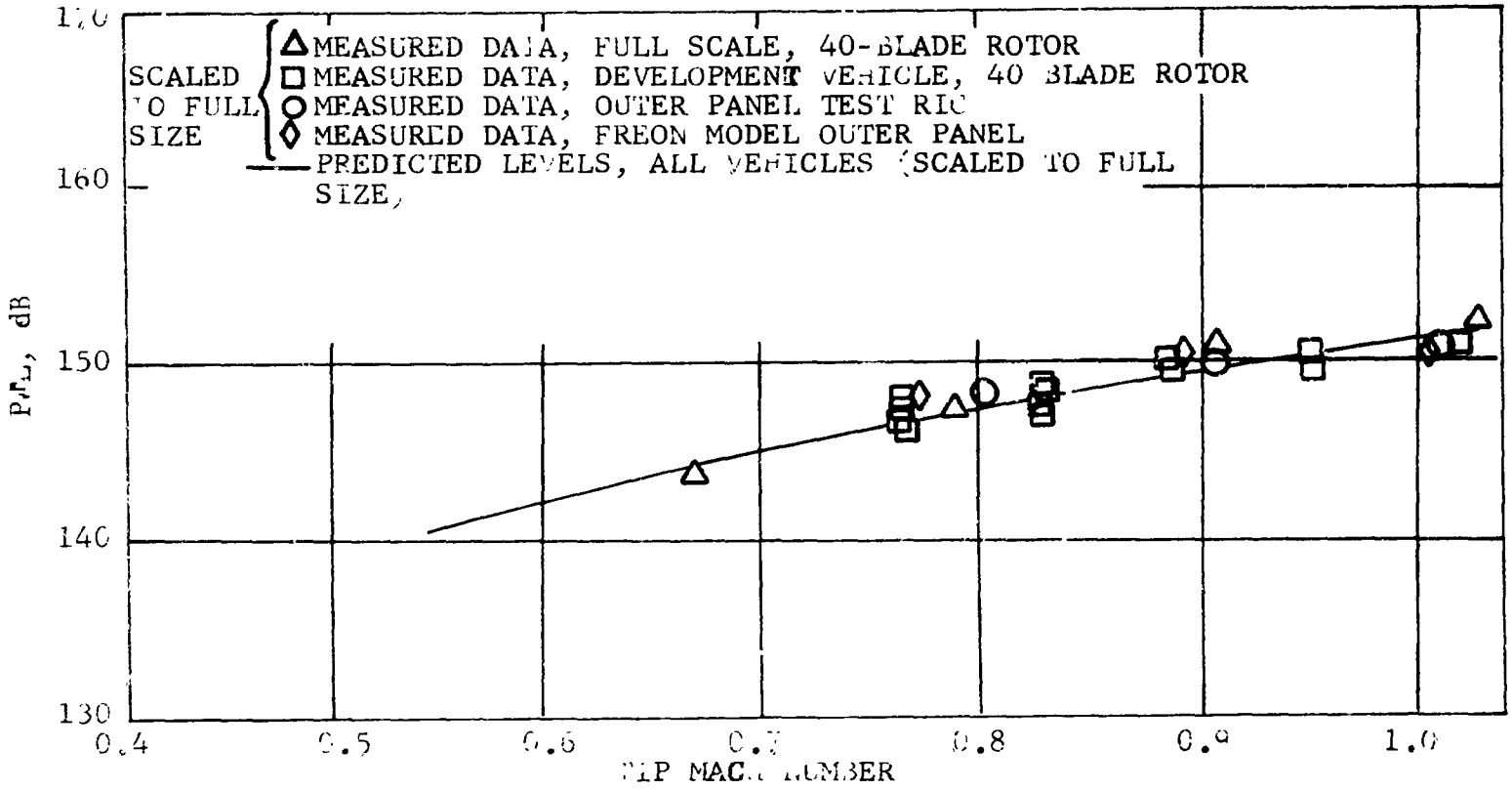

FIGURE VIII-C3 SECOND HARMONIC PWL - TF39 TEST VEHICLES - SCALED TO FULL SIZE TF39

REFERENCES SECTION VIII-C

1. Wells, R. J. and McGrew, J.M. "Model Freon Compressor Acoustical Studies," FAA Report FAA DS-68-5, February 1968.

IX. SEMI-EMPIRICAL PREDICTION OF COMPRESSOR NOISE

The basic mechanisms of compressor noise generation, transmission and radiation are the same as those which apply to fan noise. Accordingly, if the proper geometric and aerodynamic performance input parameters are known, it is possible to use the mechanisms developed in Sections II and III of this report to predict multi-stage compressor noise.

In the case of low speed single stage axial flow compressor, the pure tone mechanisms described in Section II are readily applied with good accuracy. This is shown in Section X of this report.

In the relatively simple case of pure tone noise from the first stage of a multi-stage compressor, analytical predictions can still be applied with a reasonable degree of success. This is also demonstrated in Section X. More comprehensive prediction of the noise radiated by the rear stages of high speed multi-stage compressors is, however, somewhat more difficult to establish. As described in Section VII, the aerodynamic data necessary to establish the prediction parameters is often not available. With multi-stage compressors, the problem is several times greater than that experienced with fans. In such vehicles, prediction of the effects of interstage flow and acoustic wave interactions, interstage pressure field interactions and transmission reflections through multiple blade row sets require analysis and/or data which is not available.

The most logical way to correlate compressor noise data is to do it with respect to parameters which are readily available in preliminary compressor design. Two such parameters are the tip relative Mach number (M_R) of the first stage of the compressor and the compressor's weight flow.

As with the fan correlation of Section VII the 1/3 octave power levels (PWL) were curve fitted using the polynomial:

$$PWL^* = \sum_{n=0}^{4} A_N \, (M_R)^N \qquad \text{(IX-A1)}$$

The coefficients for this equation for the 1/3 octave bands were obtained from the GE4 compressor data obtained in the farfield from 630 Hz to 10 KHz and are shown in Table XI-A1. Figures IX-A1 and IX-A2 show the data calculated with IX-A1 and the experimental data.

In each case the PWL's have been normalized by the weight flow such that

$$PWL^* = PWL - 10 \log_{10} (\dot{W}/\dot{W}_o) \qquad \text{(IX-A2)}$$

$$FWL^* \approx \sum_{N=0}^{4} A_N M_R^N$$

f	A_o	A_1	A_2	A_3	A_4
630	91.058	79.311	-179.656	108.157	0
800	102.333	39.660	-116.915	78.136	0
1000	109.840	17.787	- 77.741	57.915	0
1250	114.748	9.172	- 58.139	46.365	0
1600	116.487	13.914	- 54.684	41.064	0
2000	385.155	-1778.563	4177.288	-4093.420	1428.073
2500	172.424	- 288.921	440.144	- 194.199	0
3150	123.285	- 35.803	36.927	0	0
4000	116.453	23.082	54.339	39.681	0
5000	155.358	- 194.087	300.243	- 132.747	0
6300	129.121	- 63.327	93.290	- 33.517	0
8000	144.967	- 157.671	254.055	- 133.651	0
10000	143.165	- 149.727	238.787	- 105.258	0

TABLE IX-A1

Coefficient Table for Compressor Noise Power Level Prediction

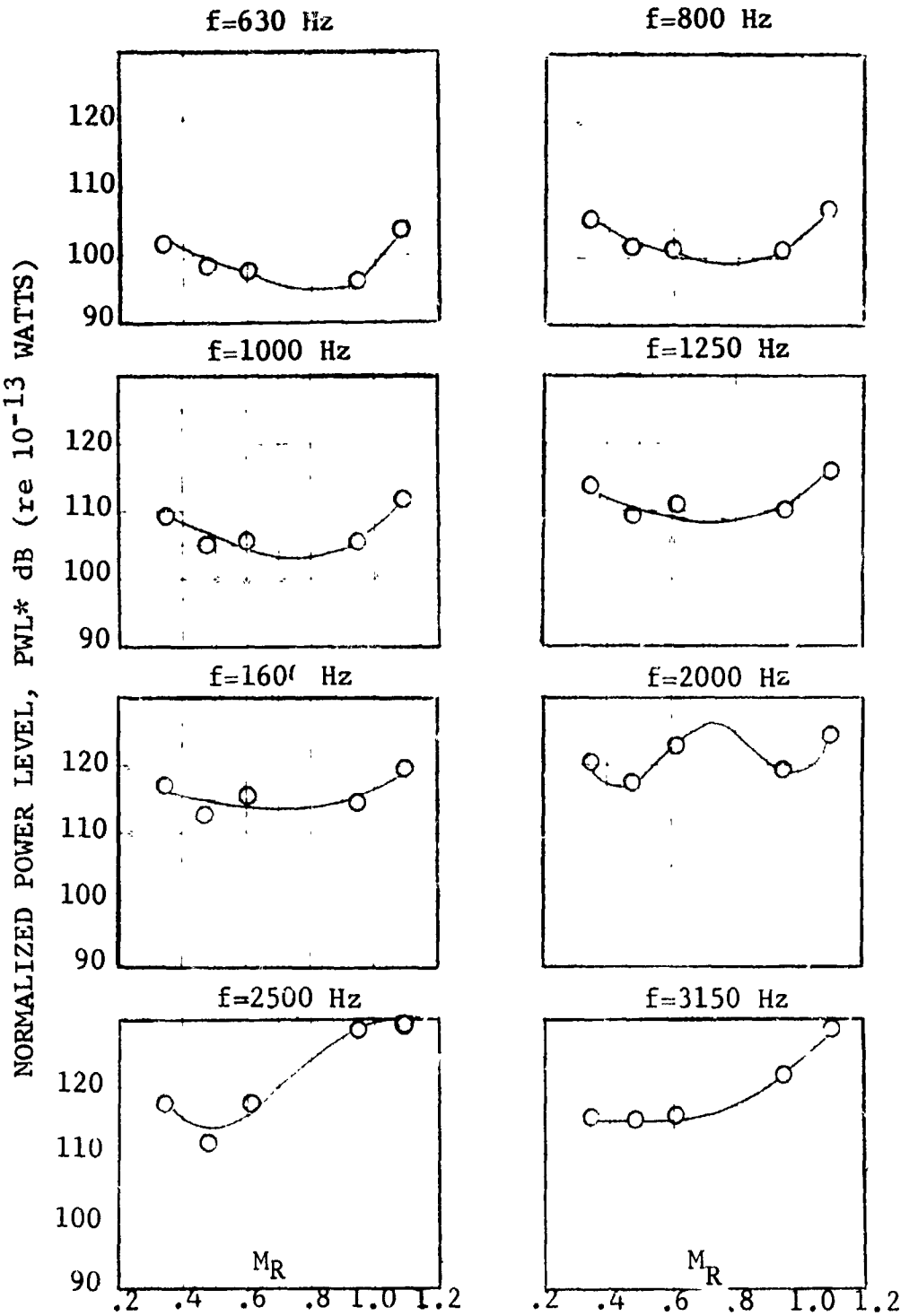

FIGURE IX-A1 NORMALIZED POWER LEVELS VERSUS M_R FOR VARIOUS 1/3 OCTAVE BAND CENTER FREQUENCIES

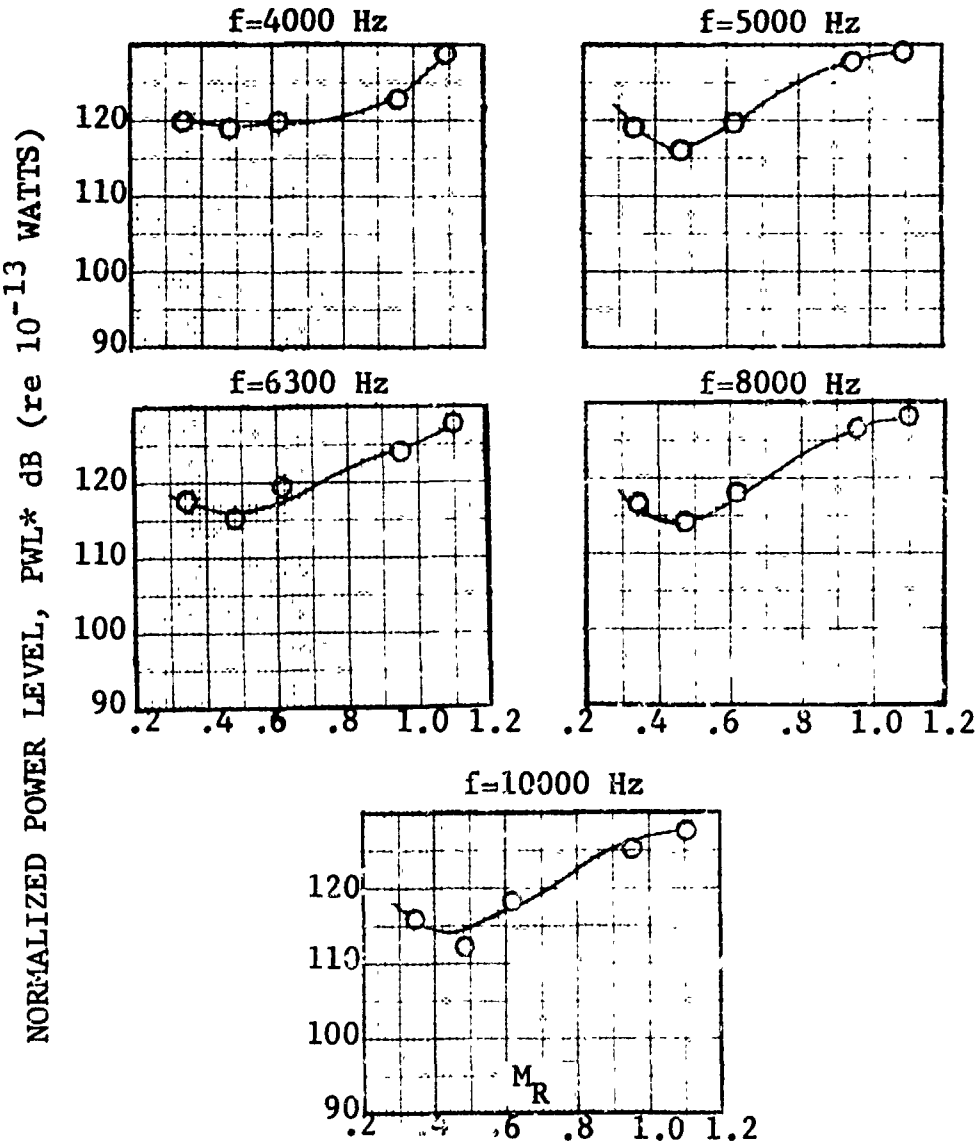

FIGURE 1X-A2 NORMALIZED POWER LEVELS VERSUS M_R FOR VARIOUS 1/3 OCTAVE BAND CENTER FREQUENCIES

where $\dot{W}$ is the weight flow of the various data used in the correlation and $\dot{W}_o$ is 1 lb/sec.

The power spectra are, of course, only part of the story. The power must be "spread" into a directivity pattern on an arc around the compressor. For this purpose a correlation has been made for directivity indices (D.I). The directivity index is defined as the difference between the measured SPL and a space averaged SPL. The space averaged SPL may be determined from the PWL as,

$$SPL_{av} = PWL - 10 \log (4\pi r^2) \qquad \text{(IX-A3)}$$

where r is the radius of the arc on which the noise level is desired <u>without</u> the effects of any attenuations such as that due to the air or any ground plane absorption. Both the SPL_{av} and the PWL in equation (IX-A3) are frequency dependent. The data of SAE ARP 866 can be used for air attenuation.

The actual SPL at any given angle can be determined from

$$SPL(f,\theta) = PWL^* (f) - 10 \log_{10} \dot{W} - 10 \log (4\pi r^2) \qquad \text{(IX-A4)}$$

$$+ D.I.(\theta)$$

The D.I.'s were correlated for a range of first stage tip relative Mach numbers from .35 to 1.09. The data for each frequency band was correlated from data for angles from 10 degress to 160 degrees in 10 degree increments. The equation used was

$$D.I. = A_o + A_1 \sin 1.5\theta + A_2 \cos 2\theta + A_3 \sin 2\theta$$

$$+ A_4 \cos^2 2\theta + A_5 \sin 1.5\theta \sin 2\theta \qquad \text{(IX-A5)}$$

The coefficients for each Mach number and frequency band are shown in Tables IX-A2 to IX-A6. The comparisons between calculated and measured data are shown in Figures IX-A3 to IX-A12. The data calculated with IX-A5 is obtained at discrete relative Mach numbers and will require interpolation to arrive at the specific Mach number desired. A linear interpolation, such as that shown in equation (IX-A6) is suitable.

$$D.I.\ (f,\theta)_{M_r} = \frac{M_r^+ - M_r}{M_r^+ - M_r^-}\ D.I.(f\theta)_{M_r^-} - D.I.(f,\theta)_{M_r^+} + D.I.(f,\theta)_{M_r^+} \qquad \text{(IX-A6)}$$

where

M_r = Tip relative Mach number at which D.I.(f,θ) is desired.

M_r^- = Tip relative Mach number just below M_r in Tables IX-A2 to IX-A6.

M_r^+ = Tip relative Mach number just above M_r in Tables IX-A2 to IX-A6.

$D.I.(f,\theta)_{M_r^-}$ = Directivity index as determined from equation IX-A5 at Mach number M_r^-.

$D.I.(f,\theta)_{M_r^+}$ = Directivity index as determined from equation IX-A5 at Mach number M_r^+.

The application of the D.I. found in Equation (IX-A5) to Equation (IX-A6) results in the prediction of a 1/3 octave spectra at each angle; however it is most likely that the frequency of the various components of the spectra are not yet compatible with the compressor whose noise level is being predicted. Scaling for frequency can be handled by shifting the 1/3 octave spectrum by the difference between the blade passing frequency of the first stage of the compressor being considered and the corresponding reference blade passing frequency of the correlated data. Figure IX-A13 indicates the tip relative Mach number versus reference blade passing frequency for the correlated data. Thus, for example suppose the blade passing frequency (BPF) of the first stage is 4000 Hz at $M_R = 1.0$ From Figure IX-A13 at $M_r = 1.0$ the reference BPF is 2660 Hz. That is, the compressor being predicted is in the 4 KHz 1/3 octave band and the reference frequency is in the 2.5 KHz band; therefore the frequency shifting of the predicted spectra (from Equation IX-A4) is two 1/3 octave bands up. That is, all the SPL's predicted by Equation (IX-A4) are indexed up two 1/3 octave bands.

$$D.I. = A_o + A_1 \sin 1.5\theta + A_2 \cos 2\theta + A_3 \sin 2\theta$$

$$+ A_4 \cos^2 2\theta + A_5 \sin 1.5\theta \sin 2\theta$$

f	A_1	A_2	A_3	A_4	A_5	A_6
630	2.255	8.8084	7.7390	- 2.6628	- 4.3337	- 6.9789
800	.9207	10.6488	8.7751	- 3.585[illegible]	- 3.4498	- 6.1865
1000	- .3257	12.7055	9.9286	- 4.85[illegible]3	- 2.7476	- 5.2026
1250	-1.8089	14.8687	11.0745	- 6.1007	- 1.9714	- 4.1571
1600	1.2147	9.0903	8.1874	- .9045	- [illegible].9033	- 6.4497
2000	-4.8067	17.5589	12.7426	- 5.1683	- .6566	- 4.5025
2500	-14.6484	31.0667	18.7949	-18.0481	6.8868	4.2273
3150	5.9820	1.9490	4.3595	3.1827	- 5.1894	-10.8703
4000	12.1398	- 4.4720	1.9914	9.7863	-10.8500	-17.7690
5000	14.2436	- 6.0790	.1279	9.3138	-12.7208	-19.7954
6300	8.8670	- .3277	3.2616	3.7231	- 7.4987	-14.4182
8000	5.3952	2.0414	4.5474	.7623	- 3.7237	-[illegible].3915
10000	5.8034	.1481	2.9077	1.1791	- 5.1920	- 8.7171

TABLE IX-A2

Coefficient Table for Compressor Directivity Indices

$M_R = .35$

$$D.I. = A_o + A_1 \sin 1.5\theta + A_2 \cos 2\theta + A_3 \sin 2\theta$$

$$+ A_4 \cos^2 2\theta + A_5 \sin 1.5\theta \sin 2\theta$$

f	A_o	A_1	A_2	A_3	A_4	A_5
630	-10.1540	19.0277	6.9371	-13.2974	3.1016	7.7781
800	- 8.2156	18.1126	7.4738	-11.4055	2.1461	5.1436
1000	- 6.2909	16.9501	7.9313	- 9.4921	1.1415	2.3978
1250	- 4.6541	16.1861	8.5038	- 7.6932	.0118	- .1928
1600	- 1.7234	13.1642	8.1989	- 4.1447	- 2.0977	- 4.1319
2000	.2280	11.4590	8.4365	- 1.4254	- 3.7014	- 7.8002
2500	10.3282	- 1.1406	2.6684	7.7667	- 9.9849	-15.6687
3150	5.5931	2.7608	3.9441	3.9164	- 5.3528	-11.0228
4000	4.0020	6.3698	6.5063	1.9610	- 3.8199	-11.9135
5000	- .4426	10.0848	6.7236	- 6.0509	- 1.2158	- 4.0095
6300	- 1.4406	12.2328	8.6187	- 6.9190	- .1119	- 4.1951
8000	- .0578	8.5616	6.3940	- 4.2200	- .7005	- 4.3971
10000	.5437	5.5359	4.3885	- 3.1634	- 1.4455	- 2.9825

TABLE IX-A3

Coefficient Table for Compressor Directivity Indices

$M_R = 0.48$

$$D.I. = A_o + A_1 \sin 1.5\theta + A_2 \cos 2\theta + A_3 \sin 2\theta$$

$$+ A_4 \cos^2 2\theta + A_5 \sin 1.5\theta \sin 2\theta$$

f	A_o	A_1	A_2	A_3	A_4	A_5
630	26.9497	-27.0112	- 6.8965	24.4[illegible]	-20.5382	-30.3101
800	20.5041	-1[illegible].8592	- 2.1037	16.5[illegible]78	-16.7684	-24.398[illegible]
1000	15.8747	- [illegible].6823	.9643	11.8[illegible]5	-13.5310	-20.3252
1250	7.5821	2.8250	5.4264	3 4[illegible]55	- 8.2778	-12.6247
1600	- .6128	13.3704	9.3294	- [illegible].1120	- 3.2742	- 5.3922
2000	-17.3591	35.5341	19.9540	-[illegible]0.6502	6.7971	6.0262
2500	-18.0760	34.8565	19.5933	-21.2382	8.5588	7.9331
3150	7.9203	- 2.0806	2.5763	6.5595	- 6.0605	-12.2950
4000	14.1891	- 8.9672	- .1814	14.1395	-11.64540	-18.9440
5000	14.1596	- 7.7898	- 1.1078	11.1042	-12.6665	-17.7372
6300	7.8332	- .4286	1.4187	4.2643	- 8.0380	-11.2750
8000	5.3007	3.3479	3.4783	.8482	- 5.7712	- 9.5669
10000	9.7613	- 5.1978	- 1.1816	6.9207	- 8.6088	-12.4767

TABLE IX-A4

Coefficient Table for Compressor Directivity Indices

$M_R = .61$

$$D.I. = A_o + A_1 \sin 1.5\theta + A_2 \cos 2\theta + A_3 \sin 2\theta$$

$$+ A_4 \cos^2 2\theta + A_5 \sin 1.5\theta \sin 2\theta$$

f	A_o	A_1	A_2	A_3	A_4	A_5
630	- 8.9686	13.5477	6.3445	-11.2108	5.6640	8.1304
800	- 7.5695	12.2524	5.9222	- 9.6746	4.9896	6.1408
1000	- 6.6617	10.7516	5.2935	- 8.0211	4.8095	4.9729
1250	- 6.1887	9.9517	4.9436	- 7.0288	4.9136	4.0654
1600	- 4.5092	8.1632	4.2966	- 4.9338	3.9503	1.7913
2000	1.5713	- 2.3546	- 1.1173	3.8264	- .0731	- 3.1351
2500	- 7.0328	13.1167	9.7105	- .9355	- 2.5734	- 5.6797
3150	9.1695	- 6.3610	- 1.5721	8.4161	- 6.1453	-13.3345
4000	16.6994	-21.7983	-10.7712	19.3683	-11.8539	-18.6154
5000	14.9300	- 9.2674	- 1.7108	14.9458	-14.2170	-19.1561
6300	2.8488	- .4303	- .9265	1.6617	- 2.9331	- 5.8828
8000	.6204	7.4318	5.1692	- .9635	- .9929	- 6.0634
10000	16.7360	-19.2541	- 7.5308	18.4456	-10.7421	-19.4379

TABLE IX-A5

Coefficient Table for Compressor Directivity Indices

$M_R = .95$

$$D.I. = A_0 + A_1 \sin 1.5\theta + A_2 \cos 2\theta + A_3 \sin 2\theta$$

$$+ A_4 \cos^2 2\theta + A_5 \sin 1.5\theta \sin 2\theta$$

f	A_0	A_1	A_2	A_3	A_4	A_5
630	- 4.2870	5.4685	3.8490	- 4.4687	4.3464	2.2410
800	- 1.7651	2.9986	2.7701	- 1.4986	2.0958	- .0441
1000	3.9207	- 4.8214	- .3461	5.8085	- 1.5100	- 5.2295
1250	5.6198	- 5.6782	- .8018	7.5108	- 3.4831	- 6.9424
1600	8.0230	- 7.6669	- 1.7510	10.3976	- 6.0728	- 9.7671
2000	8.7986	- 7.3551	- 1.7723	11.0371	- 7.5537	-10.9422
2500	9.3096	- 4.8031	.6451	11.1482	- 8.9343	-13.8721
3150	10.4953	- 7.9768	- 1.6374	11.9229	- 8.2782	-14.0221
4000	17.7885	-25.7920	-12.6438	21.4618	-12.1552	-18.7621
5000	14.0283	-11.9904	- 4.3371	13.1416	-11.5241	-16.4060
6300	5.5782	- 2.3120	.0995	4.1858	- 4.8623	- 7.5810
8000	6.8321	- 4.8311	- .4866	6.2383	- 4.9810	- 8.3562
10000	9.0967	-13.5881	- 5.8123	11.2285	- 5.6833	- 8.6756
500	- 6.4821	6.0234	4.2513	- 6.2550	6.7496	4.5338

TABLE IX-A6

Coefficient Table for Compressor Directivity Indices

$M_R = 1.09$

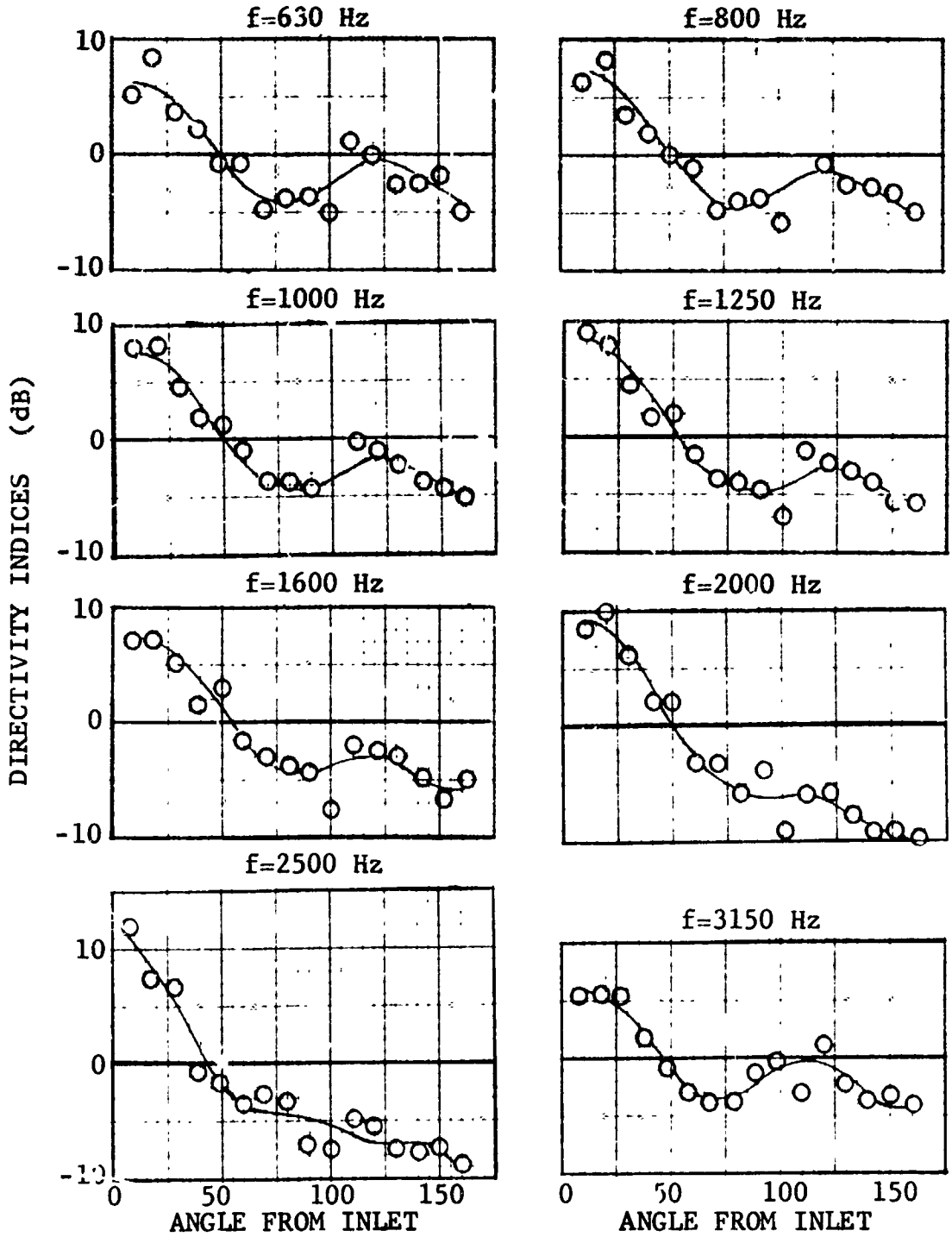

FIGURE IX-A3 DIRECTIVITY INDEX VERSUS ANGULAR POSITION FOR M_R=.35

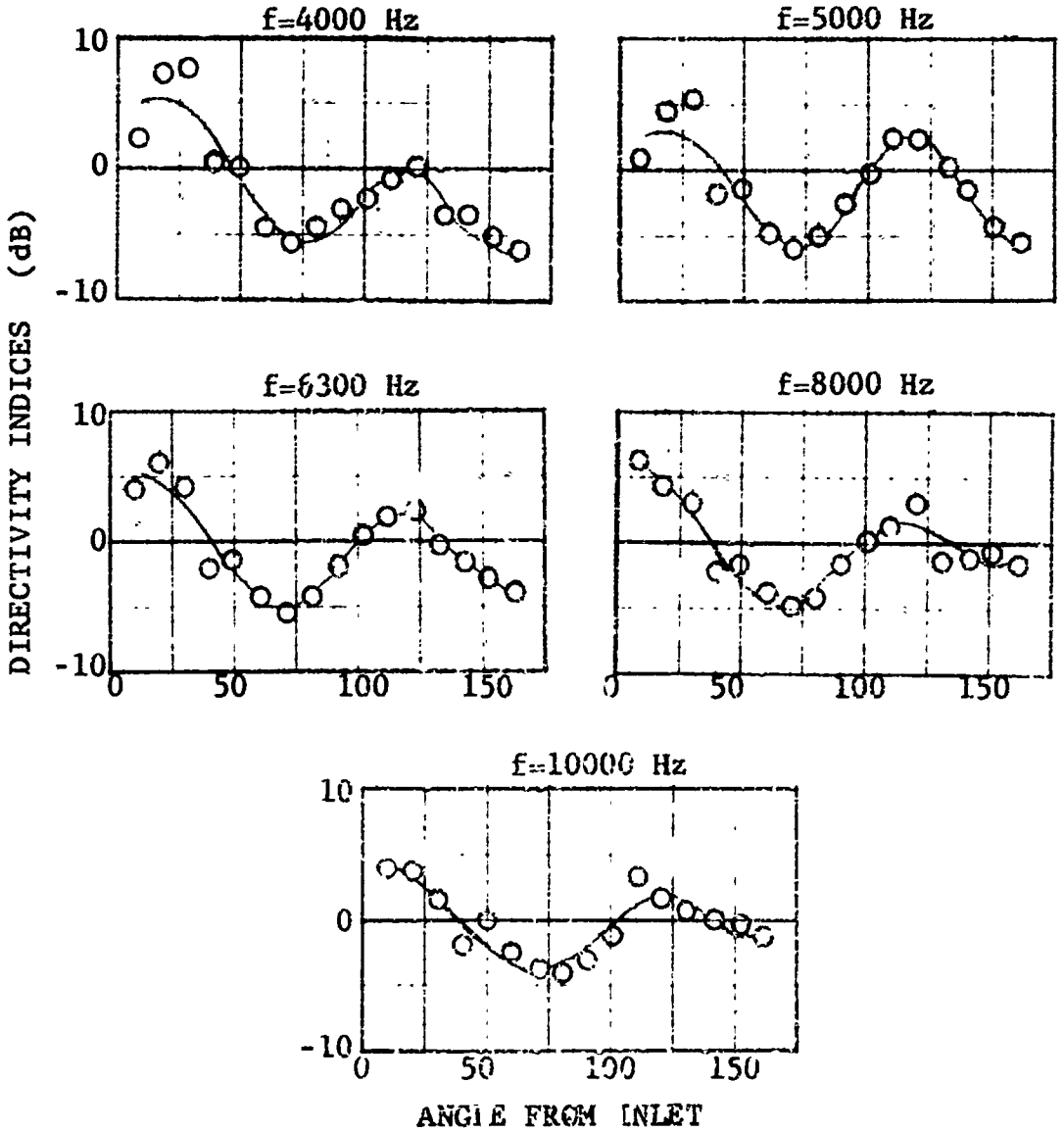

FIGURE IX-A4 DIRECTIVITY INDEX VERSUS ANGLAR POSITION FOR M_R=.35

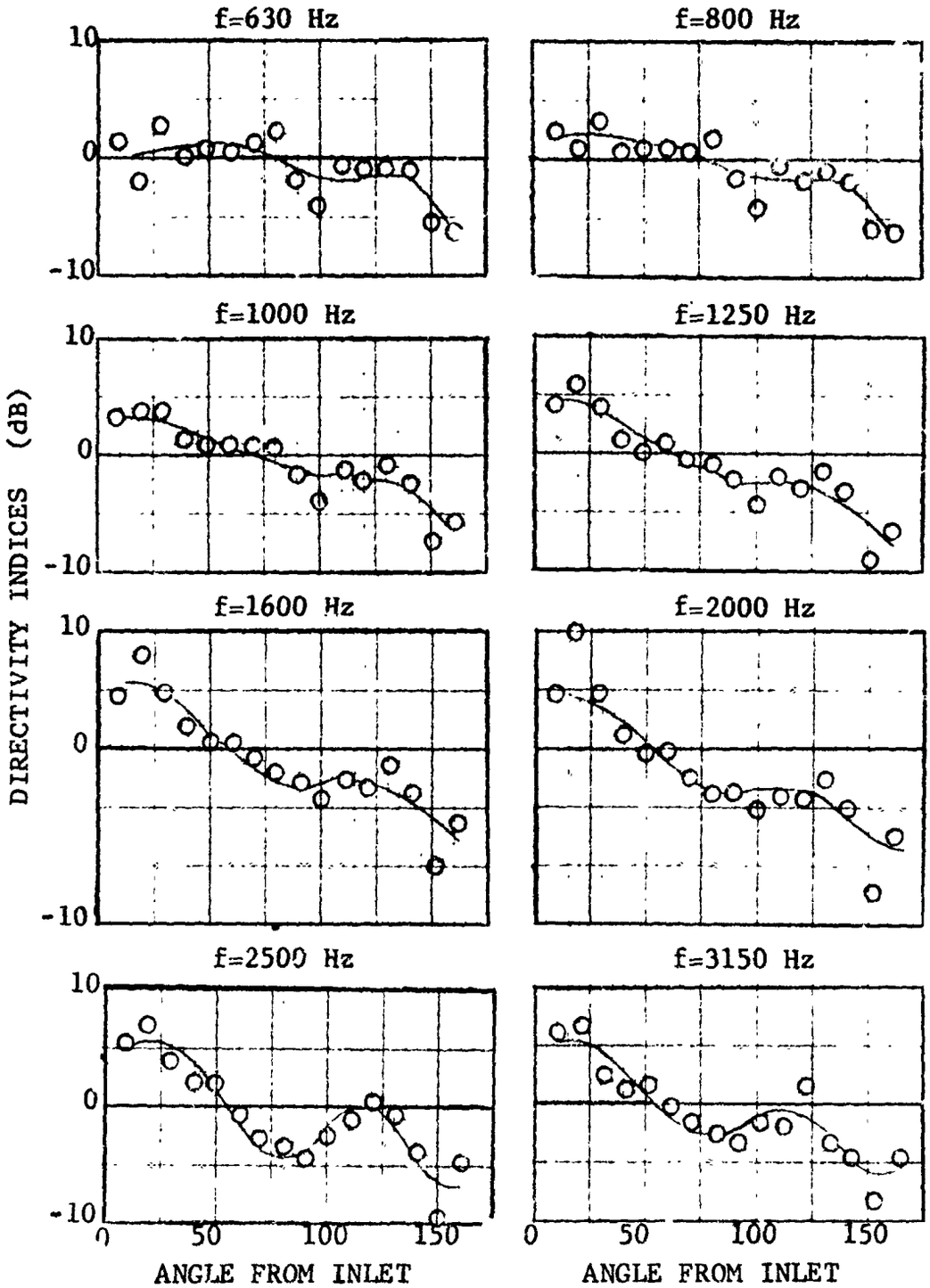

FIGURE IX-A5 DIRECTIVITY INDEX VERSUS ANGULAR POSITION FOR M_R=.48

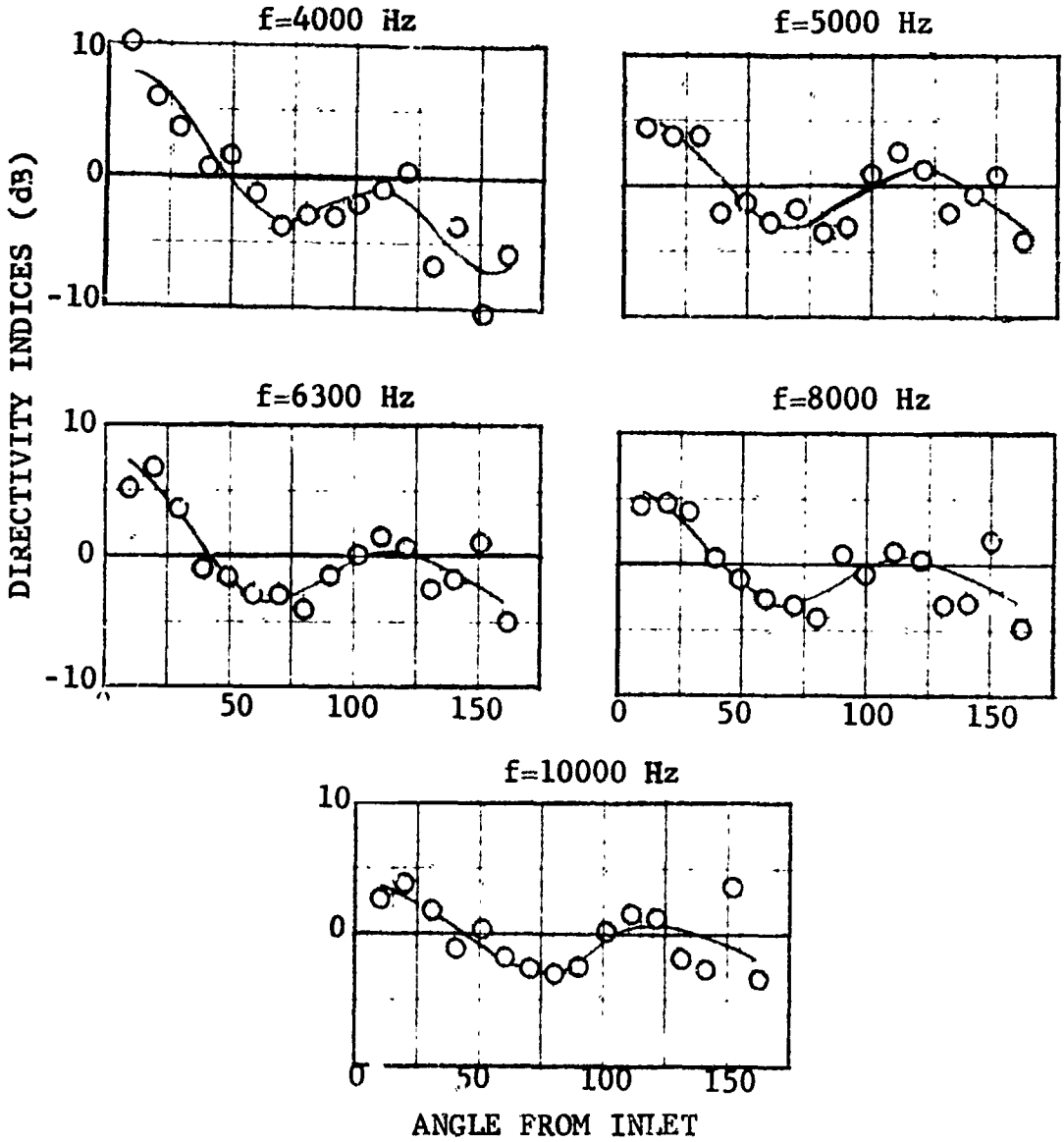

FIGURE IX-A6 DIRECTIVITY INDEX VERSUS ANGULAR POSITION FOR M_R=.48

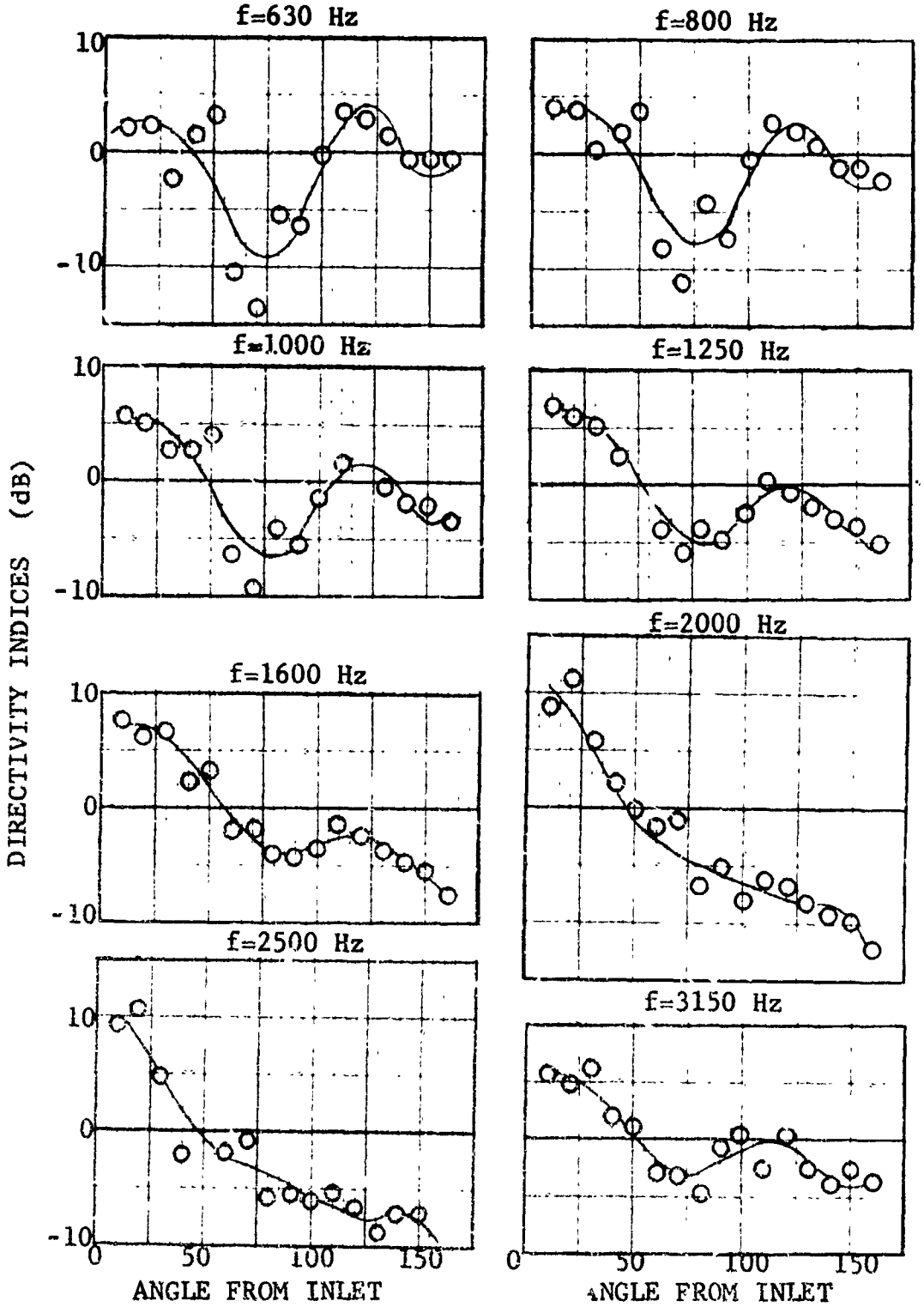

FIGURE IX-A7 DIRECTIVITY INDEX VERSUS ANGULAR POSITION FOR M_R=.61

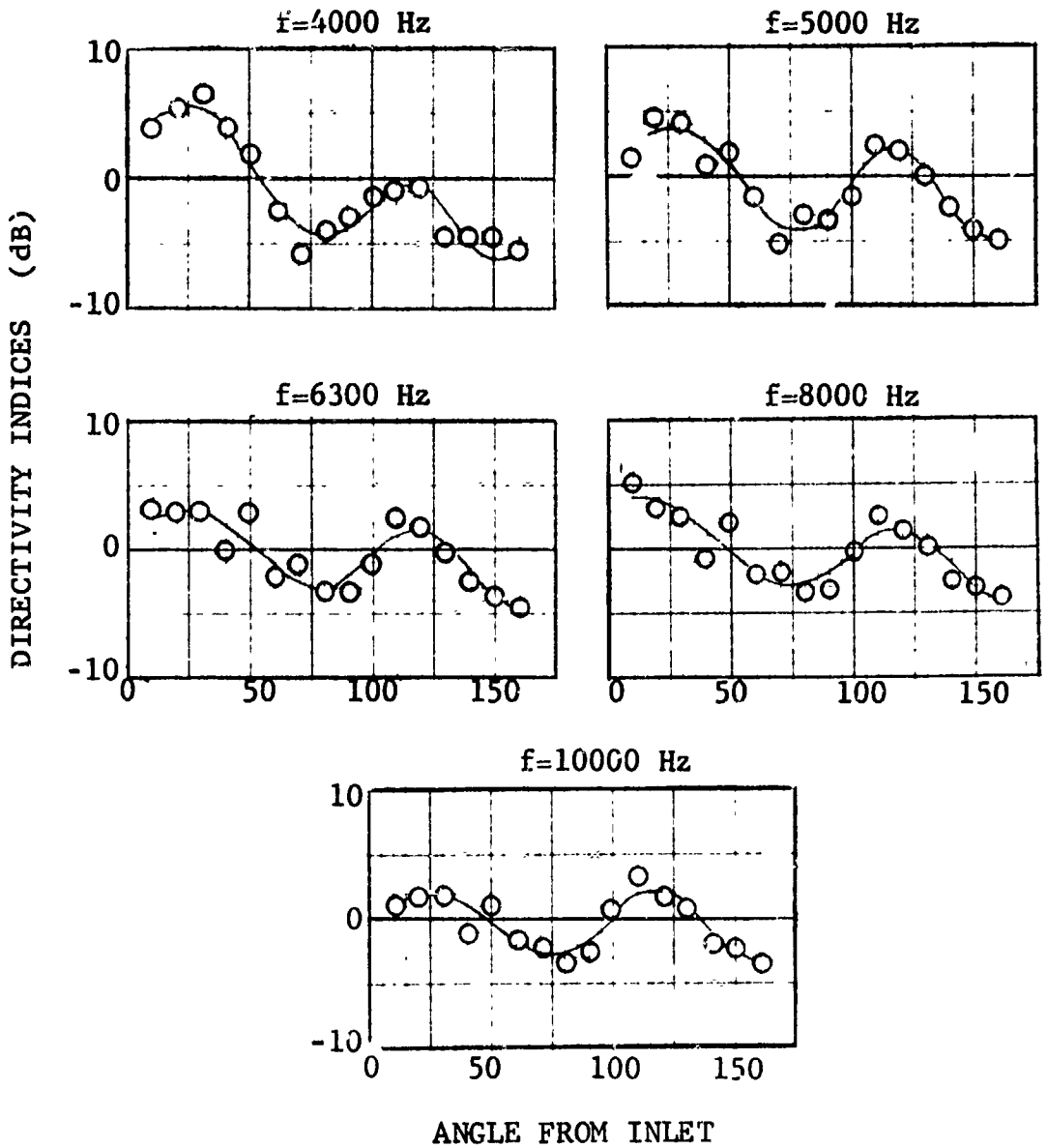

FIGURE IX-A8 DIRECTIVITY INDEX VERSUS ANGULAR POSITION FOR M_R=.61

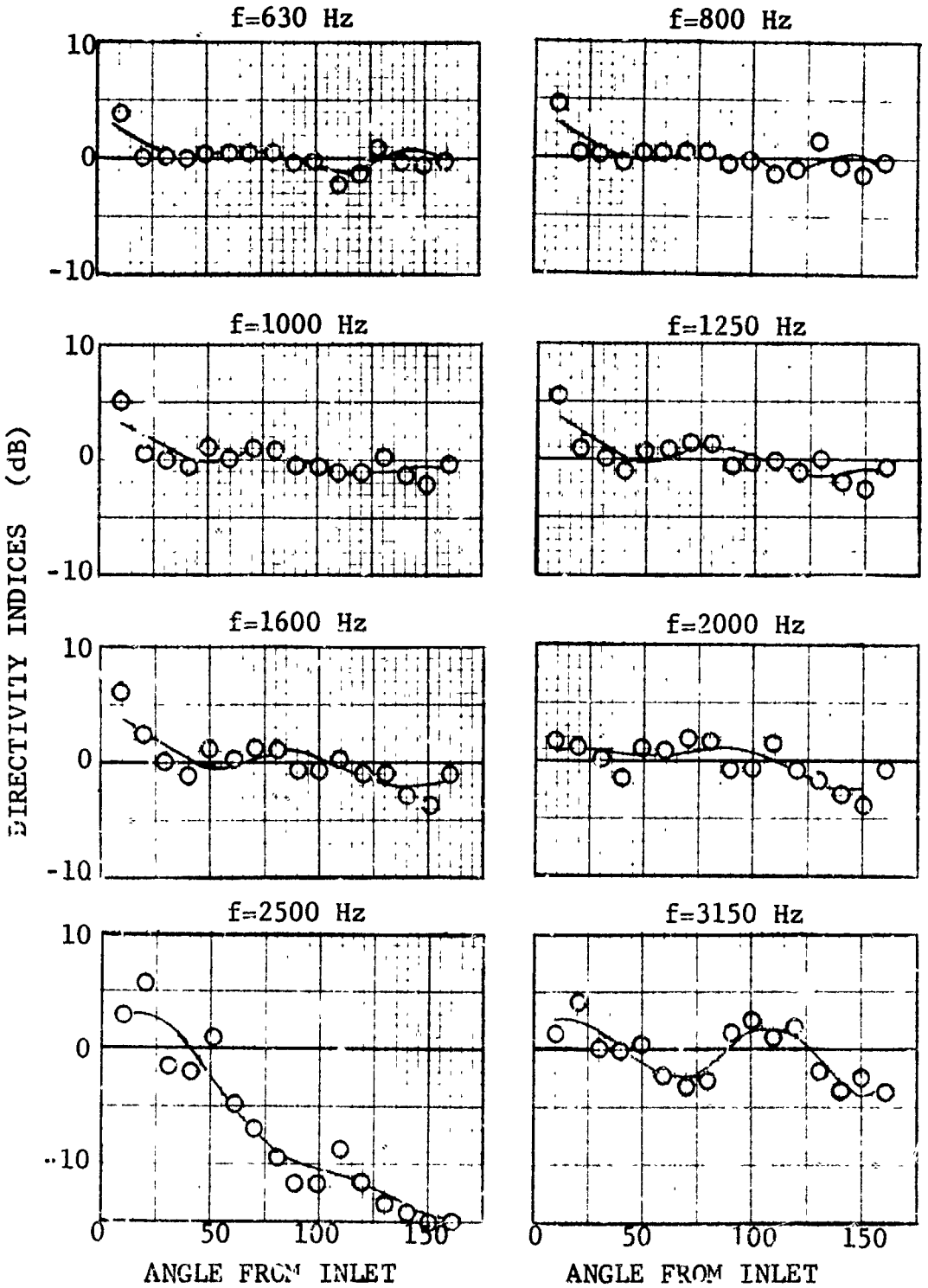

FIGURE IX-A9 DIRECTIVITY INDEX VERSUS ANGULAR POSITION FOR M_R=.95

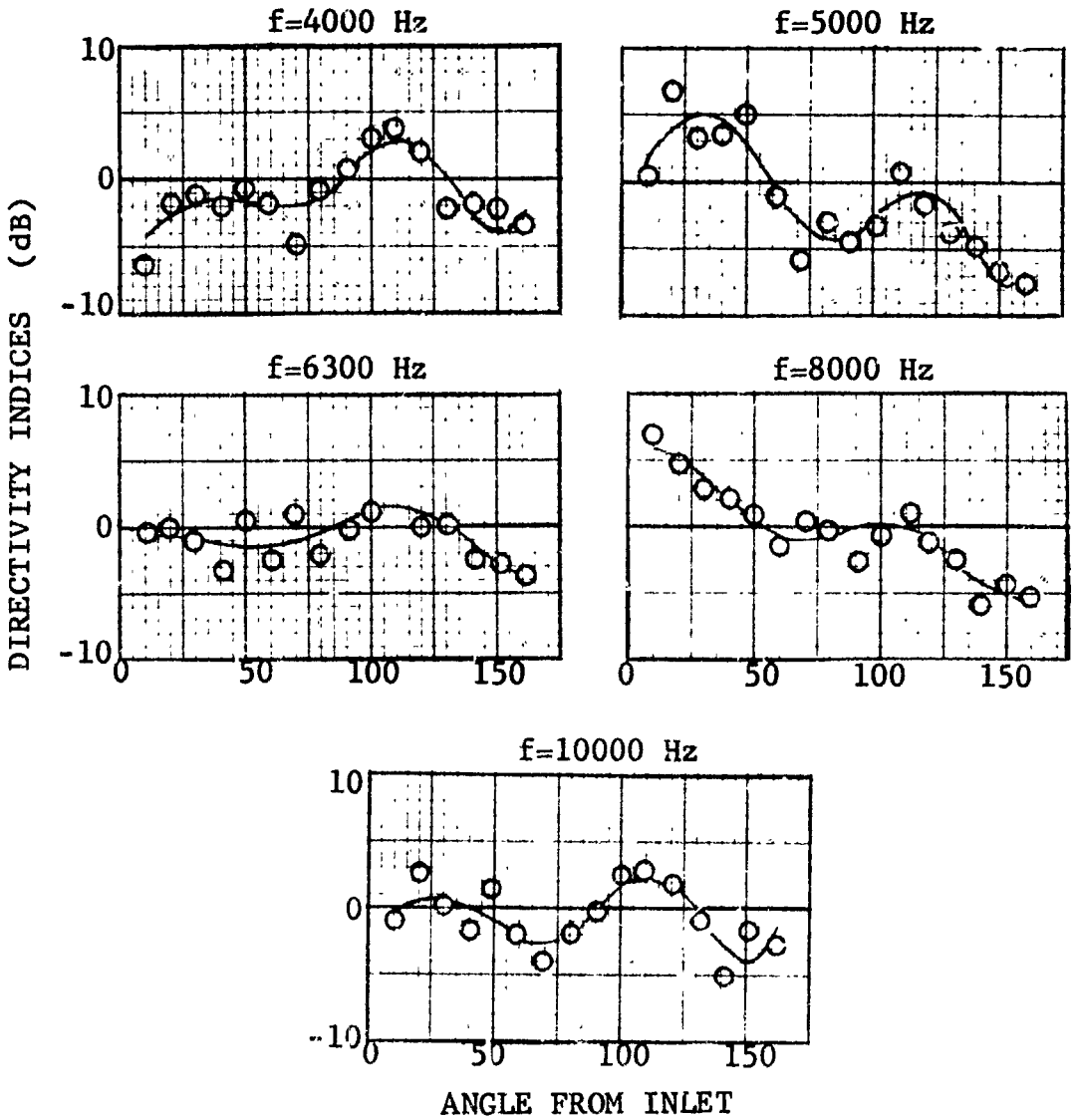

FIGURE IX-A10 DIRECTIVITY INDEX VERSUS ANGULAR POSITION FOR M_R=.95

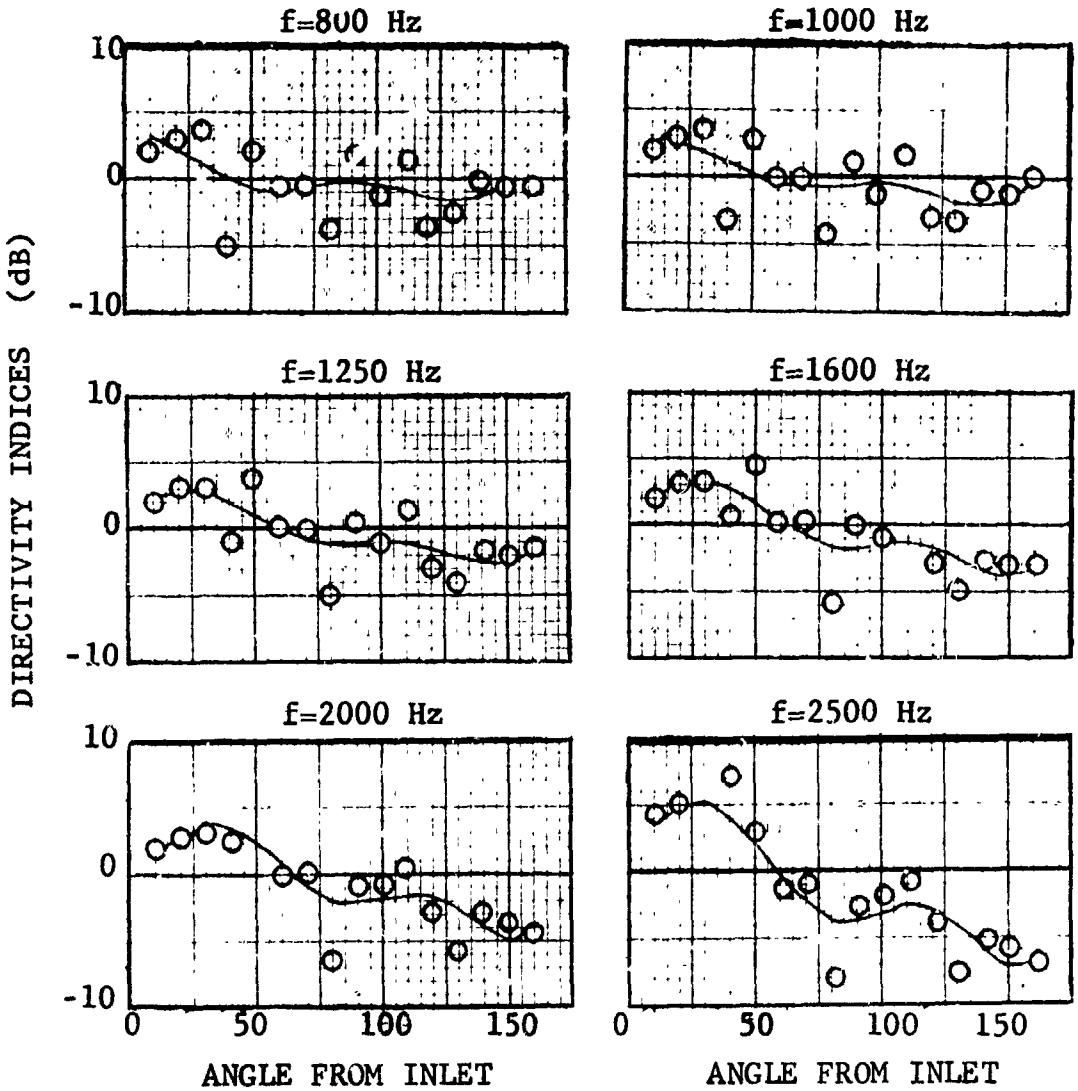

FIGURE IX-A11 DIRECTIVITY INDEX VERSUS ANGULAR POSITION FOR M_R=1.09

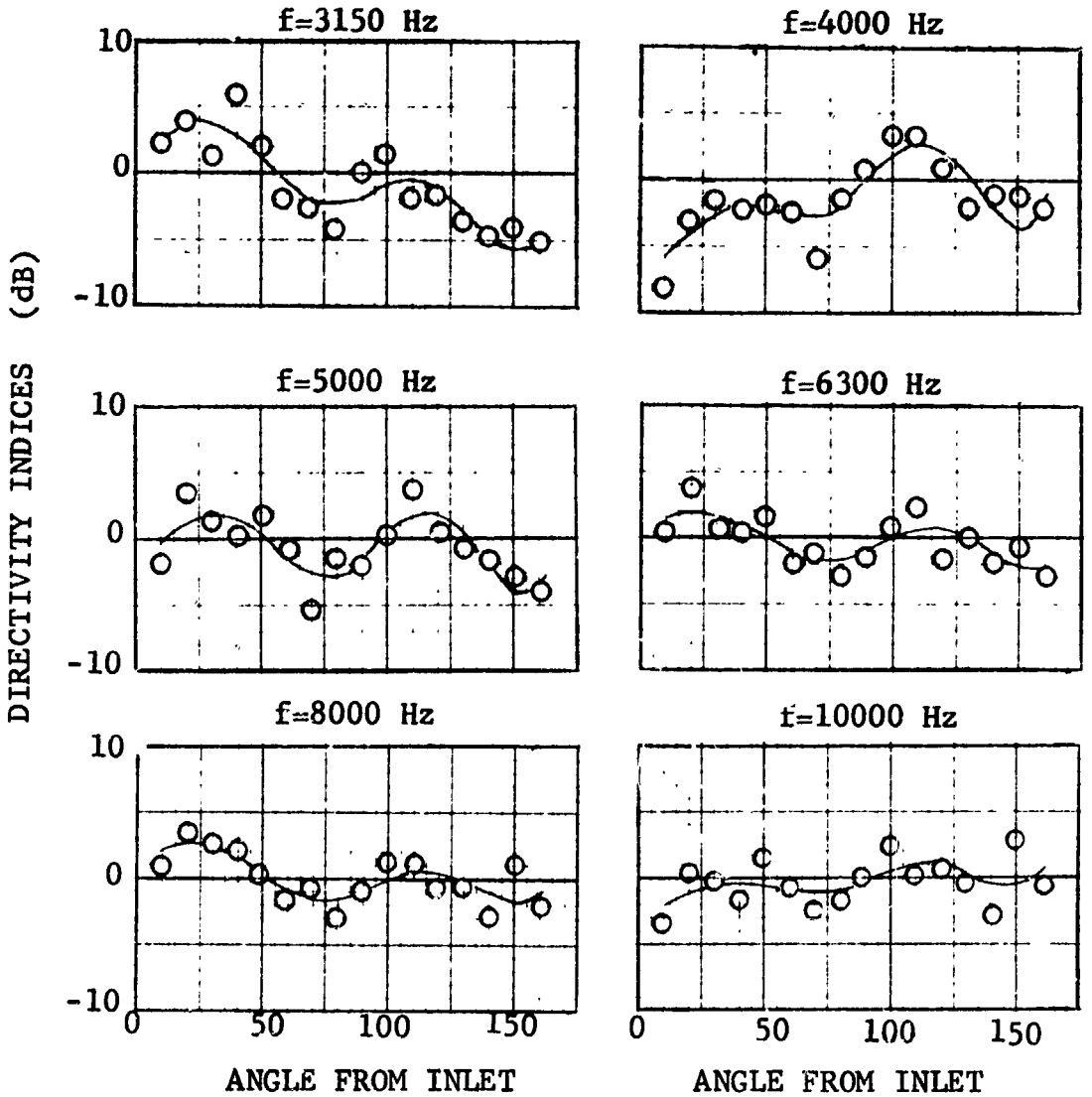

FIGURE IX-A12 DIRECTIVITY INDEX VERSUS ANGULAR POSITION FOR M_R=1.09

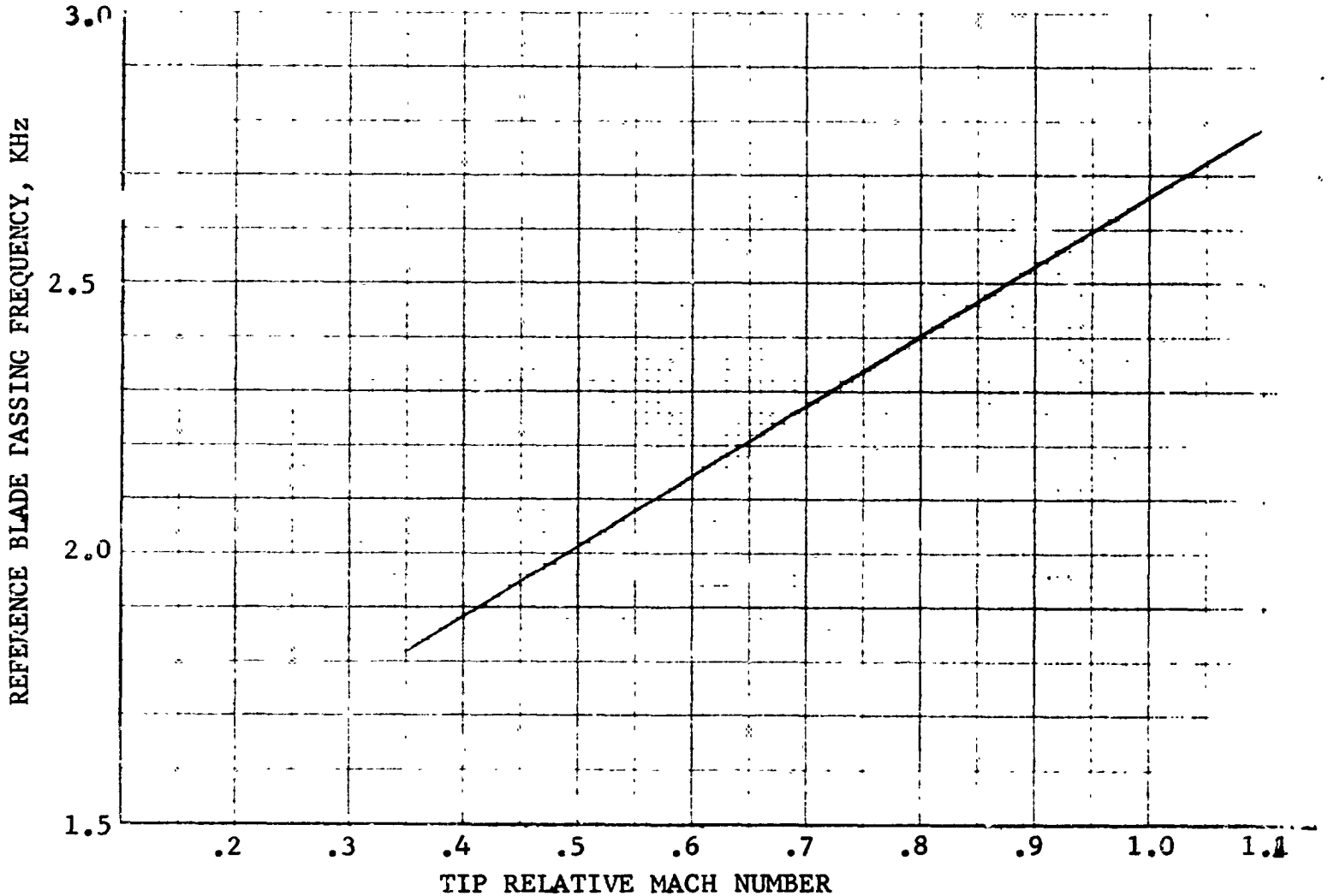

FIGURE IX-A13 REFERENCE BLADE PASSING FREQUENCY VS. TIP RELATIVE MACH NUMBER

In summary, the compressor noise prediction is made by application of the following flow chart:

Step #1	Find the normalized 1/3 power spectra as a function of first stage tip relative Mach number, equation (IX-A1) and Table IX-A1.
Step #2	Find the directivity index at tip relative Mach numbers just above and just below the desired M_r, equation (IX-A5) and Tables IX-A2 to IX-A6.
Step #3	Use linear interpolation to find the D.I. (f,θ) at the desired tip relative Mach number, equation IX-A6.
Step #4	Apply the PWL's of Step #1 and the D.I.'s of Step #2 to equation (IX-A4) with the appropriate weight flow and arc radius
Step #5	Scale the spectra of Step #4 by the number of 1/3 octave bands between the first stage blade passing frequency of the compressor being predicted and the reference blade passing frequency at the same M_r

X. VERIFICATION OF COMPRESSOR NOISE PREDICTION METHOD

(A) Low Speed Single Stage Axial Flow Compressor Pure Tone Levels. A series of configurations on low speed single stage axial flow compressor was tested by Copeland, et.al. (Reference 1) in an anechoic chamber at NASA's Langley Research Center. The blade-passing fundamental tone power levels were measured (at one speed point) for each of four configurations These measured values are compared to the corresponding predictions in Figure X-A1 details of each configuration are also given. The prediction technique again yields values which closely agree with measured data, irrespective of changes in vane-blade number ratio and vane-blade spacing.

The pure tone noise prediction method is thus seen to be accurate with this type of vehicle.

(B) High Speed Multistage Compressor Pure Tone Levels. The pure tone noise prediction technique was exercised for two multi-stage compressors (J-79 and GE-4). The measured first stage fundamental PWL's for the two machines are presented in Figures X-B1 and X-B2, along with the associated predictions. Since the predictions were to be for noise radiated forward, it was necessary to account for the fact that some of noise which might be transmitted downstream (if the stage were isolated) is in fact reflected upstream. In order to compensate for this phenomena, the flow convection effects developed in Reference 2 were used to project the resultant noise levels radiating out of the inlet. Good correlation is seen to be achieved.

(C) Multistage Compressor Directivity Predictions. The prediction method presented in Section IX was applied to the first stage of the J93 compressor, in order to predict the blade-passing fundamental sound pressure levels and directivities. Figure X-C1 is a comparison of predicted and measured 250 ft. arc data, for the forward quadrant. Good correlation was achieved.

CONFIGURATION 1: IGV-ROTOR (62 VANES, 53 BLADES)
SPACING: 0.535 CHORD

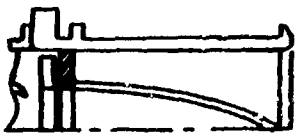

MEASURED (NASA LANGLEY) 132.0 dB

CALCULATED 132.2 dB

CONFIGURATION 2: ROTOR-OGV (53 BLADES, 62 VANES)
SPACING: 0.535 CHORD

MEASURED (NASA LANGLEY) 123.0 dB

CALCULATED 123.5 dB

CONFIGURATION 3: IGV-ROTOR-OGV (62 VANES, 53 BLADES, 62 VANES) SPACING: (I-R) 0.535 CHORD, (R-O) 0.535 CHORD

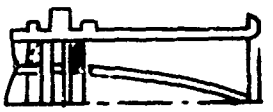

MEASURED (NASA LANGLEY) 132.0 dB

CALCULATED 132.3 dB

CONFIGURATION 4: IGV-ROTOR-OGV (62 VANES, 53 BLADES, 62 VANES) SPACING: (I-R) 0.25 CHORD, (R-O) 0.535 CHORD

MEASURED (NASA LANGLEY) 124.0 dB

CALCULATED 124.0 dB

FIGURE X-A1 COMPARISON OF MEASURED AND CALCULATED SOUND POWER LEVELS FOR NASA 14.75-INCH DIAMETER COMPRESSOR

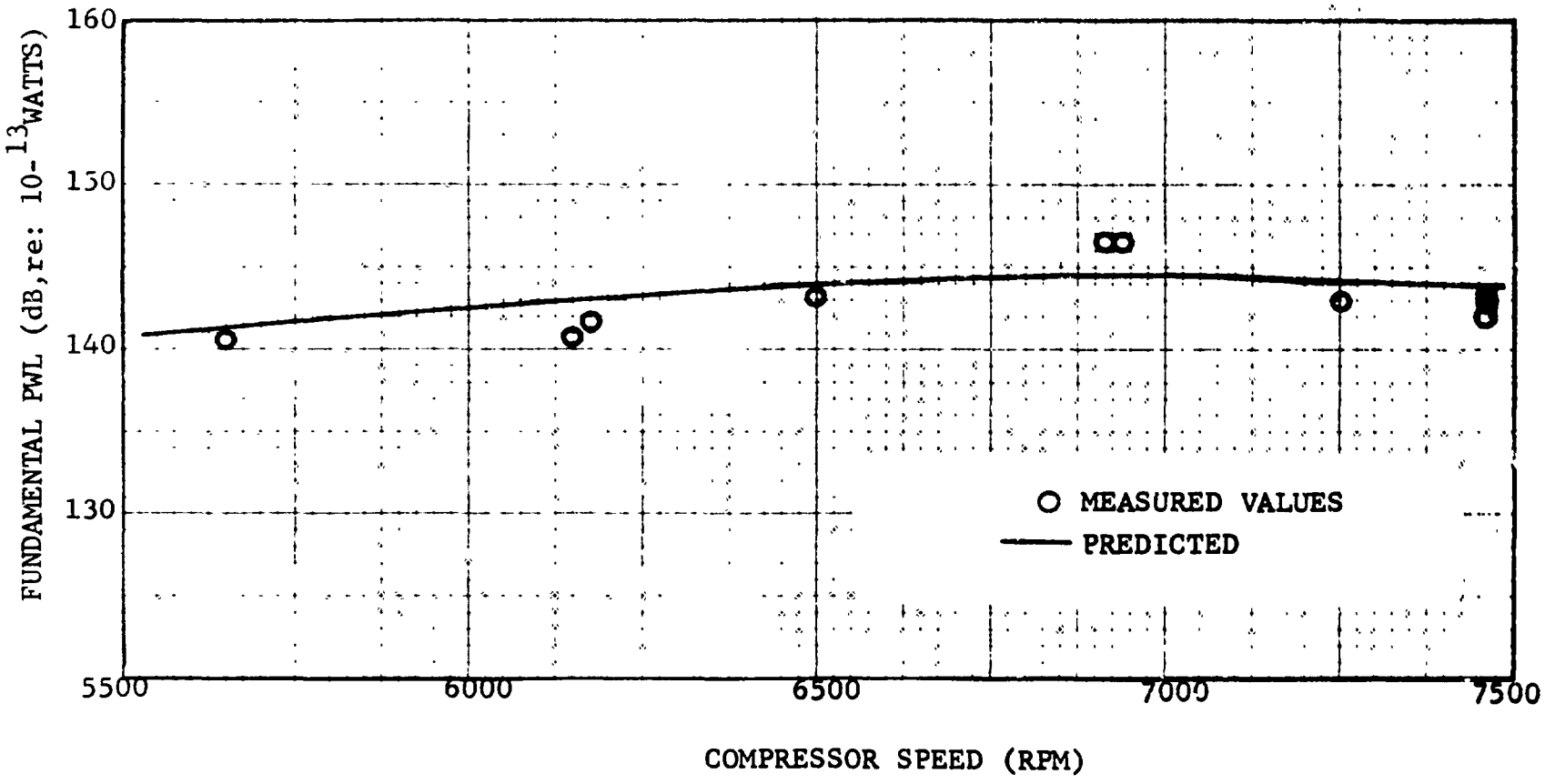

FIGURE X-B1 FUNDAMENTAL PWL - STAGE ONE J-79 COMPRESSOR

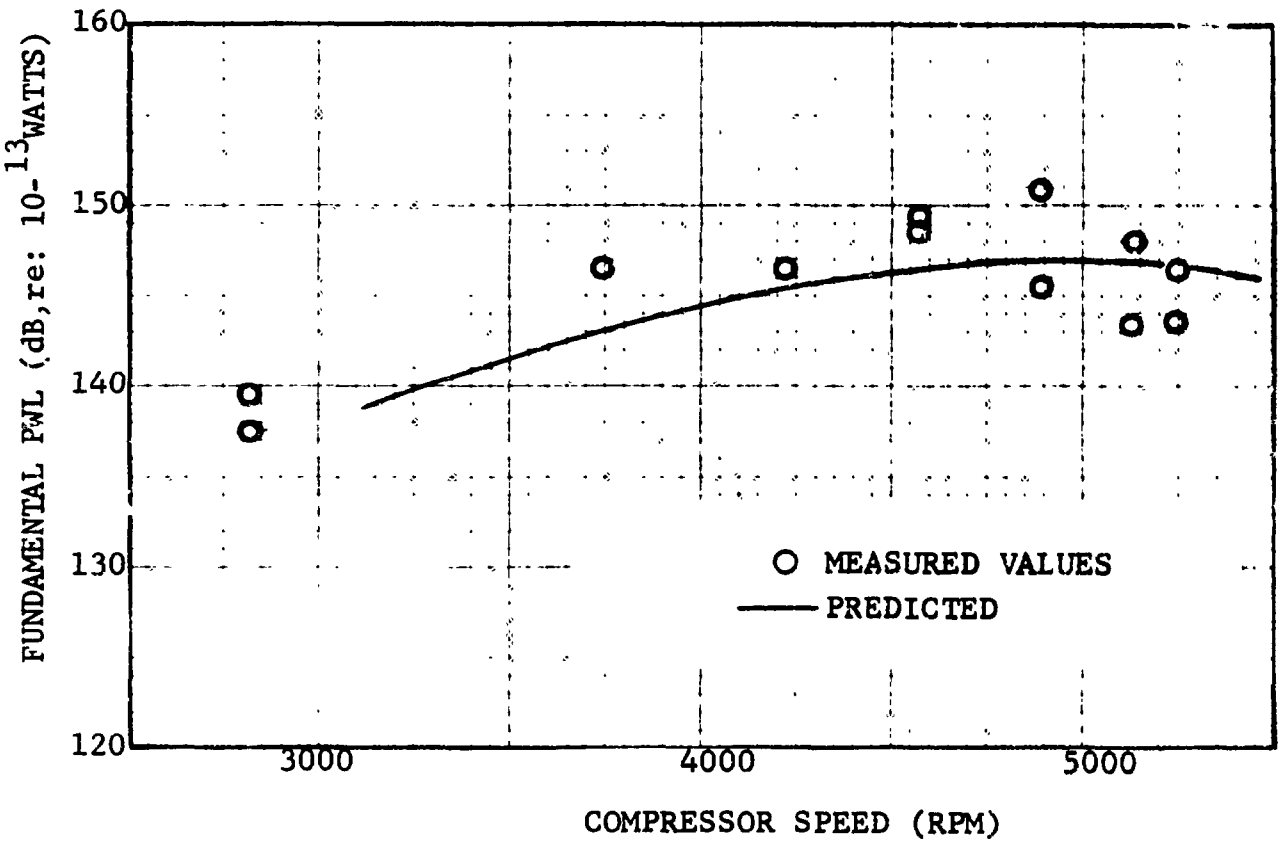

FIGURE X-B2 FUNDAMENTAL PWL - STAGE ONE GE-4 COMPRESSOR

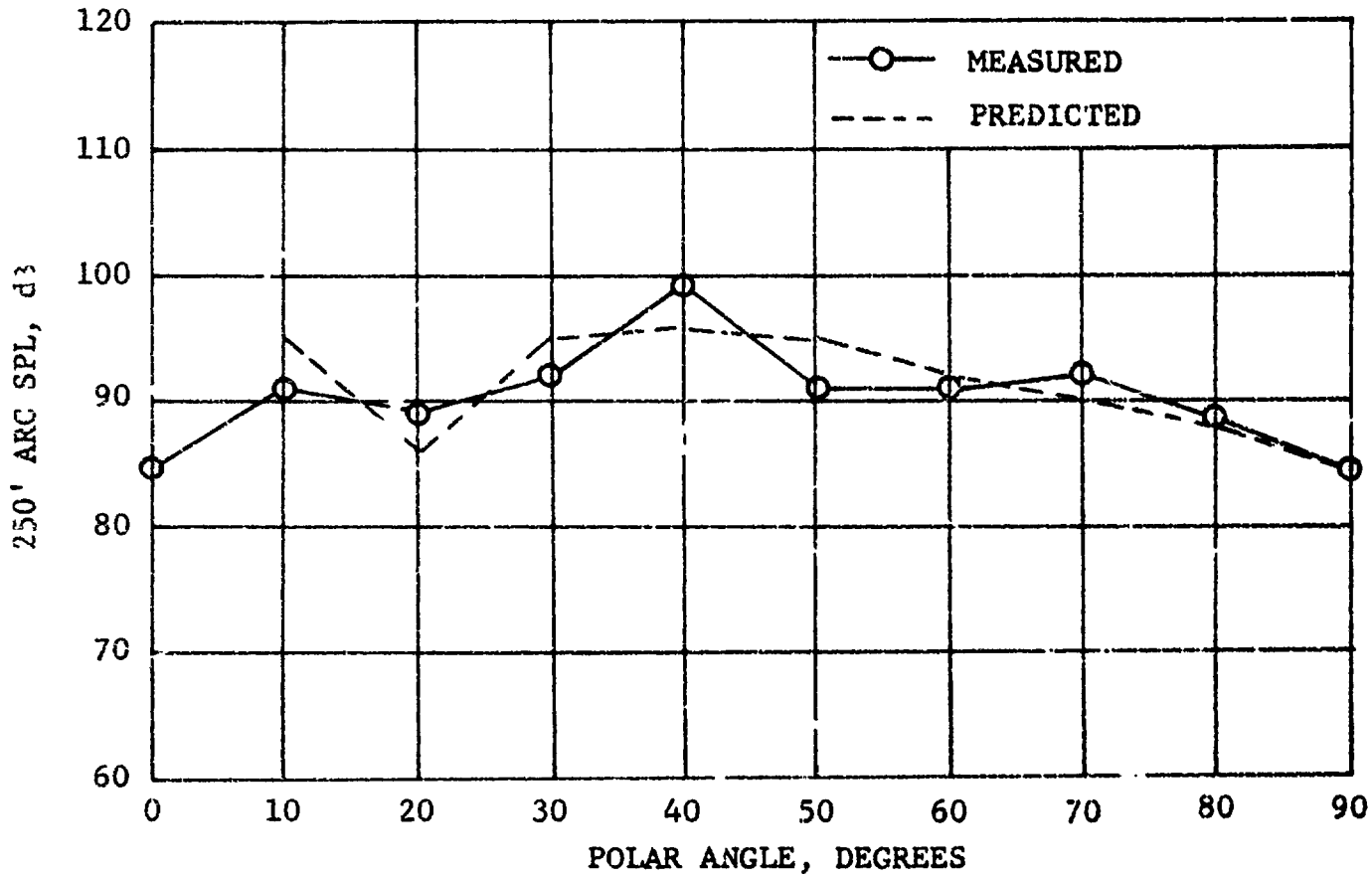

FIGURE X-C1. COMPARISON OF PREDICTED AND MEASURED SPL'S FOR FUNDAMENTAL TONE OF J93 COMPRESSOR FIRST STAGE. DESIGN POINT - ROTOR UNITY MACH NUMBER

REFERENCES SECTION X-A

1. Copeland, W.L., Crigler, J.L., and Dibble, A.C. Jr., "Contribution of Downstream Stator to the Interaction Noise of a Single-Stage Axial Flow Compressor", NASA-TND-3892.

2. Smith, M.J.T., and House, M.E., "Internally Generated Noise From Gas Turbine Engines - Measurement and Prediction", ASME Paper No. 66-GT/N-43, March 1966.

XI. NOISE REDUCTION METHODS

(A) Results of Analytical Studies. The previous sections have examined the various noise generation and transmission mechanisms present in fans and compressors. These mechanisms are influenced, both directly and indirectly, by certain physical and aerodynamic design parameters. Quite obviously, a knowledge of the ultimate acoustic effect of these parametric concepts will be applicable to the design of "quiet" fans and compressors.

The following sections present the effects on fan/compressor noise of several key design/performance parameters as predicted by the procedures summarized in Sections VII and IX of this report. Note that while specific designs have been used for purposes of illustrating the effects of certain parameters, the quantitative differences due to design changes cannot be generalized and every vehicle must be evaluated on its own merits (Reference 1). As an example, the effect of a 10% decrease in rotor tip speed may decrease noise by .5 dB on some vehicles whereas the decrease could be 5 dB on other vehicles. On yet other vehicles, if the tip speed reduction is accompanied by an increase in blade loading, the noise could increase.

In summary, quantitative evaluation of the effects of design parameters on any specific design must be evaluated on an individual basis according to the procedures summarized in Sections VII and X . Generalizations of these effects cannot be made on a reliably accurate basis.

(1) Rotor-Tip Speed. Some previous noise prediction schemes have employed tip speed as the main correlation parameter. This is quite satisfactory for broadband noise, as reference to the aforementioned generation mechanisms indicates that broadband levels do increase as the 4th to 6th power of blade relative velocity.

Increases in pure tone noise with tip speed are only incidental. This conclusion is apparent from the equations which define the noise generating mechanisms. It is seen that for rotor alone pure tone noise, the sound pressure levels generated are a direct function of circulation around the blade row. The larger the circulation, the higher the pure tone levels. Now, with pressure ratio held constant, predicted rotor-alone pure tone levels decrease as the design speed goes up (Figure XI-A1, for example). This results from the fact that the rotor loading, and consequently the circulation, goes down with increasing tip speed.

A similar effect exists for blade-vane wake interaction pure tone noise. As before, the radial unsteady circulation about the blade is the controlling factor. The defining equation indicates that, for wake interaction, the major variable influencing the circulation is the unsteady upwash on the rotor G_m^s. From the equation defining G_m^s (Equation II-25), it can be seen that there is no unique relationship with tip speed. The quantities V_s/V_r (velocity ratio, rotor inlet to rotor discharge) and β (rotor turning angle) vary with varying tip speed, but are dependent on pressure ratio as well. Indeed, for a constant pressure ratio, V_s/V_r and β would decrease as tip speed increases; as before, this would result in a decrease in predicted wake interaction pure tone levels with increasing tip speed (Figure XI-A2).

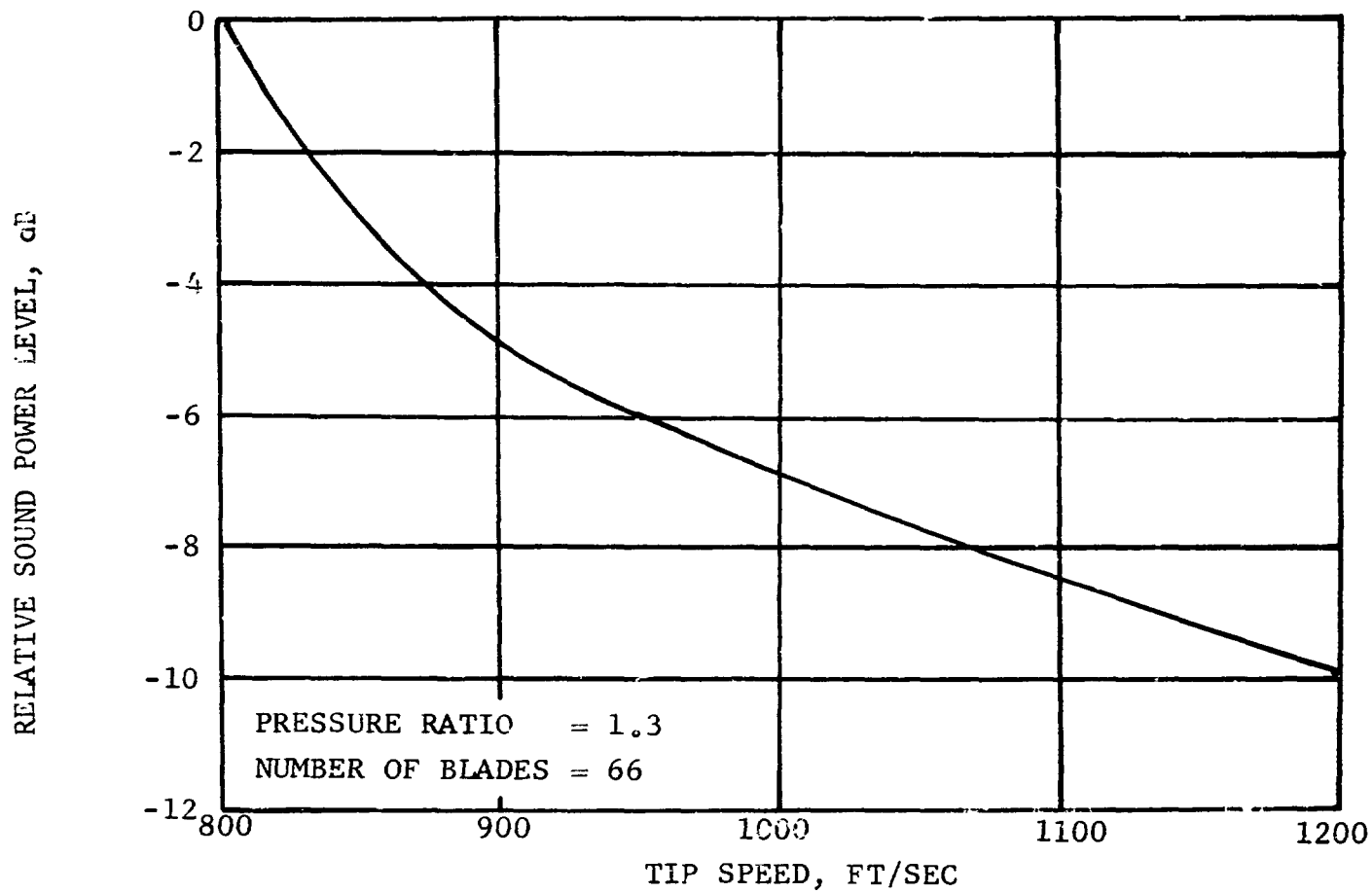

FIGURE XI-A1 EFFECT OF TIP SPEED ON ROTOR - ALONE PURE TONE NOISE FOR A TYPICAL FAN

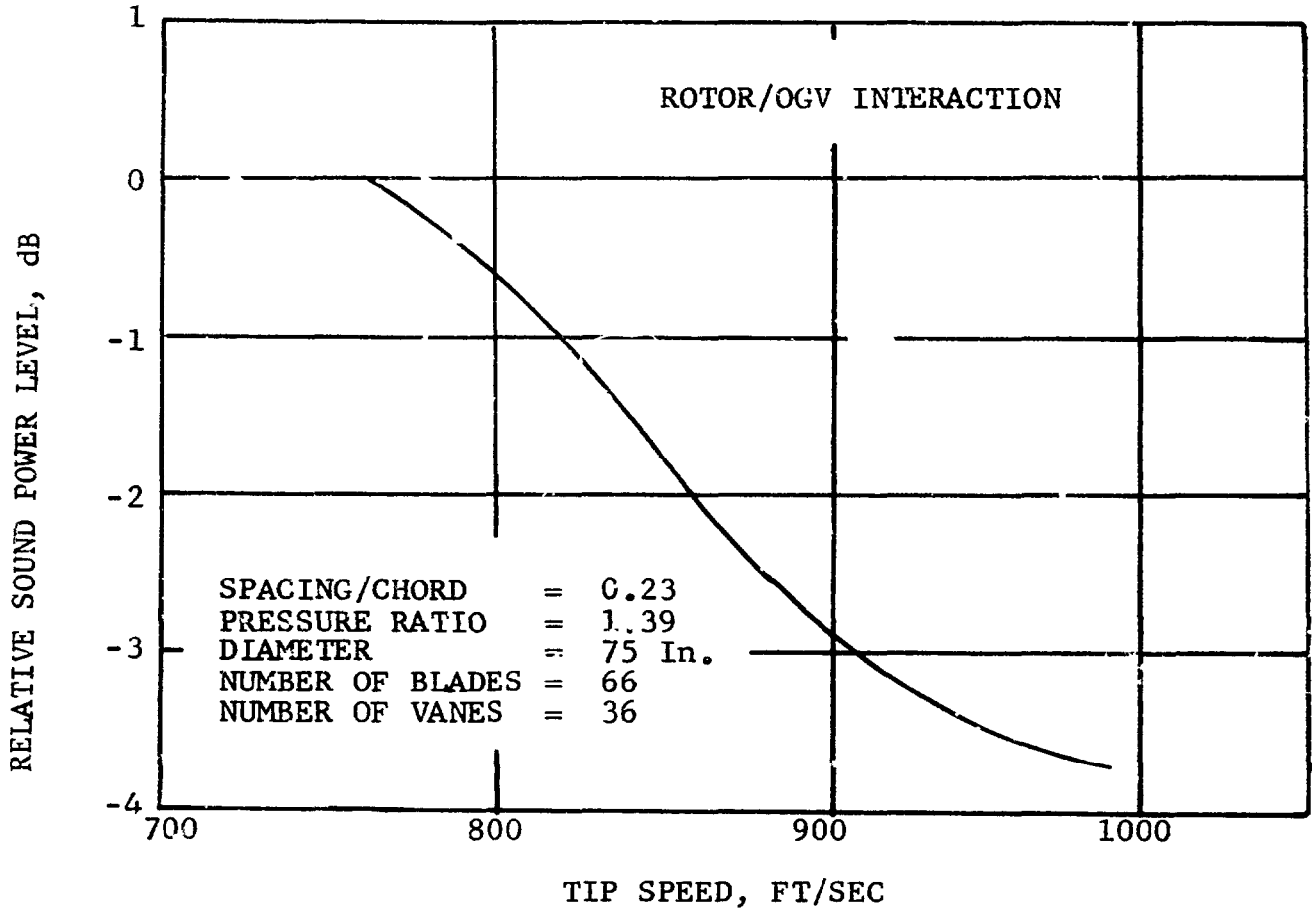

FIGURE XI-A2 EFFECT OF TIP SPEED ON WAKE INTERACTION PURE TONE NOISE FOR A TYPICAL FAN

(2) Pressure Ratio. Conversely to those effects noted in the previous analysis, predicted rotor-alone pure tone levels increase with increasing pressure ratio (speed held constant) (Figure XI-A3). Increasing pressure ratio at constant speed causes the blade loading (and circulation) to increase.

Again, a parallel exists for blade-vane pure tone interaction noise. When the pressure ratio across the fan is increased (at constant speed), more turning has to be done in the blade row and the loading goes up. The terms V_s/V_r and δ subsequently increase, and this in turn dictates an increase in predicted wake interaction pure tone noise. Figure XIA-4 presents a theoretical example study; separate curves are included for the case of constant fan size, and for that of constant fan thrust.

The concept of pure tone noise increasing with speed can, therefore, be quite misleading. It is true that the pure tone levels rise as the speed is increased on a particular vehicle, but so do the rotor loading and stage pressure ratio. Blade loading, (a more important factor in fan pure tone noise generation than tip speed) should be a major consideration of the designer.

(3) Number of Rotor Blades. For constant solidity, Section II-B indicates no broadband noise change with blade number changes. However, in the equations defining both rotor-alone and wake interaction pure tone noise, the numbers of blades present are important variables. These numbers dictate the solidities, number of rotating line sources, number of diametral modes, etc., which are employed in the equations. For both rotor alone and wake interaction noise, the theory indicates that increasing the numbers of rotor blades (all other parameters constant) will decrease the generated pure tone power levels. This predicted effect is illustrated for rotor-alone noise in Figure XI-A5, and for wake-interaction noise in Figure XI-A6.

This of course should not lead to the automatic supposition that a fan design should incorporate the maximum number of fan blades physically possible, psychoacoustic effects must be considered. Since the number of fan blades directly determines the frequencies of the pure tones generated (for constant speed), this number should be so adjusted as to keep the pure tones out of the critical areas of psychoacoustic annoyance. Tradeoff studies must be conducted in order to arrive at an optimum number of blades.

(4) Vane-Blade Number Ratio. Again there is no effect on broadband noise. The defining equations for all of the pure tone noise generating mechanisms contain N, the number of spinning lobes, as a variable. At the blade-passing fundamental frequency, N is determined by:

$$N = B - kV$$

wherein:

B = number of rotor blades
V = number of stator vanes
k = any interger (or zero)

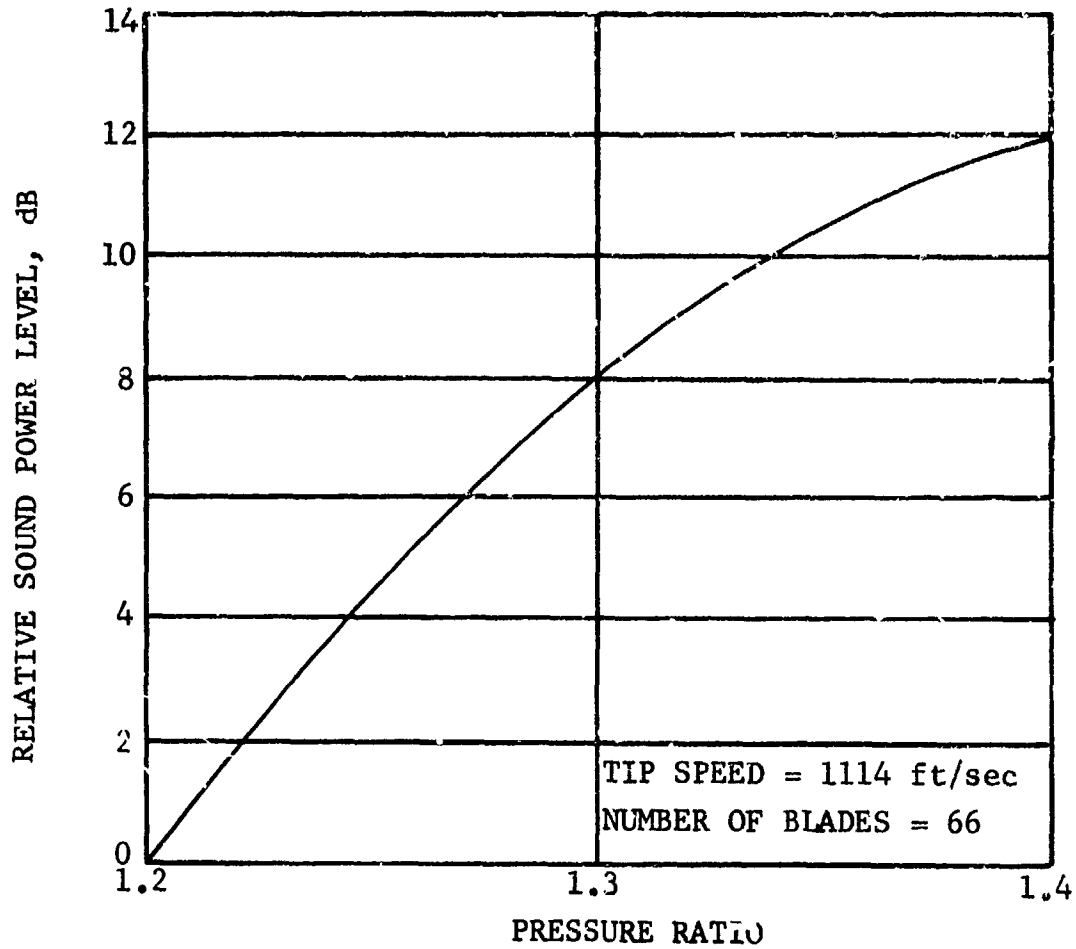

FIGURE XI-A3 EFFECT OF PRESSURE RATIO ON ROTOR - ALONE PURE TONE NOISE FOR A TYPICAL FAN

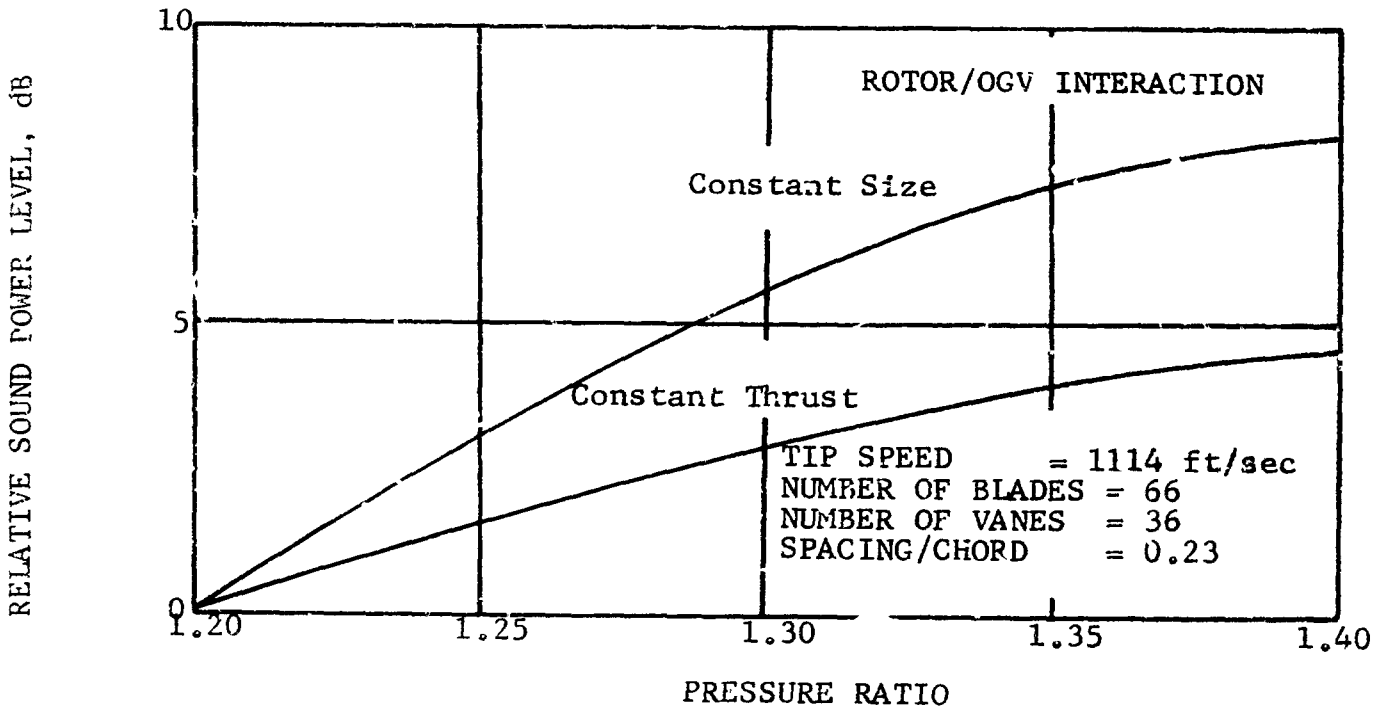

FIGURE XI-A4 EFFECT OF PRESSURE RATIO ON WAKE INTERACTION PURE TONE NOISE FOR A TYPICAL FAN

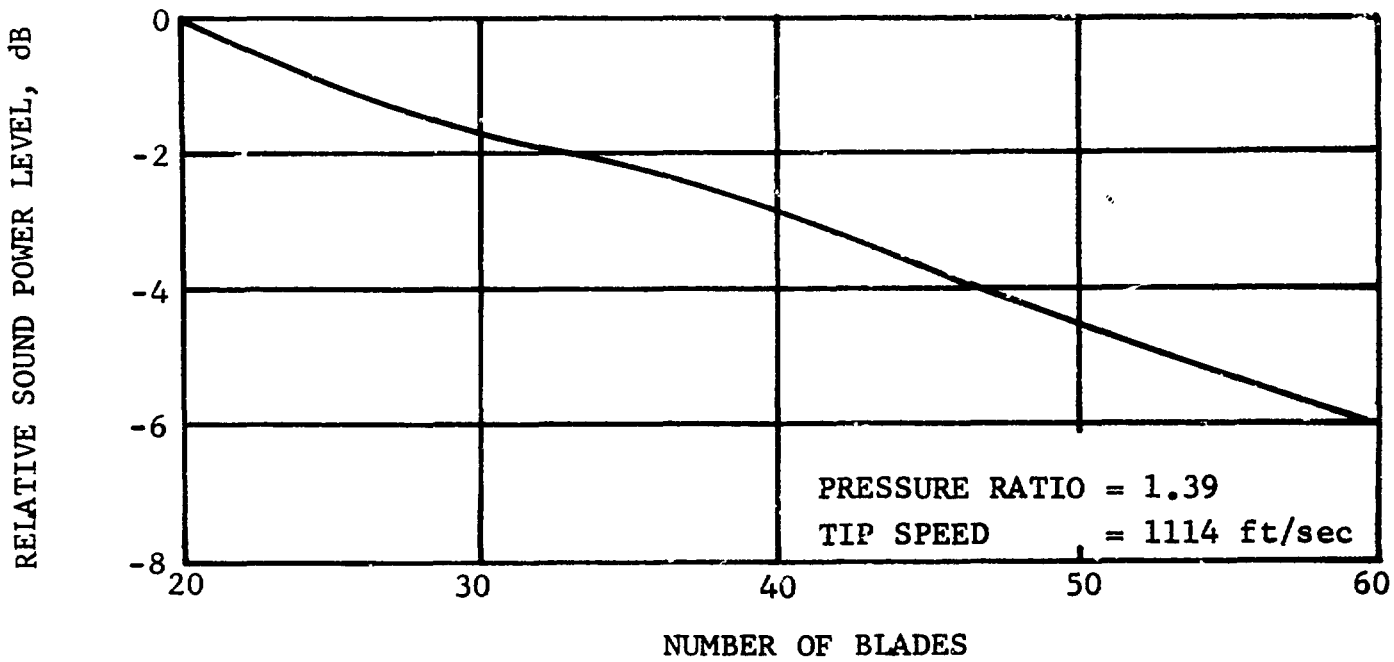

FIGURE XI-A5 EFFECT OF ROTOR BLADE NUMBERS ON ROTOR - ALONE PURE TONE NOISE FOR A TYPICAL FAN

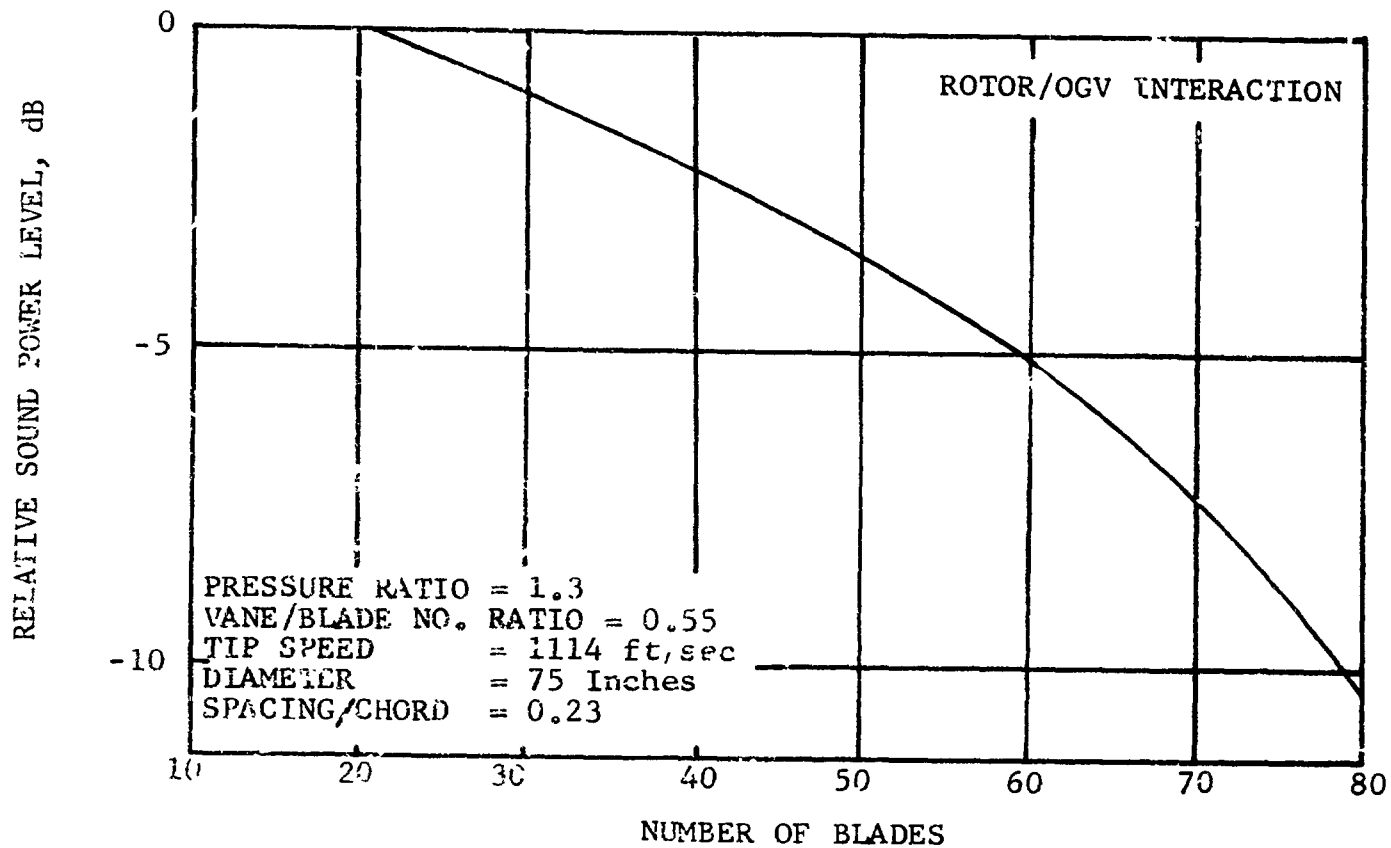

FIGURE XI-A6 EFFECT OF ROTOR BLADE NUMBERS ON WAKE INTERACTION PURE TONE NOISE FOR A TYPICAL FAN

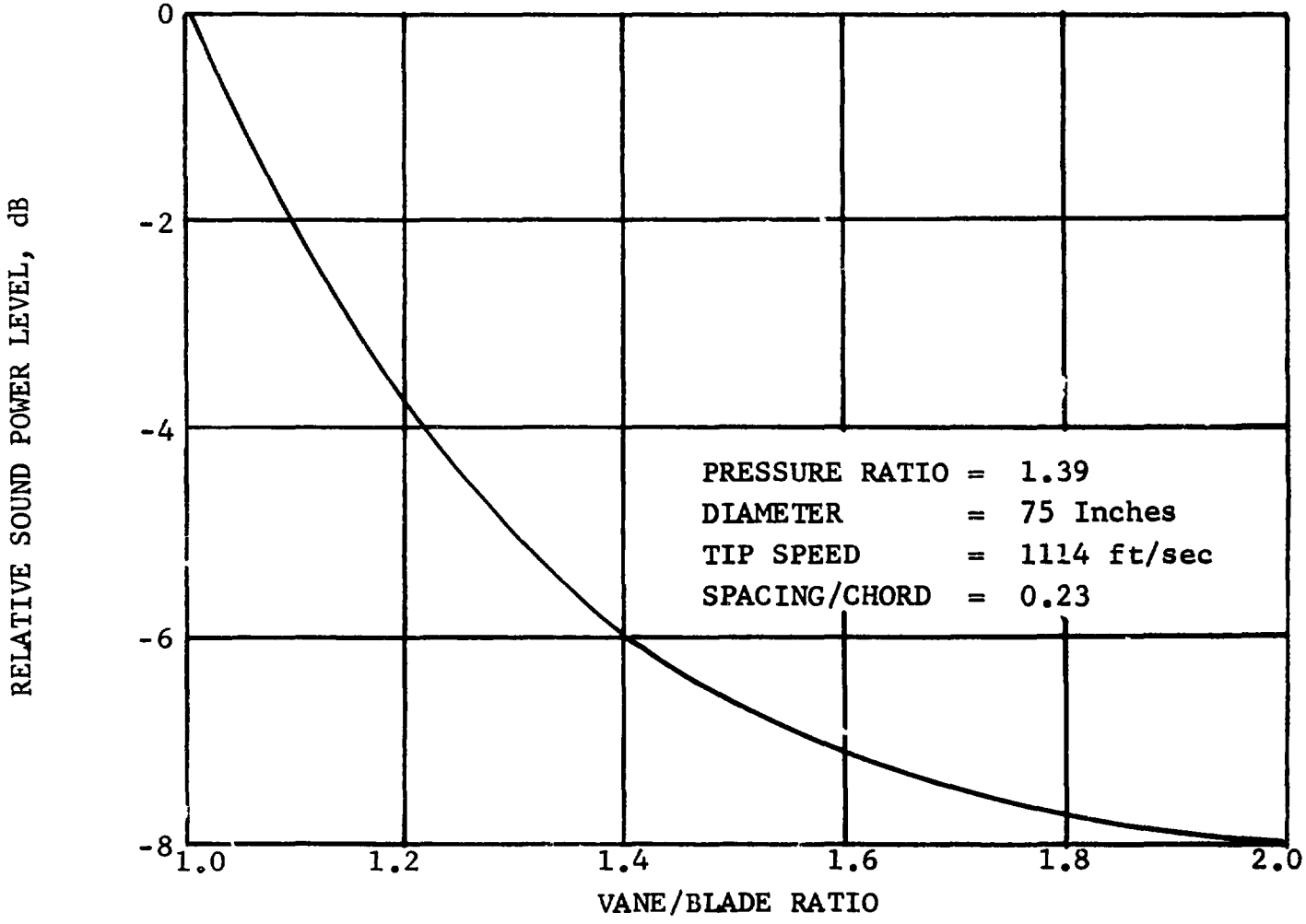

FIGURE XI-A7 EFFECT OF VANE/BLADE RATIO ON WAKE INTERACTION PURE TONE NOISE FOR A TYPICAL FAN

It can be shown from the relationships in Section II that the lower are the minimum values of N obtainable, the greater is the pure tone acoustic energy generated. For low noise it is, therefore, desirable to design the fan such that these lowest obtainable values of N are as large as possible: the above equation indicates that this may be done by making the ratio "V/B" high. As the vane-blade number ratio increases, the predicted pure tone interaction noise levels indeed decrease (Figure XI-A7). As was previously shown, however, high blade numbers are also desirable, and there are of course practical limits to the number of vanes employable. Optimization studies are again necessary.

(5) Blade-Vane Spacing. Changes in spacing do not affect broadband noise output. The effect of spacing on pure tone noise is somewhat more complicated. This parameter is directly contained in the wake interaction pure tone noise equations, and the predicted change in pure tone level with spacing is presented in Figure XI-A8. It can be seen that an appreciable reduction in pure tone levels is obtainable with increased spacing.

The qualitative effects of increasing the blade row spacing are well known, and several researchers have investigated this phenomenon. Quantitive results have been inconsistent, however, with some researchers reporting a 2 dB reduction in pure tone sound pressure levels per doubling of axial spacing, while others have found 4 or even 6 dB decreases per doubling. This inconsistency can be explained first by the fact that several other parameters besides axial spacing are involved in the wake decay process, and second, because the concept of "per doubling" is not strictly correct for pure tones. Reference to the equations (II-22 to II-30) indicates that geometric quantities (such as the solidity of the upstream blade row, the blade chords, etc.) as well as aerodynamic quantities (drag coefficient, air exit angle, etc.) are of major importance in the wake interaction decay. These parameters vary from one configuration to another, and ignoring them is bound to lead one to inconsistent conclusions. Also, it can be seen that the wake decay is not a simple function of blade row spacing, and will not result in a constant ratio "per doubling" of the axial spacing.

(6) Vane Lean. A leaned vane is non-radial. Leaned vanes reduce noise generation by decreasing the strength of the viscous wake interaction and by phasing that interaction so as to produce a degree of phase cancellation. In order to determine an optimum lean angle an analytic model was constructed under a NASA contract (NAS2-6056). Typical results of blade passing frequency versus lean angle for an IGV rotor interaction are shown in Figure XI-A9 for two spinning lobe numbers. The unique features of this figure are that the higher lobe number (greater vane blade ratio) gives a greater noise reduction for a given lean angle and that both curves have optimum lean angles, i.e., angles beyond which noise increases. The decreasing and then increasing curve is a result of multiple blade wake-stator interactions which occur as the lean angle is increased. In some cases the leaning weakens the wake interaction; however at some point the multiplicity of interactions exceeds the affect of the weaker interactions and noise increases.

The rising and falling curve is a result of multiple blade wake-stator interactions occuring as lean is increased. As more and more wakes are overlapped by a given stator, the noise generation fluctuates. However, the overall trend is that lean decreases blade passing frequency noise.

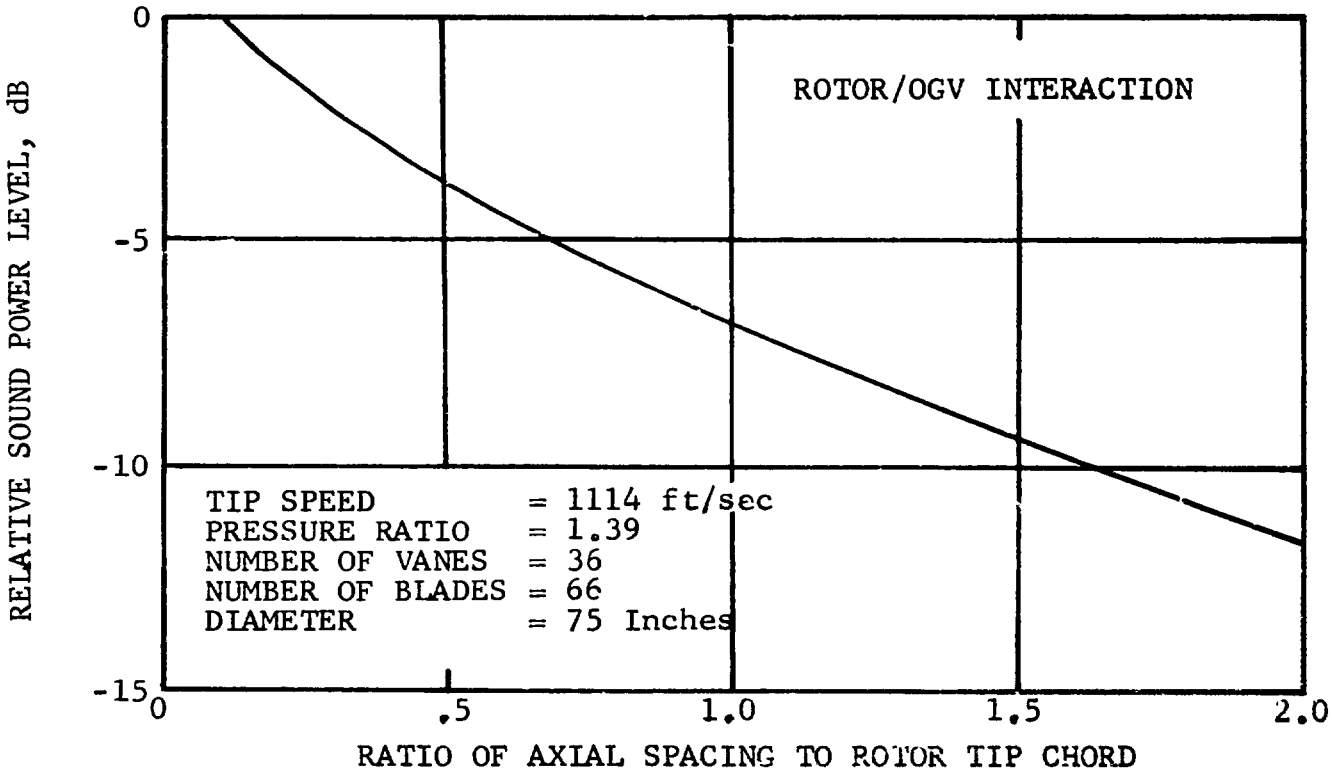

FIGURE XI-A8 EFFECT OF AXIAL VANE-BLADE SPACING ON WAKE INTERACTION PURE TONE NOISE FOR A TYPICAL FAN

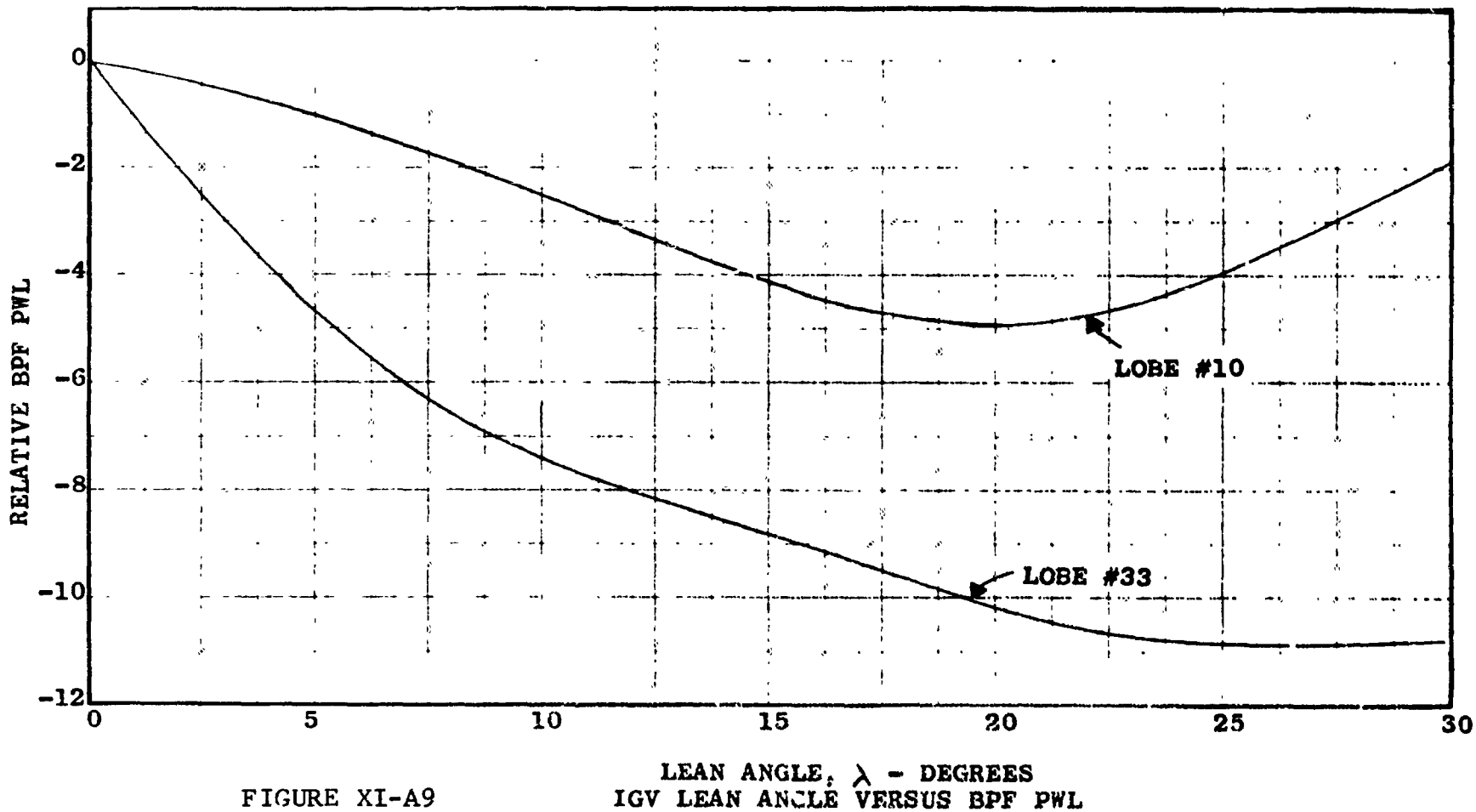

FIGURE XI-A9 IGV LEAN ANGLE VERSUS BPF PWL

(7) Vane Sweep. In the event that axial translation of an entire stator with respect to an adjacent rotor for the purpose of increasing spacing is not possible, stator sweeping may be a viable alternative. The swept stator puts more rotor-stator spacing at the tip than at the hub.

A typical study for a high solidity rotor is shown in Figure XI-A10. In this instance the swept stator is an outlet guide vane of a single stage front fan. The "half way measure" of blade sweep is seen to produce about half the noise reduction of full span spacing, although this should not be taken as a general result. Differences in the aeromechanical design of particular stages may produce significantly different results.

(8) Wake Control. A major source of noise in fans and compressors (Section II-A) is the interaction of the wakes shed by one blade row (rotating or stationary) with the following blade or vane row. The elimination or reduction of these wakes would in most practical cases result in an appreciable noise reduction. An attractive method to reduce the strength of the wake shed by a blade is to energize the low momentum region of the wake by the introduction of high energy air bled from an outside source (for example, the high pressure compressor).

The amount of air necessary will be a function of the momentum deficiency in the wake as well as the velocities at which this secondary air is introduced. The delta momentum of the secondary air should be equal to the moment deficiency in the wake. The actual mass flow necessary will depend on the geometry in question. The design as well as the results of such an experiment are reported in Section XI-B.

(9) Inlet Choking. The theoretical effects of completely choking an inlet are well known. Once the velocity of inlet air flow reaches the local sonic velocity across some plane in the duct, a"sonic block" is set up. Any pressure disturbances attempting to propagate upstream cannot penetrate this block, and consequently, the noise radiated forward is greatly reduced. (Figure III-B5, for example.) Complete choking is sometimes impractical in an actual fan or compressor inlet. An alternative concept is that of "partial" choking (localized regions of sonic flow) between the IGV's. The noise reduction would not be as great as in the case of complete choking, but substantial attenuations of forward-radiated noise are still theoretically possible.

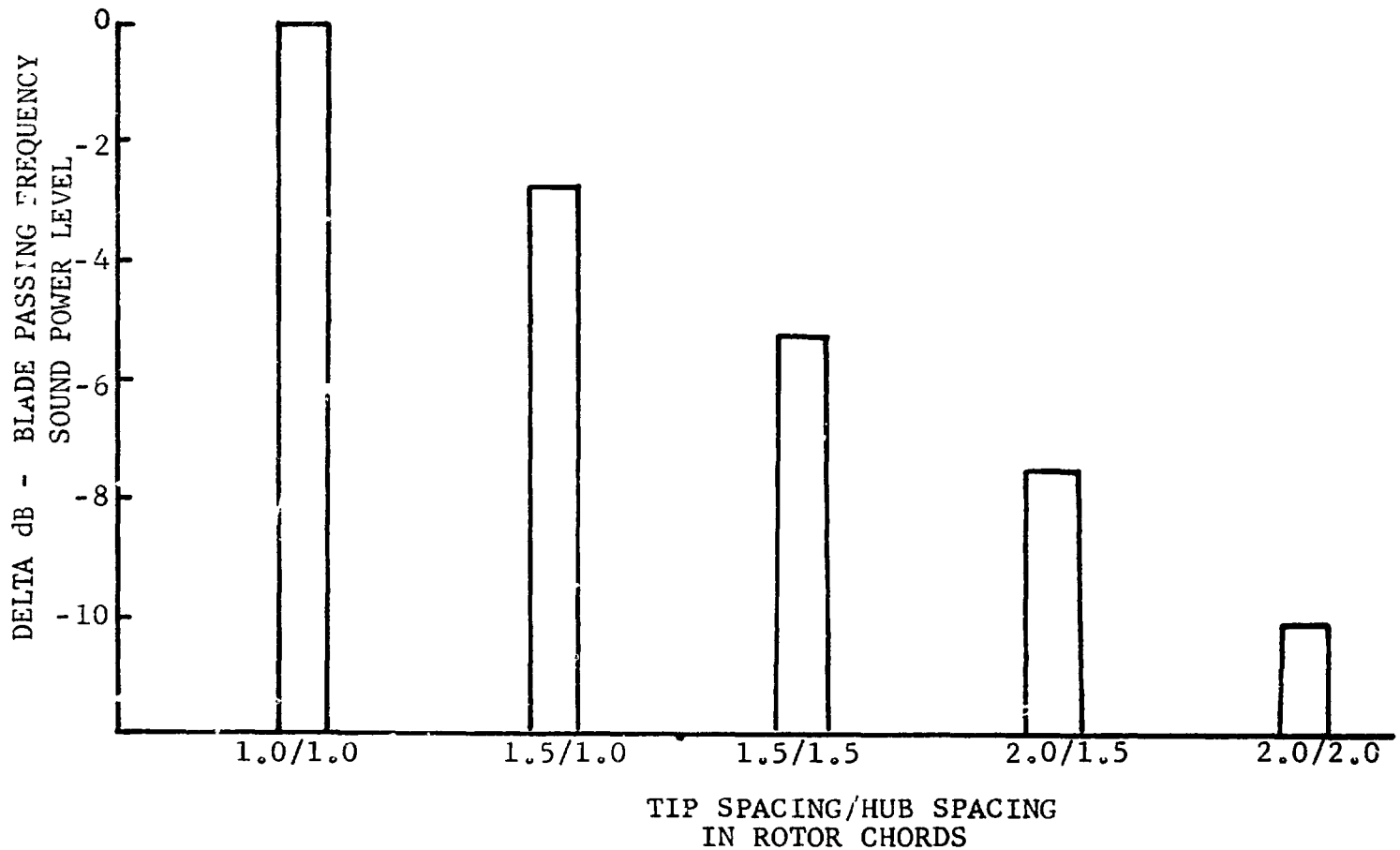

FIGURE XI-A10 BLADE PASSING FREQUENCY NOISE REDUCTION WITH STATOR SWEEP FOR A TYPICAL FAN

REFERENCES SECTION XI-A

1. Hochheiser, R. M., "Some Fan Engine Noise Design Considerations", AIAA Paper Number 69-491, June 1969.

(B) Experimental Investigation. Acoustic data, recorded from a number of fan vehicles, provides confirmation of the predicted effects of some of the concepts discussed in Section XI-A.

(1) Rotor Speed. Data showing the accuracy of predicted pure tone levels as a function of fan speed has been shown (typical examples are Figures VIII-A3, VIII-A4, and VIII-A11 to 20) in Section VIII. With respect to broadband noise, Figure II-B2 indicated that good results are available when using the procedures of Section II in predicting overall broadband sound power (PWL) as a function of fan speed on a given vehicle. Figures XI-B1 and XI-B2 are additional examples of the accuracy of those procedures. Figure XI-B1 presents the measured overall broadband sound power levels from the CJ805-23 fan, plotted as a function of rotor tip speed; the predicted values are also presented. It is apparent that the broadband sound power levels do increase with increasing tip speed, almost exactly as predicted. Figure XI-B2 is a similar plot for the TF39 Development Vehicle fan, indicating similar results.

Data from an experimental two-stage fan configuration supports the contention that tip speed alone is not the determining factor in pure tone noise generation. The two stages of this fan have common rotor tip diameters and a common shaft, hence they operate at identical tip speeds; all other parameters (pressure ratio, etc.) are different. Fundamental blade-passing sound power levels recorded for the first stage (25 blades) and the second stage(40 blades) are plotted as a function of tip speed in Figure XI-B3. Also presented are the predicted fundamental PWL's for each stage, said predictions being determined from the techniques outlined in Section II. It is apparent that throughout most of the fan operating range, the rotors generate significantly different (accurately predicted by the methods in Section II) noise levels, even though both have the same tip speed. Tip speed alone cannot, therefore, be the controlling parameter.

It is of course, not surprising to find that, on a given fan vehicle, increasing fan speed results in increase in noise when the vehicle is operating along a fixed operating line. As the fan RPM of any given fan increases, pressure ratio, loading, weightflow,etc., also increase. Any and every parameter contributing to noise becomes more intense and the noise increases.

(2) Pressure Ratio. Data from the aforementioned two-stage fan also provides examples of the importance of pressure ratio to pure tone noise generation. Figure XI-B4 presents aerodynamic and acoustic data recorded for the second stage of the fan. This data is in the form of an operating map; i.e., a plot of corrected weightflow through the stage, against pressure ratio across the stage. Three different fan nozzle areas were employed, hence three operating lines are plotted. Lines of constant fan speed are superimposed on the map, as are "isonoise" lines for the second stage fundamental PWL's. These isonoise lines are lines of constant noise level, established by plotting measured fundamental PWL as a function of fan weightflow and fan speed, then crossplotting these points onto the operating map. Examination of Figure XI-B4 indicates that as the fan pressure ratio is decreased along a constant speed line, the measured fundamental PWL's also decrease. More importantly, it can be seen that if fan speed is increased, while holding the pressure ratio constant, the fundamental PWL's remain constant or decrease.

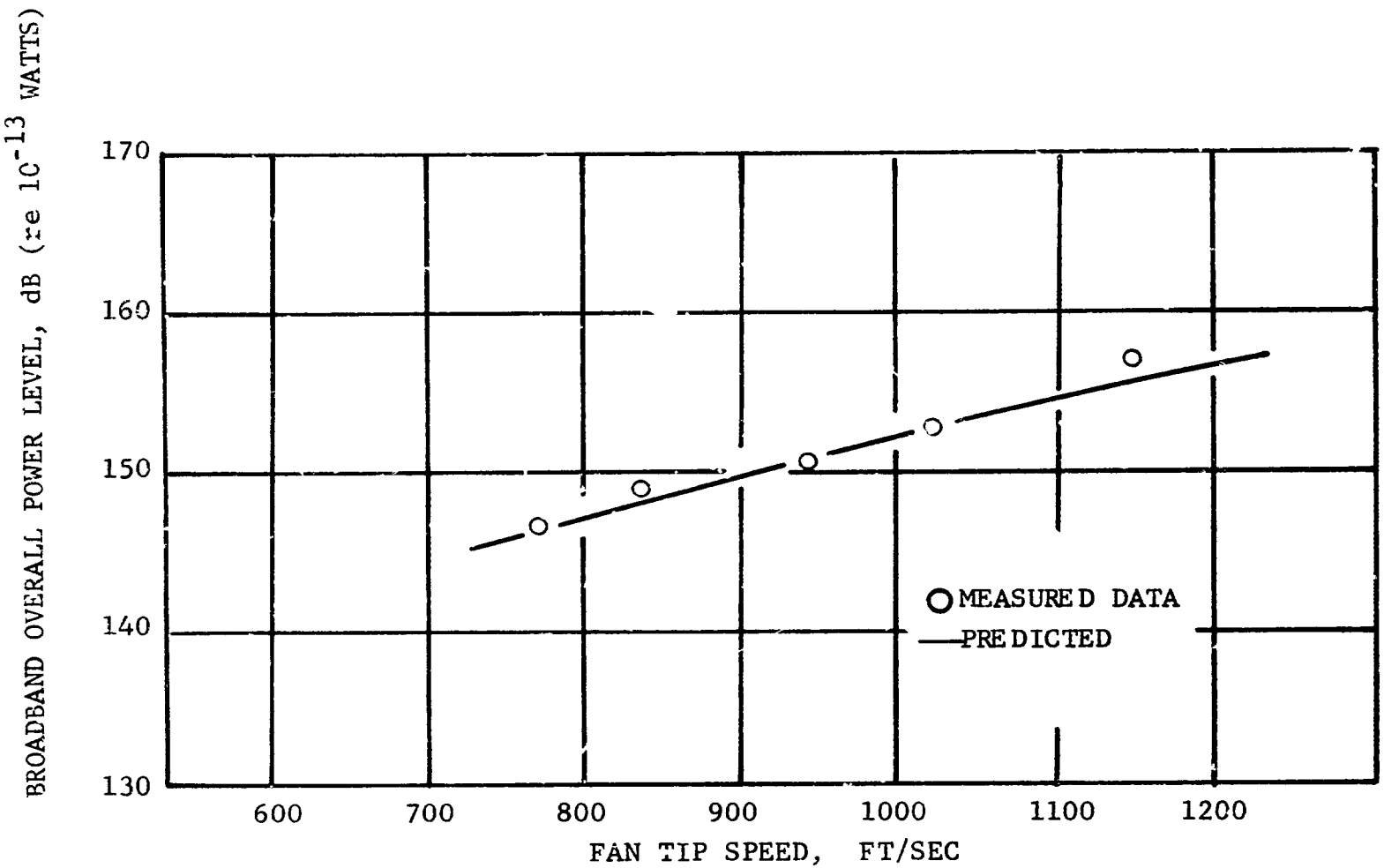

FIGURE XI-B1 BROADBAND NOISE FROM CJ805-23 FAN

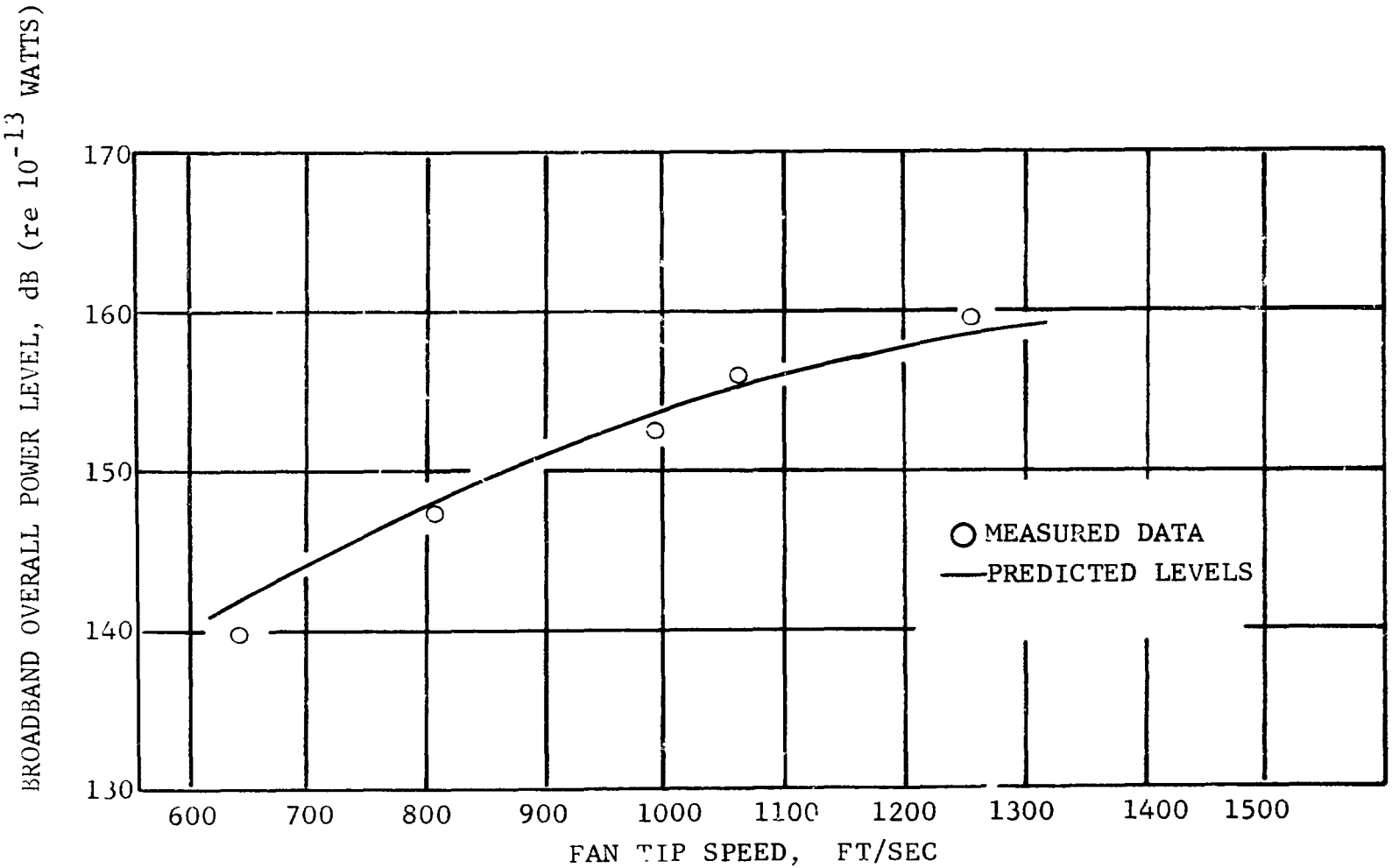

FIGURE XI-B2 TF39 D/V FAN BROADBAND NOISE

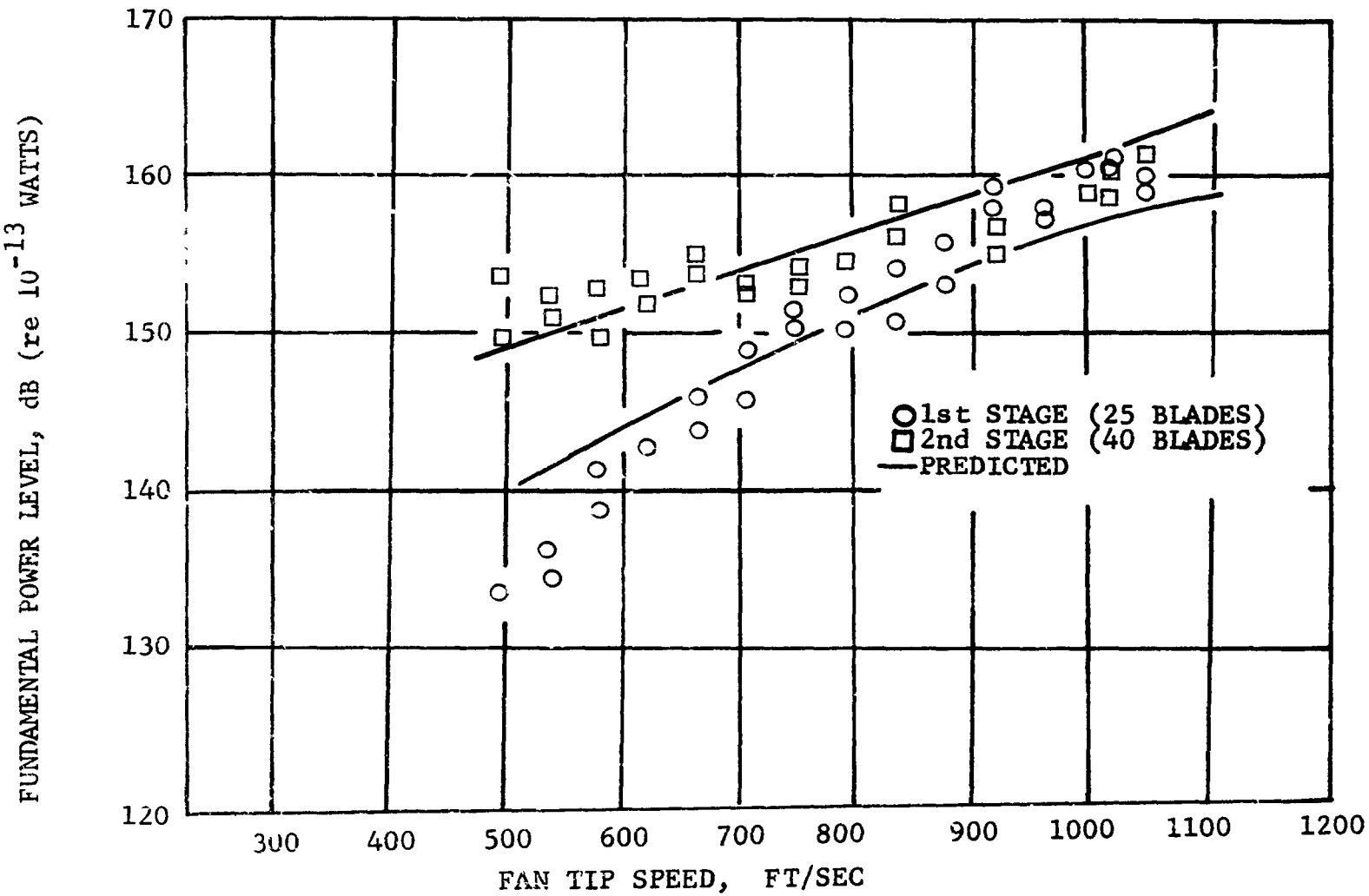

FIGURE XI-B3 FUNDAMENTAL PWLs vs. FAN TIP SPEED TWO STAGE EXPERIMENTAL FAN

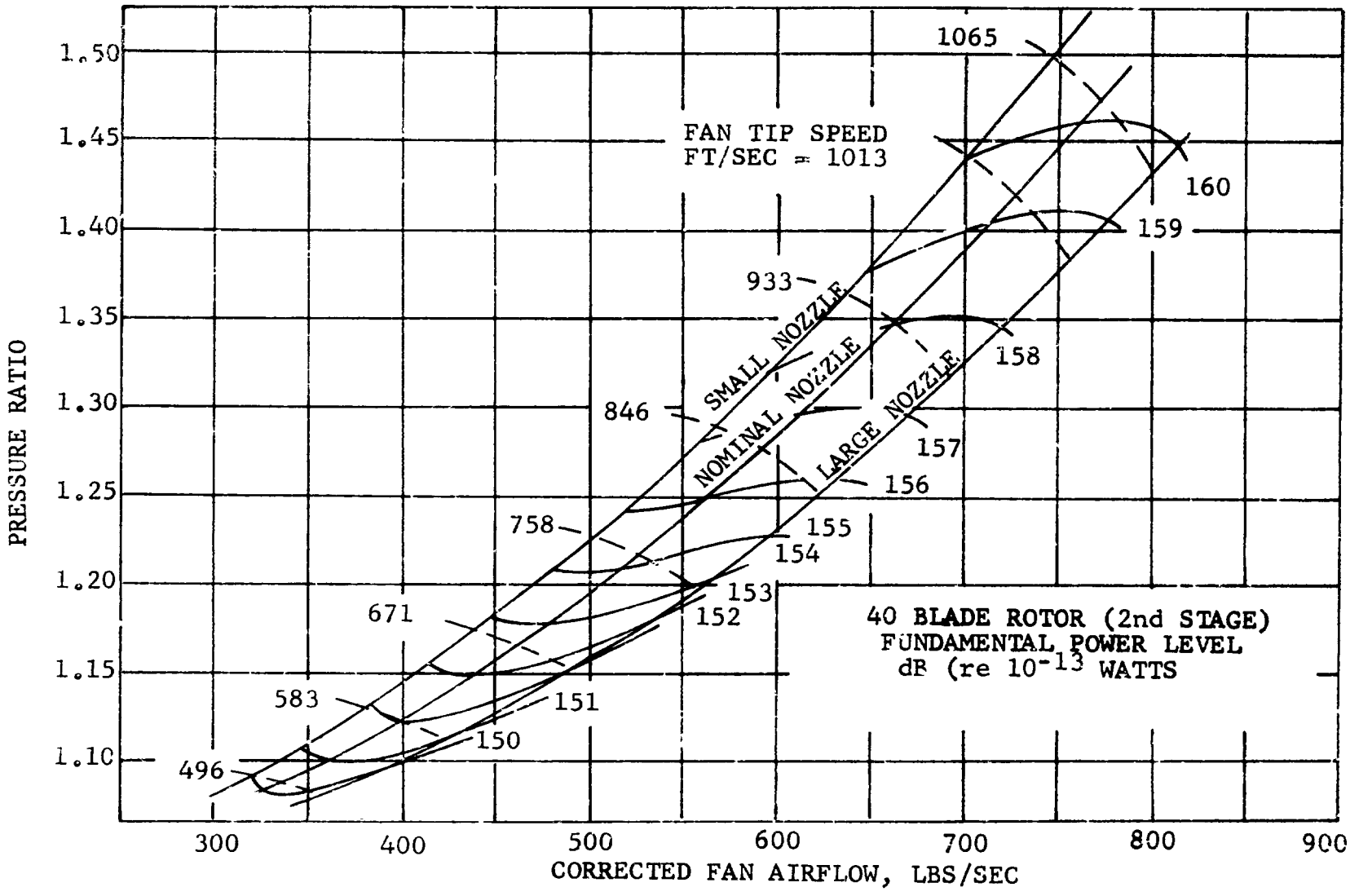

FIGURE XI-B4 ISONOISE MAP - FUNDAMENTAL PWL (SECOND STAGE)
TWO STAGE EXPERIMENTAL FAN

Rotor aerodynamic loading is a measure of the work done by the stage, and is dependent on the amount of turning done by the rotor; this is in turn dependent on rotor tip speed and pressure ratio. Ultimately, either decreasing the pressure ratio with tip speed held constant, or increasing tip speed with pressure ratio held constant, translates into a decrease in rotor loading. It is thus apparent, from Figure XI-B4, that the pure tone noise levels vary in direct proportion to the rotor loading.

From this data, one can see that a lightly loaded fan could, in fact, be as quiet or quieter than a more heavily loaded fan which ran at a lower tip speed.

Blade loading, rather than tip speed alone, is, therefore, seen to be a controlling parameter in fan pure tone noise generation. The prediction procedure was applied to this same second stage rotor, in Section VIII, (Figure VIII-A23). As was indicated therein, the predictions achieved were quite accurate.

(3) Vane-Blade Number Ratio. The testing reported in Section IV is of course the prime example for confirmation of the predicted effects of varying vane-blade ratio. As was pointed out in this section, the actual increases in pure tone noise level obtained with the reduced vane-blade ratio are very close to the predicted increases.

(4) Blade-Vane Spacing. Figure (XI-B5) presents the results of IGV spacing tests run on the TF39 Development Vehicle. The normal IGV-rotor spacing (40 blade rotor) is 0.25 IGV chords; this spacing was increased to 2 chords. The predicted decrease in noise is accurately reflected by the measured data.

Additional data on rotor-stator spacing variations has been shown in Section VIII, indicating that the procedures in Section II for pure tone noise generation are valid well beyond the 2 chord range. In fact, Figure VIII-A24 indicates that the prediction is accurate even when spacing is increased by a factor of almost 20:1 to a spacing in excess of 6 IGV chords.

Rotor-OGV spacing tests were conducted on an IGV-less single stage fan vehicle. Two OGV spacings were employed: 0.15 chord, and 2 chords. Figure XI-B6 compares the measured and predicted fundamental blade-passing sound power levels (at 100% design speed) for each spacing configuration. An appreciable reduction in fundamental PWL is seen to be achieved with increased OGV spacing; the predicted reduction is very close to that actually obtained.

(5) Swept Rotor. In principle,the swept rotor, just as the swept stator, provides a reduction in wake interaction noise by increasing the vane-blade spacing at the tip. The hub spacings are unchanged, but the great majority of the noise generation occurs at the blade tips. A test was conducted to compare swept and non-swept rotors. The two configurations employed are shown schematically in Figure XI-B7, which compares the blade-vane spacings (as a percentage of upstream blade chord) and blade numbers.

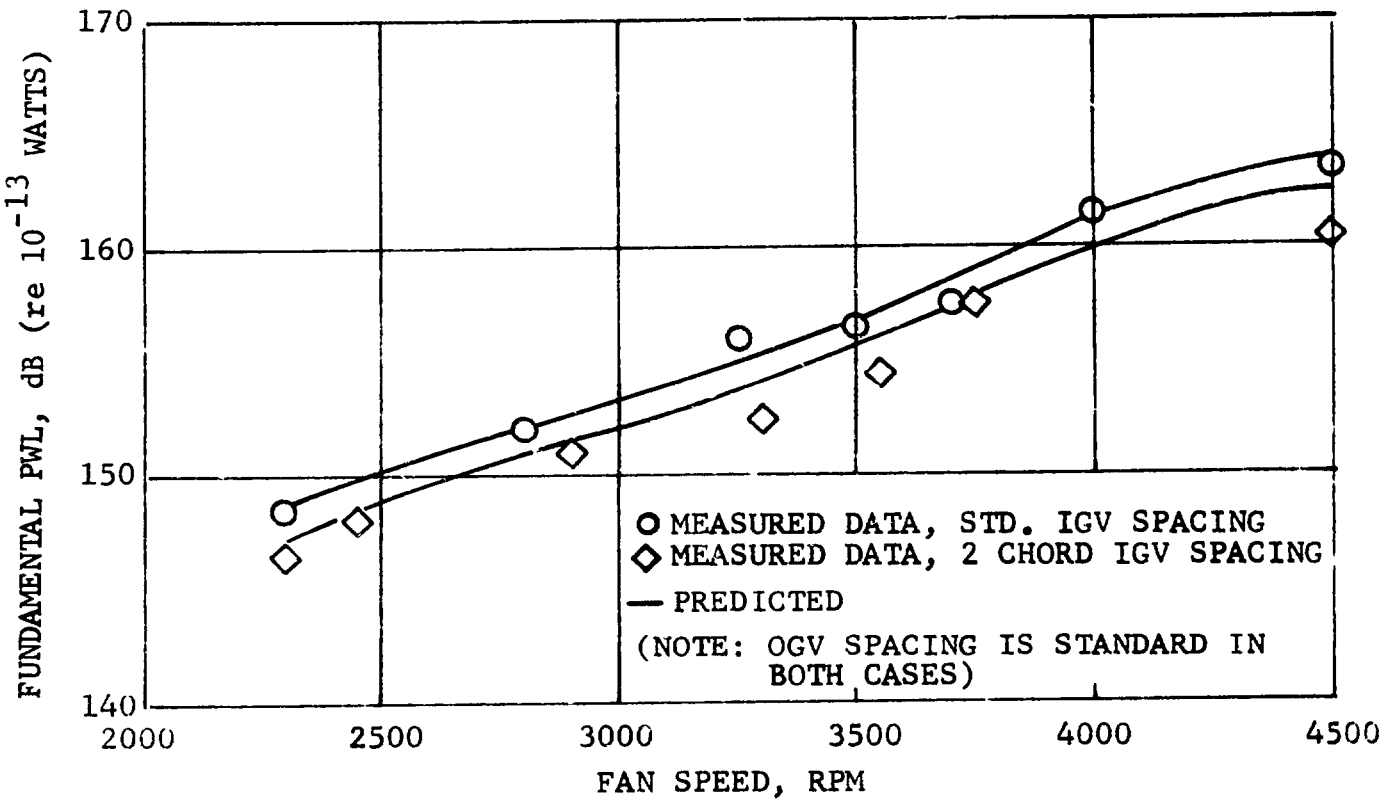

FIGURE XI-B5 EFFECT OF VARIATION OF IGV-ROTOR SPACING ON FUNDAMENTAL PWL - TF 39 D/V

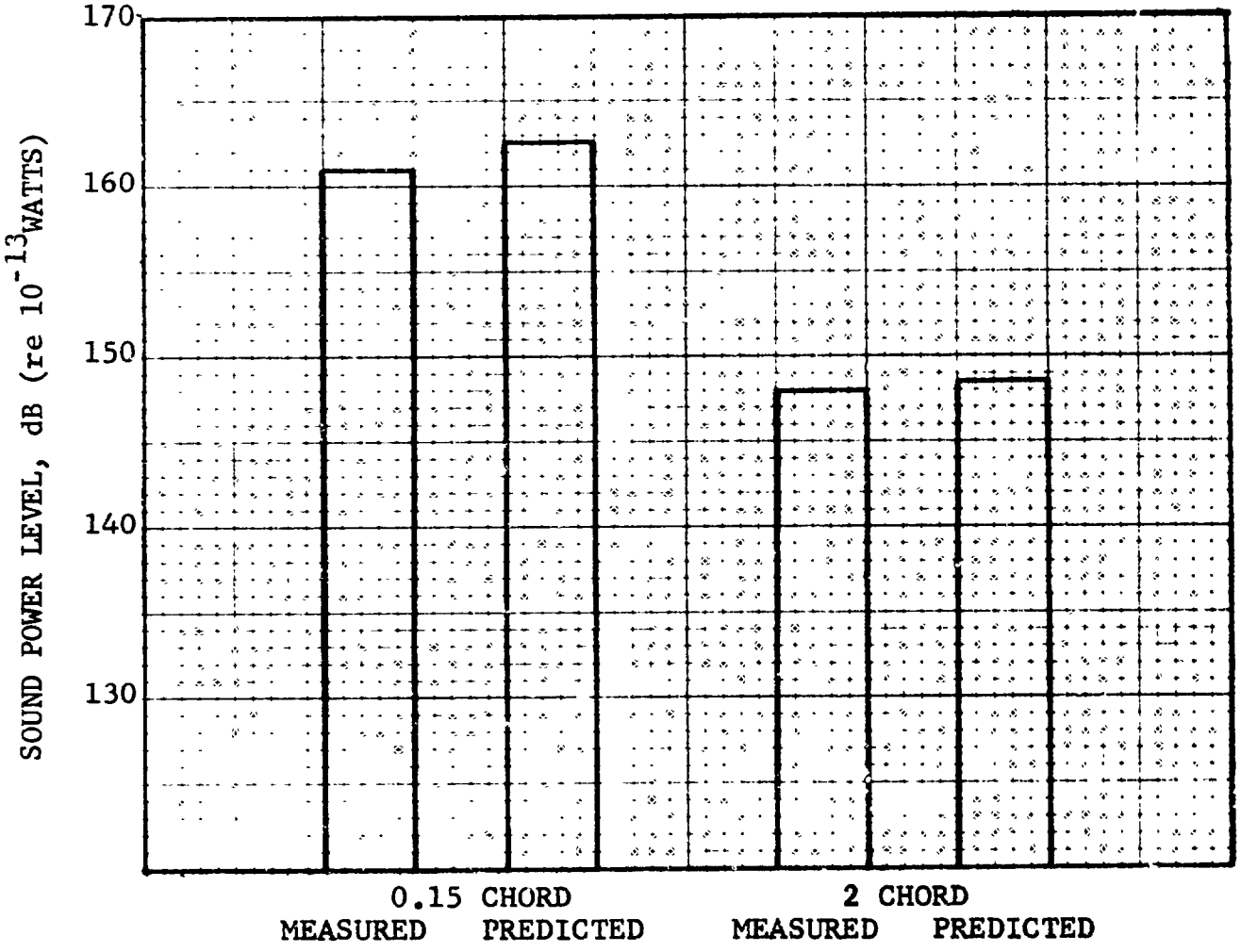

FIGURE XI-B6. VARIATION OF FUNDAMENTAL PWL WITH OGV SPACING (100% DESIGN SPEED)

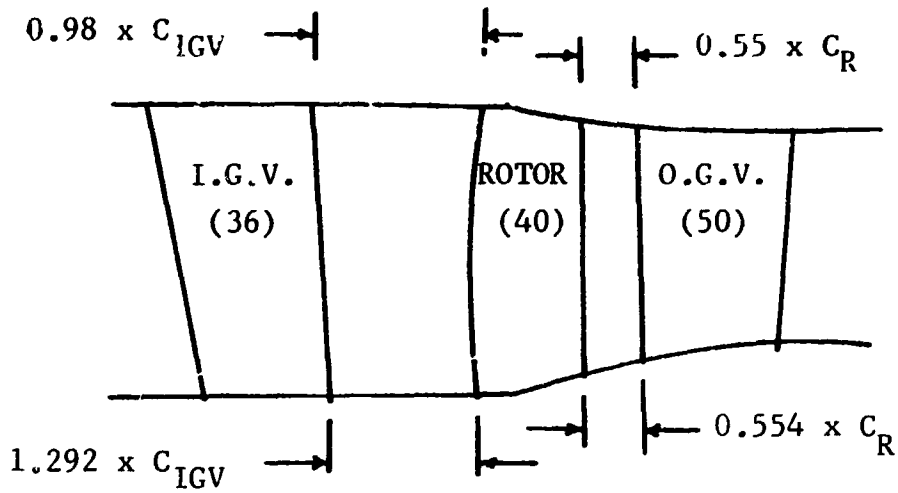

NON-SWEPT ROTOR CONFIGURATION

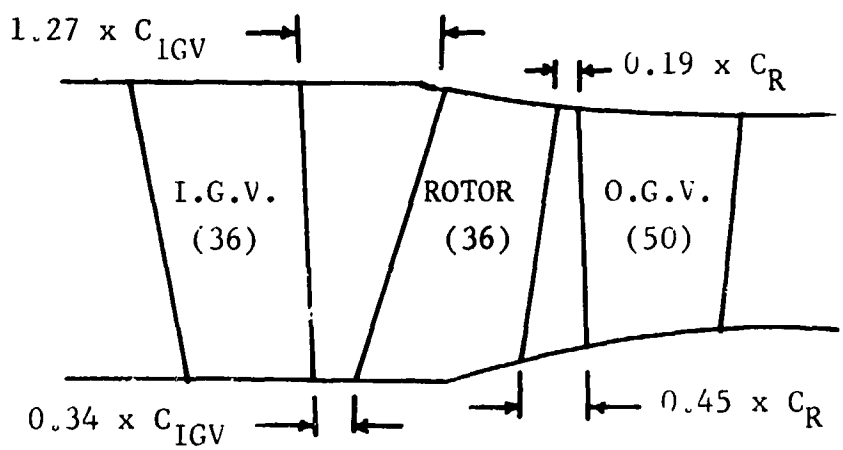

SWEPT ROTOR CONFIGURATION

(NOTE: C = TRUE CHORD OF UPSTREAM BLADE SECTION.)

FIGURE XI-B7 SWEPT ROTOR TESTS - COMPARISON OF CONFIGURATIONS

In this particular test, two salient factors would lead to the conclusion that the pure tone noise levels should be higher for the swept rotor. Obvious, from Figure XI-B7 is the fact that the swept rotor has closer blade-vane spacings than the non-swept rotor, except for the tip IGV-rotor spacing. Secondary, the vane-blade number ratio of 1:1 for the IGV-rotor combination on the swept rotor fan is worse from a noise standpoint than the 36:40 ratio present in the standard configuration.

Figure XI-B8 compares the blade-passing fundamental power levels recorded for the two vehicles, along with the associated predictions. The swept rotor fundamental levels are, as predicted, higher.

(6) Wake Control. In order to provide experimental verification of the theoretical noise reduction obtainable with wake control, the following tests were initiated:

A fifteen inch diameter single stage laboratory compressor was modified for use in the tests; a schematic of the vehicle is presented in Figure XI-B9. The compressor consists of a 32-blade rotor, driven by an electric motor; no OGV's are employed, and the IGV's are simulated by a set of 3/8 inch diameter rods, spaced 1.25 inches upstream of the rotor. For this test, eight hollow rods, each with ten 1/8 inch diameter holes evenly spaced along the span, were placed in the compressor. The rods were connected to a common air supply manifold, allowing pressurized air to be injected from the downstream side of the rods, into the wakes. An indexing system was employed with the rods, allowing variation of the angle between the compressor longitudinal axis and the direction of wake injection.

An acoustic probe, placed at the plane of the IGV rods, at mid-span height, and centered between two rods, was used to obtain sound data. The raw data was recorded on magnetic tape for reduction at a later time.

Comparative measurements were thus made between configurations with and without IGV rods, and with various rates of wake injection flow, at various injection angles. Compressor speed was kept constant (2635 RPM) throughout the tests.

Calculations of wake strength from the rods showed that the optimum total wake-injection flow rate (distributed through all rods) for this particular speed was 4.0% of the total compressor weightflow (4.42 lbs/sec, corrected, at 2635 RPM). This 4.0% flow rate should yield the maximum possible "filling" of the rod wake velocity decrements, and hence provide the maximum reduction in the wake interaction noise. Preliminary acoustic measurements, however, indicated that maximum noise reduction was actually achieved with a wake injection flow rate of only 2.9%. In order to investigate this phenomena, a total pressure probe was used to traverse the rod wakes for each of the two flow rates (at 0° injection angle) as well as for zero injection flow. The changes in the total pressure drop (ΔP_T) downstream of the rod would then provide a comparison of the effectiveness of each wake filling rate.

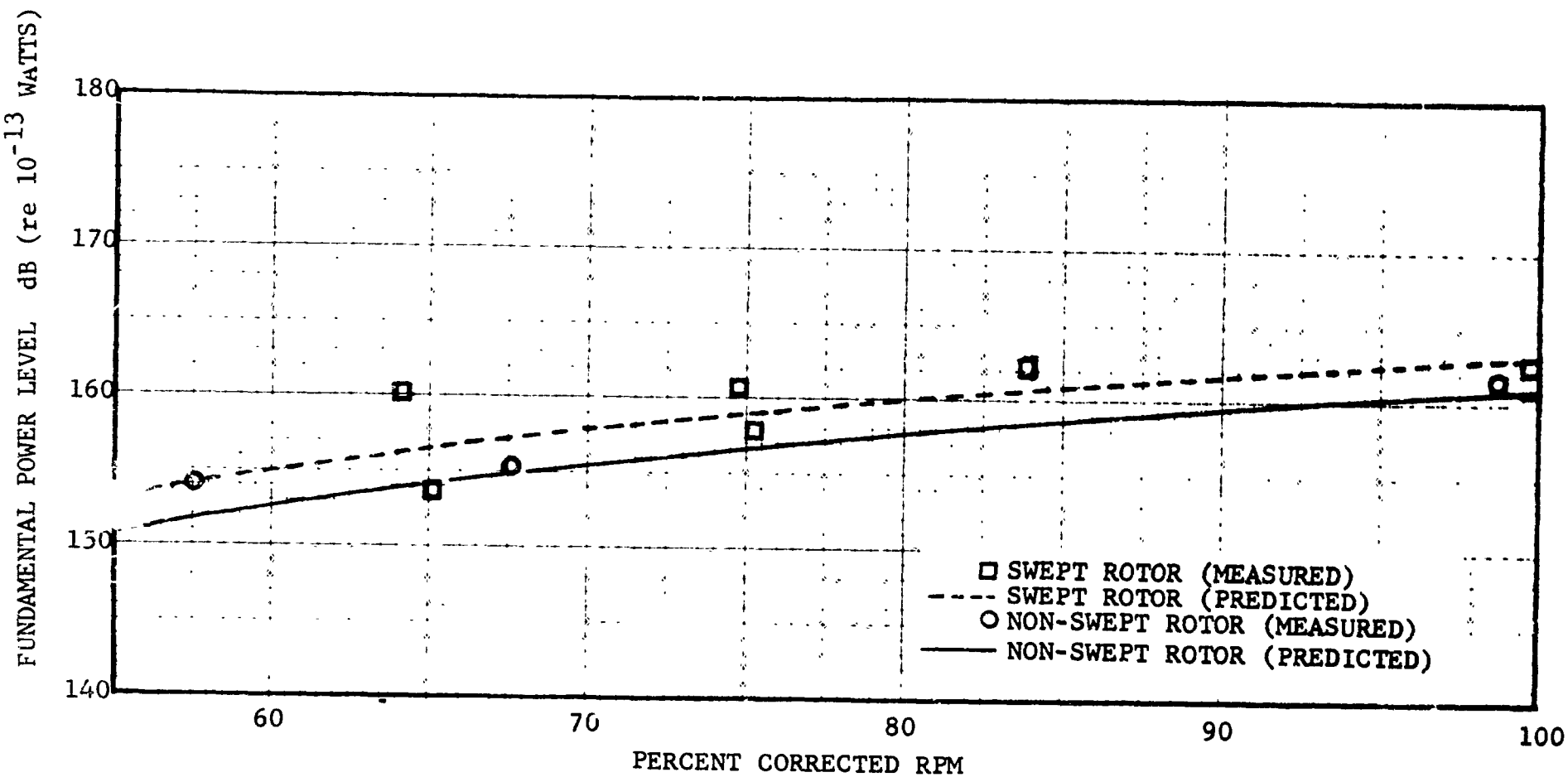

FIGURE X1-B8 FUNDAMENTAL PWL vs. PERCENT SPEED: SWEPT ROTOR vs. NON-SWEPT ROTOR

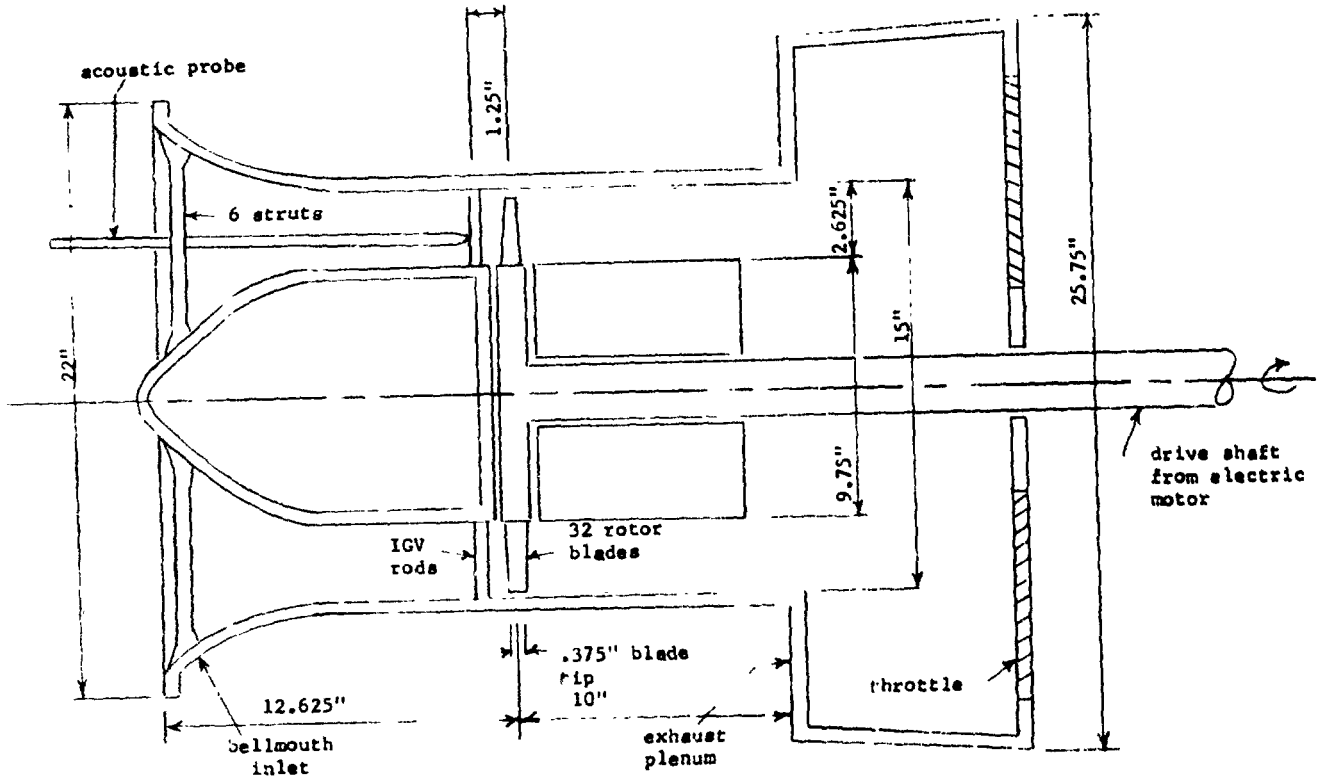

FIGURE XI-B9 15 - INCH LABORATORY COMPRESSOR WAKE INJECTION TESTS

Figures XI-B10 through XI-B13 are typical comparative plots of the ΔP_T's transversely across the wake (referenced to the freestream values of PT), measured approximately 1 inch downstream of the rods, for 0, 2.9% , and 4.0% wake injection flow rates. Each plot is at a different immersion depth (across the total annulus height of 2.63 inches). Examination of the plots indicates that for certain immersions (Figures XI-B10 and XIB-12) the 4.0% flow rate did result in smaller pressure drops than the 2.9% rate. At other immersions, however, (notably Figures XI-B11 and XI-B13)the larger flow rate "overfilled" the wake, actually increasing the total pressure to a point higher than the freestream value. With the 4.0% rate, therefore, the absolute change in total pressure experienced by a blade passing behind the rod is at certain immersions, as great or greater than that for the unfilled wake. The total effect across the blade span is to negate the potentially better performance of the 4.0% flow rate.

Figures XI-B14 through XI-B18 are comparisons of the probe sound pressure levels recorded for various configurations. These are presented in the form of 50 Hz narrowband frequency sound pressure level (SPL) spectra.

Figure XI-B14 compares the SPL's from the compressor without IGV rods, to those from the compressor with 8 IGV rods in place (no wake injection). Addition of the rods is seen to cause an increase in broadband noise levels; however, the most dramatic effect of the rods is the increase in pure tone levels, particularly for the second harmonic of the blade-passing frequency. Indeed, the SPL spectrum measured for the compressor with IGV rods in place is dominated by this strong second harmonic tone.

Figure XI-B15 compares the noise spectra recorded for the wake injection process (2.9% flow rate) operating alone (without compressor operation) to that recorded for the compressor running with IGV rods and no wake injection. Figure XI-B16 is a similar comparison for the 4.0% flow rate. These comparisons indicate the maximum noise reduction possible with wake injection. The wake-injection noise for the 2.9% flow rate is 5 - 10 dB lower than the operating system (compressor + rod) noise floor, all across the frequency spectrum. However, for the 4.0% flow rate, the injection noise floor is equal in level to the compressor noise floor at frequencies above 5000 Hz; the larger injection flow rate would thus be expected to increase the compressor broadband noise.

Figure XI-B17 compares the spectrum recorded for the compressor with IGV rods and no wake injection, to that recorded for the compressor with the wake injection operating at 2.9% flow rate, 0° injection angle. Figure XI-B18 is a similar comparison for the 4.0% flow rate at 0° injection angle. (Additional runs were made, in which the injection angle was varied 15° to either side of the zero position, but the 0° angle runs are typical of the results achieved for these variations.)

Figures XI-B19 through XI-B21 summarize the reductions in pure tone SPL achieved for the fundamental and first two harmonic tones, at the various injection angles tested, for the 2.9% flow rate. The pure tone noise reductions achieved with the 4.0% flow rate exhibited the same qualitative relationships to injection angle as did those for the 2.9% rate. The magnitudes of the reductions were, however, considerably smaller.

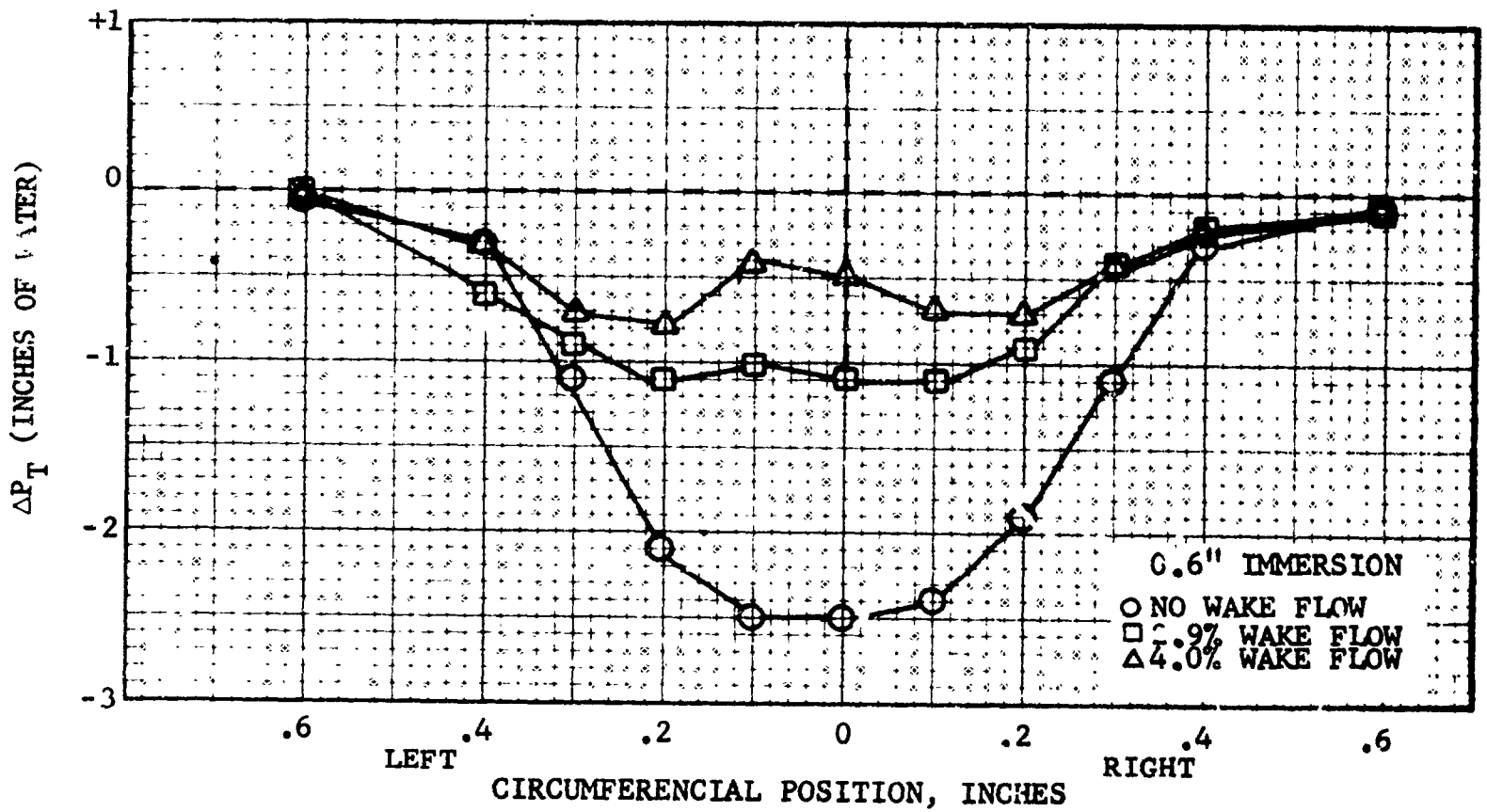

FIGURE XI-B10 WAKE TRAVERSE

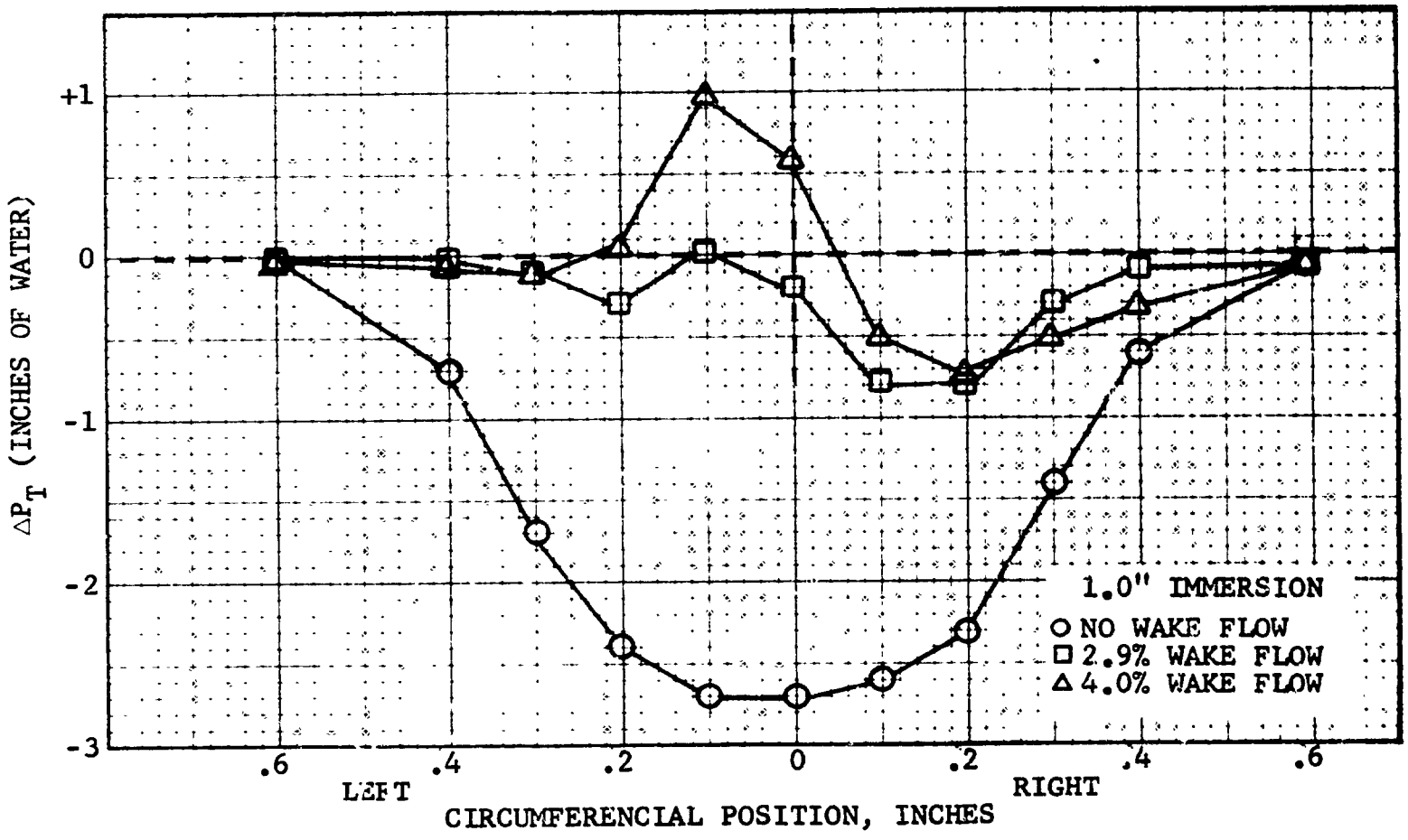

FIGURE XI-B11 WAKE TRAVERSE

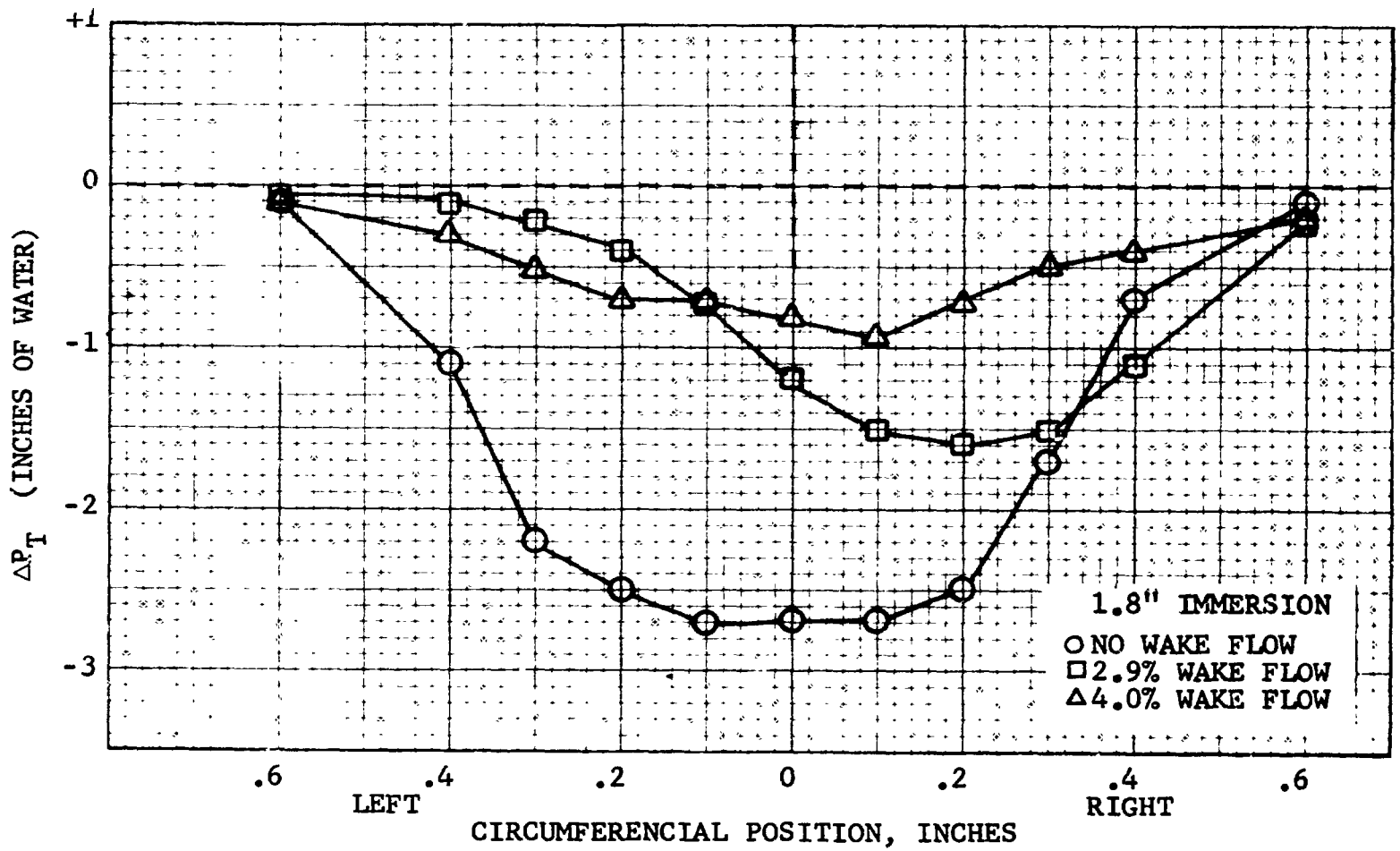

FIGURE XI-B12 WAKE TRAVERSE

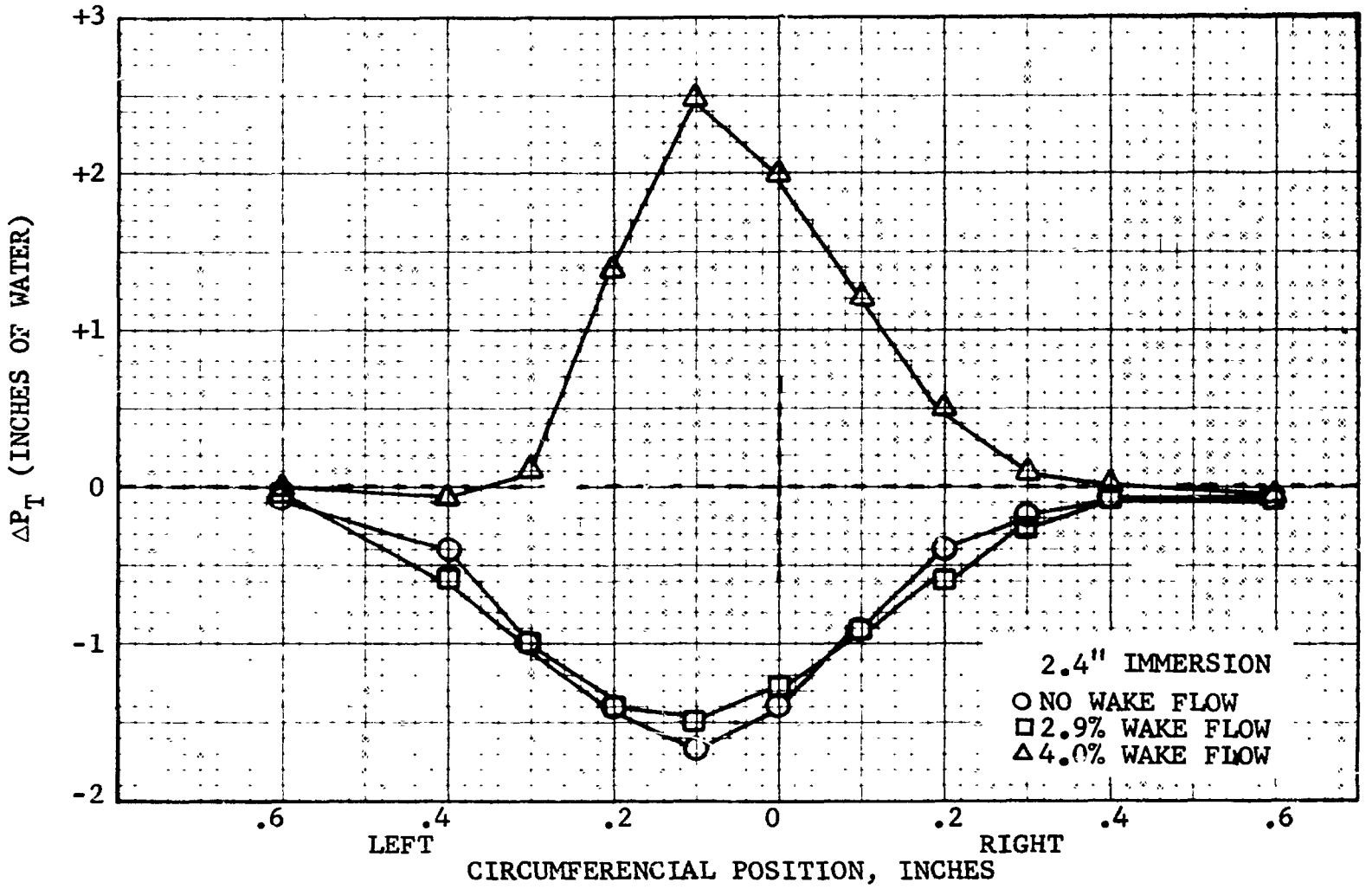

FIGURE XI-B13 WAKE TRAVERSE

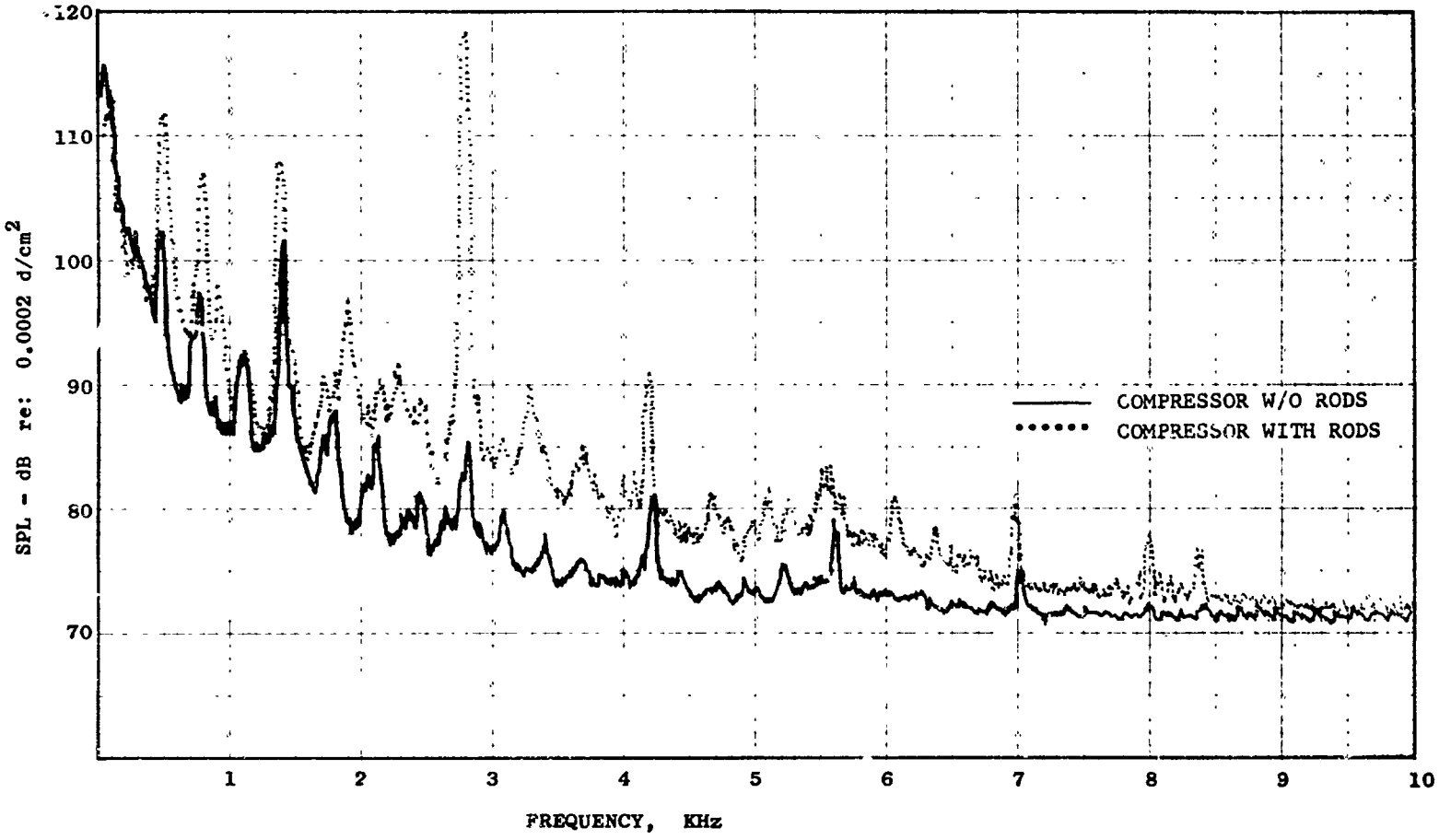

FIGURE XI-B14 50 Hz BANDWIDTH SPECTRAL COMPARISON COMPRESSOR W/O RODS vs. COMPRESSOR WITH 8 IGV RODS

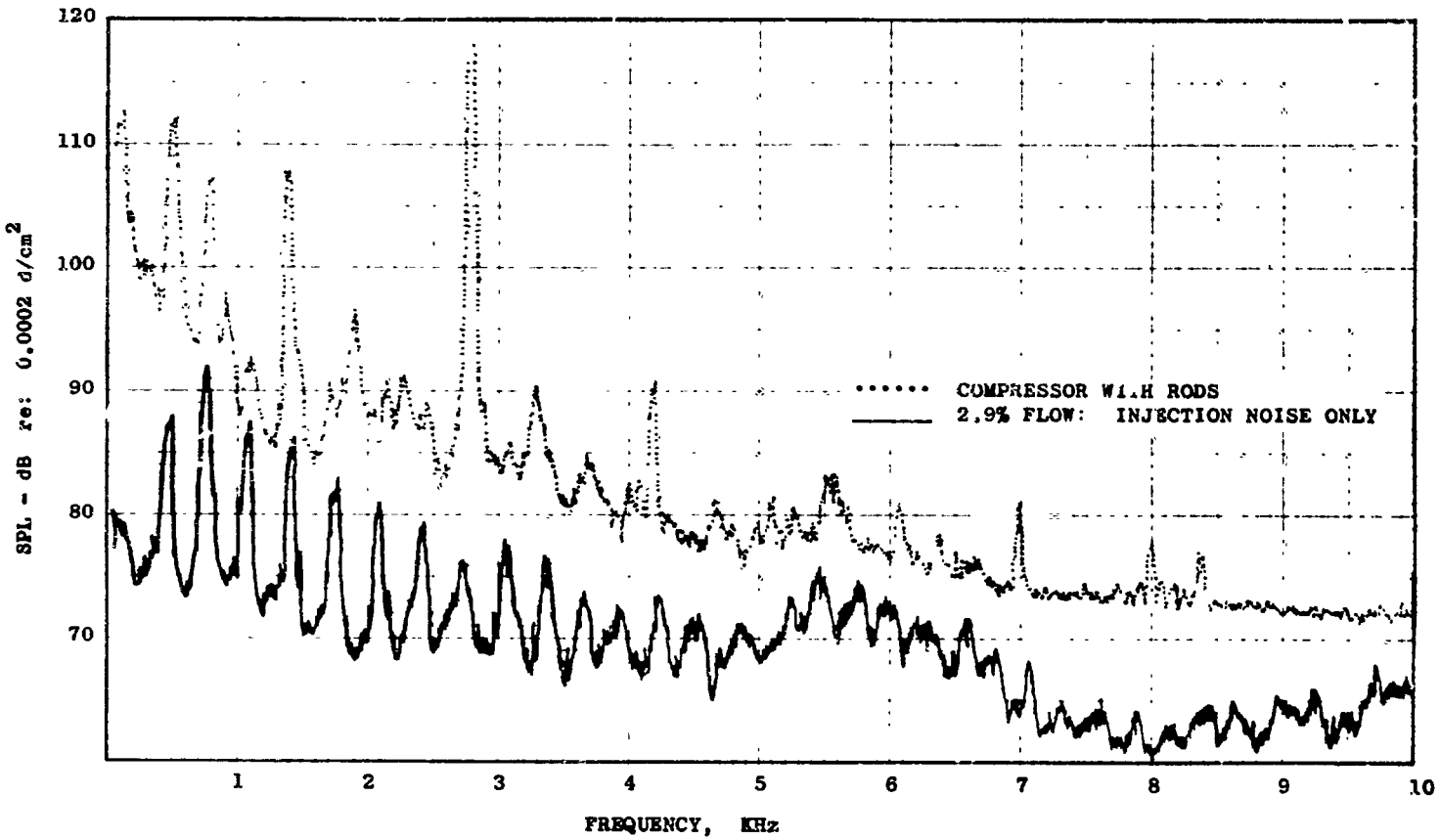

FIGURE XI-B15 50 Hz BANDWIDTH SPECTRAL COMPARISON COMPRESSOR WITH 8 IGV RODS vs. 2.9% FLOW RATE WAKE INJECTION NOISE

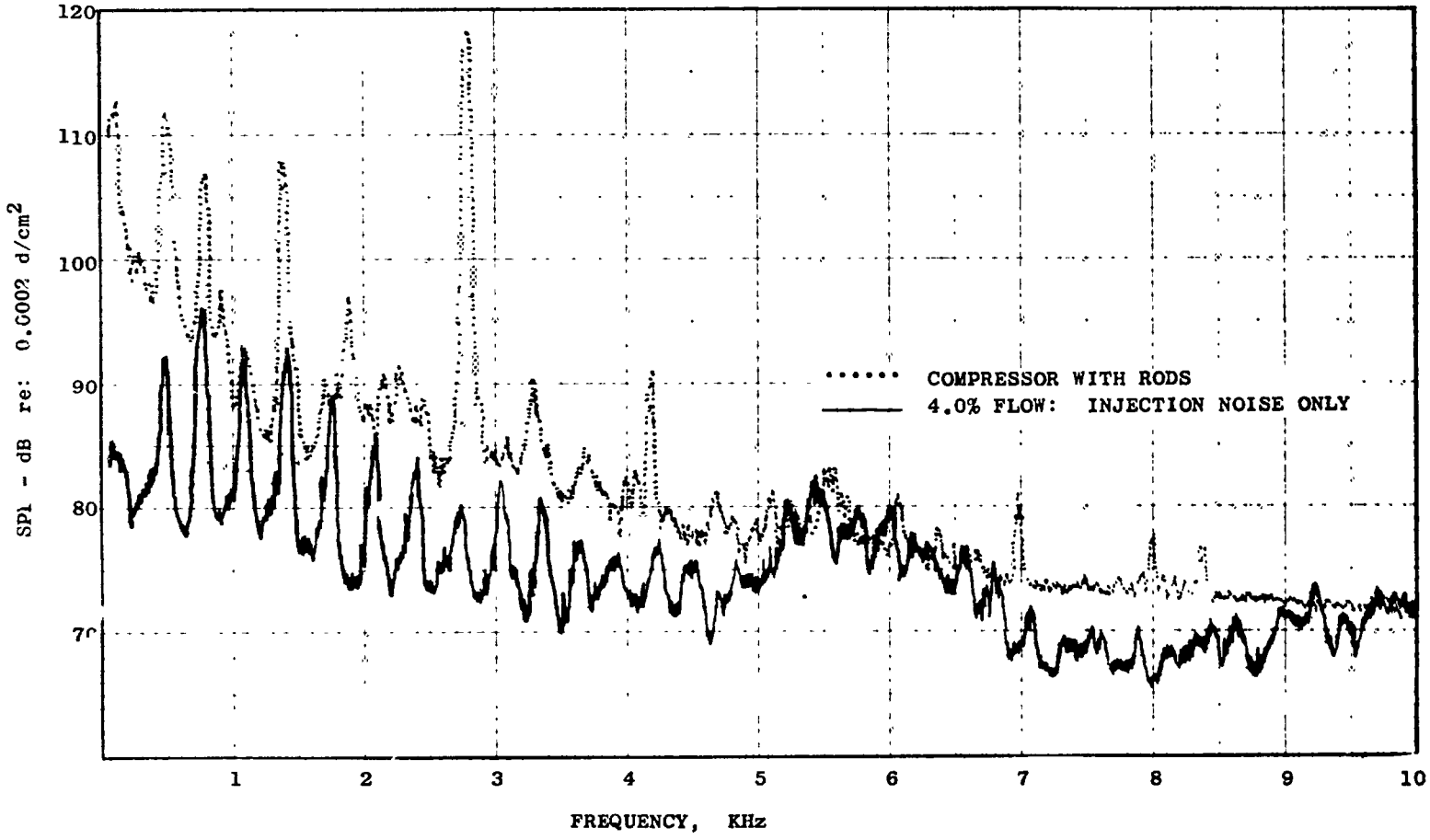

FIGURE XI-B16 50 Hz BANDWIDTH SPECTRAL COMPARISON COMPRESSOR WITH 8 IGV RODS vs. 4.0% FLOW RATE WAKE INJECTION NOISE

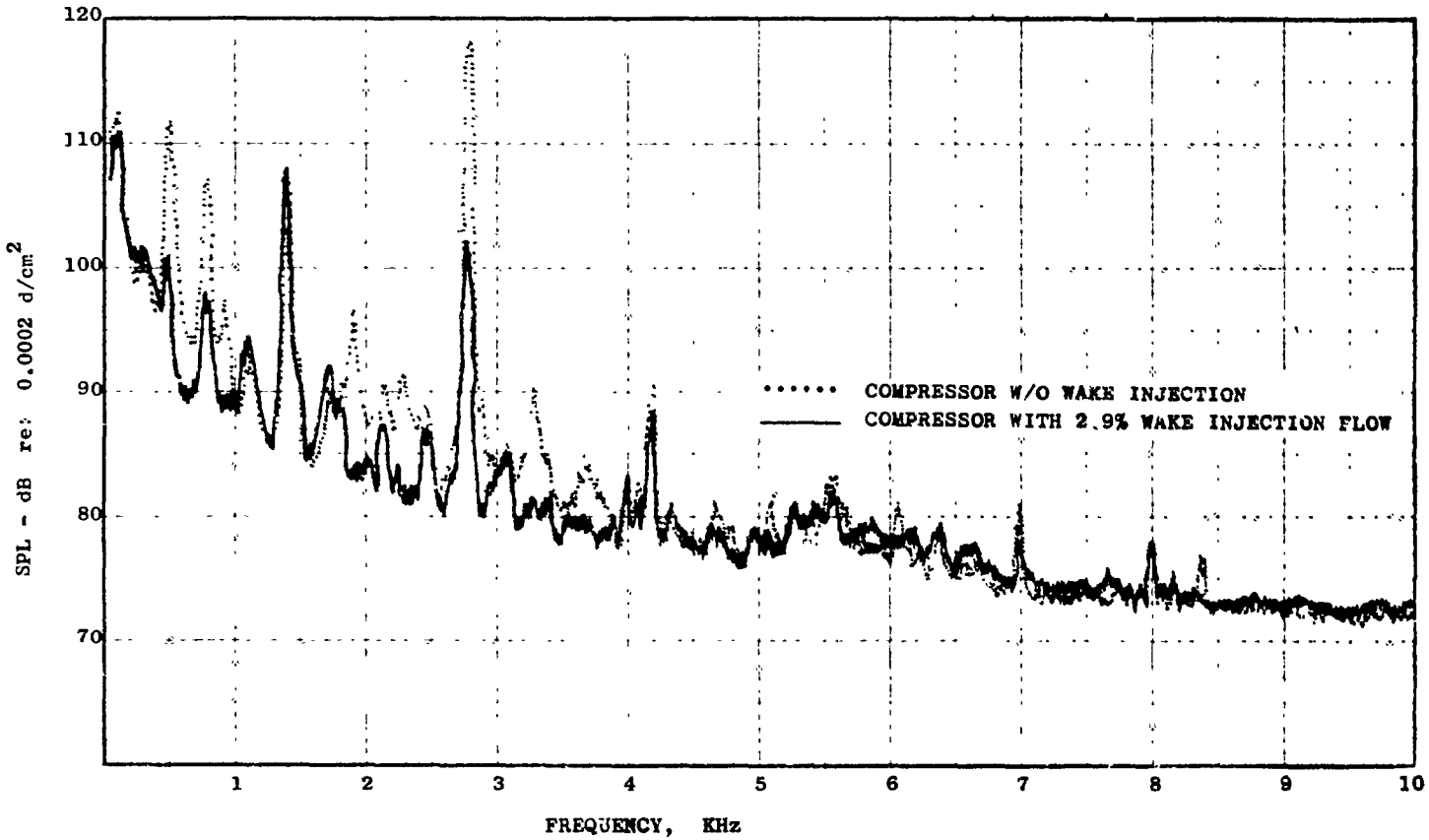

FIGURE XI-B17 50 Hz BANDWIDTH SPECTRAL COMPARISON COMPRESSOR WITH RODS AN NO WAKE INJECTION vs. COMPRESSOR WITH RODS AND 2.9% WAKE INJECTION FLOW

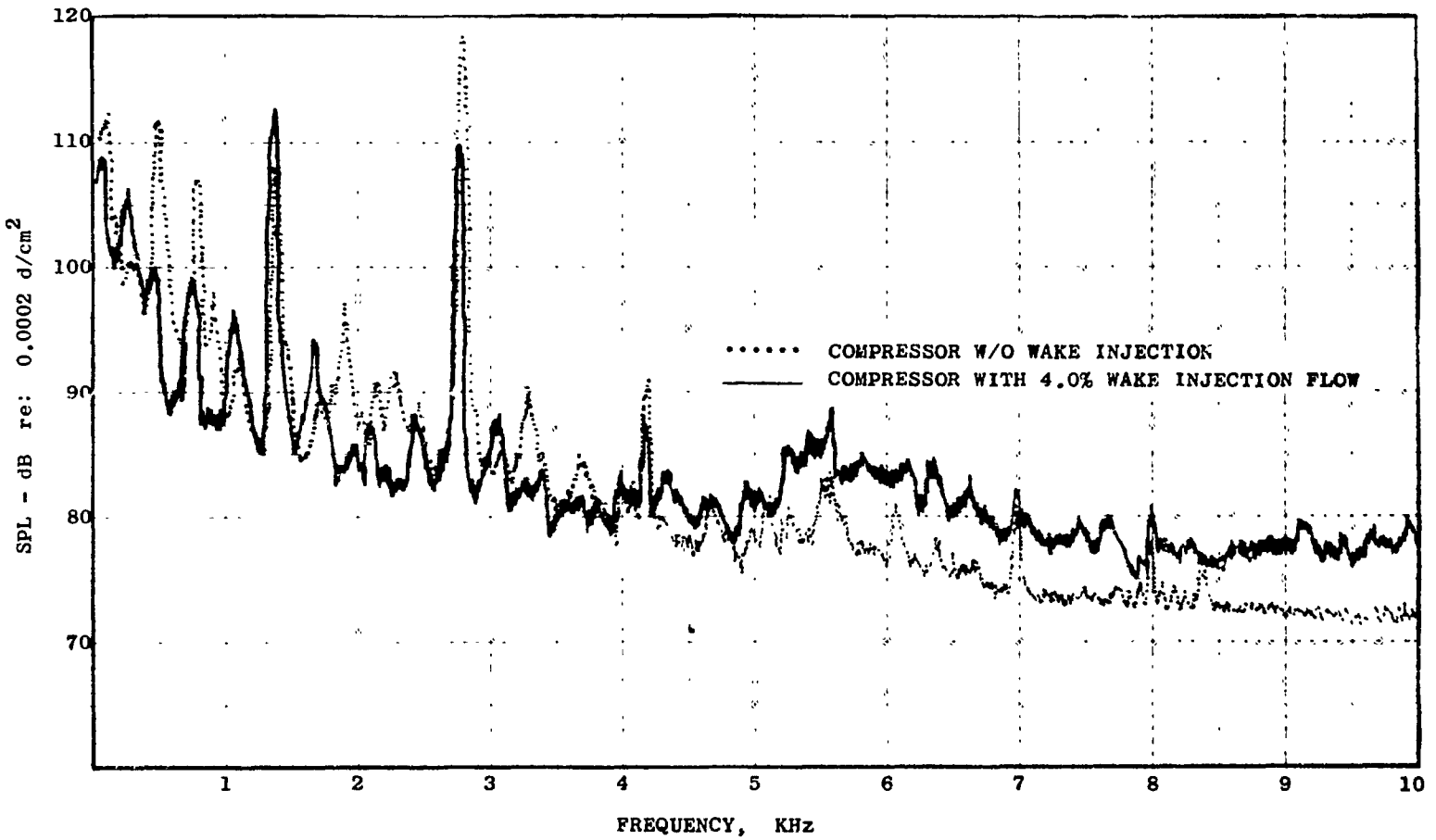

FIGURE XI-B18 50 Hz BANDWIDTH SPECTRAL COMPARISON COMPRESSOR WITH RODS AND NO WAKE INJECTION vs. COMPRESSOR WITH RODS AND 4.0% WAKE INJECTION FLOW

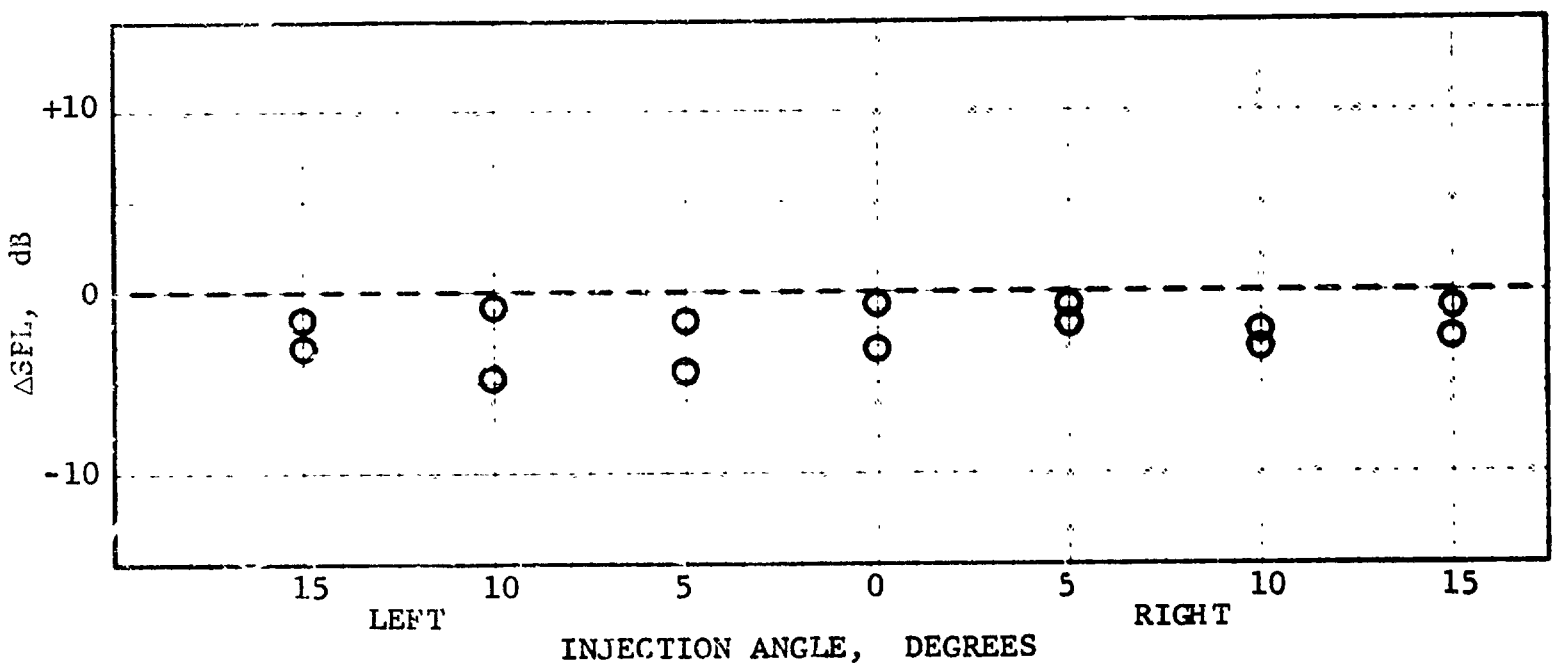

FIGURE XI-B19 PURE TONE SUPPRESSION vs. INJECTION ANGLE FUNDAMENTAL TONE 2.9% FLOW RATE

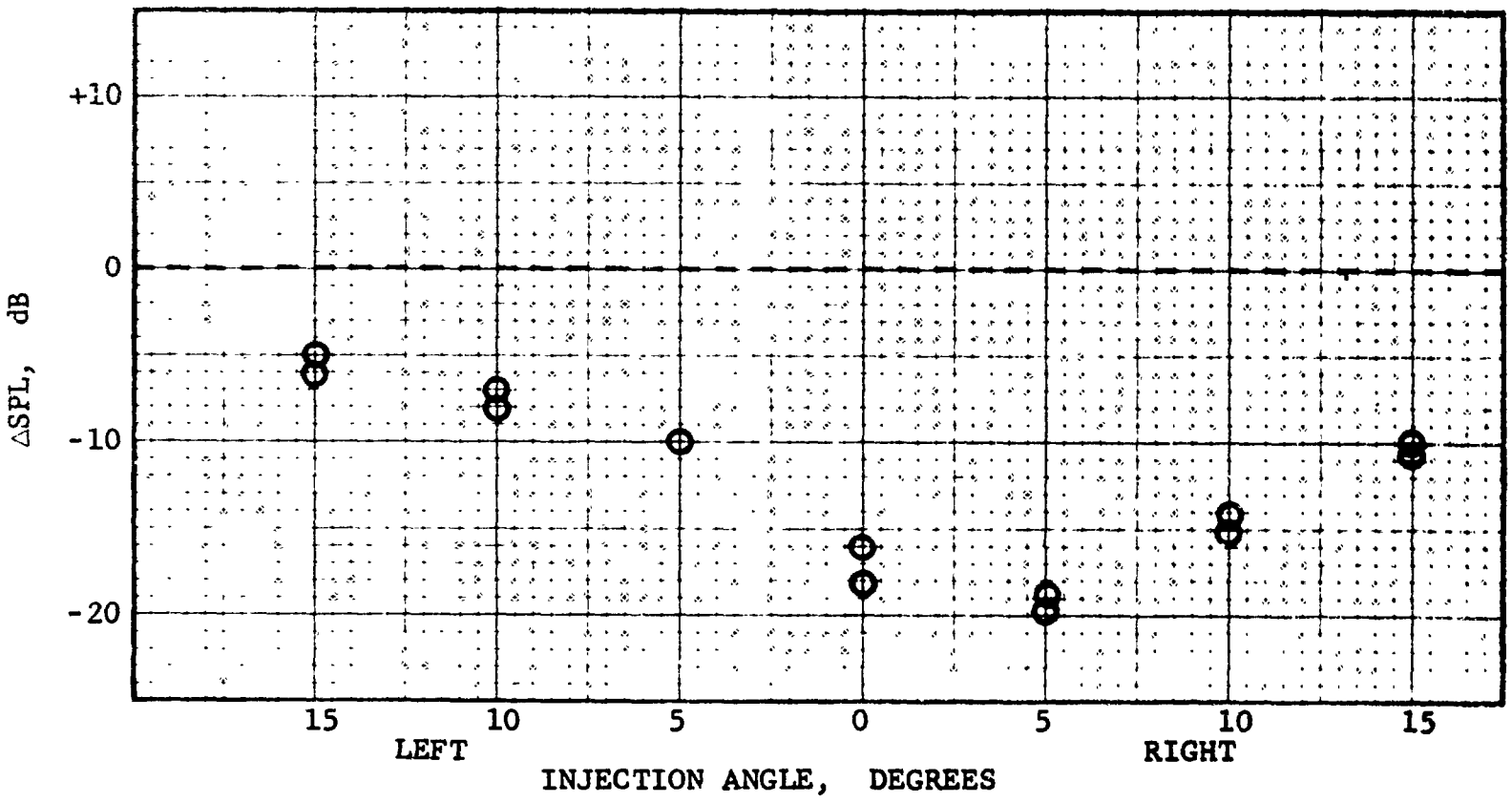

FIGURE XI-B20 PURE TONE SUPPRESSION vs. INJECTION ANGLE SECOND HARMONIC TONE 2.9% FLOW RATE

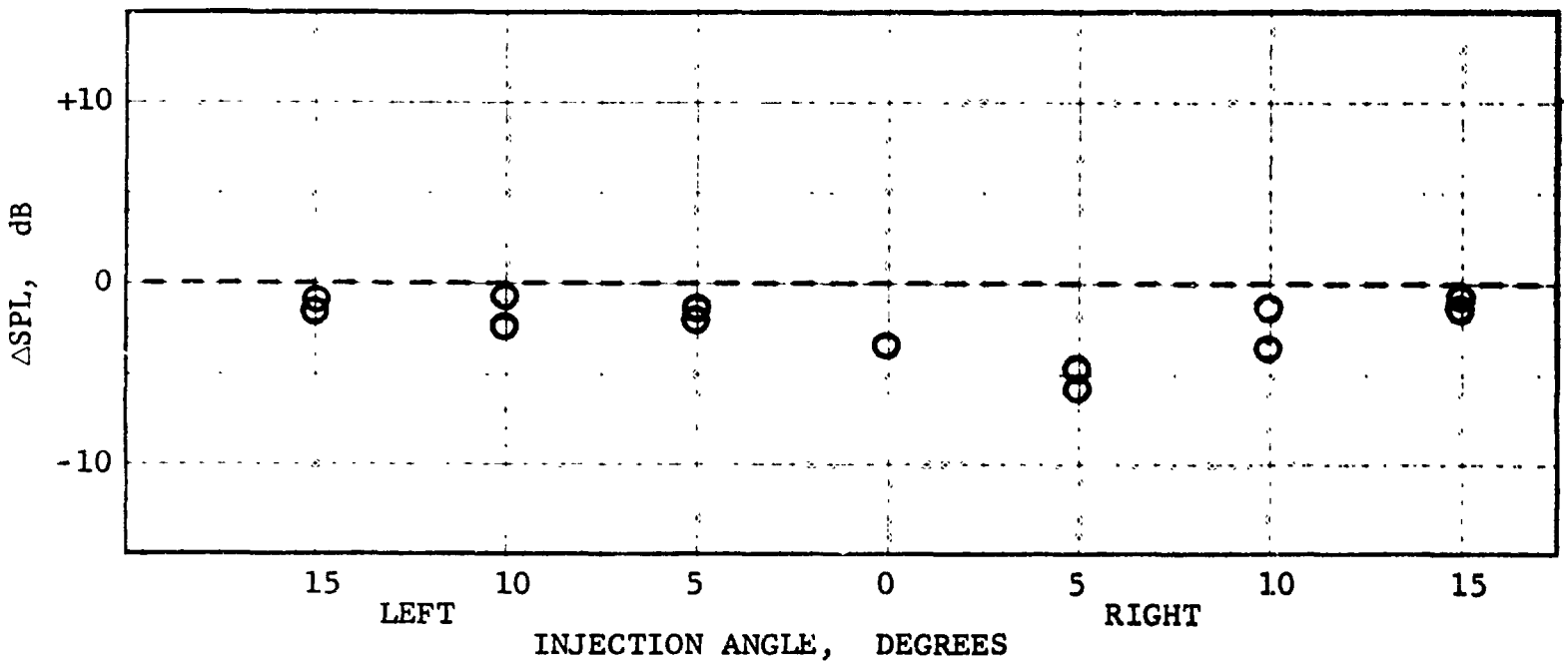

FIGURE XI-B21 PURE TONE SUPPRESSION vs. INJECTION ANGLE THIRD HARMONIC TONE 2.9% FLOW RATE

The pure tone reductions obtained by the wake injection do not seem to have been as sensitive to injection angle as might have been supposed (with the possible exception of the second harmonic levels). The "optimum" injection angle appears to be 5° to the right. However, reference to the wake PT plots (Figures XI-B10 through XI-B13 indicates that the wake injection method employed resulted in some preswirl to the left; hence it is thought that angling the rods to the right may have merely offset this effect.

The results of the wake control tests can be summarized in Figure XI-B22. It is seen that most of the pure tone wake interaction noise created by the presence of the rods has been eliminated by the "wake filling" process.

With respect to broadband noise, the presence of the inlet rods increased broadband noise levels. This increase is entirely consistent with the IGV vs. No IGV data reported in Section V. Since much of this is believed due to inlet turbulence, reduction of the rod broadband noise would not be expected to result from trailing edge wake filling.

It was shown that care must be taken in the selection of the wake injection flow in that too much flow can "overfill" the wake and can also generate excessive noise in the injection process. Such conditions have been shown to generate more noise than the no-injection case.

It is thus apparent that the concept of wake control can be applied, in practice, to obtain substantial reductions in wake interaction pure tone noise. Particular care must be taken, however, in the design of the wake injection system, to avoid localized "overfilling" of the wake.

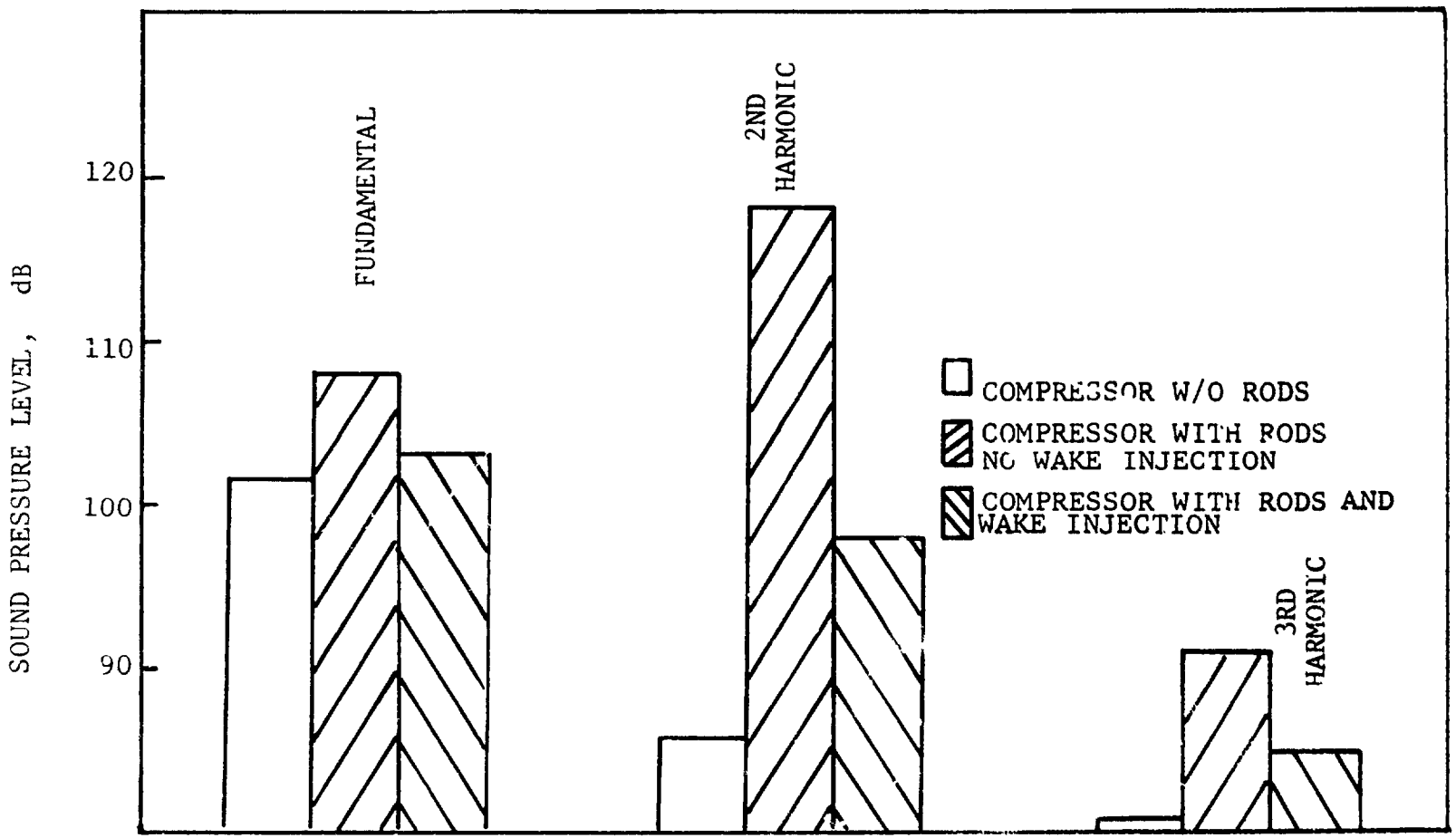

FIGURE XI-B22 MEASURED REDUCTIONS IN PURE TONE SOUND PRESSURE LEVEL WITH WAKE INJECTION

XII. SUMMARY AND CONCLUSIONS

As a result of this program, the following conclusions can be drawn:

1. A mathematical model has been derived for the generation of fan/compressor blade passing frequency tones and their higher harmonics. The model describes the different generation mechanisms (rotor alone, wake and potential blade row interaction, etc.) in terms of basic turbomachinery geometry and aerodynamics. The mathematical model enables the engine designer to study parametrically the effects on fan/compressor noise of such parameters as blade and vane numbers, tip speed, pressure ratio, blade loading, blade/vane lean and sweep, blade and vane solidities, and blade row spacing.

2. The mathematical model for pure tone generation has been checked against a number of different types and sizes of subsonic and transonic vehicles. The comparison between predicted and measured data has been shown to be extremely good.

3. A theoretical model of the overall broadband sound power generated in fans and compressors has been shown to correlate the experimental data obtained on three high speed fans extremely well.

4. A mathematical model has been derived for the broadband noise spectrum prediction. The model incorporates velocity profiles and unsteady fluctuations in airfoil wakes and permits the prediction of airfoil noise vs. frequency.

5. Detailed velocity fluctuation measurements were made in the wakes of cylinders, symmetric airfoils and typical sections of transonic airfoils. The results were very helpful in the understanding and quantitative evaluation of vortex shedding noise.

6. Experiments conducted on a research compressor indicated that trailing edge wake control can be a very effective means of significantly reducing viscous wake interaction noise.

7. A mathematical model for the sound transmission through rotating and stationary blade rows has been derived and checked against experimental data. The model permits the engine designer to parametrically study the effects of blade stagger, vane/blade ratio, and vane solitities on sound transmission.

8. It was shown that refraction effects at the terminations of turbomachinery ducts were the key phenomena controlling the sound radiation pattern. Refraction experiments were conducted and showed that sound directivities could be controlled by refraction parameters.

9. An experimental investigation of vane/blade ratio effects on fan/compressor noise has been carried out on a high speed transonic fan. The results indicate that a high vane/blade ratio reduced the blade passing frequency sound generated by about 4-5 dB at low speeds and about 1 to 2 dB at high speeds. This vane/blade ratio variation did not have any appreciable effects on broadband noise generation and on sound radiation directivity.

10. In the prediction of actual noise levels for ground or flight cases, and especially in the comparison of test data to predictions or to other test results taken under differing conditions, the factors affecting propagation of sound from the source to the receiver must be taken into account. The work done on reflection indicates that much of the experimentally observable variations in data can be correlated and systematized on an empirical basis.

11. An experimental investigation of the effects of the presence of IGV's of fan noise was conducted on a high speed transonic fan. The results indicated that IGV's if properly designed and placed far away from the rotor, will not affect the sound power generated at the blade passing frequency. They will increase the broadband noise generated at low speeds and decrease the multiple pure tones radiated at high speeds.

12. The prediction methods for fan/compressor noise derived as result of this program show good correlation across a wide range of sizes and design parameters with a number of different fans and compressors. The methods expressed have been summarized in terms of prediction flow charts which incorporate analytical relationships derived in the report and influence functions which have been put in tabular form.

XIII. RECOMMENDATIONS

At the completion of this program, the following recommendations for further research can be made:

1. A similar program on turbine noise generation, transmission and radiation should be initiated. The progress in fan/compressor noise reduction and suppression that was made in the last few years has resulted in a situation wherein turbine noise is becoming a primary source of noise in low noise high bypass-ratio engines. A similar program to the one just completed on fan/compressor noise is needed for studies of turbine noise. The effects of vane/blade ratio, vane/blade spacing, vane lean, number of blades and vanes on turbine noise will be investigated on turbines to the same degree as they have been on fans and compressors in this report.

2. The work initiated on this program on detailed aeroacoustic measurements on airfoils in cascades should be continued. The analytical developments on broadband noise reported in Section II-B indicate that a detailed knowledge of the unsteady aerodynamics of airfoils in cascades is necessary before a meaningfull broadband source noise reduction program can be implemented. A step in this direction was taken on this program but it is felt that considerable research still remains to be done in terms of measurements in two and three dimensional cascade systems.

3. Based upon the demonstrated strong influence of refraction on tone directivities, additional studies should be conducted to further investigate the effects of velocity, and temperature ratios in co-annular ducts upon refraction and tone scattering. Such experiments would enable more detailed analyses to be made of whether certain flow conditions provide more beneficial directivity patterns on engines designed for low sideline or flyover noise. These tests should cover not only the range of conditions applicable to fan tones, but also to the refraction and scattering of turbine tones.

4. It is recommended that efforts to correlate the coefficient of reflection and the phase factor for a variety of surfaces and source-observer geometries be continued, and that further studies be made into the effects of atmospheric absorption, gradients and wind on far field acoustic data.

5. One of the major barriers in further propulsion system noise reductions for CTOL and particularly V/STOL aircraft is created by the exhaust jet noise. Considerable work is needed to develop the understanding necessary to reveal the basic mechanisms of jet produced noise through the range of efflux velocities, and temperatures typical of present and future commercial aircraft propulsion systems. An analytical and experimental program based on fundamental jet noise mechanisms and leading to meaningful jet noise prediction and reduction techniques should, therefore, be initiated.

XIV. ACKNOWLEDGMENT

The authors wish to express their appreciation of Mr. Russ Motsinger for his work on refraction effects on sound directivity. They also like to thank Mr. Dodd for his efforts in organizing and coordinating the preparation of this report.